



University
of Glasgow

Bezenšek, Boštjan (2003) Elastic-plastic crack problems in the ductile-brittle transition. PhD thesis

<http://theses.gla.ac.uk/6946/>

Copyright and moral rights for this thesis are retained by the author

A copy can be downloaded for personal non-commercial research or study, without prior permission or charge

This thesis cannot be reproduced or quoted extensively from without first obtaining permission in writing from the Author

The content must not be changed in any way or sold commercially in any format or medium without the formal permission of the Author

When referring to this work, full bibliographic details including the author, title, awarding institution and date of the thesis must be given

**Elastic-plastic crack problems in
the ductile-brittle transition**

By

Boštjan Bezenšek

**A thesis submitted for the degree of
Doctor of Philosophy (Ph.D.)
to the
Department of Mechanical Engineering
Faculty of Engineering, University of Glasgow**

October 2003

© Boštjan Bezenšek 2003

SUMMARY

Structural integrity in the ductile-brittle transition has been discussed within the framework of elastic-plastic fracture mechanics. The work has addressed benefits from arguments based on constraint loss and probabilistic arguments in defect assessment schemes. Crack extension in homogeneous and fracture toughness of functionally graded materials, such as laser welds, has also been examined.

Margins in defect assessment procedures such as BS 7910 and R6/4 have been examined for cleavage and ductile tearing from complex and re-characterised defects. A range of crack profiles with re-entrant sectors developed from two co-planar surface breaking defects by fatigue has been examined experimentally and numerically. Both studies show enhanced crack driving forces in the re-entrant sector combined with a loss of crack tip constraint. Cleavage failures from complex and re-characterised defects demonstrated that the re-characterisation procedure is not conservative when cleavage occurs at small fractions of the limit load. Failures close to the limit load benefit from constraint loss which counteract the amplified crack driving forces in re-entrant sectors and cause re-characterised defects to be more detrimental than the original complex defects. Benefit may be taken from statistical size effects, which are strongly dependent on the crack geometry. Experimental fatigue and ductile tearing studies show similar development of complex cracks towards the re-characterised shape and re-characterisation procedures, such as those given in BS 7910 and R6/4, are conservative for fatigue and ductile tearing.

A procedure has been developed to quantify enhanced temperature margins due to constraint loss by comparing the self similar stress fields at a critical local fracture stress (the Ritchie-Knott-Rice approach) and through the Weibull stress. Agreement with the experimental data has been demonstrated and the temperature dependence of the material parameters has been discussed.

Following Li (1997) and Karstensen (1996) a toughness mapping techniques was discussed that allows mode I toughness to be translated into mixed-mode I+II toughness for stress controlled fracture. In support of the arguments, toughness of Mode I and mixed-mode I+II configurations was measured on a mild steel. The experimental data clearly show increased

cleavage toughness for unconstrained mode I and mixed-mode fields and the correlation with the predictions from the numerical models was demonstrated.

The work has examined fracture behaviour of single-pass laser welds under cleavage conditions in the ductile-brittle transition using deep and shallow cracks. Configurations with fatigue cracks contained in the weld metal, the HAZ and the base material were tested to failure. The highest fracture toughness was consistently recorded for cracks located in the heat affected zones and lowest for weld metal or the edge of heat affected zone. A strong correlation between the spatially distributed fracture toughness and crack propagation direction was observed. An attempt to model the experimental results with a probabilistic Weibull stress analysis has required gradation in the local toughness and yield strength to be considered.

ACKNOWLEDGEMENTS

I am sincerely grateful to my supervisor, Professor John Hancock for honouring me with an enviable research opportunity on problems of practical and academic implications. His numerous advises, words of wisdom and valuable suggestions have benefited our knowledge and produced a noteworthy contribution to the engineering community. I am excited and grateful to be entrusted projects of magnitude and responsibility. Likewise I am in dept to John for his support and assistance in dispensing my work to the scientific community and industrial partners at several conferences, often accompanied with memorable backdrops. Thank you for taking the bother of going through numerous revisions of my "a, an, the" English.

I am pleased to acknowledge our industrial partner, British Energy Generation Ltd and enlightening discussions with Dr. R.A. Ainsworth and the TAGSI group members. I was thrilled to be able to work on problems of immediate concern to the power generation industry.

Acknowledgements are due to the University of Glasgow, Faculty of Engineering for the Faculty scholarship and to the Universities UK for granting the Overseas Research Student (ORS) award that have made this work possible.

I am grateful to Prof. Zoran Ren and Prof. Jože Flašker of Faculty of Mechanical Engineering, University of Maribor, Slovenia for their continuing support and for granting leave of absence that allowed me to complete this work in Glasgow.

Sincere thanks is due to Mr. Alex Torry for his patience with putting up with my multitasking eagerness and occasionally rushed experimental work. Without his words of engineering wisdom, trustworthiness and confidence in keeping to the deadlines, all these wouldn't have been possible in the short time. To Mr. Alan Birkbeck for his words of advice and effort in keeping the fatigue machines running throughout these years.

To all the staff and students of the Materials group, who have put up with me. In particular to Julian and Anuradha for the company and entertaining chats that have made those lunches so much more exciting. To Dr. Hodgkiess for kindly assisting and making available the imaging equipment on top of his busy schedule.

To my parents for understanding and supporting my decision to complete this work in Glasgow. I am also grateful for all the financial and moral support I have received throughout the years of education.

And to everyone who have in some way or the other contributed in putting this work together over the past months.

Thank you all!

CONTENTS

Summary	i
Acknowledgements	iii
Contents	iv
Nomenclature	xi
List of Figure Captions	xvi
List of Tables	xxix
1. INTRODUCTION	1
2. INTRODUCTION TO FRACTURE MECHANICS	8
2.1. Linear Elastic Fracture Mechanics	8
2.1.1. The Griffith criterion	8
2.1.2. The elastic stress at the crack tip	10
2.1.3. Small scale yielding	12
2.1.4. Crack tip stress field under mixed-mode loading	14
2.2. Elastic - Plastic Fracture Mechanics	15
2.2.1. The crack tip opening displacement (CTOD)	15
2.2.2. The J-integral	16
2.3. Two parameter characterisation	19
2.3.1. Limitation of single parameter characterisation	19
2.3.2. Two parameter characterisation	21
2.3.3. Determination of the T-stress	23
2.3.4. The Q parameter	23
2.3.5. J-T/Q toughness locus	24
2.4. Measurement of fracture toughness	25
3. INFINITE PERIODICAL SINUSOIDAL CRACK	28
3.1. Introduction	28
3.2. Geometry	28
3.3. Numerical method	28
3.3.1. Line spring technique	29
3.3.2. Boundary conditions	29

3.4. Results	30
3.4.1. Linear elastic analysis	30
3.4.2. Elastic-plastic analysis	31
3.5. Discussion	34
3.5.1. Effect of crack front perturbation	34
3.5.2. Local force and bending moment redistribution	35
3.5.3. Stability of a perturbed crack front	36
4. WEAKEST LINK STATISTICS	37
4.1 Theoretical background	37
4.2 The Weakest link model	38
4.3 Transferability of fracture toughness data	40
4.4 Application to straight and semi-elliptical cracks	42
4.4.1 Statistical effects associated with straight cracks	42
4.4.2 Statistical effects associated with semi-elliptical cracks	43
4.4.3 Statistical effects associated with straight and semi-elliptical cracks	45
4.5 Results	46
4.5.1 Analytically computed values of χ for semi-elliptical cracks	46
4.5.2 The effect of semi-elliptical crack shape on fracture resistance	47
4.5.3 Discrete evaluation of the effective crack front length	47
4.5.4 Comparison with the experimental data	48
4.6 Discussion	48
5. THE RE-CHARACTERISATION OF COMPLEX DEFECTS	50
6. LINE SPRING ANALYSIS OF COMPLEX DEFECTS	53
6.1. Introduction	53
6.2. Numerical study of planar coalescence	53
6.2.1. Geometry	53
6.2.2. Numerical model	54
6.2.3. Results	55
6.2.3.1. Linear elastic analysis	55
6.2.3.2. Elastic-plastic analysis	56
6.3. Numerical study of non co-planar coalescence	58

6.3.1. Geometry and numerical methods	58
6.3.2. Results	59
6.4. Modified failure assessment diagrams for complex defects	60
6.4.1. Failure assessment diagrams	60
6.4.2. Modified failure assessment diagrams	61
6.4.3. Results	62
6.5. Discussion	63
7. DEVELOPMENT OF COMPLEX DEFECTS IN FATIGUE	65
7.1. Introduction	65
7.2. Test procedure	65
7.3. Results	66
7.3.1. Experimental observations	67
7.3.2. Analysis of fatigue crack growth	68
7.4. Discussion	70
7.4.1. Fatigue life and re-characterisation	70
7.4.2. Non co-planar coalescence	71
8. DUCTILE TEARING OF COMPLEX DEFECTS	75
8.1. Introduction	75
8.2. Test procedure	75
8.3. Results	76
8.3.1. Interacting defects before coalescence	76
8.3.2. Defect with a moderate re-entrant sector	77
8.3.3. Defect with a modest re-entrant sector	78
8.3.4. Bounding semi-elliptical defect	79
8.4. Discussion	79
9. BRITTLE FAILURE FROM COMPLEX DEFECTS	83
9.1. Introduction	83
9.2. Experimental details	83
9.2.1. Experimental procedure	83
9.2.2. Experimental results	84
9.3. Deterministic analysis	85

9.3.1. Deterministic procedure	85
9.3.2. Results of a deterministic analysis	86
9.4. Probabilistic analysis	87
9.5. Failure assessment diagrams	88
9.5.1. Introduction	88
9.5.2. General failure assessment diagram	88
9.5.3. Constraint modified failure assessment diagram	89
9.5.4. Failure assessment diagram with statistical size corrections	89
9.6. Failure initiation site	90
9.7. Discussion	92
9.8. Approximate amplification factors	94
9.9. Main conclusions to defect re-characterisation	95
10. MICROMECHANICAL MODELLING OF CLEAVAGE FRACTURE IN FERRITIC STEELS	97
10.1 Ritchie-Knott-Rice cleavage model	97
10.1.1 The local fracture stress	98
10.1.2 The microstructural distance	99
10.2 Statistical treatment of cleavage fracture	100
10.3 The Weibull stress model	101
10.3.1 Elastic material	102
10.3.2 Elastic-plastic material	102
10.4 Probabilistic toughness scaling model	103
10.5 Crack trajectory	104
11. THE TEMPERATURE DEPENDENCE OF MATERIAL PARAMETERS IN THE RKR MODEL	106
11.1 Introduction	106
11.2 Temperature dependent Young's modulus	106
11.3 Temperature dependent local fracture stress	107
11.4 Temperature dependent microstructural distance	107
11.5 Discussion	108

12. A PROCEDURE TO QUANTIFY ENHANCED TEMPERATURE MARGINS ASSOCIATED WITH CONSTRAINT LOSS	110
12.1 Introduction	110
12.2 Procedure	110
12.3 Numerical model	111
12.4 Self-similarity in contained yielding	112
12.5 Matching J-T/Q crack tip fields	113
12.5.1 Comparing fields at a fixed distance	113
12.5.2 Comparing fields at a local fracture stress	114
12.5.3 The Weibull stress approach	115
12.6 Results	115
13. TEMPERATURE MARGINS DUE TO CONSTRAINT LOSS FOR A533B-1 DATA	118
13.1 Summary of experimental data	118
13.2 Determination of the local fracture stress	118
13.3 Enhanced toughness margins from constraint loss	119
13.4 Enhanced temperature margins due to constraint loss	120
13.5 The effect of simulated neutron irradiation on the temperature shift	121
13.5.1 Stress-strain curves for the irradiated material	122
13.5.2 Constraint effects for the irradiated material	122
13.5.3 Temperature shift for a simulated irradiated material	123
13.6 Main conclusions to temperature shift due to constraint loss	123
14. MODE I AND MIXED-MODE CRACK TIP FIELDS UNIFIED BY CONSTRAINT	125
14.1 Mixed-mode fields	125
14.1.1 Slip-line fields	125
14.1.2 Strain hardening solutions	127
14.2 Fracture criteria	128
14.3 Experimental details	128
14.4 Experimental results	130
14.5 Conclusions	131

15. FRACTURE MECHANICS OF LASER WELDED JOINTS	132
15.1 Introduction	132
15.2 Numerical examination of crack tip fields in mismatched joints	133
15.3 Laser beam welding	134
15.4 Fracture mechanics of laser welds	135
15.5 Limit load solutions for overmatched welds	137
15.6 Procedures for structural assessment of mismatched joints	138
15.7 Estimation of J-integral from experimental quantities	139
15.8 Fracture toughness of laser welded joints	140
16. WEAKEST LINK ANALYSIS OF A BI-MATERIAL JOINT	143
16.1 Introduction	143
16.2 Procedure	143
16.3 Crack propagation direction	145
16.4 Numerical method	146
16.5 Results and discussion	146
17. EXPERIMENTAL EXAMINATION OF THE INTEGRITY OF LASER WELDED JOINTS	148
17.1 Experimental details	148
17.2 Results of cleavage tests in contained yielding	149
17.2.1 Fracture toughness	149
17.2.2 Crack paths	150
17.3 Results of cleavage tests in ductile-brittle transition	151
17.3.1 Deep cracks	152
17.3.2 Shallow cracks	153
17.4 Ductile tearing of laser welded joints	154
17.5 Charpy V-notched tests	154
17.5.1 Impact tests	154
17.5.2 Slow bend Charpy tests	155
17.6 Discussion	155

18. FRACTURE ASSESSMENT OF LASER WELDED JOINTS	157
18.1 Numerical model	157
18.2 Assessment using failure assessment diagrams	158
18.3 Crack initiation direction using maximum hoop stress criteria	159
18.4 Crack initiation direction based on local stress triaxiality	159
18.4.1 Charpy V-notch geometry	160
18.4.2 Geometry with a fatigue pre-crack	160
18.5 Statistics of crack propagation in graded material	160
18.5.1 Plastic zones and process zones	162
18.5.2 Results	163
18.6 Discussion	163
19. OVERALL CONCLUSIONS	165
BIBLIOGRAPHY	169
APPENDIX	181
A. List of conference publications	
B. List of journal papers	

NOMENCLATURE

a	Crack depth
a_A	Crack depth in the re-entrant sector on a complex crack
a_B	Crack depth of the deepest segment of a semi-elliptical crack
a_D	Crack depth of the deepest segment of a semi-elliptical crack or re-characterised crack
\bar{a}	Mean crack depth
a/c	Aspect ratio of a semi-elliptical crack
b	Width of a plate geometry containing sinusoidal and complex cracks
c	Half crack surface length
e_o	Yield strain
e^*	Constant in Ramberg-Osgood relation
e_{ij}	All strain components
$e_x, e_y, e_z, e_{zx}, e_{xy}, e_{yz}$	Strain components in Cartesian co-ordinate system
$f_{ij}(\theta)$	Angular function describing the influence of a strength mismatch on the stress field
h	Weld semi-width
k	Yield stress in shear
m	Weibull modulus
n	Strain hardening exponent, also strength of leading singularity in the HRR solution
p	Probability density function
r	Radial distance in polar co-ordinate system
r_o	Radius of a cracked particle
r_p	Plastic zone size
$r(\theta)$	Radius of a plastic zone
s	Crack front length
s_o	Incremental crack length used for calculating failure probability
s^{st}	Crack front length of a straight crack
s^{SE}	Crack front length of a semi-elliptical crack
t	Strength of leading singularity using small-scale yielding solution, also thickness of the plate geometry containing sinusoidal and complex cracks
u,v	Displacements in Cartesian co-ordinate system
v	The parameter which measures position along the crack front
w	Width of geometry
w_p	Plastic work of fracture
x,y,z	Co-ordinated in a right handed Cartesian system

A	Amplitude of a sinusoidal crack
A_{pl}^{CMOD}	Plastic work under the load – CMOD curve
B	Thickness of geometry
D_f	Fast neutron dose
D_t	Slow neutron dose
E	Young's modulus
F	Failure load
F_T	Function of irradiation temperature
F_Y	Limit load of a mismatched joint
F_{YBM}	Limit load of a base material
F_{YW}	Limit load of a weld metal
F_{lim}	Plastic collapse load
$F_{lim,local}$	Local plastic collapse load
$F_{lim,global}$	Global plastic collapse load
G	Elastic energy release rate
$G(\frac{a}{T})$	Geometry function for an edge cracked bar
HV	Vickers hardness
I_n	Integration constant in HRR field
J	J –integral
$J_{(T)}$	Constraint enhanced fracture toughness
$J_{(T=0)}$	Plane strain fracture toughness
J^{ref}	J value of a reference geometry
J^{-ve}	J value of an unconstrained geometry
$J_{0.5}$	J value of an $a/w=0.5$ geometry
$J_{0.075}$	J value of an $a/w=0.075$ geometry
J_{el}	Elastic component of the J-integral
J_{pl}	Plastic component of the J-integral
\bar{J}	Mean toughness of a homogeneous material
K	Stress intensity factor
\bar{K}	Mean toughness
K_{mat}	Critical value of stress intensity factor used in FAD
K_o	Constant in Weibull expression for failure probability
K_{ref}	Reference stress intensity factor, considered as loading parameter
K_{IC}	Plane strain fracture toughness
$K_{0.5}$	Stress intensity factor for $a/w=0.5$ geometry
$K_{0.075}$	Stress intensity factor for $a/w=0.075$ geometry

K_I	Mode I stress intensity factor
K_{II}	Mode II stress intensity factor
K_{III}	Mode III stress intensity factor
K_J	J-integral expressed in stress intensity factor notation
K_c	Critical stress intensity factor
K_r	Normalised stress intensity factor in failure assessment diagram
$K_{(v)}$	Stress intensity factor as a function of position along the crack front
L	Span between supports, also length of the specimen
L_r	Normalised load in failure assessment diagram
M	Strength mismatch
M	Parameter of Zhang <i>et al</i> used in J-Q-M characterisation of strength mismatched fields.
M^e	Elastic mode mixity
M^p	Plastic mode mixity
$M_{(x)}$	Local bending moments per unit crack length
$N_{(x)}$	Local forces per unit crack length
P	Probability of failure
R	Resistance to crack growth
Q	Elastic-plastic constraint parameter
Q^{ref}	Elastic-plastic constraint parameter for a reference field
Q^{-ve}	Elastic-plastic constraint parameter for an unconstrained field
$Q_{0.5}$	Elastic-plastic constraint parameter for $a/w=0.5$ geometry
$Q_{0.075}$	Elastic-plastic constraint parameter for $a/w=0.075$ geometry
T	Elastic T-stress
U	Potential energy for crack advance
U_a	Elastic strain energy
U_γ	Energy required to form a new surface
W	External work
V_o	Volume of a unit cell, for definition of Weibull stress
X, Y	Generalised local forces and moments plotted in the yield space
Y	Geometry function
α	Constant in Ramberg-Osgood relation
$\alpha_{(v)}$	Non-dimensional stress intensity factor as a function of crack tip position
β	Biaxiality parameter
γ	Factor to quantify a change in the yield stress
γ_s	Energy density to form new surface

$\gamma(\frac{a}{c})$	Function of a semi-elliptical geometry
ξ	Effective crack front length
λ	Wavelength of a sinusoidal crack
λ	Non-dimensional size of the process zone, for Weibull calculations
η_{plCMOD}	J_{plastic} calibration factor
δ	Crack tip opening displacement (CTOD)
δ_{ij}	Kroneker delta
φ	Notch opening angle, also parameter that defined angular position on the semi-elliptical crack front
ϕ	Temperature in °C
ρ	Non-dimensional radius of the process zone
θ	Angle in polar co-ordinate system
$\bar{\theta}$	Macroscopic crack initiation angle
χ	Non-dimensional angular function of a stress intensity factor for semi-elliptical cracks
ν	Poisson's ratio
σ	Applied stress
$\bar{\sigma}$	Average stress
σ_b	Outer fibre stress in bending
σ_c	Critical stress for crack propagation in ideal brittle materials
σ_{eq}	Equivalent (Mises) stress
σ_f	Local fracture stress
σ_{ij}	All stress components
σ_m	Mean stress
σ_o	Yield stress
$\sigma_{o,0.5}$	Yield stress of a $a/w=0.5$ geometry at a fixed toughness
$\sigma_{o,0.075}$	Yield stress of a $a/w=0.075$ geometry at a fixed toughness
σ_o^*	New yield stress of a stress field matched to another stress field
$\sigma_{o,0.5}^*$	New yield stress of a $a/w=0.5$ geometry to match with the $a/w=0.075$ geometry at a fixed toughness
$\sigma_{o,0.075}^*$	New yield stress of a $a/w=0.075$ geometry to match with the $a/w=0.5$ geometry at a fixed toughness
$\Delta\sigma_o$	Change in the yield stress
σ_{ref}	Yield stress of a reference solution, identified with the small-scale yielding solution
σ_{oW}	Yield stress of the weld metal
σ_{oBM}	Yield stress of the base material

σ_t	Remotely applied tensile stress
σ_u	Constant with dimensions of stress
σ_w	Weibull stress
σ_r	Radial stress in a polar co-ordinate system
$\sigma_{r\theta}$	Shear stress in a polar co-ordinate system
$\sigma_x, \sigma_y, \sigma_z$	Stress components in Cartesian co-ordinate system
σ_θ	Tangential (hoop) stress in a polar co-ordinate system
σ_{HRR}	Stresses in the HRR field
σ_{TS}	Tensile strength
σ_1	Maximum principal stress
$\sigma_1, \sigma_2, \sigma_3$	All principal stresses
$\tilde{\sigma}(n, \theta)$	Tabulated functions in HRR field
σ_{ij}^{SSY}	Small scale yielding stress field
$\tilde{\sigma}_w^m$	Non-dimensional Weibull stress parameter
$(\tilde{\sigma}_w^m)^{ref}$	Non-dimensional Weibull stress parameter for a reference field
$(\tilde{\sigma}_w^m)^{-ve}$	Non-dimensional Weibull stress parameter for an unconstrained field
$(\tilde{\sigma}_w^m)_{0.5}$	Non-dimensional Weibull stress parameter for a/w=0.5 geometry
$(\tilde{\sigma}_w^m)_{0.075}$	Non-dimensional Weibull stress parameter for a/w=0.075 geometry
$\tau_{r\theta}$	Shear stress in a polar co-ordinate system
υ	Function of geometry with dimensions of K_{ref}
ψ	Variance
Γ	Gamma function
Δa	Increase in crack length in fatigue crack growth law
Δc	Crack growth on the free surface of a surface breaking defect
ΔK	Change of stress intensity factor in fatigue crack growth law
ΔN	Number of loading cycles in fatigue crack growth law
Φ	Integration angle for a semi-elliptical crack front
Ω	Load independent Weibull stress parameter

LIST OF FIGURE CAPTIONS

Chapter 2

- Figure 2.1: Stresses in the vicinity of a crack.
- Figure 2.2: Load-displacement curves for (a) fixed load and (b) fixed displacement conditions.
- Figure 2.3: Characteristic modes of crack opening.
- Figure 2.4: Conditions of small scale yielding.
- Figure 2.5: Irwin's plastic zone model.
- Figure 2.6: Plane stress and plane strain plastic zone sizes.
- Figure 2.7: Dependence of fracture toughness on the thickness of the geometry.
- Figure 2.8: Illustration of the crack mouth opening displacement (CMOD) and definition of the crack tip opening displacement (CTOD) with the 45° intersection lines.
- Figure 2.9: Definition of the J-integral after Rice (1968).
- Figure 2.10: Illustration of the boundary layer formulation.
- Figure 2.11: Slip line fields in Mode I plane strain, showing the effect of T-stress, after Du and Hancock (1991).
- Figure 2.12: Application of the J-Q toughness locus.

Chapter 3

- Figure 3.1: Plate geometry.
- Figure 3.2: Definition of an infinite periodical sinusoidal crack.
- Figure 3.3a: A sinusoidal crack of varying amplitude.
- Figure 3.3b: A sinusoidal crack of varying wavelength.
- Figure 3.3c: Illustration of the perturbation of a sinusoidal crack.
- Figure 3.4: Finite element model of the plate.
- Figure 3.5: The line-spring model of a surface breaking crack.
- Figure 3.6: A representative cell of an infinite periodic sinusoidal crack.
- Figure 3.7: Stress intensity factor for surface touching sinusoidal crack of varying wavelength for $A = 0.25t$ and $\bar{a} = 0.25t$ in tension.
- Figure 3.8: Stress intensity factor for surface touching sinusoidal crack of varying wavelength for $A = 0.25t$ and $\bar{a} = 0.25t$ in three-point bending.
- Figure 3.9: Stress intensity factor for deep sinusoidal crack of varying wavelength for $A = 0.25t$ and $\bar{a} = 0.25t$ in tension, normalised with a constant.
- Figure 3.10: Stress intensity factor for deep sinusoidal crack of varying wavelength for $A = 0.25t$ and $\bar{a} = 0.25t$ in three-point bending, normalised with a constant.

- Figure 3.11: The elastic T-stress for surface touching sinusoidal crack of varying wavelength for $A = 0.25t$ and $\bar{a} = 0.25t$ in tension.
- Figure 3.12: The elastic T-stress for surface touching sinusoidal crack of varying wavelength for $A = 0.25t$ and $\bar{a} = 0.25t$ in three-point bending.
- Figure 3.13: Normalised local forces (b) and bending moments (c) for surface touching sinusoidal crack (a) of varying wavelength for $A = 0.25t$ and $\bar{a} = 0.25t$ in tension.
- Figure 3.14: Dependence of the stress intensity factor on the amplitude and wavelength for a deep sinusoidal crack ($\bar{a} = 0.5t$) in tension.
- Figure 3.15: Dependence of the stress intensity factor on the amplitude and wavelength for a deep sinusoidal crack ($\bar{a} = 0.5t$) in three-point bending.
- Figure 3.16: Dependence of the T-stress on the amplitude and wavelength for a deep sinusoidal crack ($\bar{a} = 0.5t$) in tension.
- Figure 3.17: Dependence of the T-stress on the amplitude and wavelength for a deep sinusoidal crack ($\bar{a} = 0.5t$) in three point bending.
- Figure 3.18: Dependence of the stress intensity factor on the amplitude and wavelength for a surface touching sinusoidal crack in tension.
- Figure 3.19: Dependence of the stress intensity factor on the amplitude and wavelength for a surface touching sinusoidal crack in three point bending.
- Figure 3.20: Dependence of the elastic T-stress on the amplitude and wavelength for a surface touching sinusoidal crack in tension.
- Figure 3.21: Dependence of the elastic T-stress on the amplitude and wavelength for a surface touching sinusoidal crack in three point bending.
- Figure 3.22: Global limit load for surface touching sinusoidal crack in tension, normalised with values for $\lambda = 2t$.
- Figure 3.23: Determination of local critical values for surface touching sinusoidal crack of $\lambda = 10t$ in tension; deepest and shallowest point analysed.
- Figure 3.24: Global and local limit load for surface touching sinusoidal crack in tension; normalised with global limit load for $\lambda = 2t$ configuration.
- Figure 3.25: Global and local limit load for surface touching sinusoidal crack in three-point bending; normalised with global limit load for $\lambda = 2t$ configuration.
- Figure 3.26: Development of plasticity for a surface touching sinusoidal crack of $A = 0.25t$ and $\bar{a} = 0.25t$ at $F=0.5F_{lim}$ in tension.
- Figure 3.27: Development of plasticity for a surface touching sinusoidal crack of $A = 0.25t$ and $\bar{a} = 0.25t$ at $F=F_{lim}$ in tension.
- Figure 3.28: Development of plasticity for surface touching sinusoidal crack of $A = 0.25t$ and $\bar{a} = 0.25t$ at $F=0.5F_{lim}$ in three point bending.
- Figure 3.29: Development of plasticity for surface touching sinusoidal crack of $A = 0.25t$ and $\bar{a} = 0.25t$ at $F=F_{lim}$ in three-point bending.

- Figure 3.30: Development of crack tip constraint, parameterised with the T- stress, for a surface touching sinusoidal crack of $A = 0.25t$ and $\bar{a} = 0.25t$ at $F=0.5F_{lim}$ in tension.
- Figure 3.31: Development of crack tip constraint, parameterised with the T-stress, for a surface touching sinusoidal crack of $A = 0.25t$ and $\bar{a} = 0.25t$ at $F=F_{lim}$ in tension.
- Figure 3.32: Development of crack tip constraint, parameterised with the T-stress, for a surface touching sinusoidal crack of $A = 0.25t$ and $\bar{a} = 0.25t$ at $F=0.5F_{lim}$ in three-point bending.
- Figure 3.33: Development of crack tip constraint parameterised with the T-stress, for a surface touching sinusoidal crack of $A = 0.25t$ and $\bar{a} = 0.25t$ at $F=F_{lim}$ in three-point bending.
- Figure 3.34: Comparison of line spring data with results of Eq. (3.5) for a surface touching sinusoidal crack of $A = 0.1t$, $\bar{a} = 0.12t$ in tension.
- Figure 3.35: Comparison of line spring data with results of Eq. (3.5) for a surface touching sinusoidal crack of $A = 0.3t$, $\bar{a} = 0.32t$ in tension.
- Figure 3.36: Increase in the crack front perturbation shifts the location of the maximum K or J towards the shallower segments in tension and bending.

Chapter 4

- Figure 4.1: Parametric definition of a semi-elliptical crack..
- Figure 4.2: Values for the parameter χ for a semi-elliptical crack in tension, computed from Newman-Raju (1981) expression.
- Figure 4.3: Values for the parameter χ for a semi-elliptical crack in pure bending, computed from Nemanw-Raju (1981) solution.
- Figure 4.4: The increased fracture resistance expressed in terms of K_{ref} of a semi-elliptical crack compared to a straight crack of equal lengths, arising from the shape of the crack: (a) tension and (b) pure bending.
- Figure 4.5: Definition of the line segment Δv_i for approximating the effective crack front length using discrete values.

Chapter 5

- Figure 5.1: Crack geometry and the re-characterisation of adjacent co-planar defects.

Chapter 6

- Figure 6.1: Semi-elliptical and complex crack shapes developed in fatigue; $b=6t$.
- Figure 6.2: Modelled segment of the experimental geometry.
- Figure 6.3: Finite element mesh representing a quarter of the experimental geometry.
- Figure 6.4: Stress intensity factor in the re-entrant sector (position A) and at the deepest crack segments (position B) from line spring analysis. Data for a bounding

- semi-elliptical and a single defect before coalescence are superimposed from data of Raju Newman (1981).
- Figure 6.5: Stress intensity factor between the line-of-coalescence (position A) and deepest crack segments (Position B) from line spring analysis.
- Figure 6.6: Normalised local forces along surface length between positions A and B from the line spring analysis.
- Figure 6.7: Normalised bending moments along surface length between positions A and B from the line spring analysis.
- Figure 6.8: T-stress between the line-of-coalescence (position A) and deepest crack segments (position B) from the line spring analysis.
- Figure 6.9: T-stress between at line-of-coalescence (position A) in the re-entrant sector and for a straight edge crack of equivalent depth from Sham (1991).
- Figure 6.10: Biaxiality parameter β between the line-of-coalescence (position A) and deepest crack segments (Position B) from the line spring analysis.
- Figure 6.11: Local and global limit loads for complex crack; normalised with global limit load of uncracked geometry.
- Figure 6.12: Definition of the local and global limit load for a coalesced crack shape of $a_A=0.05t$.
- Figure 6.13: Force-bending moment histories for the re-entrant position A of coalesced cracks with re-entrant sectors.
- Figure 6.14: Values of J-integral in the re-entrant sector and at the deepest positions. Values are normalised with local ligament lengths and taken for the same fraction of local limit load in the re-entrant sector.
- Figure 6.15: Values of J-integral in the re-entrant sector and at the deepest positions. Values are normalised with constant ligament lengths of each profile and taken for the same fraction of global limit load of the uncracked geometry.
- Figure 6.16: Values of J-integral in the re-entrant sector and at the deepest positions. Values are normalised with constant ligament length of each profile and taken for the displacements of a fixed fraction of plate thickness.
- Figure 6.17: T-stress in the re-entrant sector as a function of applied load. Values are normalised with the yield stress and taken for the same fraction of local limit load of each profile.
- Figure 6.18: T-stress in the re-entrant sector as a function of crack depth. Values are normalised with the thickness and taken for the same fraction of global limit load of the uncracked geometry.
- Figure 6.19: Modelled geometry containing two non co-planar cracks.
- Figure 6.20: Finite element mesh used for modelling non co-planar coalesced profiles.
- Figure 6.21: Mode I stress intensity factor between positions A and B for non co-planar cracks and step height of $0.04t$.
- Figure 6.22: Mode I stress intensity factor in the re-entrant sector of co-planar and non co-planar cracks.
- Figure 6.23: Mode III stress intensity factor in the non co-planar re-entrant sector.
- Figure 6.24: T-stress in the re-entrant sector for co-planar and non co-planar cracks.

- Figure 6.25: Biaxiality parameter β in the re-entrant sector of co-planar and non co-planar cracks.
- Figure 6.26: The general failure assessment diagram (Option 1).
- Figure 6.27: FAD for three coalesced crack shapes and constraint sensitivity $k=1$. Applied load is normalised with the local limit load in re-entrant sector.
- Figure 6.28: FAD for three coalesced crack shapes and constraint sensitivity $k=3$. Applied load is normalised with the local limit load in re-entrant sector.
- Figure 6.29: FAD for three coalesced crack shapes and constraint sensitivity $k=1$. Applied load is normalised with the global limit load of a bounding semi-ellipse.
- Figure 6.30: FAD for three coalesced crack shapes and constraint sensitivity $k=3$. Applied load is normalised with the global limit load of a bounding semi-ellipse.

Chapter 7

- Figure 7.1: Plate geometry, all dimensions in [mm].
- Figure 7.2: Illustration of the beachmark technique.
- Figure 7.3: Initial crack propagation by coalescence of microcracks.
- Figure 7.4: Development of a complex crack from adjacent co-planar notches (Specimen S13).
- Figure 7.5: Through thickness crack growth of specimen S13.
- Figure 7.6: Through thickness crack growth rate of specimen S13.
- Figure 7.7: Crack growth on the free surface of specimen S13.
- Figure 7.8: Development of the aspect ratio for specimen S13 in fatigue.
- Figure 7.9: Formation of a crack overlap (a) and sub-surface coalescence of (b) a step on the crack front during fatigue crack growth and the initial coalesced shape.
- Figure 7.10: Stress intensity factor in the through thickness direction at positions A and B, from experimental and numerical studies. Values are normalised with applied stress and the greatest crack depth of each crack shape.
- Figure 7.11: Stress intensity factor on free surface of a complex crack, from the experimental study.
- Figure 7.12: Crack lengths on free surface (positions E and F) with loading cycles.
- Figure 7.13: Crack length on free surface (positions E and F) with distance to coalescence (s/d).
- Figure 7.14: Stress intensity factors at positions E and F, normalised with applied stress and free surface length.
- Figure 7.15: Interaction factor K^E/K^F for the adjacent defects extending in bending.
- Figure 7.16: Growth of crack on free surface in fatigue.

- Figure 7.17: Illustration of the effect of leading grooves on the crack path on free surface. In (a) leading grooves are cut part way between notches and in (b) leading groove connects both notches.
- Figure 7.18: Photographs of fatigue crack growth on free surface from co-planar leading grooves, leading to coalescence on surface.
- Figure 7.19: Photograph of the effect of the leading groove on the growth near free surface, as indicated by arrows.
- Figure 7.20: Photograph of a development of a fatigue crack from co-planar notches connected with leading groove (specimen S16).

Chapter 8

- Figure 8.1: Photographs of fracture surface in ductile torn configurations. Arrows mark boundary of cleavage failure.
- Figure 8.2: A view on the tested specimens from the free surface.
- Figure 8.3: Illustration of load - deflection paths recorded during the ductile tearing of complex defects.
- Figure 8.4: Assessment of a defect with re-entrant sector (specimen S7) using the failure assessment diagram of R6, Rev 4. All J values are taken for the re-entrant tip and load is normalised with the local limit load in the re-entrant sector: $F_{lim}^A = 0.88 \cdot F_{lim}^{global}$.
- Figure 8.5: Assessment of a re-characterised defect (specimen S9) using the failure assessment diagram of R6, Rev 4. Assessment is performed for the near surface position (C) and deepest position (D). Load is normalised with the local limit loads.
- Figure 8.6: Illustration of the plasticity patterns observed on the free surface during testing.
- Figure 8.7: The von Mises stress patterns, modelled for a defect with a moderate re-entrant sector (specimen S7).

Chapter 9

- Figure 9.1: Photographs of tested crack configurations, with the recorded failure loads to cleavage.
- Figure 9.2: Deterministic assessment of complex defects (S11 at -196°C and S6 at -100°C) and re-characterised defects.
- Figure 9.3: Probability of failure of complex defects (S11) at -196°C and (S6) at -100°C and re-characterised defects, at measured failure load on complex defects.
- Figure 9.4: Assessment of the complex defect (S11) tested at -196°C and the re-characterised defect using general failure assessment diagram.
- Figure 9.5: Assessment of the complex defect (S6) tested at -100°C is shown in Figure 9.5(a) and the re-characterised defect in Figure 9.5(b) using general failure assessment diagram.
- Figure 9.6: Assessment of a complex tested (S6) at -100°C using constraint modified failure assessment diagram.

- Figure 9.7: Assessment of complex defects (S11 at -196°C and S6 at -100°C) and re-characterised defects using failure assessment diagram including statistical size and shape corrections.
- Figure 9.8: Probability density function (pdf) for complex defects (S11) at -196°C and (S6) at -100°C and the re-characterised defects, at measured failure loads on complex defects.
- Figure 9.9: The transition of failure from a complex defect to a re-characterised defect determined using a modified failure assessment diagram. The transition is governed by the constraint effects in the re-entrant sectors.
- Figure 9.10: Assessment of a complex defect (S10) tested at -196°C and the re-characterised defect using failure assessment diagram.
- Figure 9.11: The definition of a complex geometry used to define the approximate amplification factors.

Chapter 10

- Figure 10.1: Illustration of the Ritchie-Knott-Rice (1973) cleavage model at two temperatures. Stress intensification that will initiate failure at temperature T_1 will not initiate failure at a higher temperature T_2 when the microstructural distance is temperature independent.
- Figure 10.2: Example of stress distributions at failure for SENB specimens, showing locations of initiation sites, after Wall, Lane and Hipsley (1994).
- Figure 10.3: Local fracture stress for two microstructures of A533B steel, after Bowen *et al* (1987).
- Figure 10.4: The ratio of local fracture stress to yield stress for the two microstructures of A533B steel examined by Bowen *et al* (1987).
- Figure 10.5: A schematic diagram showing the active zone for cleavage fracture, taken from Wang *et al* (2002b).
- Figure 10.6: The microstructural distance for the two microstructures of A533B steel, after Bowen *et al* (1987).
- Figure 10.7: Average angle of crack initiation as a function of remote mode mixity angle for a homogeneous material, taken from Becker *et al* (2002). The deterministic criterias: maximum hoop stress, energy release rate and maximum principal stress are superimposed.

Chapter 11

- Figure 11.1: The underprediction of cleavage toughness at elevated temperatures using the RKR model on $a/w=0.5$ A533B-1 data at a fixed local fracture stress and microstructural distance.
- Figure 11.2: Comparison of the RKR fit to A533B-1 $a/w=0.5$ data for a fixed E , σ_f and r_c and a fit where Young's modulus is temperature dependent at a fixed σ_f and r_c .

Figure 11.3: The necessary temperature dependence of the local fracture stress to account for the ration of unconstrained ($a/w=0.075$) to constrained ($a/w=0.5$) toughness data from Sherry *et al* (2001).

Figure 11.4: The temperature dependent critical microstructural distance for deep and shallow cracked data, normalised with the individual lower shelf values.

Chapter 12

Figure 12.1: Plots of applied principal stress directly ahead of the crack over a range of applied J values in (a) and yield stresses in (b).

Figure 12.2: Plots of normalised principal stresses directly ahead of the crack, examined over a range of applied J values in (a) and yield stresses in (b).

Figure 12.3: Principal stress directly ahead of the crack for a reference ($T=0$) and an unconstrained ($T=-0.25\sigma_0$) and ($T=-0.5\sigma_0$) fields. In (a) examined at a fixed yield stress and in (b) at a fixed J.

Figure 12.4: Multiplicative factor β proposed by Anderson and Dodds (1991) to quantify the relaxation of stresses in unconstrained fields of shallow cracked bend bars compared to the constrained field characteristic of a deep cracked bend bars, at $\theta=0$.

Figure 12.5: Constrained ($T=0$) field is matched to the unconstrained ($T=-0.25\sigma_0$) field by a change in J in (a) and by a change in σ_0 in (b), at a fixed distance ahead of the crack.

Figure 12.6: Constrained ($T=0$) field is matched on unconstrained ($T=-0.5\sigma_0$) field by J in (a) and by σ_0 in (b), at a fixed distance ahead of the crack.

Figure 12.7: Unconstrained field is matched to the $T=0$ field at a local fracture stress of $\sigma_f = 3\sigma_{0, \text{fixed}}$ by J in (a) and yield stress in (b), as illustrated with plots of principal stress ahead of the crack ($\theta=0$).

Figure 12.8: Unconstrained field is matched to the $T=0$ field at a local fracture stress of $\sigma_f = 3\sigma_{0, \text{fixed}}$, by J in (a) and yield stress in (b), as shown by contours of principal stress.

Figure 12.9: Unconstrained and $T=0$ field match close to the crack tip by adjusting J, based on the small strain Weibull stress approach for $\lambda=3$ and $m=20$.

Figure 12.10: Unconstrained and $T=0$ field match at a fracture process zone boundary ($\lambda=3$) by adjusting J, based on the small strain Weibull stress approach for $\lambda=3$ and $m=10$.

Figure 12.11: Unconstrained and $T=0$ field match close to the crack tip by adjusting yield stress. Based on the small strain Weibull stress approach for $\lambda=3$ and $m=20$.

Figure 12.12: Principal stress ahead of the crack for crack tip fields characteristic of $K_J=150-250\text{MPa}\sqrt{\text{m}}$ toughness data. The fields differ by constraint and temperatures (yield stresses) and are matched at a fracture stress taken as three times the yield stress of the field to which values are matched.

Figure 12.13: Principal stress ahead of the crack for constrained ($T=+0.1\sigma_0$) and unconstrained ($T=-0.61\sigma_0$) field, characteristic of $K_J=150-250\text{MPa}\sqrt{\text{m}}$ toughness data. Fields are matched by yield stress computed from finite

strain Weibull stress procedure in the plastic zone ($\lambda=1$) and normalised with a fixed value σ_0 and $J/\sigma_0 e_0$ for the constrained field.

Chapter 13

- Figure 13.1: Experimental low and high constraint toughness data from Sherry *et al* (2001) as a function of temperature. Data are curve-fit for clarity.
- Figure 13.2: Constraint values in experimental data from Sherry *et al* (2001) as a function of temperature.
- Figure 13.3: Toughness data from Sherry *et al* (2001) as a function of constraint. Data are curve-fit for clarity.
- Figure 13.4: Temperature dependent yield stress re-drawn from data of Sherry *et al* (2001). A linear curve-fit over the temperature range of interest is superimposed.
- Figure 13.5: The stress fields based on the HRR and SSY ($T=0$) singularity directly ahead of the crack. The hoop stress for the field representative of constrained ($a/w=0.5$) data having $T=+0.1\sigma_0$ is superimposed
- Figure 13.6: High constraint data ($a/w=0.5$) fitted with the RKR model using SSY singularity on the lower shelf at three microstructural distances.
- Figure 13.7: Constraint correction to the shallow cracked experimental data ($a/w=0.075$) obtained by matching fields at a local fracture stress of $\sigma_f=2300$ MPa.
- Figure 13.8: Constraint correction to the shallow cracked ($a/w=0.075$) experimental data obtained by comparing stress fields using the Weibull stress model evaluated in the plastic zone ($\lambda=1$).
- Figure 13.9: Temperature shifts due to constraint loss for the $a/w=0.075$ data obtained by matching the crack tip fields at a local fracture stress of $\sigma_f=2300$ MPa.
- Figure 13.10: Temperature shifts due to constraint loss for the $a/w=0.075$ data obtained by matching the crack tip fields at a local fracture stress of $\sigma_f=1830$ MPa after Ritchie *et al* (1979).
- Figure 13.11: Temperature shifts from constraint loss for the $a/w=0.075$ data, obtained using the Weibull stress approach evaluated in the plastic zone ($\lambda=1$).
- Figure 13.12: Q parameter for the irradiated and unirradiated material, determined at a fixed toughness for the $a/w=0.075$ data set.
- Figure 13.13: Temperature shift due to constraint loss for unirradiated and irradiated $a/w=0.075$ data by matching stress fields directly ahead of the crack at a local fracture stress of 2300 MPa.
- Figure 13.14: Temperature shift due to constraint loss for unirradiated and irradiated $a/w=0.075$ data by matching stress fields directly ahead of the crack at a local fracture stress of 1830 MPa.
- Figure 13.15: Temperature shift due to constraint loss for unirradiated and irradiated $a/w=0.075$ data using the Weibull stress model with Weibull modulus of 20 evaluated in the plastic zone.

Chapter 14

- Figure 14.1: Mean stress non-dimensionalised by the yield stress as a function of angle for a range of mixities in a non-hardening material, after Li (1997).
- Figure 14.2: Mises stress non-dimensionalised by the yield stress as a function of angle for a range of mixities in a non-hardening material, after Li (1997).
- Figure 14.3: Slip line fields for a family of mixed-mode problems at $T=0$, after Li (1997).
- Figure 14.4: The maximum hoop stress of mixed-mode cracks as a function of the non-dimensionalised distance from the crack tip, after Li (1997).
- Figure 14.5: The hoop stress directly ahead of a Mode I crack as a function of the non-dimensionalised distance from the crack tip for a range of $\frac{T}{\sigma_0}$ values, after Li (1997).
- Figure 14.6: T-stress as a function of mixity for a range of hardening rates, after Li (1997).
- Figure 14.7: Q as a function of mixity for a range of hardening rates, after Li (1997).
- Figure 14.8: The stress deviator, $S_{\theta\theta}$, non-dimensionalised by the yield stress directly ahead of Mode I crack for a range of $\frac{T}{\sigma_0}$ values, after Li (1997).
- Figure 14.9: The stress deviator, $S_{\theta\theta}$, non-dimensionalised by the yield stress on the plane of maximum hoop stress in mixed-mode cracks, after Li (1997).
- Figure 14.10: Illustration of the asymmetric four-point bend loading arrangement, after Maccagno and Knott (1989).
- Figure 14.11: Photographs of specimens tested to cleavage under mixed-mode loading, showing crack propagation direction as a function of mixity.
- Figure 14.12: Results of fracture toughness tests on unconstrained Mode I cracks shown in (a) and mixed-mode I+II cracks shown in (b).
- Figure 14.13: Unconstrained Mode I and mixed-mode I/II toughness data plotted in a failure assessment diagram.
- Figure 14.14: Unification of mode-mixity and in-plane constraint loss, shown by Mode I data and mapped mixed mode I+II data into a common constraint-mixity locus.
- Figure 14.15: Constraint-mixity locus derived from the experimental data and superimposed predictions obtained by matching fields at a local fracture stress or by using the Weibull stress procedure of Gao and Dodds (2001).
- Figure 14.16: Correlation between the constraint parameter and remote mixity for interfacial cracks, after Li (1997).

Chapter 15

- Figure 15.1: Comparison of plastic strain contours for 40% mismatched welds at two weld widths loaded to $J/h\sigma_{0w}=0.1$, from Burstow *et al* (1998).
- Figure 15.2: The effect of mismatch, m , and weld width, $2h$, on the distribution of stresses ahead of a crack, from Burstow *et al* (1998).

- Figure 15.3: The crack tip stresses directly ahead of the crack as a function of mismatch, showing self-similarity of crack tip fields when normalised by $J/h\sigma_{0w}$, after Burstow *et al* (1998).
- Figure 15.4: Effect of base material strength on crack tip stress distribution with increasing load, after Burstow *et al* (1998).
- Figure 15.5: Schematic representation of plasticity development in mismatched SENB specimens, after Eripret *et al* (1997).
- Figure 15.6: The definition of the plasticity development patterns for mismatched SENB specimens: a) the weld joint is large enough to contain the plasticity and b) plasticity extends to the base material, after Hornet *et al* (1995).
- Figure 15.7: Defect assessment procedures for structural integrity and extension for mismatch effects, after Schwalbe *et al* (1997).
- Figure 15.8: Ductile tearing of a crack located in the weld centerline at 0°C, taken from Cam *et al* (1999).
- Figure 15.9: Cleavage crack path for a crack located at the weld centerline under dynamic loading, after Sumpter (1996).

Chapter 16

- Figure 16.1: The ratio of the local fracture stresses and yield stresses of the two microstructures in A533B steel, using data of Bowen *et al* (1987).
- Figure 16.2: Contours of principal stress for $\lambda=2.5$ and plastic zone sizes for a range of strength mismatches in Mode I plane strain.
- Figure 16.3: Failure probability for a bi-material joint as a function of normalised load in plane strain. λ is 2.5 and Weibull modulus is 10 in Figure 16.3(a) and 20 in Figure 16.3(b).
- Figure 16.4: The dependence of toughness in a bi-material joint on the strength mismatch and Weibull modulus at $\lambda=2.5$.
- Figure 16.5: The probability density function for a bi-material joint as a function of angle over a range strength mismatches at $\lambda=2.5$. The Weibull modulus is 10 in Figure 16.5(a) and 20 in Figure 16.5(b).
- Figure 16.6: Average crack propagation angle into the soft side of a bi-material joint at $\lambda=2.5$, as a function of strength mismatch and Weibull modulus (m).

Chapter 17

- Figure 17.1: Geometry of laser welded specimens.
- Figure 17.2: Illustration of typically weld cross-section and a crack location in the heat affected zone, near fusion line.
- Figure 17.3: Cross-section of laser weld showing and example of a crack located in the heat affected zone (HAZ), near fusion line and a photograph of the cross-section.
- Figure 17.4: Measurement of Vickers hardness across the width of the weld, starting from the fusion line.

- Figure 17.5: Strength mismatch from collection of hardness measurements across the laser welded joint, simplified for use in the finite element model.
- Figure 17.6: Schematic representation of crack locations in test geometries and associated plots of the plastic strains.
- Figure 17.7: Fracture toughness in contained yielding at $-130\text{ }^{\circ}\text{C}$ for a range of crack configurations, with crack location measured in the centre of specimens. The local yield stresses are shown in Figure 17.7(b).
- Figure 17.8: Photographs of crack paths at $-130\text{ }^{\circ}\text{C}$ tests in the center of the specimen, measured on cross-sections 2 mm apart.
- Figure 17.9: Photographs of crack path on the surface of laser welded specimens, tested at $-130\text{ }^{\circ}\text{C}$.
- Figure 17.10: Plots of the plastic strains under plane stress conditions for a representative sample of test geometries at $-130\text{ }^{\circ}\text{C}$ conditions.
- Figure 17.11: Fracture toughness for a deep crack ($a/w=0.5$) configuration in ductile-brittle transition at $-60\text{ }^{\circ}\text{C}$. Crack location is measured in the centre of the specimen.
- Figure 17.12: Load – load-line-displacement records from tests on deep cracks at $-60\text{ }^{\circ}\text{C}$, showing pop-in failures.
- Figure 17.13: Photographs of crack paths in the center of laser welded specimens, for $a/w=0.5$ configurations tested at $-60\text{ }^{\circ}\text{C}$. Photographs are taken at cross-sections 2mm apart.
- Figure 17.14: Photograph of a fracture surface of specimen LW-31 showing pop-in failure. The specimen had a crack front fully contained in the weld metal.
- Figure 17.15: Photographs of crack location along the width of the weld for $a/w=0.1$ crack prior to cleavage tests.
- Figure 17.16: Photographs of crack paths in the center of laser welded specimens, for $a/w=0.1$ configurations tested at $-90\text{ }^{\circ}\text{C}$. Photographs are taken at cross-sections 2 mm apart.
- Figure 17.17: Fracture toughness for shallow crack ($a/w=0.1$) configurations in ductile-brittle transition at $-90\text{ }^{\circ}\text{C}$. Crack location is measured in the centre of the specimen.
- Figure 17.18: T-stress for shallow crack ($a/w=0.1$) configurations in ductile-brittle transition at $-90\text{ }^{\circ}\text{C}$. Crack location is measured in the centre of the specimen and T-stress is normalised with the yield stress of material at the crack tip.
- Figure 17.19: Photographs showing ductile tearing of laser welded joint at room temperature.
- Figure 17.20: Photographs of Charpy specimens, tested in ductile-brittle transition. Notch was cut along the fusion line.
- Figure 17.21: Photographs of Charpy geometries tested under quasi-static three-point bending.
- Figure 17.22: Curve-fit to the deep crack K_{IC} data at $-130\text{ }^{\circ}\text{C}$ and crack propagation direction with respect to fracture toughness.

Chapter 18

- Figure 18.1: Detail of the finite element mesh near the crack tip.
- Figure 18.2: Illustration of crack locations in the yield stress gradient at $-130\text{ }^{\circ}\text{C}$.
- Figure 18.3: Benchmark of the procedure where nodal temperature are used to prescribe the stress-strain relation to elements.
- Figure 18.4: Failure assessment diagrams for cracks in laser welded joints, showing general (Option 1) and geometry and material specific (Option 3) failure assessment curves (FAC).
- Figure 18.5: Assessment of configurations tested at $-130\text{ }^{\circ}\text{C}$ using failure assessment diagrams. J is non-dimensionalised with the J_c measured on the weld configuration and load with the limit load of the configuration.
- Figure 18.6: Limit loads for cracks in the laser welded joint are shown in figure (a) and illustrated with respect to the yield stress gradient in figure (b).
- Figure 18.7: Limit load of a homogeneous crack tip material, as a function of crack tip yield stress.
- Figure 18.8: Plots of maximum hoop stress around the crack tip for experimental configurations. Stresses are normalised with the crack tip yield stress and distances with crack tip yield stress and measured J .
- Figure 18.9: Illustration of the configuration with crack on the fusion line, showing paths along which stress triaxiality was determined.
- Figure 18.10: Plastic zone size for slow bend Charpy geometry at failure at $-85\text{ }^{\circ}\text{C}$.
- Figure 18.11: Stress triaxiality ahead of the Charpy V-notch located on the fusion line.
- Figure 18.12: Contours of 2% principal plastic strain ahead of a fatigue pre-crack and Charpy notch.
- Figure 18.13: Stress triaxiality ahead of the fatigue pre-crack located on the fusion line.
- Figure 18.14: Evolution of plastic zone with increased loading, for a crack located at a fusion line.
- Figure 18.15: Evolution of plastic zone with increased loading, for a crack located in the heat affected zone.
- Figure 18.16: The process zone for a crack in a laser welded joint, defined with plastic zone size and contour of 2% plastic strain.
- Figure 18.17: Average crack initiation angles as a function of load for cracks on a fusion line and in HAZ. Weibull moduli are 22 and 30 for the base material and interpolated to the value of 10 for the weld metal.
- Figure 18.18: Probability density functions for a crack on the fusion line at low and high loads. Weibull modulus is 22. Measured angle from specimen LW-5 is superimposed.
- Figure 18.19: Probability density functions for a crack in the heat affected zone at low and high loads. Weibull modulus is 22. Measured angles from experiments are superimposed
- Figure 18.20: Probability density functions for a crack in the base material near heat affected zone, at low and high loads. Weibull modulus is 22. Measured angles from experiments are superimposed.

LIST OF TABLE CAPTIONS

Chapter 3

- Table 3.1: The location of the maximum stress intensity factors for sinusoidal cracks in (a) tension and (b) three-point bending.
- Table 3.2: The location of the local limit load for a surface touching sinusoidal cracks in tension and three-point bending.

Chapter 4

- Table 4.1: Evaluation of the transferability schemes, by comparing measured failure loads with those obtained using the Eq. (4.43).

Chapter 7

- Table 7.1: Chemical composition of BS4360 grade 50D steel
- Table 7.2: Crack depth in the re-entrant sector with number of cycles to coalescence, number of cycles in the test and crack growth direction

Chapter 8

- Table 8.1: The coalescence of two surface breaking defect by ductile tearing. The crack depths at positions A and B are shown at the end of each stage, with the load to initiate gross plasticity in each stage and the extension on the free surface, Δc .

Chapter 9

- Table 9.1: Results of experimental cleavage tests showing characterising crack dimensions, failure and limit loads of real defect and the failure load for the re-characterised defect, obtained from statistical procedure (in Chapter 4).
- Table 9.2: The physical and effective crack front lengths are given with the size and shape corrected mean values of fracture toughness, \bar{K}_{mat} , and the standard deviation, σ .

Chapter 13

- Table 13.1: Summary of average values of experimental data at a fixed toughness for high constrained ($a/w=0.5$) data.
- Table 13.2: Summary of average values of experimental data at a fixed toughness for unconstrained ($a/w=0.075$) data.
- Table 13.3: Summary of average values of irradiated constrained data ($a/w=0.5$) over a fixed toughness range.
- Table 13.4: Summary of average values of irradiated unconstrained data ($a/w=0.075$) over a fixed toughness range.

Chapter 14

- Table 14.1: Elastic mixity for range of plane strain mixed mode fields.
- Table 14.2: Chemical composition of En32 steel (in wt%).
- Table 14.3: Tensile properties of En32 steel.
- Table 14.4: η_{plCMOD} calibration factors for deep cracked ($a/w=0.5$) bend bars over a range of mode-mixities in asymmetric four-point-bending.
- Table 14.5: Results of fracture toughness tests on Mode I cracks in three-point bending at -90°C .
- Table 14.6: Results of fracture toughness tests on mixed-mode cracks having $a/w=0.5$ in asymmetric four-point bending at -90°C .

Chapter 17

- Table 17.1: Chemical composition of Lloyd's Grade L36N steel [in wt%].
- Table 17.2: Welding specifications.
- Table 17.3: Summary of tests on laser welds in contained yielding (-130°C). Test were performed on deep cracks ($a/w=0.5$) in four-point bending.
- Table 17.4: Summary of tests on laser welds in ductile-brittle transition at -60°C . Test were performed on deep cracks ($a/w=0.5$) in four-point bending.
- Table 17.5: Summary of tests on shallow cracked ($a/w=0.1$) laser welds at -90°C . Test were performed in three-point bending.

Chapter 18

- Table 18.1: Measured and computed average crack initiation angles using Weibull stress model for -130°C test conditions.

Chapter 1

INTRODUCTION

The development of fracture mechanics was originally motivated by a series of failures of high strength welded structures. The advent of welding in the first half of the nineteenth century changed the design and the production techniques of many steel structures including pressure vessels and ships. The fabrication of the first all welded merchant ship in 1921 started a design shift from all riveted to all welded construction. The economic and fabrication advantages of welding were overwhelming. However within a few years this new method was to experience a catalogue of disasters. The first all welded truss bridge collapsed in Belgium in 1931, followed by the first all welded tanker in 1943, which broke in half in the fitting docks. During the second world war dozens of catastrophic and near catastrophic failures of ships were reported. By 1953, out of 4694 all welded ships constructed, 233 had been subject to hull failure and 1056 had been subject to potentially dangerous structural failure. The cause of these failures was attributed to the stress concentrations and material defects. The fractures were found to be brittle low energy failures, promoted by low temperatures and the state of triaxiality at the flaw. Under these conditions steels can fail by cleavage, with minimal energy absorption.

The importance of evaluating defects in structures and components is still a critical area despite advances in manufacturing technology. Many engineering structures develop cracks during manufacture or during the operational life. Large flaws detected with non-destructive methods are repaired on site. Small flaws which are not detected or judged to be uneconomical to repair are left in the structure. During the operational life of a structure these small defects may grow under cyclic loading or propagate in a stable manner under overloads. Consequently small defects may interact and merge into larger complex defects. These may become critical to the integrity of the structure under fatigue, ductile tearing or cleavage. Defect assessment procedures, such as R6/4 (2001), BS 7910 (1999) and ASME Section XI (1992), recommend replacing complex defects with an idealised shape during a process known as defect re-characterisation. An assessment is then performed for the idealised defect. During re-characterisation interaction effects and the specific geometry of the complex defect are largely ignored. This may compromise the safety margins of the re-characterisation procedure. Significant efforts have been devoted into analysing defect

interaction in fatigue, which has led to revised interaction criteria in the BS 7910 and R6/4. Cleavage failures from complex and re-characterised defects and failures by ductile tearing have yet to be examined. To apply the re-characterisation procedure to these failure modes, the procedure must be demonstrated to give conservative assessments.

Cleavage failures from complex and re-characterised defects have been examined and detailed analyses of the test results have been performed using deterministic and probabilistic approaches. The deterministic analysis compares the maximum stress intensity factor or the J-integral, to a critical value obtained from tests on standard test geometries or from the Master curve. The probabilistic analysis is based on weakest link statistics extended to complex crack fronts and applied to cleavage failure. Both the deterministic and probabilistic approaches have been extended to include constraint effects. The interaction and coalescence of adjacent defects under ductile tearing is also examined and compared with results from finite element analysis.

Several aspects of low energy cleavage failures still remain unresolved despite 50 years of research to address catastrophic crack induced failures. Mechanistic models, such as the Ritchie-Knott-Rice model (Ritchie *et al* 1973), have been introduced with aim of relating fracture toughness with material microstructure and operating environment. Confidence in such models is dependant on the intrinsic material properties, such as the local fracture stress and the characteristic size scale of the microstructure. Correlations have been achieved for pressure vessel steels at temperatures on the lower shelf. Nevertheless the fundamental aspects of stress and strain induced cleavage failure have not been fully researched through the ductile-brittle transition. An aspect of cleavage failure from a mechanistic viewpoint is addressed in the work where a temperature dependence of critical parameters in the Ritchie-Knott-Rice model is examined using data on an A533B pressure vessel steel.

The operation of power plant is required to demonstrate pressure and temperature margins on critical components which may develop shallow cracks. A procedure is developed in the work to quantify enhanced temperature margins due to constraint loss by comparing the self-similar stress fields at a critical local fracture stress (the Ritchie-Knott-Rice approach) and through the Weibull stress. Agreement with the experimental data was achieved and the temperature dependence of the material parameters has been discussed.

Fracture toughness data are derived from standard test procedures, largely concerned with mode I toughness. Mode I toughness is usually the lowest and therefore most important failure mode. However the toughness for mixed-mode loading may also be required. As mixed-mode test are more difficult to perform or not available, it is important to be able to translate measured mode I toughness to a mixed-mode loading. Following Li (1997) and Karstensen (1996) a toughness mapping techniques may be developed that allows mode I toughness to be translated into mixed-mode toughness for stress controlled fracture. However the procedure has been hampered by the lack of a consistent experimental data. An experimental examination of the toughness of Mode I and mixed-mode I+II configurations was performed on a mild steel. The experimental data clearly show increased cleavage toughness for unconstrained mode I and mixed-mode fields and the correlation with the predictions from numerical models is excellent, giving confidence to data transferability schemes.

In real structures defect and flaws are frequently associated with welds. Consequently it is appropriate that part of the current work is concerned with the integrity of laser welded joints. Little experimental data is available in the literature and most of the data is concerned with impact testing. It is argued that a crack located in highly overmatched joints, such as laser welds, deviates into the base material. As the toughness of the base material is usually higher than that of the weld metal, and the values of the weld metal are difficult to obtain, this has led to the use of fracture toughness of the base material in integrity assessments. An experimental study was performed to examine fracture behaviour of laser welds under cleavage conditions in the ductile-brittle transition using deep and shallow cracks. The highest fracture toughness was consistently recorded for cracks located in the heat affected zones and lowest for weld metal or edges of heat affected zone. The crack paths propagated into the weld or the base material depending on the crack location in a spatially distributed fracture toughness profile. An attempt to model the experimental results with a probabilistic Weibull stress analysis has required material gradation to be considered.

The thesis is structured by initially presenting a review of the relevant literature, which allows the research to be placed in the context of existing knowledge. Initially elastic, and elastic-plastic fracture mechanics is reviewed, leading to a discussion of developments on two parameter fracture mechanics. A major component of the present work is concerned with re-characterisation of complex defects. The fundamental features of the problem are captured by an infinite sinusoidal crack, which is discussed in chapter 3. The influence of the crack front size and shape are discussed in Chapter 4 using weakest link arguments. The re-characterisation procedures proposed in BS7910, ASME XI and R6/4 are reviewed in chapter 5, followed by a numerical study of complex defects with re-entrant sectors in chapter 6. The results of an experimental programme on the development of complex defects in fatigue is presented in chapter 7. This is followed by an investigation into ductile tearing from complex defects in Chapter 8, and cleavage failures from complex and re-characterised defects in chapter 9.

The second part of the work addresses the micromechanics of cleavage failure, and starts with a literature review in chapter 10, followed by a discussion of temperature dependence of Ritchie-Knott-Rice model in chapter 11 using the existing experimental data of Sherry *et al* (2001). Procedures to evaluate enhanced temperature margins due to constraint loss are presented in chapter 12 and applied to the experimental data of Sherry *et al* (2001) in chapter 13.

In Chapter 14 a transferability scheme between mode I and mixed mode I/II cleavage toughness is presented and evaluated with the novel experimental data.

The final part of the work in chapters 15 to 18 addresses crack propagation in laser welded joints. In chapter 15 observations from numerical studies on crack propagation in strength overmatched materials are summarised and experimental data on laser welded joints are reviewed. Chapters 16 and 18 present results of the numerical examination into bi-material and graded joints, respectively, while chapter 17 summarises results of the experimental studies on integrity of laser welded joints.

The final conclusions are presented in chapter 19. Two journal papers and 8 conference papers have been published during the course of this work and summarised are attached in appendices A and B.

It is helpful to differentiate between the original contributions and the literature review. Chapters 1 and 2 are introduction of the problems considered and literature review on constraint based fracture mechanics, respectively.

In chapter 3 a parametric study of the infinite periodical sinusoidal defect identified the load redistribution along the crack front as a fundamental mechanism leading to amplified crack driving forces and loss of constraint in shallow cracked segments. A strong correlation has also been observed with the crack front perturbation.

In chapter 4 the weakest link statistics, which was derived to consider size effects in fracture, was extended to consider mechanics of curved crack fronts. A new approach is derived that allows spatial crack driving force or average strength of the material to be incorporated in the modified weakest link theory. On this basis a parameter transferability scheme between different geometries is derived and a new evaluation of the fracture resistance of semi-elliptical defect shapes is given. The chapter introduces the new approach that is later extensively used in chapter 9, as part of analysing cleavage fracture from complex defects.

Chapter 5 comprises a literature review on the re-characterisation of complex defects.

Chapter 6 presents new studies of crack tip parameters in complex defects with re-entrant sectors. In planar crack fronts a significantly amplified K and J are observed in the re-entrant sector, complemented by a negative T . This suggests low failure loads at low temperatures where K (or J) exceed K_{IC} before sufficient constraint effects develop in the re-entrant sector, which is a potentially dangerous situation. A similar, previously not reported, analysis of non-planar crack front with a shear step in the re-entrant sector shows crack tip parameters in the re-entrant sector are less amplified due to the presence of a shear step. Finally the implications of amplified crack tip parameters in re-entrant sectors on assessment using failure assessment diagrams have been determined.

In chapter 7 fatigue crack growth tests on interacting defects have shown amplified crack growth rates in the re-entrant sectors. This confirms the numerical calculations and highlights concern using simplified (level 1) defects assessment procedures for cleavage. A significant contribution in this chapter is the evaluation of the crack interaction criteria

in the context of recent revision to the defect assessment codes. As a direct result of this work, a significant progress has been made in revising the ASME Section XI flaw interaction rules (document IWA-3330) for cracks extending by fatigue.

Chapter 8 examines ductile tearing from complex defects with re-entrant sectors. This work is an original contribution to the behaviour of complex defects, which is significant for a practising engineer. Similar to chapter 7, the results of this work are being helpful to the ASME subcommittee working on flaw interaction rules for ductile tearing.

Chapter 9 reports on extensive cleavage tests on complex and re-characterised defects and the assessments using simplified and detailed numerical approaches. The deterministic and probabilistic analyses based on the novel weakest link statistics are used. Significantly it has been observed that the simplified defect assessment guidelines based on re-characterised defects are not safe when failure occurs at small fractions of the limit load. This result has merited significant attention and revised guidelines for defect assessment are given, that draw benefit of constraint and statistical size effects.

Chapters 10 presents a review of the literature on micromechanics of cleavage fracture.

In chapter 11 a temperature dependence of microstructural parameters in the Ritchie-Knott-Rice model is examined using existing fracture toughness data. The chapter clarifies the role of individual parameters and clearly shows that the microstructural distance has to be temperature dependent.

Chapters 12 and 13 present a new method to benefit from the constraint effect by quantifying constraint loss in a form of a temperature shift. The approach is based on using the temperature dependant yield stress at a temperature independent local fracture stress, which is a novel, simple and more accurate method than for example by expressing temperature shift from the constraint corrected temperature dependent J . The influence of irradiation on the constraint benefit is also examined.

Chapter 14 addresses a new topic: mixed-mode fracture. It presents and verifies a new failure locus that allows constraint of mode I fields to be unified with the mixity of mixed-mode I/II fields. The numerical work performed by Li (1997) has been complemented by

new and comprehensive sets of experiments on shallow and deep cracked mode I and mixed-mode I/II data using mild steel.

Chapters 15 to 18 also address a new topic, laser welded joints. Chapter 15 gives a detailed literature review on the recent advances in laser welding and the assessment of strength mismatch joints.

In chapter 16 the weakest link model is applied to study relative strengths and crack paths in bi-material systems, which differ by a strength at a fixed toughness. A new argument is introduced that allows connection to be made between the strength mismatch and the local fracture stress of each constituents.

Chapter 17 presents previously unreported results of cleavage fracture tests on laser welded joints. Significant new information relating to the fracture toughness and crack path deviations are reported, that are of interest in fracture assessments.

Chapter 18 presents various types of analysis that can be applied to laser welded joints, ranging from a simple R6 type of approaches to a detailed finite element local approach calculations.

In chapter 19 the main conclusions are drawn from the various studies reported in the thesis.

Chapter 2

INTRODUCTION TO FRACTURE MECHANICS

2.1 Linear elastic fracture mechanics

2.1.1 The Griffith criterion

Griffith (1921) considered the energetics of crack advance in brittle materials, such as glass. His studies focused on a plate of thickness, t , containing a through thickness centre crack of length $2a$ (Figure 2.1), remotely loaded with either a fixed displacement, or a uniformly distributed load. Griffith argued that crack propagation occurs, when the release of elastic strain energy is sufficient to produce a new surface.

$$\frac{\partial}{\partial A}(U_a - W) \geq \frac{\partial}{\partial A} U_\gamma \quad (2.1)$$

Here W represents external work, U_a is the strain energy of the body and U_γ is the energy required to form new surface, A . The right hand part of (2.1) represents the energy required to form two new crack surfaces, i.e. the resistance to crack growth, R :

$$R = \frac{\partial}{\partial A} U_\gamma = \frac{\partial}{\partial a} (2 \cdot 2aB\gamma_s) \quad (2.2)$$

Griffith considered the resistance to crack growth to be the specific surface energy necessary for decohesion of atomic bonds, as quantified by the surface energy density, γ_s . Orowan (1952) and Irwin (1957) subsequently modified Griffith's criterion after observing that even in brittle materials, like glass, the main energy absorption process was plastic flow in a small region at the crack tip. However the Griffith equation is still valid, if γ_s is interpreted as the total work per unit area resisting crack growth, including plastic work at the crack tip.

The left hand side of (2.1) is the difference between the external work done and the accumulated elastic strain energy and represents energy released during crack extension, defined as elastic energy release rate, G :

$$G = -\frac{\partial}{\partial A}(U_a - W) \quad (2.3)$$

The external work depends on the loading configuration and the geometry of the cracked body. Under fixed load conditions (Figure 2.2), the external work is given by the integral of the applied load, P , with respect to the work conjugate displacement, Δ :

$$W = \int_0^{\Delta} P \cdot d\Delta = P\Delta \quad (2.4)$$

The strain energy released as crack propagates from a to $a + da$ is:

$$U_a = \int_0^{\frac{\Delta}{2}} P \cdot d\Delta = P \cdot \frac{\Delta}{2} \quad (2.5)$$

giving the elastic energy release rate as:

$$G = -\frac{\partial}{\partial A}(-U_a) = \frac{P}{2B} \left(\frac{\partial \Delta}{\partial a} \right)_P \quad (2.6a)$$

In the case of fixed displacement ($\Delta_1 = \Delta_2$), no work is done by the external forces, such that energy available for crack extension is the accumulated elastic strain energy:

$$G = -\frac{\partial}{\partial A}(U_a) = -\frac{\Delta}{2B} \left(\frac{\partial P}{\partial a} \right)_\Delta \quad (2.6b)$$

which reduces with crack extension. By introducing a compliance, $C = \Delta/P$, it can be shown that

$$G = \frac{P^2}{2B} \frac{\partial C}{\partial a} \quad (2.7)$$

for both load and displacement control.

The elastic strain energy of an infinite body containing a Griffith's crack is given by Inglis (1913) as:

$$U_a = \frac{\pi \sigma^2 a^2 B}{E'} \quad (2.8)$$

where $E' = E$ is Young's modulus for plane stress and $E/(1-\nu^2)$ for plane strain, ν being the Poisson's ratio. The remotely applied critical stress required for crack extension can then be expressed for an ideally brittle material as:

$$\sigma_c = \sqrt{\frac{2E'\gamma_s}{\pi a}} \quad (2.9)$$

where the only resistance to crack propagation considered is the resistance to decohesion of atomic bonds.

2.1.2 The elastic stress at the crack tip

Local criteria for crack advance consider the nature of the near crack-tip stress, strain and displacement fields. For this purpose a through thickness crack in a linear elastic solid under remote tension is considered, as shown in Figure 2.1. A right-handed Cartesian coordinate system $\{x,y,z\}$ is employed at the center of the crack, while cylindrical coordinates $\{r,\theta,z\}$ are centered at the crack tip. The stresses appearing in an elementary unit of material ahead of crack tip can be expressed by a stress function, ϕ , that satisfies boundary conditions, equilibrium conditions and the compatibility. By using an appropriate complex stress function, Westergaard (1939) expressed the asymptotic stresses at the crack tip in cylindrical coordinates for a mode I loading as a series expansion:

$$\begin{aligned}\sigma_x &= \frac{\sigma\sqrt{\pi a}}{\sqrt{2\pi r}} \cos\frac{\theta}{2} \left(1 - \sin\frac{\theta}{2} \sin\frac{3\theta}{2}\right) + \dots \\ \sigma_y &= \frac{\sigma\sqrt{\pi a}}{\sqrt{2\pi r}} \cos\frac{\theta}{2} \left(1 + \sin\frac{\theta}{2} \sin\frac{3\theta}{2}\right) + \dots \\ \sigma_{xy} &= \frac{\sigma\sqrt{\pi a}}{\sqrt{2\pi r}} \sin\frac{\theta}{2} \left(\cos\frac{\theta}{2} \cos\frac{3\theta}{2}\right) + \dots\end{aligned}\quad (2.10)$$

This is identical to the first term of the Williams (1957) series expansion of the elastic stress field in cylindrical coordinates:

$$\sigma_{ij}(r, \theta) = A_{ij}(\theta)r^s + B_{ij}(\theta)r^t + C_{ij}(\theta)r^u + \dots \quad (2.11)$$

where $\{s,t,u,\dots\}$ are $\{-1/2,0,1/2,\dots\}$. The corresponding Cartesian displacements can be derived through the elastic stress-strain relations:

$$\begin{aligned}e_x &= \frac{1}{E}[\sigma_x - \nu(\sigma_y + \sigma_z)] \\ e_y &= \frac{1}{E}[\sigma_y - \nu(\sigma_z + \sigma_x)] \\ e_z &= \frac{1}{E}[\sigma_z - \nu(\sigma_x + \sigma_y)] \\ e_{xy} &= \frac{\sigma_{xy}}{2G}, \quad e_{yz} = \frac{\sigma_{yz}}{2G}, \quad e_{zx} = \frac{\sigma_{zx}}{2G}\end{aligned}\quad (2.12)$$

where G represents the shear modulus, $G = \frac{E}{2(1+\nu)}$ and ν is Poisson's ratio. The strains can be related to the Cartesian displacements (u,v,w) through the strain-displacement equations, here given for a two dimensional problem:

$$e_x = \frac{\partial u}{\partial x}, \quad e_y = \frac{\partial v}{\partial y}, \quad e_{xy} = \frac{\partial u}{\partial y} + \frac{\partial v}{\partial x} \quad (2.13)$$

Strains must fulfill the compatibility equation:

$$\frac{\partial^2 e_x}{\partial y^2} + \frac{\partial^2 e_y}{\partial x^2} = \frac{\partial^2 e_{xy}}{\partial x \partial y} \quad (2.14)$$

For simplicity it is convenient to consider two limiting cases: thin plates and long bars. Thin plates or membranes are effectively subject to in-plane stresses only: the condition of plane stress. The out-of-plane stresses ($\sigma_z, \tau_{zx}, \tau_{zy}$) are zero on both free surfaces ($z=\text{constant}$) and the through thickness stress gradients can be assumed to be negligible:

$$\begin{aligned} \sigma_z = \sigma_{zx} = \sigma_{yz} = 0, \quad \frac{\partial \sigma_z}{\partial z} = \frac{\partial \sigma_{zx}}{\partial z} = \frac{\partial \sigma_{yz}}{\partial z} = 0 \\ e_z = -\frac{2(1+\nu)}{E} \nu (\sigma_x + \sigma_y) \end{aligned} \quad (2.15)$$

The deformation of a slice of material near the center of a thick plate is restrained in the out-of-plane direction. The adjacent material imposes an out-of-plane stress, limiting the deformation to three in-plane components of strain (e_x, e_y, e_{xy}). This defines the plane-strain condition, in which:

$$\begin{aligned} e_z = e_{yz} = e_{zx} = 0, \quad \frac{\partial e_z}{\partial z} = \frac{\partial e_{zx}}{\partial z} = \frac{\partial e_{yz}}{\partial z} = 0 \quad \text{and} \\ \sigma_z = \nu (\sigma_x + \sigma_y) \end{aligned} \quad (2.16)$$

The displacement field (u, v) ahead of the crack tip for plane strain or plane stress conditions under tensile loading are of the form:

$$\begin{aligned} u = 2(1+\nu) \frac{\sigma \sqrt{\pi a}}{E} \sqrt{\frac{r}{2\pi}} \cos \frac{\theta}{2} (\kappa - 1 + 2 \sin^2 \frac{\theta}{2}) \\ v = 2(1+\nu) \frac{\sigma \sqrt{\pi a}}{E} \sqrt{\frac{r}{2\pi}} \sin \frac{\theta}{2} (\kappa + 1 - 2 \cos^2 \frac{\theta}{2}) \end{aligned} \quad (2.17)$$

where κ is defined as:

$$\begin{aligned} \kappa = 3 - 4\nu \quad \text{in plane strain and} \\ \kappa = \frac{3 - \nu}{1 + \nu} \quad \text{in plane stress.} \end{aligned} \quad (2.18)$$

Close to the crack tip the first, singular, term is dominant and the strength of the singularity is measured by the stress intensity factor, K , (Irwin (1958)). In an elastic body the elastic stresses near the crack tip must be proportional to the remotely applied stress. A dimensional argument shows that K must also be proportional to the square root of a characteristic dimension, such as crack length:

$$K = Y \sigma \sqrt{\pi a} \quad (2.19)$$

In finite geometries the function Y describes the effect of geometry and loading on the stress singularity, and is tabulated for many standard geometries in compendia (Tada *et al* (1973), Murakami (1987)). Solutions similar to Eq. (2.10) can be derived for the displacements in the vicinity of the crack as well as the stresses and displacements under mode II and mode III loading (Anderson (1995)). Under load the crack flanks may displace in combination of three characteristic modes as illustrated in Figure 2.3; the tensile mode, denoted with subscript I, the in-plane shear or sliding mode II and in the out-of-plane shear or tearing mode III.

For a linear elastic material the elastic energy release rate, G , and the stress intensity factor, K , are related, as evidenced by the Griffith criterion. In Mode I loading:

$$G_I = \frac{K_I^2}{E'} \quad (2.20)$$

where $E' = E$ in plane stress and $E' = E/(1 - \nu^2)$ in plane strain.

2.1.3 Small scale yielding

The argument so far has been based on linear elasticity for which a stress singularity is predicted to occur at the crack tip. In metals plastic deformation occurs when the yield criterion is met. When the plastic zone ahead of the crack is small compared to the dimensions of the body and crack length, the arguments of small scale yielding may be invoked. Under these conditions the linear elastic stress intensity factor approach can be used to characterise the stresses close to the crack tip but outside the plastic zone, as illustrated in Figure 2.4, in an asymptotic manner. The exact determination of the size and shape of a plastic zone through-out the crack front length frequently presents a challenge (Schijve (2003)), due to the transition between plane stress to plane strain stress states. A simplified approach to crack tip plasticity is frequently used, where either, the plastic zone at an approximated shape is determined (Irwin (1960), Dugdale (1960)) or a yield criteria is employed to estimate the shape of the plastic zone. An estimation of the size of the crack tip plastic zone has been made by Irwin (1960) by substituting critical value of stress intensity factor and the uniaxial yield stress, σ_0 , in the stress field of Eq. (2.10) for $\theta = 0$:

$$\sigma_y = \frac{K_c}{\sqrt{2\pi r_p}} = \sigma_0 \Rightarrow r_p = \frac{1}{2\pi} \left(\frac{K_c}{\sigma_0} \right)^2 \quad (2.21)$$

Irwin (1960) considered a circular plastic zone in an elastic-perfectly plastic material and observed that the effective plastic zone must be larger to accommodate truncation of the stresses above the yield stress, as illustrated in Figure 2.5. Similar conclusions were drawn by Dugdale (1960), who assumed that all plastic deformation is confined to a strip of material ahead of the crack, known as the strip yield model of crack tip plasticity.

Models that determine the shape of the crack tip plastic zone are based on the von Mises or Tresca yield criteria, applied to perfectly plastic material. The von Mises yield criteria can be expressed in terms of principal stresses, $(\sigma_1, \sigma_2, \sigma_3)$ as:

$$(\sigma_1 - \sigma_2)^2 + (\sigma_2 - \sigma_3)^2 + (\sigma_3 - \sigma_1)^2 = 2\sigma_0^2 \quad (2.22)$$

For the two-dimensional problem of plane stress under Mode I the in-plane principal stresses near the crack tip are :

$$\begin{aligned} \sigma_1 &= \frac{K_I}{\sqrt{2\pi r}} \cos \frac{\theta}{2} \left(1 + \sin \frac{\theta}{2}\right) \\ \sigma_2 &= \frac{K_I}{\sqrt{2\pi r}} \cos \frac{\theta}{2} \left(1 - \sin \frac{\theta}{2}\right) \end{aligned} \quad (2.23)$$

This gives the plastic zone shape, $r(\theta)$, as:

$$r(\theta) = \frac{1}{4\pi} \left(\frac{K_I}{\sigma_0} \right)^2 \left(1 + \frac{3}{2} \sin^2 \theta + \cos \theta \right) \quad (2.24a)$$

For plane strain, $\sigma_3 = \nu(\sigma_1 + \sigma_2)$, and the plastic zone shape is obtained from:

$$r(\theta) = \frac{1}{4\pi} \left(\frac{K_I}{\sigma_0} \right)^2 \left(\frac{3}{2} \sin^2 \theta + (1 - 2\nu)^2 (1 + \cos \theta) \right) \quad (2.24b)$$

The plastic zone shapes are illustrated in Figure 2.6. It should be noted that these estimates fail to satisfy the compatibility or the stress-strain equations. These plastic zone models define the limiting cases for real 3-dimensional bodies, with plane stress approximation for the surface of the body, plane strain representation in the center and a transition region defined by the stress triaxiality at the crack tip.

The stress state at the elastic-plastic boundary depends on the plastic zone size relative to the plate thickness (Anderson (1995)). In an uncracked plate a state of plane stress exists and must also exist in a cracked plate at a sufficiently remote distance from the crack. The material close to crack tip is loaded to higher stresses than the surrounding material and

tries to contract in the x and z directions. This is prevented by surrounding material imposing a triaxial state of stress at the crack tip. When the size of the plastic zone is in the order of the plate thickness, plane stress conditions prevail at the elastic-plastic boundary, transverse yielding reduces the stress triaxiality at the crack tip, resulting in greater critical values of stress intensity, K_C . With decreasing plastic zone sizes relative to the thickness of the plate, the transverse yielding becomes constrained and plane strain conditions develop at the boundary. The critical stress intensity factor saturates at a material property, defined as K_{IC} , close to an empirical thickness of $2.5\left(\frac{K}{\sigma_0}\right)^2$, as illustrated in Figure 2.7. ASTM E399-88 (1988) method uses this criteria to define the size requirement for a plane strain fracture toughness test.

Small scale yielding requires the plastic zone to be much smaller than the relevant crack and body dimensions. The validity criteria for use of linear elastic fracture mechanics compare the plastic zone size with the crack length, a , the unbroken ligament, $w-a$, width, w and the thickness, B , (ASTM E399 (1988)):

$$\begin{aligned} a &\geq 2.5\left(\frac{K_{IC}}{\sigma_0}\right)^2, \quad w-a \geq 2.5\left(\frac{K_{IC}}{\sigma_0}\right)^2, \\ w &\geq 2.5\left(\frac{K_{IC}}{\sigma_0}\right)^2, \quad B \geq 2.5\left(\frac{K_{IC}}{\sigma_0}\right)^2 \end{aligned} \quad (2.25)$$

K_{IC} is the critical plane strain value of the stress intensity factor and σ_0 is the uniaxial yield stress. Under these restrictions the critical value of stress intensity factor is considered to be a material property and is termed the fracture toughness. The ASTM E399-88 or ESIS P1-92 are frequently used to establish the fracture toughness values by testing edge cracked bars or compact tension specimens.

2.1.4 Crack tip stress field under mixed-mode loading

In mixed-mode I+II plane strain conditions the crack tip stress field can be written in polar coordinates as:

$$\begin{aligned} \begin{Bmatrix} \sigma_r \\ \sigma_\theta \\ \sigma_{r\theta} \end{Bmatrix} &= \frac{K_I}{\sqrt{2\pi r}} \begin{Bmatrix} \cos\frac{\theta}{2}(1 + \sin^2\frac{\theta}{2}) \\ \cos^2\frac{\theta}{2} \\ \sin\frac{\theta}{2}\cos^2\frac{\theta}{2} \end{Bmatrix} + \frac{K_{II}}{\sqrt{2\pi r}} \begin{Bmatrix} \sin\frac{\theta}{2}(1 - 3\sin^2\frac{\theta}{2}) \\ -3\sin\frac{\theta}{2}\cos^2\frac{\theta}{2} \\ \cos\frac{\theta}{2}(1 - 3\sin^2\frac{\theta}{2}) \end{Bmatrix} \\ \sigma_{rz} &= \sigma_{\theta z} = 0 \end{aligned} \quad (2.26)$$

Under fully elastic conditions the ratio of tension to shear can be defined by an elastic mixity parameter introduced by Shih (1974):

$$M^e = \frac{2}{\pi} \tan^{-1} \left(\frac{K_I}{K_{II}} \right) = \frac{2}{\pi} \tan^{-1} \left\{ \lim_{r \rightarrow 0} \frac{\sigma_{\theta\theta}(r,0)}{\sigma_{r\theta}(r,0)} \right\} \quad (2.27)$$

Under elastic-plastic conditions the near tip mode mixity is defined by a plastic mixity factor:

$$M^p = \frac{2}{\pi} \tan^{-1} \left\{ \lim_{r \rightarrow 0} \frac{\sigma_{\theta\theta}(r,0)}{\sigma_{r\theta}(r,0)} \right\} \quad (2.28)$$

which gives the relative contributions of the local shear to tension in the plastic zone at the crack tip. The remote elastic mixity and the local plastic mixity are given by Shih (1974) for plane strain small-scale yielding conditions and are generally not identical.

2.2 Elastic – plastic fracture mechanics

Linear elastic fracture mechanics (LEFM) is appropriate as long as crack tip plasticity is small compared to the dimensions of the body. In tough materials large plastic zones invalidate the LEFM approach. Under elastic-plastic conditions, criteria for crack propagation include a critical value of crack tip opening (Wells (1961)) or an argument based on the J-integral (Rice (1968), Eshelby (1968), Cherepanov (1967)).

2.2.1. The crack tip opening displacement (CTOD)

Wells (1961) observed that the stresses at the crack tip are limited by yielding and suggested that plastic strains directly ahead of the crack tip must be the controlling parameter in fracture. Wells argued that the displacement of crack flanks close to the crack tip, Figure 2.8, is a measure of the crack tip plastic strains. Failure is assumed to occur at a critical value of the local plastic strain, which is considered to be a material property. Wells utilised the strip yield model of Dugdale (1960) to express the crack tip opening displacement, δ , in terms of the stress intensity factor:

$$\delta = \frac{4}{\pi} \frac{K_I^2}{E' \sigma_o} \quad (2.29)$$

Under large scale plasticity the small scale yielding expression is modified by a constant λ , which depends on the strain hardening properties (Burdekin and Stone (1966)):

$$\delta = \frac{K_I^2}{\lambda E' \sigma_0} \quad (2.30)$$

The geometry of crack blunting prior to onset of crack advance hampers the unambiguous determination of δ . Rice (1968) and Rice and Johnson (1970) have determined λ computationally and experimentally and found to be 1 for plane stress and 2 for plane strain conditions.

The applicability of the CTOD criterion to fracture mechanics is twofold: firstly the postulate of a critical value of crack opening displacement as a measure of the onset of crack propagation suggests failures at the same values of CTOD regardless of the crack length. This allows the use of a laboratory specimens to measure the critical CTOD, avoiding the need for large scale testing (Robinson and Tetelman (1973)). Secondly for materials with high toughness valid K_{IC} values cannot be determined. These materials could be characterised by a critical CTOD, through the COD Design Curve approach suggested by Burdekin and Stone (1966).

2.2.2 The J-integral

The evaluation of a stress, strain and displacement fields for a non-linear elastic material through an energy balance approach was proposed independently by Cherepanov (1967), Eshelby (1968) and Rice (1968). The J-integral is a path independent contour integral which can be understood as a measure of the difference between the potential energy of a non-linear elastic cracked body, when crack advances by some infinitesimal amount. Expressing the total potential energy of a body as $U=U_a-W$, the change in potential energy per unit thickness, when crack advances by an infinitesimal amount, is given as:

$$J = -\frac{1}{B} \frac{\partial U}{\partial a} \quad (2.31)$$

For a linear elastic material $-\frac{1}{B} \frac{\partial U}{\partial a} = G$, giving the identity:

$$J = G \quad (2.32)$$

The J-integral is based on an energy conservation theorem applied to a non-linear elastic behavior and can be used to model the plastic behavior, providing that no unloading occurs, since plasticity is irreversible. Following Eshelby (1968), Rice (1968) considered a

closed contour path in a stressed solid and obtained the change in potential energy due to the internal and external work done (Figure 2.9) in a two-dimensional problem as:

$$J = \int_{\Gamma} \left(w dy - T \frac{\partial u}{\partial y} ds \right) \quad (2.33)$$

The J-integral is defined as a counter-clockwise contour integral, where the w is the strain energy density ($w = \int_0^{\epsilon} \sigma_{ij} d\epsilon_{ij}$), T is the traction vector normal to the contour integration path, u is the displacement vector and s is the arc length. This description is based upon deformation plasticity or equivalently non-linear elasticity.

An important feature of the J-integral is its path independence. This allows the selection of any closed contour around the crack tip, which can be taken to simplify the analysis. The postulate also allows the transferability of the values between geometries.

In order to develop the J-integral as a fracture criterion, the critical values, J_C that characterises the resistance to crack growth must be established. Under linear conditions the identity $J=G$ gives a simple correlation between the values of J_{IC} and G_{IC} and K_{IC} . For non-linear elastic behavior it was shown experimentally by Begley and Landes (1972a, 1972b) and Kobayashi *et al* (1973) that critical values of J_C can be determined from load-displacement diagrams through the compliance, or more recently, using the crack mouth opening measurement (Sumpter (1987), Kirk and Dodds (1993)). In both cases the area under the load-displacement or crack mouth opening curve represents the plastic work done, which can be related to the J-integral through a calibration factor. Details of the procedure are given later.

The J-integral is related to the crack tip opening displacement by an expression:

$$J = \lambda \sigma_o \delta \quad (2.34)$$

where λ is a tabulated function of σ_o/E and strain hardening exponent (Robinson (1976), Shih (1981)).

The analogy between J and G suggests that J could also be a stress field parameter as is G through the $K^2 = GE'$ relation. This is the case for a linear elastic material, where $J = G$,

but it remains valid for a non-linear elastic material, such as described by the Ramberg-Osgood stress-strain relation:

$$\frac{e}{e_0} = \frac{\sigma}{\sigma_0} + \alpha \left(\frac{\sigma}{\sigma_0} \right)^n \quad (2.35)$$

σ_0 and e_0 are reference stresses and strains and n is the strain hardening exponent. The curve fitting constant σ_0 is often identified with the yield stress. However with this identity, e_0 does not correspond to the yield strain at $\sigma=\sigma_0$, but the corresponding strain becomes $e=(1+\alpha)e_0$. The relation is general and gives good description for materials with large strain hardening capacity (austenitic steels). For mild steels with defined upper and lower yield points the relation can be meaningfully fitted only at strains that are large compared to the yield strain. Through out the thesis the material flow behavior is therefore described by the elastic deformation below the yield stress, σ_0 and merged into Ramberg-Osgood relation for strains that are large compared to the yield strain.

Hutchinson (1968) and Rice and Rosengren (1968) unified fields close to the crack tip, where the elastic strains are assumed to be negligible and have consequently simplified the stress-strain relation to:

$$\frac{e}{e_0} = \alpha \left(\frac{\sigma}{\sigma_0} \right)^n \quad (2.36)$$

On this basis the strength of the stress and strain singularities in non-linear elastic material is a function of material flow properties:

$$\sigma(r) \propto \frac{D}{r^{\frac{1}{n+1}}} \quad \text{and} \quad e(r) \propto \frac{C}{r^{\frac{n}{n+1}}} \quad (2.37)$$

C and D are proportionality constants that define the amplitude of the stress and strain singularities. The singularities given by Eq. (2.37) are referred to as HRR singularities after Hutchinson (1968) and Rice and Rosengren (1968), and are for a non-linear material under Mode I:

$$\begin{aligned} \sigma_{ij} &= \sigma_0 \left[\frac{J}{\alpha r \sigma_0 e_0 I_n} \right]^{\frac{1}{n+1}} \tilde{\sigma}_{ij}(\theta, n) \\ e_{ij} &= \alpha e_0 \left[\frac{J}{\alpha r \sigma_0 e_0 I_n} \right]^{\frac{n}{n+1}} \tilde{e}_{ij}(\theta, n) \end{aligned} \quad (2.38)$$

$\tilde{\sigma}_{ij}(\theta, n)$ and $\tilde{\epsilon}_{ij}(\theta, n)$ are tabulated functions of angle, strain hardening exponent, the mode of loading and whether plane stress or plane strain condition is assumed. The form of the expression for the strains is written two ways in the literature (EPRI (1981), Anderson (1995)), depending on whether the angular function $\tilde{\epsilon}_{ij}(\theta, n)$ is allowed to contain α . I_n is an integration constant, which is a function of the strain hardening exponent. Equation (2.38) suggests that J can be regarded as quantifying the amplitude of the singularity of the elastic-plastic crack tip field, in a similar way to the way in which K defines the amplitude of singularity of the elastic crack tip stress field. Indeed, for a linear elastic behavior $n=1$ and Eq. (2.37) reduces to the Westergaard field, given by Eq.(2.10).

The HRR field is a small geometry change solution in which the crack tip is essentially assumed to remain sharp. The HRR field is regarded as being equivalent to the asymptotic small-scale yielding field that develops under contained plasticity ahead of cracks in real structures. As crack tip undergoes large geometry changes during the crack tip blunting, the HRR and small-scale yielding fields field remain a valid descriptor of the deformation field at distances large compared to the crack tip opening displacement, $r \geq 2J/\sigma_0$ (McMeeking (1977)).

The application of J-integral concept to fracture mechanics is limited by its definition on deformation plasticity, whereas crack extension in real structures follows incremental theory of plasticity. A path dependence of J-integral inside the zone of large strains ($r < 2\delta$) has also been observed (McMeeking (1977)).

2.3 Two parameter characterisation

2.3.1 Limitation of Single Parameter Characterisation

Single parameter or J-dominant fields, such as the HRR or the small-scale yielding fields, can be uniquely described by a single parameter, such as J or δ . Single parameter characterisation of the near tip field requires that the dominant singularity completely encompasses the zone of large strains. The analyses of Rice and Johnson (1970) and McMeeking (1977) using blunt crack tips and finite strain theory shows that the maximum stresses occur close to 2δ and merge with the small geometry change solution as given by

HRR and small-scale yielding field. As there is a unique relation between K , J , and δ in small scale yielding, deformation and fracture can be described with a single parameter.

McClintock (1968) argued that the crack tip stress field in a fully plastic fracture is not unique, but dependant on the geometry and the type of loading. In order to determine the limits of J-dominance, McMeeking and Parks (1979) compared the stress ahead of the crack in finite geometries such as edge cracked bend bars or center cracked panels with a reference solution. The reference solution used was the large geometry change solution in small scale yielding. In contrast Shih and German (1981) used the HRR field as the reference solution. Both McMeeking and Parks (1979) and Shih and German (1981) found a range of crack geometries in which J alone no longer uniquely characterises the crack tip fields and the J-dominance depends on geometry and mode of loading. This specifies requirements on a size of test specimens to obtain near-tip stress triaxialities corresponding to those of small-scale yielding. Crack-tip fields in geometries which meet such geometric constraints are defined as J-dominant fields. A dimensional argument shows that the J-dominance may be expressed through a size requirement of the form:

$$c > \mu \frac{J}{\sigma_0} \quad (2.39)$$

where the characteristic dimension, c , is identified with the unbroken ligament in deeply edge cracked geometries and must be greater than $25J/\sigma_0$ for bending and $200J/\sigma_0$ for tension.

Al-Ani and Hancock (1991) examined the size requirements for valid J-dominant field in deep and shallow edge cracked bars using full field solutions. Using small and finite strains, the near tip stresses closely correspond to the HRR field, when plasticity is confined to the ligament, such as occurs in deep cracks having $a/w > 0.3$ in bending and $a/w > 0.5$ in tension. Under small-scale yielding conditions such crack tip fields can be uniquely described with a single parameter. In shallow cracked geometries ($a/w < 0.3$ in bending and $a/w < 0.5$ in tension) the plasticity breaks through to the crack face and the stresses ahead of the crack fall from the small scale yielding values characteristic of deep cracks to another geometry dependant distribution. In deep cracks the ligament determines the plastic flow and characterizes the stress field and can be identified as the size requirement for the valid J-dominant characterization. In shallow cracks Al-Ani and

Hancock (1991) pointed out that the crack length is a more appropriate controlling dimension. Al-Ani and Hancock showed that J-dominance was lost before $J \leq \frac{a\sigma_o}{200}$ in shallow edge crack bend bars and correlated the observations with the development of a compressive T-stress acting parallel with the crack flanks.

2.3.2 Two parameter characterization

Larsson and Carlsson (1973) used a boundary layer technique introduced by Rice and Tracey (1973) to investigate the development of crack tip plasticity in compact tension, double edge cracked and centre cracked panels under small scale yielding conditions. The crack configurations were also modelled using full field solution. Boundary layer technique replaces the actual elastic-plastic problem by a boundary layer problem, in which a semi-infinite crack in an infinite body is considered. The full field boundary conditions are replaced by the asymptotic boundary conditions, applied as displacement to the outer domain of the model, as illustrated in Figure 2.10. Contained yielding is modelled by restricting plasticity to a small fraction of the domain radius such that the outer field exhibits an elastic field characterised by the stress intensity factor. Under contained yielding the same crack tip stress fields develop in boundary layer model as in the actual geometry subject to the same stress intensity factor. Boundary layer formulations are thus computationally efficient techniques to study near crack tip stress fields. However Larsson and Carlsson observed significant difference between plastic zone radii obtained from boundary layer model compared to full field analyses of complete geometries loaded to the same stress intensity factor. Their results showed significant deviations from the small scale yielding solutions, characterised by a single parameter, such as J . Larsson and Carlsson showed that by adding a non-singular stress parallel with the plane of the crack to the boundary tractions of the boundary layer model, the agreement between plastic zone radii was achieved. The non-singular stress in the outer elastic field was determined as the difference between σ_{xx} components of the detailed finite element model and the boundary layer computation, and expressed as the proportion of the applied load, K/\sqrt{a} . Following Williams (1957), Rice (1974) expressed the in-plane stress components of the elastic near tip stress field as:

$$\begin{bmatrix} \sigma_{xx} & \sigma_{xy} \\ \sigma_{yx} & \sigma_{yy} \end{bmatrix} = \frac{K_I}{\sqrt{r}} \begin{bmatrix} f_{xx}(\theta) & f_{xy}(\theta) \\ f_{yx}(\theta) & f_{yy}(\theta) \end{bmatrix} + \begin{bmatrix} T & 0 \\ 0 & 0 \end{bmatrix} + \text{terms which vanish at crack tip} \quad (2.40)$$

and showed that near the crack tip the non-singular stresses amount to the uniform stress, $\sigma_{xx}=T$. Significantly, Rice (1974) showed that the effects of J and T on the crack tip stress fields are independent, that is the effects of singularity and constraint can not be described by a single parameter.

Betegón and Hancock (1991) examined plane strain elastic-plastic crack tip fields under contained yielding using modified boundary layer technique based on the first two terms, K and T , of the elastic field. Betegón and Hancock observed that a compressive T -stress reduces the stresses ahead of the crack by an amount, which is independent of the radial distance, corresponding to the introduction of the second term to the boundary layer tractions. The significance of their result was discussed by Du and Hancock (1991) using modified boundary layer formulation in perfect plasticity, where T -stress was observed to influence the form of the asymptotic fields. Directly ahead of the crack the fields exhibit a constant stress sector. The stress in this sector differs hydrostatically depending on the T -stress, such that the full Prandtl field is obtained in the limit of a positive (tensile) T -stress. A compressive T -stress influences the radial span of the centred fan sectors and reduces the mean stresses in the constant stress sector ahead of the crack. Al-Ani and Hancock (1991) observed a similar effect in the strain hardening plasticity of deep and shallow cracked bend bars and correlated the compressive T -stresses with the loss of in-plane constraint. The influence of the T -stress on the crack tip plastic zone is illustrated in Figure 2.11 after Du and Hancock (1991). Compressive T -stresses enlarge the maximum radius of plastic zones and causes the plastic lobes to swing forward. In contrast a tensile T -stress reduces the maximum size of the plastic zones and causes lobes to swing towards the crack flanks. The T -stress is proportional to the applied load and the $T=0$ field is significant in the sense that applies in all geometries at low loads, hence can be used to define conditions of small scale yielding. Betegón and Hancock (1991) observed that geometries which maintain J -dominance are characterised by the zero or positive T stress, while geometries with the negative T stress can be described by a two parameter characterisation using J and T .

2.3.3 Determination of the T-stress

The T-stress can be determined directly from the stress or the displacement field in a plane strain finite element analysis. Rearranging the first two terms of the Williams expansion gives the T-stress:

$$T = \lim_{r \rightarrow 0} \left(\sigma_{ij} - \frac{K}{\sqrt{2\pi r}} f_{ij}(\theta) \right) \delta_{1j} \delta_{i1} \quad (2.41)$$

The simplest approach is to examine the stress field in the crack flanks, where $f_{ij}(\theta) = 0$ for $\theta = \pi$ and the T-stress is identical to σ_{xx} .

Following Leivers and Radon (1986) the elastic T-stress can be expressed in terms of a biaxiality parameter β as:

$$\beta = \frac{T\sqrt{\pi a}}{K} \quad (2.42a)$$

or

$$\frac{T}{\sigma} = \lambda\beta, \quad (2.42b)$$

where λ is the calibration constant for the stress intensity factor, which depends on the loading and geometry. In a linear elastic analysis λ and β can be evaluated separately for tension and bending and then superimposed, giving the T-stress in the form:

$$T = \lambda_t \beta_t \sigma_t + \lambda_b \beta_b \sigma_b \quad (2.43)$$

where subscripts t and b represent tension and bending. This formulation is particularly useful for determining higher order terms from shell analyses in which the crack is represented by line springs, as discussed in Chapters 3 and 6.

2.3.4 The Q parameter

O'Dowd and Shih (1991a, 1991b) investigated higher order terms in the elastic-plastic stress field by comparing detailed numerical solutions with the two parameter boundary layer solutions and described the stresses as a series expansion with the singular term, the constraint parameter Q and the higher order terms which vanish remote from crack tip. They parameterised the constraint with the elastic-plastic parameter, Q, and argued that is independent of distance ($z \ll 1$) and of the angular position in the forwards stress sector ($-\pi/4 < \theta < \pi/4$) and scales with the yield stress:

$$\sigma_{ij} = \sigma_o \left[\frac{J}{\alpha \sigma_o \epsilon_o I_n r} \right]^{\frac{1}{n+1}} f_{ij}(n, \theta) + Q \left(\frac{r \sigma_o}{J} \right)^z \tilde{\sigma}_{ij}(n, \theta) + \text{higher order terms} \quad (2.44)$$

On this basis Q is defined as:

$$Q = \lim_{\frac{r \sigma_o}{J} \rightarrow 2} \frac{\sigma_{ij} - \sigma_{HRR}}{\sigma_o} \quad \text{at } \theta=0 \text{ and } \frac{r \sigma_o}{J} = 2 \quad (2.45)$$

where σ_{HRR} represents the HRR stress field and $Q\sigma_o$ scales with the hydrostatic stresses. The small-scale yielding field ($T=0$) is also used to determine Q as HRR and SSY fields are within 2% directly ahead of the crack (Du and Hancock (1991)). In small-scale yielding, T and Q are uniquely related and both can be used as a measure of the loss of constraint. Betegón and Hancock (1991) have given a relation based on the numerical calculations for $n=13$:

$$Q = 0.64 \frac{T}{\sigma_o} - 0.4 \left(\frac{T}{\sigma_o} \right)^2 \quad (2.46)$$

O'Dowd and Shih (1991a,b) observed that the elastic-plastic crack tip fields of deep and shallow edge cracked bars are deviatorically similar, but differ hydrostatically. The magnitude of the hydrostatic stresses can be scaled with either, the elastic plastic parameter Q or with the T-stress acting in the enveloping elastic field. There is no unique choice for the second parameter to describe the crack tip stress field. The T-stress is based on an asymptotic elastic stress field solution. Although it is formally rigorous in contained yielding, it has no rigorous physical background in full plasticity, despite good agreement in qualitative and quantitative data past the limit load has been made by number of researchers (Betegón and Hancock (1991), Du and Hancock (1991) and Al-Ani and Hancock (1991), Wang (1993)). The Q parameter can more accurately describe constraint in fully plastic conditions, but it entails detailed finite element modeling for every geometry, whereas T-stress solutions are easily obtainable and available from various sources (Leevers and Radon (1986), Kfoury (1986) and Sham (1991)).

2.3.5 J-T/Q toughness locus

The development of a compressive T-stress is associated with high level of toughness. Betegón and Hancock (1991) and Sumpter *et al* (1991,1992) have examined the relationship between the constraint parameter T and cleavage fracture toughness for a number of standard geometries. Specimens with the highest compressive T-stress values

were found to be tougher than deeply cracked geometries with a positive T-stress. Enhanced toughness values were observed in shallow edge cracked geometries, for which Al-Ani and Hancock (1991) demonstrated the development of a compressive T-stress. A similar enhancement of initiation fracture toughness under ductile tearing of a range of unconstrained cracked geometries was correlated with the development of compressive T-stress by Hancock, Reuter and Parks (1993). These observations have led to developments of J-T/Q toughness loci for structural integrity assessments, where the conditions at failure can be inferred from specific geometry and load dependant toughness values by matching the constraint at fracture with the laboratory tests at the same constraint level. An example shown in Figure 2.12 gives the J-T/Q toughness locus with the scatter band from the collection of experimental results. The applied J vs T/Q curve is then computed from the finite elements analysis for the configuration of interest and superimposed. Failure is predicted when the applied driving force curve passes through the toughness locus.

2.4 Measurement of fracture toughness

In geometries that comply with the requirements of ASTM E399-88 (1988) for fracture toughness testing, the plane strain and small scale yielding conditions develop at the crack tip, and the value of the stress intensity factor at failure is defined to be the measure of the fracture toughness. This is typically the case in cleavage tests on the lower shelf. When large scale yielding develops, fracture toughness is usually measured by a critical J value, J_c . Fracture mechanics standards ASTM E813-88 (1988) and ESIS P1-92 (1992) estimate the fracture toughness for deeply notched SENB specimens by measuring the load and load-line-displacement. Typically the J-integral is decomposed into elastic and plastic components:

$$J = J_{el} + J_{pl} \quad (2.47)$$

The elastic component is parameterised with the stress intensity factor, which is tabulated in handbooks, such as Tada *et al* (1973):

$$J_{el} = \frac{K^2(1-\nu)}{E} \quad (2.48)$$

The plastic component is determined from the plastic work under the load – load-line-displacement record:

$$J_{pl} = \frac{\eta_{pl}A}{(w-a)B} \quad (2.49)$$

where η_{pl} is the calibration factor ($\eta_{pl}=2$ for SENB specimens), A is the plastic work done, $(w-a)$ is the unbroken ligament and B is the thickness of the test geometry. The elastic and plastic parts of J-integral are additive and the combined toughness can be expressed in the stress intensity factor notation:

$$K_{Jc} = \sqrt{\frac{(J_{el} + J_{pl})E}{1 - \nu^2}} \quad (2.50)$$

The approach based on the area under the load – load-line displacement record also includes dissipation of energy on gross deformation occurring remote from crack tip and local deformation around the supports and indenter. The estimated J-integral value is therefore no longer the value for crack initiation and propagation, but rather a measure of the plastic strain energy dissipated in the whole structure. The approach in present codes is restricted to tests on deeply cracked geometries ($a/w \sim 0.5$) where local plasticity is confined to the unbroken ligament and the calibration factor can be determined from slip line analysis. For shallow cracks the standards ASTM E813-88 (1988) and ESIS P1-92 (1992) are unsuitable, as gross section yielding occurs and plasticity is no longer confined to the ligament, but extends to the front face. Sumpter (1987), Joch (1993) and Kirk and Dodds (1993) proposed to use plastic work determined under the load - crack-mouth-opening-displacement (CMOD) record to estimate the plastic part of the J-integral. They argue that the local measurement of strain energy close to the crack mouth is able to represent the crack tip region load, thus excluding the contribution from the global strain energy which may not contribute to crack opening. The plastic part of the J-integral obtained from the work done under load – crack-mouth-opening-displacement record is:

$$J_{pl} = \frac{\eta_{plCMOD}}{B(w-a)} A_{pl}^{CMOD} \quad (2.51)$$

where η_{plCMOD} values were given by Kirk and Dodds (1993) as a curve-fit to numerical simulations:

$$\eta_{plCMOD} = 3.785 - 3.101 \cdot \frac{a}{w} + 2.018 \left(\frac{a}{w}\right)^2 \quad (0.05 \leq a/w \leq 0.70) \quad (2.52)$$

valid for deep and shallow edge cracks and all strain hardening rates. A similar expression was also obtained by Wang and Gordon (1992):

$$\eta_{plCMOD} = 3.5 - 1.4167 \cdot a/w \quad (0.1 \leq a/w \leq 0.5) \quad (2.53)$$

Fracture toughness is measured using crack mouth opening displacement throughout the work and specific η_{plCMOD} factors are calculated from a finite element model where not available in the literature.

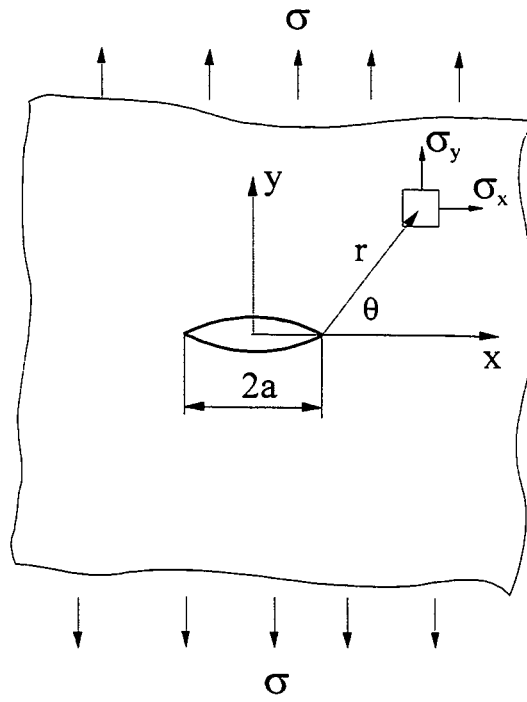


Figure 2.1:
Stresses in the vicinity of a crack.

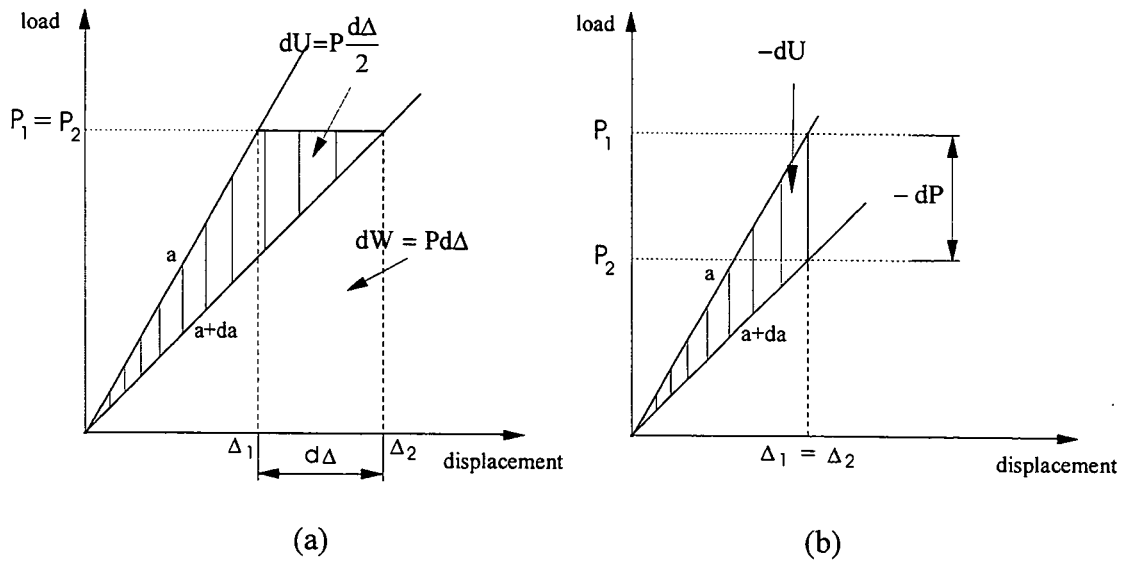


Figure 2.2:
Load-displacement curves for (a) fixed load and (b) fixed displacement conditions.

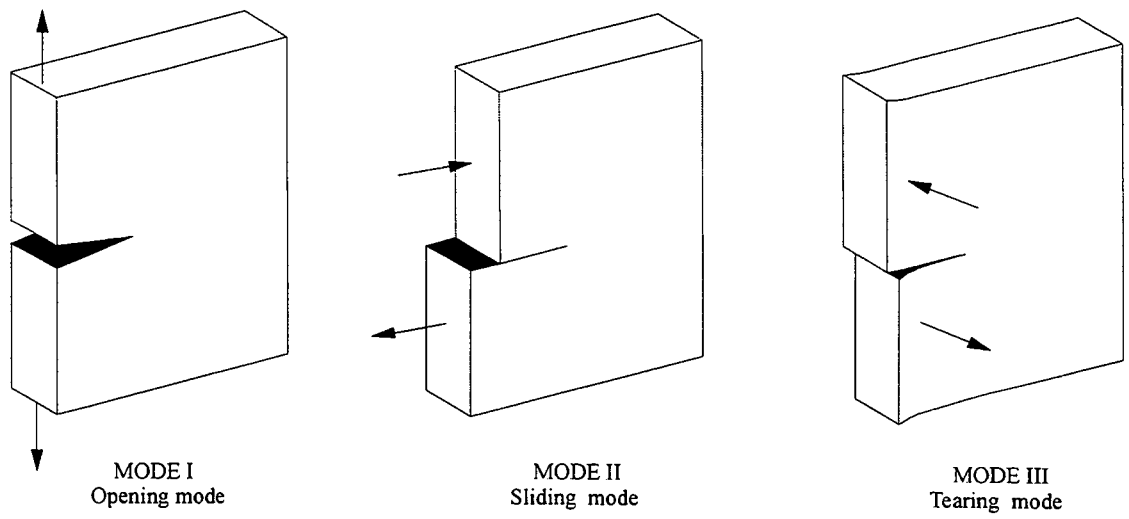


Figure 2.3:
Characteristic modes of crack opening

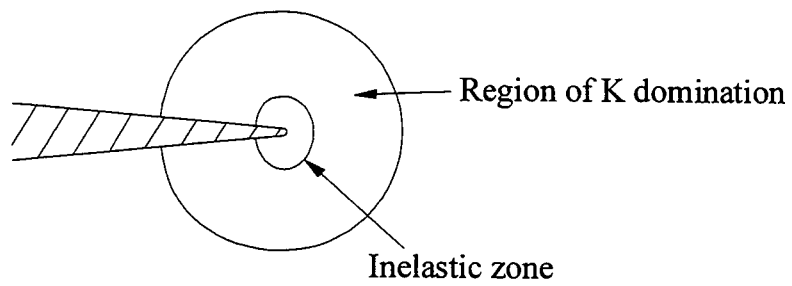


Figure 2.4:
Conditions of small scale yielding

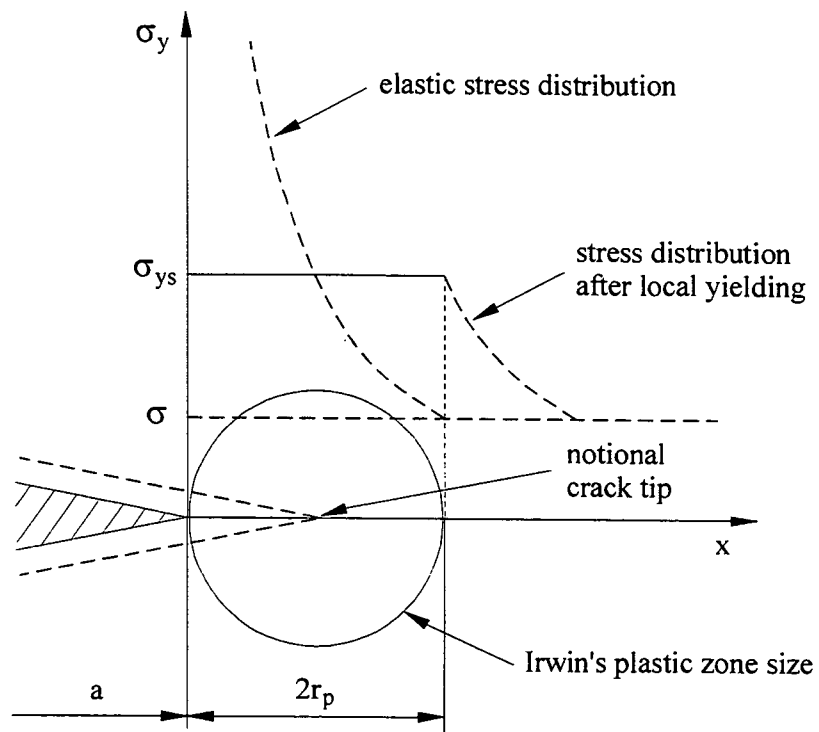


Figure 2.5:
Irwin's plastic zone model

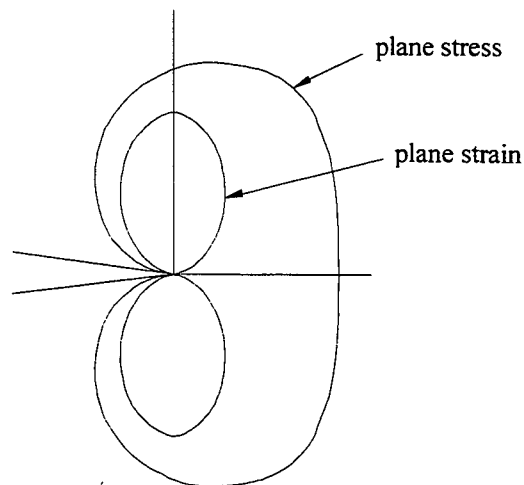


Figure 2.6:
Plane stress and plane strain plastic zone sizes

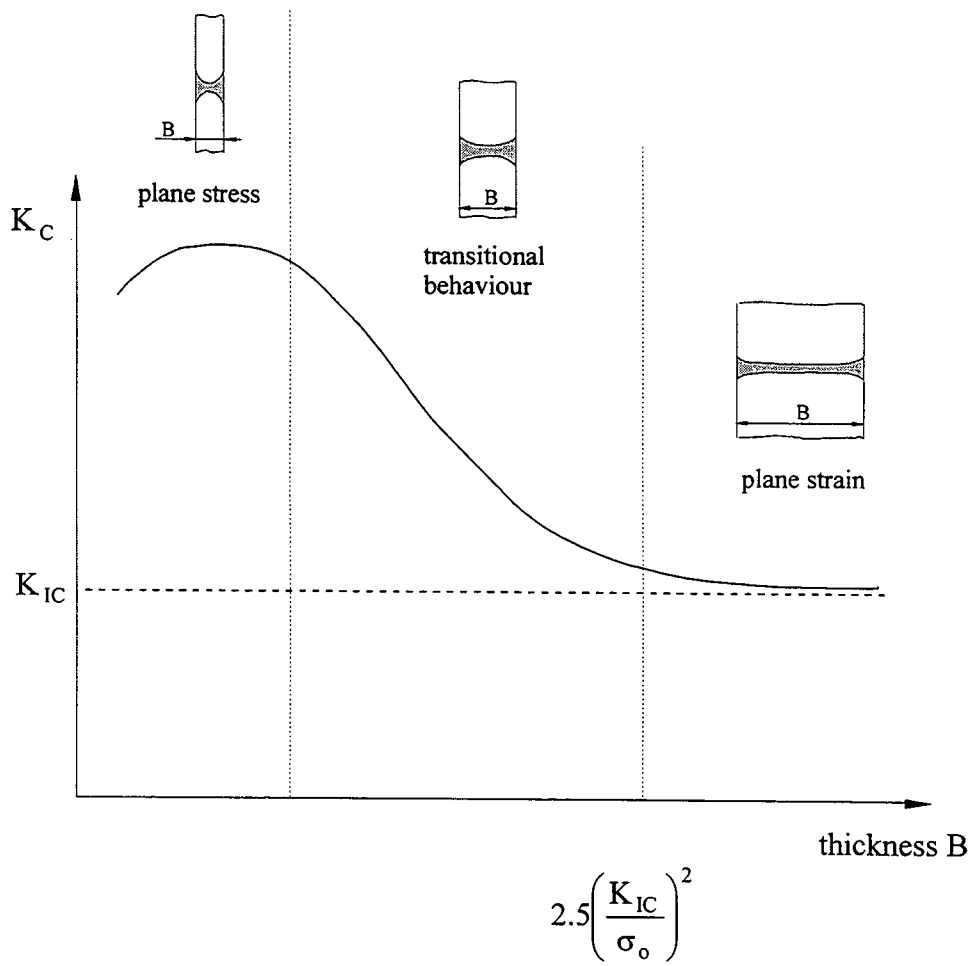


Figure 2.7:
Dependence of fracture toughness on the thickness of the geometry.

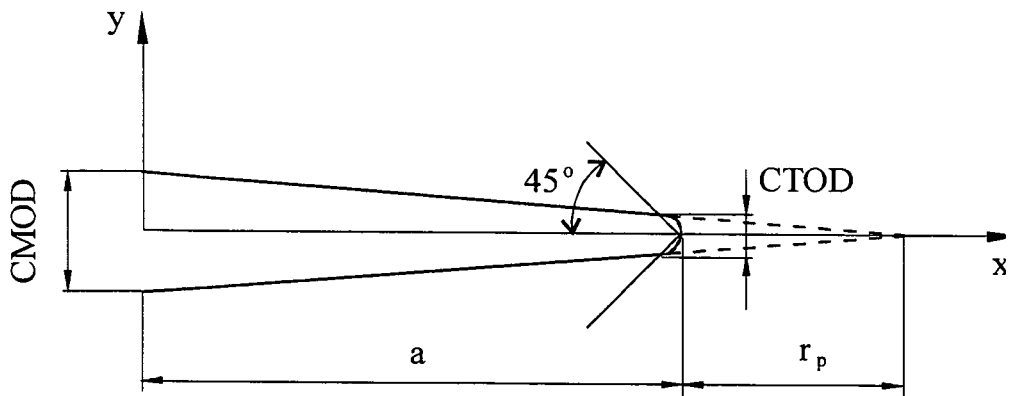


Figure 2.8:
 Illustration of the crack mouth opening displacement (CMOD) and definition of the crack tip opening displacement (CTOD) with the 45° intersection lines.

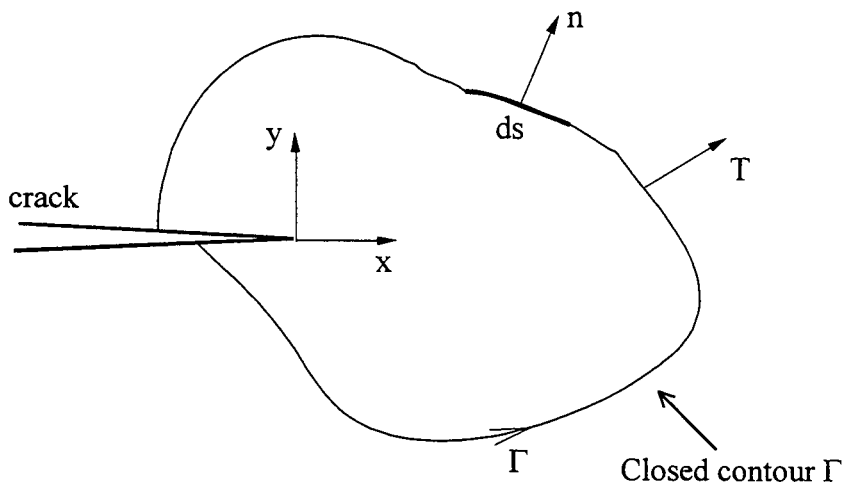


Figure 2.9:
 Definition of the J-integral after Rice (1968)

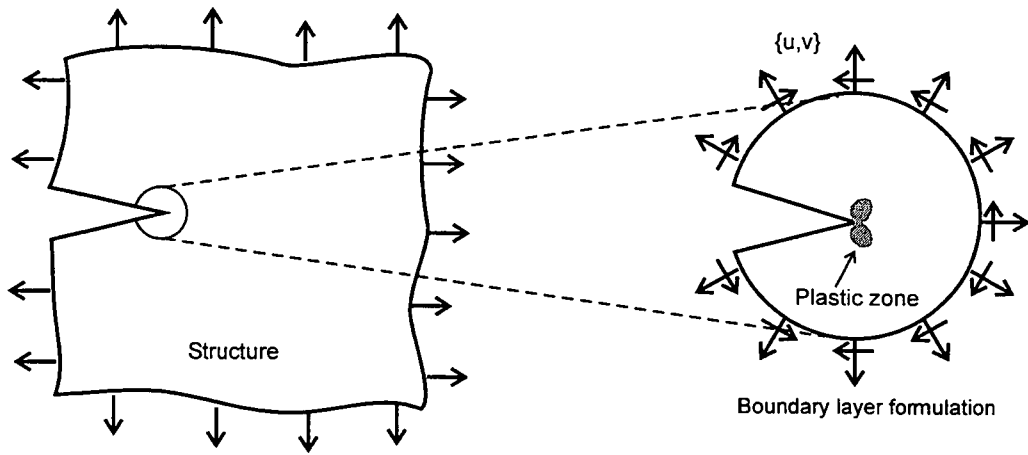


Figure 2.10:
Illustration of the boundary layer formulation.

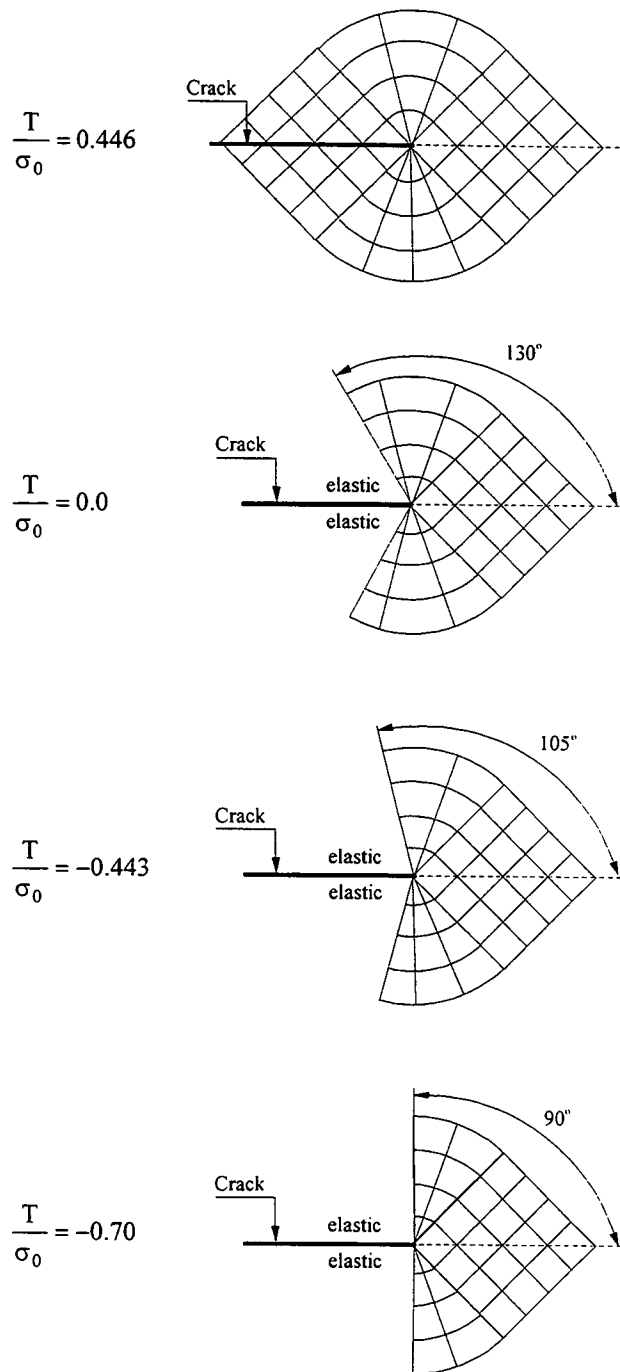


Figure 2.11: Slip line fields in Mode I plane strain, showing the effect of T-stress, after Du and Hancock (1991).

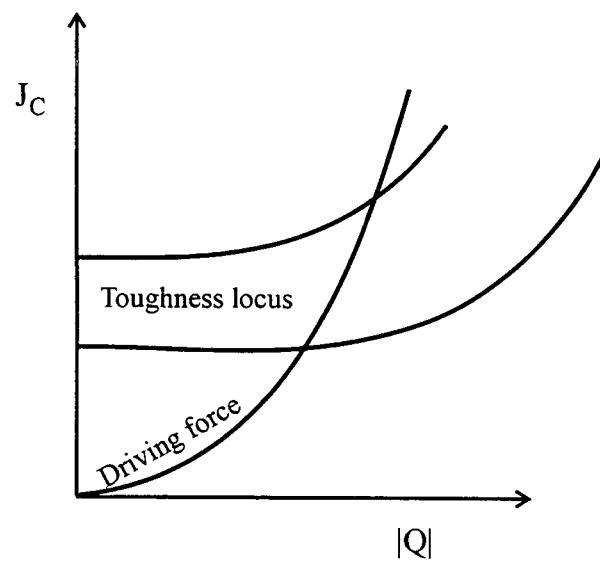


Figure 2.12:
Application of the J-Q toughness locus.

Chapter 3

INFINITE PERIODICAL SINUSOIDAL CRACK

3.1 Introduction

An infinite periodic sinusoidal crack has been investigated to gain fundamental insight into the mechanics of complex cracks. Periodicity minimises the influence of a finite geometry, while allowing a systematic correlation of crack front perturbations with parameters, such as K , T and J . A linear elastic analysis has estimated the stress intensity factors and T -stresses for tension and three-point bending for a range of sinusoidal cracks. Elastic-plastic analysis examined the limit load and the way the J -integral depends on crack front curvature under net section yield.

3.2 Geometry

An infinite sinusoidal crack was modelled in a flat plate using a right-handed Cartesian coordinate system (x,y,z) defined in Figure 3.1. The sinusoidal crack is defined by its wavelength, λ , amplitude, A and mean depth \bar{a} , as shown in Figure 3.2. The crack depth at any point along the crack length is thus described by:

$$a_{(x)} = A \cos\left(\frac{2\pi}{\lambda} x\right) + \bar{a} \quad (3.1)$$

Sinusoidal defects with fully embedded (deep) and surface touching crack fronts have been examined at a fixed amplitude or a fixed wavelength under tension and three-point bending. The crack fronts are illustrated in Figure 3.3 and the crack front perturbation is described by the ratio of amplitude to wavelength, A/λ .

3.3 Numerical method

The geometry was modelled numerically using a finite element method under plane strain conditions and utilising ABAQUS (HKS (1998)) as a solver. A symmetric half of the geometry was represented with 1140 isoparametric second order shell elements, compatible with the line spring elements to represent a surface breaking crack. The mesh shown in Figure 3.4 was uniform along the x axis and weighted towards the $y=0$ plane, where a sinusoidal crack was introduced using symmetric line-spring elements.

3.3.1 Line spring technique

Rice and Levy (1972) introduced the elastic line spring technique as a computationally efficient way of analysing surface cracked plates and shells. The method essentially idealises a part-through surface crack of surface length $2c$ as a through crack with a series of one dimensional springs placed across the crack faces, as illustrated in Figure 3.5. The compliance of each spring is matched to the compliance of a plane strain edge crack bar of matching local crack depth. The additional rotations and displacements arising from the increased compliance of the cracked bar are combined with the constitutive relation to give the local force and bending moments per unit length along the crack front. The stress intensity factors are then determined by combining the local forces and moments with the geometry calibration functions for a plane strain edge crack bar. The line spring method was extended by Parks and White (1982) to include elastic-plastic behaviour. Limit load behaviour is introduced using an upper bound solution to limit load of the edge cracked strip in combined tension and bending, while the J-integral is determined by equating the plastic work done by the line springs and an edge-cracked strip. The accuracy of elastic and elastic-plastic line spring solutions is discussed by Parks and White (1982) and Parks (1981), and shown to give acceptable level of accuracy when compared with the detailed 3-dimensional solutions of Raju and Newman (1981). The elastic T-stress is calculated by combining forces and moments (Wang and Parks (1992)) with the calibration functions of T-stress of an edge crack bar, given by Sham (1991).

3.3.2 Boundary conditions

Periodicity allows a representative cell to be analysed as illustrated in Figure 3.6. The left hand side of the finite element model had prescribed symmetric boundary condition about the plane $x=0$. The nodes on the right hand side of the mesh were unconstrained in x direction but restrained to have identical but undefined displacements. The upper nodes of the model were allowed to rotate freely about the x axis.

The model was subject to displacement loading. In tension a displacement of 1% of plate height was imposed on upper nodes in the positive y -direction. In three point bending the upper nodes of the model were displaced by 10% of the plate height in the negative z direction, while the surface breaking crack was located on the positive side of the z axis. Results are presented in a normalised manner where possible.

3.4 Results

3.4.1 Linear elastic analysis

Stress intensity factors and T-stresses for deep and surface touching sinusoidal cracks are shown in Figures 3.7 to 3.12, normalised with the applied load, and either, a local crack depth or a mean crack depth. Shallow crack fronts typically exhibit amplified values of stress intensity factors and more compressive T stresses compared to the reference straight edge crack of the same local depth in both, tension and three-point bending. Conversely, deeper crack segments show reduced values of K and T. The trend can be related to the local forces and bending moments per unit crack length, shown in Figure 3.13. The local forces are normalised in tension with remote force per unit length, defined as the $\frac{\text{total applied tensile force}}{\text{geometry width}}$. The local moment was normalised by $\frac{\text{applied tensile force} \times \text{geometry thickness}}{\text{geometry width}}$ in tension. In three point bending the local forces were normalised with $\frac{\text{remotely applied bending force} \times \text{geometry height}}{\text{geometry width} \times \text{geometry thickness}}$ and local moments with $\frac{\text{remotely applied bending force} \times \text{geometry height}}{\text{geometry width}}$. Shallow crack segments experience enhanced opening forces and opening bending moments under remote tension, while deeper segments feature reduced local forces and closing bending moments, compared to a reference straight edge crack of the same depth. Similarly, remote bending gives rise to local tensile forces and amplified local bending moments for shallow segments and compressive values for deeper segments of the sinusoidal crack.

The difference between the crack tip parameters for the reference straight edge crack and the sinusoidal crack depends on the perturbation of the crack front. An increase in amplitude or a reduction in wavelength, hence increase in perturbation, increases the difference, as illustrated in Figures 3.7 to 3.10. Of most interest are crack front segments with the greatest values of the stress intensity factors. These are the deeper crack segment, however with increase in perturbation (A/λ) the enhanced stress intensity factors shift to the shallower segments, as shown in Table 3.1. The trends are influenced by both, the loading mode and the position of sinusoidal crack within the plate (fully embedded or surface touching).

The dependence of the stress intensity factor and elastic T-stress on the crack front perturbation is examined for a fixed position at the shallowest crack segments on the

perturbed crack front. The effects of both, amplitude and wavelength on K and T are summarised in Figures 3.14 to 3.21. In all cases an increase in crack front perturbation increases the stress intensity factor and reduces the elastic T-stress at the shallowest position, irrespective of loading, confirming that the critical position shifts towards shallow segments as the perturbation (A/λ) increases.

3.4.2 Elastic-plastic analysis

As similar K and T distributions were observed for both, deep and surface touching sinusoidal cracks in the linear elastic analysis, the elastic-plastic analysis examined the surface touching sinusoidal cracks. Three wavelengths were examined: $\lambda=40t$, $\lambda=10t$ and $\lambda=2t$, at a constant amplitude, $A=0.25t$ and mean depth $\bar{a}=0.25t$, giving the crack front perturbations (A/λ) of 0.00625, 0.025 and 0.125 and w is the plate width. The limit loads and crack tip parameters are presented in Figures 3.22 to 3.33 for a sinusoidal crack in perfectly plastic (non-hardening) and strain hardening materials under tension and three point bending.

Local and global limit loads

Defect assessment schemes require knowledge of the local and global limit loads. The limit loads for standard straight cracked geometries depend on the yield stress and the size of the unbroken ligament. For a uniform crack in an homogeneous material, both are constant along the crack front. In irregular cracks the net section ligament changes along the crack front, and may experience spatially dependent yield stresses (material or temperature gradients). In such cases a distinction must be made between the local and global limit loads. The global limit load is the plastic collapse load of the structure at which the plastic strains become unbounded for a non-hardening material response. Local plasticity may however extend across the ligament at a local limit load which is less than the global limit load.

In order to find the local limit load, the stress history at a given position along the crack front has been analysed. The local stress history is expressed in terms of the local forces and bending moments, which under elastic deformation define the local elastic stresses. The elastic-plastic conditions however require interpolation between the elastic stress field and fully plastic (non-hardening) stress field. Rice (1972) proposed a yield surface, as an

upper bound solution to the limit load of a straight plane strain crack in combination of tension and bending. The yield surface comprises normalised local forces on the abscissa and combination of normalised local forces and local moments on the ordinate, where the values are normalised with unbroken ligament:

$$X = \frac{\sqrt{3}N_{(x)}}{2\sigma_0(t-a)}, \quad (3.2a)$$

$$Y = \frac{\sqrt{3}}{2\sigma_0(t-a)^2} \left(M_{(x)} + \frac{t}{2} N_{(x)} \right)^2 \quad (3.2b)$$

The stress state at any point along the crack front is defined by a combination of the local force and bending moment compared to the yield surface. Points within the yield surface correspond to elastic stress states, while points on the yield envelope correspond to fully plastic local behaviour. The proximity of the stress point to the yield envelope determines the proximity of local crack tip to net section yield and local plastic collapse. By comparing the stress history of all points on the crack front, the point which reaches the yield envelope first, defines the critical site on the crack front and the corresponding local limit load.

An alternative method of locating the critical site is based on the plastic component of the J-integral. In line springs the elastic and fully plastic part of J-integral are defined separately and are dependant on the local stress history. The plastic part of the J-integral becomes significant when the local stress history reaches the yield envelope. This simplifies the task of finding critical site by identifying the critical site as that which develops J_{plastic} component at the lowest applied load. This is a convenient method for determining the location of the critical site on the crack front and the corresponding local limit load.

All the sinusoidal configurations had similar global limit loads, as illustrated in Figure 3.22. The procedure for determining the local limit load by tracing the stress histories is illustrated in Figure 3.23, where stress histories corresponding to the deepest ($a=0.5t$) and the shallowest ($a=0.02t$) crack tips of a surface touching sinusoidal crack having $\lambda=10t$ ($A/\lambda=0.025$) are examined. In this case the stress history of the deepest crack tip reaches the yield envelope at the lower applied load than the shallowest tip. As expected, the

analysis of J_{plastic} indicated, that for this configuration the deepest crack tip is the critical location.

As the limit load is reached at the critical site, the local force to moment ratio changes as plasticity extends along the remainder of the crack front, towards the shallower sections. This is observed as sliding of the stress point along the yield envelope, until the shallowest location reaches the yield envelope. At that load the whole cross-section becomes plastic and global plastic collapse occurs. All subsequent values of the local stress state then coincide.

In remote tension the competition between the ligament size and the local tension to bending ratio shifts the critical site from the deepest position for small perturbations ($A/\lambda=0.00625$) to the crack mid-depth for a perturbation of $A/\lambda=0.125$ ($\lambda=2t$), as illustrated in Table 3.2. Under remote bending the local crack tip stresses are bending dominated and the critical site was always the shortest unbroken ligament, largely due to the relatively small perturbations that could be examined. Full plasticity of the largest net section ligament (shallowest location on the crack front) corresponds to the attainment of the global plastic collapse under both, tension and bending. The corresponding local limit loads are compared with global limit loads in Figures 3.24 and 3.25 for tension and three-point bending. The local limit load is influenced by the crack front perturbation, where an increase in the perturbation increases the local limit loads towards the global collapse load. This is due to the redistribution of local forces and bending moments, such that where greater perturbations feature more compressive stresses at the critical (deepest) site and delay the plastic collapse of the adjacent ligament to greater loads.

Crack tip plasticity and constraint

The J-integral along the crack front is shown in Figures 3.26 and 3.27 for remote tension and in Figures 3.28 and 3.29 for remote three-point bending for a surface touching sinusoidal crack. The J-integral is normalised with yield stress and the smallest net section ligament and is presented as a function of crack depth, which defines the position along the crack front. As the net section ligament changes along crack front, the smallest (fixed) net section ligament was used to normalise J in all cases. This gives a better comparison between tensile and bending results. The load is normalised with the global limit load. Superimposed on these figures is the value of J for a straight crack, obtained with the same

numerical model for the current crack at the same F/F_{lim} ratios. Large J develops at the deepest crack tips for small perturbations ($\lambda=40t$). As the perturbation increases, plasticity shifts from the deepest sites to shallower segments, and the J -integral increases for shallower segments. This is most pronounced under bending conditions. For all loads even small deviations from a straight crack (e.g. $\lambda=40t$) has a pronounced effect on the J -integral, which increases in magnitude compared to a straight edge crack. As the perturbation increases, the magnitude of J -integral reduces and approaches that of the straight edge crack. The results suggest that under both, small-scale yielding and fully plastic conditions crack advance is strongly governed by crack front perturbations.

The development of crack tip constraint for sinusoidal cracks is shown in Figures 3.30 to 3.33, in which the T -stress normalised with the yield stress is compared with a straight edge crack. The applied load is normalised with the global limit load. A sinusoidal crack with a long wavelength in tension shows similar values of T stress to the straight edge crack. With an increase in crack front perturbation the T -stresses become more compressive for the shallow crack segments under remote tension. In three-point bending the effect of crack front perturbation on the T -stress is less pronounced, and the extent of constraint loss is comparable to that of a straight edge crack.

3.5 Discussion

3.5.1 Effect of crack front perturbation

There is a close relation between the magnitude and location of amplified values of crack driving force and the crack front perturbation. The perturbation can be expressed in terms of a local crack front curvature, ρ , (Stoker (1969)):

$$\rho = \frac{-A \cdot \left(\frac{2\pi}{\lambda}\right)^2 \cdot \cos\left(\frac{2\pi}{\lambda} x\right)}{\left[1 + \left(A \cdot \frac{2\pi}{\lambda} \cdot \sin\left(\frac{2\pi}{\lambda} x\right)\right)^2\right]^{\frac{3}{2}}} \quad (3.3)$$

This suggests that the local stress intensity factor may be expressed in a form:

$$K = g_{(\rho)} \sigma \sqrt{\pi a} G\left(\frac{a}{t}\right) \quad (3.4)$$

where the effect of crack front perturbation is introduced through a function of local crack front curvature, $g_{(\rho)}$, multiplied by the solution for a straight edge crack. Substituting Eq.

(3.3) in Eq. (30) of Rice's (1985) solution for a periodic surface cracks in a semi-infinite solid and rearranging gives a first-order expression for the curvature:

$$g_{(\rho)} = 1 + \frac{\rho\lambda}{4\pi} \left[1 + \left(-2\pi \frac{A}{\lambda} \sin\left(\frac{2\pi}{\lambda} x\right) \right)^2 \right]^{\frac{3}{2}} \quad (3.5)$$

This estimate of SIF is superimposed in Figures 3.34 and 3.35 for a surface touching sinusoidal crack of amplitude $0.1t$ at wavelengths $40t$, $10t$ and $2t$. The difference between the numerical results and equation (3.5) in Figures 3.34-3.35 arises from the finite geometry. Rice's (1985) equation was derived for a small perturbations in an infinite half plane. Qualitatively the distribution of stress intensity factors along the crack fronts is similar in both, finite and semi-infinite geometries. A similar difference between the numerical results and Eq. (3.5) for a surface touching sinusoidal crack of amplitude $0.3t$ in Figure 3.35 suggests that the effect of a finite geometry accounts for up to 30% of the difference in results. The difference is also influenced by the crack front perturbation, such that greater perturbations increase the discrepancy.

3.5.2 Local force and bending moment redistribution

Characterising parameters such as the stress intensity factor and the T-stress depend on the local forces and moments along the crack front. Shallow sections of the sinusoidal crack experience enhanced local opening forces and moments, while deeper sections are subject to reduced values. A remote uniform tensile loading on a sinusoidal crack produces local forces which vary around the local force on a straight crack. To maintain equilibrium the normalised sum of local forces along the total crack length must equal unity:

$$\int_{-\infty}^{+\infty} \frac{N_{(x)}}{N_0} \cdot dx = 1 \quad (3.6)$$

where N_0 represent local forces on a straight crack. The crack geometry contributes to the appearance of local moments although the applied loading is simply tensile. Local opening moments develop in shallow sections and local closing moments at deeper section of the crack front. Equilibrium requires that the sum of local moments across the total crack length has to equal the remotely applied moment, which in case of uniform tension, is zero:

$$\int_{-\infty}^{+\infty} M_{(x)} dx = 0 \quad (3.7)$$

In bending the roles of the local forces and moments are reversed. The remotely applied moment is balanced by local moments which vary around value for equivalent straight crack. Similarly, local normalised forces arising from the crack shape sum to zero, when summarised over the crack length.

3.5.3 Stability of a perturbed crack front

The results suggest a correlation between the perturbation, crack driving force and the crack front stability. Sinusoidal configurations with small perturbations from the straight crack show (in tension and bending) the greatest crack driving force at the deepest crack segments. As the perturbation reaches a critical value, it shifts the crack driving force to the less advanced crack segments, as illustrated in Figure 3.36. Perturbation also increases the magnitude of the crack driving force, in particular in elastic analyses.

From these analysis, crack front stability argument can be related with the crack front curvature. There is a critical crack front curvature, at which the greatest crack driving force moves from more to less advanced crack sections. Sinusoidal cracks with crack front curvature less than this value tend to advance from the more advanced crack segments. At higher crack front curvature than a critical value crack advance shifts to the less advanced crack sections, consistent with Rice's (1985) discussion of a perturbed crack front in a semi-infinite body. A perturbed crack front experiencing uniform global conditions tends to straighten by a cycling movement of critical segment between more and less advanced crack segments and in a process maintains a perturbed crack front.

Deep sinusoidal crack ($\bar{a} = 0.5t$) in tension			
Perturbation, A/λ	0.0075	0.03	0.15
Location of max K	Deepest segment	Mid-section	Mid-section to shallower tips

Surface touching sinusoidal crack ($a = A$) in tension			
Perturbation, A/λ	0.00625	0.025	0.125
Location of max K	Deepest segment	Deepest segment	Mid-section

(a)

Deep sinusoidal crack ($\bar{a} = 0.5t$) in three-point bending			
Perturbation, A/λ	0.0075	0.03	0.15
Location of max K	Mid-section	Mid-section to shallower tips	Shallowest segments

Surface touching sinusoidal crack ($\bar{a} = A$) in three-point bending			
Perturbation, A/λ	0.00625	0.025	0.125
Location of max K	Deepest segment	Mid-section	Shallowest segments

(b)

Table 3.1:
The location of the maximum stress intensity factors for sinusoidal cracks in (a) tension and (b) three-point bending.

Surface touching sinusoidal crack ($\bar{a} = A$) in tension			
Perturbation, A/λ	0.00625	0.025	0.125
Location of the local limit load	Deepest segment	Deepest segment	Mid-section

Surface touching sinusoidal crack ($\bar{a} = A$) in three-point bending			
Perturbation, A/λ	0.00625	0.025	0.125
Location of the local limit load	Deepest segment	Deepest segment	Deepest segment

Table 3.2:
The location of the local limit load for a surface touching sinusoidal cracks in tension and three-point bending.

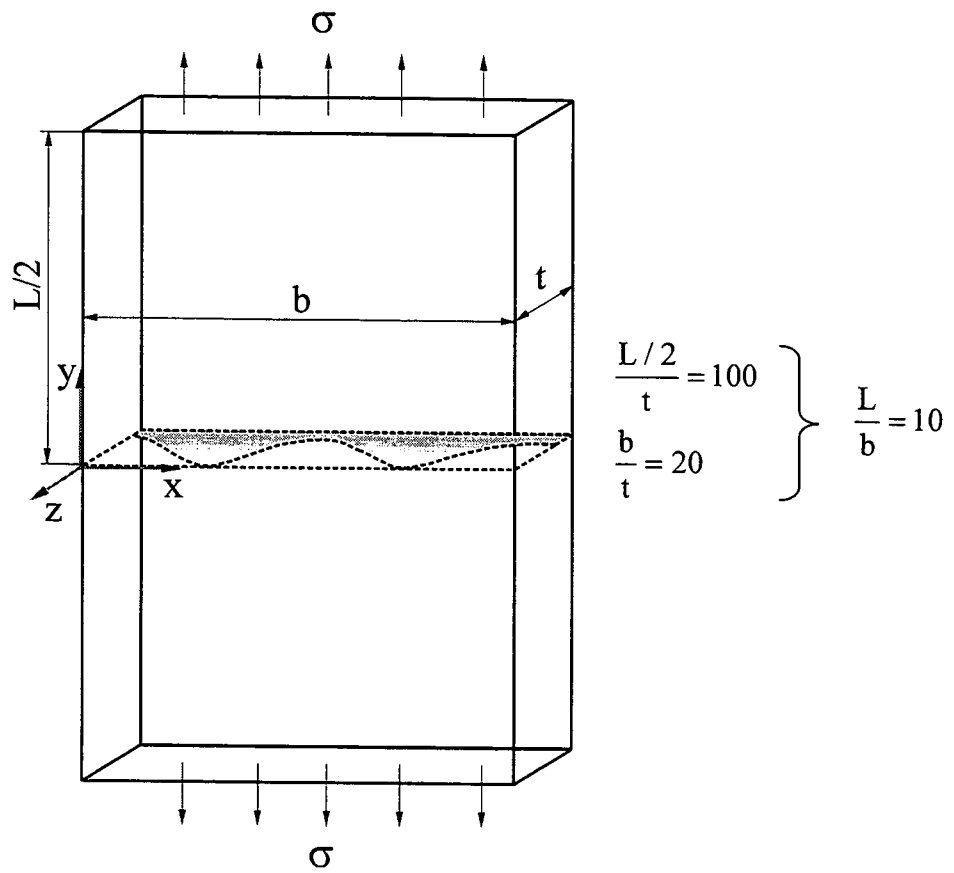


Figure 3.1:
Plate geometry.

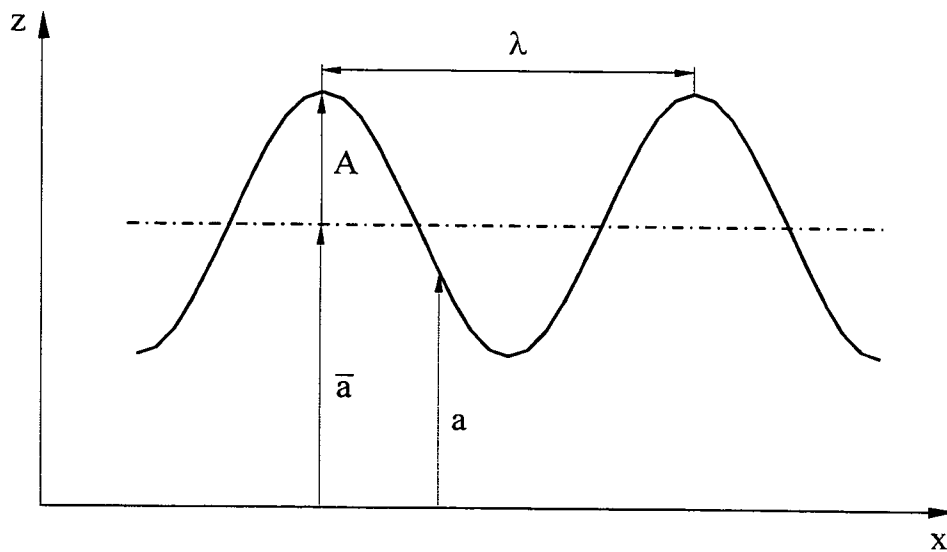


Figure 3.2:
Definition of an infinite periodical sinusoidal crack.

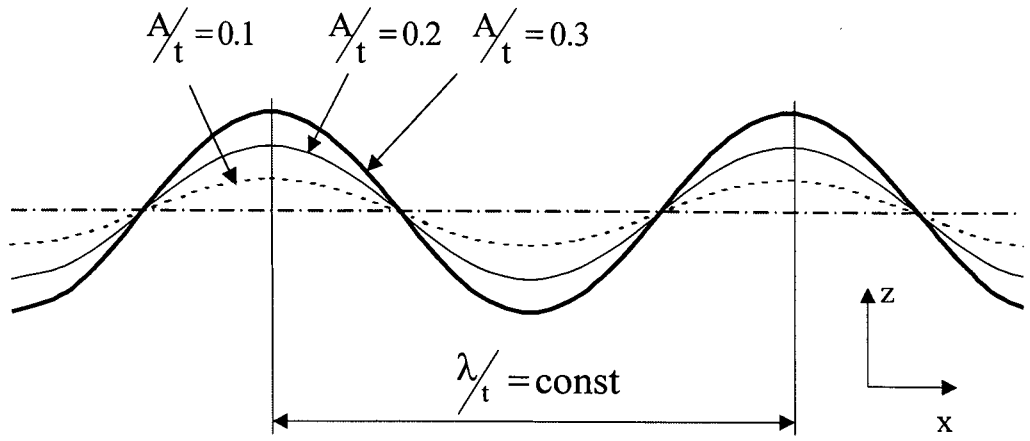


Figure 3.3a:
A sinusoidal crack of varying amplitude.

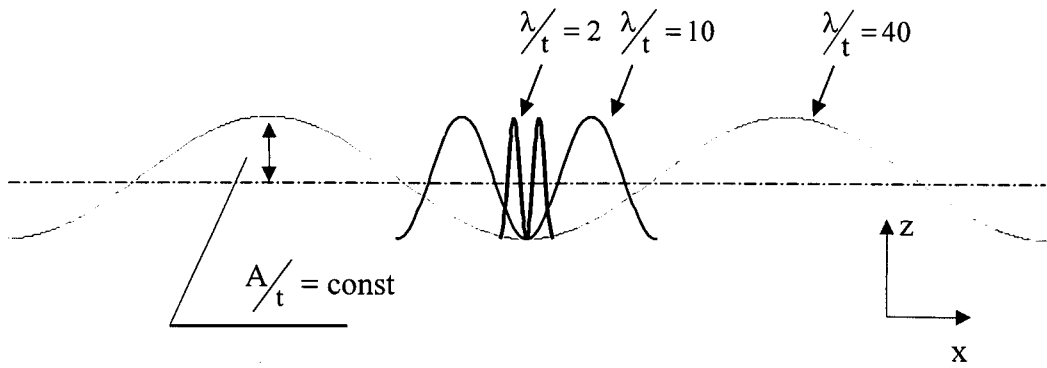
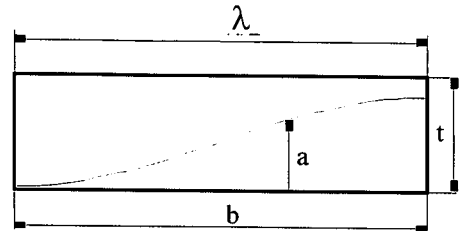


Figure 3.3b:
A sinusoidal crack of varying wavelength.

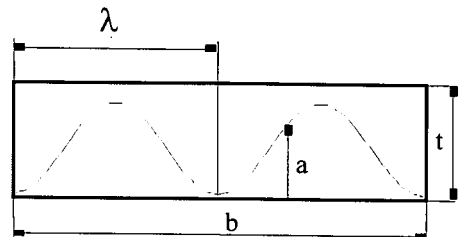
Low perturbation

$$\frac{\lambda}{t} = 40 \quad \Leftrightarrow \quad \lambda = 2b$$



Medium perturbation

$$\frac{\lambda}{t} = 10 \quad \Leftrightarrow \quad \lambda = \frac{1}{2}b$$



High perturbation

$$\frac{\lambda}{t} = 2 \quad \Leftrightarrow \quad \lambda = \frac{1}{10}b$$

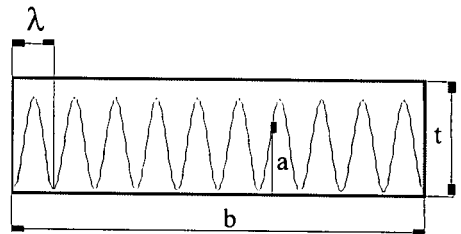


Figure 3.3c:
Illustration of the perturbation of a sinusoidal crack.

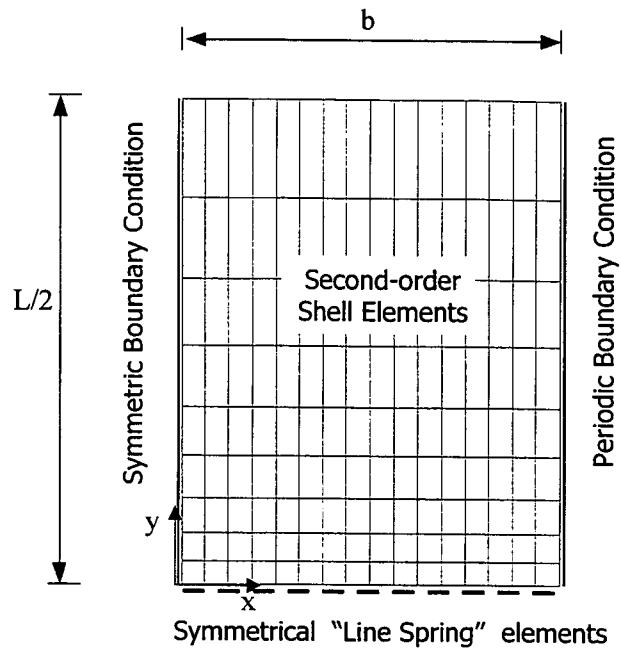


Figure 3.4:
Finite element model of the plate.

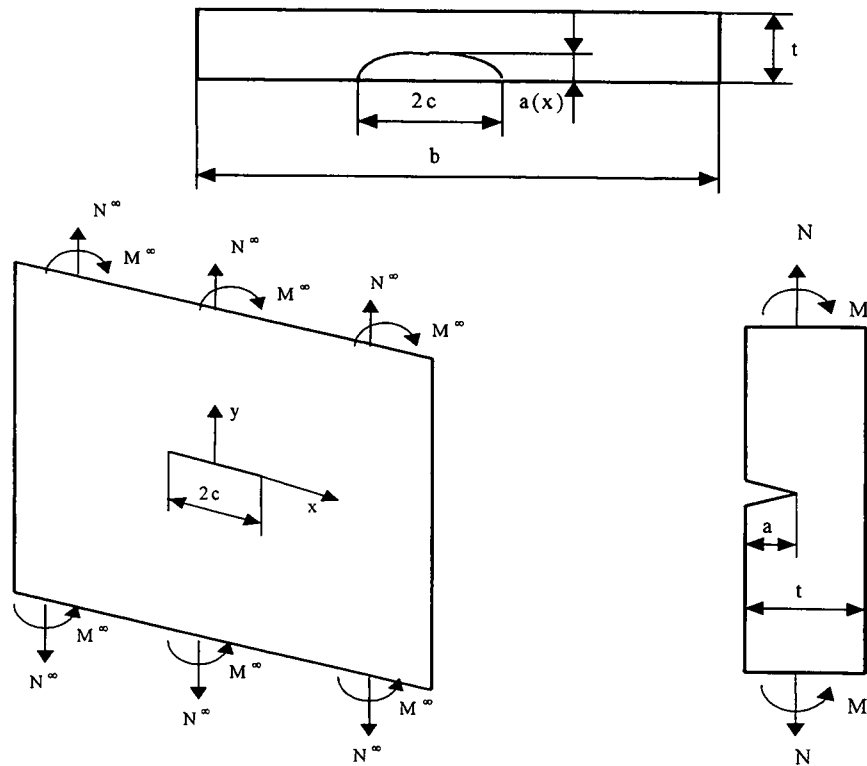


Figure 3.5:
The line-spring model of a surface breaking crack.

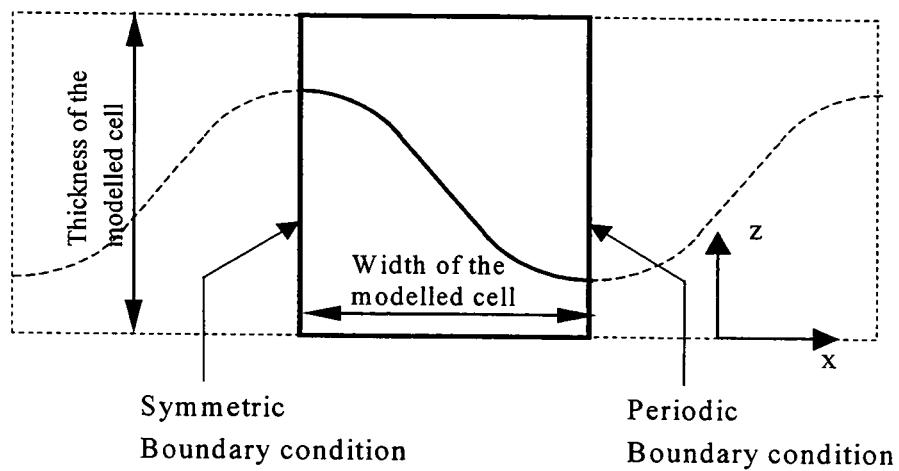


Figure 3.6:
A representative cell of an infinite periodic sinusoidal crack.

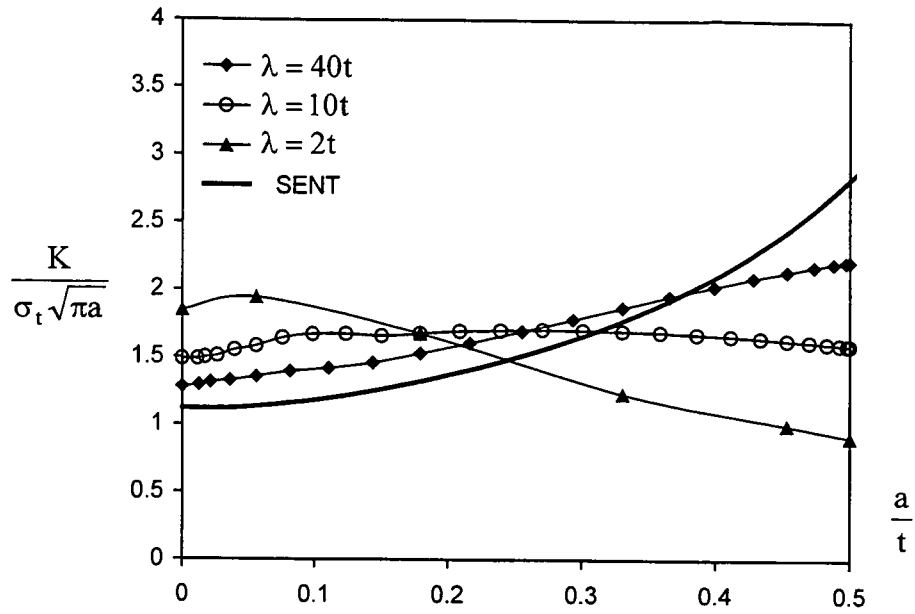


Figure 3.7:
Stress intensity factor for surface touching sinusoidal crack of varying wavelength for $A = 0.25t$ and $\bar{a} = 0.25t$ in tension.

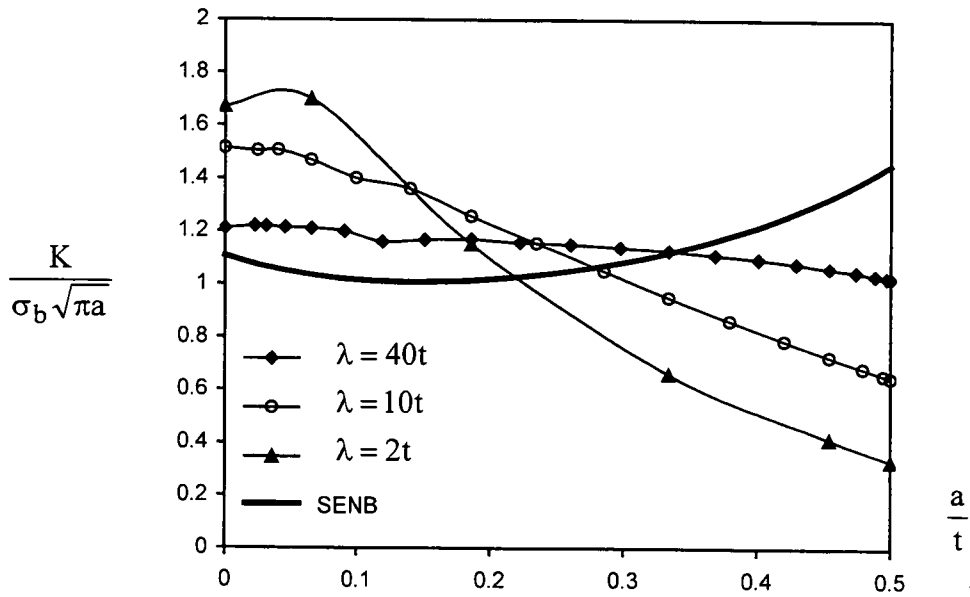


Figure 3.8:
Stress intensity factor for surface touching sinusoidal crack of varying wavelength for $A = 0.25t$ and $\bar{a} = 0.25t$ in three-point bending.

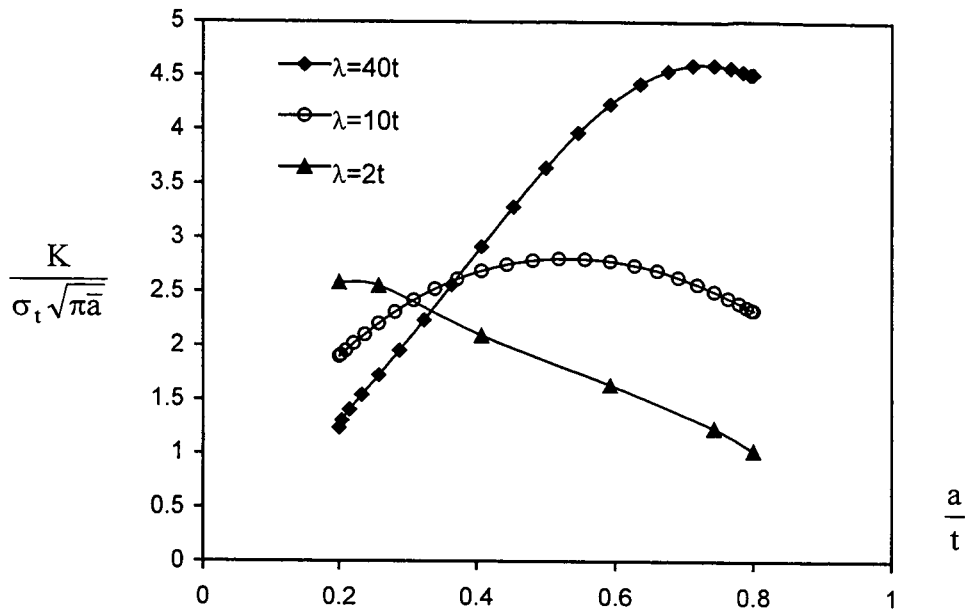


Figure 3.9:
Stress intensity factor for deep sinusoidal crack of varying wavelength for $A = 0.25t$ and $\bar{a} = 0.25t$ in tension, normalised with a constant.

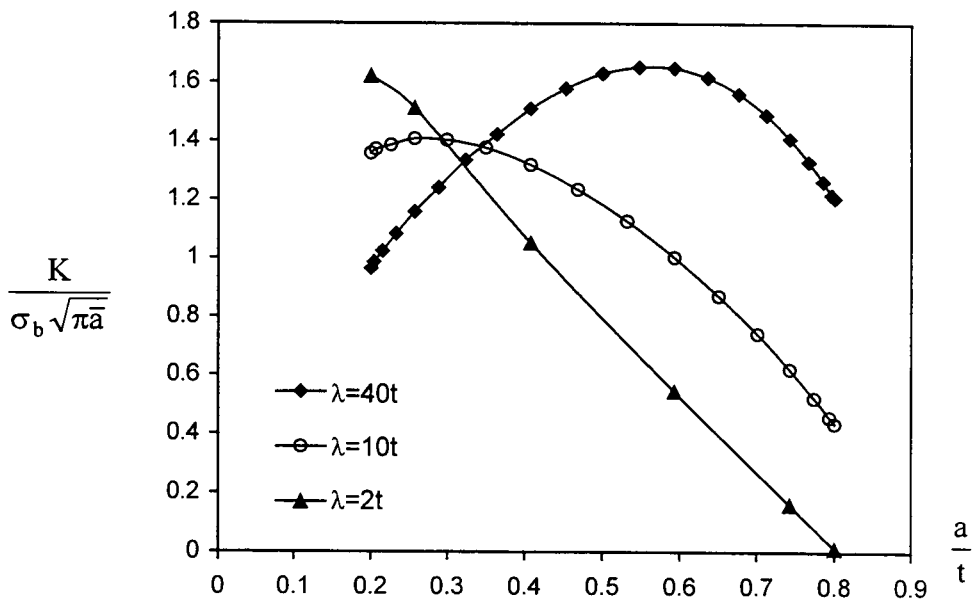


Figure 3.10:
Stress intensity factor for deep sinusoidal crack of varying wavelength for $A = 0.25t$ and $\bar{a} = 0.25t$ in three-point bending, normalised with a constant.

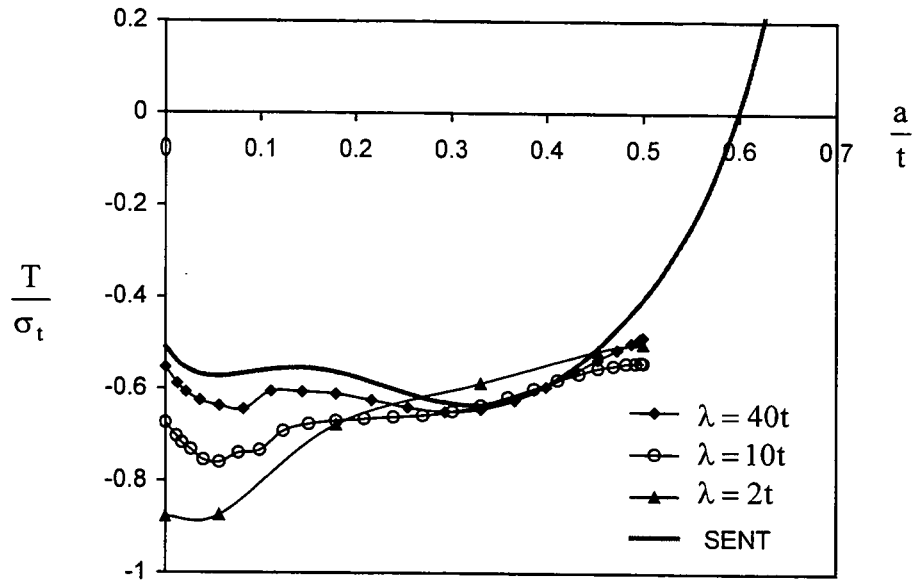


Figure 3.11:
The elastic T-stress for surface touching sinusoidal crack of varying wavelength for $A = 0.25t$ and $\bar{a} = 0.25t$ in tension.

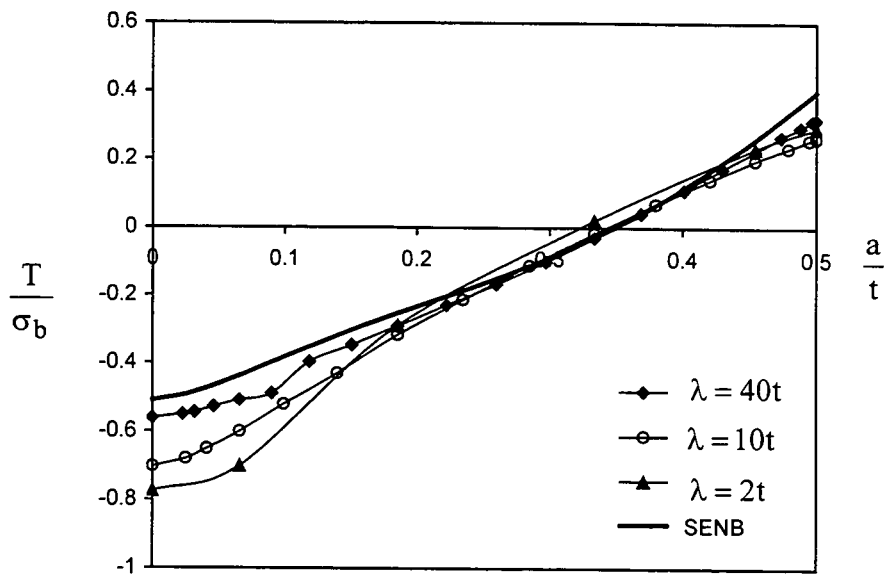


Figure 3.12:
The elastic T-stress for surface touching sinusoidal crack of varying wavelength for $A = 0.25t$ and $\bar{a} = 0.25t$ in three-point bending.

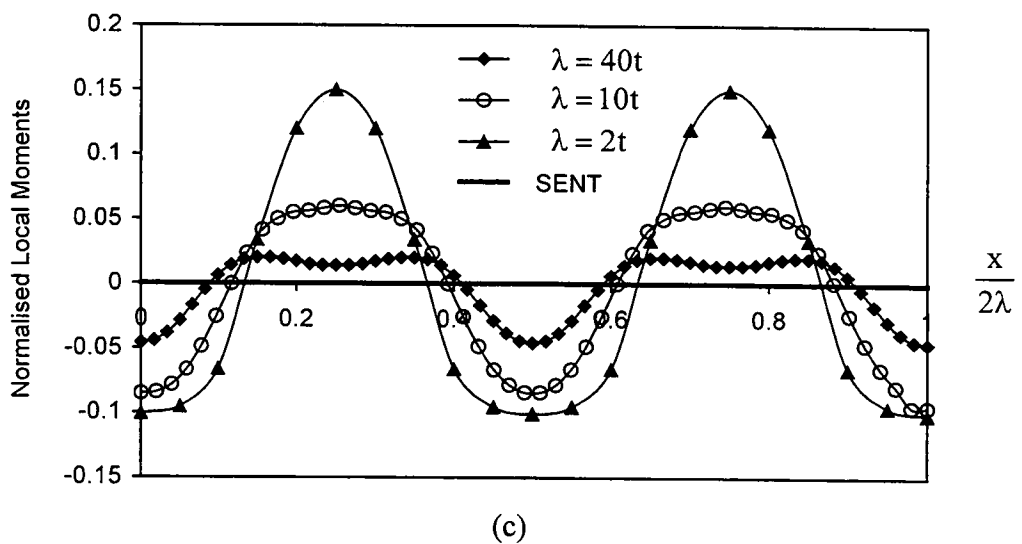
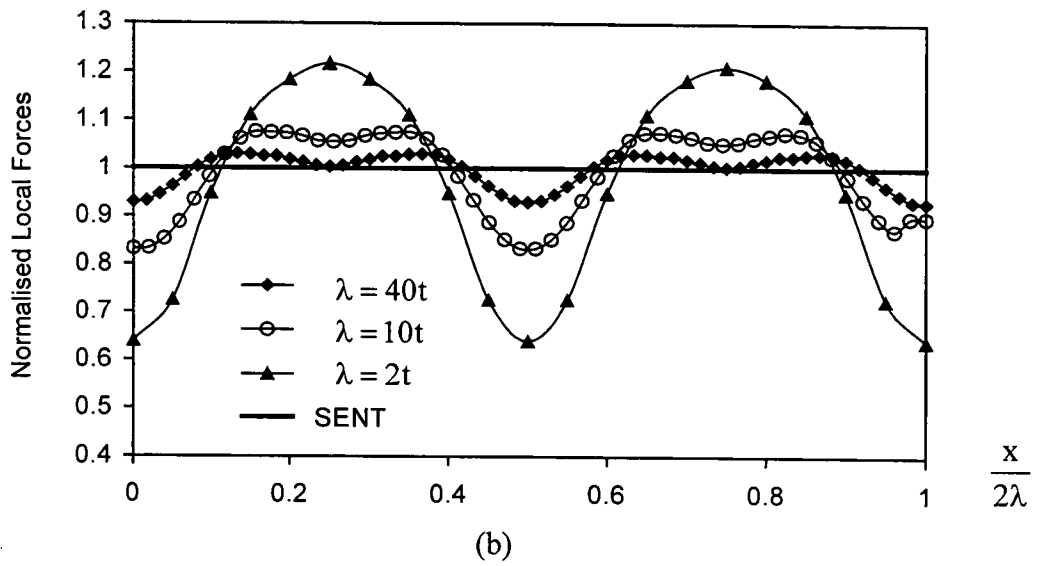
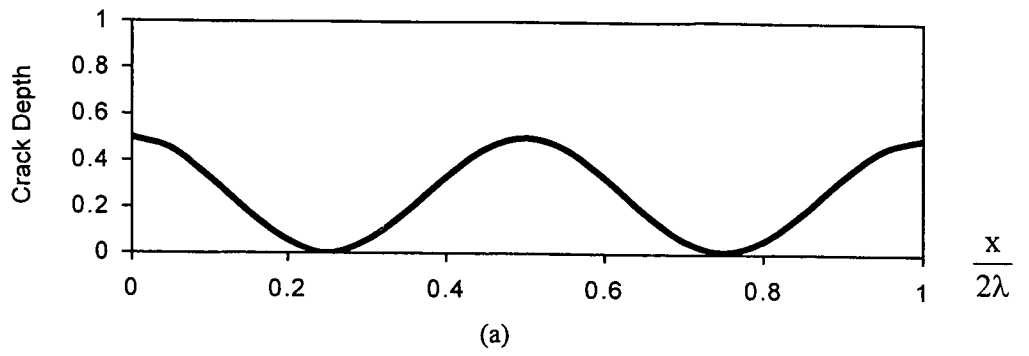


Figure 3.13:
 Normalised local forces (b) and bending moments (c) for surface touching sinusoidal crack (a) of varying wavelength for $A = 0.25t$ and $\bar{a} = 0.25t$ in tension.

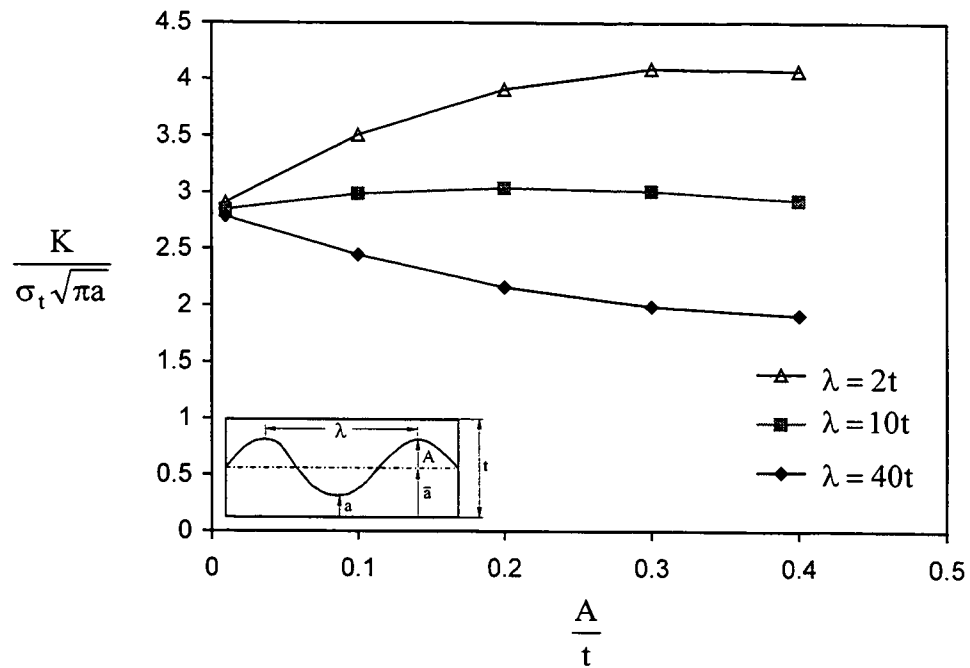


Figure 3.14: Dependence of the stress intensity factor on the amplitude and wavelength for a deep sinusoidal crack ($\bar{a} = 0.5t$) in tension.

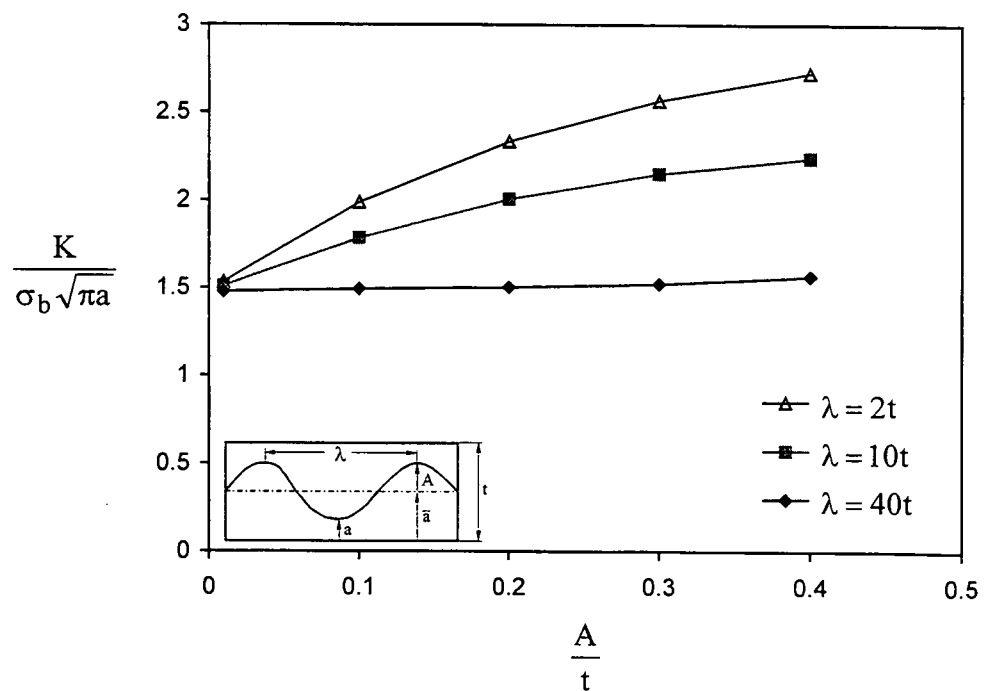


Figure 3.15: Dependence of the stress intensity factor on the amplitude and wavelength for a deep sinusoidal crack ($\bar{a} = 0.5t$) in three-point bending.

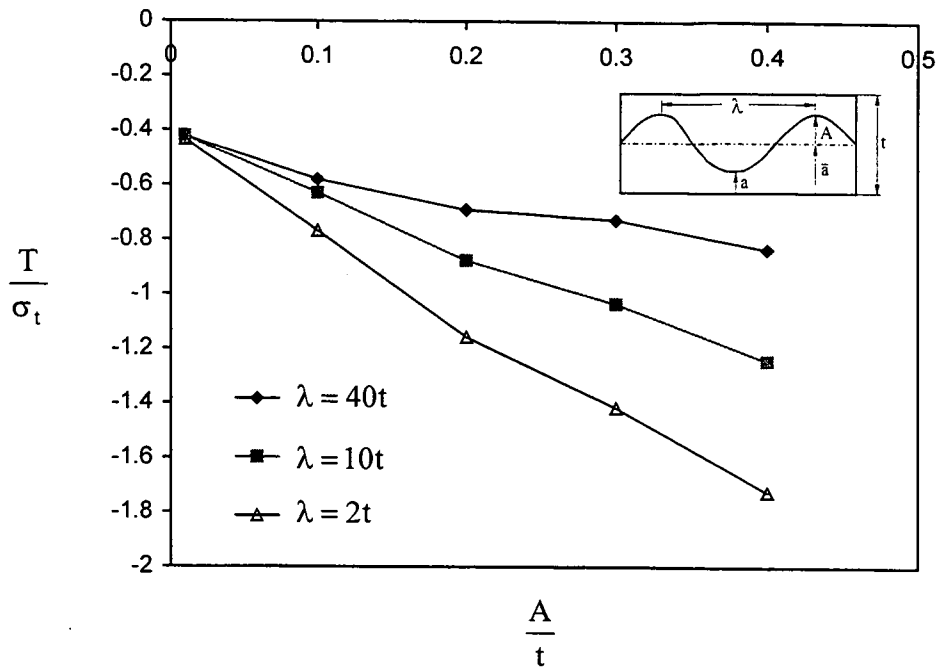


Figure 3.16: Dependence of the T-stress on the amplitude and wavelength for a deep sinusoidal crack ($\bar{a} = 0.5t$) in tension.

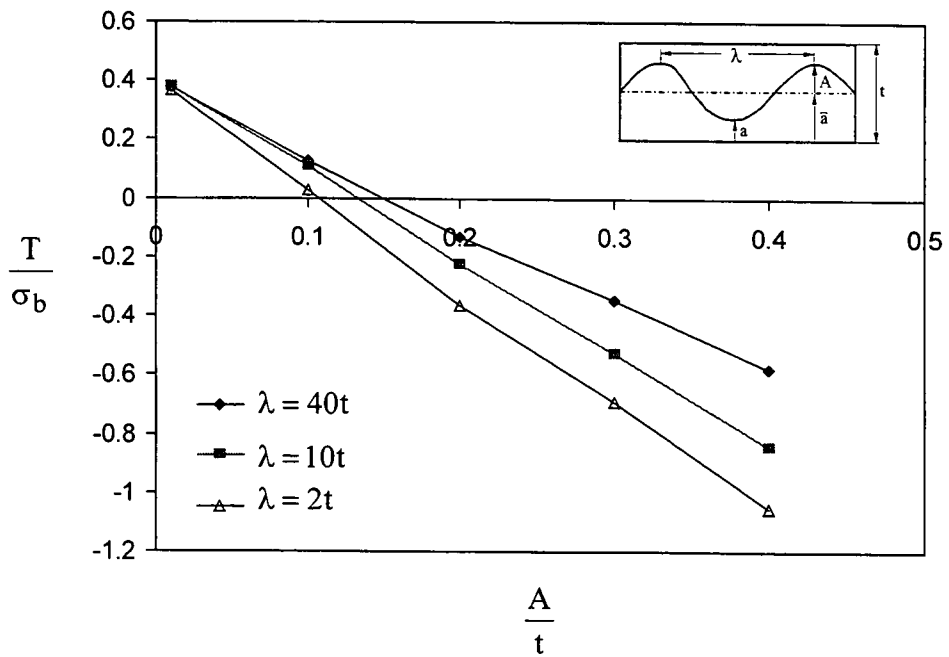


Figure 3.17: Dependence of the T-stress on the amplitude and wavelength for a deep sinusoidal crack ($\bar{a} = 0.5t$) in three point bending.

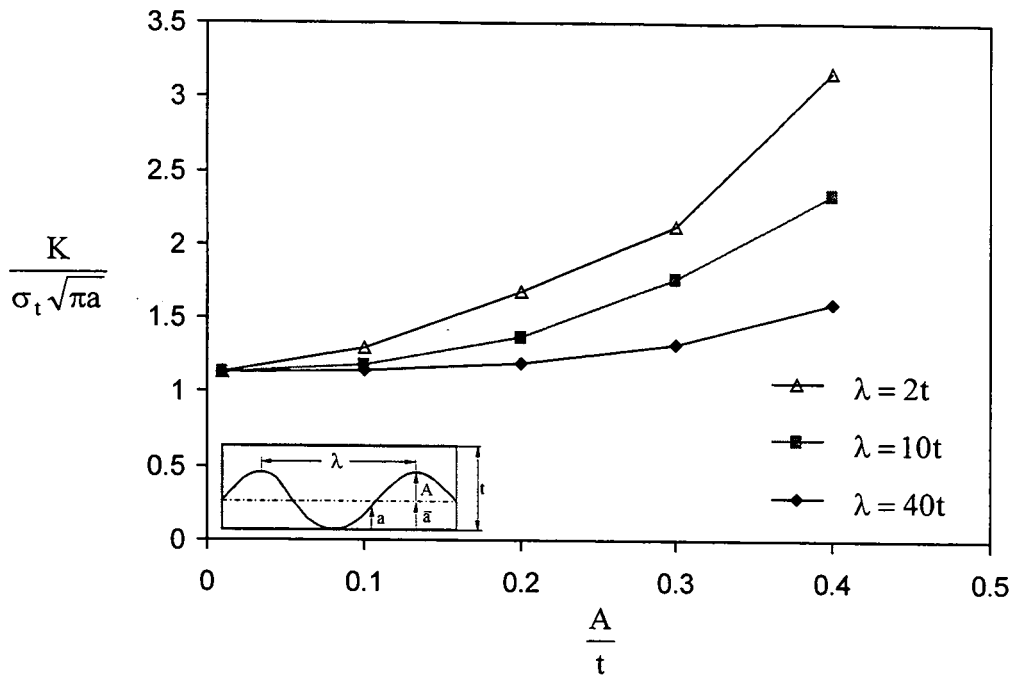


Figure 3.18: Dependence of the stress intensity factor on the amplitude and wavelength for a surface touching sinusoidal crack in tension.

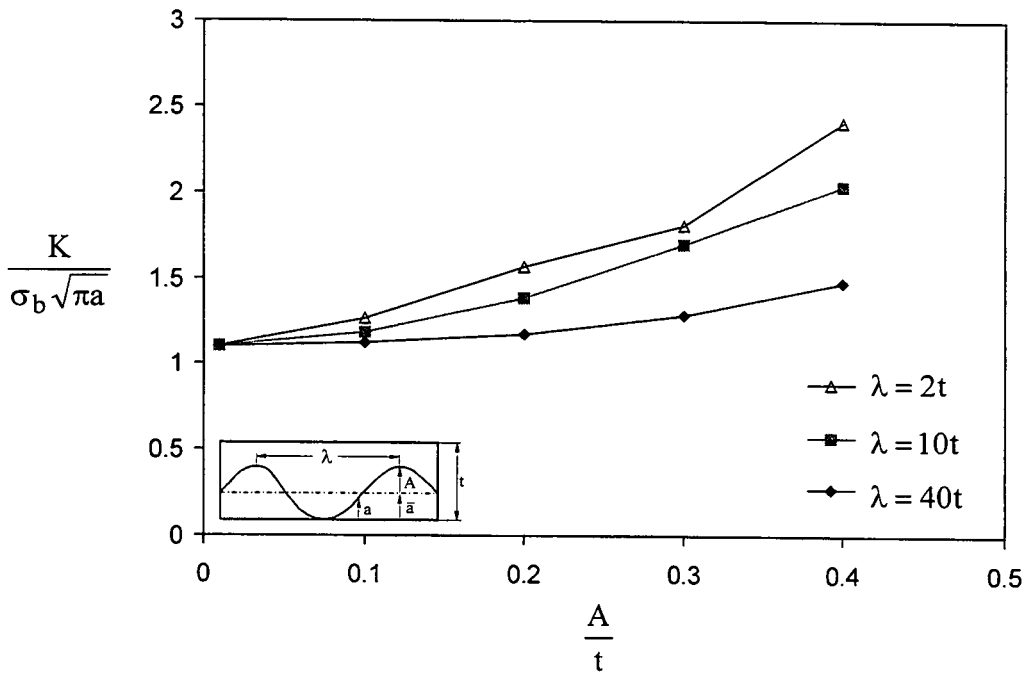


Figure 3.19: Dependence of the stress intensity factor on the amplitude and wavelength for a surface touching sinusoidal crack in three point bending.

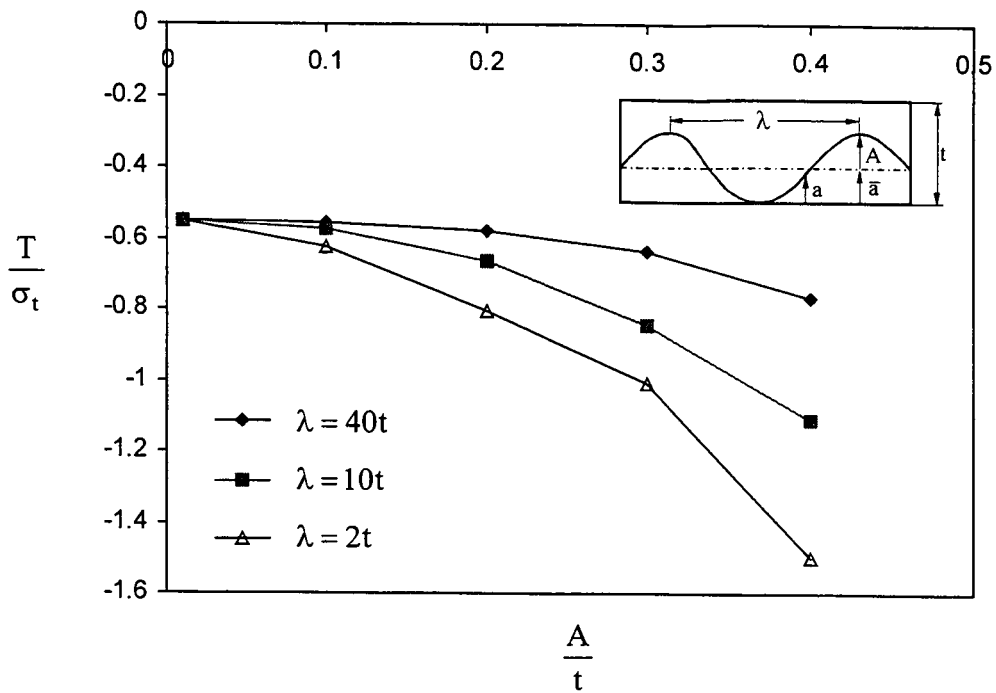


Figure 3.20: Dependence of the elastic T-stress on the amplitude and wavelength for a surface touching sinusoidal crack in tension.

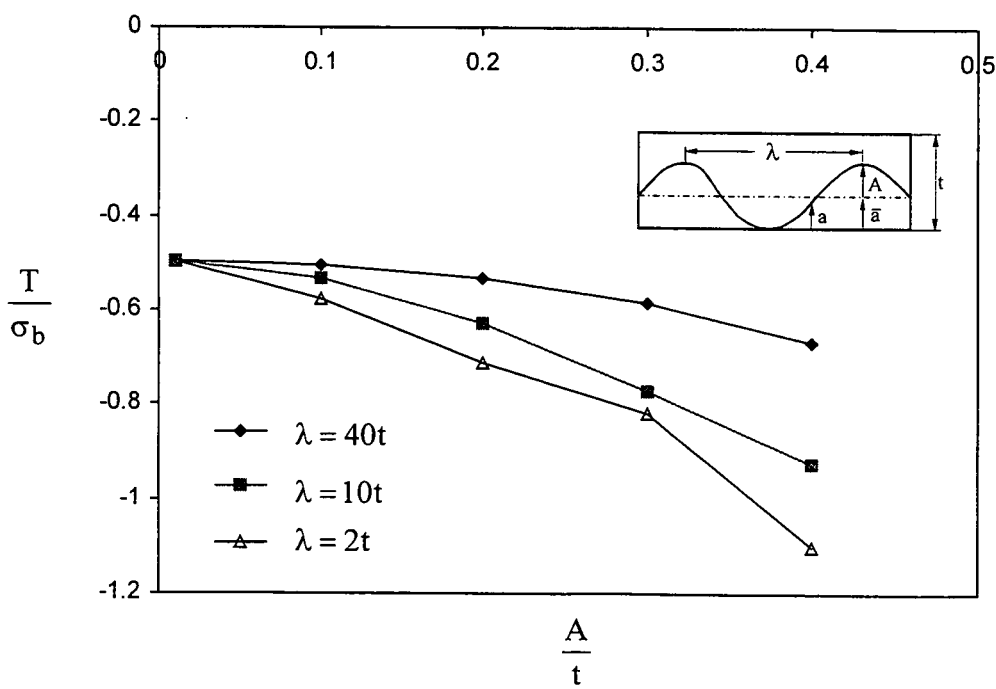


Figure 3.21: Dependence of the elastic T-stress on the amplitude and wavelength for a surface touching sinusoidal crack in three point bending.

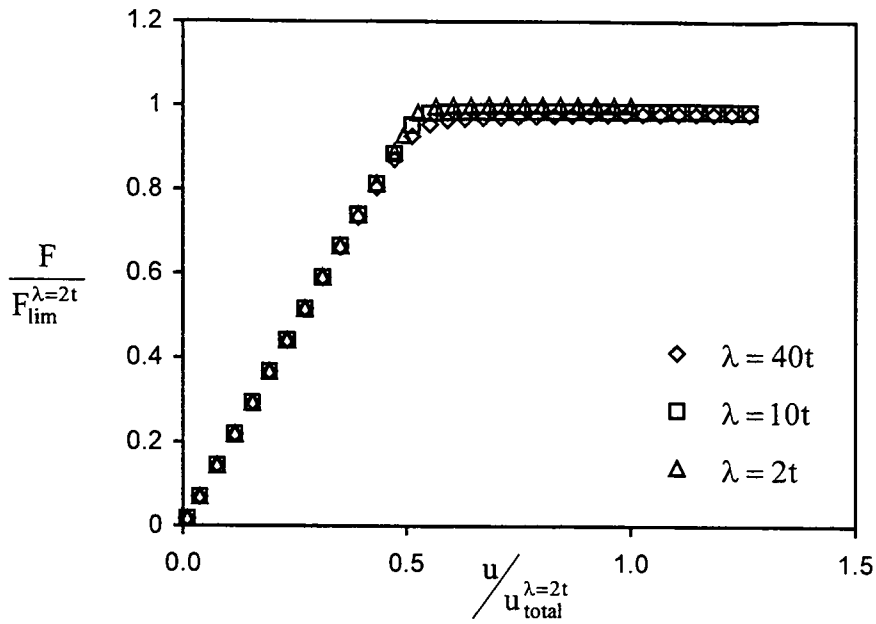


Figure 3.22 :

Load-displacement relationship for a surface touching sinusoidal crack in tension. The forces, F , are normalised by the global limit load, $F_{lim}^{\lambda=2t}$, of $\lambda=2t$ configuration, while the displacements, u , are normalised by the displacement at the global limit load of $\lambda=2t$ configuration.

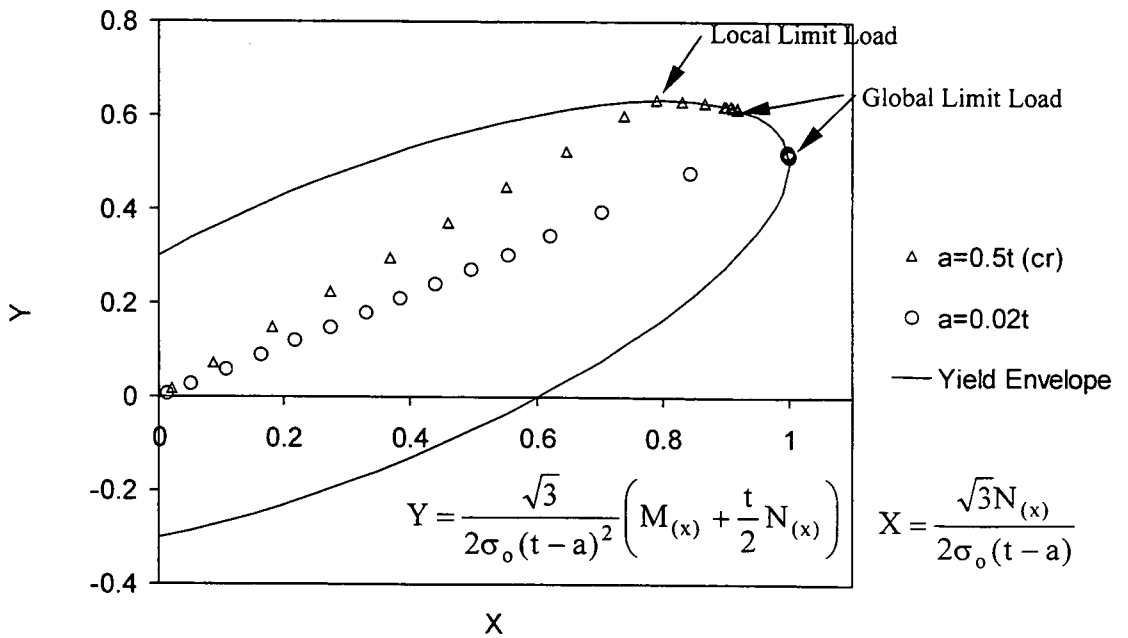


Figure 3.23:

Determination of local critical values for surface touching sinusoidal crack of $\lambda = 10t$ in tension; deepest and shallowest point analysed.

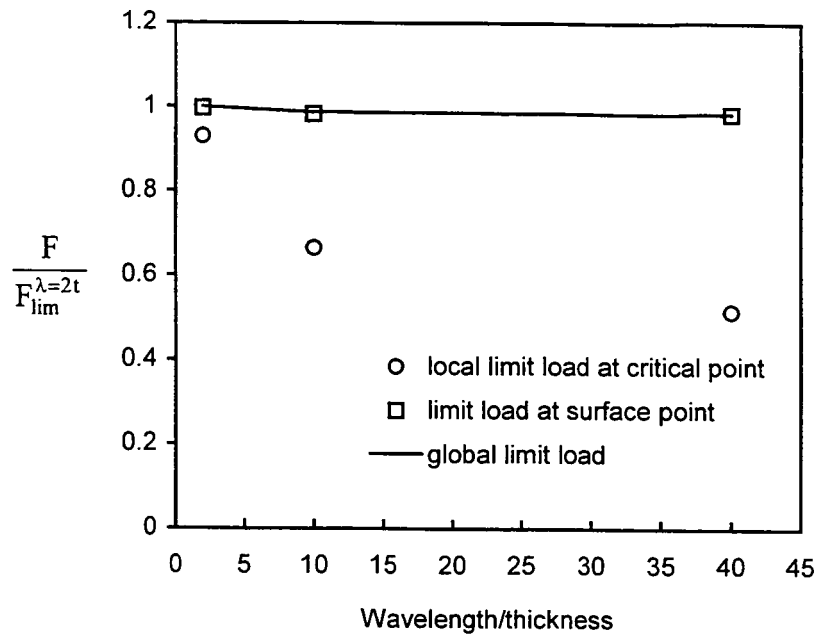


Figure 3.24:
Global and local limit load for surface touching sinusoidal crack in tension; normalised with global limit load for $\lambda = 2t$ configuration.

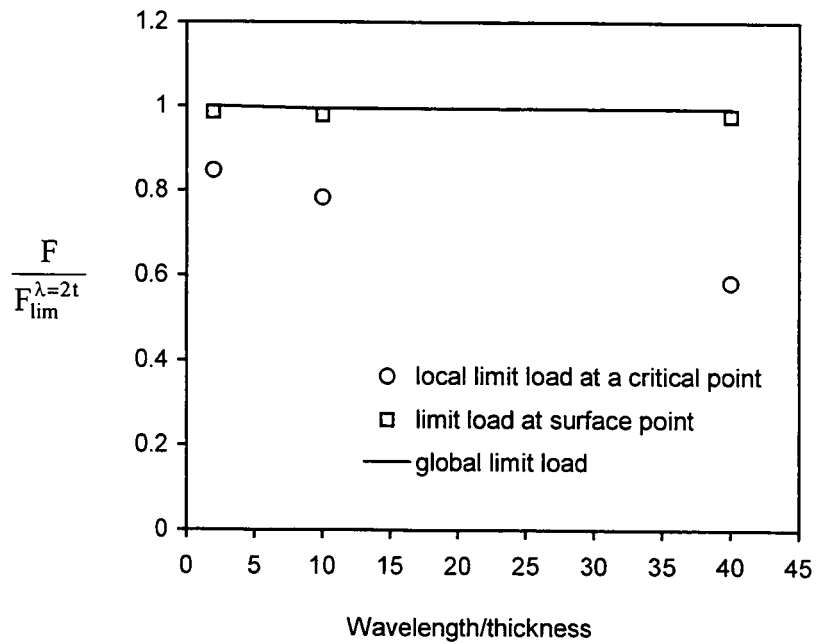


Figure 3.25:
Global and local limit load for surface touching sinusoidal crack in three-point bending; normalised with global limit load for $\lambda = 2t$ configuration.

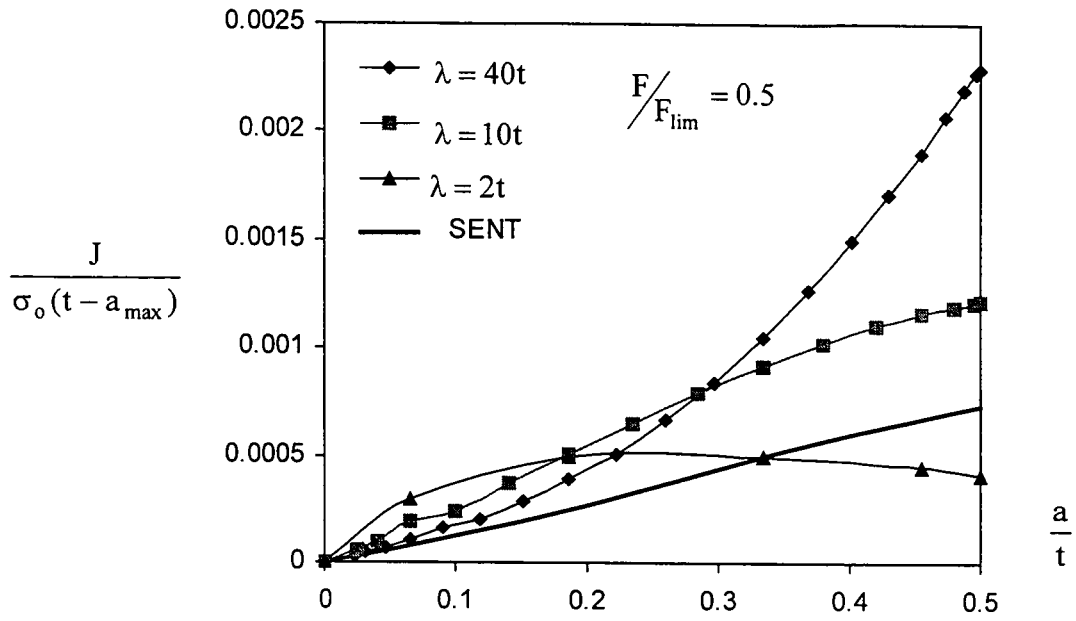


Figure 3.26:
Development of plasticity for a surface touching sinusoidal crack of $A = 0.25t$ and $\bar{a} = 0.25t$ at $F = 0.5F_{lim}$ in tension.

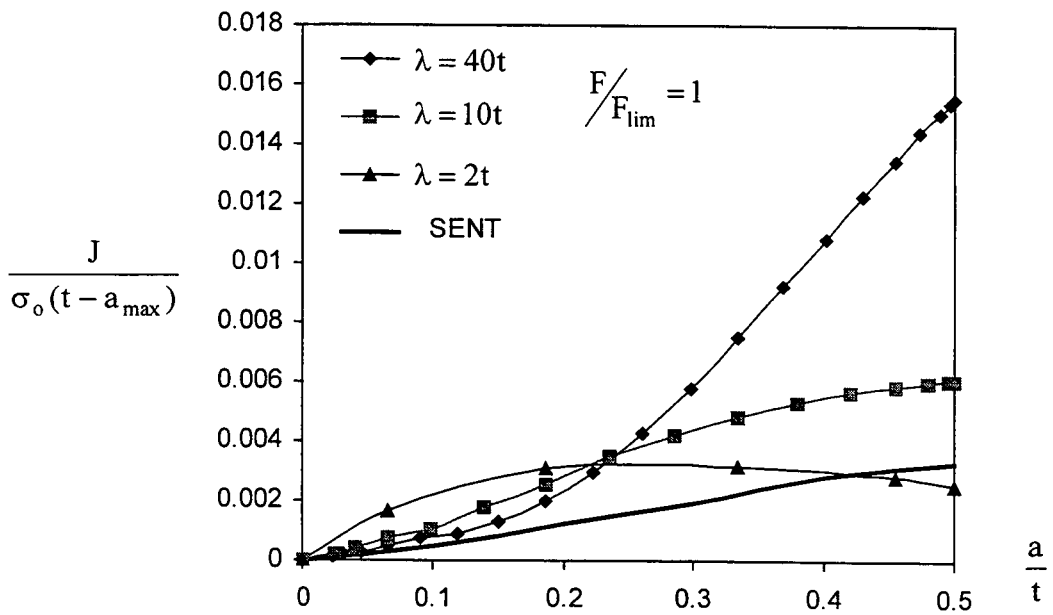


Figure 3.27:
Development of plasticity for a surface touching sinusoidal crack of $A = 0.25t$ and $\bar{a} = 0.25t$ at $F = F_{lim}$ in tension.

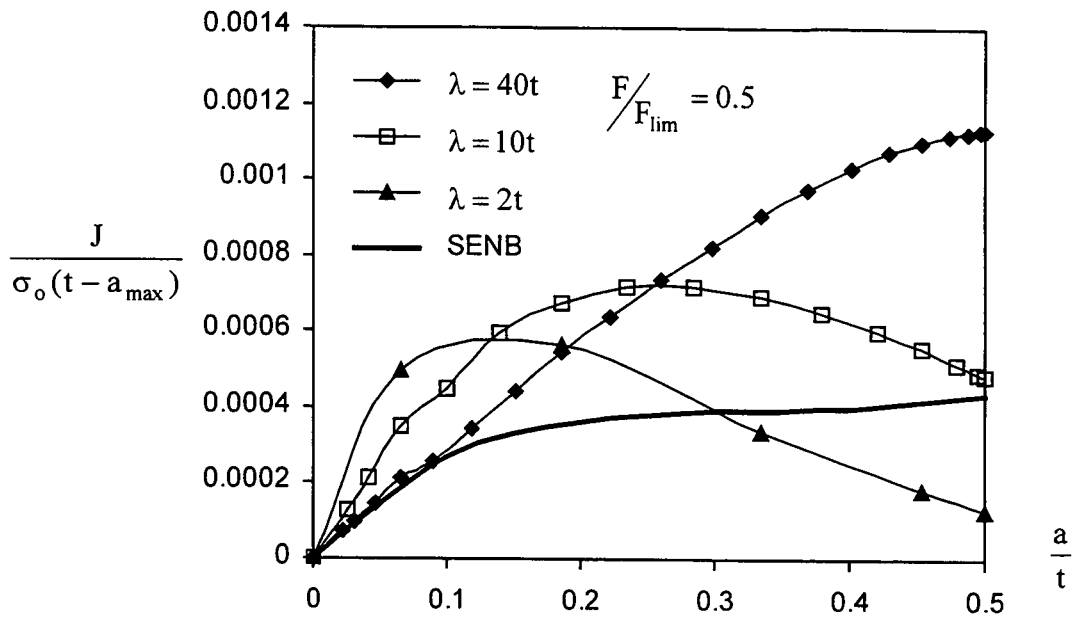


Figure 3.28:
Development of plasticity for surface touching sinusoidal crack of $A = 0.25t$ and $\bar{a} = 0.25t$ at $F=0.5F_{lim}$ in three point bending.

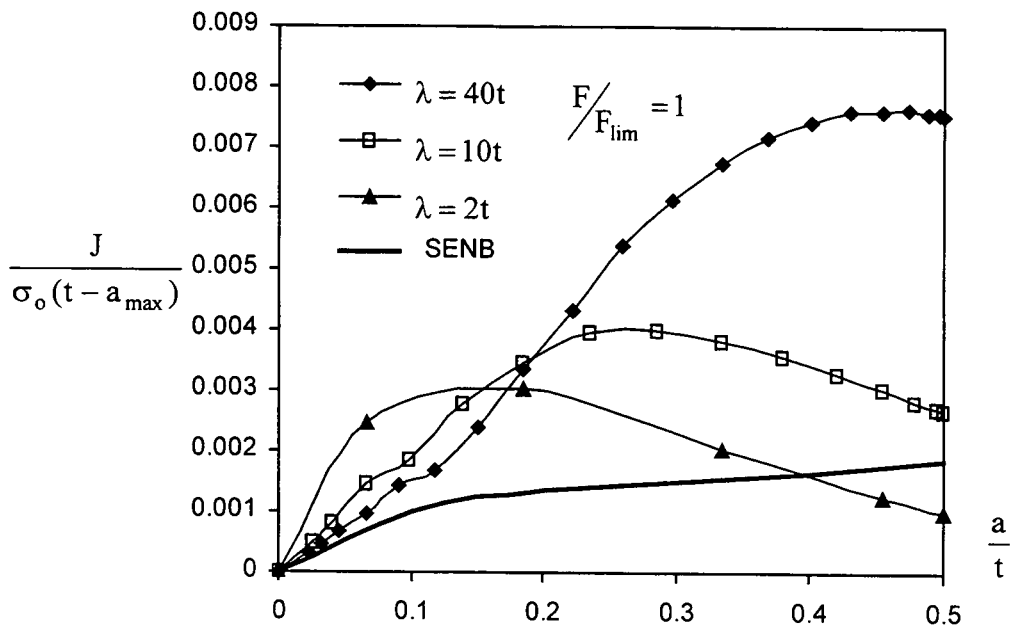


Figure 3.29:
Development of plasticity for surface touching sinusoidal crack of $A = 0.25t$ and $\bar{a} = 0.25t$ at $F=F_{lim}$ in three-point bending.

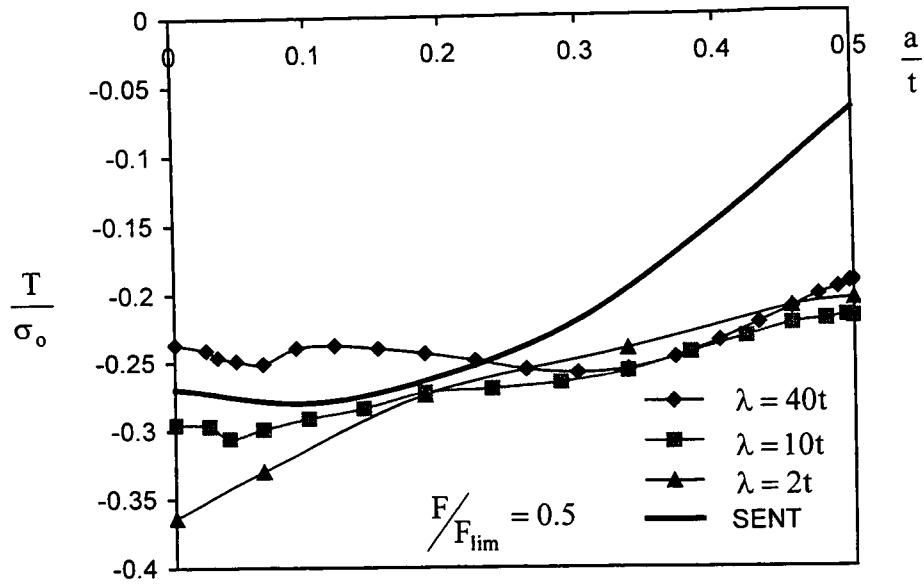


Figure 3.30:
Development of crack tip constraint, parameterised with the T-stress, for a surface touching sinusoidal crack of $A = 0.25t$ and $\bar{a} = 0.25t$ at $F = 0.5F_{lim}$ in tension.

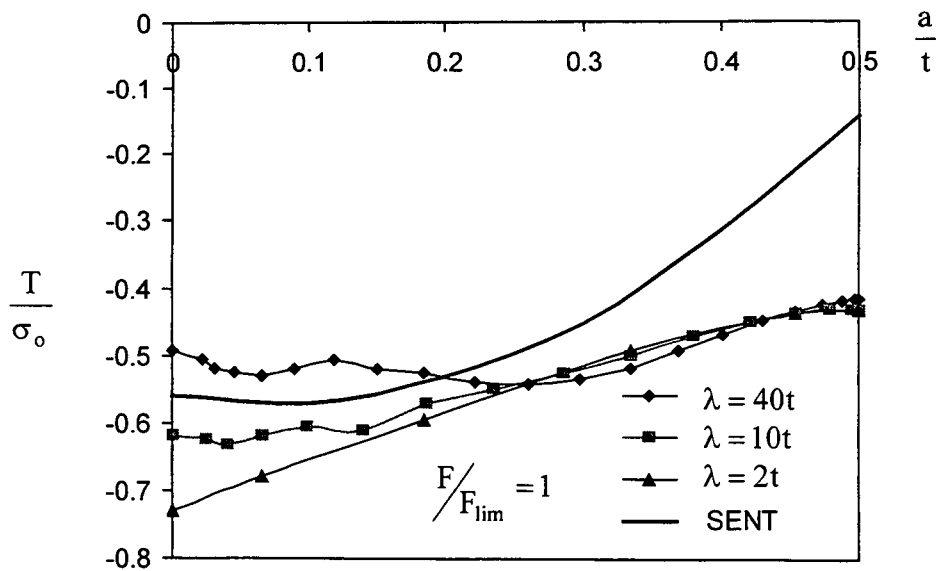


Figure 3.31:
Development of crack tip constraint, parameterised with the T-stress, for a surface touching sinusoidal crack of $A = 0.25t$ and $\bar{a} = 0.25t$ at $F = F_{lim}$ in tension.

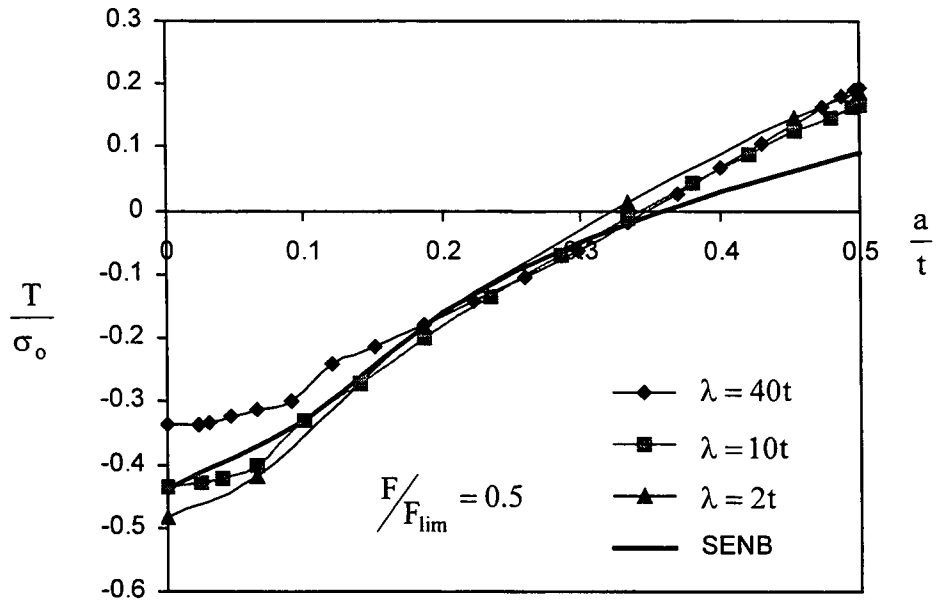


Figure 3.32:
Development of crack tip constraint, parameterised with the T-stress, for a surface touching sinusoidal crack of $A = 0.25t$ and $\bar{a} = 0.25t$ at $F = 0.5F_{lim}$ in three-point bending.

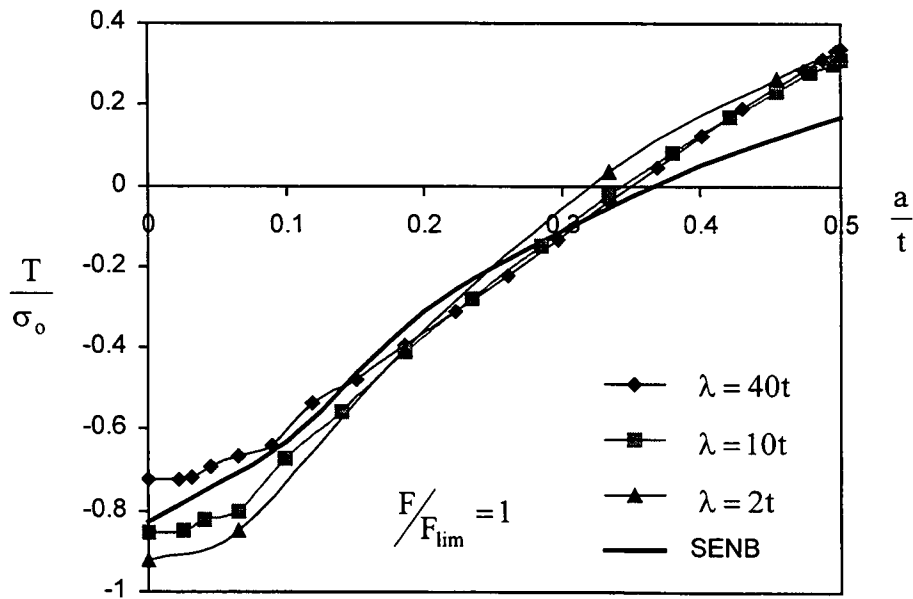


Figure 3.33:
Development of crack tip constraint parameterised with the T-stress, for a surface touching sinusoidal crack of $A = 0.25t$ and $\bar{a} = 0.25t$ at $F = F_{lim}$ in three-point bending.

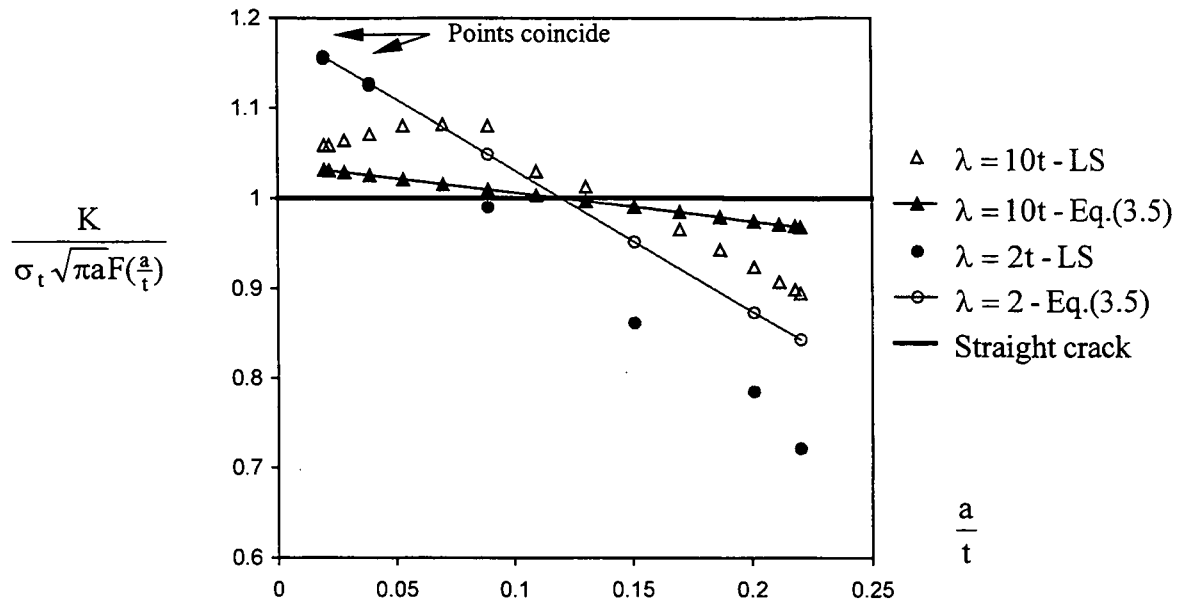


Figure 3.34:
Comparison of line spring data with results of Eq. (3.5) for a surface touching sinusoidal crack of $A = 0.1t$, $\bar{a} = 0.12t$ in tension.

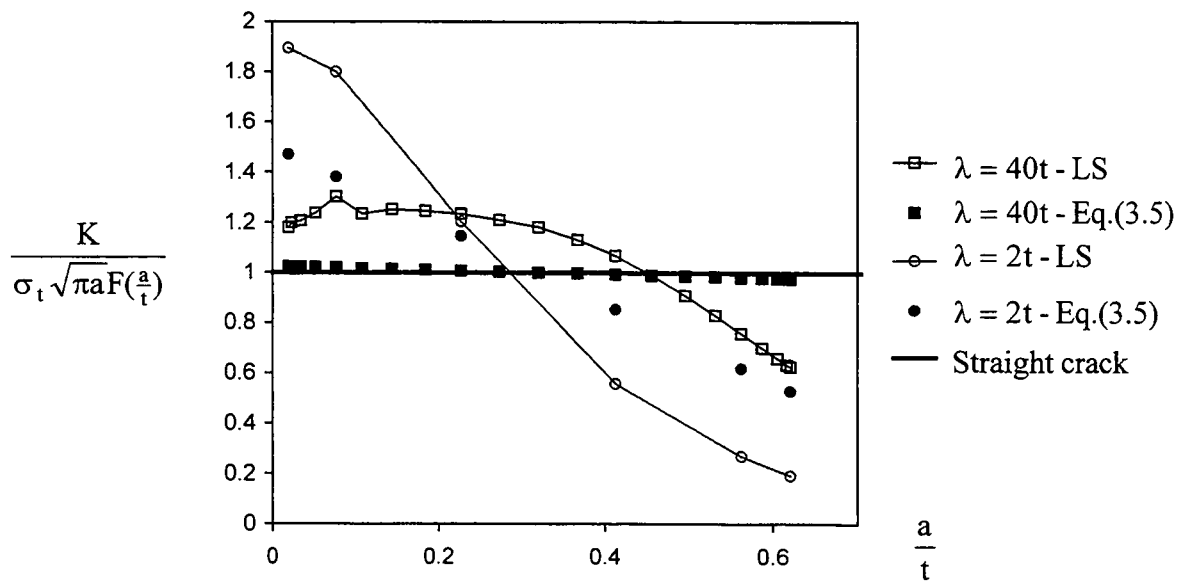


Figure 3.35
Comparison of line spring data with results of Eq. (3.5) for a surface touching sinusoidal crack of $A = 0.3t$, $\bar{a} = 0.32t$ in tension.

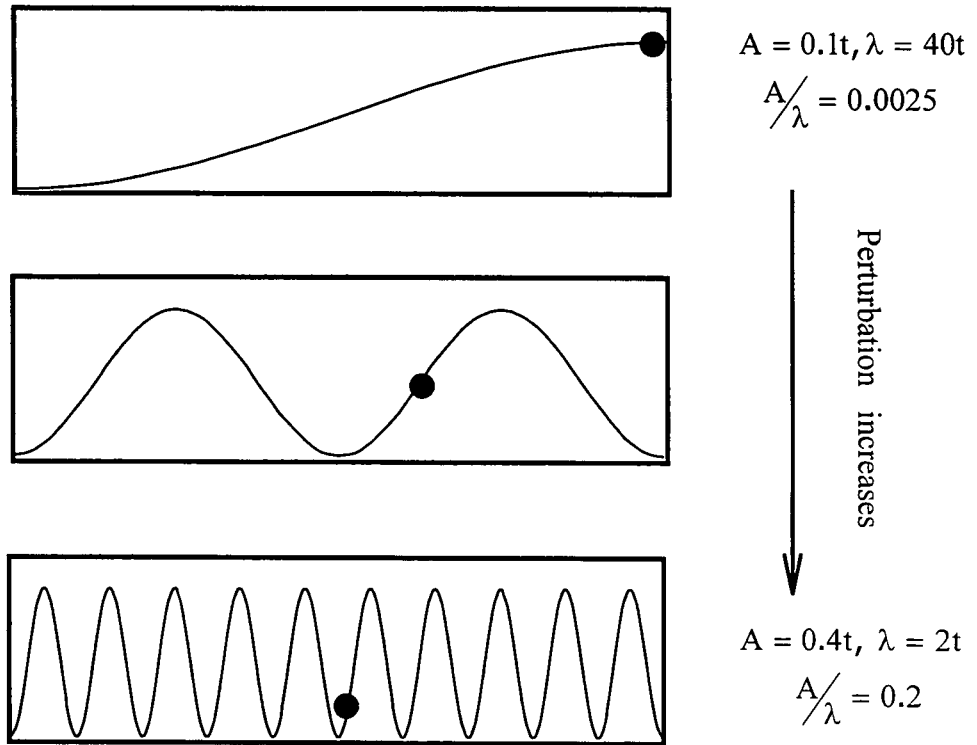


Figure 3.36:
 Increase in the crack front perturbation shifts the location of the maximum K or J towards the shallower segments in tension and bending.

Chapter 4

WEAKEST LINK STATISTICS

The failure of brittle materials has been widely discussed as a statistical process (Freudenthal (1968)) and analysed using weakest link statistics (Wallin (1984), Slatcher and Oystend (1986), Bruckner-Fort *et al* (1990)). These studies are concerned with the effect of crack front length on the overall resistance to failure by examining the stress intensity factor along the crack front of standard fracture mechanics specimens. This simplification was relaxed by Beremin (1983) by considering the probability of failure initiating within the process zone. Cleavage failure is considered to result from a high local tensile stress acting over a sufficiently large volume of material that allows the cleavage of a hard particle and the unstable propagation of the resulting micro-cracks (Ritchie *et al* (1973)). This is essentially a statistical process governed by the probability of finding a favourable initiating particle.

4.1 Theoretical background

Weakest link arguments were developed by considering a chain composed of a series of identical links. The chain is point loaded at both ends to ensure the same load on the links, which have randomly distributed strengths. The failure of the chain occurs when the critical strength is exceeded in the weakest link. Slatcher and Oystend (1986) argue that the weakest link argument describes the failure of a structure containing a sharp crack if:

- (a) structure is defined to be brittle with respect to its components, that is the entire structure fails when one of its sub-segment fails.
- (b) The components are equally loaded,
- (c) The strength of the components is identically distributed,
- (d) The strength of the components is mutually independent.

The brittleness condition can be illustrated with failure from two specimens which differ in the crack front lengths. If a specimen A having a long crack front is divided in specimens B of a shorter crack front length and each specimen B fails in brittle manner, than the specimen A is defined to be brittle. The brittleness condition is not satisfied when a cleavage crack that causes total failure in specimen B, arrests in a larger specimen A, such

as the pop-in effects in inhomogeneous materials. The condition is also not satisfied when the micromechanism of crack extension is ductile.

The criterion that the crack driving force should not vary along the crack front allows a connection to be made with the mechanics of the point loaded chain. However cracks in real structures seldom have shapes with constant crack driving forces along the crack length. In a deterministic assessment structural integrity is evaluated for the position with the greatest value of K or J , which is in the weakest link model equivalent of assuming the entire structure is point loaded to the greatest value. The restriction can be relaxed if the chain is conceptually allowed to have a spatially distributed both, load and strength, as discussed in subsequent sections.

The criterion of identically distributed fracture toughness requires that the fracture toughness does not depend on position or orientation of the micro-crack with respect to the body, hence fracture toughness of any link can be described with identical distribution function. However toughness distribution frequently varies spatially along crack fronts, such as due to stress triaxiality or material gradation. If the spatial and statistical variation of fracture toughness is known, the failure probability can be calculated. At a fixed failure probability this allows fracture toughness to be expressed as a function of spatial parameters, leading to transferability schemes between crack configurations.

Experimental fracture toughness data measured on standard specimens of different thickness (crack front lengths) largely conforms to the weakest link governed failure (Wallin (1984, 1985, 1989), Slatcher and Oystend (1986)). Propositions have been made to scale the toughness data with the thickness of the test piece and describe the data throughout the ductile-brittle transition with a single toughness curve, the "Master curve" method of ASTM E1921 (1997).

4.2 The weakest link model

The weakest link model partitions the crack front into small segments of sufficient volume to contain a weak particle from which cleavage originates (Ritchie *et al* (1973)). The failure of each segment is considered to be statistically independent and described with a cumulative distribution function, P , such as that proposed by Weibull.

$$P^i = 1 - \exp\left(-\left(\frac{K}{K_o}\right)^n\right) \quad (4.1)$$

Here P^i is a probability of failure of segment i at or below the stress intensity factor, K , and K_o is a material property with dimensions of $\text{MPa}\sqrt{\text{m}}$. If a crack front of length s , is divided into incremental segments of length s_o , the survival of the crack front requires survival of all segments, giving:

$$1 - P = (1 - P^i)^{s/s_o} \quad (4.2)$$

Agreement with experimental cleavage data (Landes and Shaffer (1980)) has been achieved using a two parameter Weibull cumulative distribution, although three parameter distributions have also been used (Bezensek and Hancock (2003)). For a straight crack of length s , subject to uniform stress intensity factor, K , the probability of failure, P , can be written as:

$$P = 1 - \exp\left\{-\frac{s}{s_o}\left(\frac{K}{K_o}\right)^n\right\} \quad (4.3)$$

where K_o and s_o are scaling constants. Wallin (1984) has argued that the shape factor for J-dominant cracks should be 4. To extend the method to materials with spatially dependent crack tip parameters, the material property, K_o , can be written in terms of the mean toughness, \bar{K} , of any link:

$$\bar{K} = K_o \Gamma\left(1 + \frac{1}{n}\right) \quad (4.4)$$

where $\Gamma\left(1 + \frac{1}{n}\right)$ is the Gamma function. This allows Eq. (4.3) to be rewritten as:

$$P = 1 - \exp\left\{-\frac{s}{s'_o}\left(\frac{K}{\bar{K}}\right)^n\right\} \quad (4.5)$$

where

$$s'_o = \frac{s_o}{\Gamma\left(1 + \frac{1}{n}\right)} \quad (4.6)$$

The mean fracture toughness, \bar{K} , is now considered to be a function of constraint, K_{mat} . Similar arguments can be developed to consider effects of material gradation. In general the constraint and the mean local toughness vary with spatial position, allowing Eq. (4.5) to be written more generally as:

$$P = 1 - \exp - \left\{ \frac{1}{s'_0} \int_s \left(\frac{K_{(v)}}{K_{\text{mat}}} \right)^n dv \right\} \quad (4.7)$$

$K_{(v)}$ is the stress intensity factor at position v on the crack front of length s , and K_{mat} is the local toughness. The failure probability is determined by integrating the ratio $K_{(v)}/K_{\text{mat}}$ along the entire crack front. Alternatively the argument can be developed to define the mean failure condition.

4.3 Transferability of fracture toughness data

The stress intensity factor, $K_{(v)}$, can always be separated into load and geometry dependent parts using a reference stress intensity factor, K_{ref} , and a non-dimensional function of geometry, $\alpha_{(v)}$:

$$K_{(v)} = K_{\text{ref}} \cdot \alpha_{(v)} \quad (4.8)$$

The reference stress intensity factor is essentially a loading parameter which can be chosen in a number of arbitrary ways. In the present context it is advantageous to identify K_{ref} with the maximum stress intensity factor along the crack front. The probability of failure can then be expressed by substituting Eq. (4.8) into the cumulative failure probability of Eq. (4.3):

$$P = 1 - \exp - \left\{ \frac{\xi}{s'_0} \left(\frac{K_{\text{ref}}}{K_0} \right)^n \right\} \quad (4.9)$$

where ξ is:

$$\xi = \int_s \alpha_{(v)}^n dv \quad (4.10)$$

Slatcher and Oystend (1986) show that ξ is essentially an effective crack front length. This may readily be evaluated for geometries for which a closed-form expression for the non-dimensional stress intensity factor is available or by a numerical evaluation of computational results.

The probability density function is defined by differentiating the cumulative probability function with respect to K_{ref} :

$$p = \frac{\partial P}{\partial K_{\text{ref}}} \quad (4.11)$$

This allows the mean value of K_{ref} to be written as:

$$\bar{K}_{\text{ref}} = \int_0^{\infty} K_{\text{ref}} \cdot p \cdot dK_{\text{ref}} = K_o \left(\frac{S_o}{\xi} \right)^{\frac{1}{n}} \Gamma\left(1 + \frac{1}{n}\right) \quad (4.12)$$

with the variance:

$$\psi^2(K_{\text{ref}}) = \int_0^{\infty} p \cdot (K_{\text{ref}} - \bar{K}_{\text{ref}})^2 dK_{\text{ref}} \quad (4.13)$$

The ratio of the mean values of K_{ref} for two configurations, A and B, then depends on the ratio of the effective crack front length parameters, ξ^A and ξ^B :

$$\frac{\bar{K}_{\text{ref}}^A}{\bar{K}_{\text{ref}}^B} = \left(\frac{\xi^B}{\xi^A} \right)^{\frac{1}{n}} \quad (4.14)$$

and variance of the two geometries also scales with the effective crack front lengths:

$$\frac{\psi^2(K_{\text{ref}})^A}{\psi^2(K_{\text{ref}})^B} = \left(\frac{\xi^B}{\xi^A} \right)^{\frac{2}{n}} \quad (4.15)$$

The variances are proportional to the second power of the mean values of fracture toughness, a relation that is implicit to using the Weibull cumulative distribution function in describing toughness data.

The loading parameter K_{ref} can also be expressed with the failure probability by rearranging Eq. (4.9):

$$K_{\text{ref}} = K_o \left(\frac{S_o}{\xi} \right)^{\frac{1}{n}} \left[\ln \frac{1}{1-P} \right]^{\frac{1}{n}} \quad (4.16)$$

By combining Eq. (4.14) and (4.16) the critical value of a loading parameter to be used in the assessment schemes on a geometry A (K_{ref}^A) can be inferred from the mean value of critical loading parameter (fracture toughness) of a geometry B (\bar{K}_{ref}^B), at a chosen survival probability (1-P):

$$\frac{K_{\text{ref}}^A}{\bar{K}_{\text{ref}}^B} = \left(\frac{\xi^B}{\xi^A} \right)^{\frac{1}{n}} \left[\ln \frac{1}{1-P} \right]^{\frac{1}{n}} \frac{1}{\Gamma\left(1 + \frac{1}{n}\right)} \quad (4.17)$$

Two geometries may have different geometric shapes and sizes, but for straight cracks in similar shaped test specimen, Eq. (4.14) is equivalent to the statistical size corrections of

ASTM E1921 (1997). Equation (4.14) can also be used to map fracture mechanics parameters from one geometry to another, by invoking size and shape corrections at a given failure probability (Eq. (4.17)). Given the ratio of the reference stress intensity factors in two configurations, it is also straight forward to compare the failure loads.

$$\frac{\bar{F}^A}{\bar{F}^B} = \frac{\upsilon^B}{\upsilon^A} \left(\frac{\xi^B}{\xi^A} \right)^{\frac{1}{n}} \quad (4.18)$$

and

$$\frac{F^A}{F^B} = \frac{\upsilon^B}{\upsilon^A} \left(\frac{\xi^B}{\xi^A} \right)^{\frac{1}{n}} \left[\ln \frac{1}{1-P} \right]^{\frac{1}{n}} \frac{1}{\Gamma(1 + \frac{1}{n})} \quad (4.19)$$

and the variance of load:

$$\frac{\Psi^2(F)^A}{\Psi^2(F)^B} = \frac{\upsilon^B}{\upsilon^A} \left(\frac{\xi^B}{\xi^A} \right)^{\frac{2}{n}} \quad (4.20)$$

where υ is function of geometry and the dimension chosen to define K_{ref} .

4.4 Applications to straight and semi-elliptical cracks

4.4.1 Statistical effects associated with straight cracks

The stress intensity factor for a straight crack has a form (Tada (1973)):

$$K_{(v)} = \sigma \sqrt{\pi a} G\left(\frac{a}{t}\right), \quad (4.21)$$

which can be separated into a reference stress intensity factor and a function of the crack shape:

$$K_{(v)} = \left\{ \sigma \sqrt{\pi a} \right\} \cdot \left\{ G\left(\frac{a}{t}\right) \right\} = K_{ref} \cdot \alpha_{(v)} \quad (4.22)$$

Here K_{ref} is chosen to be the nominal stress intensity factor, which is in particular advantageous for examining the effect of size and shape on the fracture resistance of semi-elliptical cracks in the next section. In this manner the semi-elliptical cracks can be conveniently described by a set of parameters defined by Raju-Newman. For a chosen semi-elliptical geometry a relation between the nominal K and the maximum K , which depends on the position on the crack front, can be described using Raju-Newman

expression and based on results of this chapter the fracture resistance can than be expressed in terms of $K_{\text{ref}}=K_{\text{max}}$.

For a straight crack the stress intensity factor is independent of position on the crack front and the crack shape function, $\alpha_{(v)}$, is constant for a given geometry. For a straight crack the integral of Eq. (4.9) can then readily be solved along the crack length, s , giving the mean value of K_{ref} :

$$\bar{K}_{\text{ref}} = K_o \left(\frac{s_o}{s \cdot G(\frac{a}{t})^4} \right)^{\frac{1}{4}} \Gamma(1 + \frac{1}{4}) \quad (4.23)$$

and the mean load \bar{F} , as:

$$\bar{F} = \frac{K_o}{v} \left(\frac{s_o}{s \cdot G(\frac{a}{t})^4} \right)^{\frac{1}{4}} \Gamma(1 + \frac{1}{4}) \quad (4.24)$$

with the variances:

$$\psi^2(K_{\text{ref}}) = K_o^2 \left(\frac{s_o}{s \cdot G(\frac{a}{t})^4} \right)^{\frac{1}{2}} \left[\Gamma(1 + \frac{1}{2}) - (\Gamma(1 + \frac{1}{4}))^2 \right] \quad (4.25)$$

$$\psi^2(F) = \frac{K_o^2}{v} \left(\frac{s_o}{s \cdot G(\frac{a}{t})^4} \right)^{\frac{1}{2}} \left[\Gamma(1 + \frac{1}{2}) - (\Gamma(1 + \frac{1}{4}))^2 \right] \quad (4.26)$$

When \bar{K}_{ref} is considered for two straight cracks of equal crack depth, ($\frac{a}{t}=\text{fixed}$), but different crack front length, s , the statistical size effect given in ASTM E1921 (1997), is recovered.

$$\frac{\bar{K}_{\text{ref}}^A}{\bar{K}_{\text{ref}}^B} = \left(\frac{s^B}{s^A} \right)^{\frac{1}{4}} \quad (4.27)$$

4.4.2 Statistical effects associated with semi-elliptical cracks

A closed-form expression for the stress intensity factor around a semi-elliptical crack front is given by Raju-Newman (1981). The crack shape is defined by its depth to surface length ratio, a/c , the crack depth, a/t , and the ratio of the free surface length to the width of the geometry, c/b . The position around the crack front is described in terms of the angular

parameter φ , defined in Figure 4.1. The stress intensity factor is given in a general form as a function of the parametric angle, φ :

$$K_{(\varphi)} = (\sigma_t + H\sigma_b) \sqrt{\pi \frac{a}{Q}} \cdot G\left(\frac{a}{t}, \frac{a}{c}, \frac{c}{b}, \varphi\right) \quad (4.28)$$

This can be separated into a reference SIF, ($K_{\text{ref}} = \sigma \sqrt{\pi a}$), and a function of geometry $\alpha_{(\varphi)}$, as before. For tension Eq.(4.28) becomes:

$$K_{(\varphi)} = \{\sigma_t \sqrt{\pi a}\} \cdot \left\{ \sqrt{\frac{1}{Q}} \cdot G\left(\frac{a}{t}, \frac{a}{c}, \frac{c}{b}, \varphi\right) \right\} \quad (4.29a)$$

and for bending:

$$K_{(\varphi)} = \{\sigma_b \sqrt{\pi a}\} \cdot \left\{ \sqrt{\frac{1}{Q}} \cdot H\left(\frac{a}{t}, \frac{a}{c}, \varphi\right) \cdot G\left(\frac{a}{t}, \frac{a}{c}, \frac{c}{b}, \varphi\right) \right\} \quad (4.29b)$$

The cumulative probability of failure for a semi-elliptical crack follows by substituting above expressions (4.29) in expression (4.9). The integration along the crack arc length, s , can be replaced by integration around the angle Φ . The line segment dv is related to the angle φ through the relationship:

$$dv = c \cdot \sqrt{\sin^2 \varphi + \left(\frac{a}{c}\right)^2 \cos^2 \varphi} \cdot d\varphi \quad (4.30)$$

The failure probability for a semi-elliptical crack then becomes:

$$P_{(K)} = 1 - \exp\left\{-\frac{K_{\text{ref}}^4 \cdot c}{K_o^4 \cdot s_o} \cdot \chi\left(\frac{a}{c}, \frac{a}{t}, \frac{c}{b}\right)\right\} \quad (4.31)$$

where the function $\chi\left(\frac{a}{c}, \frac{a}{t}, \frac{c}{b}\right)$ incorporates effects of crack length and crack shape and is a function of the crack geometry:

$$\chi\left(\frac{a}{c}, \frac{a}{t}, \frac{c}{b}\right) = \int_{\Phi} \alpha_{(\varphi)}^4 \cdot \sqrt{\sin^2 \varphi + \left(\frac{a}{c}\right)^2 \cos^2 \varphi} \cdot d\varphi \quad (4.32)$$

The effective crack front length for a semi-elliptical defect is simply: $\xi = c\chi$.

The mean value of K_{ref} for a semi-elliptical crack follows as:

$$\bar{K}_{\text{ref}} = K_o \left(\frac{s_o}{c \cdot \chi\left(\frac{a}{c}, \frac{a}{t}, \frac{c}{b}\right)} \right)^{\frac{1}{4}} \Gamma\left(1 + \frac{1}{4}\right) \quad (4.33)$$

with the mean load :

$$\bar{F} = \frac{K_o}{\nu} \left(\frac{s_o}{c \cdot \chi\left(\frac{a}{c}, \frac{a}{t}, \frac{c}{b}\right)} \right)^{\frac{1}{4}} \Gamma\left(1 + \frac{1}{4}\right) \quad (4.34)$$

and variances:

$$\psi^2(K_{\text{ref}}) = K_o^2 \left(\frac{s_o}{c \cdot \chi\left(\frac{a}{c}, \frac{a}{t}, \frac{c}{b}\right)} \right)^2 \left[\Gamma\left(1 + \frac{1}{2}\right) - \left(\Gamma\left(1 + \frac{1}{4}\right)\right)^2 \right] \quad (4.35)$$

$$\psi^2(F) = \frac{K_o^2}{\nu} \left(\frac{s_o}{c \cdot \chi\left(\frac{a}{c}, \frac{a}{t}, \frac{c}{b}\right)} \right)^2 \left[\Gamma\left(1 + \frac{1}{2}\right) - \left(\Gamma\left(1 + \frac{1}{4}\right)\right)^2 \right] \quad (4.36)$$

4.4.3 Statistical effects associated with straight and semi-elliptical cracks

Safety margins on the defect re-characterisation procedure can be assessed by comparing the mean values of loading parameter, \bar{K}_{ref} , or the mean values of failure loads for semi-elliptical and straight cracks. The ratio of \bar{K}_{ref} for a semi-elliptical crack, $\bar{K}_{\text{ref}}^{\text{SE}}$, and an equivalent long straight crack, $\bar{K}_{\text{ref}}^{\text{st,eq}}$, shows the contribution to the safety margins from the shape of the crack front:

$$\frac{\bar{K}_{\text{ref}}^{\text{SE}}}{\bar{K}_{\text{ref}}^{\text{st,eq}}} = \left(\frac{s^{\text{SE}} \cdot G\left(\frac{a}{t}\right)^4}{c \cdot \chi\left(\frac{a}{c}, \frac{a}{t}, \frac{c}{b}\right)} \right)^{\frac{1}{4}} = \left(\frac{\gamma\left(\frac{a}{c}\right)}{\chi\left(\frac{a}{c}, \frac{a}{t}, \frac{c}{b}\right)} \right)^{\frac{1}{4}} \cdot G\left(\frac{a}{t}\right) \quad (4.37)$$

The length of an equivalent straight crack is defined as the crack front length of a semi-elliptical crack and can be written in terms of the surface length, c , and a function of geometry, $\gamma\left(\frac{a}{c}\right)$:

$$s^{\text{SE}} = c \cdot \gamma\left(\frac{a}{c}\right) \quad (4.38)$$

$$\gamma\left(\frac{a}{c}\right) = \int_{\phi} \sqrt{(\sin \phi)^2 + \left(\frac{a}{c}\right)^2 (\cos \phi)^2} \, d\phi \quad (4.39)$$

A more general form of the mean values of the loading parameter for a semi-elliptical crack and a straight crack of arbitrary length, s^{st} , is:

$$\frac{\bar{K}_{\text{ref}}^{\text{SE}}}{\bar{K}_{\text{ref}}^{\text{st}}} = \left(\frac{s^{\text{st}}}{s^{\text{SE}}} \right) \left(\frac{\gamma\left(\frac{a}{c}\right)}{\chi\left(\frac{a}{c}, \frac{a}{t}, \frac{c}{b}\right)} \right)^{\frac{1}{4}} \cdot G\left(\frac{a}{t}\right) \quad (4.40)$$

with a variance:

$$\frac{\Psi^2(K_{ref}^{SE})}{\Psi^2(K_{ref}^{st})} = \left(\frac{s^{st}}{s^{SE}} \right)^{\frac{1}{2}} \left(\frac{\gamma(\frac{a}{c})}{\chi(\frac{a}{c}, \frac{a}{t}, \frac{c}{b})} \right)^{\frac{1}{2}} \cdot G(\frac{a}{t})^2 \quad (4.41)$$

As an example of the use of Eq. (4.40) consider \bar{K}_{ref} as the average fracture toughness of a standard test geometry (K_{mat}). The average resistance to failure of a semi-elliptical geometry, \bar{K}_{ref}^{SE} , can be determined using Eq. (4.40). Likewise the critical value of the loading parameter to be used in the assessment schemes follows from the value for the standard geometry and a survival probability: :

$$\frac{K_{ref}^{SE}}{K_{ref}^{st}} = \left(\frac{s^{st}}{s^{SE}} \right)^{\frac{1}{4}} \cdot \left(\frac{\gamma(\frac{a}{c})}{\chi(\frac{a}{c}, \frac{a}{t}, \frac{c}{b})} \right)^{\frac{1}{4}} \frac{G(\frac{a}{t})}{\Gamma(1 + \frac{1}{4})} \left[\ln \frac{1}{1-P} \right]^{\frac{1}{4}} \quad (4.42)$$

The mean failure loads of semi-elliptical and a straight cracks scale through the functions of their crack size and shape:

$$\frac{\bar{F}^{SE}}{\bar{F}^{st}} = \frac{v^{st}}{v^{SE}} \cdot \left(\frac{s^{st}}{s^{SE}} \right)^{\frac{1}{4}} \cdot \left(\frac{\gamma(\frac{a}{c})}{\chi(\frac{a}{c}, \frac{a}{t}, \frac{c}{b})} \right)^{\frac{1}{4}} G(\frac{a}{t}) \quad (4.43)$$

with a variance ratio:

$$\frac{\Psi^2(F^{SE})}{\Psi^2(F^{st})} = \frac{v^{st}}{v^{SE}} \left(\frac{s^{st}}{s^{SE}} \right)^{\frac{1}{2}} \left(\frac{\gamma(\frac{a}{c})}{\chi(\frac{a}{c}, \frac{a}{t}, \frac{c}{b})} \right)^{\frac{1}{2}} G(\frac{a}{t})^2 \quad (4.44)$$

The failure load for a semi-elliptical crack geometry follows from the average failure load of a straight crack at a chosen probability of survival, as:

$$\frac{F^{SE}}{F^{st}} = \frac{v^{st}}{v^{SE}} \left(\frac{s^{st}}{s^{SE}} \right)^{\frac{1}{4}} \cdot \left(\frac{\gamma(\frac{a}{c})}{\chi(\frac{a}{c}, \frac{a}{t}, \frac{c}{b})} \right)^{\frac{1}{4}} \frac{G(\frac{a}{t})}{\Gamma(1 + \frac{1}{4})} \left[\ln \frac{1}{1-P} \right]^{\frac{1}{4}} \quad (4.45)$$

4.5 Results

4.5.1 Analytically computed values of χ for semi-elliptical cracks

The Raju-Newman (1981) parametric stress intensity factor expression describes a broad range of semi-elliptical crack configurations, with the ratios of crack depth to plate thickness from 0 to 1.0 and the ratio of crack depth to crack surface length from 0 to 1.0. The effects of plate width on the stress intensity factor are included through the parameter c/b for values between 0 and 0.5. For greater values of $\ln c/b$ the effects of the free edges are

more pronounced. However the stress intensity factor solution is found to be reasonably accurate for cracks in the range $c/b \leq 0.7$.

The parameter χ was determined for shallow semi-elliptical cracks by solving Eq. (4.32) using *Mathematica*TM software package. The results are presented in Figure 4.2 for tension and in Figure 4.3 for pure bending.

4.5.2 The effect of semi-elliptical crack shape on fracture resistance

The effects of crack shape on the critical stress intensity factor is shown in Figure 4.4, where the ratio of average reference stress intensity factors for semi-elliptical and equivalently long straight cracks after Eq. (4.37) is shown as a function of the parameters defining the semi-elliptical crack. Higher values of K_{ref} are observed for the semi-elliptical defect compared to the value for the equivalent straight crack in both, tension and pure bending. For shallow crack segments ($a/t < 0.3$) that are subject to predominant tensile local loading, the amplification of the reference SIF over that of the straight crack is independent of the type of remotely applied loading. With increasing depth the remote bending effect is observed under bending. The results suggest that the fracture resistance of a semi-elliptical geometry (as measured by K_{ref}) is higher compared to the straight crack front of equal lengths, an effect that arises from the curvature of the semi-elliptical crack shape.

4.5.3 Discrete evaluation of the effective crack front length

Statistical size and shape effects can be determined exactly when closed-form expressions for the stress intensity factor are known. When only numerical values are available an approximate method may be used. A continuous integration domain, defined along the crack front length, is divided into discrete segments. Each segment has defined a discrete value of the distributed variable, $\alpha_{(t)}$. The size and shape of the irregular crack are expressed as an effective crack front length, ξ , through the summation :

$$\xi_{\text{discrete}} = \sum_i \left(\frac{\alpha_{(v)_i}^4 + \alpha_{(v)_{i+1}}^4}{2} \right) \cdot \Delta v_i \quad (4.46)$$

and the non-dimensional expression $\alpha_{(t)}$ is defined by :

$$\alpha_{(v)_i} = \frac{K_i^{\text{FE}}}{\sigma \sqrt{\pi a_{\text{deepest}}}} \quad (4.47)$$

K_i^{FE} is the applied stress intensity factor at a discrete position on the crack front, calculated from finite element model and the incremental crack length, Δv_i , is defined as (see Figure 4.5):

$$\Delta v_i = \sqrt{(x_{i+1} - x_i)^2 + (y_{i+1} - y_i)^2} \quad (4.48)$$

4.5.4 Comparison with the experimental data

The procedure is applied to a series of cleavage tests on complex defects, semi-elliptical surface breaking defects and standard straight crack 25 mm thick three point bend specimens. The test were performed using 50D steel at temperature -196 °C. Crack geometries, failure loads and further details of the test procedure are given in Chapter 9, section 9.2 and in Table 9.1. The effective crack front length, ξ , was determined numerically by integrating the stress intensity factor calculated by line spring analysis. The results shown in Table 4.1 demonstrate good agreement between the ratio of experimental failure loads and the average values derived from the size and shape corrections, using Eq. (4.43). Semi-elliptical cracks were also analysed using the Newman-Raju (1981) solutions for ξ and the results agree closely with the line spring analysis.

4.6 Discussion

During integrity assessments under brittle conditions, the critical values of stress intensity factors are estimated at critical locations on real or re-characterised defects. These are compared with values measured on standard geometries of nominally straight cracks of “preferred” width (ASTM E399-88) under high constraint conditions. The effect of thickness on the fracture toughness measured on straight cracks can be assessed through the size-effect arguments (Wallin (1985), ASTM E1921 (1997)). However in practice defects are seldom straight and are usually idealised to be semi-elliptical with a low aspect ratio. Such defects benefit from the shape of the crack front, as illustrated in Figure 4.4. The use of fracture toughness data obtained from standard deep cracked geometries with straight crack fronts and a predetermined width is not realistic and may be over-

conservative. The above procedure allows for crack shape and size to be included in integrity assessment, to evaluate the safety margins of the re-characterised defect by comparing the crack tip parameters. Similarly the technique allows realistic design parameters for a component to be transferred from data obtained on standard test geometries.

Test No.	Test geometry		Comparison	
	Characteristic crack dimension, a_D [mm]	Effective crack front length, ξ [mm]	$(F^{\text{test}}/F^{\text{straight}})$ measured	$(F^{\text{test}}/F^{\text{straight}})$ from Eq. (4.43)
S11	11.2	21.51	3.0	3.4
S12	11.0	24.50	3.4	3.3
S13	14.0	17.60	3.3	3.2
S15	13.7	7.51	3.9	4.0
S16	13.5	7.36	3.6	4.1

Table 4.1:
Evaluation of the transferability schemes, by comparing measured failure loads with those obtained using the Eq. (4.43).

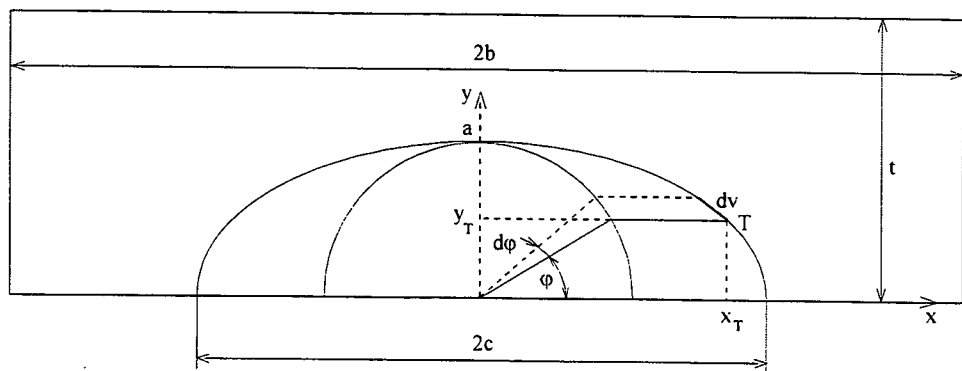


Figure 4.1:
Parametric definition of a semi-elliptical crack.

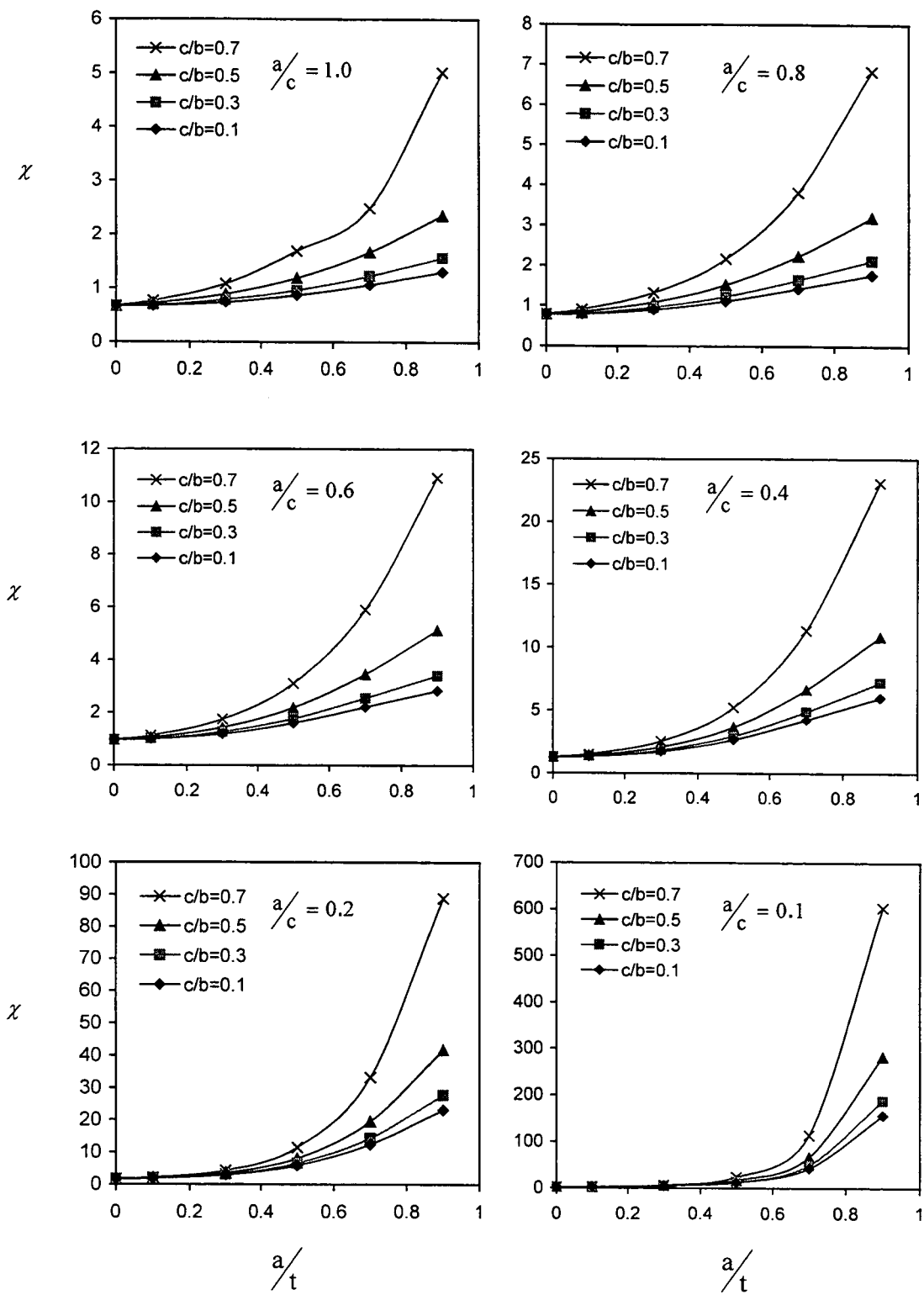


Figure 4.2:
 Values for the parameter χ for a semi-elliptical crack in tension, computed from Raju-Newman (1981) expression.

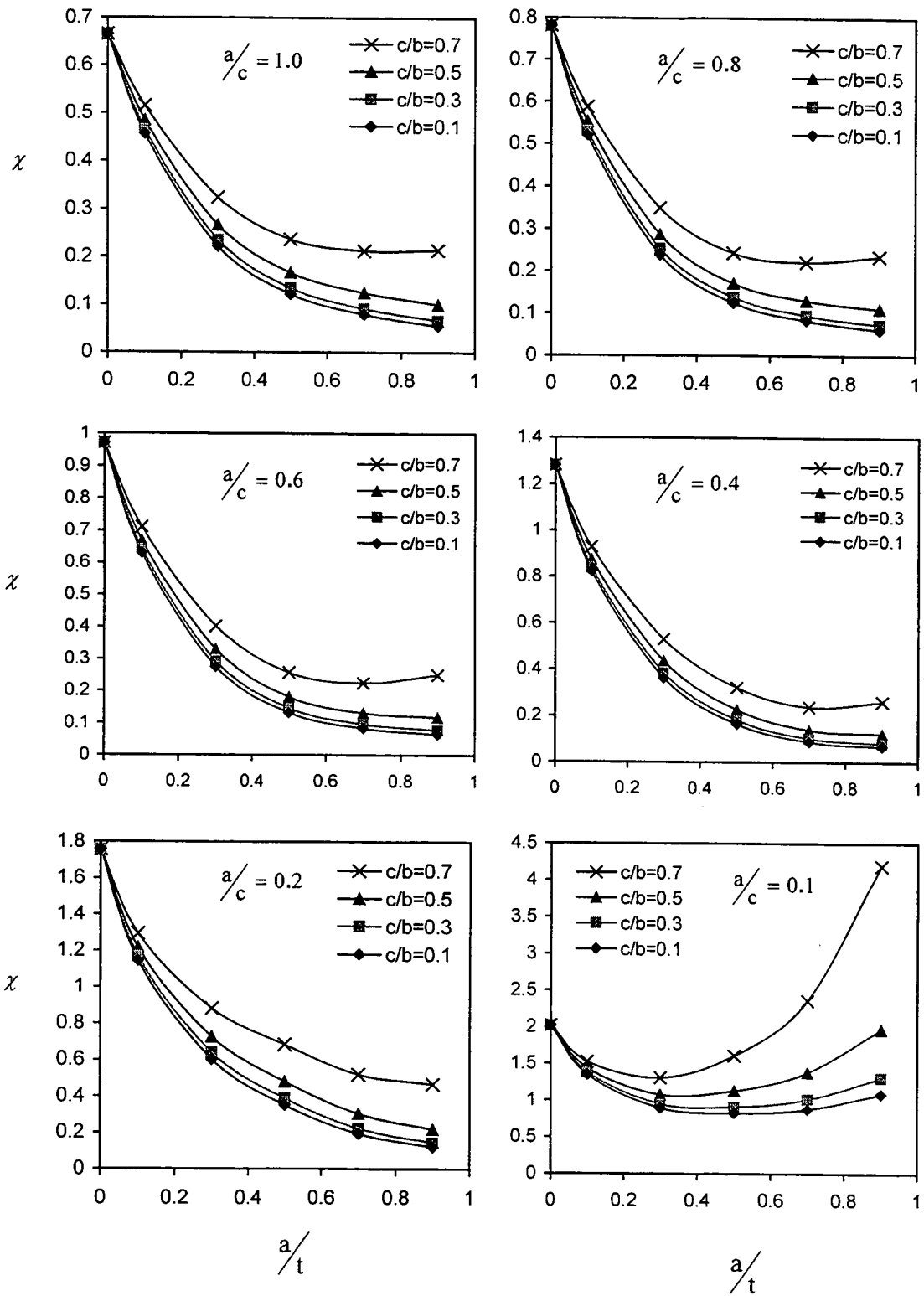


Figure 4.3:
 Values for the parameter χ for a semi-elliptical crack in pure bending, computed from Raju-Newman (1981) solution.

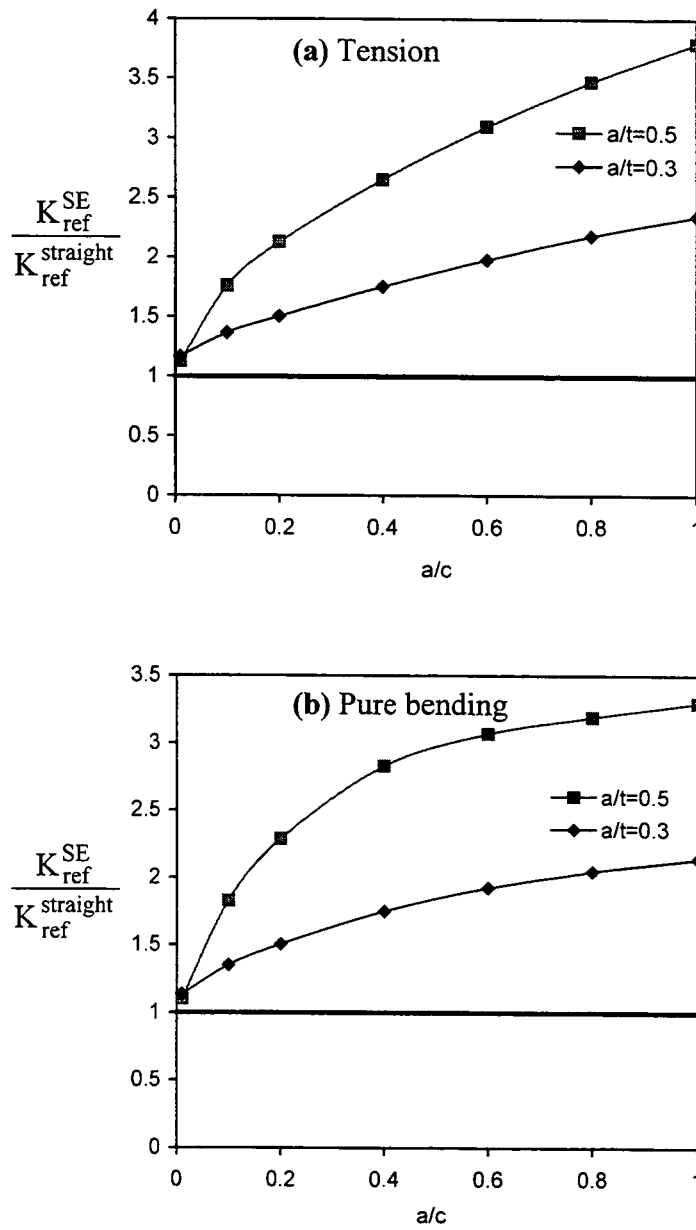


Figure 4.4:

The increased fracture resistance expressed in terms of K_{ref} of a semi-elliptical crack compared to a straight crack of equal lengths, due to the shape of the crack: (a) tension and (b) pure bending.

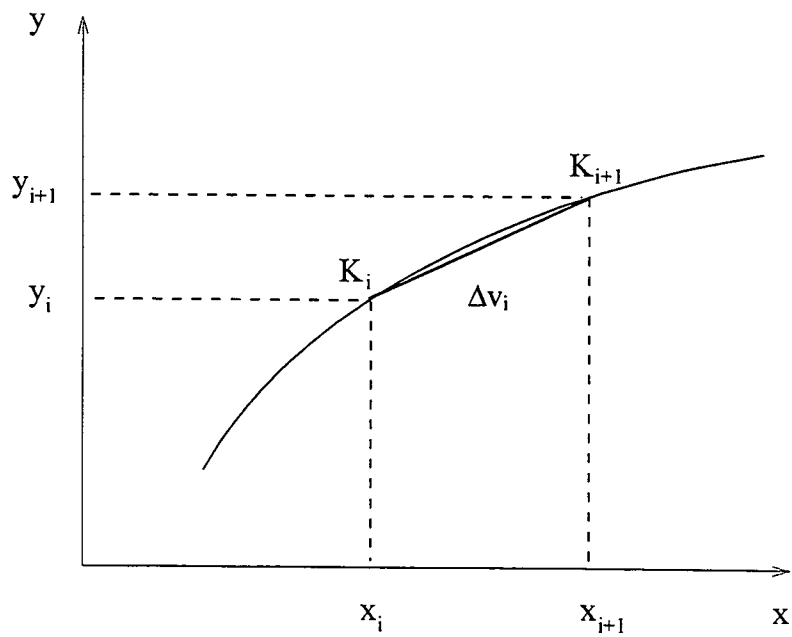


Figure 4.5:
Definition of the line segment Δv_i for approximating the effective crack front length using discrete values.

Chapter 5

THE RE-CHARACTERISATION OF COMPLEX DEFECTS

Defect assessment procedures ensure the integrity of structures which may contain cracks or flaws. Assessments are based on toughness data obtained from standard tests on specimens with straight crack fronts. The integrity of the structure is then demonstrated by comparing a characterising parameter, such as the stress intensity factor, K , or the J -integral, J , around the perimeter of a real or idealised defect with critical values obtained from standard test geometries. However real structures may contain neighbouring defects, or defects with complex shapes. Codes, such as BS 7910 (1999), R6/4 (2001) and ASME Section XI (1992), invoke procedures which allow multiple interacting or complex defects to be idealised as simpler shapes, which are more amenable to analysis. To ensure the procedure is conservative, the re-characterised defects must be demonstrated to be more detrimental than the original defect. Although the re-characterisation procedures are primarily intended for complex defects which extend by fatigue, they may also be applied to monotonic loading failures under both cleavage and ductile tearing conditions.

The re-characterisation procedure can be applied to single defects, or to multiple interacting defects, on a single or adjacent planes. Multiple non co-planar defects are assessed either as co-planar defects or as separate defects, depending on proximity rules set out in the codes. The re-characterisation procedure is approached in two stages illustrated in Figure 5.1 for defects on a single plane. The defect is enclosed in a rectangular box and a re-characterised defect is generated by inscribing a semi-elliptical profile for a surface breaking defect, or an elliptical profile for sub-surface defect, within the box. One axis of the semi-ellipse is parallel to the free surface length, while the other axis extends in the through-thickness direction.

The criteria for defect interaction and re-characterisation originated from the interaction of plastic zones of adjacent near surface crack tips. In document PD 6493 (1991) that preceded the BS 7910 and R6/4, the interaction criteria is based on the free surface lengths of both defects. The two co-planar surface breaking defects, shown in Figure 5.1, are considered as through-thickness cracks of length equal to free surface length. The plastic zone sizes are estimated for plane stress conditions at the crack tip as:

$$\begin{aligned} r_{p1} &= 2r_{o1} = 2K_I^2 / (2\pi\sigma_o^2) = (\sigma / \sigma_o)^2 c_1 \\ r_{p2} &= 2r_{o2} = (\sigma / \sigma_o)^2 c_2 \end{aligned} \quad (5.1)$$

where σ_o is the yield stress and r_{p1} and r_{p2} are plastic zone sizes for defects 1 and 2. An interaction criteria follows by equating the plastic zone sizes with the distance between the crack tip:

$$s = r_{p1} + r_{p2} = (\sigma / \sigma_o)^2 (c_1 + c_2) \quad (5.2a)$$

or

$$s \leq c_1 + c_2 \quad \text{for} \quad (\sigma / \sigma_o) \leq 1 \quad (5.2b)$$

The approach developed in the ASME Section XI code is identical, apart from idealising surface breaking defects as a semi-circular cracks ($a=c$), with the interaction criteria depending on the average depth of both defects:

$$s \leq 0.508(a_1 + a_2) \quad \text{for} \quad (\sigma / \sigma_o) \leq 1 \quad (5.3a)$$

or in practical, conservative, manner:

$$s \leq 2a_1 \quad \text{or} \quad 2a_2, \text{ whichever is greater.} \quad (5.3b)$$

Several experimental studies (Iida *et al* (1984), Twaddle and Hancock (1986), Soboyejo *et al* (1990), Leek and Howard (1996)), have demonstrated limited crack interaction effects under bending as the adjacent crack tips approach, and numerical analyses (O'Donoghue *et al* (1984), Soboyejo *et al* (1990), Perl *et al* (1997), Hasegawa *et al* (2001)) show enhanced values of stress intensity factors only for very closely spaced crack tips. Recent revisions of PD6493, now issued as BS 7910, and the R6/4 code incorporate limited interaction effects in fatigue but preclude the contribution of coalescence to the fatigue life, by re-characterising interacting defects only when the adjacent crack tips touch ($s=0$).

The present work focuses on the implication of significantly amplified local stress intensity factors in relatively long crack fronts, on failure and re-characterisation of complex defects in ductile-brittle transition. The fatigue study determines safety margin introduced by the new crack interaction rules in the BS7910 standard in relation to the coalescence and re-characterisation of adjacent defects extending by fatigue. The fatigue crack growth is also used to generate a family of complex cracks with re-entrant sectors, which show rapid fatigue crack growth rates in the re-entrant sectors (Twaddle and Hancock (1986),

Soboyejo *et al* (1990), Leek and Howard (1996), Bayley and Bell (1997)) associated with amplified stress intensity factors. In this context a particular concern arises from monotonic failures. This is examined for ductile tearing and cleavage from complex defect, to address the appropriateness of using the interaction rules and the re-characterisation procedure developed for fatigue.

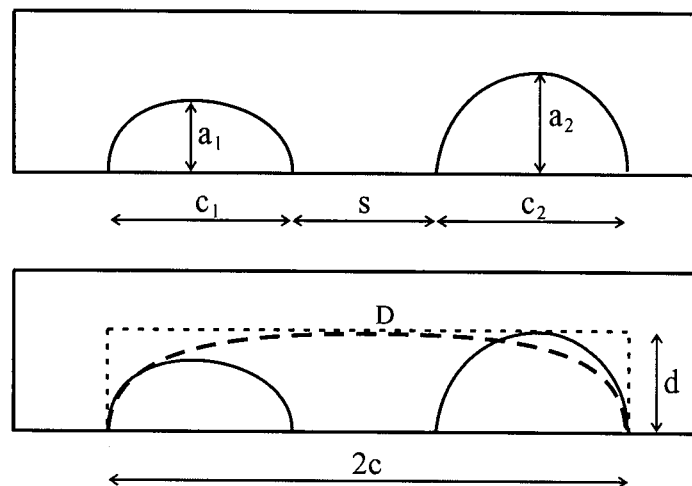


Figure 5.1:
Crack geometry and the re-characterisation of adjacent co-planar defects.

Chapter 6

LINE SPRING ANALYSIS OF COMPLEX DEFECTS

6.1 Introduction

The generic problem of an infinite periodic sinusoidal crack discussed in Chapter 3 demonstrated the way in which K and T depend on the crack front shape. It is to be expected that K and T depend on the shape and curvature of a finite irregular crack in qualitatively the same way.

Surface breaking semi-elliptical cracks have been the subject of many investigations; from the analytical evaluation of Irwin (1962), to fatigue behaviour and interaction, mostly in context of fatigue life predictions (Twaddle and Hancock (1986), Soboyejo *et al* (1990), Leek and Howard (1996)). Analyses of the interaction of two surface breaking semi-elliptical cracks in fatigue (Murakami *et al* (1981, 1982), O'Donoghue *et al* (1984), Iida *et al* (1980,1984)) treat the process of coalescence as occurring almost instantaneously. When two semi-elliptical surface cracks meet at the surface, they are re-characterised with a bounding semi-elliptical crack. However fatigue crack growth is a stable process, during which a family of coalesced cracks with re-entrant sectors form. Many investigations also simplify the problem to one of co-planar coalescence, whereas experiments frequently indicate non co-planar coalescence (Twaddle and Hancock (1986), Soboyejo *et al* (1990), Leek and Howard (1996)). Such cracks are of interest to structural integrity assessments.

In this chapter a family of representative coalescing cracks are investigated under monotonic loading for elastic and elastic-plastic conditions. The analyses examine co-planar cracks and cracks with steps in the re-entrant sector. Failure from co-planar coalesced configurations is also addressed in terms of modified failure assessment diagrams.

6.2 Numerical study of planar coalescence

6.2.1 Geometry

The family of cracks considered in the study were adopted from the experimental programme described in Chapter 7, and are summarised in Figure 6.1. In all, 18 cracks were considered. These include six specimens with adjacent semi-elliptical cracks before

coalescence, eight specimens with coalesced cracks forming re-entrant sectors and four bounding semi-elliptical defects. The coalesced crack profiles exhibit a distinct cusp of high local curvature, which is termed a re-entrant sector. The re-entrant sector is defined as position A in the study, while position B is the deepest segment of the complex crack front. During coalescence the re-entrant sector evolves towards a bounding crack, accompanied by a reduction in local crack front curvature in the re-entrant sector. Each crack was modelled individually in a flat plate of a thickness, t , width, b , and span, L , as shown in Figure 6.2, corresponding to the experimental geometry described in Chapter 7. Scott and Thorpe (1981) showed that the type of loading (tension, bending) affects the shape of a fatigue grown surface breaking crack. In order to examine the development of complex defects of low aspect ratio containing re-entrant sectors, three point bending was used in the experiments and in the numerical simulations.

6.2.2 Numerical model

The geometry was modelled with isoparametric second-order thick shell elements and crack was represented by the line spring technique of Rice and Levy (1972) and Parks and White (1982). Due to symmetry of the problem, one quarter of the geometry was modelled, as shown in Figure 6.3. The finite element mesh consisted of 660 second order small strain shell elements and 30 symmetric line spring elements along the bottom edge of the mesh, as shown in Figure 6.3. In the x direction the mesh was uniform, while in the y direction it was weighted towards the edge, where line spring elements were introduced. Symmetric boundary conditions were applied on the plane $x=0$ (Figure 6.3), combined with symmetric line springs on the plane $y=0$ to ensure a consistency with the experimental geometry. Displacement controlled three point bending was imposed by displacing the upper nodes of the model by $0.1t$, although results are presented in non-dimensional manner. A non-linear material was defined for non hardening and work hardening plasticity, using a power hardening exponent of ∞ and 9 and a constant 2 in a Ramberg-Osgood power hardening law (Eq. (2.35)) to describe the plastic strains. Material was defined to be linear elastic below the yield stress and merged with Ramberg-Osgood relation using two strain hardening rates, $n= \infty$ and 9 to model non-hardening and strain hardening plasticity. The constant α was 2. Stress σ_0 was defined as 0.2% proof stress and corresponds to the lower yield stress of 345 MPa measured on 50D steel used in the experiments. Reference strain e_0 was taken as σ_0/E , while Young's modulus is 210 GPa.

The numerical analysis focused on the crack front from the re-entrant sector to the deepest sectors. Line spring analysis limits the accuracy of the analysis close to the free surface. However since the emphasis of the study is on the re-entrant sector, this limitation is not significant. Nevertheless for cracks with very pronounced re-entrant sectors, the rapid variation of depth in the re-entrant sector flank may compromise numerical accuracy (Parks (1981)).

6.2.3 Results

6.2.3.1 Linear elastic analysis

The key elastic results are presented in Figures 6.4 to 6.9. The stress intensity factors are presented in Figures 6.4 and 6.5, normalised with the outer fibre stress in bending and the greatest crack depth of each profile. In Figure 6.4 the stress intensity factor is presented at positions A and B, as the crack depth at each site increases. SIFs at positions A and B are compared to the solutions of Raju-Newman (1981), for a single semi-elliptical crack and for a bounding defect. The results for the single defect agree with the Raju-Newman solution. In the shallow re-entrant sector just after coalescence, significantly amplified stress intensity factor are observed compared to the value for a bounding defect. This is further demonstrated in Figure 6.5, where stress intensity factors are shown along the crack length, between positions A and B. Away from the re-entrant sector there is no significant effect of the cusp region on the stress intensity factor. As the coalesced crack shapes develop into the bounding semi-elliptical crack, the stress intensity factors at positions A and B merge to the same levels, and match the data of Raju and Newman (Figures 6.4 and 6.5).

The qualitative trend of SIF along the crack length exhibits the features of the generic problem of an infinite periodic sinusoidal crack, with enhanced values in the shallow crack regions. For the sinusoidal crack this effect arises from the redistribution of local forces and bending moments along the crack front. A similar effect was found for complex cracks with re-entrant sectors, as shown in Figure 6.6 and 6.7. The local force per unit surface length of the crack, $N_{(x)}$, is shown in Fig. 6.6, while the bending moment, $M_{(x)}$, defined as the bending stress per unit surface length of the crack, is shown in Fig. 6.7. Both are presented between positions A and B and normalised with the remotely applied values, defined in Figures 6.6 and 6.7. The crack shape contributes to the appearance of opening local forces and enhanced values of local moments in the re-entrant sector under bending.

These values are combined with the calibration functions in the line spring model to give the stress intensity factors and the T-stress. The force and moment redistribution along the crack length thus cause an amplification of the stress intensity factor in the re-entrant sector and contribute to the loss of in-plane crack tip constraint, as parameterised by T. The T-stress is shown in Figures 6.8, between the line of coalescence and deepest crack segment and in Figure 6.9 in the re-entrant sector as a function of crack depth. The T-stress is normalised with the outer fibre stress. The Figure 6.9 demonstrates greater loss of constraint compare to those for an edge crack of the same depth taken from Sham (1991). This is due to the load redistribution. The enhanced stress intensities in the re-entrant sector in Figure 6.5 are matched by enhanced constraint loss, shown in Figures 6.8 and 6.9 by a strongly compressive T-stress. As may be expected, only coalesced cracks with pronounced re-entrant sectors show significant constraint loss effects in bending. Crack tips located deeper in the geometry are subject to high constraint as indicated by a tensile T-stress.

The biaxiality parameter β is shown in Figure 6.10 between the line of coalescence and the deepest crack segments and indicates that coalesced cracks with pronounced re-entrant sectors benefit from constraint loss.

6.2.3.2 Elastic-plastic analysis

Elastic-plastic analysis focused on crack shapes with re-entrant sectors. The crack driving force was monitored through development of the J-integral (Rice (1968)), and crack tip constraint was parameterised with the T-stress. Analysis examined both parameters between the line of coalescence (position A) and the deepest crack segments (position B). Local and global limit loads were determined using an elastic perfectly-plastic material response, followed by analysis for a work hardening material.

Local and global limit loads

The global limit load was determined from the global response of the structure, whereas the local limit load was determined from the local stresses, or the plastic component of the J-integral, as discussed in Chapter 3. Twelve coalesced and bounding geometries, ranging from $a_A=0.05t$ to $a_A=0.67t$ were evaluated for an incompressible, perfectly-plastic material. The local and global limit loads are shown in Figure 6.11, normalised with the limit load of an uncracked geometry (F_0). The global limit loads decrease with increasing crack size,

with the greatest value established for the configuration containing a coalesced crack with the greatest ligament ($a_A=0.05t$). Figure 6.11 suggests, that the sharp re-entrant sector does not significantly influence the global limit load, which largely depends on the load bearing area.

The coalesced crack of $a_A=0.05t$ with a pronounced re-entrant sector was used to investigate the local limit load at the shallowest ($a_A=0.05t$) and deepest ($a_B=0.4t$) positions, by monitoring the stress history for both positions. This is shown in Figure 6.12 where the stress history is plotted on the yield surface following arguments of Rice (1972), as discussed in Chapter 3. Due to the local load redistribution and pronounced local curvature, shallow crack segments in pronounced re-entrant sectors develop large scale plasticity before the rest of the crack front, despite having the largest ligament. Large local opening forces in the shallow re-entrant sector shift the total stresses in a tensile dominated region of the stress space. The deepest segment of the crack is in compression throughout, favouring crack advance from the re-entrant sector. A systematic study of local stress histories for re-entrant sectors and deepest crack segments is shown in Figure 6.13. As the crack depth on the line of coalescence increases, the re-entrant sectors become increasingly dominated by bending. At a crack depth of $a_A=0.4t$, the process of coalescence is near completion, and the coalesced crack closely resembles the bounding crack. The deepest segments of the bounding crack (position A) exhibit compressive local forces and reduced opening moments. Crack advance in a bounding crack of low aspect ratio shifts closer to the free surface, as indicated by the plastic component of the J-integral.

Local limit loads for configurations with re-entrant sectors were analysed for positions A and B and are shown in Figure 6.11 with matching global limit loads. All the values in Figure 6.11 are normalised with the global limit load of an uncracked geometry. The study found the local limit loads in the pronounced re-entrant sectors to be a small fraction of the global limit load. For all cracks with re-entrant sectors, the local limit load in the re-entrant sector is less than the local limit load at the deepest segments.

Crack driving force and constraint

The J-integral was examined on the line of coalescence (position A) and the deepest segment (position B) of each crack. The size of the unbroken ligament of these cracks varies with position around the crack front and between the cracks. Values of J in the re-

entrant sector are compared to J values in the deepest segments, by presenting data sets for positions A and B with the same abscissa value. This allows a comparison of J at two positions on the same complex crack front. Examples of J normalised with local unbroken ligament and smallest unbroken ligament of each profile are shown in Figures 6.14 and 6.15, while Figure 6.16 compares J at A and B under fixed displacement. The results show amplified values of J in the shallow re-entrant sectors compared to deeper crack segments at the same remote loading. This suggests that complex defect has a tendency to extend from the re-entrant sector in plasticity.

Crack tip constraint was examined in the re-entrant sectors using the T-stress and is presented in Figures 6.17 and 6.18, normalised with the yield stress. In Figure 6.17 the T-stress is presented at a fraction of local limit load in the re-entrant sector of each crack and in Figure 6.18 the T-stress is shown as a function of crack depth along the line of coalescence at a fixed load. The results show the same features as observed in the elastic analysis: a compressive T-stress develops in pronounced re-entrant sectors which saturates as large scale plasticity develops close to local limit load. The magnitude of T depends on the crack depth in the re-entrant sector, and may be comparative to the yield stress for very shallow re-entrant sectors ($a_A=0.05t$).

6.3 Numerical study of non co-planar coalescence

Experiments on fatigue growth of neighbouring surface breaking cracks, originating from two co-planar notches, show a surface deviation from the notched plane before coalescence. This feature is discussed in Chapter 7 and may influence brittle failure. Here a numerical analysis is presented for a coalesced crack with a step in the re-entrant sector. The analysis is presented for elastic conditions, relevant to brittle failure.

6.3.1 Geometry and numerical methods

Representative crack profiles were taken from the study of a co-planar coalescence, shown in Figure 6.1 and comprised cracks with re-entrant sectors: $a_A=0.14t$, $a_A=0.20t$, $a_A=0.27t$, $a_A=0.37t$ and a bounding crack of $a_A=0.52t$. These are introduced in a simplified experimental geometry, shown in Figure 6.19, introducing a step along the line of coalescence by mis-aligning the two halves of the crack. Two step heights of $0.04t$ and $0.08t$ were chosen to correspond with a 1 mm and a 2 mm step heights observed in the

experimental work. The shear step was modelled as an edge crack segment, in which the depth of the crack through the shear step was the same as the depth of the crack in the re-entrant sector (along the line).

Fracture mechanics parameters have been determined by line spring analysis (Rice and Levy (1972)), by using a subgroup of elements formulated to represent the three deformation modes (I, II and III) under linear elastic conditions. The finite element mesh representing the full geometry is schematically shown in Figure 6.20, and was subject to displacement controlled three point bending. The line spring elements placed on horizontal planes show largely Mode I Stress Intensity Factors, whereas the vertical line spring elements show largely Mode III components.

6.3.2 Results

Mode I (K_I) and Mode III (K_{III}) stress intensity factors are shown in Figures 6.21 to 6.23, normalised with the outer fibre stress in bending and the greatest crack depth. This is crack depth at position B for cracks with re-entrant sectors and at position A for the bounding crack. In Figures 6.21 K_I is shown along the quarter free surface length for a non co-planar crack with a step height of $0.04t$. The effect of the step height on K_I is further examined in Figure 6.22 as a function of crack depth in the re-entrant sector. The introduction of a small step significantly reduces the magnitude of the K_I in the shallow re-entrant sector compared to the values for a co-planar crack front and gives rise to a Mode III component, shown in Figure 6.23. The K_{III} is smallest in the pronounced re-entrant sector and rises as the crack depth in the re-entrant sector increases.

In-plane constraint parameterised by T and β is presented in Figures 6.24 and 6.25. Figure 6.24 shows the T -stress, normalised with the outer fibre stress in bending, for the co-planar geometry and non co-planar geometry with two step heights. Co-planar re-entrant sectors generate amplified compressive T -stresses, which markedly reduce as the step is introduced in the crack front. The non co-planar crack experiences a mixed mode loading in the re-entrant sector, which reduces both, the opening mode I SIF and the in-plane crack tip constraint, as indicated by the biaxiality parameter β , shown in Figure 6.25.

A numerical line spring study of non co-planar cracks indicates that the introduction of a relatively small step in the re-entrant sector has a significant effect on the crack tip parameters and may affect the evolution of such cracks under monotonic loading.

6.4 Modified failure assessment diagrams for complex defects

6.4.1 Failure assessment diagrams

The concept of failure assessment diagrams has evolved from the work at the CEGB in the United Kingdom and originates from the “two criteria” approach of Dowling and Townley (1975). The diagrams are convenient way of demonstrating safety margins of a flawed structure, by comparing the load with that to cause plastic collapse or failure under contained yielding. The plastic collapse load F_0 is determined on a basis that collapse occurs at the yield stress. The resulting term L_r is then taken as an indication of the proximity to plastic collapse:

$$L_r = \frac{F}{F_0} \quad (6.1)$$

Similarly, the proximity to failure under contained yielding is quantified by the ratio of the applied stress intensity factor K to an experimentally measured material toughness, K_{mat} .

$$K_r = \frac{K}{K_{mat}} \quad (6.2)$$

Interpolation between the extreme modes: elastic fracture in contained yielding ($K_r=1$) and plastic collapse ($L_r=1$) is achieved with a failure assessment curve (FAC), as illustrated in Figure 6.26. The vertical axis represents the normalised stress intensity factor, whereas the horizontal axis is the load normalised with the limit load. The region bounded by the axis and the failure line is the safe regime. Any load and crack size combination that falls beyond the failure line may lead to failure.

Three choices for failure assessment diagrams are distinguished based on the available data. Option 1 requires the minimum knowledge of material and geometry and is constructed as conservative lower bound to a pool of experimental data. Options 2 and 3 are increasingly more realistic, but require specific material data and full-field solutions. Other more specific applications are also considered in Revision 4 of R6 (2001).

Option 3 failure assessment curve in R6, Rev 4 allows a failure assessment diagram to be generated through a J-integral analysis for a specific material and geometry. To maintain the agreement with the notation of J based fracture mechanics, the ordinate of the FAD can be written in terms of J_{mat} and its elastic component $J_{elastic}$.

$$K_r = \frac{K_I}{K_{mat}} = \sqrt{\frac{J_{elastic}}{J_{mat}}} \quad (6.3)$$

The abscissa is still given by the ratio of the applied to limit load. The FAC is truncated at the abscissa value of L_r^{max} , defined in terms of a yield stress σ_0 and ultimate tensile strength σ_{TS} :

$$L_r^{max} = \frac{\sigma_0 + \sigma_{TS}}{2\sigma_0} \quad (6.4)$$

6.4.2 Modified Failure Assessment Diagrams

The failure assessment diagram based on J-controlled crack growth concept is based on a J-dominant crack tip field and does not account for the geometry dependant constraint effects. Consequently data can not be directly transferred from one geometry to the other, unless both configurations are J-dominant.

Modified failure assessment diagrams developed by Ainsworth and O'Dowd (1995) and MacLennan and Hancock (1995) aim to take advantage of enhanced levels of toughness associated with constraint loss. The effect of constraint loss is incorporated in the FAD in one of two ways; If the material toughness K_{mat} is identified with K_{IC} for plane strain problem, the enhanced toughness associated with the constraint loss generates a new failure assessment curve (Ainsworth and O'Dowd (1995)) for a particular level of constraint loss. Alternatively, K_{mat} may be defined as constraint matched fracture toughness, which allows the original FAC to be retained (MacLennan and Hancock (1995)), while the crack-tip load becomes a non-linear function of remote load. The use of the constraint matching techniques allow the relevant toughness to be used, rather than the lower bound toughness associated with deeply cracked laboratory specimens. The appropriate failure condition is given by a failure locus in which the critical value of J is given as a function of constraint parameterised with T. Following MacLennan and Hancock (1995) a J-T failure locus is idealised by the equation:

$$\frac{J_{(T)_c}}{J_{(T=0)_c}} = \left[\frac{1}{\exp\left(\frac{T}{\sigma_0}\right)} \right]^k, \quad \frac{T}{\sigma_0} < 0 \quad (6.5a)$$

$$J_{(T)_c} = J_{(T=0)_c}, \quad \frac{T}{\sigma_0} \geq 0 \quad (6.5b)$$

Constraint sensitivity is determined by the exponent k , such that constraint insensitivity is represented by $k=0$ when failure occurs at a critical value of J . Non-zero values of k correspond to increased levels of constraint enhanced toughness for negative values of T . The constraint sensitive toughness values are denoted $J_{(T)_c}$, to indicate that the critical values of J is a function of the constraint parameter, T . Fully constraint deformation is identified with the $T \geq 0$ and given the notation $J_{(T=0)_c}$. Failure initiation is taken to occur at the intersection of a $(J-T)$ loading history with the failure locus.

6.4.3 Results

Modified failure assessment diagrams were constructed for the re-entrant sectors of coplanar coalesced cracks defined with crack depths at the line of coalescence of: $0.05t$, $0.14t$ and $0.27t$. Constraint loss was quantified by T and margins on J_{Ic} were evaluated using Eq. (6.5) at several load increments. The option 1 failure assessment curve was then used as a base line. Constraint enhanced failure assessment curves were derived by multiplying the option 1 FAC with the square root of expression (6.5), obtained for the same increments of the limit load. Low ($k=1$) and high ($k=3$) constraint sensitivities were considered. The applied load was normalised with the local limit load in the re-entrant sector. Since complex defects exhibit local limit loads that differ from global limit loads and between crack configurations, the modified FAD were also constructed for a load normalised with a fixed limit load. In a view of re-characterisation procedures it was appropriate to use the global plastic collapse load for a bounding semi-elliptical defect shape as a normalising load, which is constant for all configurations analysed.

The results presented in Figures 6.27 to 6.30 show that constraint loss in the re-entrant sector elevates the corresponding failure assessment curves over the baseline, allowing for more realistic assessment when constraint benefits may be invoked.

6.5 Discussion

The interaction of coplanar defects has been investigated with numerical techniques of varying complexity (O'Donoghue *et al* (1984), Murakami and Nemat-Nasser (1982), and Miyazaki *et al* (1989)). These results agree as to the general variation of the stress intensity factors around the periphery of interacting co-planar surface breaking cracks. The present study used a simple and efficient line spring analysis and shown amplified values of fracture mechanics parameters in the re-entrant sector, with results closely matched by the literature and the experimental trends (see Chapter 9). When two co-planar semi-elliptical cracks approach each other, an interaction effect elevates the stress intensity factors for adjacent crack tip, with the magnitude depending on the separation between the adjoining tips (Perl *et al* (1997), Moussa (1999)) This has been observed in the numerical study and is further elaborated using experimental data in Chapter 7. As the adjacent crack tips merge on a single plane, the newly formed re-entrant sector experiences amplified values of stress intensity factor, which rapidly reduce as the crack depth in the re-entrant sector increases and the crack shape approached that of the bounding defect.

The variation of crack tip parameters with the shape of the complex crack can be discussed in two ways. The generic infinite sinusoidal crack problem indicated a form of inter-relation between the crack tip parameters and the local forces and moments. The shape of the irregular crack determines redistribution of local forces and moments, causing additional local tensile forces and enhanced bending moments in the re-entrant sectors under remotely applied bending. This affects the near crack tip stress field and is reflected in the characteristic variation of K and T along the crack front.

An alternative qualitative explanation for the amplification of the stress intensity factor in the re-entrant sector can be given in terms of the crack face displacement. Analysis of an embedded elliptical defect under uniform tension (Green and Sneddon (1950)) showed that the maximum stress intensity factor at the end of the minor axis and the minimum stress intensity at the end of the major axis. Given that the displacement in the centre of the crack must be the same for both axes, the crack tip opening on each axis depends on the distance from the centre to the crack tip and resulting in the minor axis being under greater crack tip displacement. Since the crack tip displacement can be related to the stress intensity factor directly, it follows that the stress intensity factor must be largest on the minor axis. If this

argument is transferred to the re-entrant sector, it can be seen that as soon as the two defects coalesce, the crack faces along the major axis would attempt to displace in a similar manner.

The introduction of a relatively small non co-planar step in the re-entrant sector of a complex crack has a significant effect on the crack tip parameters. Co-planar coalescence generates amplified stress intensity factors in the re-entrant sector, which are reduced by up to 60 per cent by a small step. The step may also shift the location of the maximum stress intensity factor towards the flank of the re-entrant sector. Similarly the magnitude of the compressive T-stress reduces in a non co-planar geometry. The presence of a shear step introduces a mixed mode loading in the re-entrant sector, with larger plastic zones. The combination of mode I and mode III loading and in-plane constraint loss may compensate for amplified crack driving forces along the line of coalescence. In such cases monotonic failure may initiate from the flanks of the re-entrant sector, which feature moderately amplified stress intensity factors and no loss of constraint, rather than from the centre of the re-entrant sector. Fracture surface of specimens containing complex defects with re-entrant sectors fracture at $-100\text{ }^{\circ}\text{C}$ showed chevron patterns in the re-entrant sector, running along the line of coalescence, but were not obvious at the line-of-coalescence. Such consideration supports the influence of a step, which introduces the mixed mode loading and reduces amplified stress intensity factors along the line of coalescence.

Modified failure assessment diagrams have been constructed for planar cracks with re-entrant sectors, which experience constraint loss in the re-entrant sectors. Modified FACs are dependant on the level of constraint sensitivity, the crack shape and to some extent on the way in which the applied load is normalised. Higher levels of constraint sensitivity lead to elevated modified FACs for pronounced re-entrant sectors. The largest effect is noted for the values of normalised loads close to the limit load ($0.6 \leq L_r \leq 1$). As coalesced cracks develop towards the high constraint bounding semi-elliptical cracks, failure is governed by the general failure assessment curve.

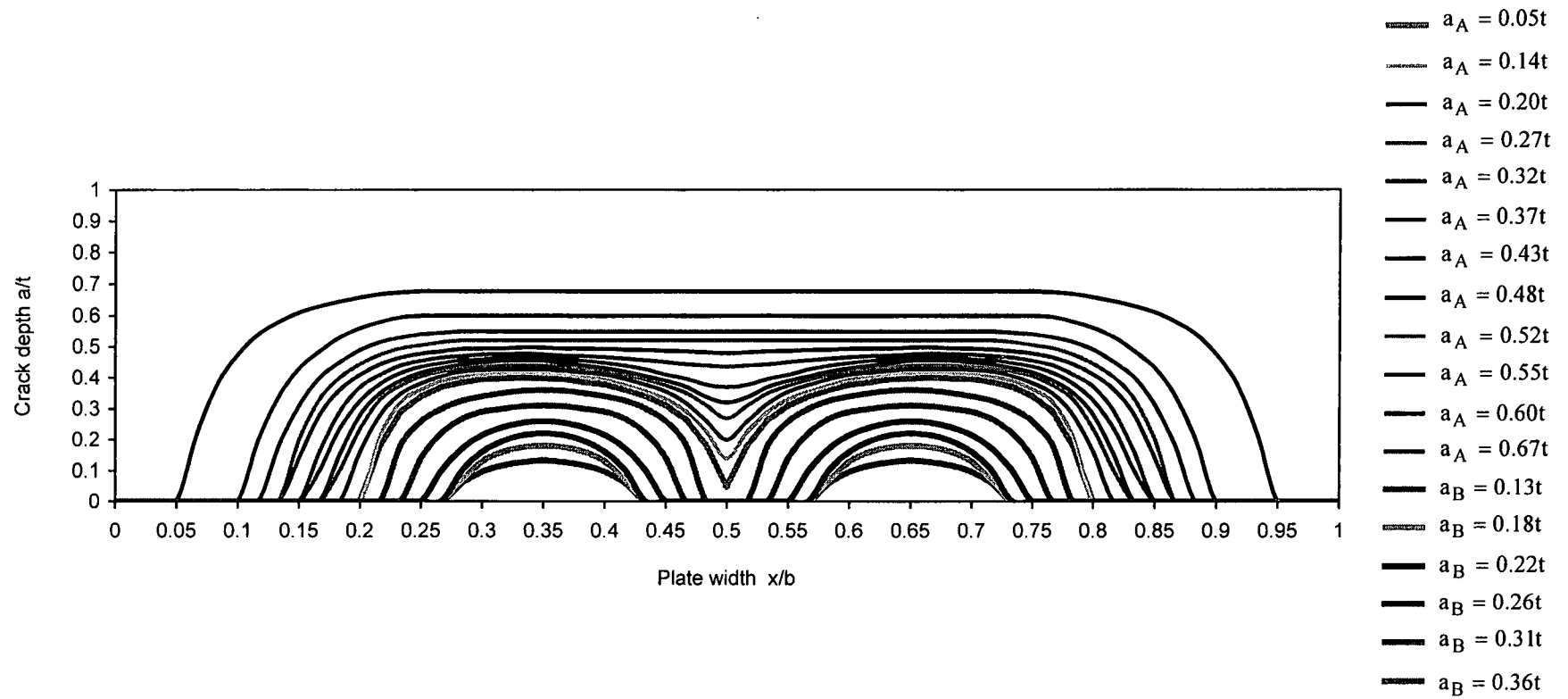


Figure 6.1:
Semi-elliptical and complex crack shapes developed in fatigue; $b=6t$.

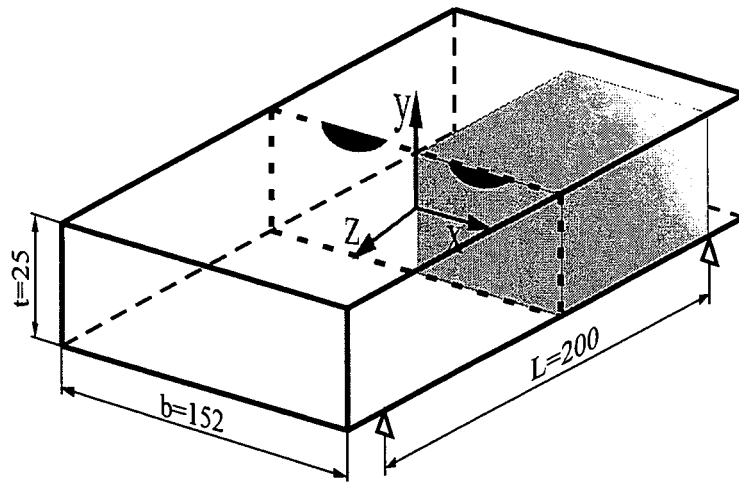


Figure 6.2:
Modelled segment of the experimental geometry.

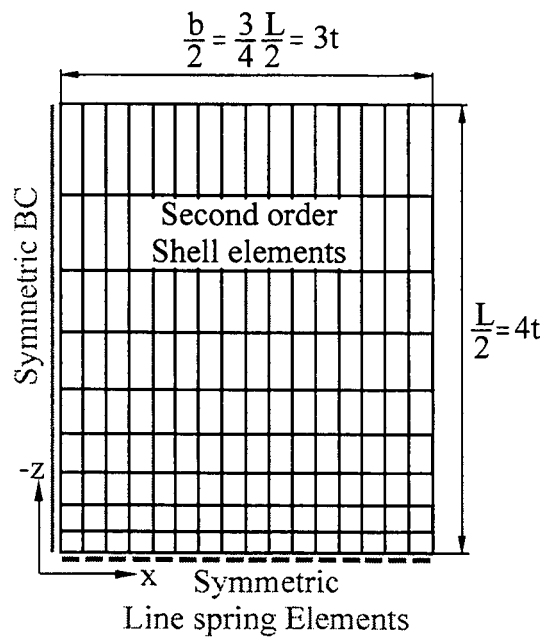


Figure 6.3:
Finite element mesh representing a quarter of the experimental geometry.

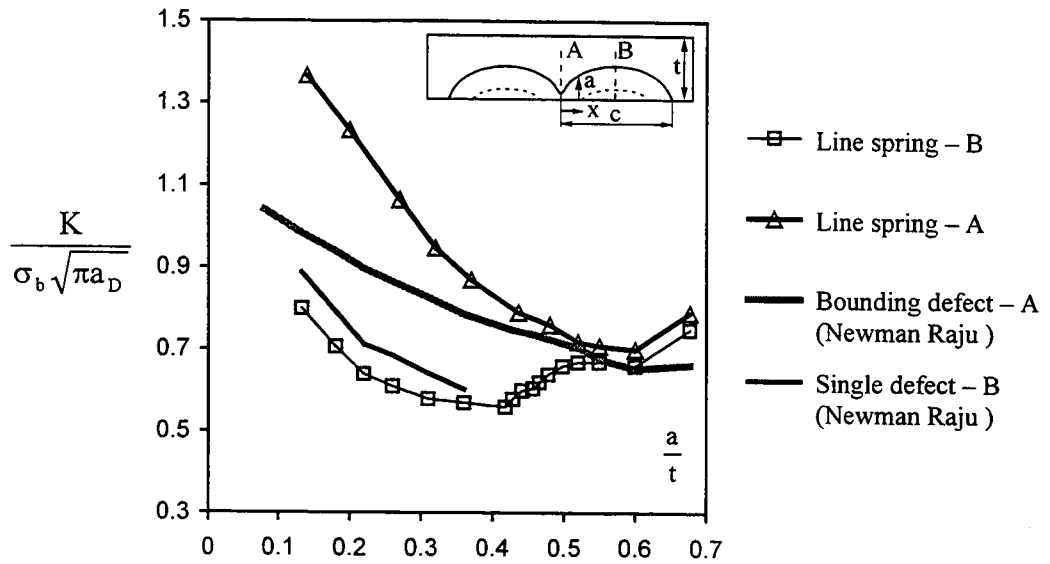


Figure 6.4:
 Stress intensity factor in the re-entrant sector (position A) and at the deepest crack segments (position B) from line spring analysis. Data for a bounding semi-elliptical and a single defect before coalescence are superimposed from data of Raju Newman (1981).

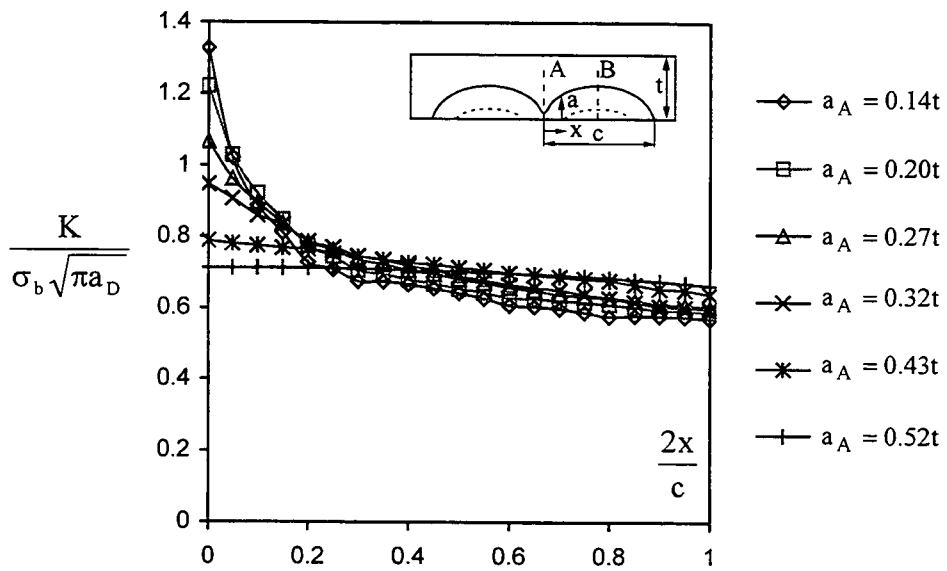


Figure 6.5:
 Stress intensity factor between the line-of-coalescence (position A) and deepest crack segments (Position B) from line spring analysis.

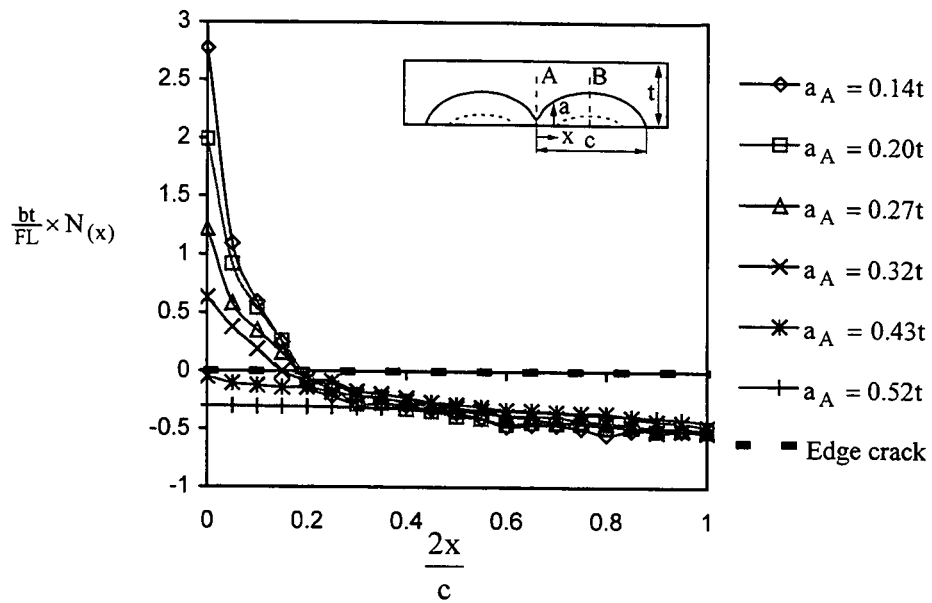


Figure 6.6:
Normalised local forces along surface length between positions A and B from the line spring analysis.

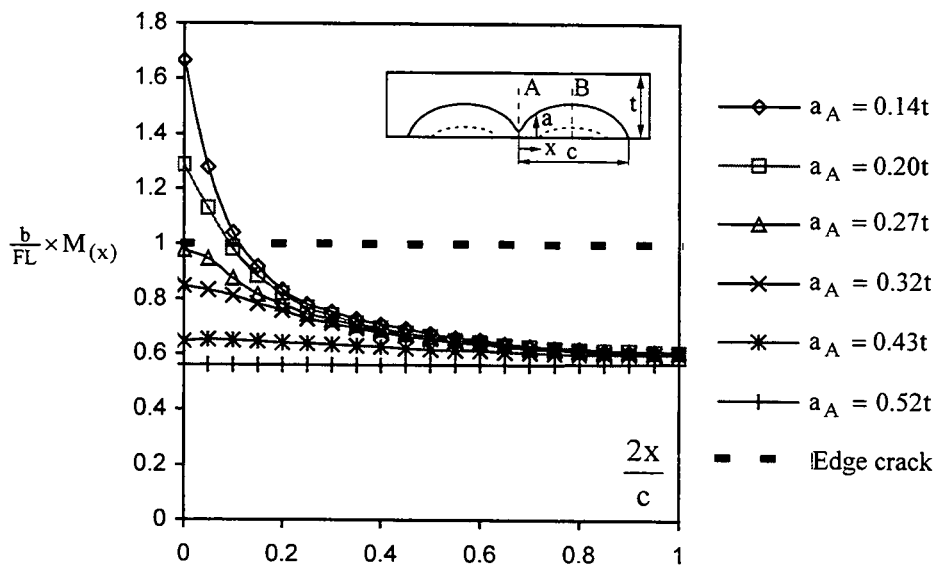


Figure 6.7:
Normalised bending moments along surface length between positions A and B from the line spring analysis.

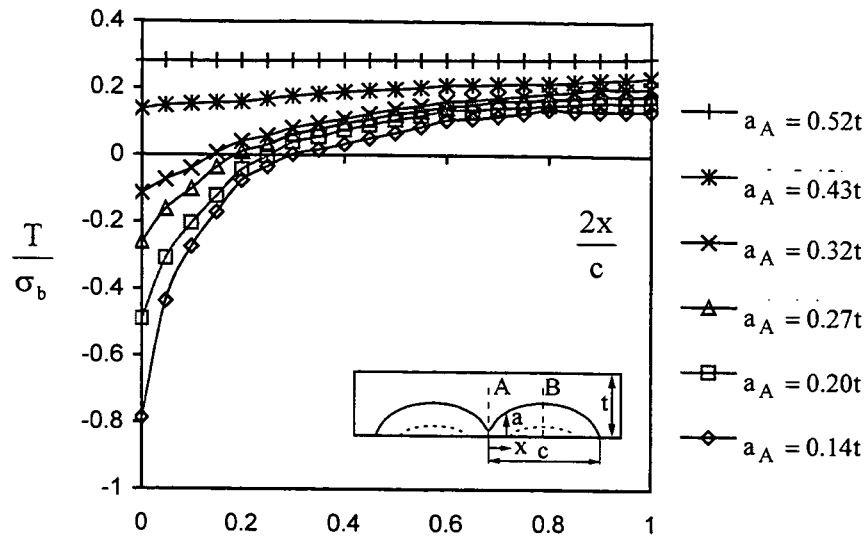


Figure 6.8:
T-stress between the line-of-coalescence (position A) and deeper crack segments (position B) from the line spring analysis.

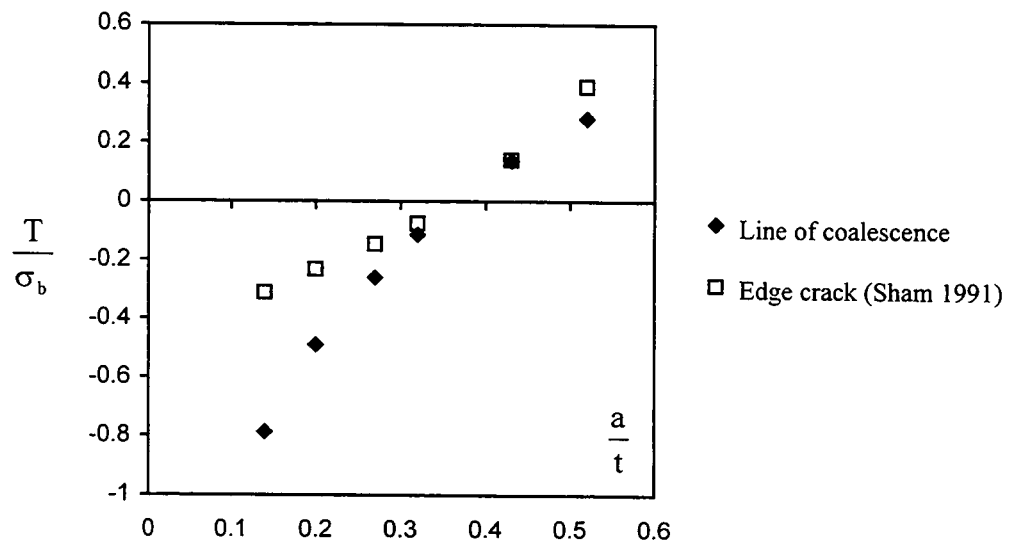


Figure 6.9:
T-stress between at line-of-coalescence (position A) in the re-entrant sector and for a straight edge crack of equivalent depth from Sham (1991).

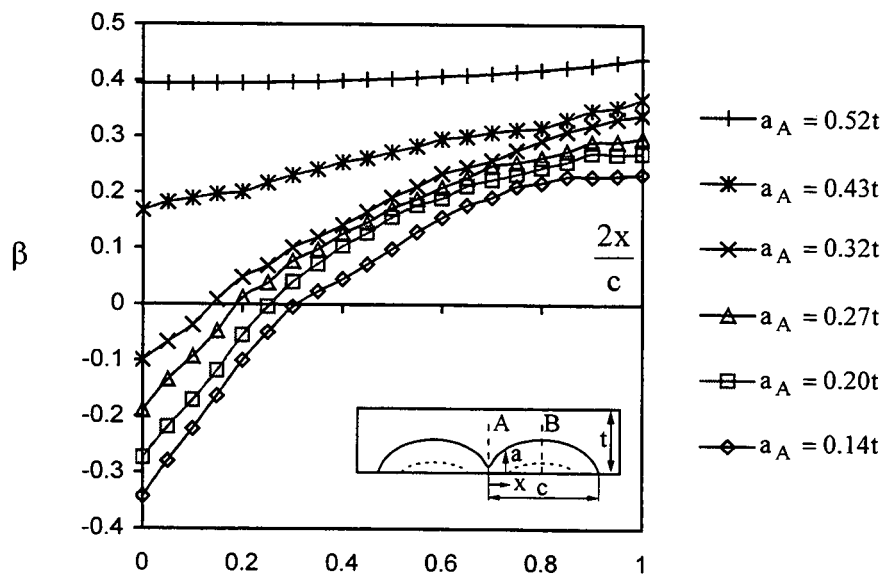


Figure 6.10:
 Biaxiality parameter β between the line-of-coalescence (position A) and deepest crack segments (Position B) from the line spring analysis.

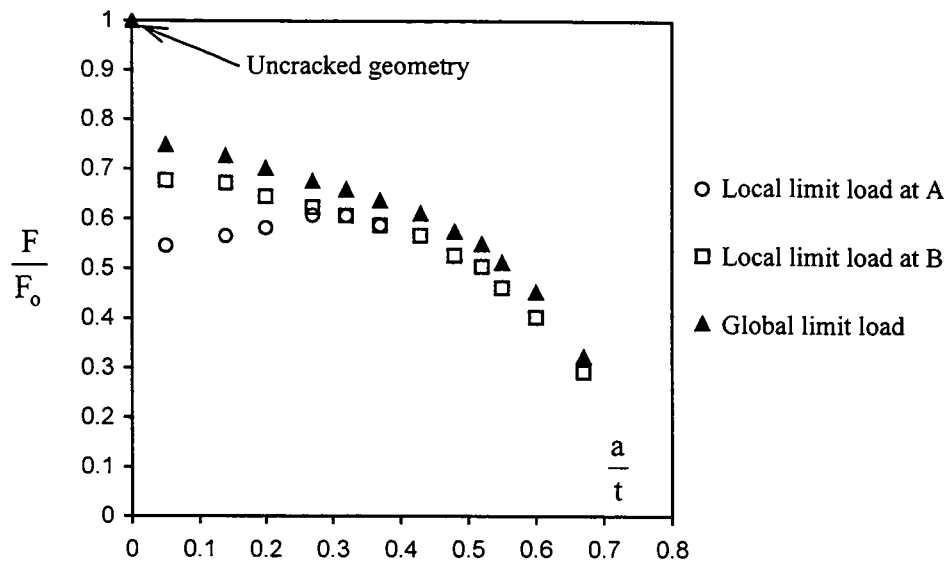


Figure 6.11:
Local and global limit loads for complex crack; normalised with global limit load of uncracked geometry.

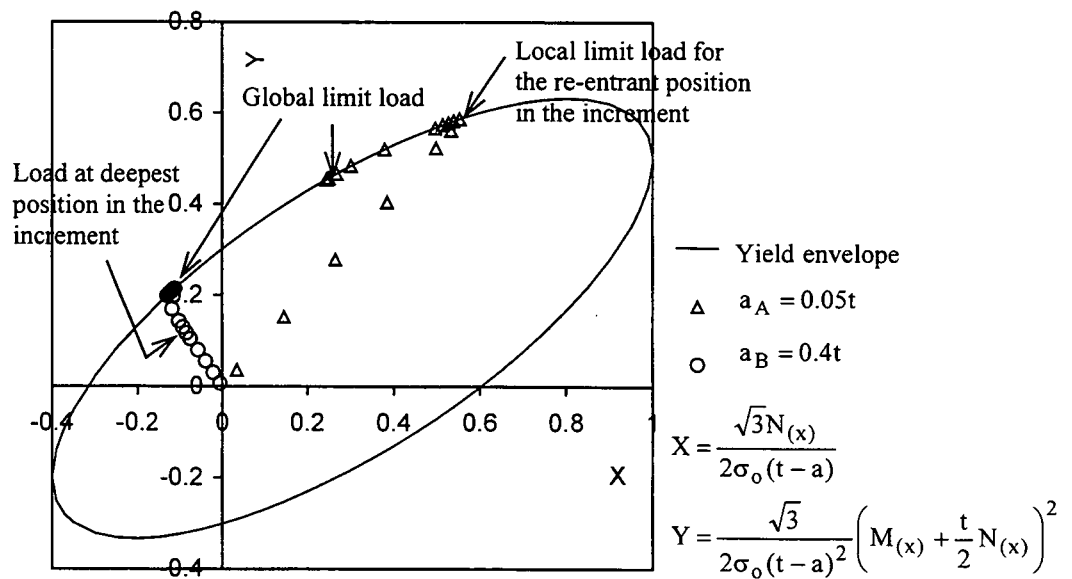
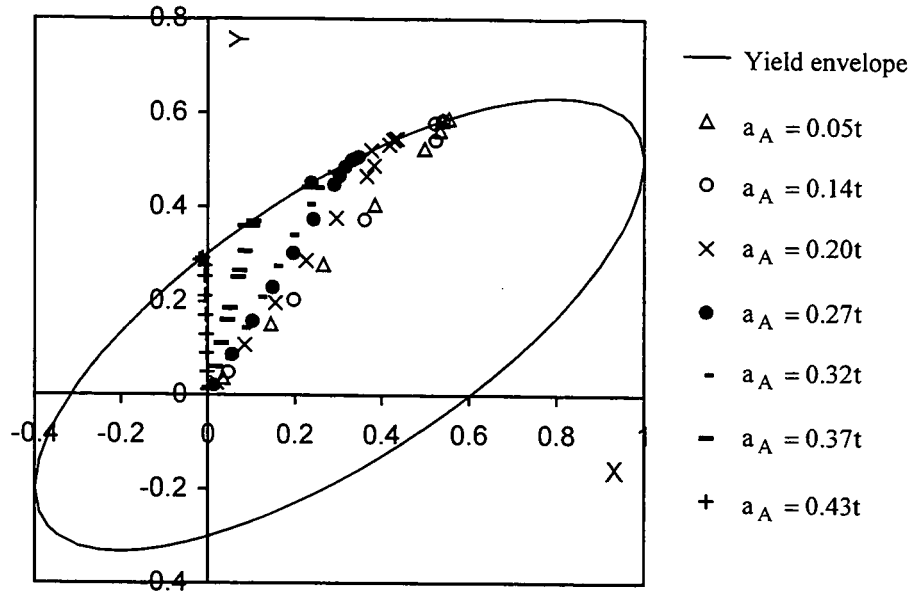


Figure 6.12:
Definition of the local and global limit load for a coalesced crack shape of $a_A = 0.05t$.



$$X = \frac{\sqrt{3}N(x)}{2\sigma_0(t-a)} \quad , \quad Y = \frac{\sqrt{3}}{2\sigma_0(t-a)^2} \left(M(x) + \frac{t}{2}N(x) \right)^2$$

Figure 6.13:
Force-bending moment histories for the re-entrant position A of coalesced cracks with re-entrant sectors.

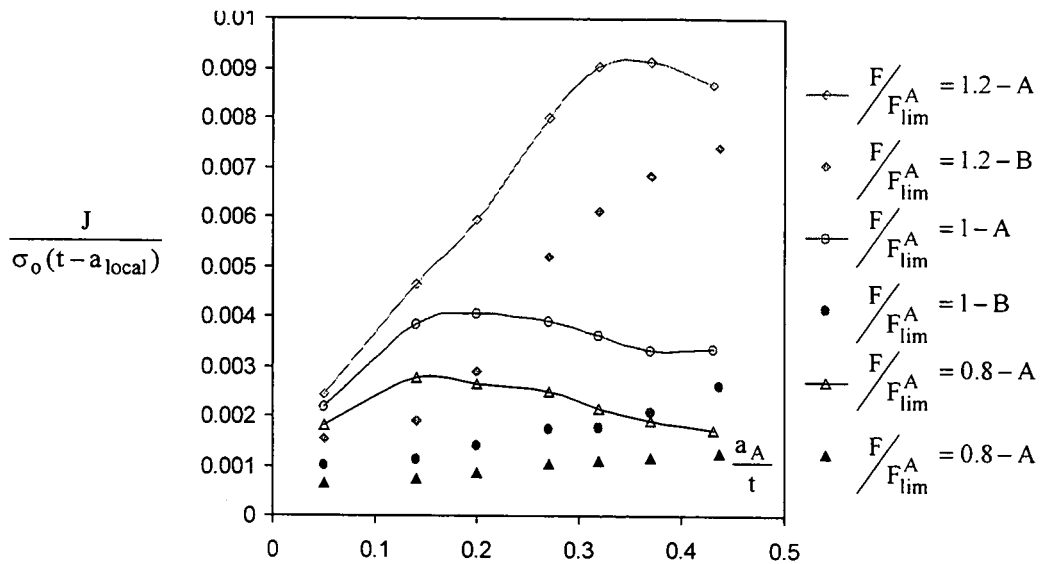


Figure 6.14:
Values of J-integral in the re-entrant sector and at the deepest positions. Values are normalised with local ligament lengths and taken for the same fraction of local limit load in the re-entrant sector.

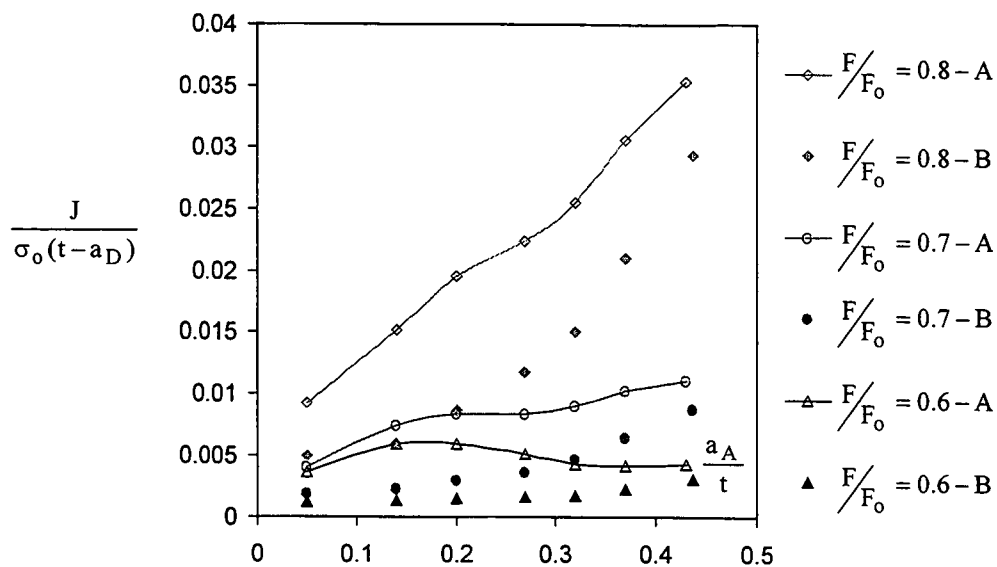


Figure 6.15:
 Values of J-integral in the re-entrant sector and at the deepest positions. Values are normalised with constant ligament lengths of each profile and taken for the same fraction of global limit load of the uncracked geometry

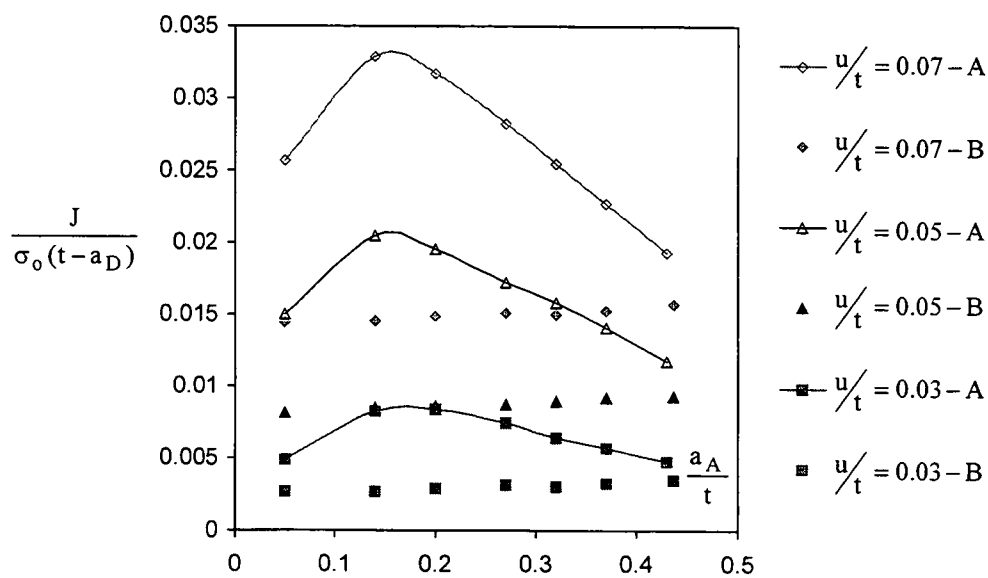


Figure 6.16:
 Values of J-integral in the re-entrant sector and at the deepest positions. Values are normalised with constant ligament length of each profile and taken for the displacements of a fixed fraction of plate thickness.

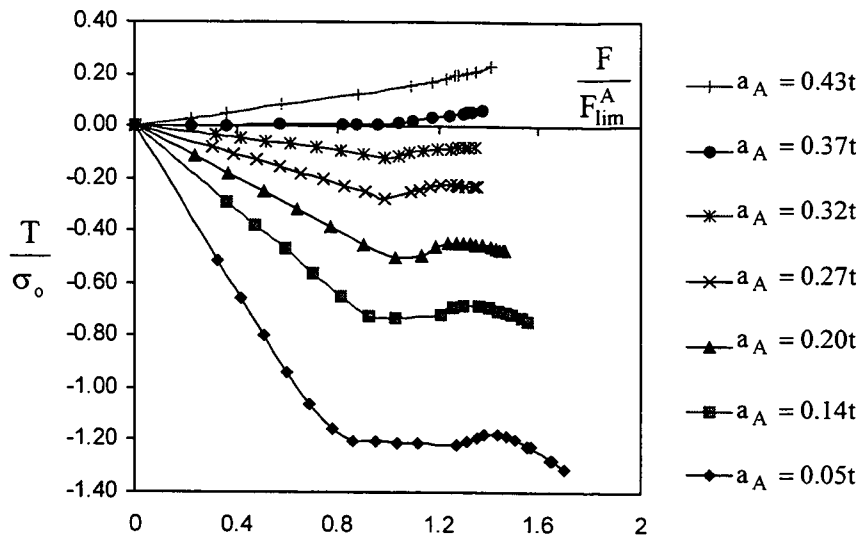


Figure 6.17:
 T-stress in the re-entrant sector as a function of applied load. Values are normalised with the yield stress and taken for the same fraction of local limit load of each profile.

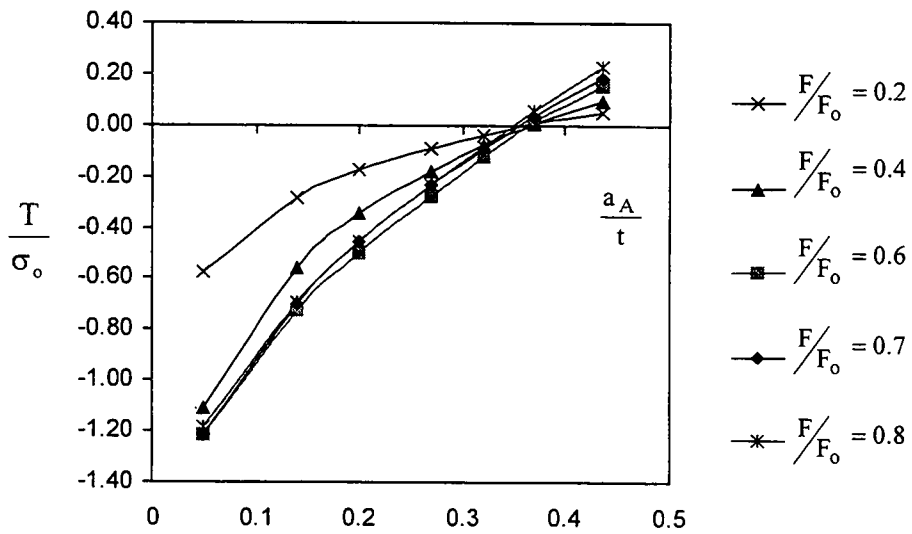


Figure 6.18:
 T-stress in the re-entrant sector as a function of crack depth. Values are normalised with the thickness and taken for the same fraction of global limit load of the uncracked geometry.

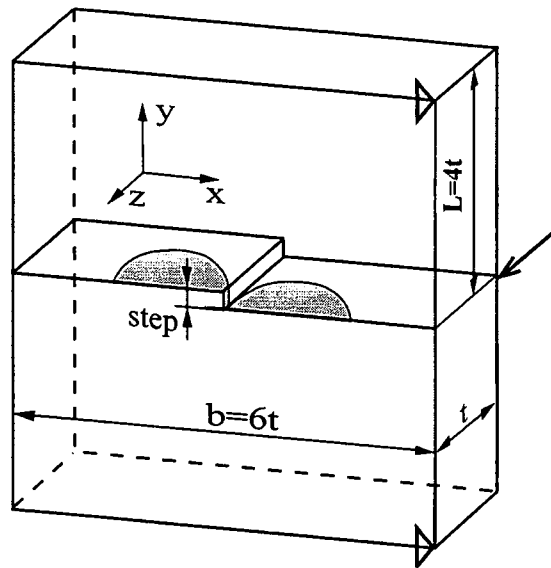


Figure 6.19:
Modelled geometry containing two non co-planar cracks.

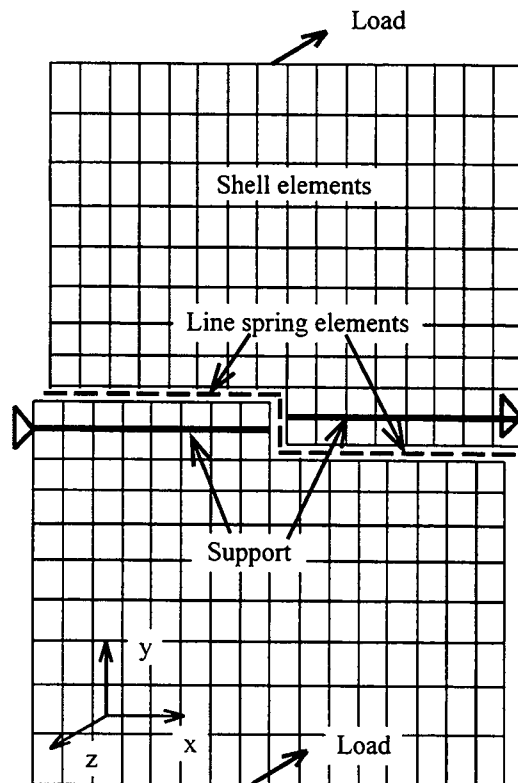


Figure 6.20:
Finite element mesh used for modelling non co-planar coalesced profiles.
(Note the mesh is split along the crack front for visualisation purposes.)

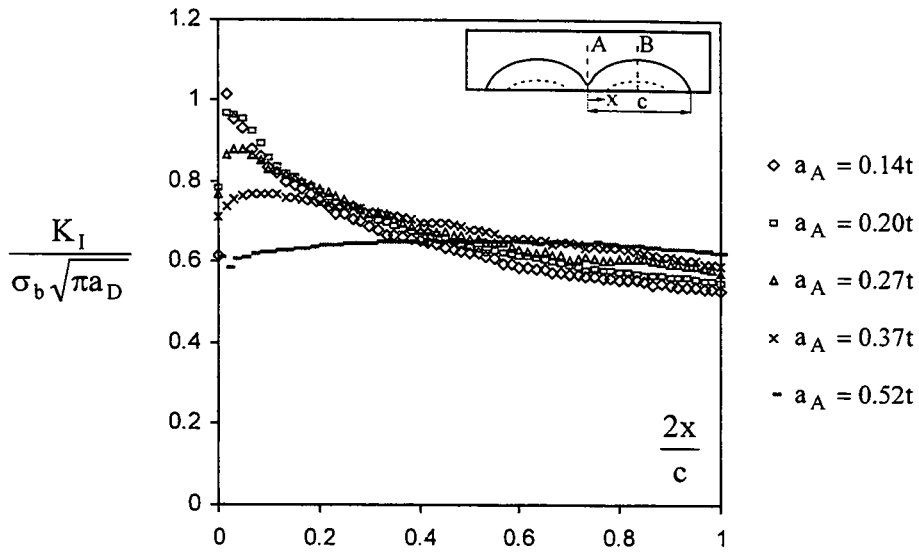


Figure 6.21:
Mode I stress intensity factor between positions A and B for non co-planar cracks and step height of $0.04t$.

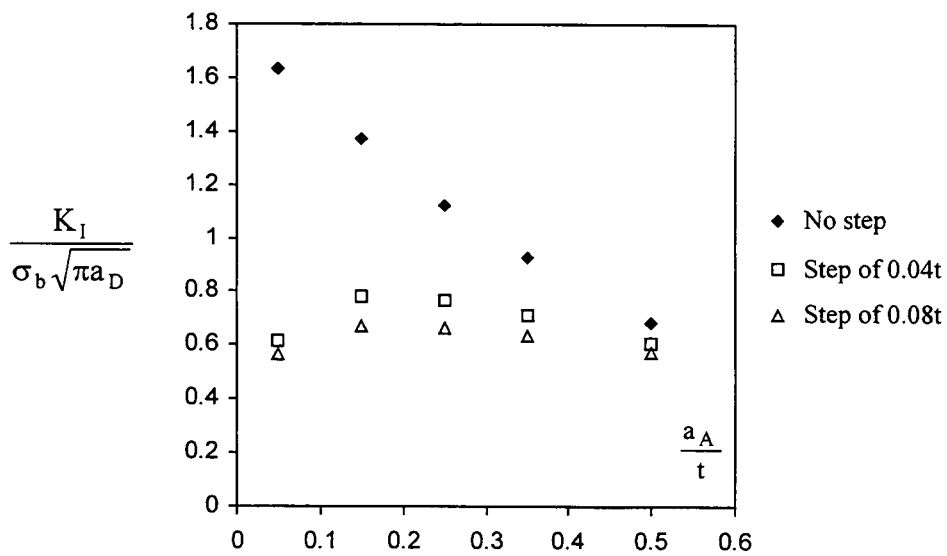


Figure 6.22:
Mode I stress intensity factor in the re-entrant sector of co-planar and non co-planar cracks.

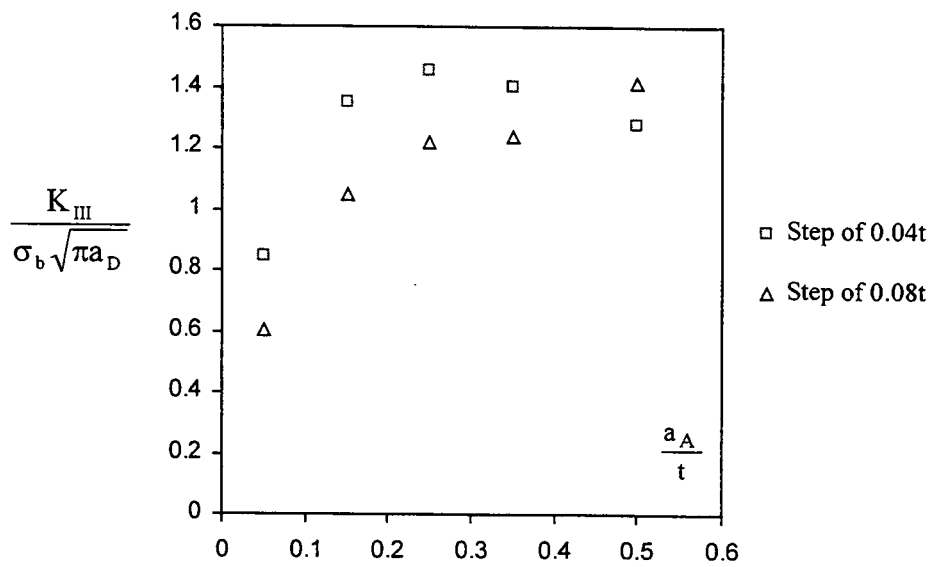


Figure 6.23:
Mode III stress intensity factor in the non co-planar re-entrant sector.

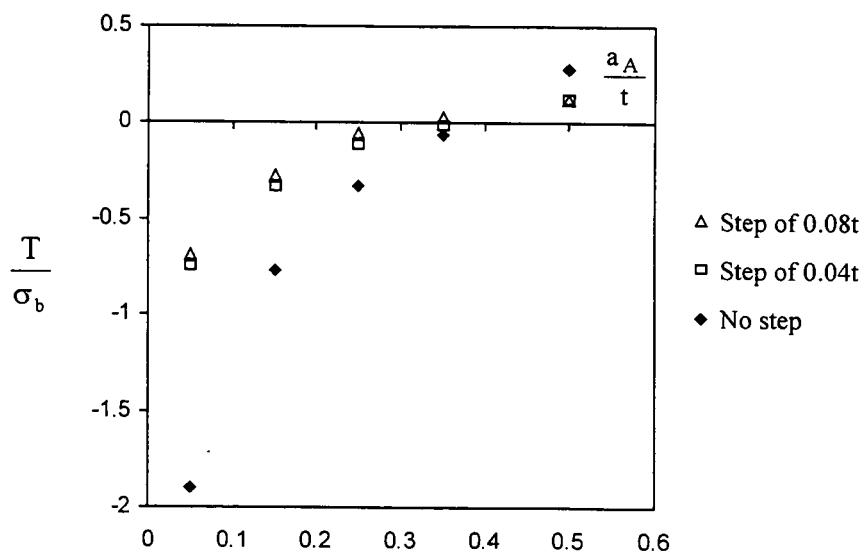


Figure 6.24:
T-stress in the re-entrant sector for co-planar and non co-planar cracks.

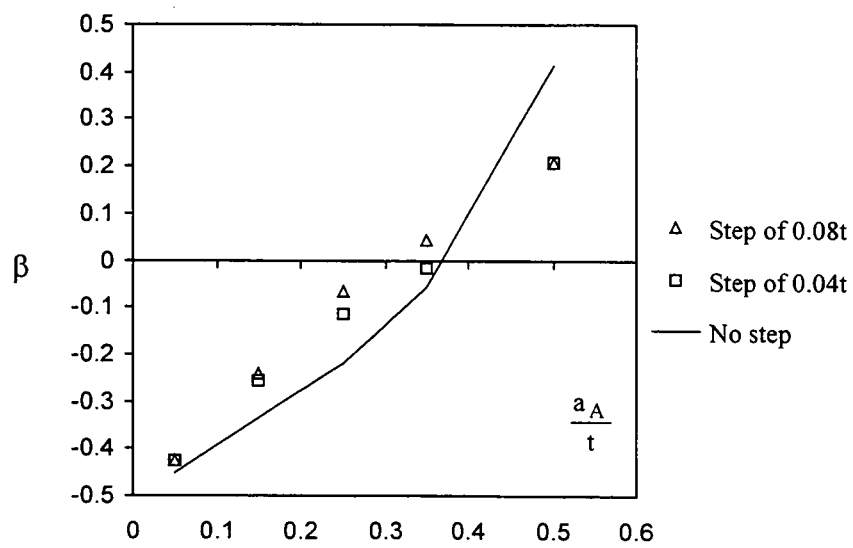


Figure 6.25:
 Biaxiality parameter β in the re-entrant sector of co-planar and non co-planar cracks.

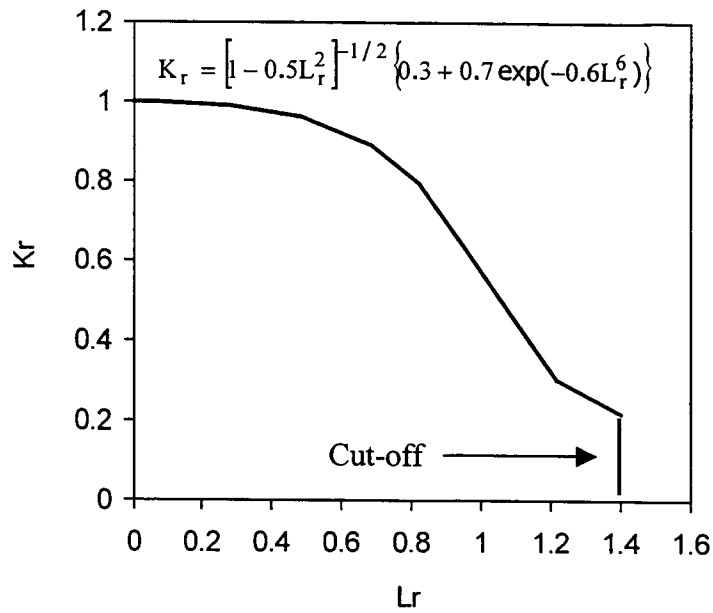


Figure 6.26:
The general failure assessment diagram (Option 1).

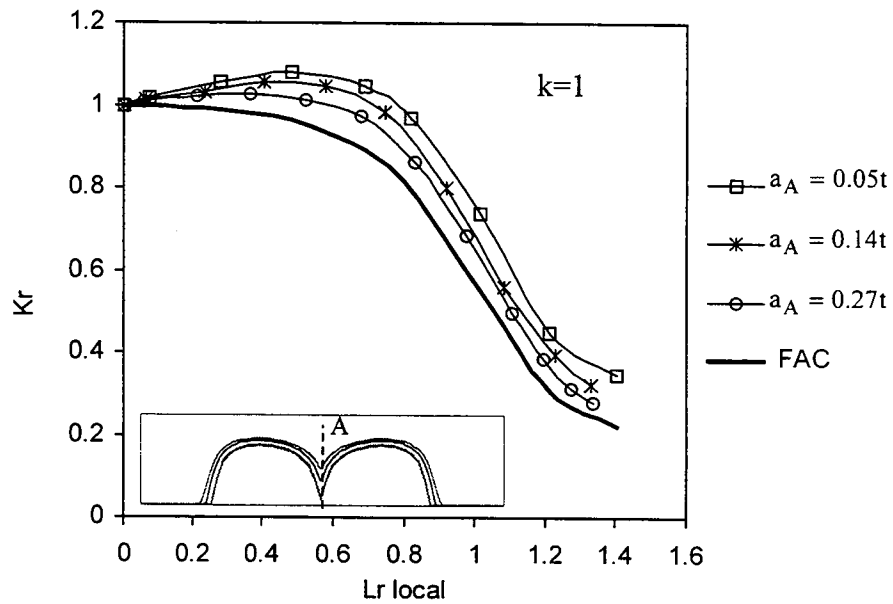


Figure 6.27:
FAD for three coalesced crack shapes and constraint sensitivity $k=1$.
Applied load is normalised with the local limit load in re-entrant sector.

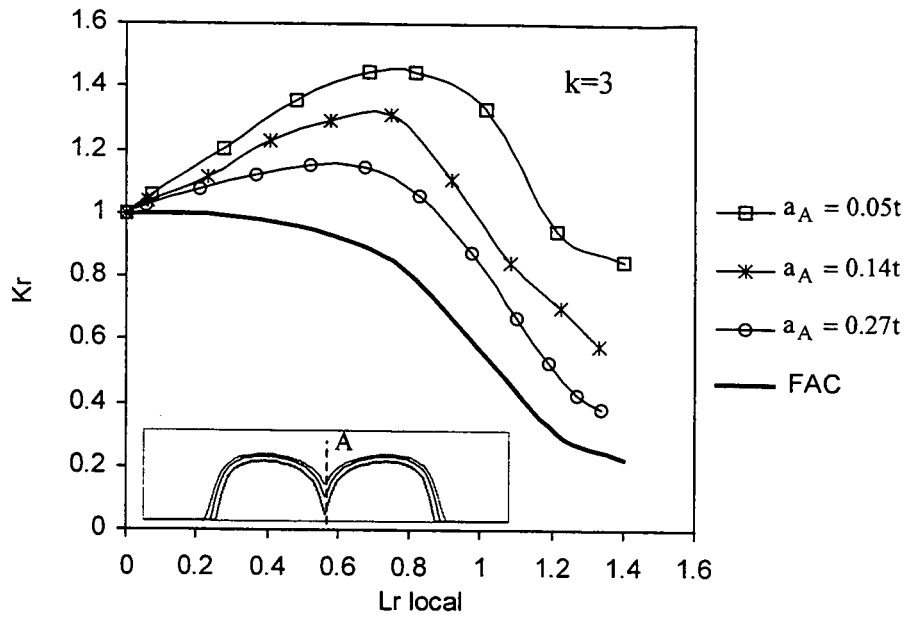


Figure 6.28:
FAD for three coalesced crack shapes and constraint sensitivity $k=3$.
Applied load is normalised with the local limit load in re-entrant sector.

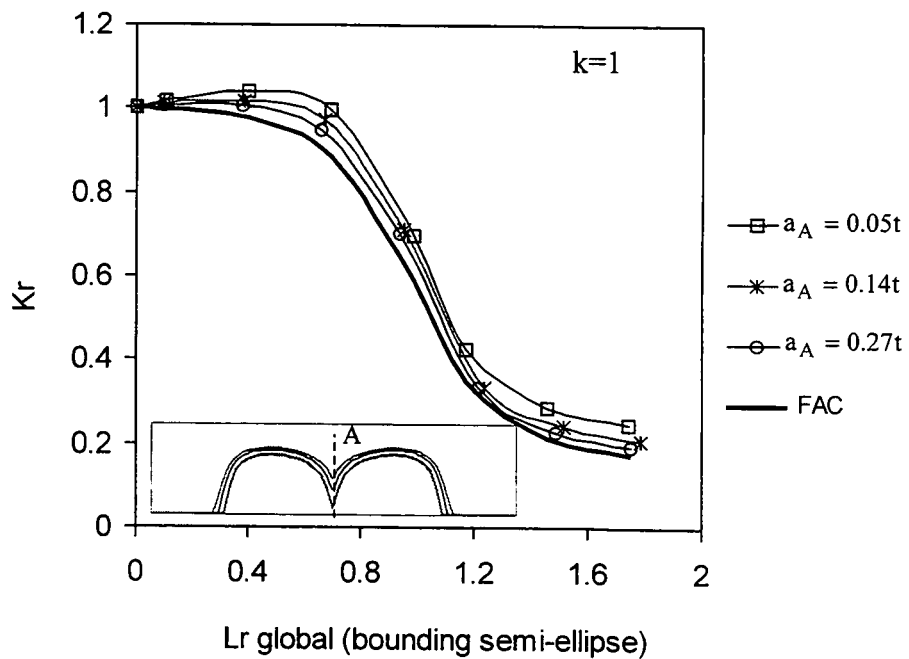


Figure 6.29:
FAD for three coalesced crack shapes and constraint sensitivity $k=1$.
Applied load is normalised with the global limit load of a bounding
semi-ellipse.

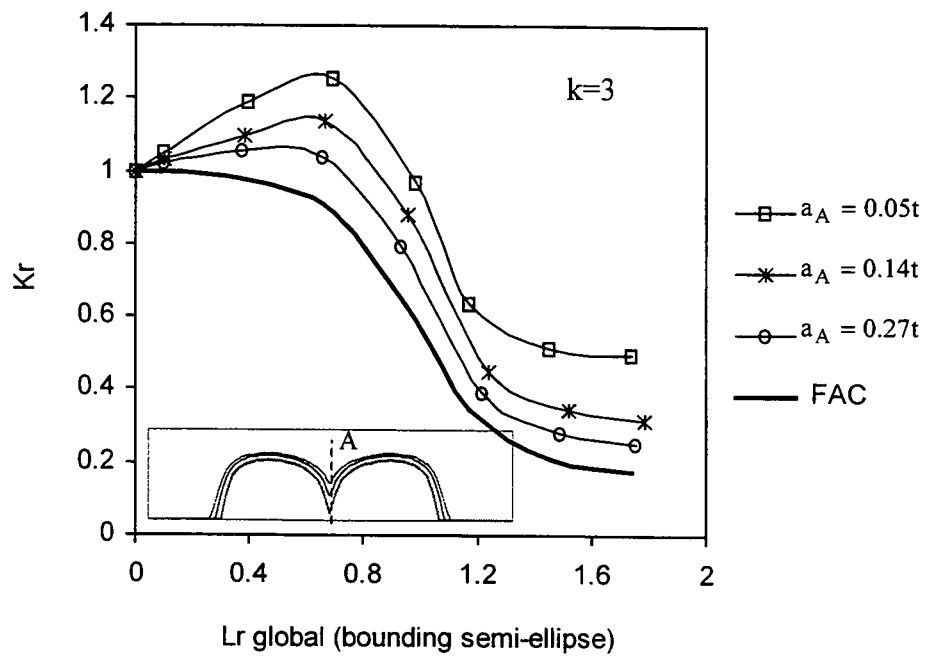


Figure 6.30:
 FAD for three coalesced crack shapes and constraint sensitivity $k=3$.
 Applied load is normalised with the global limit load of a bounding
 semi-ellipse.

Chapter 7

DEVELOPMENT OF COMPLEX DEFECTS IN FATIGUE

7.1 Introduction

The development of complex defects resulting from coalescence of adjacent defects in fatigue has been examined experimentally. The study addresses the growth of individual defects leading to coalescence, the development of re-entrant sectors and the evolution of such complex defects in fatigue towards a bounding shape. Emphasis was placed on the interaction of adjacent defects in the light of the revised interaction rules in BS 7910 and R6/4.

7.2 Test procedure

Experiments were performed on a plain carbon manganese steel, defined as grade 50D in BS 4360. The chemical composition of this steel is given in Table 7.1. Specimens were cut from a steel plate and machined to the geometry, shown in Figure 7.1. Two starter notches were machined in the centre-plane, with a slitting wheel of 70 mm in diameter and 0.15 mm thick. The notches were machined to a nominal depth of 2 mm and a surface length of 25 mm. The separation of adjacent notch tips was 25 mm. Specimens are denoted with letter S and consecutive test number.

Fatigue crack growth tests were conducted on a 100 kN servo-hydraulic testing machine using a standard three-point bending setup at a frequency of 4 Hz and a stress ratio of 0.1. During testing care was taken to maintain the peak stress intensity factor below $30 \text{ MPa}\sqrt{\text{m}}$ to maintain valid LFM conditions at the crack tips. The development of the crack shape was monitored using a "beach mark" technique, which produced distinct striations on the fracture surface. This was achieved by altering the load ratios at a constant frequency, such that the minimum load during the beach mark stage corresponded to the mean load of the main fatigue growth, while keeping the maximum load fixed. This is illustrated in Figure 7.2. The procedure can be summarised in seven steps:

- (1) The stress intensity factor at the deepest point and at the free surface of the semi-elliptical defect was evaluated, using Raju - Newman (1981) solution.

- (2) The number of cycles required for a through thickness crack growth of 1 mm was calculated from the Paris fatigue crack growth law (Paris and Erdogan (1963)). A spacing of 1 mm between the adjoining beach marks gave an accurate description of the coalescence. The stress intensity factor was determined in (1) and constants C and n were calibrated on standard three-point bend 25mm thick specimens and agree well with reports of Hancock *et al* (1986) on a similar steel. The fatigue crack growth law used was:

$$\frac{da}{dN} = 8.02 \cdot 10^{-12} (\Delta K)^{2.92} \quad [\text{m/cycle}] \quad (7.1)$$

where ΔK is given in $\text{MPa}\sqrt{\text{m}}$.

- (3) The crack extension on the free surface was calculated by assuming a through thickness crack of length $2c$, combined with the stress intensity factor determined in (1).
- (4) The applied stress range was then modified for a beach marking period, typically of 5000 cycles.
- (5) The number of loading cycles during the beach marking was calculated using the crack shape prior to beach marking. Crack growth increments of 0.1mm were found to give a distinct beach mark.
- (6) The stress range was then redefined prior to the main crack growth cycle block to maintain valid LEFM condition.
- (7) The defect shape was updated prior to the start of the next increment of crack growth (i.e. return to step (1)).

Tests were performed according to this procedure. For prediction purposes, coalescence was neglected and the stress intensity factor in (1) was calculated for a semi-ellipse with surface length equal to the sum of surface lengths of individual defects and a crack depth equal to the depth of the individual defect. Rapid fatigue crack growth was account for during coalescence, by empirically adjusting the cycle limit calculated during this period.

7.3 Results

Sixteen specimens were cyclically loaded to produce a systematic range of coalesced crack shapes. Specimens S1, S4, S9, S13, S15 and S16 were cyclically loaded until a bounding defect had developed. Specimens S2, S5, S6, S7, S11, S12 and S14 were grown to coalesced shapes with a re-entrant sector, while crack growth in specimens S3, S8 and S10

was stopped before coalescence occurred. A representative fractograph showing coalescence by fatigue is shown in Figure 7.4. The fractographs of fatigue tests terminated by ductile tearing and brittle failure are shown in Chapters 8 and 9.

7.3.1 Experimental observations

After a few thousand cycles fatigue crack initiated from several small regions around the notch periphery. The proximity of these microcracks resulted in a rapid coalescence to produce a uniform semi-elliptical crack front. The coalescence of small cracks was observed on fractographs, which revealed several small shear lips around the premachined notches. Some of these fractographs are shown in Figure 7.3.

The photographs shown in Figure 7.4 clearly showed beach marks, from which crack lengths were measured and are presented with the corresponding loading cycles in Figures 7.5 and 7.7. Only the cycles during the main crack growth were considered; the crack growth forming the beach mark is neglected. Initially the cracks grew from the deepest point of the notch in the through-thickness direction, as shown in Figures 7.5 and 7.7, propagating a semi-elliptical crack towards a stable aspect ratio, shown in Figure 7.8. When an aspect ratio of 0.4 was established, the crack grew on the surface. Both individual cracks showed similar growth on surface towards the free edge and coalescence, as shown in Figure 7.7. As adjoining crack tips approached to a 25% of their initial spacing, the crack growth on the free surface increased above that in the through-thickness direction. At an aspect ratio of 0.45, adjacent crack tips at the free surface came close to one another and an increase in crack growth towards coalescence was noted. This acceleration in fatigue growth indicate an interaction effect, as found by the experimental observations of Soboyejo *et al* (1990) and numerical analysis of Perl *et al* (1997) and Moussa *et al* (1999). Coalescence occurred after 217,000 cycles in the representative fractograph of specimen S13 shown in Figure 7.4. The re-entrant sector grew into the bounding crack within 30,000 cycles, which is within 11 per cent of total test time of 275,000 cycles, indicating the short duration of the process. During coalescence the deepest positions experience minor retardation in crack growth rate, while crack sections near the free surface were not affected. After coalescence the free surface length of the coalesced crack doubled, resulting in a step change of aspect ratio. The aspect ratio calculated from the Raju-Newman (1981) analysis and the prediction of the model developed by Iida *et al* (1980) are superimposed on the data. Prior to coalescence, the Raju-Newman model gives the best prediction of the

developing shape of the smaller crack. The development of the larger crack is however better predicted by the Iida's model. After coalescence both predictions are in good agreement with the experimental data.

All fatigue tests showed a deviation of the surface crack path from the plane containing the notches, while in the through thickness direction cracks remained in the plane, as schematically shown in Figure 7.9. Such observation have been previously reported (Twaddle and Hancock (1986), Soboyejo *et al* (1990), Leek and Howard (1996)) and inhibit planar coalescence on the surface. The crack growth rate at the free surface accelerated and the cracks either overlapped or coalesced in a non co-planar manner, by shearing the small ligament and forming a step in the crack front, as shown on fractographs in Figure 7.4 and schematically in Figure 7.9b. In the case of an overlap, schematically shown in Figure 7.9a, the overlapping cracks turned towards each other and isolated a small cone shaped section of material between them. The coalescence then occurred sub-surface on the plane containing notches. The preferred mode of coalescence is determined by the thickness of the ligament between two crack tips, as discussed by Bezensek and Hancock (2001). Shearing of the ligament occurred for small ligaments, otherwise the cracks overlapped and coalesced sub-surface. Non-coplanar coalescence influences the size and shape of re-entrant sectors. Configurations with a substantial crack overlap resulted in the formation of modest re-entrant sectors. An example of such a re-entrant sectors is shown in the fractograph of Figure 9.2. The depth of the re-entrant sector is given in Table 7.2, with the number of cycles and the mode of coalescence. In cases with no overlap, final coalescence by shear resulted in a small step (Figure 7.4) and a pronounced re-entrant sector, with crack depths as shallow as 0.1t.

7.3.2 Analysis of fatigue crack growth

The measured crack lengths were combined with a fatigue crack growth law to give the stress intensity factors for deepest crack tips (position B) and the line of coalescence (position A). The fatigue crack growth law of Paris and Erdogan (1963) was used in the work with constants C and n determined on standard three-point bend specimens and given in Eq. (7.1). The experimentally determined stress intensity factors are shown in Figure 7.10, normalised with the outer fibre stress and the greatest crack depth of each crack shape. The high initial values of stress intensity factors for the deepest crack tips of both individual defects reduce with formation of stable aspect ratio of individual defects. The

lowest stress intensity factor is reached just prior to coalescence, agreeing with results from the numerical study by Twaddle and Hancock (1986). After coalescence the stress intensity factor at position B increased with increasing crack depth. During coalescence the stress intensity factors in the re-entrant sector were extremely high. As the crack depth in the re-entrant sector increased towards the bounding defect shape, the stress intensity factors at A and B merged towards same level. The crack depth ($0.53t$ in Figure 7.10) where this occurs, completes the process of coalescence, as the stress intensity factor distribution around the crack front returns to that of a single semi-elliptical defect, as discussed in Chapter 6 (Figure 6.4). Superimposed on the Figure 7.10 is the stress intensity factor obtained from the line spring analysis of coalescing cracks, analysed numerically in Chapter 6. The numerically modelled cracks were chosen such that represent the average aspect ratio and crack depth observed in the tests. Agreement between the experimentally determined and numerically modelled stress intensity factors is observed for both positions, A and B. The minor discrepancy for the deepest positions may arise from the statistically discrepancies in different batches of steel, that may influence the calibration of parameters in fatigue growth law. The specimens were cut from a plate and had notches machined perpendicular to the rolling direction, with the crack growth is largely in the short transverse direction. The standard fatigue crack growth specimens were machined to propagate the crack perpendicular to the rolling direction but in the long transverse direction. The stress intensity factors in Figure 7.10 show the accuracy of the line spring model applied to complex defects with re-entrant sectors, where the values in the re-entrant sector closely match the experimentally determined values.

Experimentally determined stress intensity factors close to the surface are shown in Figure 7.11 and agree with the free surface crack growth rate shown in Figure 7.6. The stress intensity factor was normalised with the outer fibre stress and the half free surface crack length c , measured from the centreline of the notch. Stable growth on the surface was reached after an initial transient, as shown by a constant stress intensity factors in Figure 7.11. Just prior to coalescence adjacent crack tips accelerated towards one another, indicating the interaction effects, which are discussed later. When crack overlap occurred on the surface, the retardation in the growth on surface in the overlap is indicated with a drop in stress intensity factors in Figure 7.11. A constant crack growth rate on the surface of a coalesced defect towards the free edge was observed through the coalescence process, as shown in Figure 7.6 and 7.7. This matches the observations from the fractographs,

where no significant effect of the coalescence was noted on the free surface growth of coalesced crack. After the bounding defect profile was reached, the free surface growth rate accelerated, corresponding to the increase in the stress intensity factors shown in Figure 7.11.

Interaction effects between the adjacent defects can be quantified by comparing the fatigue growth rates on the free surface, as shown in Figures 7.12 and 7.13, the corresponding stress intensity factors for surface crack tips, as shown in Figure 7.14 and by the ratio of applied stress intensity factors at surface positions E and F, shown in Figure 7.15. Interaction effects only become significant when the crack tip spacing becomes less than half the depth of the deepest defect ($s < d/2$). The magnitude of the interaction is dependent on the thickness of the out-of-plane ligament separating the adjacent crack tips which determines the mode of coalescence. In the case of crack overlap, interaction effects elevate the local stress intensities by 20 per cent compared to the value on a single isolated defect and in cases of coalescence by a shear step the interaction causes a 40 per cent increase in stress intensity as $s \rightarrow 0$.

7.4 Discussion

7.4.1 Fatigue life and re-characterisation

During fatigue, co-planar surface breaking defects develop largely independently until the adjacent crack tips meet and coalesce. Small interaction effects, which are sensitive to shear or overlap effects, occurred before the adjacent crack tips came into contact. The observations are consistent with the finite element work of Perl *et al* (1997) and Moussa *et al* (1999) on the interaction of non co-planar surface breaking cracks and the analysis of Murakami and Nemat-Nasser (1982) and Bayley and Bell (1997) on the interaction of co-planar surface breaking cracks. Small under-predictions of the fatigue life arise if interaction effects are omitted. However this is counteracted by re-characterising the defect as soon the crack tips touch. Although the two effects may not be equal, the resulting effect is usually conservative.

Coalescence is a rapid local process affecting the local region where a re-entrant sector is formed. The fraction of the fatigue life spent in coalescence was approximately 15 per cent in the present work, matching previous reports (Twaddle and Hancock (1986), Soboyejo *et*

al (1990), Leek and Howard (1996)), although Frise and Bell (1992) found that coalescence could constitute up to 87 per cent of total test time, depending on the geometry, defect spacing and the type of loading. In engineering applications both, crack interaction and coalescence may constitute a useful part of the operational life. Re-characterisation procedures which discard both, interaction and coalescence, shorten the operational life. Allowing a limited amount of defect interaction but precluding coalescence, as recommended in R6/4 and BS 7910 defect assessment codes, and proposed for the revised ASME XI code (Hasegawa (2002)) rationalises the assessment while maintaining the necessary conservatism. The present experimental work confirms suggestions of Iida *et al* (1980, 1984), Twaddle and Hancock (1986), and agrees with observations of Soboyejo *et al* (1990) and Leek and Howard (1996) that the defect interaction and coalescence phases in fatigue growth may be neglected and simplified procedures for fatigue life are conservative and support the revised defect re-characterisation rules of BS 7910 and R6/4.

Leek and Howard (1996) proposed a fatigue life model, which accounts for rapid fatigue crack growth in re-entrant sectors through numerically determined interaction factors. However Iida's recommendation of replacing the actual interacting crack geometry with a bounding crack as soon as adjacent crack tips touch is still maintained. This approach is an improvement over the original proposal of Iida *et al* (1984), whose fatigue life model does not incorporate interaction effects.

Defect re-characterisation rules given in BS 7910 and R6/4 recommend replacing the real defects with a re-characterised shape once the adjacent crack tips touch. This recommendation is supported in the present work, where no major interactions or abrupt changes in fatigue growth prior to recommended re-characterisation have been observed.

7.4.2 Non co-planar coalescence

Much of the experimental work on defect coalescence is concerned with configurations with initially coplanar defects. The majority of experimental observations (Twaddle and Hancock (1986), Soboyejo *et al* (1990), Leek and Howard (1996), Bayley and Bell (1997)) however suggest final crack coalescence by surface or subsurface shearing of small ligament of material, contrasting the assumed tip-to-tip coalescence on the free surface. Similar trends in fatigue growth of free surface crack tips were found in the present work

where crack growth at the free surface deviated from the initial plane into which defects were machined. This is shown schematically in Figure 7.16 and appears to be non-systematic. For cases where one crack dominated there was a greater tendency for cracks to deviate in opposite sense at coalescence. Conversely, when crack growth initiated evenly at both defects, there was a tendency for the deviations to be in the same sense but differing in magnitude.

Melin (1983) has addressed the problem of non co-planar crack interaction by considering stress intensity factors for an array of collinear cracks. For a single crack, planar crack extension is found to be stable in Mode I loading. For a combination of mixed mode loading the crack path is governed by the mode mixity. For a periodic array of cracks with closely spaced tips, Melin found crack path is unstable for any combination of loading and concludes that non co-planar coalescence is favoured in fatigue, as observed in the present work. Crack tips close to the free surface may experience effects due to the non-singular T-stress. Cottrell and Rice (1984) have shown through the perturbation analysis that to the first-order, the deviation from the crack plane is energetically favourable, when the crack tip experiences a tensile T-stress. Conversely, a compressive T-stress stabilises the crack into its initial path. Such arguments may be relevant in the present case, where the individual free surface crack paths follow a macroscopic straight path until they are close to each other. The analysis of Cottrell and Rice however does not take into consideration the interaction of multiple adjacent defects. Clearly a full explanation has not yet been developed. Significantly, the non co-planar coalescence affects the size of the re-entrant sectors, which are relevant to brittle failures.

Mechanical factors arising from specimen preparation and testing may influence crack growth. The geometries were fine ground perpendicular to the notches after the notches were cut. Observations under optical microscope did not reveal machining marks in the crack growth direction. The machining of starter notches may have affected areas close to the free surface and influenced the subsequent orientation of small cracks formed before the development of a single dominant crack. These small cracks coalesced into a dominant crack and their orientation may have affected the initial orientation of the main crack and influenced the propagation near the free surface.

The test geometry (Figure 7.1) usually exhibited free surface crack growth in opposing directions from the plane containing the notches. This resulted in crack overlap and sub-surface coalescence with a moderate re-entrant sectors. A set of leading grooves was cut between the notches, to assess the sensitivity of the deviation of free surface crack growth, which is shown schematically in Figure 7.17. The depth of these grooves was 10% of the depth of the starter notch, to minimise the influence on crack initiation, while still providing the geometric constraint for planar crack growth. Initially the leading grooves were cut half way between the notches. In the second case a leading groove was cut between the two notches.

In the first instance, which is schematically shown in Figure 7.17a, the leading groove successfully contained the main crack in the plane. However as the free surface crack tips reached the end of the leading groove, they deviated from the plane at a similar angle to that observed without leading grooves. The growth from the leading grooves is shown in more detail on the fractograph of Figure 7.18. The figure shows two plastic zones have developed and connecting the groove tips. The cracks initially followed the plastic zones, as shown in Figures 7.18 a, b and c, but then deviated and continued at an angle to the plane, as illustrated in Figure 7.18 d. The adjacent crack tips met close to the perpendicular plane (Figure 7.18 e) and coalesced by shearing the small ligament, as shown in Figure 7.18 f.

Configurations with leading grooves cut part way between notches produced coalesced configurations with a modest shear step and pronounced re-entrant sectors, when the deviation of free surface growth was of an equal sense. The size and shape of the re-entrant sectors formed depends on the separation between the adjacent tips of the leading grooves, which determines the crack overlap. The growth of the tip of the main fatigue crack within the leading groove and away from the leading groove is shown in Figure 7.19. The leading groove initiates small microcracks ahead of the main crack which are then consumed by the main crack and dictate the propagation of the main crack. At the end of the leading groove the crack tip loses its geometric restraint and propagates out of the plane.

A leading groove cut between the notches of Figure 7.17b led to coplanar coalescence, as shown in the fractograph of Figure 7.20. In this instance the notch separation was 15 mm, and a distinct re-entrant sector has formed. For cases where the notch separation is 25 mm,

a large portion of the co-planar crack front constitutes the re-entrant sector, and has a modest curvature. The entire crack profile was smaller in size, since coalescence effectively commenced earlier in the test.

The findings on a non co-planar coalescence suggests a more fundamental and systematic fracture mechanics reason for crack deviation than experimental scatter. A numerical investigation into this phenomena requires a full three dimensional model, which is beyond the scope of the current work.

Chemical composition (Wt%)								
C	Si	Mn	P	S	Cr	Mo	Cu	Nb
0.17	0.29	1.3	0.01	0.008	0.09	0.01	0.11	0.045

Table 7.1:
Chemical composition of BS4360 grade 50D steel

Configuration	Coalesced crack depth (position A) [mm]	Number of cycles to coalescence [cycles]	Number of cycles in the test [cycles]	Mode of coalescence
Specimen S1	5.5	170.000	190.000	Step
Specimen S2	6.5	156.000	162.000	Overlap
Specimen S3	Not coalesced	/	165.000	Overlap
Specimen S4	10.0	164.000	186.000	Overlap
Specimen S5	7.5	117.000	126.000	Overlap
Specimen S6	2.2	131.000	131.000	Step
Specimen S7	7.0	133.000	136.000	Overlap
Specimen S8	Not coalesced	/	144.000	Overlap
Specimen S9	0.4	75.000	117.000	Coplanar *
Specimen S10	Not coalesced	/	94.000	Coplanar *
Specimen S11	2.0	116.300	116.300	Step **
Specimen S12	1.0	117.000	117.000	Step **
Specimen S13	13.2	214.000	275.000	Step **
Specimen S14	9.8	111.000	111.000	Coplanar *
Specimen S15	13.7	91.000	140.000	Coplanar *
Specimen S16	13.5	74.000	121.000	Coplanar *

* Leading groove connecting the notches

** Leading grooves machined part way between notches

Table 7.2:
Crack depth in the re-entrant sector with number of cycles to coalescence, number of cycles in the test and crack growth direction.

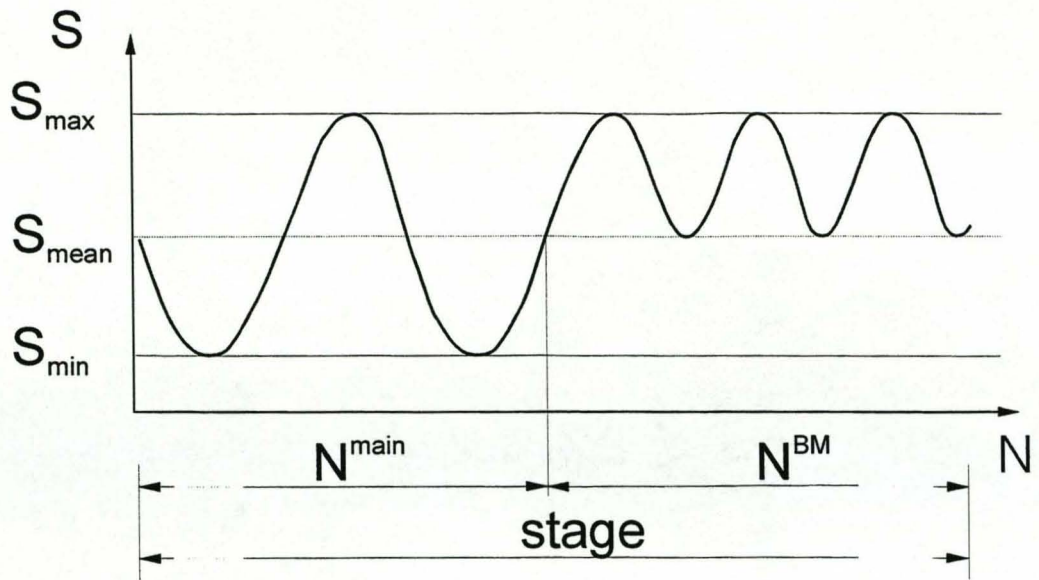


Figure 7.2:
Illustration of the beachmark technique

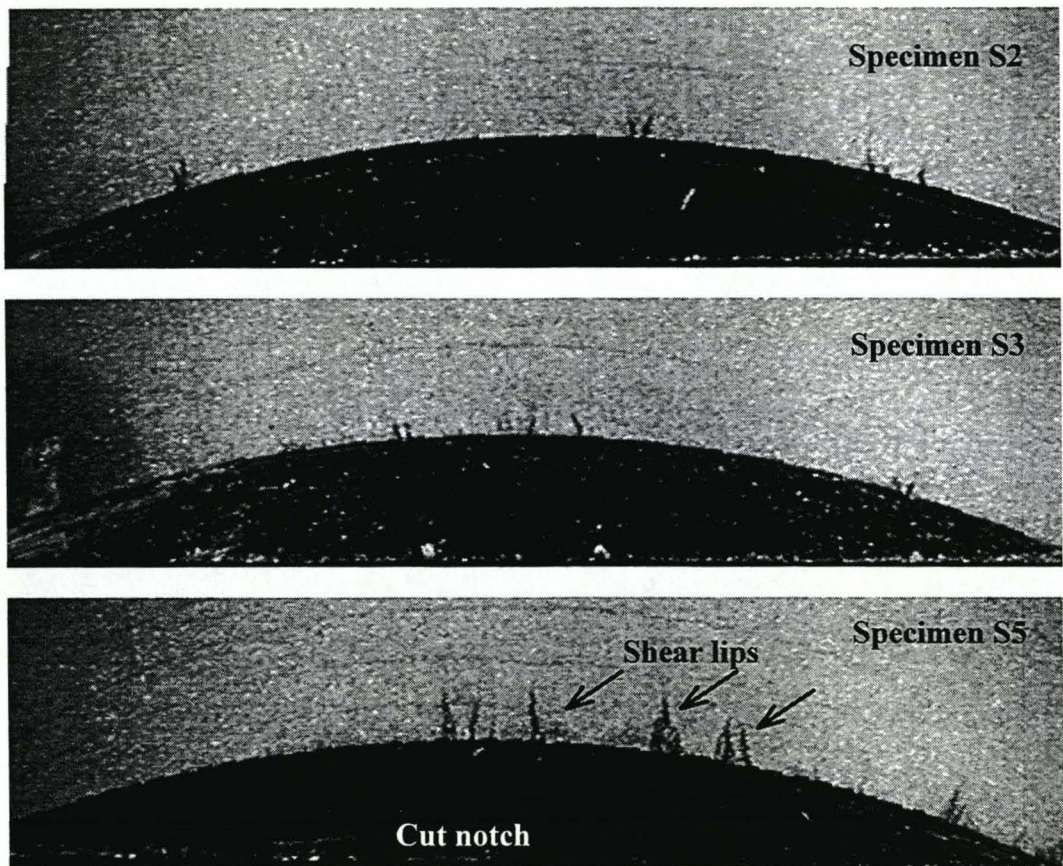


Figure 7.3:
Initial crack propagation by coalescence of microcracks

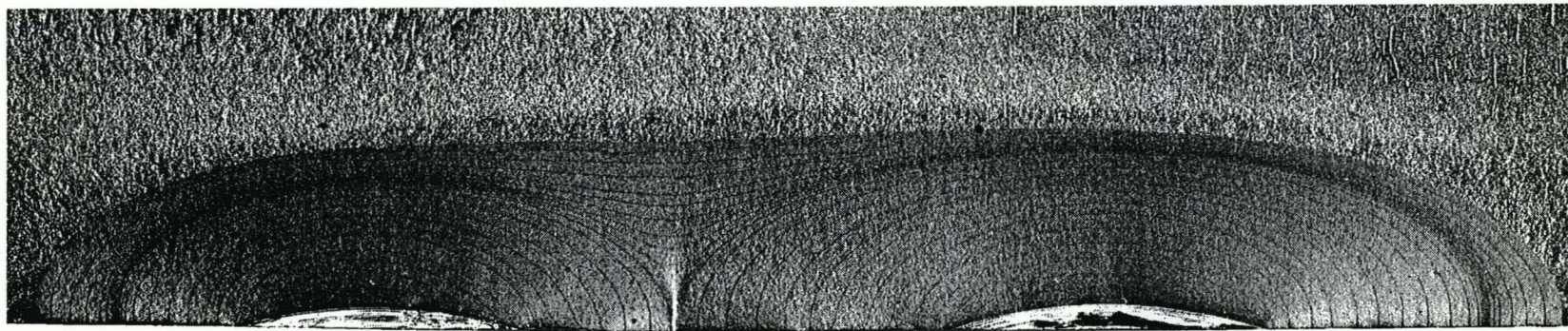


Figure 7.4:
Development of a complex crack from adjacent co-planar notches (Specimen S13).

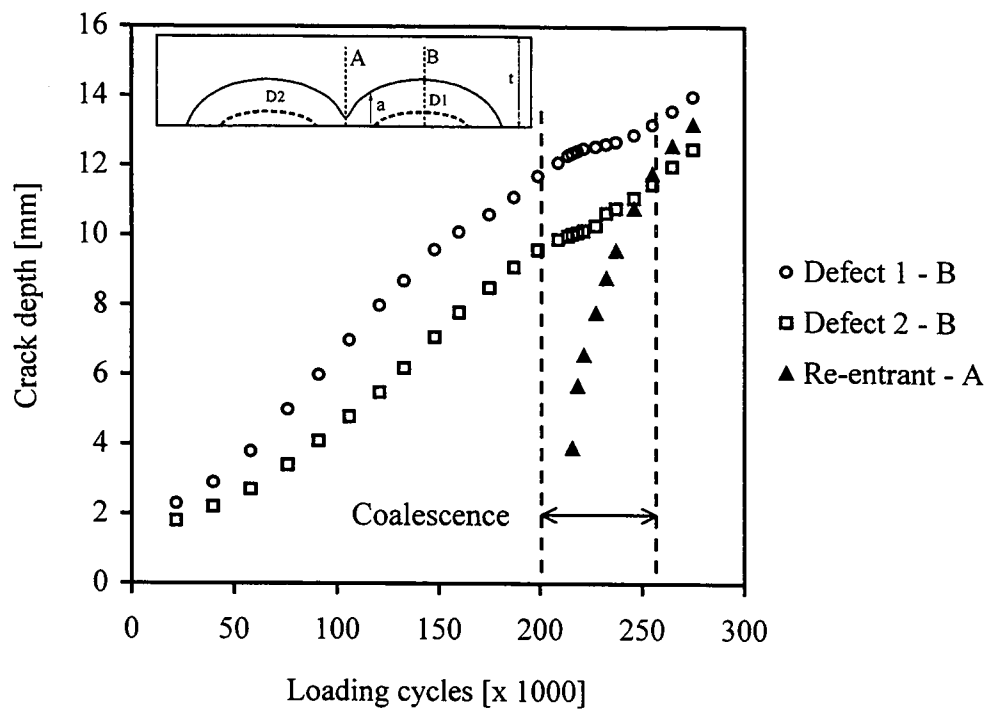


Figure 7.5:
Through thickness crack growth of specimen S13

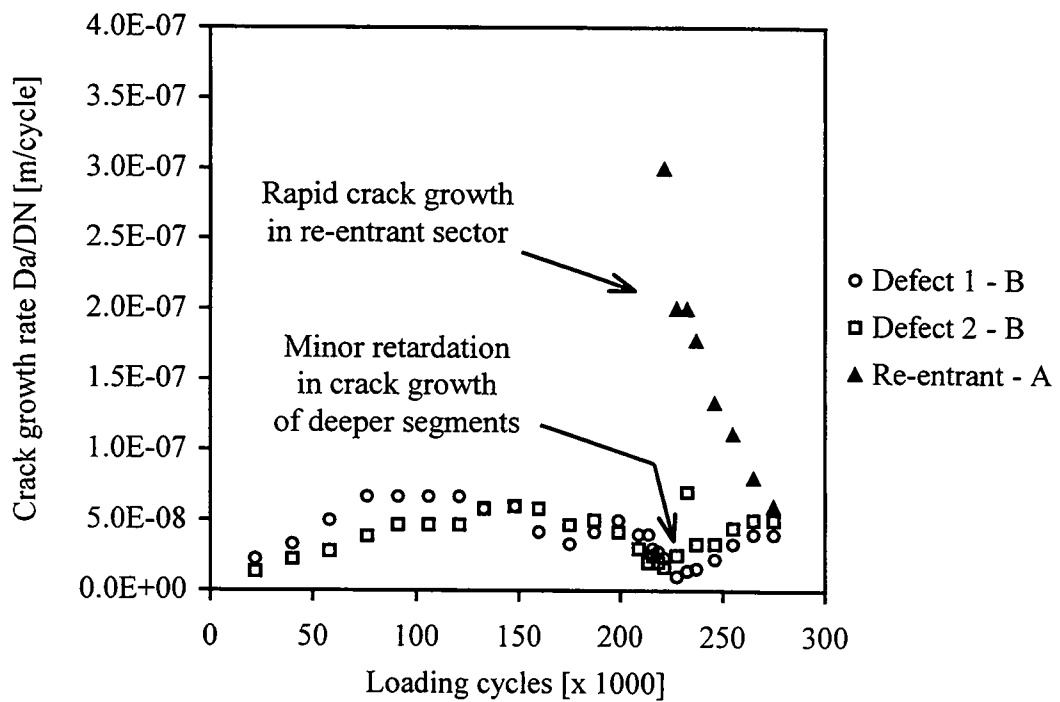


Figure 7.6:
Through thickness crack growth rate of specimen S13

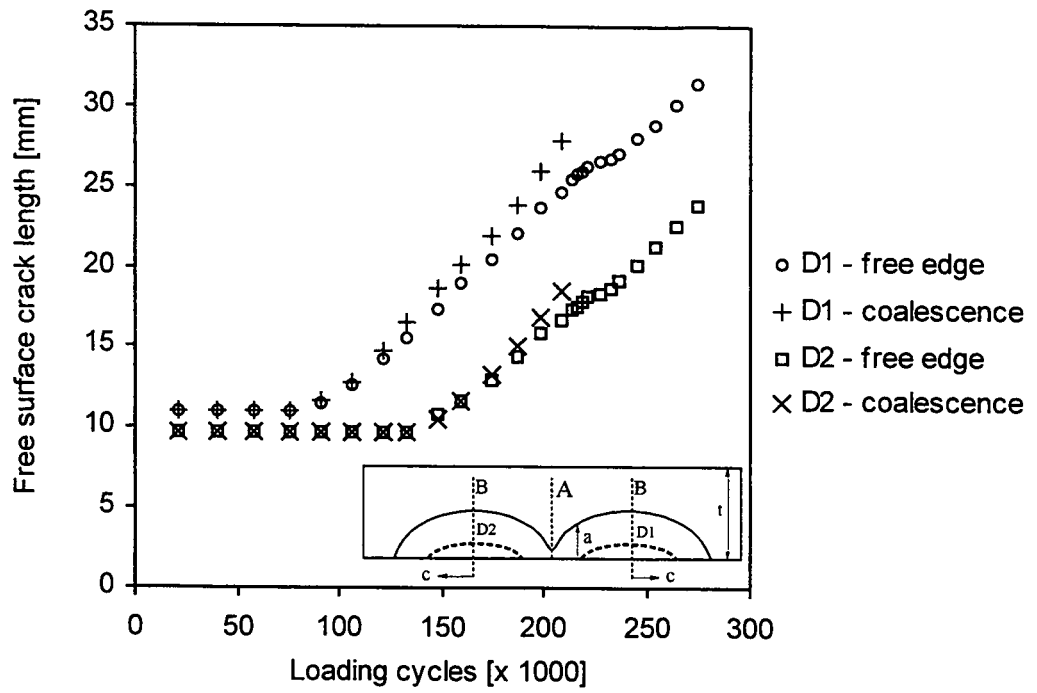


Figure 7.7:
Crack growth on the free surface of specimen S13

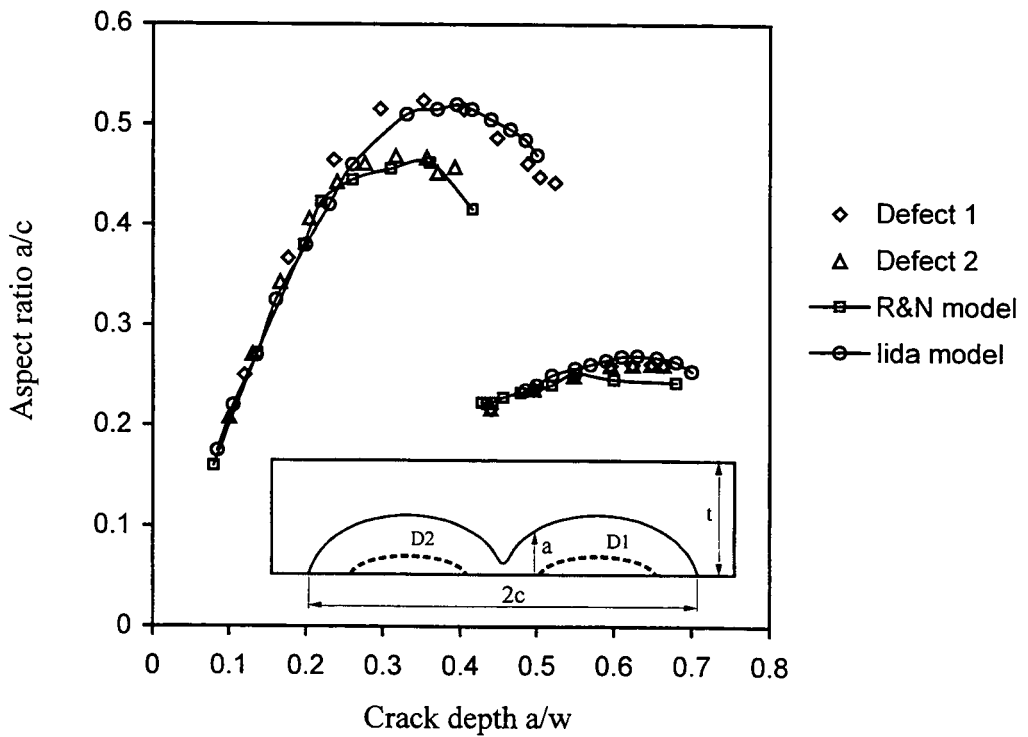
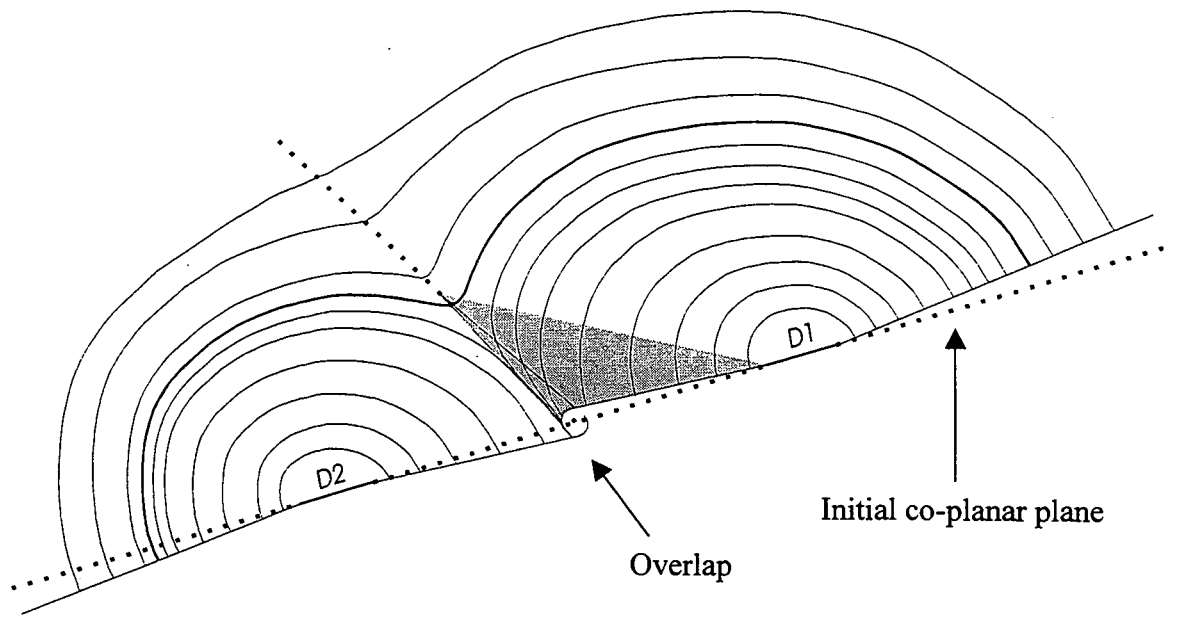
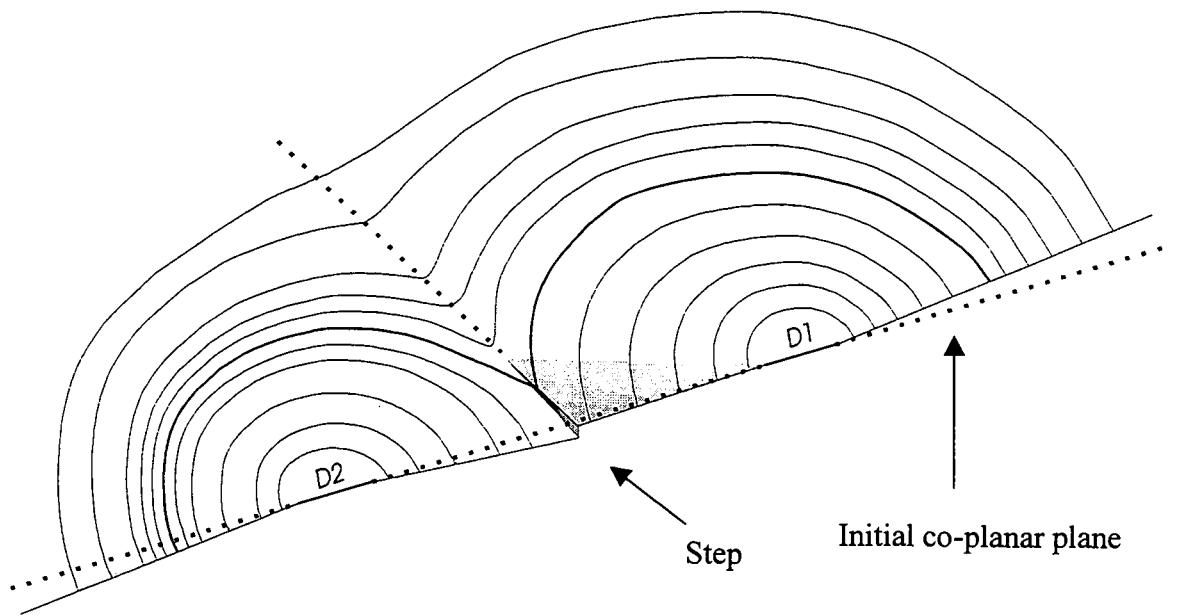


Figure 7.8:
Development of the aspect ratio for specimen S13 in fatigue



(a)



(b)

Figure 7.9:
Formation of a crack overlap (a) and sub-surface coalescence of (b) a step on the crack front during fatigue crack growth and the initial coalesced shape.

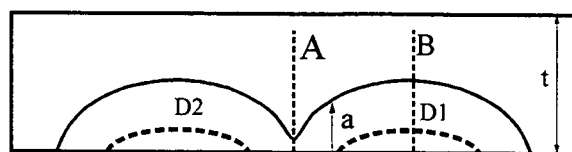
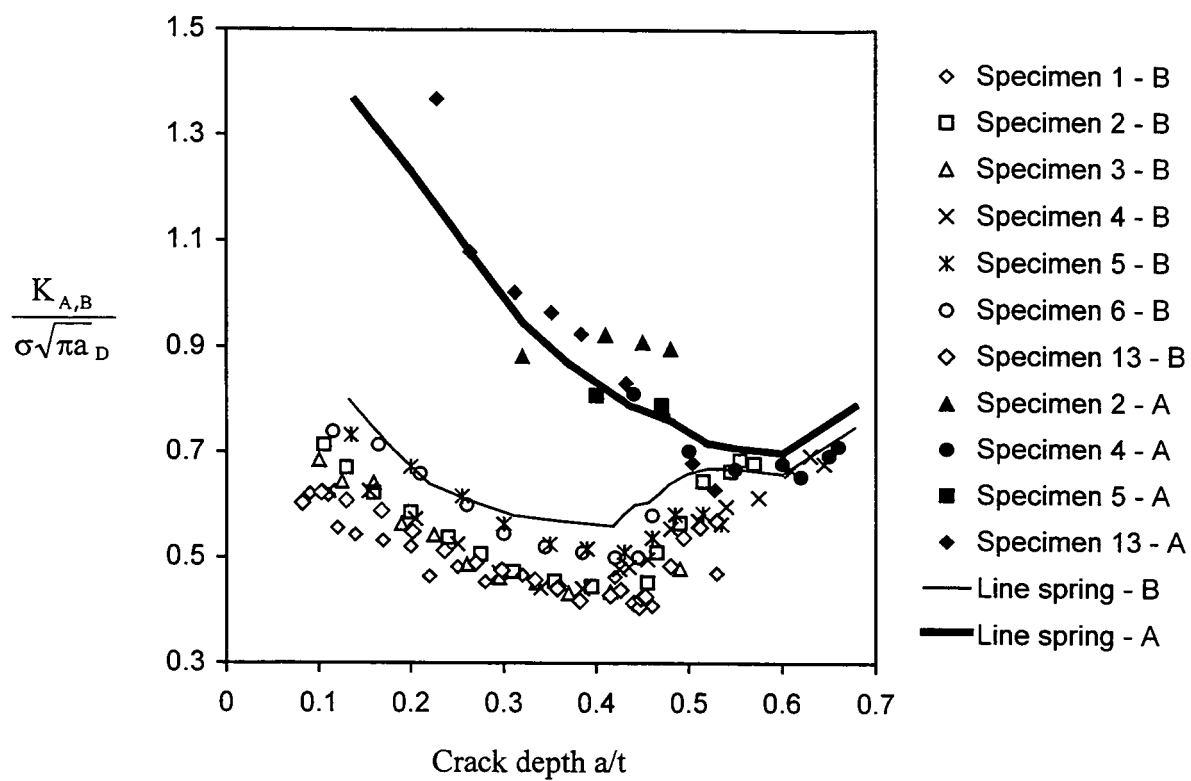


Figure 7.10: Stress intensity factor in the through thickness direction at positions A and B, from experimental and numerical studies. Values are normalised with applied stress and the greatest crack depth of each crack shape.

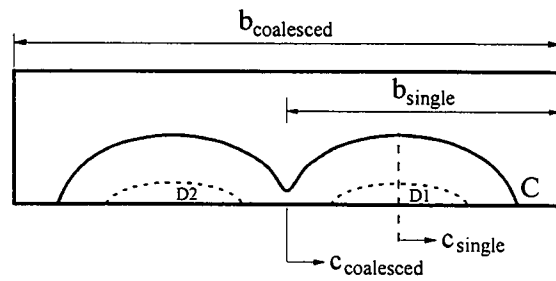
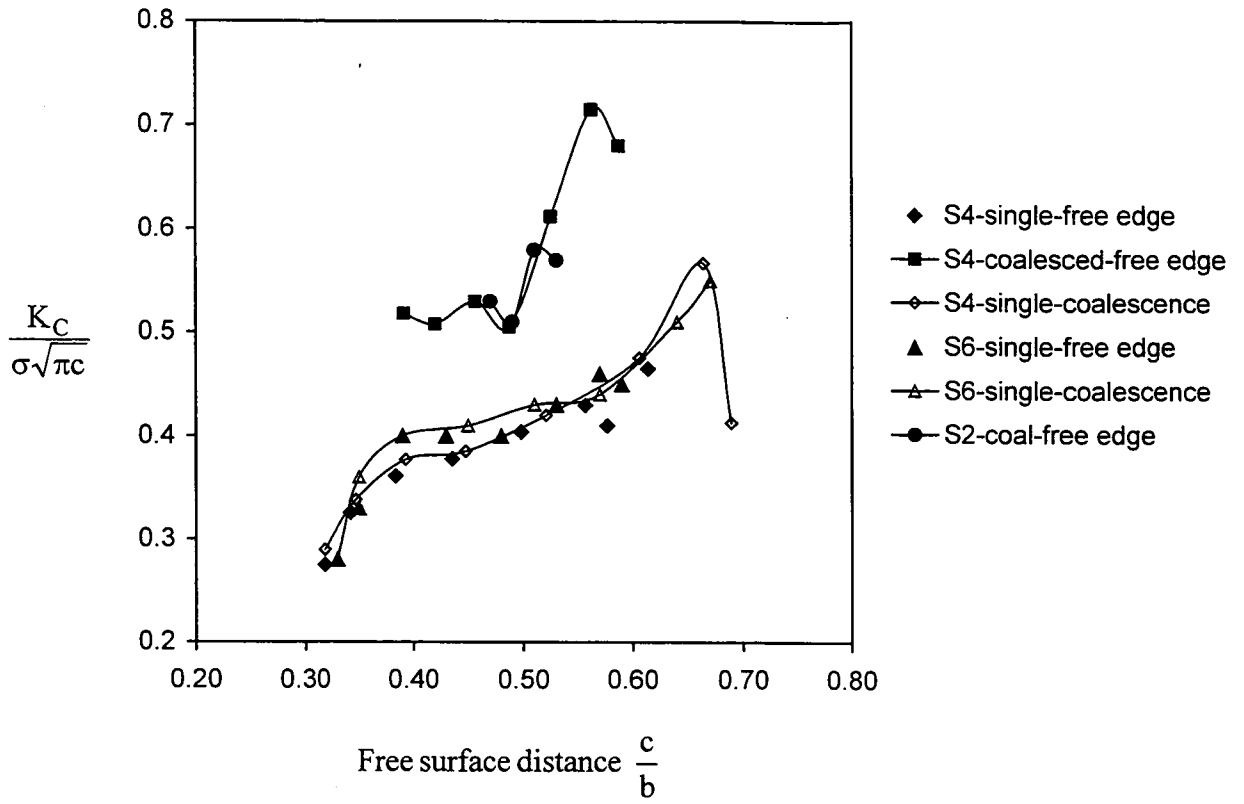
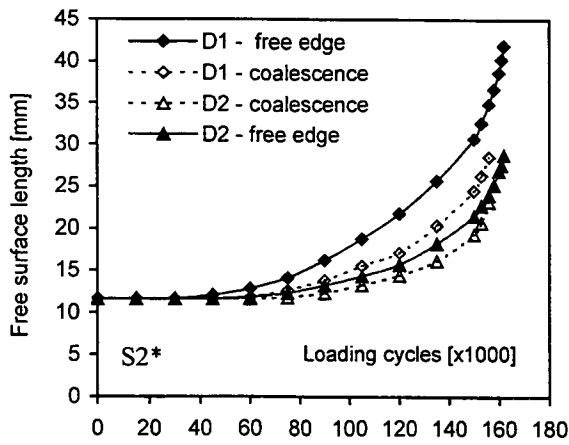
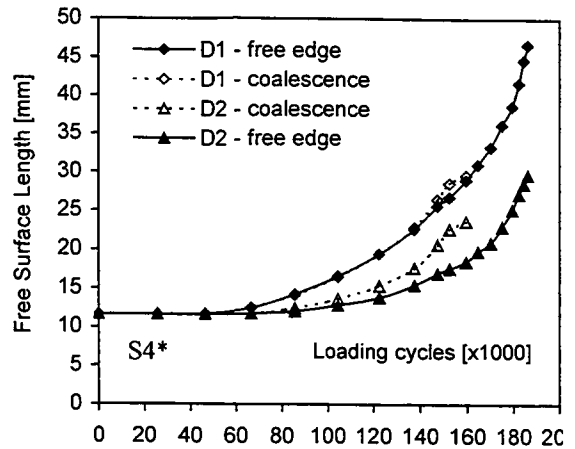


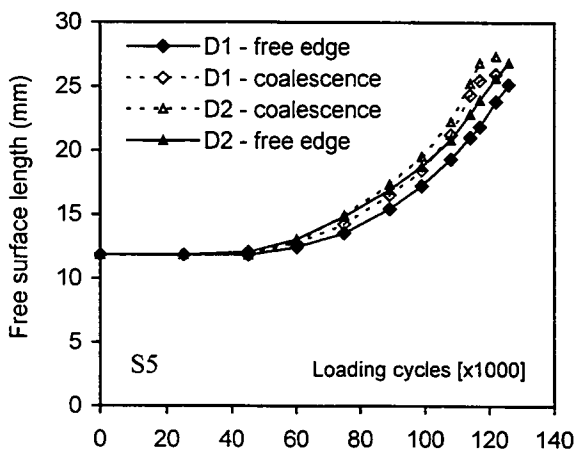
Figure 7.11:
Stress intensity factor on free surface of a complex crack, from the experimental study.



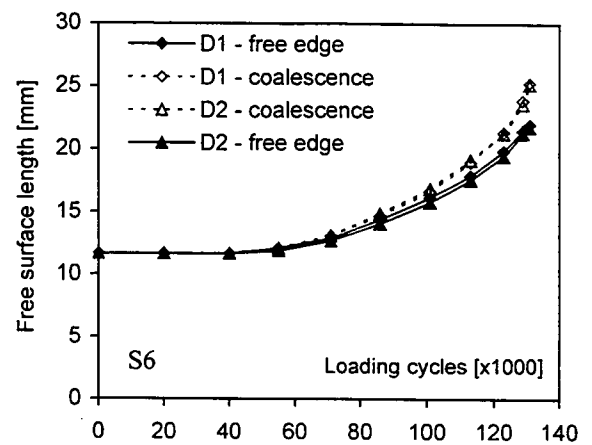
(1) S2 specimen



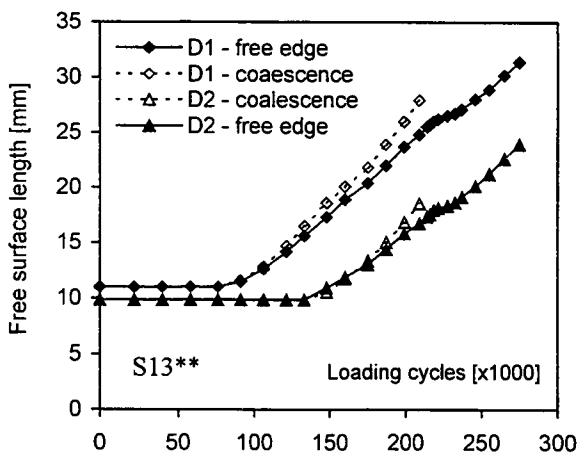
(2) S4 specimen



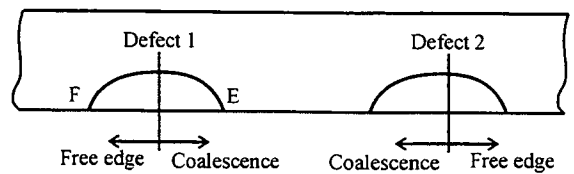
(3) S5 specimen



(4) S6 specimen



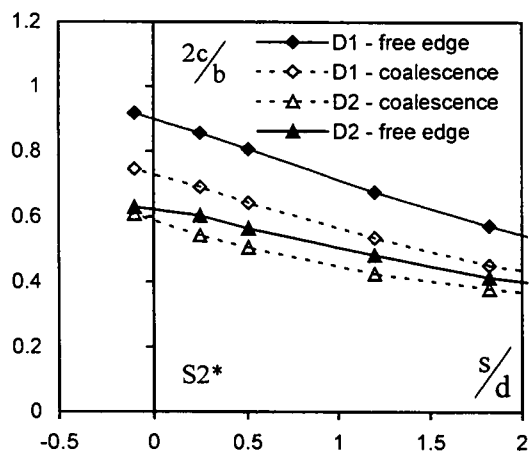
(5) S13 specimen



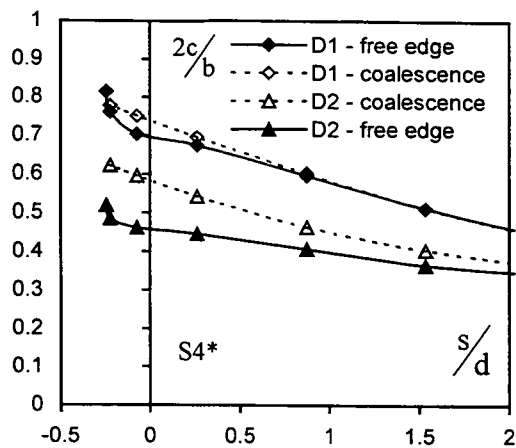
* Non-symmetric loading across plate width

** Cut notches of dissimilar size

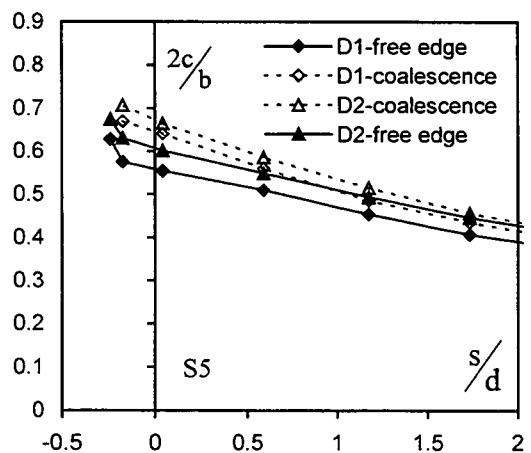
Figure 7.12:
Crack lengths on free surface (positions E and F) with loading cycles.



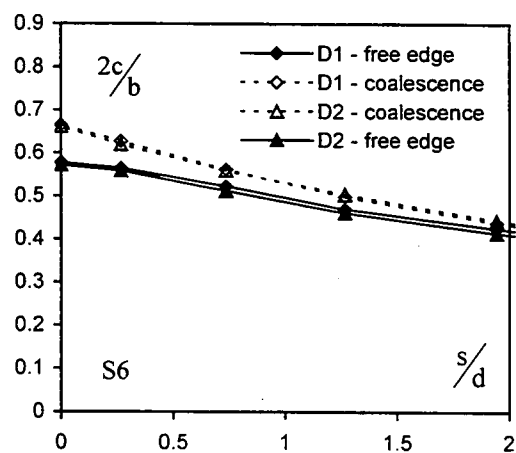
(1) S2 Specimen



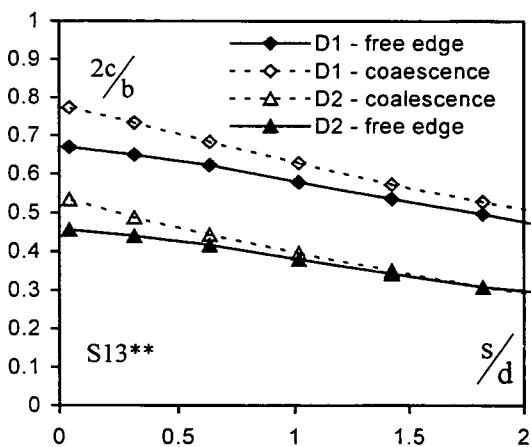
(2) S4 Specimen



(3) S5 Specimen



(4) S6 Specimen



(5) S13 Specimen

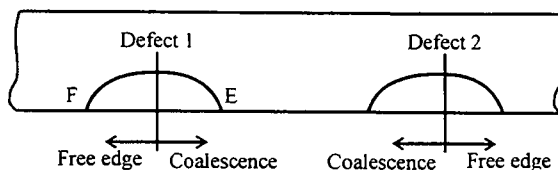
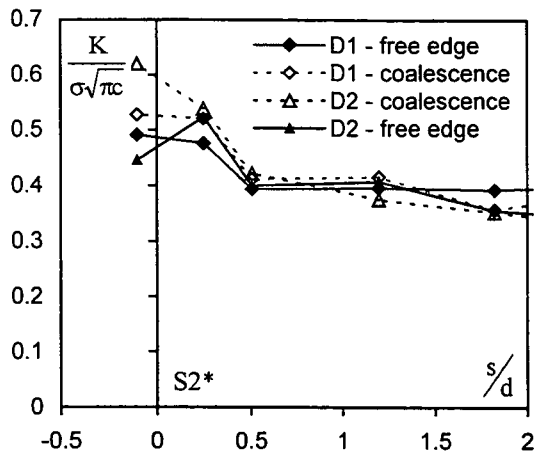
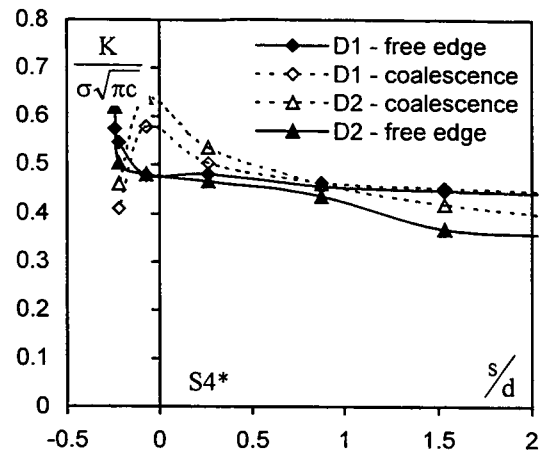


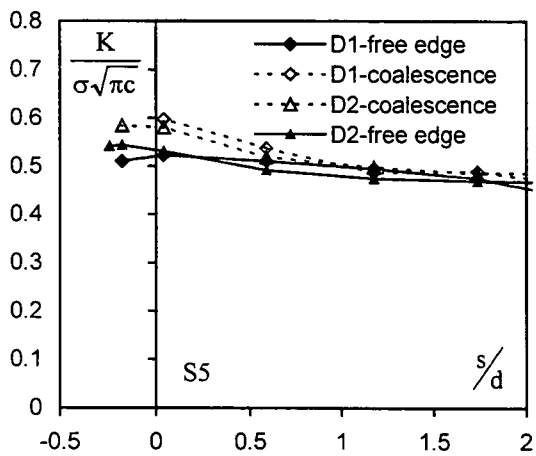
Figure 7.13:
Crack length on free surface (positions E and F) with distance to coalescence (s/d)



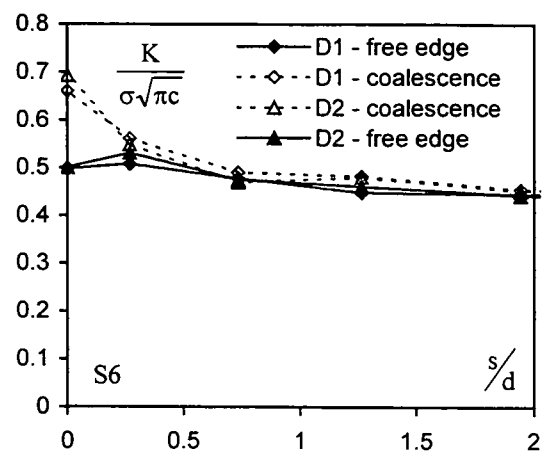
(1) S2 specimen



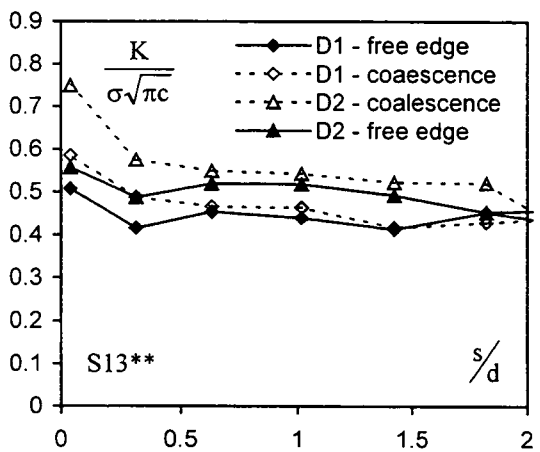
(2) S4 specimen



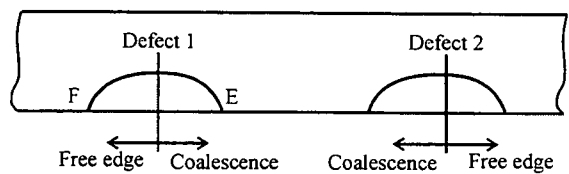
(3) S5 specimen



(4) S6 specimen

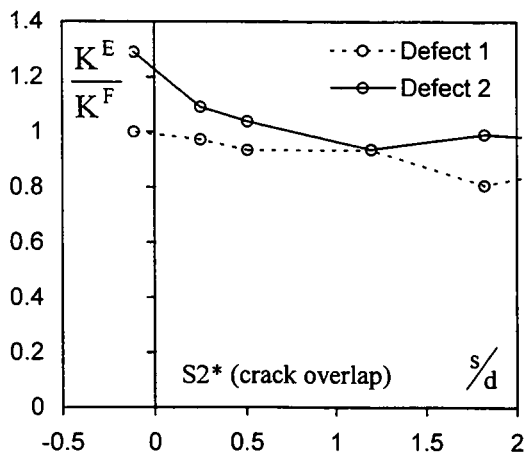


(5) S13 specimen

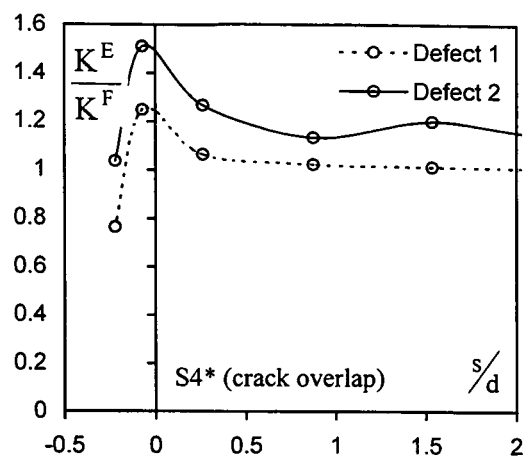


* Non-symmetric loading across specimen width
 ** Cut notches of dissimilar size

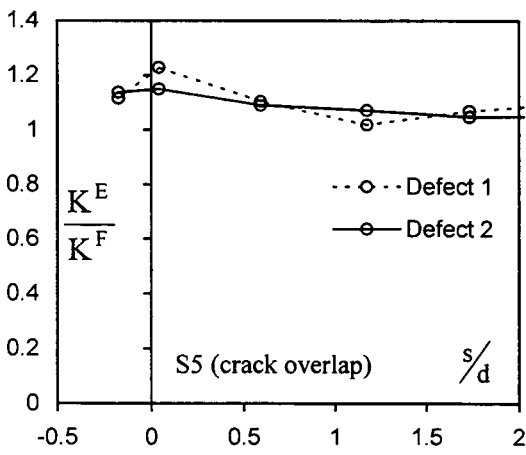
Figure 7.14:
 Stress intensity factors at positions E and F, normalised with applied stress and free surface length



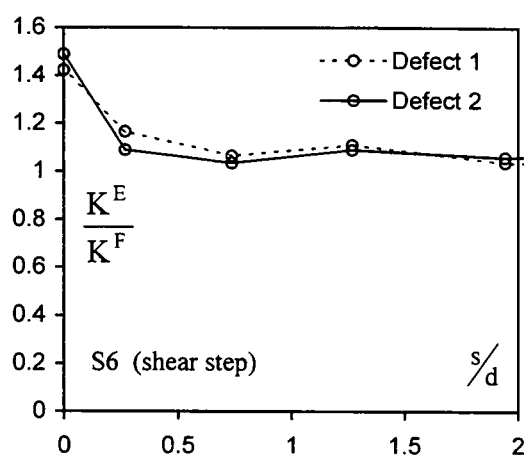
(1) S2 specimen



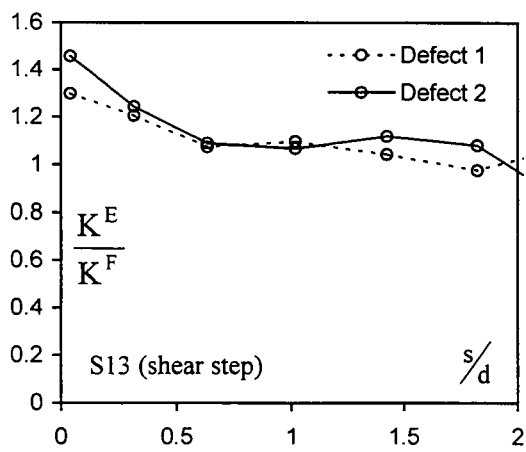
(2) S4 specimen



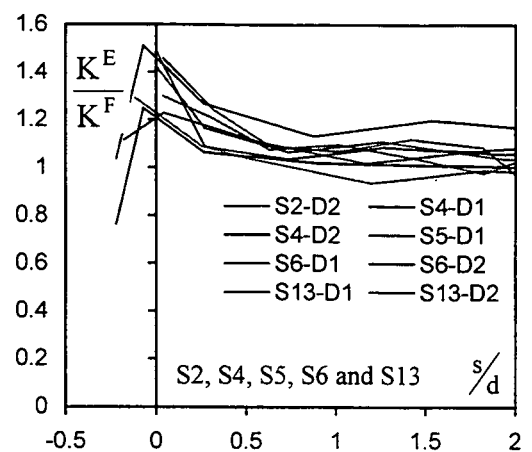
(3) S5 specimen



(4) S6 specimen



(5) S13 specimen

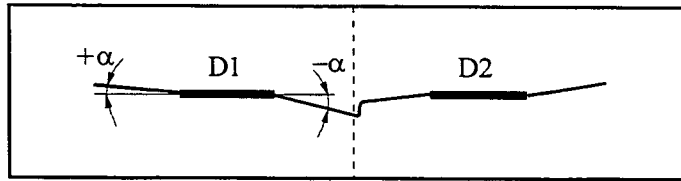


(6) S2, S4, S5, S6, S13 specimens

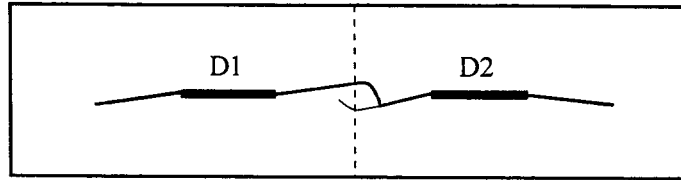
* Non-symmetric loading across plate width

Figure 7.15:
Interaction factor K^E/K^F for the adjacent defects extending in bending

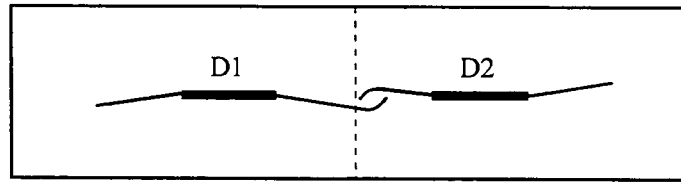
SPECIMEN 1



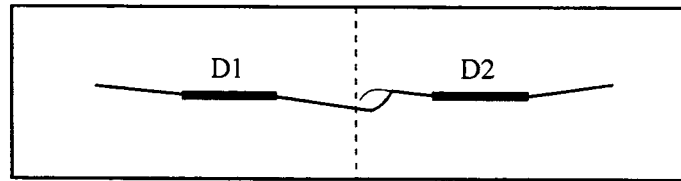
SPECIMEN 2



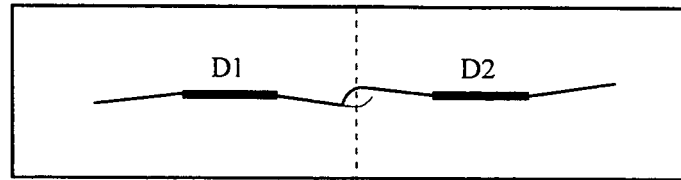
SPECIMEN 3



SPECIMEN 4



SPECIMEN 5



SPECIMEN 6

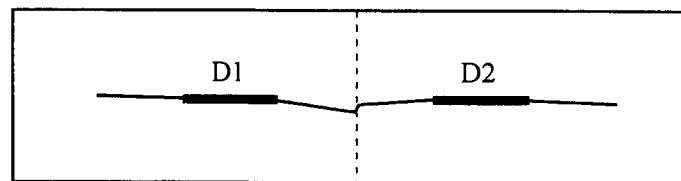


Figure 7.16:
Growth of crack on free surface in fatigue

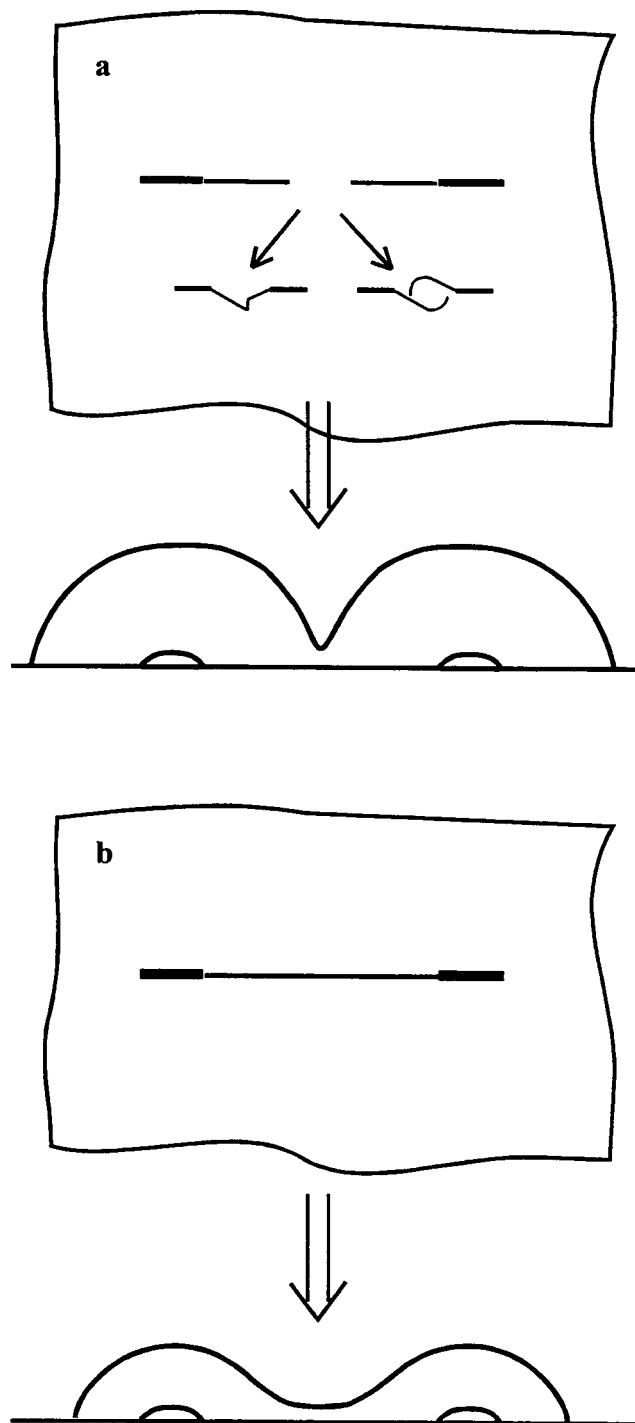


Figure 7.17:
Illustration of the effect of leading grooves on the crack path on free surface. In (a) leading grooves are cut part way between notches and in (b) leading groove connects both notches.

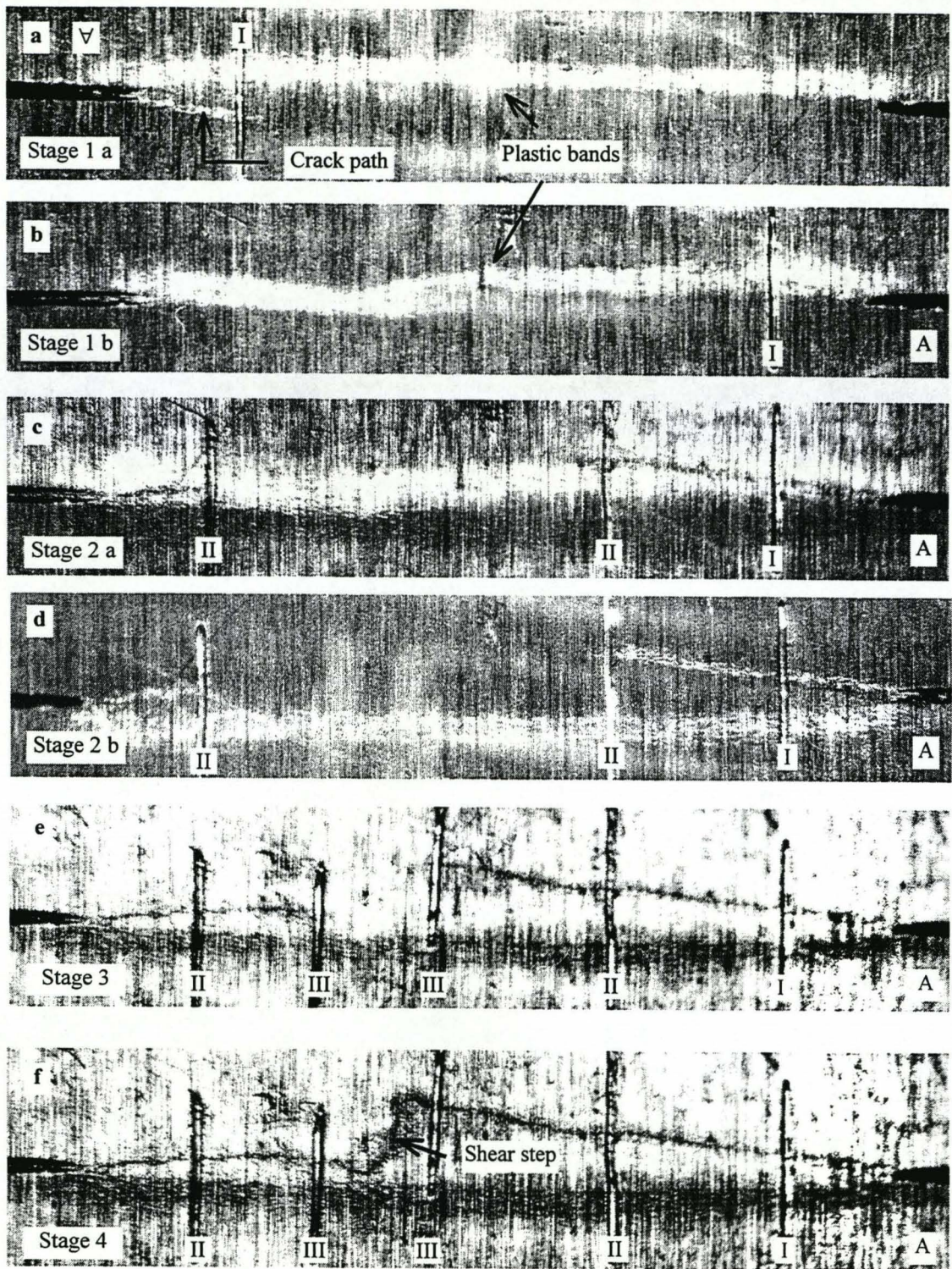


Figure 7.18:
 Photographs of fatigue crack growth on free surface from co-planar leading grooves,
 leading to coalescence on surface.



↑
Groove ends

Figure 7.19:
Photograph of the effect of the leading groove on the growth near free surface, as indicated by arrows.

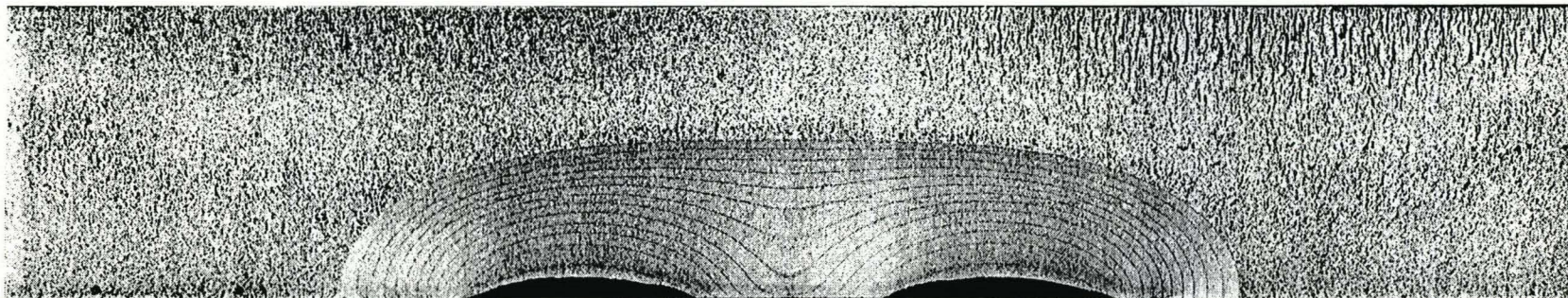


Figure 7.20:

Photograph of a development of a fatigue crack from co-planar notches connected with leading groove (specimen S16).
Notch separation is 15 mm.

Chapter 8

DUCTILE TEARING OF COMPLEX DEFECTS

8.1 Introduction

Failure on the upper shelf is preceded by significant amounts of plastic deformation and possibly crack extension by ductile tearing. Defect assessment procedures for such cases are based on elastic-plastic fracture mechanics. Such procedures may describe failure with a two parameter approach using failure assessment diagrams of R6/4 (2001), which can be modified to include constraint effects. Defects formed by the coalescence of two co-planar cracks were analysed numerically in Chapter 6 using the elastic-plastic line spring concept of Parks and White (1982). The analysis distinguished between the local limit load in the re-entrant sector and the global plastic collapse load. Similarly the development of J or CTOD is greatly amplified in the re-entrant sector. The numerical results presented in Chapter 6 suggest that crack advance starts in the re-entrant sector. Modified failure assessment diagrams have been developed for complex defects in Chapter 6 and show that the modified failure assessment curves for the re-entrant sector fall above the general curve, indicating constraint enhanced resistance to small amounts of ductile tearing in the re-entrant sector.

An experimental programme examined failure of complex defects by ductile tearing. The observations are presented in this chapter and discussed in terms of the numerical analyses presented in Chapter 6.

8.2 Test procedure

The specimens used in the work were machined to the specifications given in Chapter 7. Three representative configurations were developed by fatigue:

- i) a configuration with two separate defects before coalescence (Specimen S8), shown in Figure 8.1a,
- ii) a coalesced configuration with moderate and modest re-entrant sector (Specimens S7 and S14), shown in Figures 8.1b and 8.1c
- iii) a bounding semi-elliptical configuration (Specimen S9), shown in Figure 8.1d.

The configurations were tested at 20°C to give a representative overview of the coalescence process for large amounts of ductile tearing.

The experiments were performed using a closed-loop servo-hydraulic test machine under three point bending. The cross-head velocity of $1 \text{ mm}/\text{min}$ ensured quasi-static loading. Large amounts of ductile tearing were used to show the development of crack shape. Crack advance was monitored with a heat tinting technique described by Gahm and Jeglitsch (1981), by keeping the specimen in a furnace at 300°C for 6 hours. This procedure oxidises the fracture surface in a light blue shade and was used to mark crack advance in the first tearing stage. Crack advance in the second tearing stage was marked with a brittle fracture in the final stage, where plastic deformation was minimal and no ductile tearing occurred. The dimmer surface of the second ductile tearing stage, shown in Figure 8.1, is distinguishable from the lighter fracture surface of the brittle fracture of stage three.

8.3 Results

The significant dimensions of the crack shapes are presented in Table 8.1, with a schematic representation of the crack shape developed by ductile tearing. The crack depths in the re-entrant sector, at the deepest segments and the extension on the free surface are given in Table 8.1, with the load to cause gross plasticity in each stage of the experiment. The fractured specimens are shown in Figures 8.1 and 8.2 and the test observations are summarised below.

8.3.1 Separate defects before coalescence

The crack profile which consisted of two separate defects which have not coalesced in fatigue (specimen S8) is shown in Figure 8.1a. In fatigue the adjacent free surface crack tips grew out of the co-planar plane in opposite sense, resulting in the spacing between the adjacent crack tips of 2 mm in the x- direction (across the plate) and 2.5 mm in the y- direction (along the length of the plate) at the end of fatigue period.

Prior to the initiation of ductile tearing, local plasticity was observed on the free surface around the re-entrant sector and away from coalescence as schematically shown in Figure 8.5. This was observed for all test configurations with re-entrant sectors and is discussed in more detail in subsequent sections. After plastic deformation opened the crack flanks, coalescence occurred by shearing the remaining ligament between the adjacent surface crack tips. The extent of the shearing process could not be determined by optical observations during the test. Tearing in the first stage was stopped once a clear shear mark

was seen on the free surface. Later inspection of the fractograph (Figure 8.1a) revealed that the shear and tear in the re-entrant sector connected the deeper crack segments, resulting in a co-planar crack front with a re-entrant sector prior to the second tearing stage. A small tear was also noted close to the free surface after the first stage but not on the surface. Gross plastic deformation occurred at a load of 141 kN. The final load at the end of the first stage was 208.8 kN at a deflection of 10.4 mm. The tear was marked with heat tint, which may affect material properties and increase the load for gross plasticity in the second tearing stage by 8%, as illustrated in load-deflection diagram shown in Figure 8.3a. Consequently in the second tearing stage the gross plasticity and associated crack advance occurred at a load of 224 kN, which is 17 kN higher than the final load of the first stage. The second tearing stage was concluded at a load of 224.5 kN and the total deflection of the specimen was 15.9 mm. During the stage the load reached a peak of 230 kN at a deflection of 13.3 mm. After completion of the second tearing stage a bounding crack profile was obtained by tearing from the re-entrant sector, formed after the first tearing stage. Brittle fracture of the bounding defect in the final stage was performed at approximately -100°C and failure occurred at a load of 178 kN. Examination of the fracture surface revealed that ductile tearing of both stages was confined to the re-entrant sector. The rest of the crack front showed only minor amounts of crack advance.

8.3.2 Defect with a moderate re-entrant sector

A sub-surface coalesced crack with a moderate re-entrant sector (Specimen S7) developed in fatigue is shown in Figure 8.1b. Non co-planar fatigue crack growth led to crack overlap on the free surface and a sub-surface coalescence. Consequently a cone shaped fraction of material formed and extended from the free surface to the coplanar re-entrant crack front. The cone was still attached to both crack flanks prior to the start of the test along a thin strip, but its presence did not significantly affect ductile tearing in the re-entrant sector. During the first stage of tearing, the crack flanks opened and tearing started from the re-entrant sector, plastically deforming the cone shaped ligament. The first stage was stopped at a load of 182.7 kN and a deflection of 7.8 mm. The distinct change in slope of load-deflection paths (Figure 8.3b) indicates gross yielding of the first stage occurred at initiation load of 128 kN. The heat tint marked the extent of ductile tearing and later revealed a major ductile tear confined to the re-entrant sector. The deepest crack segments only showed crack tip blunting after the first stage. A small amount of ductile tearing was also noted near the free surface crack tips remote from coalescence, but not on the free

surface. In the second tearing stage gross plasticity initiated at a load of 191 kN, opening the crack flanks sufficiently to cause separation of the cone shaped fraction of material from one crack flank, but allowing it to remain attached to the other flank. The second stage was stopped at a load of 203.7 kN and a total deflection of 13.5 mm. During this stage ductile tearing was largely confined to the re-entrant sector and the rest of the crack front showed only minor amounts of crack advance. The load-displacement diagram in Figure 8.3b shows a 7% higher initiation load for the second tearing stage to that at the end of the first tearing stage. Superimposed on Figure 8.3b is the load-deflection curve obtained by the line spring analysis of the geometry before the first tearing stage. Only a fraction of the total measured deflection could be simulated with the finite element analysis before numerical instability. The experimental result is consistent with the small strain finite element based analysis which does not incorporate crack advance. The simulated loading path bounds the experimentally measured curve. Both paths show similar yield points, with a slightly greater compliance of the experimental path, which includes compliance of the test arrangement. In the third phase of the experiment the cleavage occurred at approximately -100°C and a load of 151 kN and marked the ductile tearing at the end of second ductile tearing stage.

8.3.3 Defect with a modest re-entrant sector

The crack with a modest re-entrant sector (Specimen S14) is shown in Figure 8.1c. It developed in fatigue from two adjacent notches, connected by a shallow leading groove, as discussed in Chapter 7. Large amounts of ductile tearing were induced in this specimen to demonstrate that the final crack shape is nearly semi-elliptical. The load-displacement paths are shown in Figure 8.3c. Full plasticity occurred at 131 kN and ductile tearing was again largely confined to the re-entrant sector, while the rest of the crack front experienced crack tip blunting. At the free surface crack did not advance. The first tearing stage was terminated at a deflection of 16.0 mm and a load of 204 kN, and was marked with a light blue heat tint. In the second tearing stage crack advanced uniformly around the entire profile, including the free surface tips. The initiation load in the second stage was 212 kN, which is 4 per cent higher to the final load in stage 1, indicating the metallurgical effect of heat tinting. The maximum load in this stage was 226 kN and the tearing was stopped at load of 221 kN and a total deflection of 31.7 mm, followed by a dark blue heat tint. In the third stage, tear initiated at the load of 226 kN and after 5.1 mm of deflection, cleavage instability occurred at room temperature. This is shown in the fractograph with a dark grey

surface. Before the cleavage crack has advanced stably for approximately 1 mm. The chevron patterns indicate cleavage initiated from crack tips near free surface, and propagated catastrophically through the entire geometry. A deterministic and a probabilistic analysis performed for brittle failures in Chapter 9 and applied here, agree with the chevron patterns and suggests that the critical site is near the free surface on the segments with greatest crack front curvature.

8.3.4 Bounding semi-elliptical defect

The fully developed bounding semi-elliptical crack (Specimen S9) developed by fatigue is shown in Figure 8.1d. A large deflection of 22.0 mm was required to produce a near-surface tear in the first tearing stage and tearing was stopped at a load of 181 kN. Heat tinting revealed that crack advanced uniformly around the crack front, apart from tips on free surface, which did not advance. Heat tinting also had an effect on the material properties by increasing the load for the second tearing stage, as shown in Figure 8.3d. The second tearing stage was extended to a total deflection of 32.0 mm and a load of 198 kN, where the load to initiate plasticity was 201 kN. The large opening of crack flanks in the second stage produced a crack advance along the entire crack front. In the third phase of the experiment the specimen was broken at $-100\text{ }^{\circ}\text{C}$ at a load of 105 kN.

8.4 Discussion

The configurations developed by the coalescence of two initially separate co-planar defects in fatigue formed a basis for the numerical analysis of extensive ductile tearing on the upper shelf. Ductile tearing experiments in bending support the numerical analysis using the non-linear line springs concept of Parks and White (1982). The tests showed that cracks with re-entrant sectors advanced from the re-entrant sector, where the local limit loads are accompanied with enhanced crack driving forces, compared to the deeper crack segments. The tests involving displacement controlled ductile tearing showed a stable tear confined to the re-entrant sector until it extended to a bounding defect. The constraint loss found by the numerical analysis for such profiles did not feature significantly in the experiments, as the complex defects only showed moderate re-entrant sectors. Unconstrained crack tip fields develop in bending only for shallow cracks (Al-Ani and Hancock (1991)), of crack depth less than $0.36t$, whereas the test geometries had crack depths in re-entrant sectors exceeding $0.25t$, where t is the thickness of the geometry.

The coalescence of adjacent defects in ductile tearing shows a similar shape development to that observed in fatigue. Tearing was initially confined to the re-entrant sector, where crack extended towards the bounding shape, while the remainder of the crack front showed only minor crack advance. This suggests that current re-characterisation procedures, BS 7910 and R6/4, applied to such defects extending by ductile tearing are conservative, since the crack profile develops initially in a similar manner to fatigue.

For surface breaking defects there are distinct differences in the evolution of crack segments close to the free surface in fatigue and ductile tearing. In fatigue, crack advance occurs around the entire crack front, with high crack growth rates near the free surface, whereas in ductile tearing the crack is initially suppressed at the free surface, due to the loss of constraint associated with out-of-plane effects.

In predominant tensile loading Leek and Howard (1996) show the development of coalescing defects in fatigue towards a high aspect ratio during coalescence. Such geometries exhibit small uncracked ligaments extending from the deepest crack segments to the back face. For such cracks gross plasticity may initially spread towards the back face due to the smaller net section ligament. Combining this with constraint loss to greater crack depths, may suggest initiation of tearing from the deeper crack segments in tension. In such cases the “leak-before-break” arguments may become relevant in demonstrating integrity.

Failure of the defect with a moderate re-entrant sector (specimen S7) was analysed by using a failure assessment diagram procedure documented in R6/4 (2001). Failure was defined with the initiation of ductile tearing in the re-entrant sector. Ductile tearing initiated in full plasticity of the local critical segment, for which the ordinate of the assessment point, based on the J_{el} , is not very sensitive to the chosen value of load. The precise value of load at which tearing initiated is not known and was chosen to be 5 per cent above the load to cause gross plasticity in this configuration (16% above the local limit load in the re-entrant sector). The crack shape prior to ductile tearing was digitised and used to determine limit loads and the J values. Assessment was performed with the general and material and geometry specific (option 3) failure assessment curve, and is shown in Figure 8.4. Load was normalised with the local limit load in the re-entrant sector. Due to the weakness of line springs in defining the transition between the elastic and

plastic behaviour (Parks (1981)) option 3 FAC does not show significant benefit of plasticity below the limit load and consequently the difference between option 1 and option 3 FACs is larger than usual. Constraint effects were observed to be weak for this configuration, and the local resistance to crack propagation, K_{mat} , was identified with the initiation plane strain toughness (extrapolated to $\Delta a=0$), J_{Ic} , measured on 25mm wide specimens in three point bending (Nekkal and Hancock (1994)), as 200 N/mm. Failure occurred between the general and specific failure assessment curves, with the proximity to option 3 FAC depending on the defined value of load at initiation of ductile tearing.

Assessment was also performed for the deepest and near surface positions of a re-characterised defect (Specimen S9), as shown in Figure 8.5. In this configuration the load to initiate ductile tearing is difficult to estimate due to extensive crack tip blunting. Gross plasticity initiated at a load of 119 kN and at the end of the stage a ductile tear of 1.5 mm was observed (see Table 8.1) at a load of 181 kN. A value of 140 kN was approximated to be the load to initiate ductile tearing. The assessment point for the near surface crack tip falls between the option 1 and option 3 failure assessment curves, while the assessment for the deepest point does not suggest failure at this load. Figure 8.5 suggests that ductile tearing initiated at near free surface crack tips, which is consistent with the experimental observations.

Large amounts of ductile tearing in complex defects were accompanied with extensive plasticity. The development of plasticity on the free surface is illustrated in Figure 8.6 for a configuration with interacting defects before coalescence, which had a small ligament between the adjacent free surface crack tips. Initially the surface plastic zone was observed as a series of circular patterns encompassing the ligament, closely followed by a wedge shaped patterns appearing away from coalescence. This is shown schematically as Area 1 in Figure 8.6. During consequent loading the circular area around the re-entrant section increased, followed by the increase of the angle of wedge shaped area away from coalescence (Area 2 in Figure 8.6). Eventually both plastic zones met and formed a distinctive profile (Area 3 in Figure 8.6), which closely resembles the profile of the coalescing crack.

The development of large scale plasticity for the re-entrant crack was modelled with the elastic-plastic line spring analysis. The test geometry of the defect with a moderate re-entrant sector (Specimen S7) before ductile tearing was analysed. The contour plots shown in Figure 8.7 show high values of the von Mises stress in the re-entrant sector and close to the surface crack tips remote from coalescence. The analysis shows a similar stress distribution pattern appearing in the numerical model to that observed on the free surface of a test geometry.

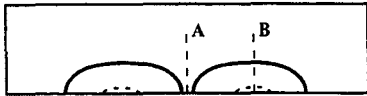
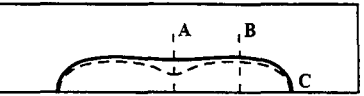
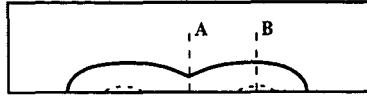
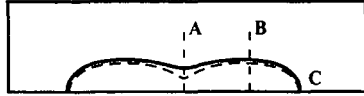
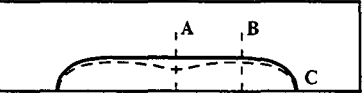
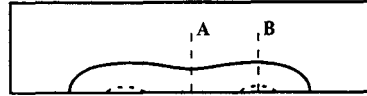
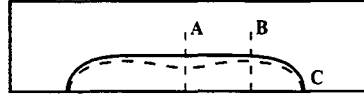
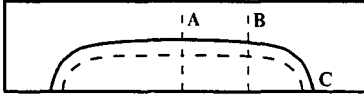
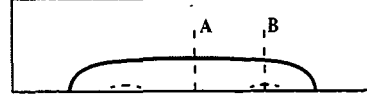
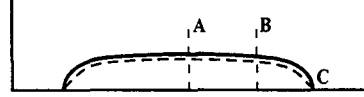
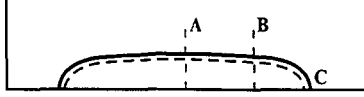
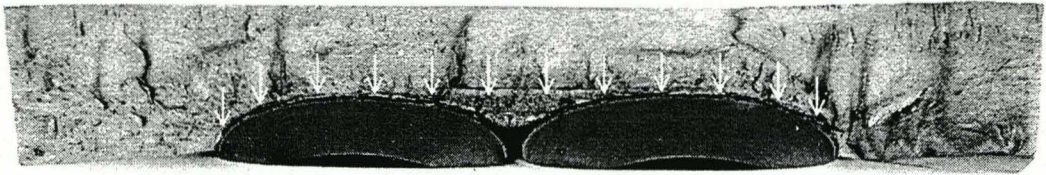
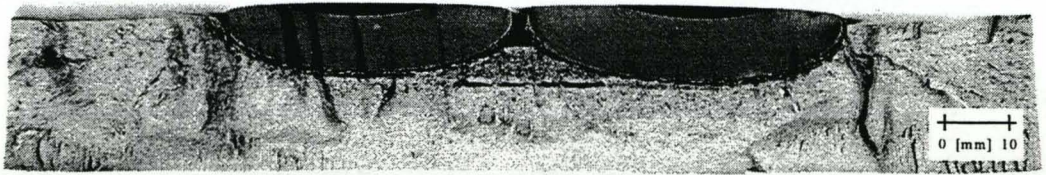
Fatigue phase			Ductile phase							
			Stage 1				Stage 2			
a_A	a_B		F_1	a_A	a_B	Δc	F_2	a_A	a_B	Δc
[mm]	[mm]		[kN]	[mm]	[mm]	[mm]	[kN]	[mm]	[mm]	[mm]
Separate defects before coalescence (S8)										
										
NA	11.3		141	6.4	12.3	0.0	224	10.8	13.0	0.0
Defect with a moderate re-entrant sector (S7)										
										
7.0	11.9		128	9.0	12.4	0.0	191	11.8	12.8	0.0
Defect with a modest re-entrant sector (S14) (large tear followed by cleavage at 20°C)										
										
9.8	11.6		131	13.2	12.8	0.0	212	16.6	16.2	3.0
Bounding semi-elliptical defect (S9)										
										
14.1	13.7		119	15.6	15.2	2.1	200	16.7	16.5	2.6

Table 8.1:

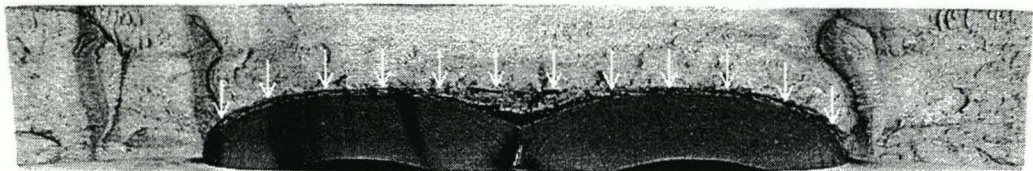
The coalescence of two surface breaking defect by ductile tearing. The crack depths at positions A and B are shown at the end of each stage, with the load to initiate gross plasticity in each stage and the extension on the free surface, Δc .



a) Separate defects before coalescence (S8)



b) Defect with moderate re-entrant sector (S7)



c) Defect with modest re-entrant sector (S14)

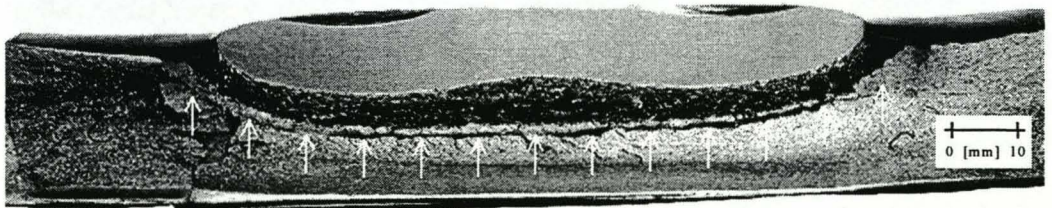
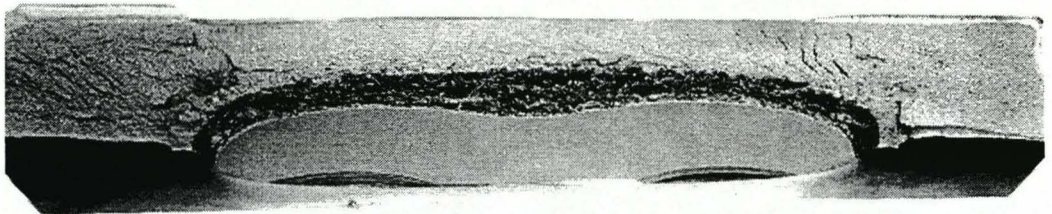
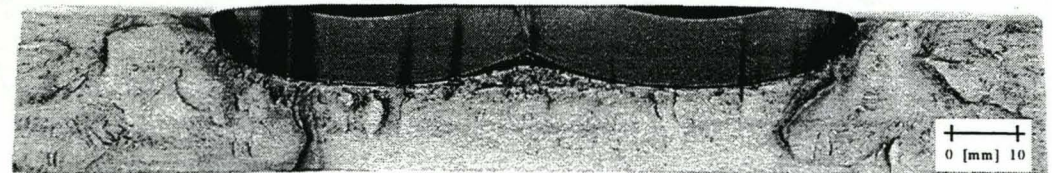
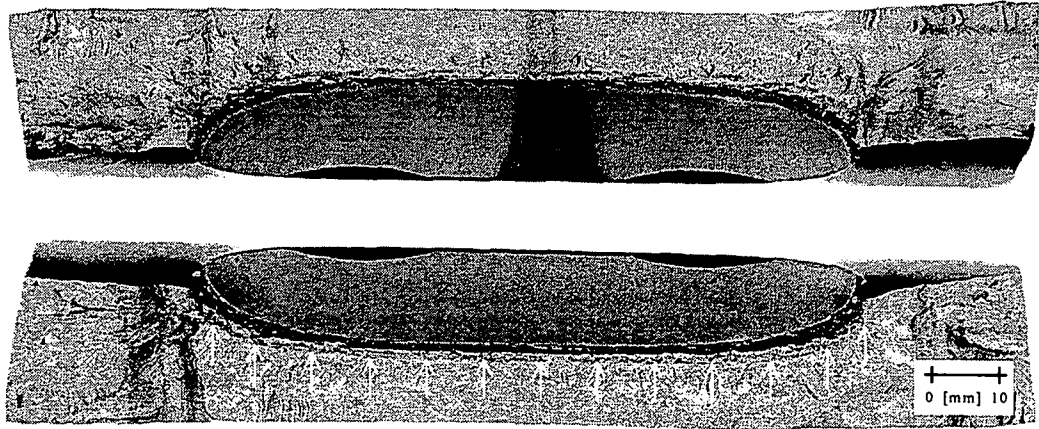
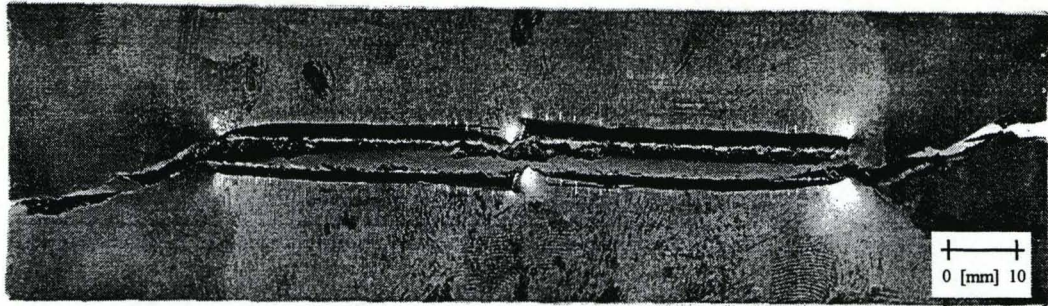


Figure 8.1:
Photographs of fracture surface in ductile torn configurations. Arrows mark boundary of cleavage failure.

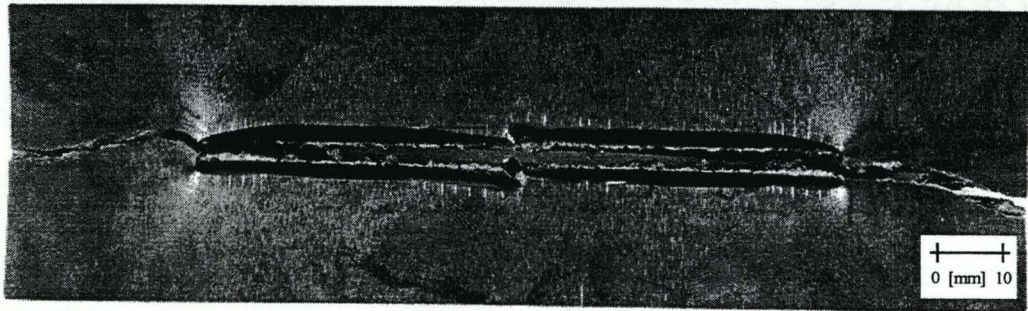


d) Bounding semi-elliptical defect (S9)

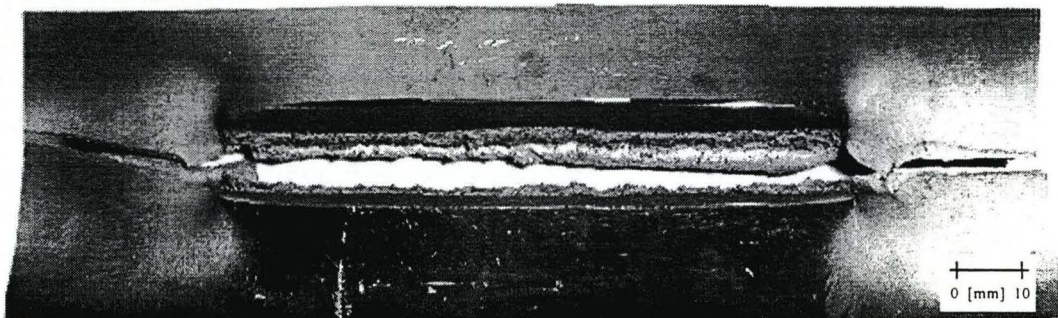
Figure 8.1 (cont):
Photographs of fracture surface in ductile torn configurations. Arrows
mark boundary of cleavage failure.



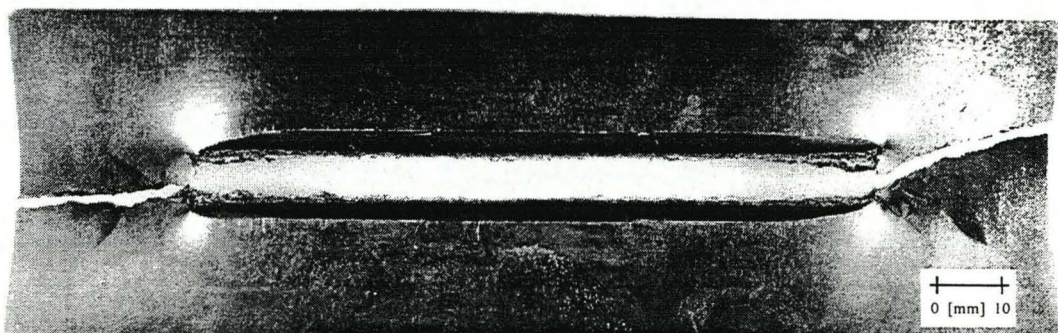
a) Separate defects before coalescence (S8)



b) Defect with moderate re-entrant sector (S7)

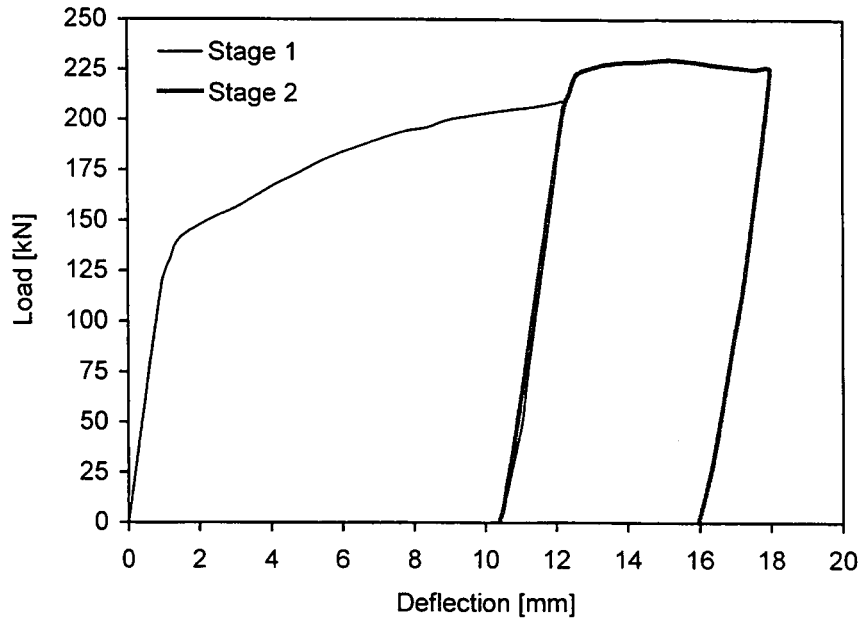


c) Defect with modest re-entrant sector (S14)

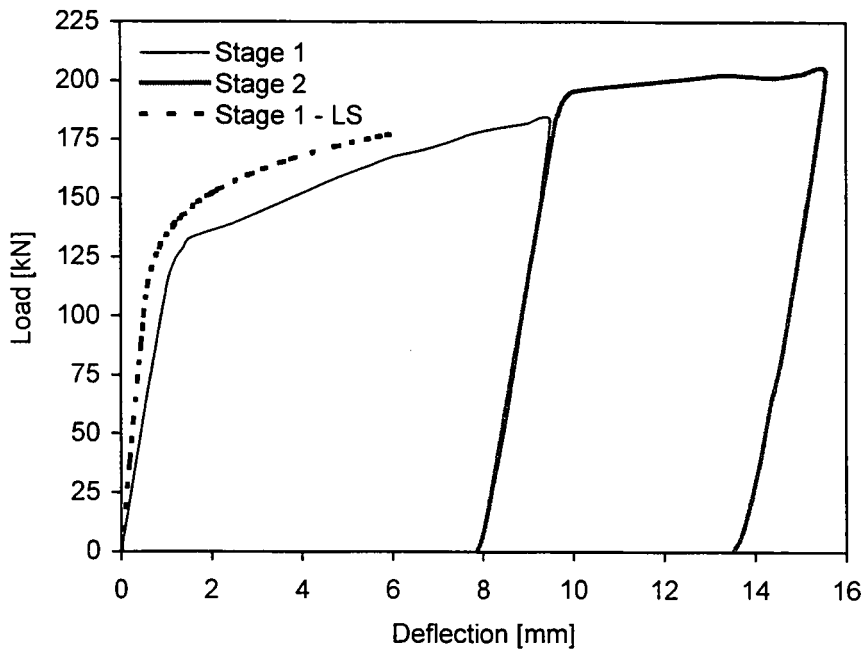


d) Bounding semi-elliptical defect (S9)

Figure 8.2:
A view on the tested specimens from the free surface.

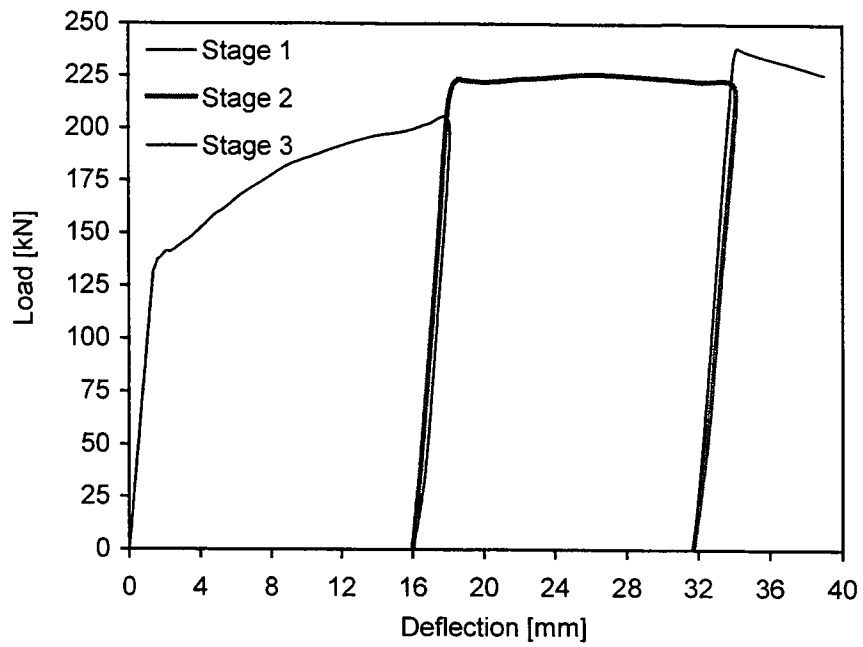


a) Separate defects before coalescence (S8)

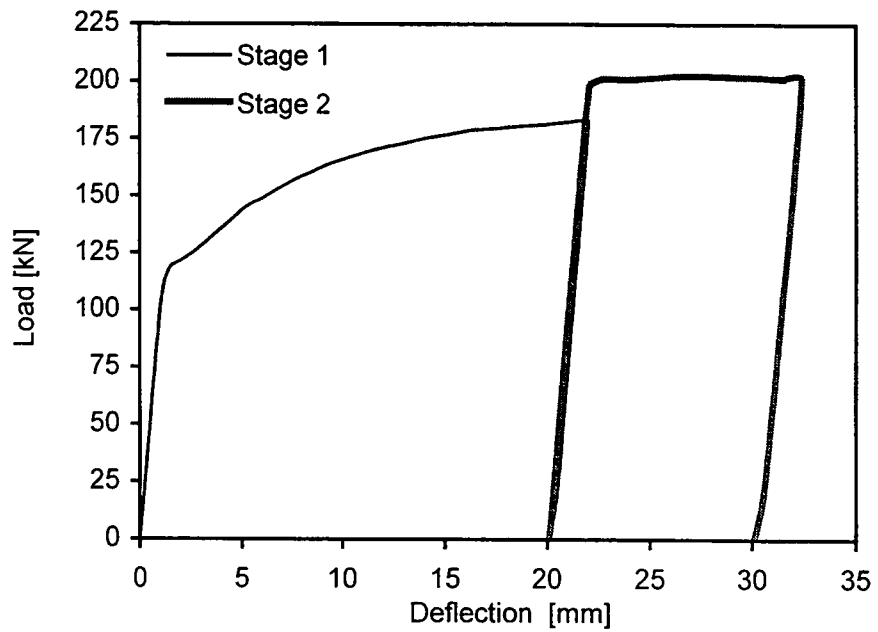


b) Defect with moderate re-entrant sector (S7)

Figure 8.3:
Illustration of load - deflection paths recorded during the ductile tearing of complex defects.

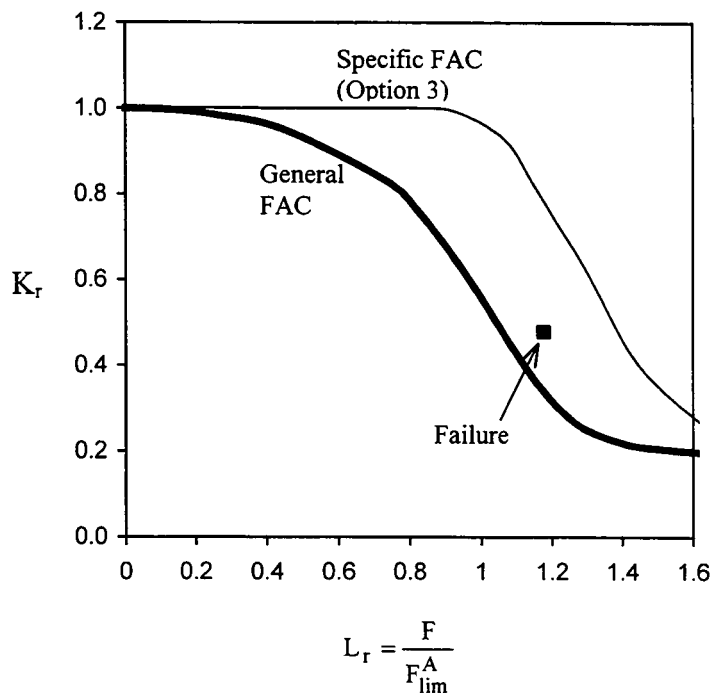


c) Defect with modest re-entrant sector (S14)



d) Bounding semi-elliptical defect (S9)

Figure 8.3 (cont):
Illustration of load - deflection paths recorded during the ductile tearing of complex defects.



General FAC : $K_r = (1 + 0.5L_r^2)^{-1/2} (0.3 + 0.7 \exp(-0.6L_r^6))$

Specific FAC : $K_r = \sqrt{\frac{J_{el}}{J_{total}}}$, obtained from the hardening analysis of the configuration

Failure : $K_r = \sqrt{\frac{J_{el}}{J_{Ic}}}$, where J_{Ic} is obtained experimentally for 50 D on 1T specimens in 3PB

Figure 8.4:

Assessment of a defect with a moderate re-entrant sector (specimen S7) using the failure assessment diagram of R6/4. All J values are taken for the re-entrant tip and load is normalised with the local limit load in the re-entrant sector: $F_{lim}^A = 0.88 \cdot F_{lim}^{global}$.

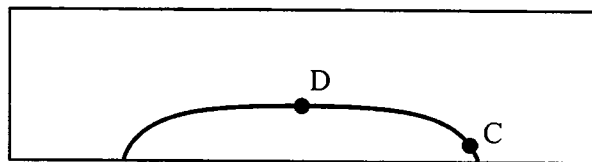
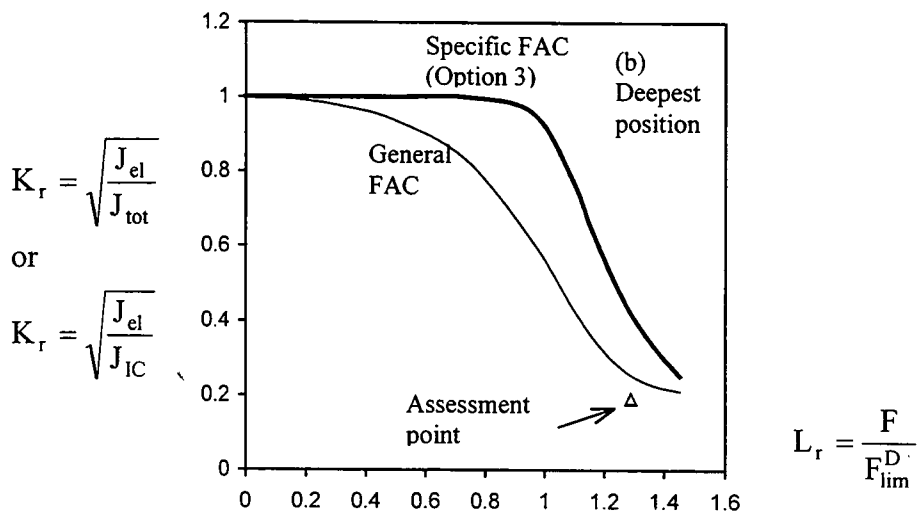
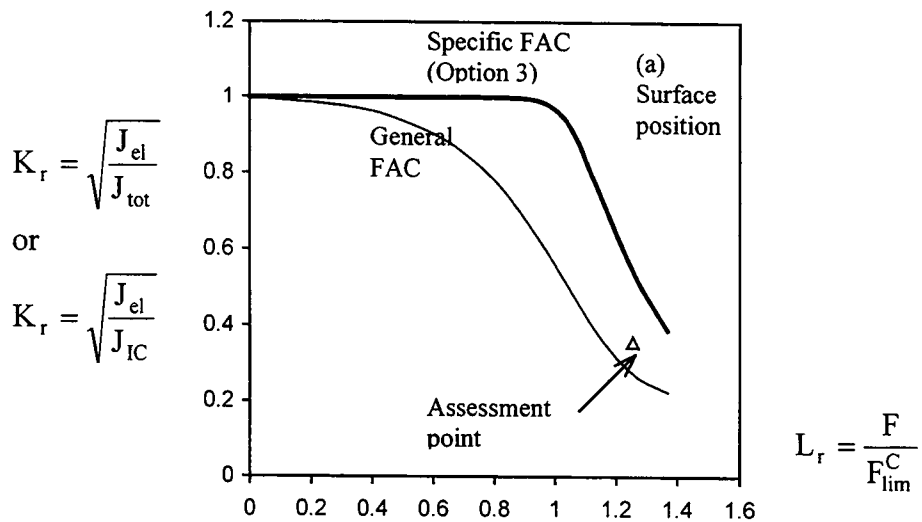


Figure 8.5: Assessment of a re-characterised defect (specimen S9) using the failure assessment diagram of R6, Rev 4. Assessment is performed for the near surface position (C) and deepest position (D). Load is normalised with the local limit loads.

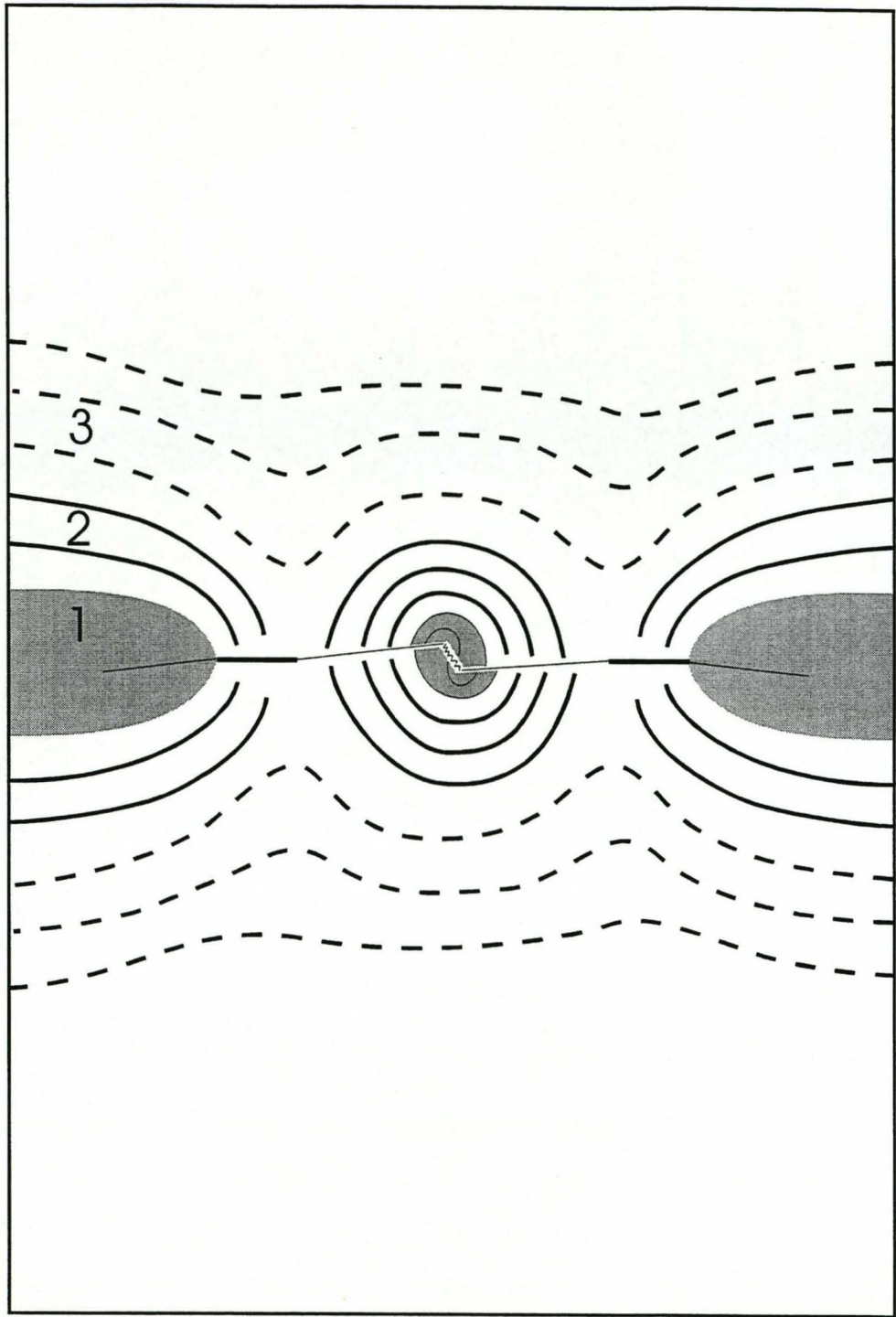
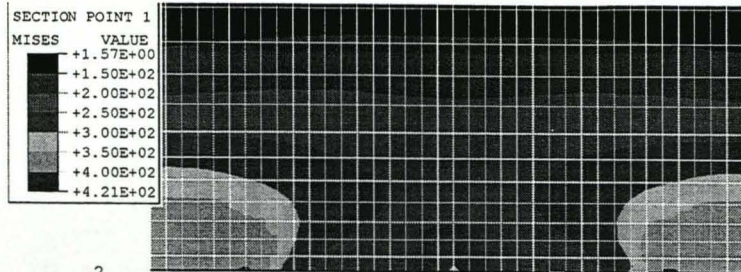
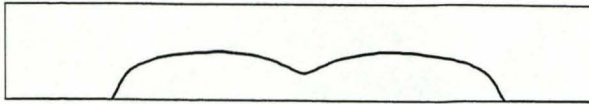
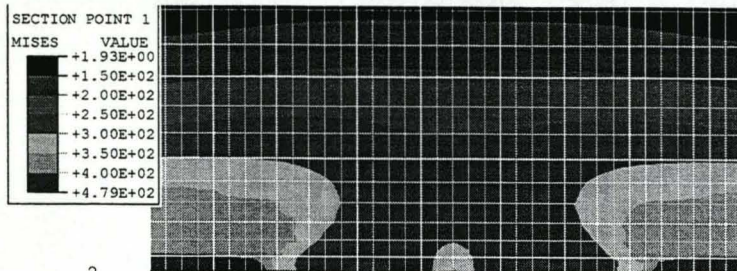


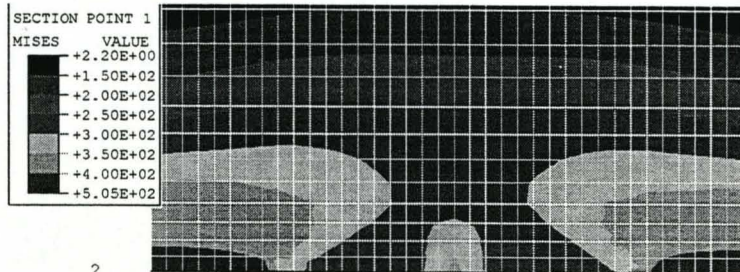
Figure 8.6:
Illustration of the plasticity patterns observed on the free surface during testing.



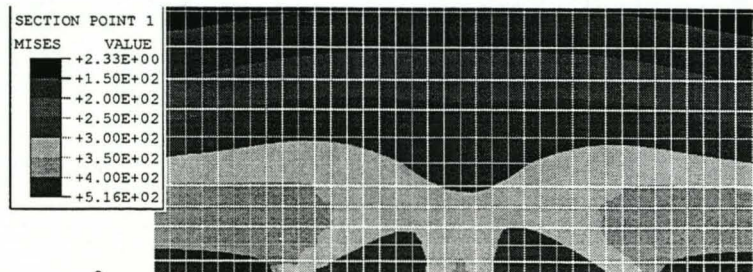
2
3 1 RESTART FILE = spec7-1-h STEP 1 INCREMENT 14
TIME COMPLETED IN THIS STEP 0.143 TOTAL ACCUMULATED TIME 0.143
ABAQUS VERSION: 5.8-14 DATE: 15-DEC-2000 TIME: 15:02:55



2
3 1 RESTART FILE = spec7-1-h STEP 1 INCREMENT 18
TIME COMPLETED IN THIS STEP 0.228 TOTAL ACCUMULATED TIME 0.228
ABAQUS VERSION: 5.8-14 DATE: 15-DEC-2000 TIME: 15:02:55



2
3 1 RESTART FILE = spec7-1-h STEP 1 INCREMENT 24
TIME COMPLETED IN THIS STEP 0.308 TOTAL ACCUMULATED TIME 0.308
ABAQUS VERSION: 5.8-14 DATE: 15-DEC-2000 TIME: 15:02:55



2
3 1 RESTART FILE = spec7-1-h STEP 1 INCREMENT 26
TIME COMPLETED IN THIS STEP 0.357 TOTAL ACCUMULATED TIME 0.357
ABAQUS VERSION: 5.8-14 DATE: 15-DEC-2000 TIME: 15:02:55

Figure 8.7:
The von Mises stress patterns, modelled for a defect with a moderate re-entrant sector (specimen S7).

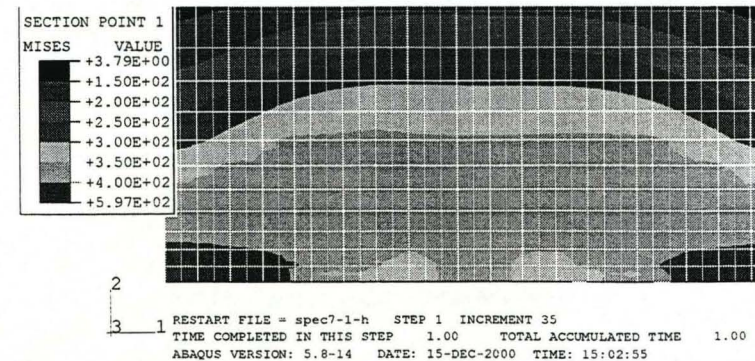
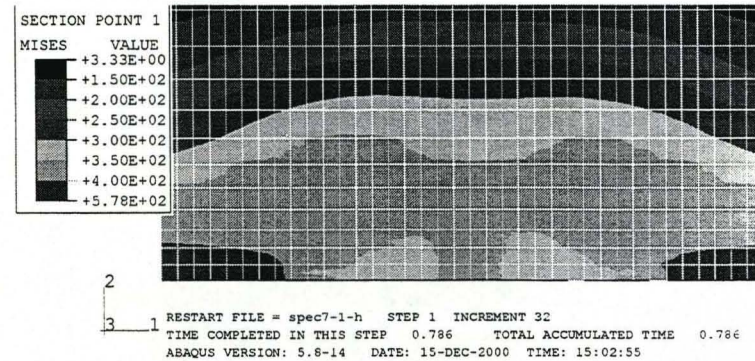
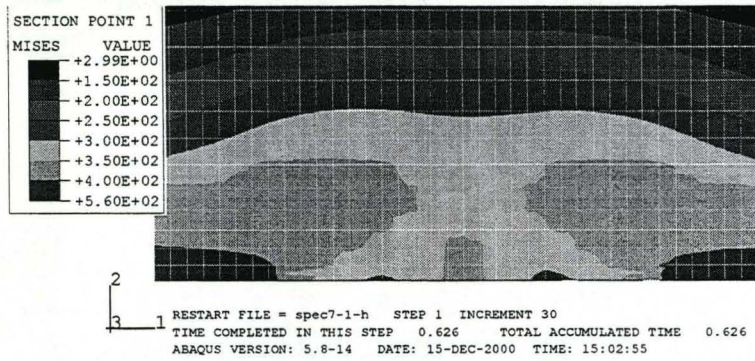
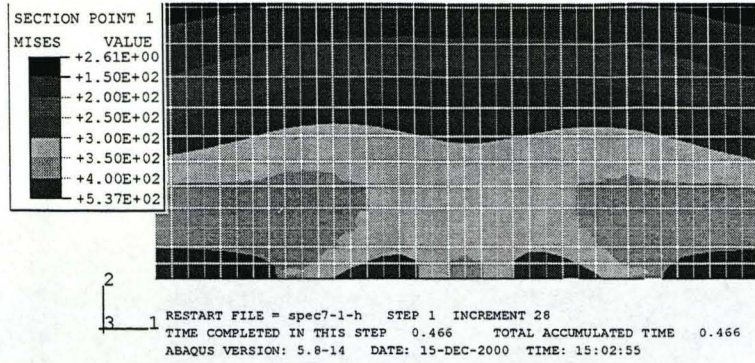
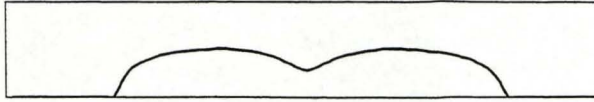


Figure 8.7 (cont):
 The von Mises stress patterns, modelled for a defect with a moderate re-entrant sector (specimen S7).

Chapter 9

BRITTLE FAILURE FROM COMPLEX DEFECTS

9.1 Introduction

The integrity of critical engineering structures is assured by considering realistic defects under severe operating conditions. This may involve cleavage failure when unstable crack propagation may occur under near elastic conditions. In general, defect assessment procedures try to avoid detailed numerical analyses and advocate simplified but conservative procedures, in which complex defects are idealised as a simple shapes in a process known as defect re-characterisation. Re-characterisation is usually applied to defects which extend by fatigue, as discussed in Chapter 5 of the current work. Chapters 6 and 7 have demonstrated that complex defects feature amplified values of the stress intensity factor and the J-integral in re-entrant sectors. This may compromise the conservatism of the re-characterisation procedure when failure occurs by cleavage.

The present work examines cleavage failures from complex and re-characterised defects on the lower shelf and in the ductile-brittle transition. Detailed analyses of an experimental programme are presented using deterministic and probabilistic approaches. The deterministic analysis compares the maximum stress intensity factor or the J-integral with a critical value obtained from tests on standard test geometries or from the Master curve (ASTM E1921 (1997)). The probabilistic analysis is based on weakest link statistics, developed for brittle failure from complex defects in Chapter 4. Both the deterministic and probabilistic approaches have been extended to include constraint effects.

9.2 Experimental details

9.2.1 Experimental procedure

Specimens with a developing family of separate, complex, and single bounding defects have been examined experimentally. The specimens were developed by fatigue as described in Chapter 7. Semi-elliptical cracks with shapes similar to those of re-characterised defects were also tested. A statistical experimental study of brittle failures has not been attempted: rather representative configurations have been tested and analysed, to address the effect of the enhanced stress intensity factor in re-entrant sectors on cleavage failure.

Tests were performed at -196°C to represent cleavage on the lower shelf and at -100°C to represent cleavage in the ductile-brittle transition. The test temperatures were obtained by cooling the specimens with liquid nitrogen: the temperature being measured at two surface positions with spot welded thermocouples. The fracture toughness on the lower shelf (-196°C) was measured on a set of five 25 mm thick three point bending specimens as $53 \pm 5 \text{ MPa}\sqrt{\text{m}}$. Master curve reference temperature T_0 was then determined based on this data to be -134°C . The fracture toughness in the ductile-brittle regime (-100°C) was estimated from the Master curve fit to be $165 \pm 23 \text{ MPa}\sqrt{\text{m}}$, which is close to the experimentally measured value of $190 \text{ MPa}\sqrt{\text{m}}$, reported by MacLennan (1996).

The temperature dependant yield stress was estimated from a relation suggested by Bennet and Sinclair (1966):

$$\sigma_o = 745.6 - 0.056 \cdot \Theta \cdot \ln\left(\frac{\zeta}{\sqrt{2\dot{\varepsilon}}}\right) \quad (9.1)$$

Here Θ is the temperature in Kelvin, ζ is a constant equal to 10^8 s^{-1} , $\dot{\varepsilon}$ is the strain rate, and σ_o is the yield stress in MPa. At room temperature this relation gives a yield stress of 350 MPa, at strain rate of $8.33 \cdot 10^{-6} \text{ s}^{-1}$, which is close to the experimentally measured 345 MPa for grade 50D steel. The yield stress in the cleavage regime was estimated to be 510 MPa at -100°C and 640 MPa at -196°C . The temperature dependence of Young's modulus is described with an expression suggested by Lidbury (1990) for ferritic steels:

$$E(\phi) = 210 - 0.054\phi \quad [\text{GPa}] \quad (9.2)$$

where ϕ is the temperature in $[^{\circ}\text{C}]$. At room temperature Young's modulus is 209 MPa and 220 MPa at -196°C .

9.2.2 Experimental results

The failure loads of the test geometries shown in Figure 9.1 are given in Table 9.1, in which the tests are denoted with the letter S followed by a number. The test configurations include defects with adjacent but separate defects (S3, S10), complex defects with re-entrant sectors (S2, S5, S6, S11, S12), as well as bounding semi-elliptical defects (S4, S13, S15, S16). The last series of defects arises from complete coalescence of initially separate defects, and result in a series of semi-elliptical defects with similar shapes to those, which would results from re-characterisation. In all cases the load-displacement records were linear until the final catastrophic failure, except for specimen S5 tested at -100°C which

showed gross plasticity prior to failure. Table 9.1 also gives the local and global limit loads calculated by elastic-perfectly-plastic line spring analysis for the crack profiles using the temperature dependent yield stress given by Eq. (9.1), and the dimensions of re-characterised defects.

On the lower shelf the failure loads for complex defects with re-entrant sectors were up to 23 per cent lower than those for the bounding defects. However, the reverse trend was observed in the ductile-brittle transition, where the highest failure load was noted for the complex defect and the lowest for a bounding defect. On the lower shelf the failure loads were only a small fraction of the global limit load, while in the ductile-brittle transition the failure loads were comparable with the global limit load.

9.3 Deterministic analysis

9.3.1 Deterministic procedure

In defect assessment procedures the applied stress intensity factor around the crack front is usually compared with the fracture toughness, K_{IC} , measured on standard test geometries with straight crack fronts. In real engineering structures, defects seldom have simple straight crack fronts and frequently have a varying depth. In such cases the crack driving force varies spatially with crack tip position. The resistance to crack advance may also vary spatially due to constraint, temperature or environmental effects, such as irradiation. Without loss of generality, the failure criterion can be defined as the ratio of an applied stress intensity factor, $K_{(v)}$, to a local resistance to crack extension, K_{mat} , both of which may be function of the crack tip position, v :

$$K_r = \frac{K_{(v)}}{K_{mat}} \quad (9.3)$$

In the present work the local fracture toughness, K_{mat} , is considered to be a function of constraint, as measured by T (Betegon and Hancock (1991)). The effect of constraint on cleavage is quantified by an expression suggested by Wallin (2000):

$$\begin{aligned} K_{mat} &= 20 + (K_{IC} - 20) \exp\left\{0.019\left(-\frac{T(v)}{10}\right)\right\} & \text{for } T < 0, \\ K_{mat} &= K_{IC} & \text{for } T > 0, \end{aligned} \quad (9.4)$$

Here K_{IC} is the plane strain fracture toughness of standard deep crack test specimen.

Configurations with pronounced re-entrant sectors (S6, S11 and S12) and the corresponding re-characterised configurations were analysed in detail using the line spring technique of Rice and Levy (1972) as extended by Parks and White (1982) to include elastic-plastic behaviour. A symmetric half of the experimental geometry was modelled at the experimental failure load. The material response was linear elastic to yield point and merged into a Ramberg-Osgood relation with the appropriate temperature dependant yield stress (510 MPa at -100°C and 640 MPa at -196°C). The strain hardening exponent was determined from uni-axial test data at room temperature to be 9, and assumed to be temperature independent.

The analysis determined the distribution of the stress intensity factor and the T-stress around the crack front. Although line spring analysis is a computationally efficient and effective numerical technique, it may not provide good estimates of crack tip parameters near the free surface. Consequently the stress intensity factor on the free surface was determined from fatigue crack growth data, using the beach marks spacing. Line spring data was used for most of the crack front. For segments close to the free surface the values of stress intensity factors were extrapolated by using a polynomial to match the value on the free surface with the value obtained from fatigue data. The same polynomial was used to determine the value of T-stress for the near-surface crack tips and the SIF and T-stress of the re-characterised defect. The values of crack tip parameters in pronounced re-entrant sectors should also be taken with caution, as they are estimated on the basis of shallow edge cracks.

9.3.2 Results of a deterministic analysis

The analyses of a complex geometries (S6, S11 and S12) and the related re-characterised geometries are summarised in Figure 9.2. Figure 9.2(a) shows the digitised complex and the re-characterised crack shapes and Figure 9.2(b) shows the corresponding stress intensity factors for both geometries. The stress intensity factors are normalised with the outer fibre stress in bending and the greatest crack depth (at position D, using the nomenclature defined in Chapter 5), and are plotted along the surface length of the defect. The T-stress is shown in Figure 9.2(c), normalised with the outer fibre stress in bending. As observed from fatigue and numerical studies, pronounced re-entrant sectors of complex defects exhibit amplified stress intensity factors and loss of in-plane crack tip constraint, as shown by a negative T-stress.

The ratio of the local stress intensity factor, $K_{(v)}$, to the local constraint matched toughness, K_{mat} , is given in Figures 9.2(d) and 9.2(e) for a complex and the re-characterised defect. Figure 9.2(d) shows data for tests (S11 and S12) at -196°C and Figure 9.2(e) for test (S6) at -100°C . The deterministic analysis shows that failure is strongly affected by in-plane constraint effects, which depend on the applied load. Failures (S11 and S12) on the lower shelf (-196°C) occurred at small fractions of the limit load, and as such gain little benefit from any increase in toughness due to constraint loss. Failure is determined by the stress intensity factor alone and the use of Eq. (9.4) per se may overestimate the constraint benefit. This is shown by the distinct peak in the ratio $K_{(v)}/K_{mat}$ in the re-entrant sector in Figure 9.2(d). However in the ductile-brittle transition, failure (S6) occurred close to the global limit load and benefited from a constraint enhanced toughness in re-entrant sectors, as shown Figure 9.2(e). The enhanced toughness, K_{mat} , associated with constraint loss counterbalances the amplified crack driving forces in the re-entrant sector. Although the complex defect is more detrimental than the re-characterised defect on the lower shelf when constraint effects are weak, the constraint enhanced toughness in the ductile-brittle transition recovers the conservatism of the re-characterisation procedure in this temperature range.

9.4 Probabilistic analysis

Probabilistic aspects of cleavage failure have been addressed using weakest link statistics for the complex and re-characterised geometries and results are shown in Figure 9.3. The relative failure probability of the complex and re-characterised defect depends on the applied load, which affects the constraint term in a non-linear manner. The relative failure probabilities quantify the level of conservatism in the re-characterisation procedure. For the procedure to be conservative the probability of failure of the complex defect must be less than the re-characterised defect.

At small fractions of the limit load, constraint effects are negligible and failure is essentially governed by the stress intensity factor. This is shown in Figure 9.3(b), in which geometrically similar complex defects (S11 and S12) with re-entrant sectors have a higher failure probability than the re-characterised defect at the failure load. In contrast, close to limit load (S6 at -100°C), shown in Figure 9.3(c), the complex defect has a lower failure probability due to the beneficial effects of constraint loss in the re-entrant sector. The probability analysis

thus confirms that the re-characterisation procedure is non-conservative on the lower shelf, but is conservative when the constraint effects are invoked in the ductile-brittle transition.

9.5 Failure assessment diagrams

9.5.1 Introduction

Cleavage failures on the lower shelf and in the ductile-brittle transition have been analysed using failure assessment diagrams (FADs) described in R6, revision 4 (2001), as shown in Figures 9.4 to 9.7. Failure assessment diagrams assess the proximity to failure by comparing the applied stress intensity factor, K , with a material property, K_{mat} , to cause crack extension. The general (Option 1) and material and geometry specific (Option 3) failure assessment curves (FAC) were constructed from the elastic and total J values, obtained from line spring analysis. The experimentally measured failure load was normalised with the local limit load, given in Table 9.1. For both, complex and re-characterised defects only the maximum stress intensity factor along the crack front is considered. This is normalised with a lower bound fracture toughness data, corresponding to 5% failure probability of the standard fracture mechanics test specimen. The maximum stress intensity factor is located in the re-entrant sector for a complex defect and near surface for the re-characterised defect. Initially in Section 9.5.2 the fracture toughness data from 25 mm thick three point bend specimens has been used without constraint or statistical size and shape corrections. The re-characterisation procedure is then applied to the defect and the analysis is performed for the same failure load. In section 9.5.3 assessment is repeated invoking the constraint enhanced fracture toughness and finally in Section 9.5.4 by incorporating the statistical size and shape effects.

9.5.2 General FAD

Figure 9.4 shows the analysis of a complex defect (S11) tested at -196°C , and Figure 9.5 the analysis of a complex defect (S6) tested at -100°C using the general failure assessment diagram. The analysis of the complex defects indicates a failure point above the general and specific failure assessment curves at both test temperatures. In contrast, the failure point of the re-characterised defect is inside the FAD at -196°C , while at -100°C it falls above both, the general and specific FACs. If the re-characterisation procedure was applied to the complex defect (S11) at -196°C , the procedure would predict a failure load obtained by extending the loading path from the origin through the failure point of the re-

characterised defect to the general failure assessment curve, as shown in Figure 9.4. Clearly the re-characterisation procedure overestimates the failure on the lower shelf and is non-conservative.

9.5.3 Constraint modified FAD

Constraint modified failure assessment diagrams defined in Chapter III.7 of R6 have been constructed for the cleavage failure of a complex defect (S6) at -100°C and its re-characterised form. The diagrams are presented in terms of the local limit loads, which are close to the global limit loads. The applied stress intensity factor was derived from the J-integral and is normalised in Figure 9.6(a) by a lower bound critical value, K_{IC} , obtained from the Master curve for 25 mm thick specimen at -100°C . Constraint effects were examined for the re-entrant sector using Eq. (9.3) and were introduced in the FAD by combining these expressions with the general failure assessment curve to produce a constraint modified failure assessment curves, as discussed by O'Dowd and Ainsworth (1995). In Figure 9.6(b) the applied K_I is normalised with a constraint enhanced fracture toughness, K_{mat} , retaining the general failure assessment curve as the relevant assessment curve, as discussed by MacLennan and Hancock (1995).

At -100°C the constraint enhanced toughness derived from constraint loss moves the failure outside the failure assessment curves, as shown in Figure 9.6. This confirms that the detrimental effects associated with enhanced stress intensity factors in re-entrant sectors can be offset by invoking constraint enhanced toughness.

9.5.4 FAD with statistical size corrections

Complex defects differ in the length and shape from the re-characterised defects and from the standard straight crack test specimens. Statistical size and shape corrections become relevant in assessments of such defects and are examined for a complex defect with a re-entrant sector and its re-characterised form. Weakest link arguments are employed for this purpose. For clarity the in-plane constraint effects are not combined with size and shape corrections. In practise these effects may be applied individually or combined, to give the most realistic integrity assessments. The maximum stress intensity factor is located in the re-entrant sector for the complex defect (as shown in Figure 9.2) and near surface for the re-characterised defect. The reference stress intensity factor is identified with the maximum value and the effective crack front lengths determined using Eq. (4.10) are

summarised in Table 9.2, for complex and re-characterised defects and standard 25mm thick edge cracked bend bars.

At -196°C the effective critical stress intensity factor for the complex defect is greater than that of the straight crack test specimen due to a decrease in the effective crack front length parameter, ξ , defined for the test geometry in Chapter 4. In contrast the effective critical stress intensity factor for the re-characterised defect is less than that of the straight edge crack geometry due to an increase in effective crack front length. The re-characterised defect has physical crack front length four times greater than the straight crack and statistically has lower resistance to crack propagation. The physical crack front length of the complex defect is also approximately 4 times longer than the straight cracked three point bend specimen, but the enhanced stress intensity factor in the short re-entrant sector decreases the effective crack front length. The competition between the physical crack front length and local amplification of stress intensity becomes less apparent at -100°C where more plasticity develops in the re-entrant sector.

An assessment of complex and re-characterised defects is shown in Figure 9.7 for tests at -196°C and -100°C , using the size and shape corrected lower bound fracture toughness. Both configurations fall on the general failure assessment curve at -196°C and outside the curve at -100°C . The failure of the re-characterised defect is correctly predicted at -196°C after employing size and shape corrections. Failure of the complex defect (S11) at -196°C coincides with the FAC due to an increase in K_{mat} resulting from size and shape corrections. To ensure conservatism, it is recommended that the lower of either, the size and shape corrected or the deterministically measured toughness, should be used in the assessment.

9.6 Failure initiation site

In analysing failures from complex defects it is relevant to identify the failure initiation site. The deterministic approach in this problem compares the crack driving force and the constraint enhanced toughness. A probabilistic approach considers the cumulative failure probability and the probability density function, to determine the most likely site from which failure initiates, as discussed in Chapter 4.

Both approaches show that configurations with pronounced re-entrant sectors fail from re-entrant sectors at a small fraction of the limit load. This is shown by the distinct peak in K_r , shown in Figure 9.2(d) for test (S11) and by the modal value of the probability density function in Figure 9.8(b). Close to the limit load (S6 at -100°C) constraint effects shift the origin of failure from the re-entrant sector towards deeper crack segments, as shown by the low values of K_r in the re-entrant sector, (Figure 9.2(e)) and by the change in pdf, (Figure 9.8(c)). The failure site is located close to the re-entrant sector, where there is a modest amplification of the stress intensity factor, but no loss of constraint to enhance the local toughness.

It is relevant to compare the probability of failure from the short re-entrant sector with the probability of failure from the remaining crack front (Figure 9.3). The contribution to the failure probability from the short re-entrant sector is approximately equal to the contribution from the rest of the crack front at -196°C . Although the re-entrant sector is the single most likely failure initiation site, failure has nearly the same probability of initiating from the rest of the crack front due to its greater length. At -100°C constraint effects clearly favour initiation outside the re-entrant sector (Figure 9.3(c)).

Whether the complex defect fails from the re-entrant sector or the deeper parts of the crack is determined by the constraint loss in the re-entrant sector. The argument may be developed to quantify the constraint loss necessary to make the re-characterised defect more detrimental than the complex defect. The deeper crack front locations are fully constrained and failure is governed by the general failure assessment curve. Failure from shallow re-entrant sectors is governed by modified failure assessment curves, which depend on the constraint sensitivity of the fracture toughness (MacLennan and Hancock (1995), Ainsworth and O'Dowd (1995)). In order to compare failure at two sites using a single failure assessment diagram, sites are compared at the same load. This can be achieved by using the stress intensity factor of the re-characterised defect, K_D , as the loading parameter in the ordinate of the FAD. In the re-entrant sector the enhanced stress intensity causes failure at the ratio K_D/K_{mat} less than unity. However constraint enhanced toughness in the re-entrant sector elevates the FAC above the general curve as the limit load is approached. The modified and general FAC intersect, as shown in Figure 9.9, defining the transition of failure from the re-entrant sector to the deeper sites of a complex defect or to the re-characterised defect. The constraint effects in the re-entrant sector may

be estimated using Eq. (9.3), through the amplification of the stress intensity factor in the re-entrant sector, which may be assessed from a detailed finite element analysis or from the approximate procedure described Section 9.8. The failure assessment diagram shown in Figure 9.9 thus expresses the lack of conservatism of the re-characterisation procedure at $L_r < 0.67$, while conservatism is recovered due to the loss of constraint at $L_r > 0.67$.

9.7 Discussion

On the lower shelf the complex defects exhibited lower failure loads than the predicted failure loads for the re-characterised defects. However at -100°C the failure loads of the complex defects were greater than the re-characterised defects due to constraint enhanced toughness. For failures at loads very much less than the global limit load (S11 and S12) on the lower shelf, the loss of crack tip constraint is negligible and insufficient to compensate for the amplified crack driving forces which develop in pronounced re-entrant sectors. In this case failure is governed by the applied crack driving force alone and failure initiates from the re-entrant sector. On the lower shelf, the re-characterisation procedure has been demonstrated to be non-conservative as exemplified by the FAD in Figure 9.4. Conservatism is recovered when constraint effects can be invoked to compensate for the amplified crack driving forces at failures close to the limit load, shown by test (S6) at -100°C and by the FAD in Figure 9.6. Conservatism of re-characterisation procedure can also be recovered by employing statistical size and shape correction to fracture toughness (Figure 9.7(a)). Both corrections may be applied concurrently.

Statistical size and shape corrections to the fracture toughness measured on standard test specimens should be employed in assessing cleavage failure. Size and shape effects can be quantified through an effective crack front length parameter, ξ , which allows the fracture resistance to be size and shape corrected. Corrections may result either in increase or decrease in the toughness, K_{mat} , as measured on standard straight crack specimens. Physically this depends on whether the resistance to crack propagation is governed by large sections of the crack front or small sections with high stress intensity factors. It is recommended that a decrease in K_{mat} associated with an increase in the effective crack length parameter, ξ , should always be used. However an increase in K_{mat} due to a decrease in the effective length parameter, ξ , should be taken with caution. The recommendation is

that size and shape corrections should only be used if they results in decrease in K_{mat} , to ensure a conservative assessment procedures.

Re-characterisation rules for adjacent but separate defects applied to cleavage failure must allow sufficient safety margins to account for the statistical nature of cleavage. In the present work a test was performed on a configuration containing two separate co-planar defects, with separation of adjacent crack tips equal to the crack depth, (specimen S10 in Figure 9.1) tested at -196°C . A small difference between the measured failure load of 103 kN and the failure load for the hypothetical re-characterised defect of 100 kN was noted (Table 9.1). In configuration (S10) the crack tips had not met, and according to BS 7910 (1999) and R6/4 (2001) the defects should be treated separately and independently. Figure 9.10 shows assessment of the configuration as individual defects and as a re-characterised defect in the failure assessment diagram using both, measured and statistical size and shape corrected fracture toughness. In both cases the defect configuration falls close to failure assessment curve. In cases where the separation of the crack tips is greater than depth of the larger defect, $s > d$, small interaction effects are present and assessment of individual defects is more realistic. As the crack tips approach, $s < d$, interaction becomes significant and must be included in the assessment. The re-characterisation procedures are non-conservative for $s < d$ and it is recommended that the procedures should only be applied for defects which are more widely separated ($s > d$).

Re-characterisation procedures, such as those given in BS 7910 and R6/4, are conservative for both, fatigue and ductile tearing, since in both failure modes the crack advances from the re-entrant sector towards the re-characterised shape. Cleavage failures close to the limit load benefit from constraint loss which counteract the amplified crack driving forces in re-entrant sectors and cause re-characterised defects to be more detrimental than the original complex defects. In such cases re-characterisation is conservative, as shown by the deterministic and a probabilistic analyses. The re-characterisation procedure for defects with re-entrant sectors which fail in cleavage is non-conservative for failures at small fractions of the limit loads. At such low loads there is minute benefit from constraint loss, but statistical size and shape corrections may recover the conservatism of the assessment.

It is proposed that two levels of assessment (for constraint and size effects) should be used to ensure safety margin against cleavage for complex defects with re-entrant sectors:

- 1) Assess the constraint effects in the re-entrant sector of a complex defect for the design load. If the constraint effects are sufficient to counteract the amplified values of crack driving force in the re-entrant sector ($K_{(T)}$ using Eq. (9.4) $\geq K$ in the re-entrant sector), the re-characterisation procedure (BS 7910) can be conservatively applied.
- 2a) Estimate statistical size and shape corrections for the complex defect and correct the K_{mat} value. Use new K_{mat} only when it is less than K_{IC} .
- 2b) The statistical size and shape effects can also be invoked for the re-characterised defect. Typically the corrected K_{mat} of the semi-elliptical defect shall be less than K_{IC} measured on standard specimens, giving smaller but more realistic margins.

Re-characterisation of separate interacting defects must take account of interaction effects which elevate the stress intensity factors of adjacent crack tips. The present data indicates that the re-characterisation procedure is conservatively applied to such defects only when the tip separation is greater than the depth of the deeper defect.

9.8 Approximate amplification factors

Simple geometry based amplification factors for the stress intensity factor and constraint effects in the re-entrant sector of complex defects are defined. The crack with a re-entrant sector is re-characterised and the stress intensity factor determined for the deepest position of the re-characterised defect. The amplification of K in the re-entrant sector is determined by multiplying this solution by an amplification factor, χ_K . The crack with a re-entrant sector is characterised with a length on the free surface, A , the depth of the re-entrant sector, B , and the width of the re-entrant sector, C , as shown in Figure 9.11. The tip of the re-entrant sector is approximated by a 60° circular arc to define the local curvature in the re-entrant sector, $\rho=1/r$. The amplification factor χ_K is:

$$\chi_K = \left[\rho \frac{A \cdot B}{C} \right]^5 \quad \text{for } r \ll A$$

$$\chi_K = \left[\rho \frac{A \cdot B}{C} \right]^{-5} \quad \text{for } r \approx A \text{ and } B > 1 \text{ unit}$$
(9.5)

from fitting the exponent of Eq. (9.5) with the detailed line spring data. The evaluation of the approximate procedure with the detailed line spring calculations gives conservative assessments when the exponent ζ is 1/10.

A similar procedure is defined for assessing amplification for constraint effects in the re-entrant sector, by using T-stress. The amplification factor for the T-stress is defined using the above described approximation to the complex geometry and is used in conjunction with the T-stress solutions of standard edge crack bar in bending (SENB) [20]. The exponent, ζ , of 1/8 gives a good agreement with the detailed line spring computations.

$$\frac{T}{\sigma_o} \Big|_{\text{re-entrant}} = \chi_T \cdot \frac{T}{\sigma_o} \Big|_{\text{SENB}} \quad (9.6)$$

$$\chi_T = \left[\rho \frac{A \cdot B}{C} \right]^\zeta$$

9.9 Main conclusions to defect re-characterisation

- Redistribution of local forces and moments along the crack front length results in amplified values of crack tip parameters in less advanced crack segments of complex crack fronts. The location of maximum values also depends on the crack front perturbation, with greater perturbations shifting the critical location towards shallower crack segments.
- Re-entrant sectors of co-planar crack fronts feature amplified values of K and J and a loss of constraint, measured by T. A step in the re-entrant sector reduces amplified values of K and T in proportional manner.
- Fatigue crack growth rates are significantly higher in the re-entrant sector compared to the rest of the crack front. Re-characterisation procedures that recombine interacting defects into a semi-elliptical defect when the adjacent crack tips touch are conservative, with the period of fatigue growth during the formation of the re-entrant sector representing a typical safety margin.
- Ductile tearing initiates from the re-entrant sector and crack develops into a bounding defect in a similar manner to fatigue. Re-characterisation rules developed for fatigue can be conservatively applied to ductile tearing from complex defects.

- In cleavage re-characterisation procedure is only conservative when constraint effects can be invoked to counteract amplified K or J in the re-entrant sector. At small fractions of limit load the re-characterisation procedure is not conservative. Conservatism can be recovered in the assessment when statistical size and shape corrections are considered.

Complex defect with a re-entrant sector						Re-characterised defect		
Test	Crack depth in re-entrant sector	Failure load	Local limit load	Global limit load	Yield stress	Crack depth at D	Free surface length	Mapped failure load
	a_A [mm]	F_f [kN]	$F_{lim,local}$ [kN]	$F_{lim,global}$ [kN]	σ_o [MPa]	a_D [mm]	$2c$ [mm]	$F_{re-charact.}$ [kN]
Lower shelf regime (-196°C)								
Separate defects before coalescence								
S10	/	103	/	289	640	9.3	82.2	100
Defect with a pronounced re-entrant sector								
S11	2.0	75	220	256	640	11.2	92	92
S12	1.0	85	216	251	640	11.4	96	89
Semi-elliptical defect								
S13*	/	83*	190	217	640	13.2	105	/
S15	/	98	206	229	640	13.7	86.9	/
S16	/	90	203	225	640	13.5	87	/
Ductile-brittle regime (-100°C)								
Individual defect before coalescence (overlapped)								
S3	/	145	/	170	510	14.2	110	112
Defect with a modest re-entrant sector								
S2	12.1	120	125	132	510	15.4	121.6	100
S5**	11.8	192**	150	162	510	13.9	112.9	109
Defect with a pronounced re-entrant sector								
S6	2.2	210	143	197	510	11.5	94	127
Semi-elliptical defect								
S4*	/	93*	102	108	510	17.2	127.4	/

* Test defect exceeded the size of recommended re-characterised defect

** Gross plasticity preceded cleavage failure

Table 9.1:

Results of experimental cleavage tests showing characterising crack dimensions, failure and limit loads of real defect and the failure load for the re-characterised defect, obtained from statistical procedure (in Chapter 4).

	-100°C			-196°C		
	Complex	Re-charac- terised	Straight crack	Complex	Re-charac- terised	Straight crack
Physical crack length [mm]	109.9	100.9	25.0	105.2	98.3	25.0
Effective crack length, ξ [mm]	26.8	63.8	25.0	9.3	71.1	25.0
\bar{K}_{mat} [MPa \sqrt{m}]	167.8	130.5	165.0	67.8	40.8	53.0
σ [MPa \sqrt{m}]	22.6	18.2	23.0	6.4	3.9	5.0

Table 9.2:

The physical and effective crack front lengths are given with the size and shape corrected mean values of fracture toughness, \bar{K}_{mat} , and the standard deviation, σ .

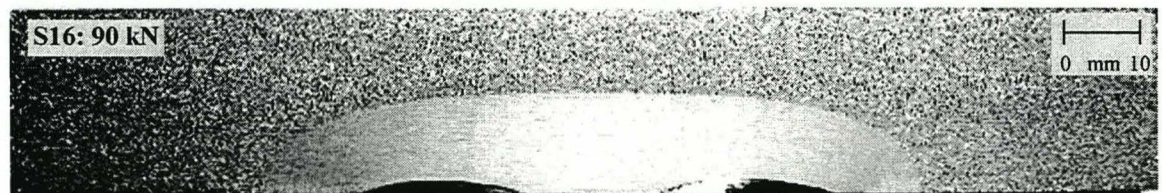
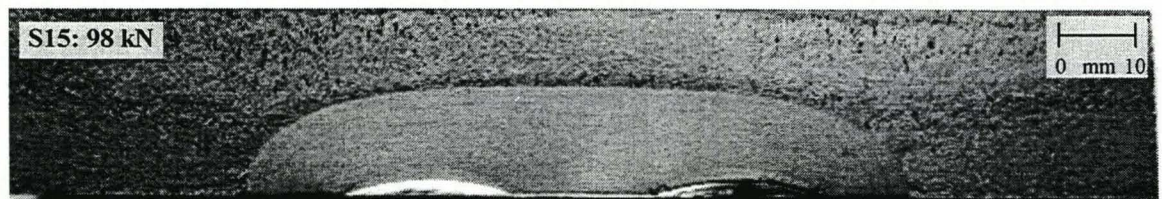
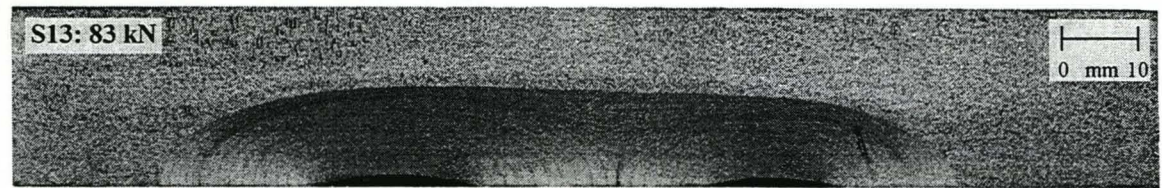
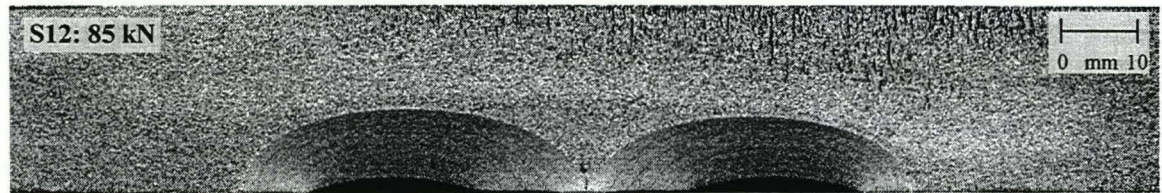
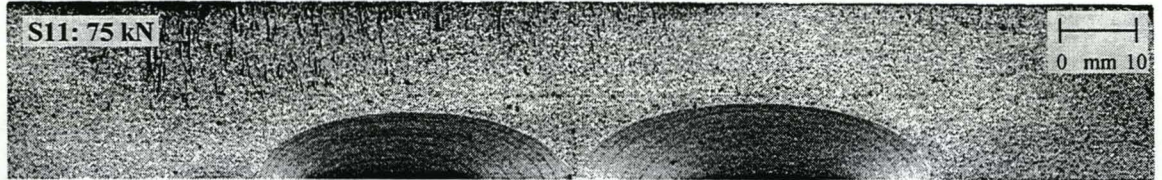
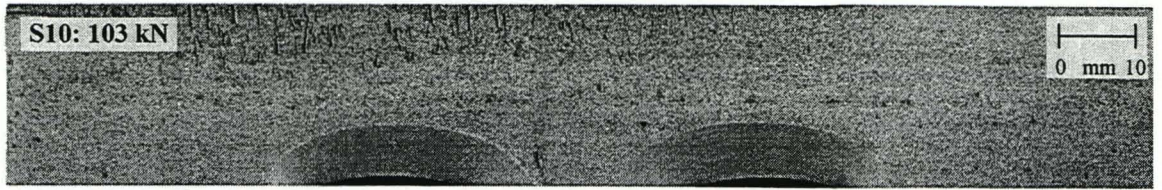


Figure 9.1:
Photographs of tested crack configurations, with the recorded failure loads to cleavage at -196°C .

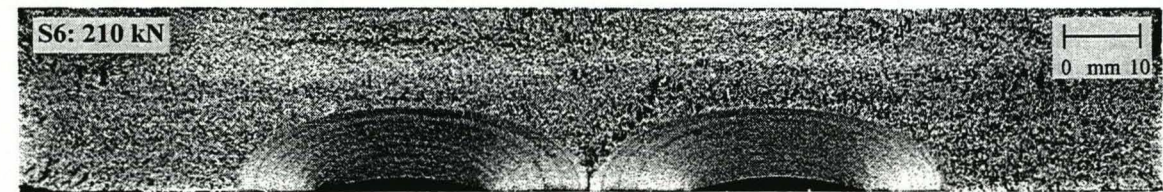
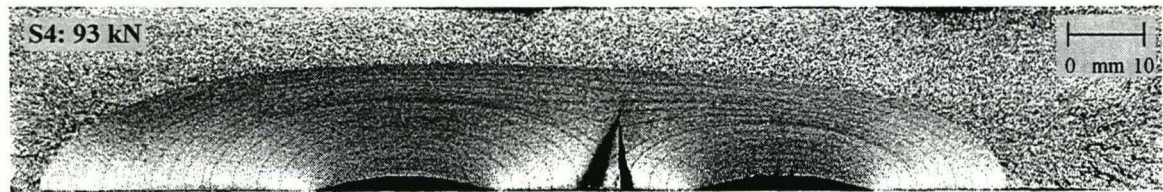
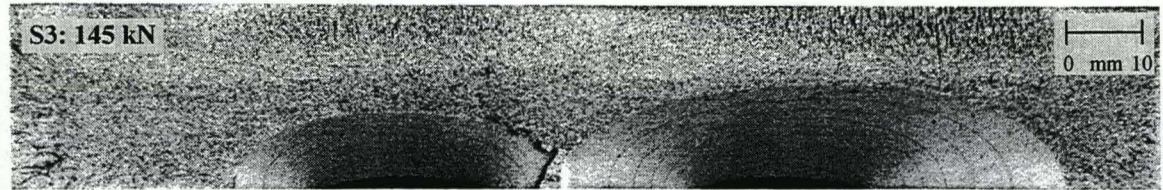
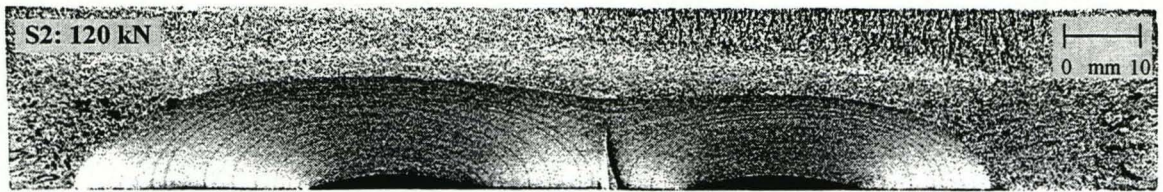


Figure 9.1 (cont):
Photographs of tested crack configurations with the recorded failure loads to cleavage at -100°C .

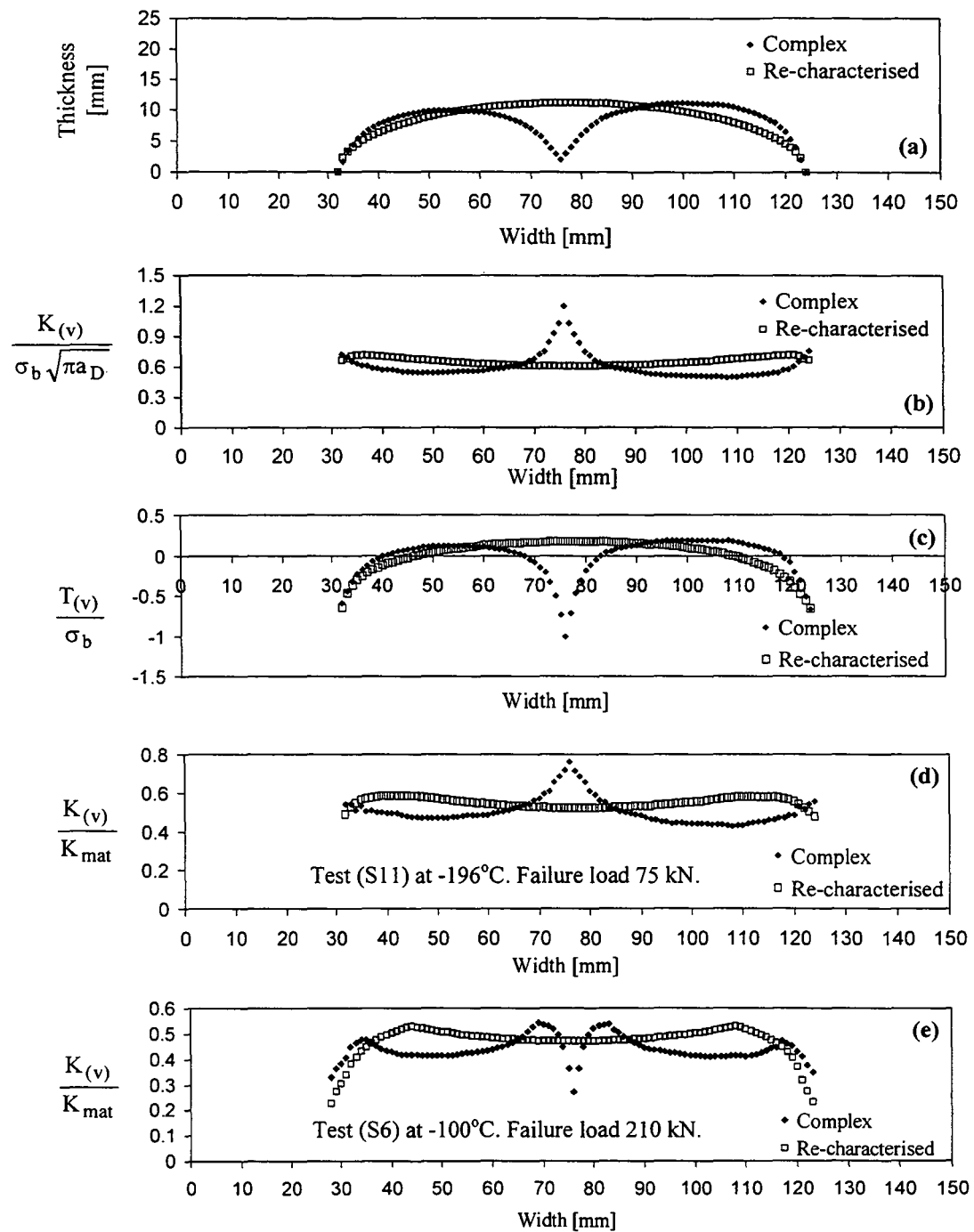


Figure 9.2:

Deterministic assessment of complex defects (S11 at -196°C and S6 at -100°C) and re-characterised defects: (a) crack profiles, (b) normalised stress intensity factors and (c) normalised T-stress. The failure criterion K_r is shown in Figure 9.2(d) for the complex defect (S11) and in Figure 9.2(e) for the complex defect (S6).

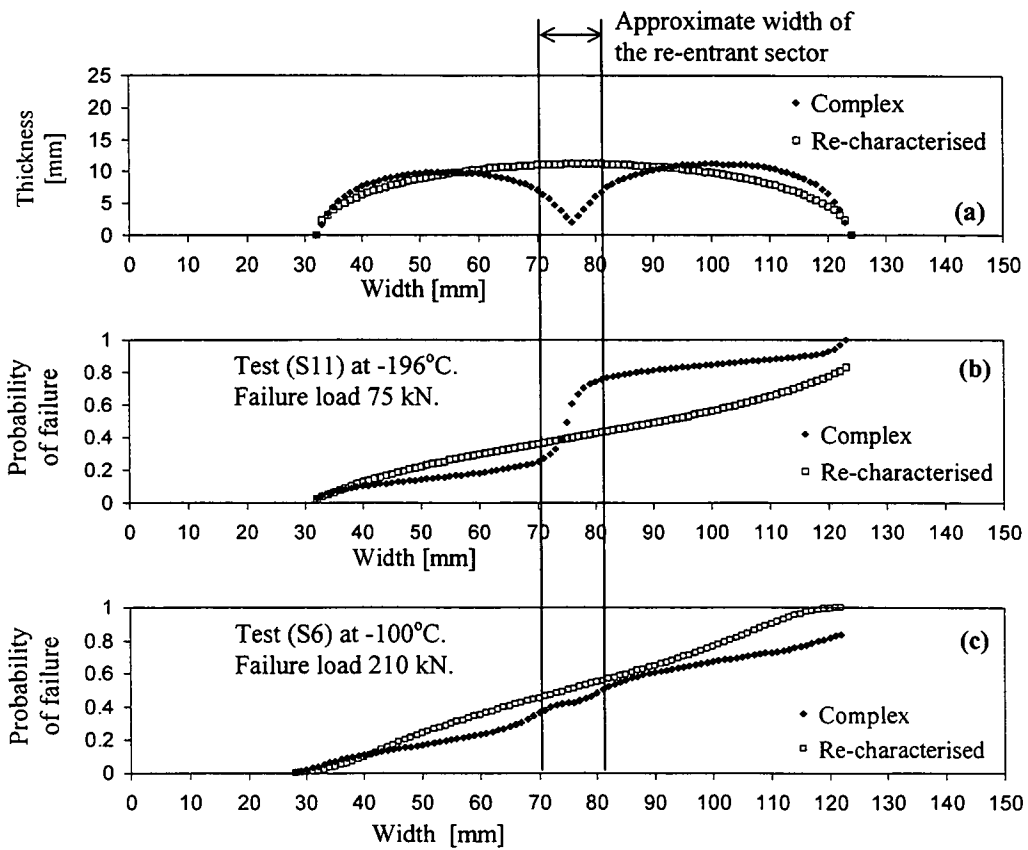


Figure 9.3.
 Probability of failure of complex defects (S11) at -196°C and (S6) at -100°C and re-characterised defects, at measured failure load on complex defects and shown as a function of position along the crack front.

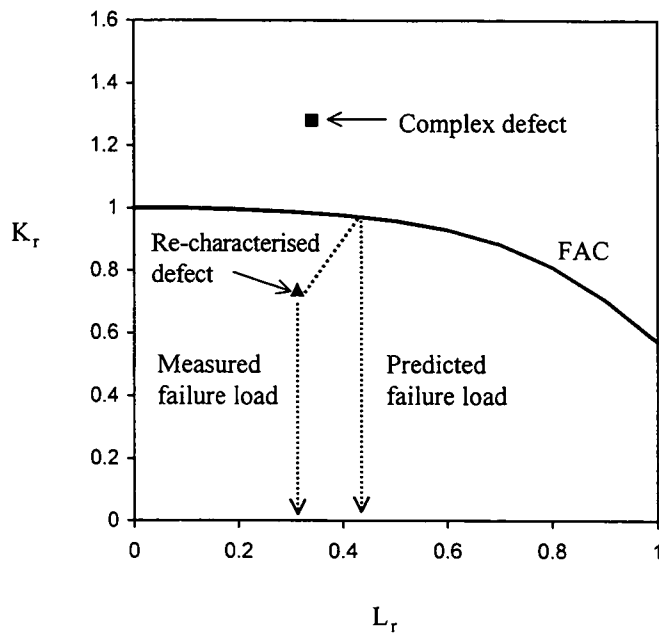


Figure 9.4:

Assessment of the complex defect (S11) tested at -196°C and the re-characterised defect using general failure assessment diagram. The stress intensity factor is normalised with lower bound fracture toughness, measured on 25mm thick specimens, without applying constraint or statistical size corrections. The load is normalised with the local limit load. The re-characterisation procedure overestimates failure load and is non-conservative.

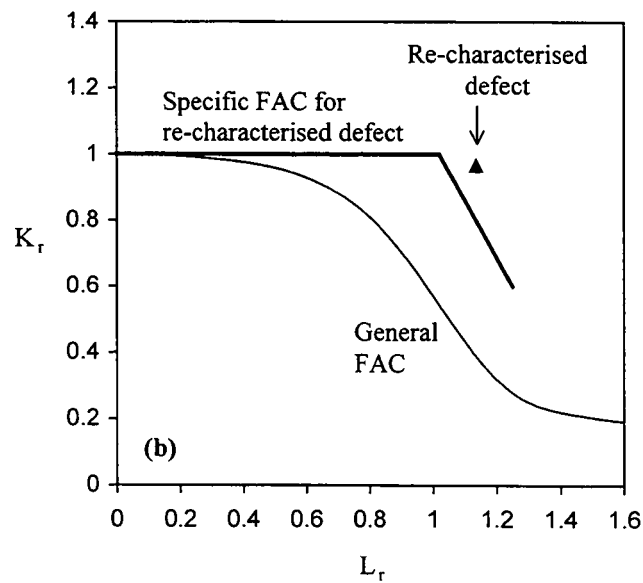
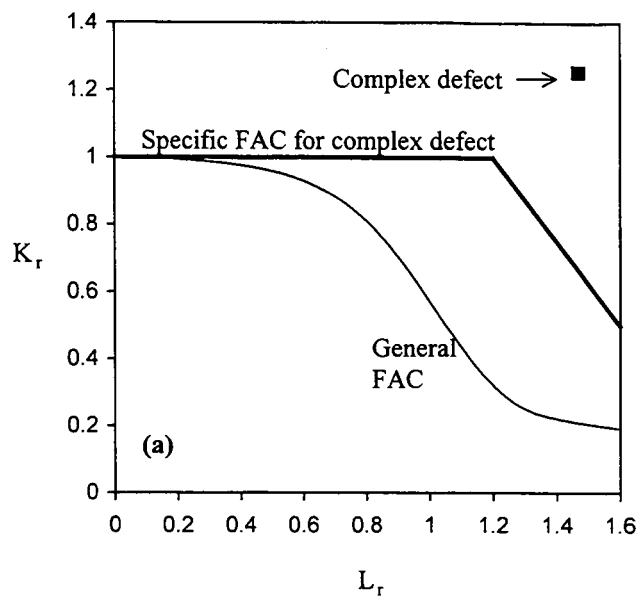


Figure 9.5:

Assessment of the complex defect (S6) tested at -100°C is shown in Figure 9.5(a) and the re-characterised defect in Figure 9.5(b) using general failure assessment diagram. The stress intensity factor, K_I , is normalised with lower bound fracture toughness using the Master Curve at -100°C , without constraint or statistical size corrections. The load is normalised with the local limit load.

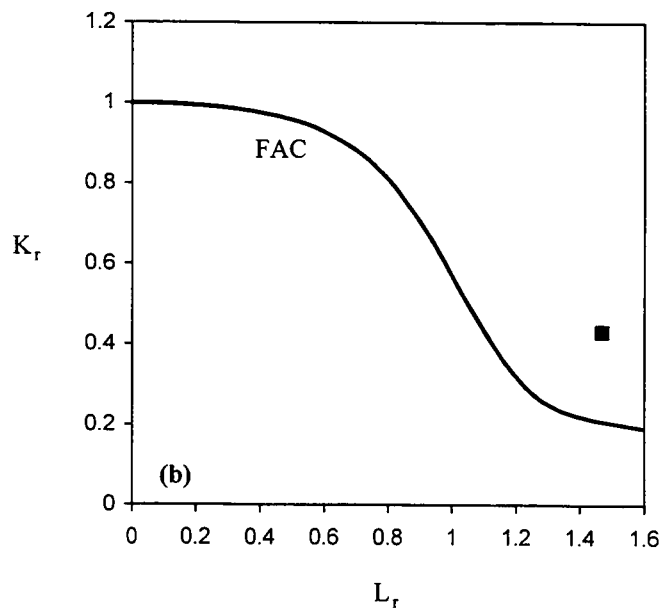
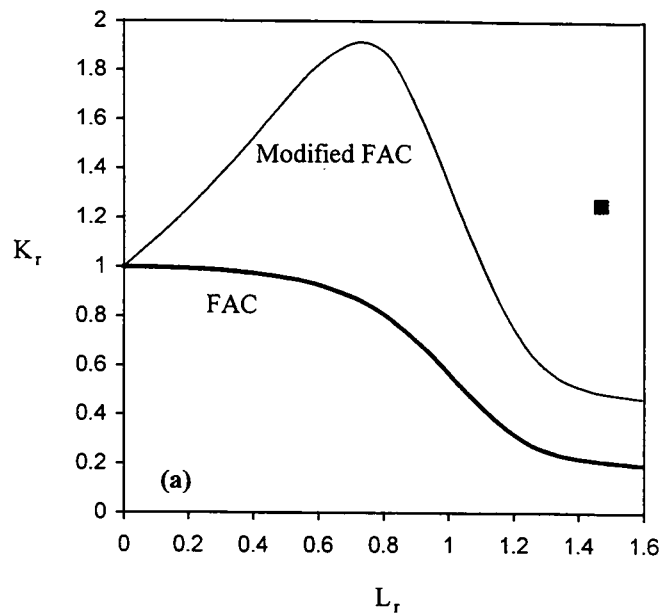


Figure 9.6.

Assessment of a complex tested (S6) at -100°C using constraint modified failure assessment diagram. In Figure 9.6(a) the modified failure assessment curve is constructed for the re-entrant sector of a complex defect, using Eq. (9.3). The stress intensity factor K_J is normalised with lower bound toughness from Master curve at -100°C . In Figure 9.6(b) the stress intensity factor K_J is normalised with constraint enhanced lower bound toughness. The load is normalised with the local limit load.

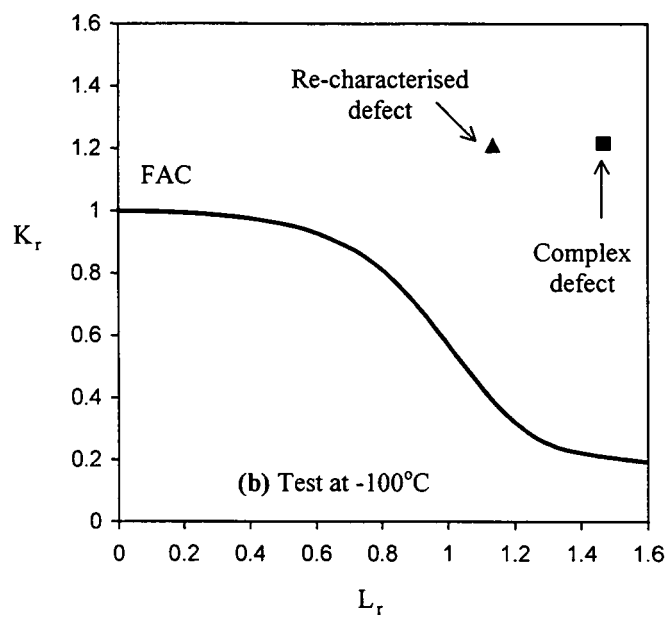
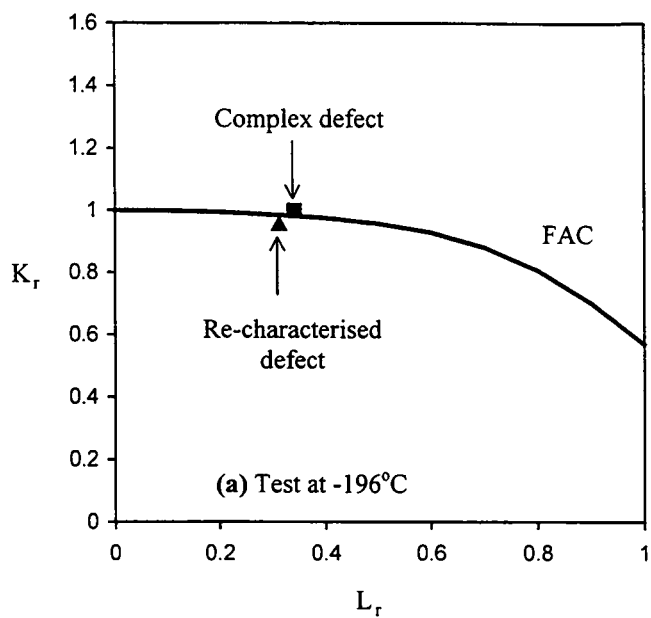


Figure 9.7:

Assessment of complex defects (S11 at -196°C and S6 at -100°C) and re-characterised defects using failure assessment diagram including statistical size and shape corrections. The stress intensity factor is normalised with lower bound size and shape corrected toughness, while measured failure load is normalised with the local limit load.

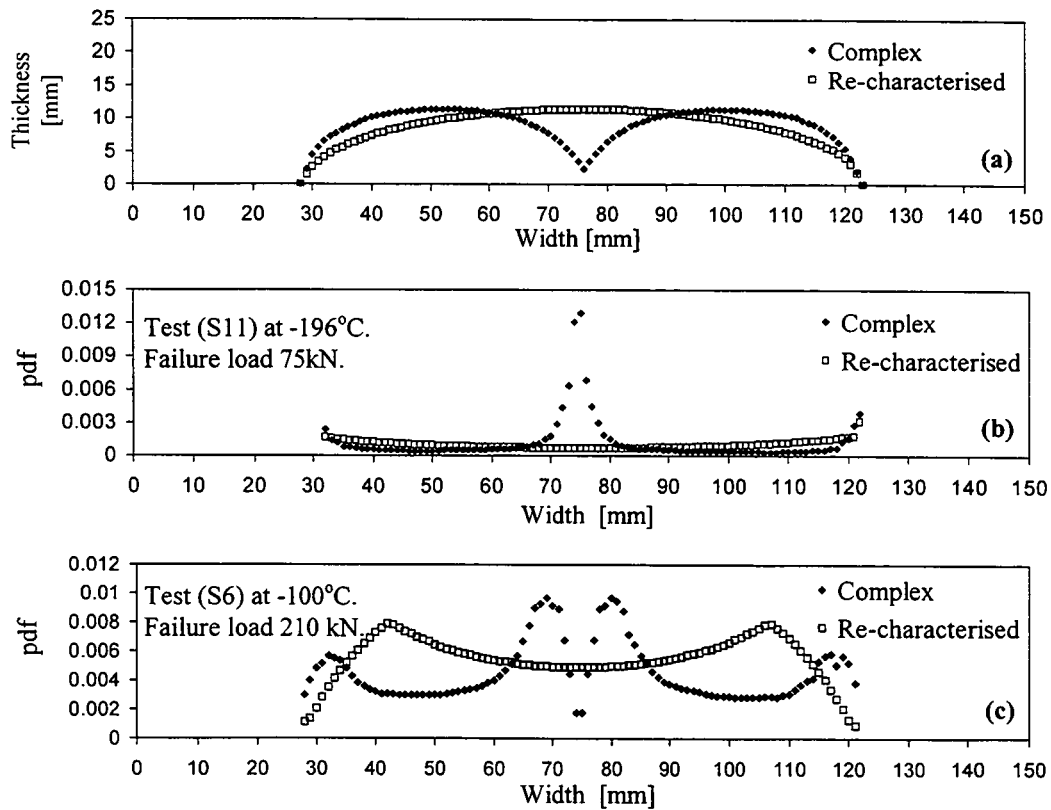


Figure 9.8:
Probability density function (pdf) for complex defects (S11) at -196°C and (S6) at -100°C and the re-characterised defects, at measured failure loads on complex defects.

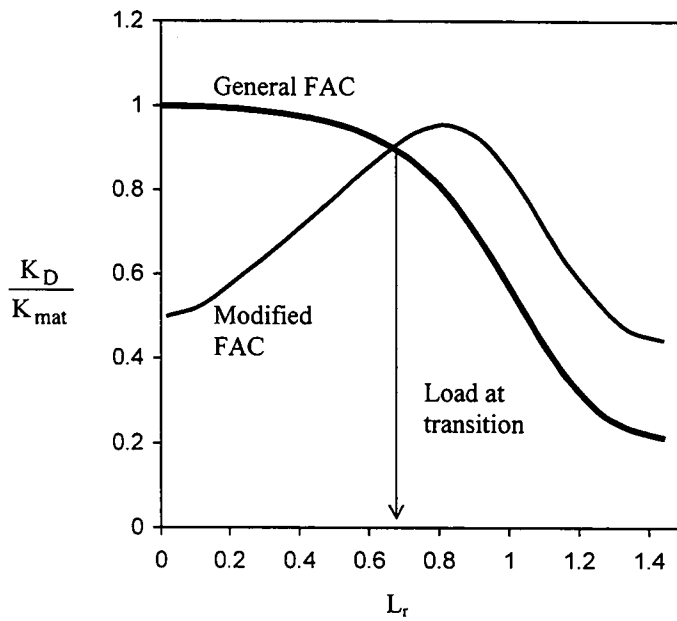


Figure 9.9:
 The transition of failure from a complex defect to a re-characterised defect determined using a modified failure assessment diagram. The transition is governed by the constraint effects in the re-entrant sectors.

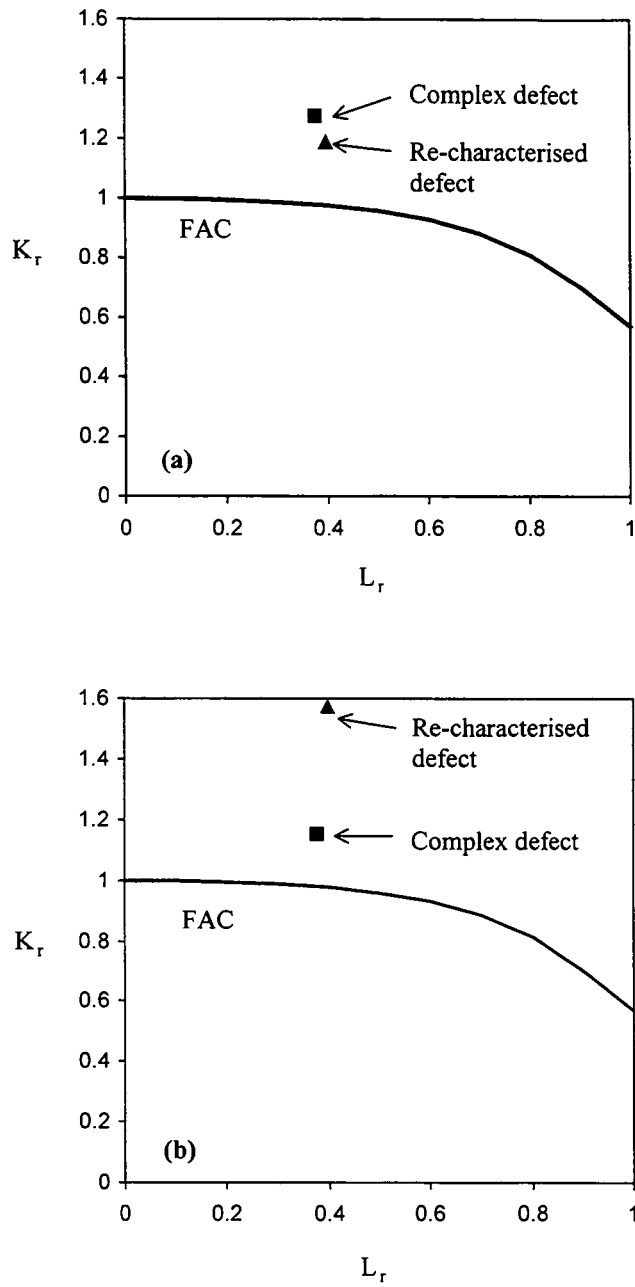


Figure 9.10:

Assessment of a complex defect (S10) tested at -196°C and the re-characterised defect using failure assessment diagram. In (a) the applied stress intensity factor, K_r , is normalised with lower bound toughness from standard 25 mm thick specimen and in (b) with size and shape corrected toughness. The load is normalised with the local limit load.

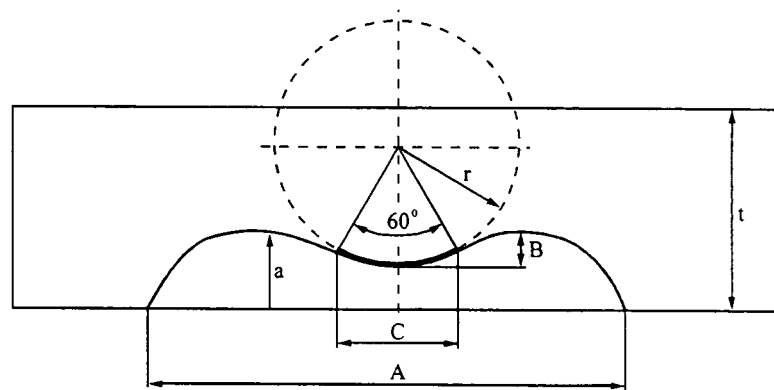


Figure 9.11:
The definition of a complex geometry used to define the approximate amplification factors.

Chapter 10

MICROMECHANICAL MODELLING OF CLEAVAGE FRACTURE IN FERRITIC STEELS

Studies of the micromechanics of cleavage fracture try to relate fracture toughness with the microscopic failure processes in the plastic zone ahead of a crack. Cleavage fracture is a low energy event, in which an unstable crack propagates along low index crystallographic planes (typically $\{100\}$ or $\{110\}$ planes) with minimum plastic distortion of the surrounding matrix. Cleavage fracture in ferritic steel is argued to occur in three stages (Bowen *et al* (1987), Wang *et al* (2002)): local plastic flow induces a dislocation pile-up which causes crack nucleation in a second phase particle or at a phase boundary. Particles such as carbides or non-metallic inclusions in the size range 0.003 - 3 μm cleave and create a ferrite grain-size microcrack of the order of 10-150 μm (Bowen *et al* 1987). The final stage is the propagation of the ferrite grain-size microcrack through the adjacent grains under stress field of the macroscopic crack.

10.1 The Ritchie-Knott-Rice cleavage model

If cleavage fracture is determined by a maximum tensile stress criterion alone, the stresses near the crack tip indicated by asymptotic solutions, such as that of the HRR field (Hutchinson (1968), Rice and Rosengren (1968)) exceed the fracture stress at vanishingly small loads, which contradicts the observed behaviour. Clearly the critical tensile stress criteria has to be supplemented with a length scale over which fracture processes are operative as suggested by Ritchie *et al* (1973). The Ritchie-Knott-Rice model uses the HRR solution to describe the near tip stress field although other solutions that describe the nature of the near tip field (such as log-spiral for blunted cracks) could also be used. Ritchie *et al* (1973) gives:

$$\frac{\sigma_{yy}}{\sigma_0} = \left(\frac{J}{\alpha r \sigma_0 e_n I_n} \right)^{\frac{1}{n+1}} \tilde{\sigma}(n, \theta) \quad (10.1)$$

where (r, θ) are cylindrical co-ordinates centered at the crack tip, σ_0 is the yield stress, I_n and $\tilde{\sigma}$ tabulated functions of angle and strain hardening exponent and J is the J-integral. The RKR model postulates cleavage when the local stresses exceed local fracture stress, σ_f over a characteristic microstructural distance, r_c . The RKR model contains two material

properties, which can in theory be measured from an independent mechanical test such a notched bar, and by inspection of the micro-structure. This is however more difficult than it seems, and in practise the lower shelf toughness is often fitted to the RKR model using the two material properties as curve fitting data.

The RKR model was developed to model the temperature dependence of fracture toughness by using the temperature dependence of the yield stress in ferritic steels, while assuming temperature independence of σ_f and r_c . The model is illustrated in Figure 10.1 by a failure from a sharp crack at two temperatures, T_1 and T_2 ($T_1 < T_2$). The associated yield stresses are σ_{o1} and σ_{o2} and the local fracture stress is σ_f . Let at T_1 hoop stress σ_{yy}/σ_{o1} suffice to initiate failure at a distance r_c . At a higher temperature T_2 the associated yield stress is lower and the critical hoop stress σ_{yy}/σ_{o2} is achieved before the distance r_c . In this case the stresses are insufficient at a distance r_c to initiate failure and a higher stress intensity has to be applied at T_2 to elevate the hoop stress and produce σ_{yy}/σ_{o2} at a distance r_c , in theory allowing modelling of temperature dependence of fracture toughness. The model has been applied to ferritic steel to predict macroscopic K_c values from independently measured data. Ritchie *et al* (1979) demonstrated good agreement with the model over a limited temperature range on to the lower shelf. However in the ductile-brittle transition the model underpredicts measured fracture toughness as demonstrated by Ritchie *et al* (1979).

10.1.1 Local fracture stress

The local event is usually described by the local fracture stress, σ_f , required for the microcrack propagation. Values of σ_f were initially determined from slip line theory for a blunt notch in plane strain (Ritchie *et al* (1973)) and identified with the opening stress on the elastic-plastic interface:

$$\sigma_f = 2k[1 + \frac{1}{2}\pi - \frac{1}{2}\phi], \quad (10.2)$$

Here k is yield stress in shear and notch opening angle, ϕ , has to be greater than 6.4° , in order to describe plasticity at the root of the notch using slip line theory. However catastrophic low temperature failures usually originate from sharp fatigue pre-cracks having much smaller crack flank opening angles, and the failure need not initiate at the elastic-plastic interface. Better estimations of the local fracture stress have been determined from tests on notched bend bars combined with the finite element model of the test

geometry. The local fracture stress was then identified with the maximum local opening stress in the asymptotic stress field ahead of the crack (Ritchie *et al* 1979). Later Wall *et al* (1994), Ortner and Hipsley (1996) and more recently Wang *et al* (2002) have identified failure initiation sites in carbon-manganese and chromium-molybdenum steels. Combining finite element analyses of the test geometry with the microscopic examination of the fracture initiation showed that the local fracture stress generally does not coincide with the maximum opening stress, but occurs between the crack tip and the site of the maximum stress, as shown in Figure 10.2 after Wall *et al* (1994). Wang *et al* (2002) also showed that the local fracture stress is typically 0.8~0.9 times the maximum opening stress ahead of the blunt notch. Significantly, Bowen *et al* (1987) and Hipsley group (1994, 1996) observed that the local fracture stress is largely independent of temperature and strain rate for many microstructures when cleavage is slip induced. Bowen *et al* (1987) examined local fracture stress for a range of microstructures in A533B steel, and observed a dependence on the microstructure. A typical value of the local fracture stress for a perlitic/bainitic microstructure was found to be around 1800 MPa, as also observed by Ritchie *et al* (1979) on the same steel. For martensitic microstructures the local fracture stress is nearly double at an approximate value of 3400 MPa, as illustrated in Figure 10.3. The results of Bowen *et al* (1987) suggest a relation between the yield stress and the local fracture stress, as shown in Figure 10.4. On the lower shelf the ratio σ_f/σ_0 is of the order 2 and increases to 2.5 in the ductile-brittle transition as the yield stress decreases.

10.1.2 The microstructural distance

The microstructural distance, r_c , was originally related to the diameter of the ferrite grains (Ritchie *et al* (1973, 1979)). Curry and Knott (1978) postulated that fracture initiates from the largest observable carbide following weakest link principle, and the characteristic distance should be identified with the spacing of the largest carbides. Subsequent investigations of brittle fracture (Curry and Knott (1979), Curry (1980), Wallin (1984), Ortner and Hipsley (1996)), emphasised statistical nature of the cleavage and interpreted the microstructural distance in terms of a volume of highly stressed material with probability of finding a microcrack nucleus to initiate failure. More recently Wang *et al* (2002b) argued that the fracture event can only initiate in the zone, where plastic strain is sufficiently large to initiate microcracks, high stress triaxialities favour particle microcracking compared to debonding of the particle-matrix interface and the opening

stresses in the zone exceed the local fracture stress, as shown schematically in Figure 10.5 from Wang *et al* (2002b). This leads to a range of characteristic distances, r_{cmin} to r_{cmax} over which the cleavage can initiate, consistent with the argument of Ritchie *et al* (1973, 1979) that characteristic distance is not fixed. Similar trends are observed for A533B data of Bowen *et al* (1987) shown in Figure 10.6. However a distance of 2-4 ferrite grain diameters is widely accepted as a good approximation for ferritic steels.

10.2 Statistical treatment of cleavage fracture

A model proposed by Wallin *et al* (1984) extends the Curry and Knott (1979) hypothesis by arguing that crack nucleation occurs at a brittle particle on the plane of maximum tensile stress, σ_1 . A cracked particle of radius r_0 will initiate fracture in a surrounding ferritic matrix or grain boundary provided that the Griffiths criterion is satisfied:

$$r_0 = \frac{\pi E(\gamma_s + w_p)}{2(1 - \nu^2)\sigma_1^2} \quad (10.3)$$

where γ_s is a ferrite surface energy, w_p is the plastic work of fracture, ν is Poisson's ratio and E is Young's modulus. To describe the statistical nature of cleavage, the plane in front of the crack is divided into discrete segments of length dX . If the probability of finding a carbide of radius $\geq r_0$ is known ($p(r > r_0)$) then the probability of fracture initiating at a distance X from the crack tip is given by:

$$P_{fx} = 1 - \prod_{X=0}^X [1 - p(r \geq r_0)]^{N, B, dX, F} \quad (10.4)$$

where N is the number of particles per unit area, B is the thickness of the specimen and F is the fraction of particles participating in the fracture process. To develop such models further, there is a necessity to establish the particle size distribution. Ortner and Hipsley (1996) examined failure initiation sites in a A533B steel and give a probability distribution of a particle size r , of the form:

$$p(r) = \frac{c^{(a-1)}}{(a-1)!} \left(\frac{r}{\bar{r}}\right)^a \exp\left[\frac{-c}{(r/\bar{r})^a}\right] \quad (10.5)$$

where c and a are constants and \bar{r} is the mean particle radius. The expression was fitted to the experimental observations and used to calculate the failure probability at the initiation sites at a given applied K from measured carbide size distribution, following arguments developed by Wallin (1984). Ortner and Hipsley (1996) observed that Wallin's (1984)

statistical approach also tends to underpredict the toughness in the ductile-brittle transition, but confirmed a specimen size dependent toughness as originally argued by Wallin (1984).

10.3 The Weibull stress model

Within the context of statistical fracture mechanics (Freudenthal (1968), Beremin (1983)), brittle failure can be modelled using a weakest link statistics. The macroscopic implications of weakest link arguments have been discussed in Chapter 4 where a failure probability was related to the crack front size and shape and remote geometry effects. Here the weakest link statistics are considered in a micromechanics sense, by interpreting crack tip fields through the Weibull stress defined by Beremin (1983). The probability of failure can be described by a two parameter Weibull distribution function:

$$P = 1 - \exp\left(-\left(\frac{\sigma_w}{\sigma_u}\right)^m\right) \quad (10.6)$$

where σ_u is a scaling parameter with the dimensions of stress and m is the dimensionless Weibull modulus. The nature of the near tip stress field is described with the Weibull stress, σ_w , defined as the weighted maximum principal stress (Beremin (1983)):

$$\sigma_w^m = \frac{1}{V_0} \int_V \sigma_1^m dV \quad (10.7)$$

where the process zone volume is taken over the zone where principal stress exceeds a defined multiple of the yield stress:

$$\sigma_1 \geq \lambda \sigma_0 \quad (\lambda \geq 1) \quad (10.8)$$

The process zone is typically in the region of $\lambda=2$ to $\lambda=3$ (Ritchie *et al* (1979), Bowen *et al* (1987), Lei *et al* (1998)), where local stresses are of the order of the fracture stress, although plastic zone has also been used as a limiting case (Gao and Dodds (2001)). The volume V_0 in Eq. (10.8) scales the Weibull stress and must be large enough to contain randomly distributed microcracks, yet small enough to eliminate stress gradient effects. Beremin argues that V_0 is of the order of 2^3 grains for a nuclear pressure vessel steel, establishing connections with the RKR, although in general V_0 can be regarded as a material constant.

The volume dependence of the Weibull stress is largely governed by the Weibull modulus, m . In the limit of a purely deterministic material, $m \rightarrow \infty$, failure is essentially dictated by

the maximum stress and is uninfluenced by the volume effects. For ferritic steels undergoing cleavage the m values are around 22 (Beremin (1983)). For sharp cracks stress field can be derived analytically and Weibull stress calculated without recourse to detailed finite element modelling. These expressions are summarised from Lei *et al* (1998).

10.3.1 Elastic material

An analytic solution to the principal stress in the asymptotic small-strain near-tip stress field was given by Hertzberg (1989):

$$\sigma_1 = \frac{K}{\sqrt{2\pi r}} (1 + \sin \frac{1}{2}\theta) \cos \frac{1}{2}\theta \quad (10.9)$$

for an elastic material and (r, θ) are polar co-ordinates centred at the crack tip. This gives Weibull stress of the form (Lei *et al* (1998)):

$$\sigma_w^m = \frac{C}{4-m} \frac{B}{V_0} \frac{K^4}{\sigma_0^{4-m}} \lambda^{m-4} \quad (10.10)$$

where the constant C is:

$$C = \frac{1}{\pi^2} \int_0^\pi [(1 + \sin \frac{1}{2}\theta) \cos \frac{1}{2}\theta]^4 d\theta = 0.456 \quad (10.11)$$

Although the elastic material does not have defined a yield stress, it is used here to define the integration domain (Eq. (10.8)) and to maintain consistency with definition for an elastic-plastic material. From Eq. (10.10) it follows that Weibull stress is finite when $m < 4$ for an elastic material. Implicitly the Weibull stress becomes dependant on the size of the process zone due to major contribution from the material close to process zone boundary. For $m \geq 4$ Weibull stress tends to infinity and the probability of failure becomes unity regardless of the applied load, which is not physically meaningful and restricts the application of Eq. (10.10).

10.3.2 Elastic-plastic material

The principal stress near the tip of the sharp crack in a power-law hardening material, such as that given by Ramberg-Osgood relation, is characterised with the HRR small-strain asymptotic solution:

$$\frac{\sigma_1}{\sigma_0} = \left(\frac{J}{\alpha r \sigma_0 e_0 I_n} \right)^{\frac{1}{n+1}} \tilde{\sigma}(\theta, n), \quad (10.12)$$

allowing the Weibull stress to be derived in the form (Lei *et al* (1998)):

$$\sigma_w^m = \frac{\hat{\Phi}(n)}{1 - \frac{m}{2(n+1)}} \frac{B}{V_o} \frac{J^2}{\alpha^2 e_o^2 \sigma_o^{2-m}} \lambda^{m-2(n+1)} \quad (10.13)$$

Where non-dimensional function $\hat{\Phi}(n)$ strongly depends on the hardening exponent n :

$$\hat{\Phi}(n) = \frac{1}{I_n^2} \int_0^\pi [\tilde{\sigma}(n, \theta)]^{2(n+1)} d\theta \quad (10.14)$$

with values 764.54 for $\hat{\Phi}(5)$ and 3.467×10^7 for $\hat{\Phi}(10)$.

The asymptotic nature of the stresses near the crack tip pose a difficulty in determining a meaningful Weibull stress values close to the sharp crack tip, especially for large Weibull moduli (~ 20), where in real structures crack blunting effects dominate. For Weibull moduli in excess of $2(n+1)$ the sharp crack solutions are no longer suitable. These limitations can be avoided by determining Weibull stress in the process zone ahead of the blunt crack tip using finite element modelling.

10.4 Probabilistic toughness scaling model

Self-similar crack tip fields that develop under contained yielding can be characterised by load-independent parameter that scales with the Weibull stress, as suggested by Gao and Dodds (2001):

$$\sigma_w^m = J^2 \frac{B\sigma_o^{m-2}}{V_o} \int_0^{2\pi\bar{\rho}} \int_0^{\bar{\rho}} f^m \rho d\rho d\theta = J^2 \frac{B\sigma_o^{m-2}}{V_o} \Omega \quad (10.15)$$

where ρ is a nondimensional radius of the process zone ($\rho = r/(J/\sigma_o)$), f is the function of material and mechanistic parameters that describe the crack tip field and scale the principal stress with the yield stress and Ω is the load independent Weibull stress parameter. This expression allows the development of a toughness scaling model between two geometries, for example geometries that differ in respect of the in-plane constraint, although the principle can be generalised to mixed-mode loading and graded materials. Requiring that Weibull stresses are the same in both geometries at failure, the ratio of fracture toughnesses becomes (Gao and Dodds (2001)):

$$\frac{J_{T \neq 0}}{J_{T=0}} = \sqrt{\frac{\Omega_{T=0}}{\Omega_{T \neq 0}}} \quad (10.16)$$

As the Weibull stress scales with the J and yield stress, and yield stress is temperature dependant, the procedure can be extended to temperature shifts by mapping self similar crack tip fields through the Weibull stress, as discussed in Chapter 12 and applied to experimental data in Chapter 13. The deterministic toughness scaling models are presented in Chapter 12 with extension to temperature shifts.

10.5 Crack trajectory

Crack propagation directions are important for cracks propagating in stress fields of graded materials or subject to mixed-mode loading. In a deterministic approach (Erdogan and Sih (1963), Williams and Ewing (1972)) the direction of maximum hoop stress is argued to determine the crack trajectory, under the assumption that crack orientates itself in such a manner to propagate in a local mode I condition. As the crack initiation angle essentially depends on the angular location of the local failure site (cracked carbide) ahead of the stationary crack, the analysis should consider stresses in the entire volume surrounding the crack tip. For such purpose the Weibull stress becomes convenient to determine the crack initiation angle, where the full planar stress field ahead of the crack is analysed. By examining the strength distribution function (probability density function) Becker *et al* (2002) observed a bi-modal nature for homogeneous mode I fields, suggesting that single most likely crack initiation directions are diametrically opposed at angles of around 40° and crack propagates on alternately inclined $\{110\}$ planes. Macroscopically mode I crack in a homogeneous material propagates straight ahead. Becker *et al* (2002) suggested to describe the macroscopic crack initiation direction by a spatial average of the strength distribution function over the process zone volume. Their approach is also followed here. First the region surrounding the crack tip is divided in large number of angular wedges extending from the tip and the failure probability is determined for each wedge, using Eq. (10.6). The probability density function is then defined for each wedge as:

$$P_{(\theta)} = \frac{P_{f,(\theta)}}{\Delta\theta} \quad (10.17)$$

Spatial average of individual probability density functions over the process zone volume gives the average angle of crack initiation as:

$$\bar{\theta} = \frac{\int_{-\pi}^{\pi} \theta \cdot p_{(\theta)} \cdot d\theta}{\int_{-\pi}^{\pi} p_{(\theta)} \cdot d\theta} \quad (10.18)$$

In Figure 10.7 the crack initiation angle is shown against the remote mixity angle for a homogeneous mixed mode configuration, taken from Becker *et al* (2002). The crack angles obtained by the above procedures are within the bounds of a deterministic procedures, using directions of maximum hoop stress, maximum energy release rate and maximum principal stress.

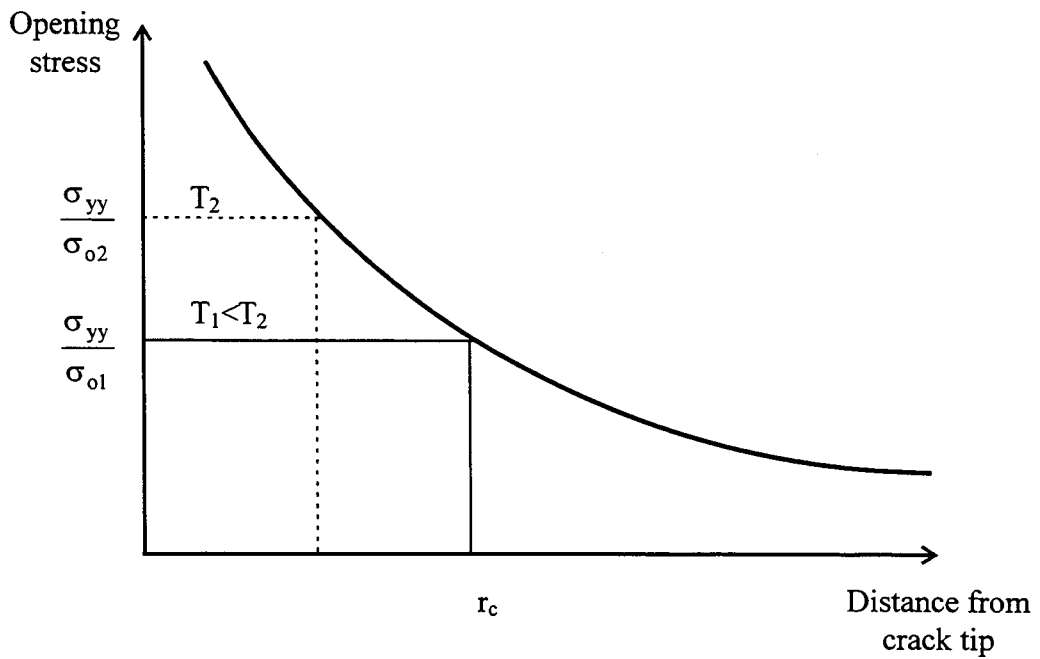


Figure 10.1:
Illustration of the Ritchie-Knott-Rice (1973) cleavage model at two temperatures.

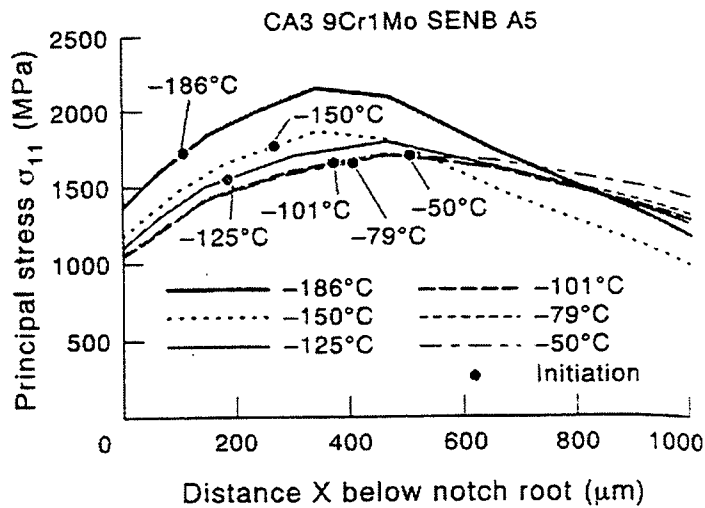


Figure 10.2:
Example of stress distributions at failure for SENB specimens, showing locations of initiation sites, after Wall, Lane and Hipsley (1994).

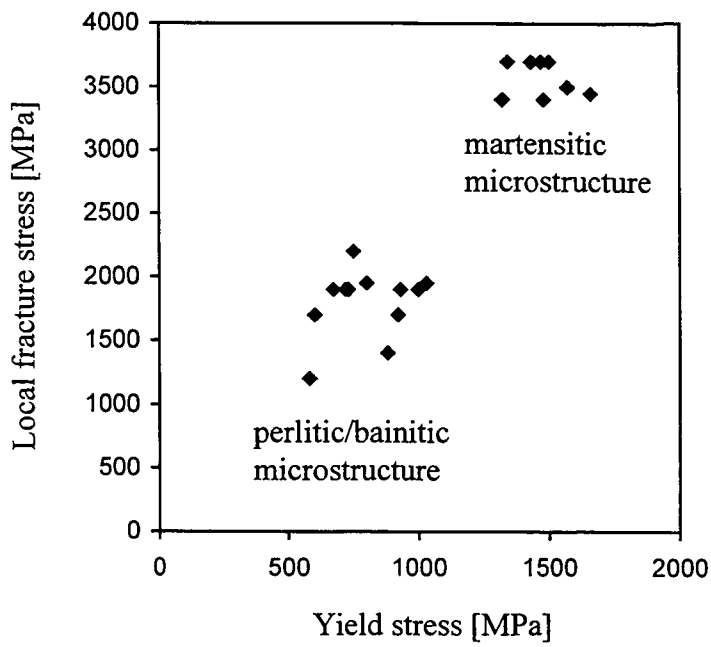


Figure 10.3:
Local fracture stress for two microstructures of A533B steel, after Bowen *et al* (1987).

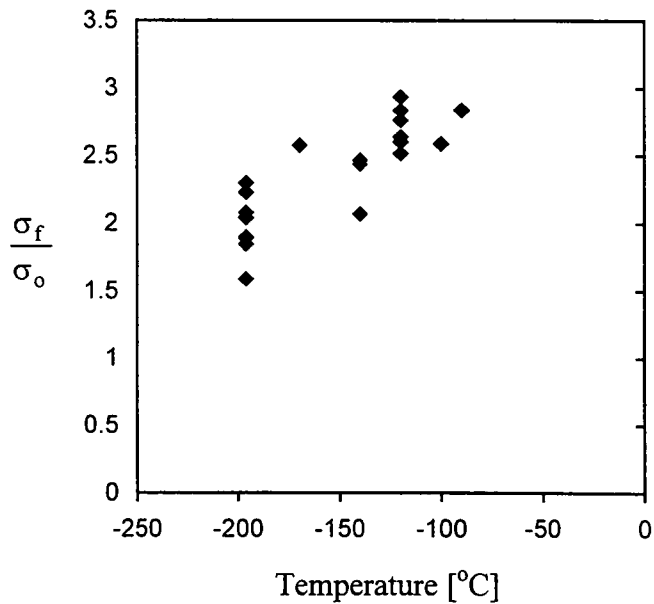


Figure 10.4:
The ratio of local fracture stress to yield stress for the two microstructures of A533B steel examined by Bowen *et al* (1987).

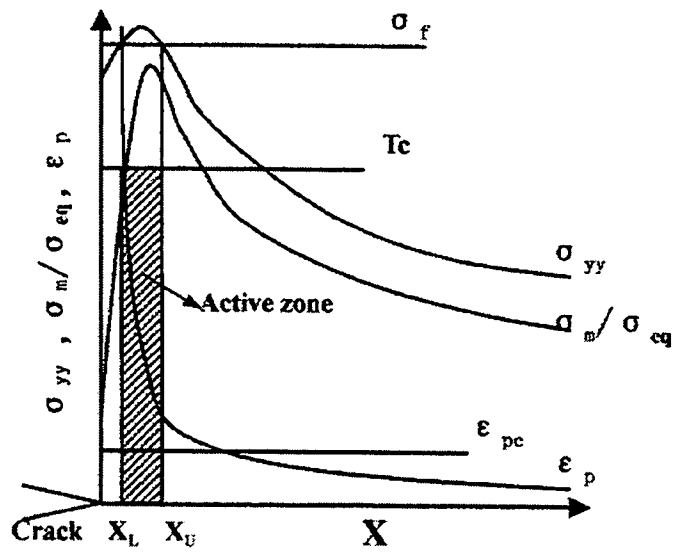


Figure 10.5:
A schematic diagram showing the active zone for cleavage fracture, taken from Wang *et al* (2002b).

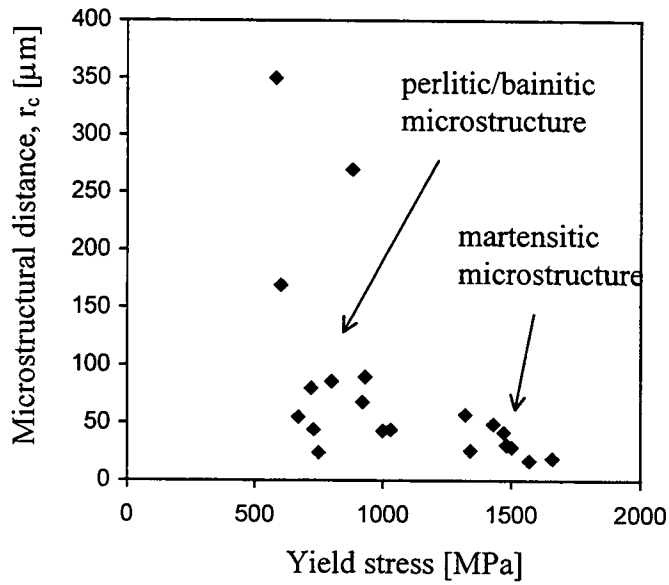


Figure 10.6:
The microstructural distance for the two microstructures of A533B steel, after Bowen *et al* (1987).

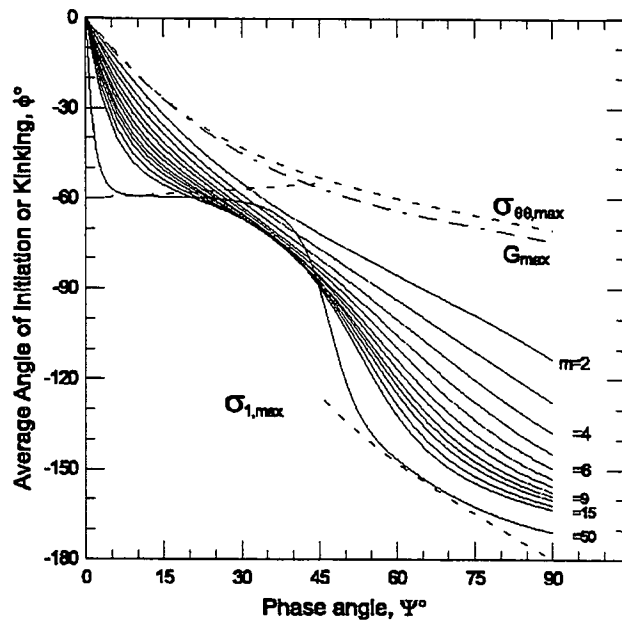


Figure 10.7:
Average angle of crack initiation as a function of remote mode mixity angle for a homogeneous material, after Becker *et al* (2002).

Chapter 11

THE TEMPERATURE DEPENDENCE OF MATERIAL PARAMETERS IN THE RKR MODEL

11.1 Introduction

The Ritchie-Knott-Rice model (Ritchie *et al* (1973)) allows the temperature dependence of fracture toughness to be modelled on the limited amount of experimental data, as discussed in Chapter 10. Ritchie *et al* (1973) argue that in cleavage the local fracture stress, σ_f , and the microstructural distance, r_c , are temperature independent and the dominant temperature dependence of toughness, as measured by J , arises largely from temperature dependence of the yield stress. However Ritchie *et al* (1979) recognises that the model underpredicts toughness in the ductile-brittle transition, as illustrated in Figure 11.1. Using the fracture toughness data of Sherry *et al* (2001) the RKR model is systematically re-examined by considering temperature dependence of key variables: the Young's modulus, the local fracture stress and the microstructural distance. The experimental data was obtained from tests conforming to ASTM E813-87 on deep cracked ($a/w=0.5$) 50x50mm and shallow cracked ($a/w=0.075$) 50x67mm specimens under three point bending throughout ductile-brittle temperature range. The toughness is expressed in terms of $K_J (= \sqrt{JE/(1-\nu^2)})$, although most tests below -100°C failed in contained yielding. Deep crack data is associated with positive T-stresses, while shallow cracked data shows loss of constraint quantified by negative T-stresses. Further details are given in Chapter 13.

11.2 Temperature dependent Young's modulus

Lidbury (1990) gives the temperature dependence of Young's modulus in ferritic steels as:

$$E(\phi) = 210 - 0.054\phi \quad [\text{GPa}] \quad (11.1)$$

which can be applied to the RKR model when the toughness is expressed in terms of J . The results in Figure 11.2 were obtained for temperature dependent Young's modulus at a fixed local fracture stress and the microstructural distance. Figure 11.2 indicates that the temperature dependent Young's modulus has a negligible effect of toughness, compared to a result for a temperature independent Young's modulus. For practical purposes Young's modulus may be considered temperature independent.

11.3 Temperature dependent local fracture stress

The necessary conclusion to account for the upswing in cleavage toughness in the ductile-brittle transition is that either the local fracture stress or the microstructural distance are temperature dependent. Comparison of the toughness of constrained ($a/w=0.5$) and unconstrained ($a/w=0.075$) fields gives an insight on this situation. Initially consider the hypothesis that the microstructural distance is identical in both the constrained and unconstrained specimens, as the stress fields operate on the same microstructure. The microstructural distance is not required to be temperature independent. By comparing fields at a fixed local fracture stress, the ratio of the unconstrained to the constrained toughness can be used to infer the fracture stress at each temperature. Details of the derivation are given in Chapter 12. Rewriting Eq. (12.8) gives the local fracture stress as:

$$\sigma_f = \left[\left(\frac{J_{0.075}}{J_{0.5}} \right)^{\frac{1}{n-1}} \cdot Q_{0.5} \cdot \sigma_o - Q_{0.075} \cdot \sigma_o \right] / \left(\frac{J_{0.075}}{J_{0.5}} \right)^{\frac{-n}{n-1}} \quad (11.2)$$

where subscript 0.075 refers to unconstrained data ($a/w=0.075$) and 0.5 to the deep cracked data ($a/w=0.5$), and Q ($\approx T/\sigma_o$) measures the constraint.

The results shown in Figure 11.3 suggest that under this hypothesis the fracture stress is temperature independent on the lower shelf, but is required to reduce with increasing temperature in the ductile-brittle transition. If this fracture stress is used with a fixed micro-crack size such as $120\mu\text{m}$ (Ritchie *et al* (1979)), it requires a decrease in toughness of the ferritic matrix to which the micro-crack propagates with increasing temperature. This is counter-intuitive and in addition the temperature dependent fracture stress fails to account appropriately for the increasing toughness of the steel as the temperature increases.

11.4 Temperature dependent microstructural distance

The necessary alternative is to assume that local fracture stress is constant over the temperature range, and investigate potential changes in the distance to nucleation sites. Ortner and Hipplesley (1996), Bowen *et al* (1987) and Wang *et al* (2002b) have investigated fracture initiation sites in compact tension specimens of A533B steel and C-Mn steel in the transition temperature and observed, that the critical event occurred at the location in the microstructure experiencing the critical local stress, σ_f . Using experimental data of Sherry *et al* (2001) combined with the RKR model the critical microstructural distance is shown in

Figure 11.4 for the deep cracked constrained ($a/w=0.5$) data, normalised with the lower shelf value of $120\mu\text{m}$. The result suggest that the distance to the initiation site increases with temperature. This can be given a physical basis on the grounds that at higher temperatures and lower yield stress cracked carbides close to the crack tip experience sufficient plastic strain to cause the micro-cracks to blunt out and subsequently to develop as voids rather than cleavage cracks, and that the increased levels of plastic strain cause interface failure of the carbides rather than transverse micro-cracking, in line with the three parameter interpretation of Wang *et al* (2002b). Applying the same argument to the unconstrained data shows the same trend, Figure 11.4, where the lower shelf value of r_c at $\sigma_f=2300\text{MPa}$ is $35\mu\text{m}$.

11.5 Discussion

The temperature dependence of Young's modulus and the local fracture stress both fail to correctly predict the upswing in toughness values with increasing temperature, suggesting that the microstructural distance to cleavage initiation sites must be temperature dependant. Recent examination of failure sites in compact tension specimens by Wall *et al* (1994) and Wang *et al* (2002) support the conclusion that the critical microstructural distance increases with temperature while the location of a failure site was observed at comparable stress levels.

A probabilistic Weibull stress model was developed by Gao and Dodds (2001) to map constraint effects into toughness margins. Contrary to the one-dimensional RKR model, the Weibull stress model considers the stresses in the volume of the fracture process zone. Gao and Dodds (2001) identified the process zone with the plastic zone. For this case it is shown in Chapter 13 that the model gives a correct upswing in the toughness values throughout ductile-brittle transition. As the model evaluates stresses in the temperature dependent plastic zone, the model implicitly contains a temperature dependant size scale, hence connects with the RKR model and a temperature dependent microstructural distance.

The maximum principal stress can be written as the sum of the mean or hydrostatic stress and a term which involves the Mises stress and hence the plastic strain. In the unconstrained specimens the loss of constraint and hydrostatic stress require that a greater contribution to the stress is made by strain hardening and plastic strain, which requires the initiation site to be closer to the crack tip. As the temperature increases the necessary

distance to cleavage initiation site increase more rapidly in the unconstrained specimens than the constrained specimens. Recalling that the stress level in the unconstrained specimens requires more plastic strain than the constrained specimens, supports the argument that micro-crack initiation sites are being made ineffective as cleavage initiation sites above critical levels of plastic strain, by developing as voids rather than acting as cleavage cracks.

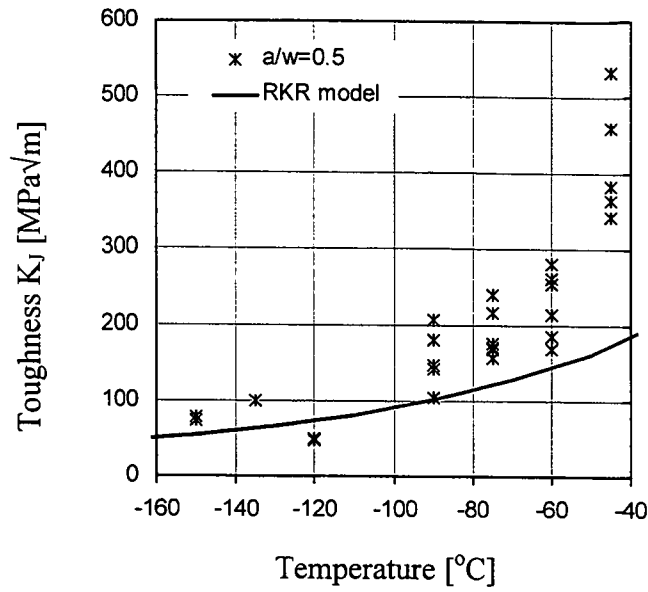


Figure 11.1:
The underprediction of cleavage toughness at elevated temperatures using the RKR model on $a/w=0.5$ A533B-1 data at a fixed local fracture stress and microstructural distance.

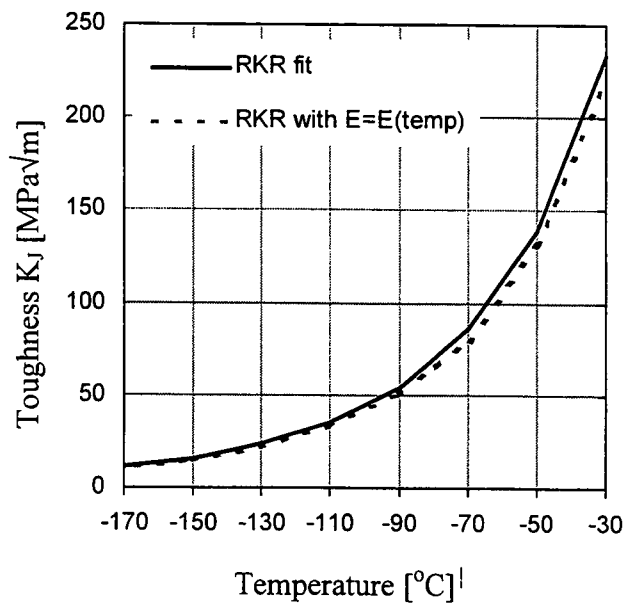


Figure 11.2:
Comparison of the RKR fit to A533B-1 $a/w=0.5$ data for a fixed E , σ_f and r_c and a fit where Young's modulus is temperature dependent at a fixed σ_f and r_c .

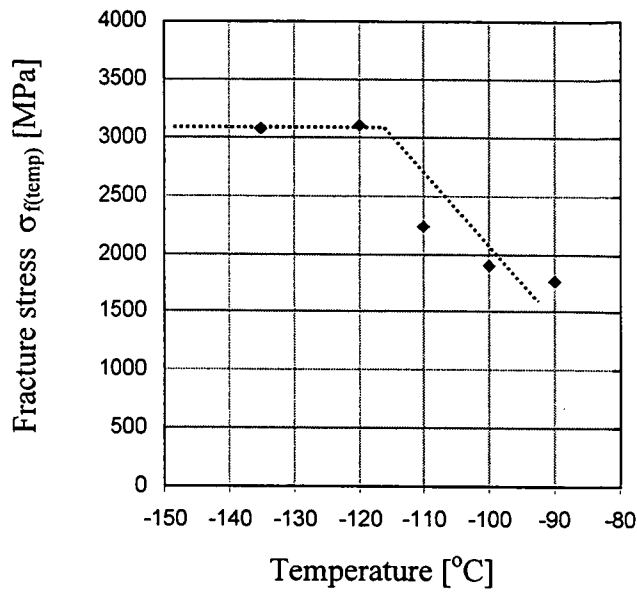


Figure 11.3:
The necessary temperature dependence of the local fracture stress to account for the ration of unconstrained ($a/w=0.075$) to constrained ($a/w=0.5$) toughness data from Sherry *et al* (2001).

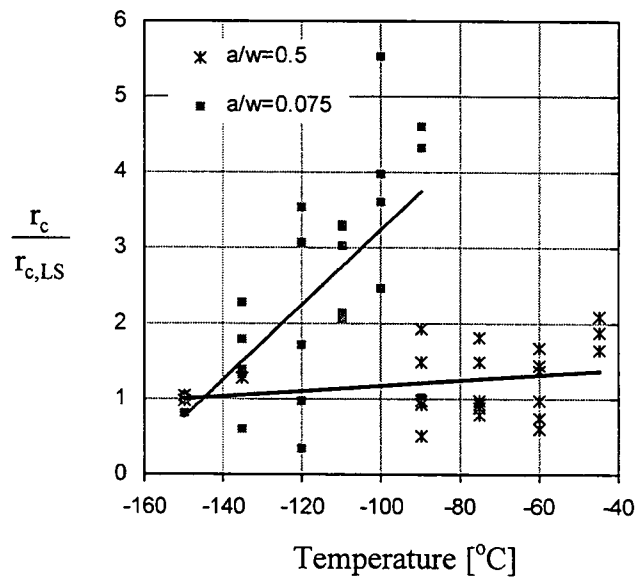


Figure 11.4:
The temperature dependent critical microstructural distance for deep and shallow cracked data, normalised with the individual lower shelf values.

Chapter 12

A PROCEDURE TO QUANTIFY ENHANCED TEMPERATURE MARGINS ASSOCIATED WITH CONSTRAINT LOSS

12.1 Introduction

Under normal operating conditions pressure vessels operate at temperatures exceeding the onset of the upper shelf fracture behaviour (OUST). In ferritic steels the criteria for a satisfactory safety case include consideration of the effects of neutron irradiation. Shortage of material frequently prevents valid sharp crack fracture mechanics tests being performed on irradiated plates. Charpy V notched tests performed on irradiated and unirradiated material indicate important trends in the ductile-brittle transition energy, which can be empirically correlated with the fracture mechanics $J_{0.2}$ toughness. At small irradiation levels the increase in yield strength through the interaction of dislocations and point defects increase the Charpy transition energy and the $J_{0.2}$ toughness. However at higher doses, interface embrittlement effects, particularly in copper rich submerged arc welds, result in significant decrease in $J_{0.2}$ toughness. The two counteracting effects complicate the systematic interpretation of data, arguing the need for a simple micro-mechanical model.

A detailed micro-mechanical modelling of near tip stresses including irradiation effects have been considered (Lidbury *et al* (1999)), however this entails complicated micro-mechanics as well as measured micromechanical parameters. This limits confidence and makes it difficult to generalise the results to give simple guidance in defect assessment procedures.

The loss of temperature and pressure margins arising from irradiation effects can be offset by appealing to arguments based on constraint. The loss of constraint associated with negative Q/T fields has been demonstrated to give an increase in both, cleavage toughness and the resistance to ductile tearing.

12.2 Procedure

A simplified method to predict the enhanced temperature margins from constraint effects is based on a scaling technique developed by Anderson and Dodds (1991) and Gao and

Dodds (2001) for cleavage fracture. Elastic-plastic crack tip fields are self-similar when stresses are non-dimensionalised by the yield stress and the distances ahead of the crack tip by J/σ_0 . The unconstrained field may be expressed as the small-scale yielding field multiplied by a factor as conceived by Anderson and Dodds (1991) or as a constrained plus a distance independent term, as conceived by Betegón and Hancock (1991) and O'Dowd and Shih (1991). By comparing the maximum principal stress contour at different levels of constraint (Q/T), it is possible to determine the increased value of J which will allow an unconstrained crack tip field to map onto the constrained (small-scale yield) field. This procedure then gives the ratio of unconstrained fracture toughness to that in small-scale yielding (J_{QT}/J_{SSY}) as a function of constraint. Similarly if the yield stress changes (due to temperature) and the cleavage fracture is temperature independent, the temperature shift to map the unconstrained field back to the small-scale yielding field can be determined by comparing the maximum principal stress contours for constrained and unconstrained configurations.

Initially the stress fields are shown to be self similar with respect to J and yield stress. Later the procedure is developed to match the crack tip fields that differ by constraint by changing the yield stress, which is in the next chapter applied to fracture toughness data from Sherry *et al* (2001).

12.3 Numerical model

Modified boundary layer formulation with displacement boundary conditions corresponding to the first two terms the Williams expansion were used:

$$\begin{aligned} u &= \frac{K_I}{2G} \sqrt{\frac{r}{2\pi}} \cos\left(\frac{\theta}{2}\right) \left[3 - 4\nu - 1 + 2 \sin^2\left(\frac{\theta}{2}\right)\right] + \frac{rT(1-\nu^2) \cos \theta}{E} \\ v &= \frac{K_I}{2G} \sqrt{\frac{r}{2\pi}} \sin\left(\frac{\theta}{2}\right) \left[3 - 4\nu + 1 - 2 \cos^2\left(\frac{\theta}{2}\right)\right] - \frac{rT(1+\nu) \sin \theta}{E} \end{aligned} \quad (12.1)$$

Material was defined to have linear elastic uniaxial response below yield stress, σ_0 :

$$\sigma = Ee, \quad \sigma \leq \sigma_0 \quad (12.2a)$$

with yield strain, e_0 , defined as σ_0/E and merged into a Ramberg-Osgood relation above the yield stress:

$$\frac{e}{e_0} = \frac{\sigma}{\sigma_0} + \alpha \left(\frac{\sigma}{\sigma_0} \right)^n, \quad \sigma > \sigma_0 \quad (12.2b)$$

Here n is the hardening exponent, σ_0 the yield stress and e_0 is a reference strain, with α taken to be unity. Calculations have been performed for a strain hardening exponent of 12, representative of a A533B-1 steel. Young's modulus was 210 GPa and Poisson's ratio 0.3. Results are generally presented in a non-dimensional form.

Crack tip stress fields were examined for a range of material properties, defined by σ_0 ranging from 200 to 600 MPa ($E/\sigma_0 = 350$ to 1050). The applied loading was quantified by the J-integral, measured at the crack tip by a domain integral method, given by Li, Shih and Needleman (1985), which is under small-scale yield conditions identical to the remotely applied stress intensity factor.

12.4 Self-similarity in contained yielding

The maximum principal stress directly ahead of the crack is shown in Figure 12.1(a) at three values of applied J and in Figure 12.1(b) over a range of yield stresses. An increase in J or an increase in yield stress increases the stress amplitude and shifts the asymptotic curves along the ordinate. All the curves collapse to a single curve when the distance, r , ahead of the crack is normalised by applied J/σ_0 and the stress is normalised with the yield stress, σ_0 , as shown in Figure 12.2. The stress field are thus self-similar, indicating that the same normalised stresses (σ_1/σ_0) are obtained over a normalised distance ($r\sigma_0/J$) regardless of yield strength or applied loading. To maintain self-similarity when changing the yield stress, the yield strain ($e_0 = \sigma_0/E$) must be included in normalising the distance.

Figure 12.3 shows that the self-similarity applies to any member from the family of unconstrained ($T < 0$) fields, such as feature in shallow edge cracked bend bars. In Figure 12.3(a) the yield stress is fixed and maximum principal stress is shown for two values of applied J and in Figure 12.3(b) for yield stresses of 400 MPa and 600 MPa. The stress profiles collapse to a single curve, when the distances are normalised by (J/σ_0) or by $(r\sigma_0 e_0/J)$ and stresses with the yield stress, (σ_1/σ_0), retaining the self-similarity. For compressive T-stresses the stress profiles reduce ahead of the crack by an amount independent of radial distance, as observed by Betegón and Hancock (1991). In Figure 12.4 the unconstrained fields are compared to the reference solution through a strain hardening dependent multiplicative factor, β , after Anderson and Dodds (1991). This is weakly dependent on the distance ahead of the crack tip, indicating that the hydrostatic

stresses govern the magnitude of stresses in the unconstrained fields. Thus the unconstrained field can be described by the constrained field plus a hydrostatic term:

$$\sigma_{ij} = \sigma_{ij}^{SSY} + Q\sigma_o \quad (12.3a)$$

or a multiplicative term:

$$\sigma_{ij} = \beta\sigma_{ij}^{SSY} \quad (12.3b)$$

12.5 Matching J-T/Q crack tip fields

Constrained and unconstrained crack tip fields are firstly shown to match at a fixed distance ahead of the crack by a change in the yield stress or equivalently temperature. Secondly, fields are matched at a local fracture stress, analogous to the Anderson and Dodds (1991) approach and thirdly by using the Weibull stress.

12.5.1 Comparing fields at a fixed distance

A family of self-similar crack tip fields can be described by two term series expansion (O'Dowd and Shih (1991)):

$$\frac{\sigma_{\theta\theta}}{\sigma_o} = \left(\frac{J}{\alpha r \sigma_o e_o I_n} \right)^t \tilde{\sigma}_{(n,\theta)} + Q \quad (12.4)$$

where the first term is the small-scale yielding ($T=0$) field. Without loss of generality, the constrained and the unconstrained fields match when their normalised hoop stresses ($\sigma_{\theta\theta}/\sigma_o$) match at some normalised distance, r , within the validity of (12.4). Self-similarity can be established either in respect of J or σ_o or combination of both. A systematic approach is adopted by examining J and σ_o separately.

Let the superscript *ref* represent parameters of the constrained field and the superscript *-ve* denote values for the unconstrained field. The two fields can be matched by adjusting J at a fixed yield stress to compensate for the constraint loss:

$$\frac{J^{ref}}{J^{-ve}} = \left[1 + Q \left(\frac{\alpha r \sigma_o e_o I_n}{J^{-ve}} \right)^t \frac{1}{\tilde{\sigma}_{(n,\theta)}} \right]^{\frac{1}{t}} \quad (12.5)$$

where the strength of leading singularity, t , arises from strain hardening exponent. The expression depends on the distance, r , at which fields are required to match.

At a fixed toughness level, the yield stress can be changed to match the constrained field to the unconstrained field, hence determine the temperature shift. The new yield stress of the constrained field, σ_o^* , that matches the unconstrained field follows as :

$$\sigma_o^* = \gamma \sigma_o^{\text{ref}} \quad (12.6)$$

$$\gamma = \left[\left(\frac{\sigma_o^{\text{ref}}}{\sigma_o^{-\text{ve}}} \right)^{2t} + (Q^{-\text{ve}} - Q^{\text{ref}}) \left(\frac{\alpha r (\sigma_o^{\text{ref}})^2 I_n}{EJ} \right)^t \frac{1}{\tilde{\sigma}_{(n,\theta)}} \right]^{-\frac{1}{2t}} \quad (12.7)$$

The disadvantage of this approach is that all parameters in HRR equation must be established and the fields match at a defined distance ahead of the crack tip.

12.5.2 Comparing fields at a local fracture stress

The same cleavage mechanisms may be assumed to operate in a constrained and unconstrained fields since the two differ only in respect of the hydrostatic stress component and experience the same microstructure. This allows connections to be established between the fields of constrained and unconstrained configurations, by comparing the fields at a local fracture stress, as discussed by Anderson and Dodds (1991). The stresses ahead of the crack are expressed using Eq. (12.4) and the microstructural distance is assumed temperature independent (Ritchie *et al* (1973, 1979)).

Identifying the hoop stress in (12.4) with the fracture stress, σ_f , over a micro-structural distance r_c , the constrained and unconstrained fields can be matched by adjusting J at a fixed yield stress (temperature) to compensate for constraint effects:

$$\frac{J^{-\text{ve}}}{J^{\text{ref}}} = \left(\frac{\sigma_f - Q^{-\text{ve}} \sigma_o}{\sigma_f - Q^{\text{ref}} \sigma_o} \right)^{\frac{1}{t}} \quad (12.8)$$

At the same toughness, $J^{\text{ref}} = J^{-\text{ve}}$, the fields can be matches by adjusting the yield stress by a factor γ . The new yield stress for the constrained specimen, σ_o^* , which reproduces the same field as in the unconstrained specimen is:

$$\sigma_o^* = \gamma \sigma_o^{\text{ref}} \quad (12.9)$$

and γ is defined as:

$$\gamma = \frac{\sigma_o^{-\text{ve}}}{\sigma_o^{\text{ref}}} \left(\frac{\sigma_f - Q^{-\text{ve}} \sigma_o^{-\text{ve}}}{\sigma_f - Q^{\text{ref}} \sigma_o^{\text{ref}}} \right)^{\frac{1}{2t-1}} \quad (12.10)$$

It is noteworthy that Eq. (12.10) does not involve the microstructural distance, r_c , which is eliminated when the fields are matched at a local fracture stress.

12.5.3 Using Weibull stress approach

The Weibull stress was used by Beremin (1983) as technique to develop the Ritchie-Knott-Rice (1973) model to incorporate statistics of micro-crack initiation in a fracture process zone. At the same failure probabilities, the identity of the Weibull stresses ($\sigma_w^{\text{constr}} = \sigma_w^{\text{unconstr}}$) can be used to match the crack tip fields. Restricting the discussion to small-scale yielding, the Weibull stress can be expressed in a non-dimensionalised manner, by normalising the stresses with the yield stress, and the volume with $(J/\sigma_o e_o)^3$:

$$\tilde{\sigma}_w^m = \frac{\sigma_w^m V_o}{\sigma_o^{m-4} J^2 E^2 B} = f(T/\sigma_o, n, \nu, \lambda, m) \quad (12.11)$$

which depends on constraint, T/Q , strain hardening exponent, the Poisson's ratio, the size of the process zone and the Weibull modulus, but is independent of J , as discussed by Gao and Dodds (2001). The enhanced toughness margins arising from constraint loss are quantified at a fixed temperature and failure probability as:

$$\frac{J^{-ve}}{J^{\text{ref}}} = \left[\frac{(\tilde{\sigma}_w^m)^{\text{ref}}}{(\tilde{\sigma}_w^m)^{-ve}} \right]^{\frac{1}{2}} \quad (12.12)$$

Which is equivalent to Gao and Dodds (2001) expression given in Chapter 10 (Eq. 10.16). At a fixed toughness, $J^{\text{ref}} = J^{-ve}$, the change in the yield stress and associated temperature shift is obtained through adjusting the yield stress by a factor γ , as before:

$$\gamma = \frac{\sigma_o^{-ve}}{\sigma_o^{\text{ref}}} \left[\frac{(\tilde{\sigma}_w^m)^{-ve}}{(\tilde{\sigma}_w^m)^{\text{ref}}} \right]^{\frac{1}{m-4}} \quad (12.13)$$

giving the new yield stress of the constrained field that matches the unconstrained field as:

$$\sigma_o^* = \gamma \sigma_o^{\text{ref}} \quad (12.14)$$

The unconstrained field can be matched to the constrained field, by dividing the yield stress of the unconstrained field by γ .

12.6 Results

In Figure 12.5 the constrained field ($T=Q=0$) is matched to an unconstrained field in which $T=-0.25\sigma_o$, ($Q=-0.22$) and in Figure 12.6 to an unconstrained field $T=-0.5\sigma_o$

($Q=-0.49$) at a fixed distance ahead of the crack. The applied stresses are normalised with the current yield stress and the distance is normalised with a fixed J/σ_0 or ($J/\sigma_0 e_0$). For both levels of constraint the crack tip fields are matched directly ahead of the crack at a distance corresponding to 4 crack tip openings ($r\sigma_0/J=4$).

Unconstrained fields are matched with the constrained field by adjusting J in Figures 12.7a and 12.8a and by changing the yield stress at a fixed local fracture stress in Figures 12.7b and 12.8b. In Figure 12.7 the maximum principal stress directly ahead of the crack is shown and in Figure 12.8 the contours of principal stress are compared. The stresses are normalised with a fixed yield stress and distances with a fixed J/σ_0 ($J/\sigma_0 e_0$) of the field to which values are matched. Comparatively small changes had to be applied to J or σ_0 to match the fields, maintaining stress fields close to their self-similar shape. In both cases an excellent match is achieved over the crack tip openings of 2-6 J/σ_0 .

To illustrate the approach using the Weibull stress procedure, constrained ($T=0$) and unconstrained ($T=-0.5\sigma_0$) fields are matched for Weibull modulus of 20 as shown in Figures 12.9 and 12.11. The Weibull modulus is close to the limiting value of $2(n+1)$ (Lei *et al* (1998) making the fields match close to the tip. At low moduli ($m=10$) the match is achieved at the process zone boundary, defined by λ , as shown in Figure 12.10. Values are normalised with a fixed yield stress and distances with a fixed J/σ_0 ($J/\sigma_0 e_0$) taken for the field to which values are matched.

A specific stress field corresponding to the experimental data of Sherry *et al* (2001) is considered in Figures 12.12 for fields representative of the constraint at failure in the toughness range of $K_J=150 \text{ MPa}\sqrt{\text{m}}$ to $250 \text{ MPa}\sqrt{\text{m}}$. As an illustration, an unconstrained field with an average yield stress $\sigma_0^{-ve}=630 \text{ MPa}$, is matched to a constrained field by increasing the yield stress of the unconstrained field to $\sigma_0^*=745 \text{ MPa}$. Here the match is achieved at a stress level three times the yield stress of the constrained field ($\sigma_0^{ref}=550 \text{ MPa}$), giving the local fracture stress of 1650 MPa , typical of the local fracture stress reported by Bowen *et al* (1987). The stresses are normalised with a fixed yield stress of 550 MPa , while the distances are normalised with a fixed value of $J/\sigma_0 e_0$ for the constrained field.

The same data is modelled using Weibull stress procedure based on a large geometry change solution to give the results shown in Figure 12.13. The fields are matched by changing the yield stress to compensate for constraint loss.

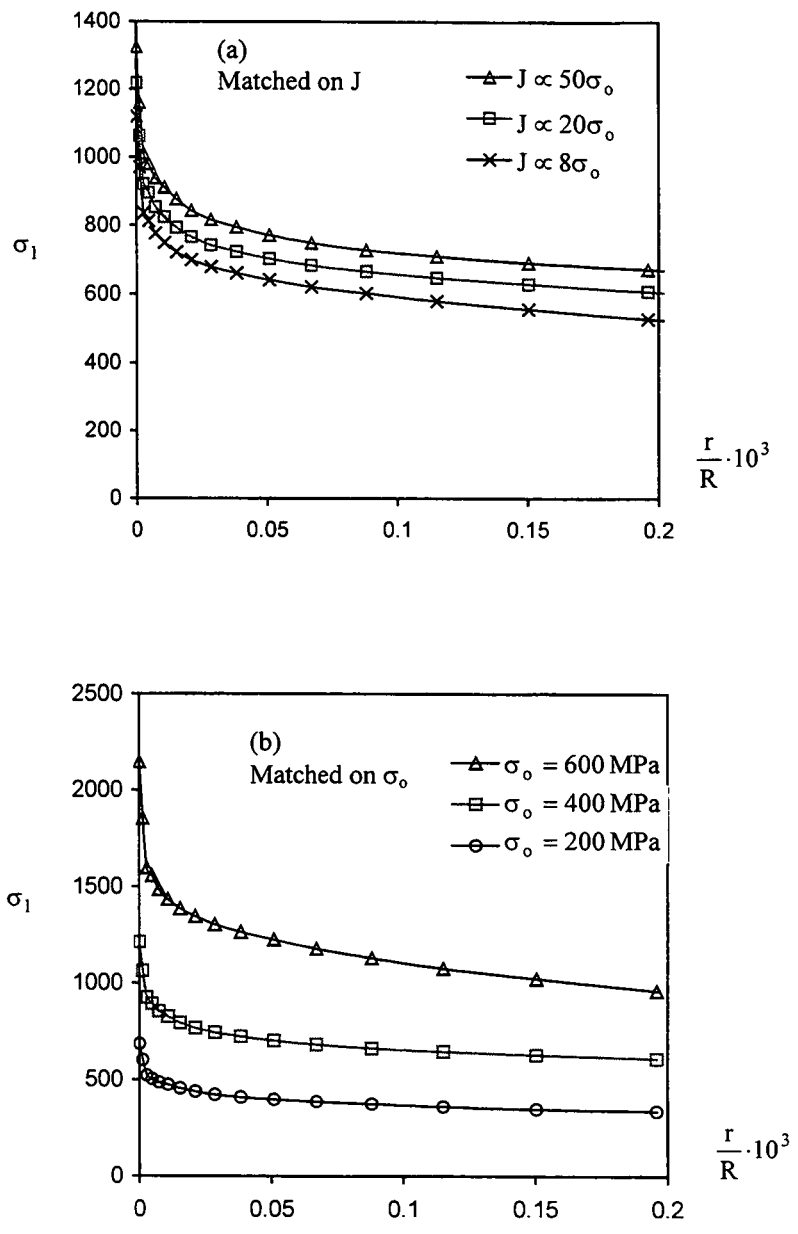


Figure 12.1: Plots of applied principal stress directly ahead of the crack over a range of applied J values in (a) and yield stresses in (b).

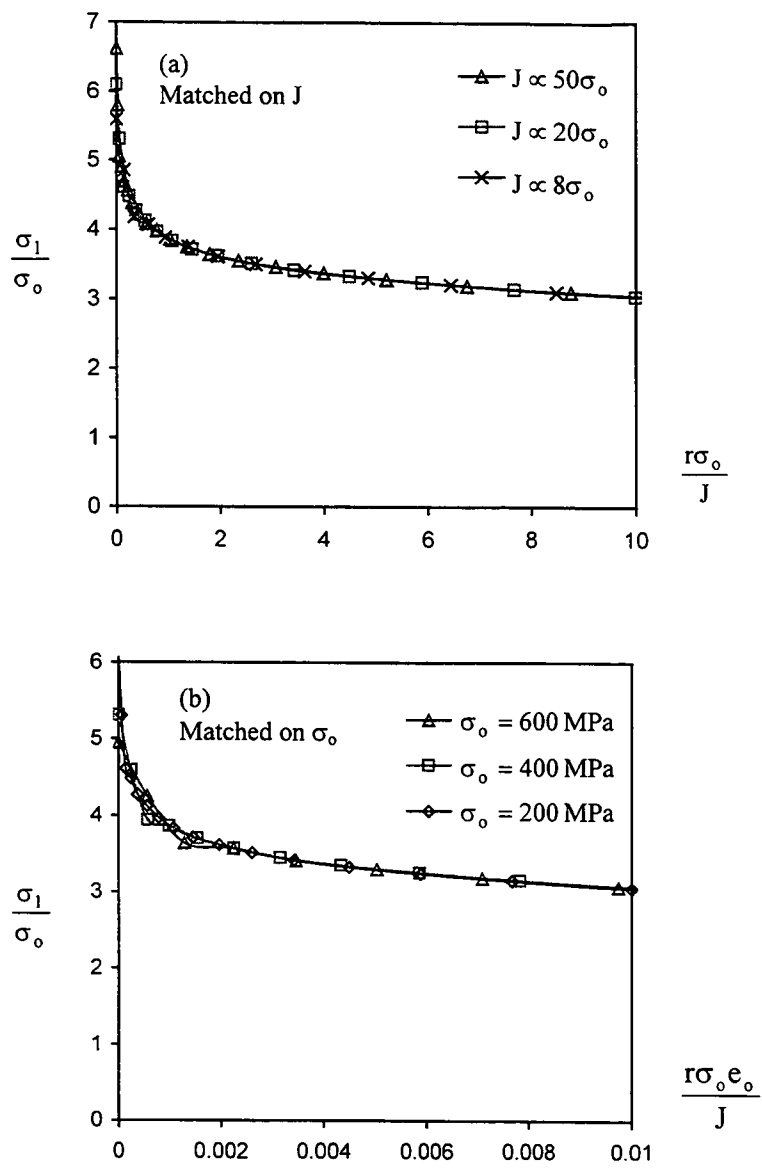


Figure 12.2:
Plots of normalised principal stresses directly ahead of the crack, examined over a range of applied J values in (a) and yield stresses in (b).

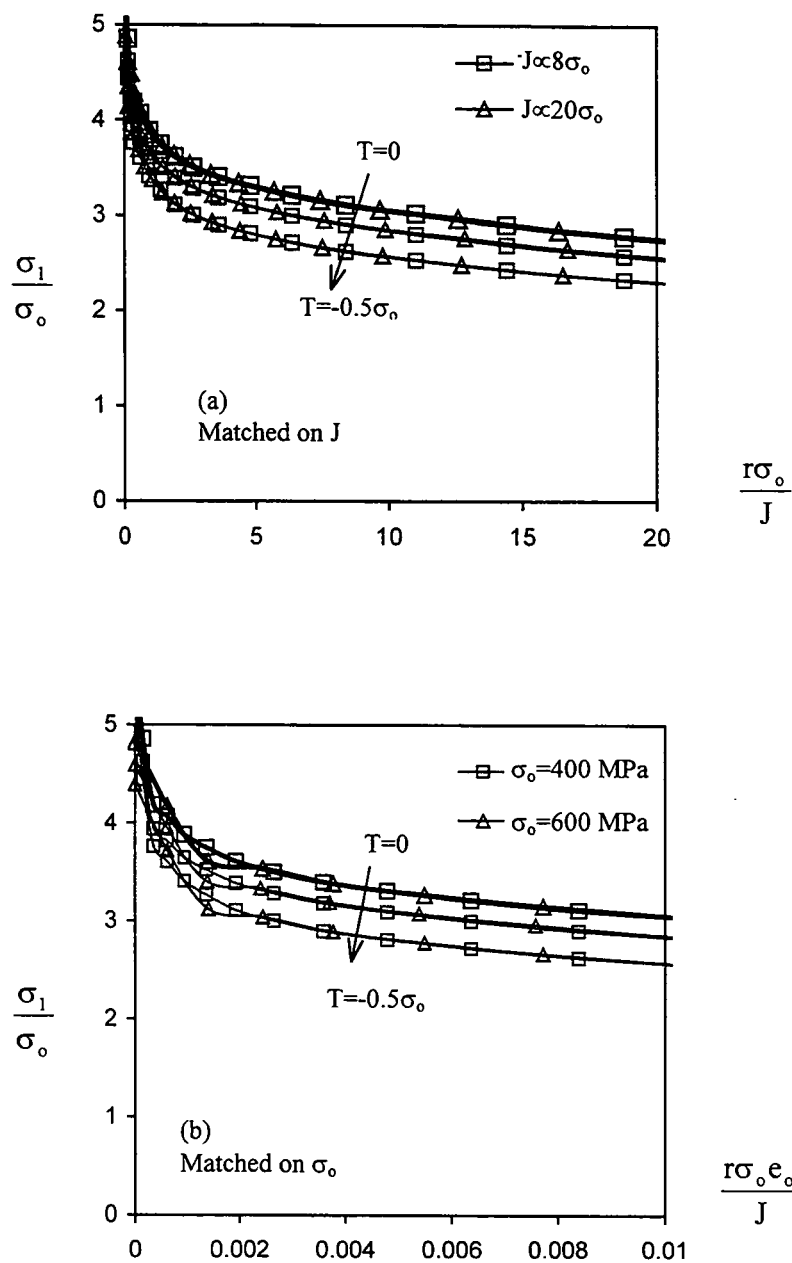


Figure 12.3:
 Principal stress directly ahead of the crack for a reference ($T=0$) and an unconstrained ($T=-0.25\sigma_0$) and ($T=-0.5\sigma_0$) fields. In (a) examined at a fixed yield stress and in (b) at a fixed J .

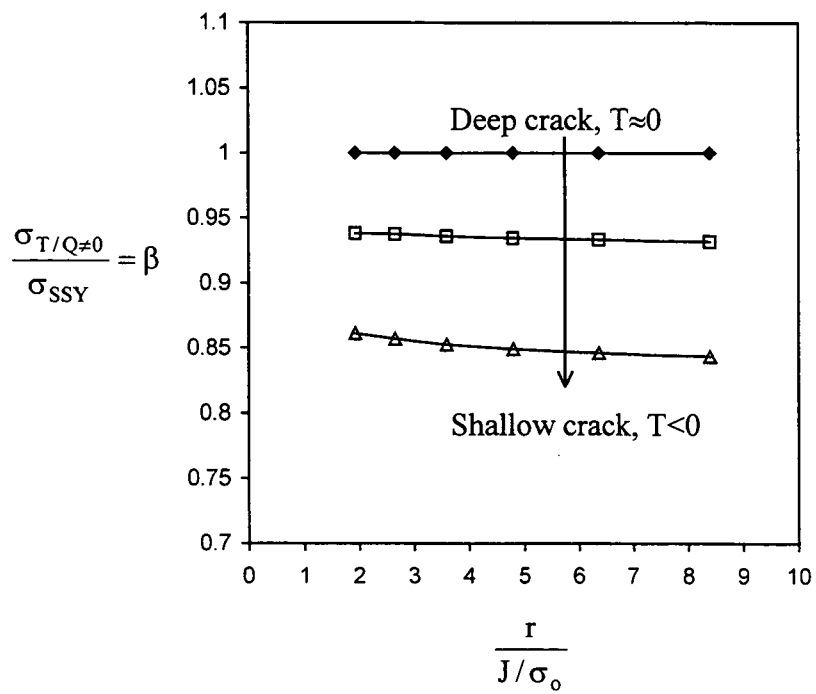


Figure 12.4:
 Multiplicative factor β proposed by Anderson and Dodds (1991) to quantify the relaxation of stresses in unconstrained fields of shallow cracked bend bars compared to the constrained field of a deep cracked bend bars, at $\theta=0$.

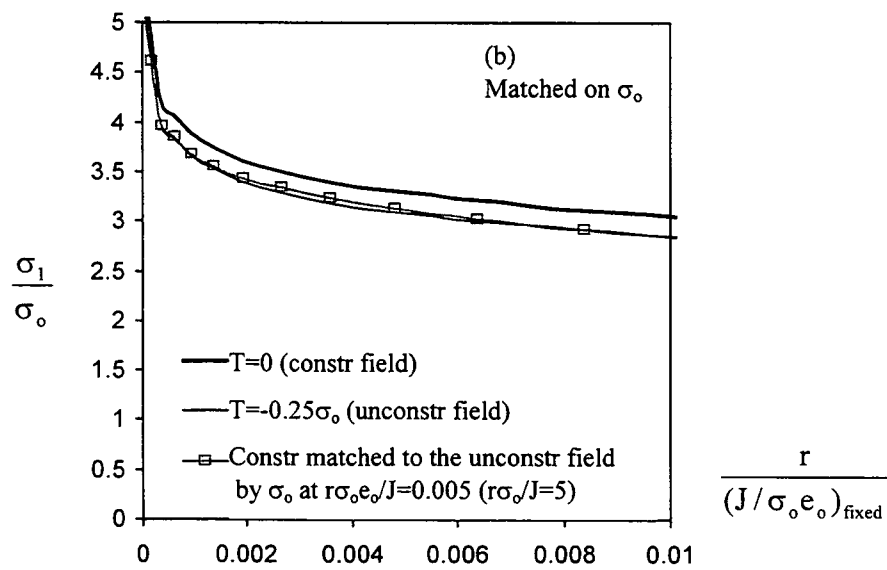
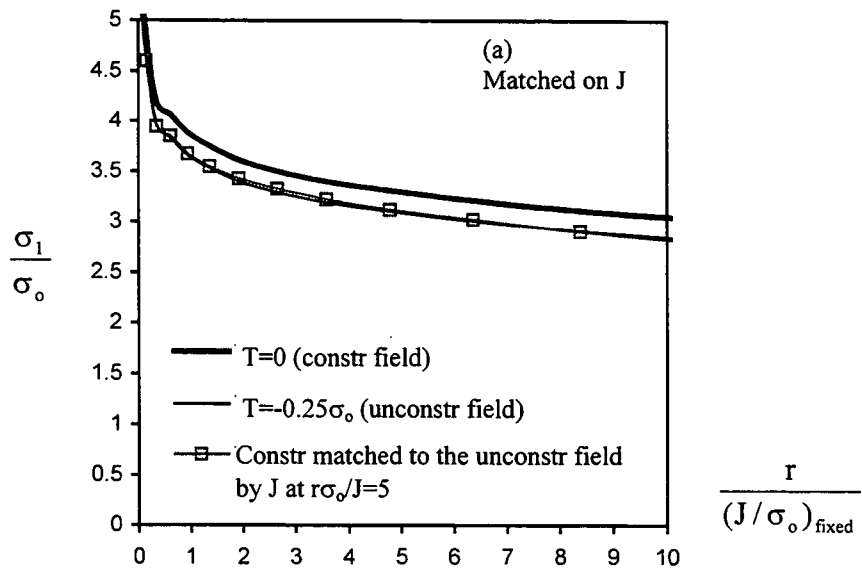


Figure 12.5:

Constrained ($T=0$) field is matched to the unconstrained ($T=-0.25\sigma_0$) field by a change in J in (a) and by a change in σ_0 in (b), at a fixed distance ahead of the crack. Stress is normalised with the current yield stress and distance is normalised with the deformation of the unconstraint field, $J/\sigma_0 \propto 8$.

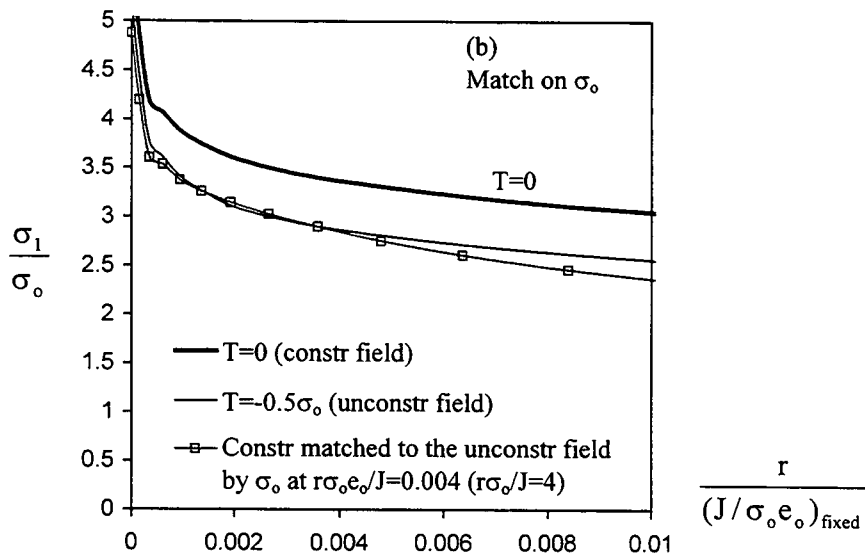
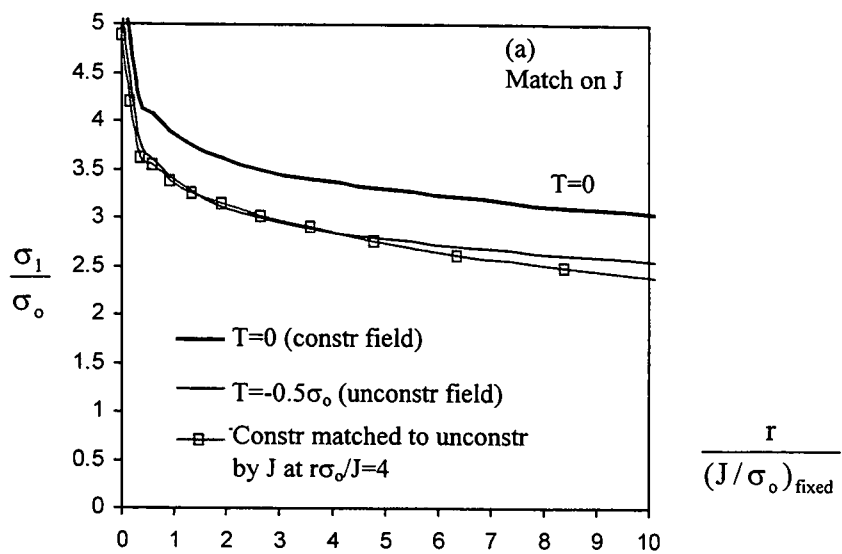


Figure 12.6:

Constrained ($T=0$) field is matched on unconstrained ($T=-0.5\sigma_0$) field by J in (a) and by σ_0 in (b), at a fixed distance ahead of the crack. Stress is normalised with the current yield stress and distance is normalised with the deformation of the unconstraint field, $J/\sigma_0 \propto 8$.

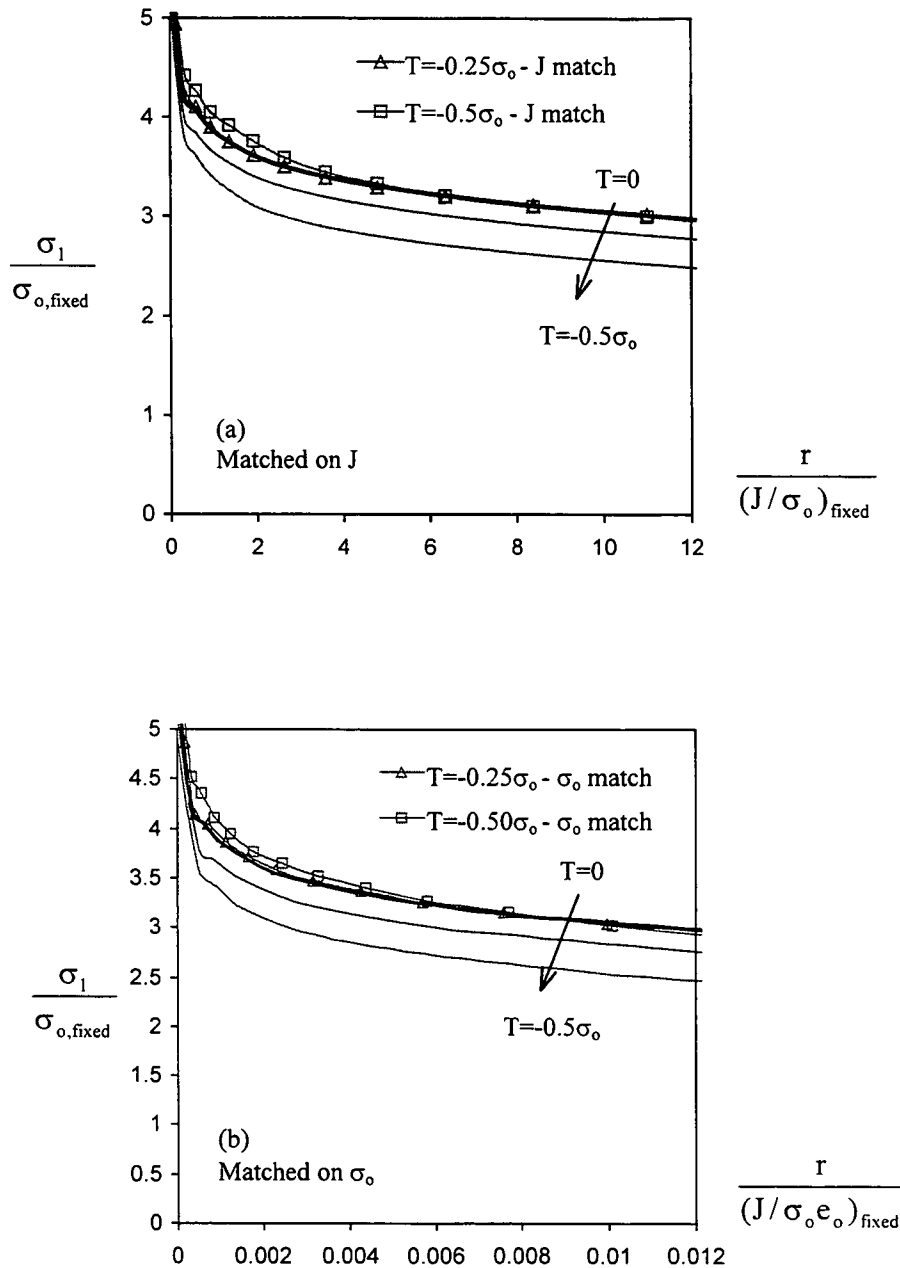


Figure 12.7: Unconstrained field is matched to the $T=0$ field at a local fracture stress of $\sigma_f = 3\sigma_{o, \text{fixed}}$ by J in (a) and yield stress in (b), as illustrated with plots of principal stress ahead of the crack ($\theta=0$). Values are normalised with fixed σ_o and J/σ_o ($J/\sigma_o e_o$) for the constrained field.

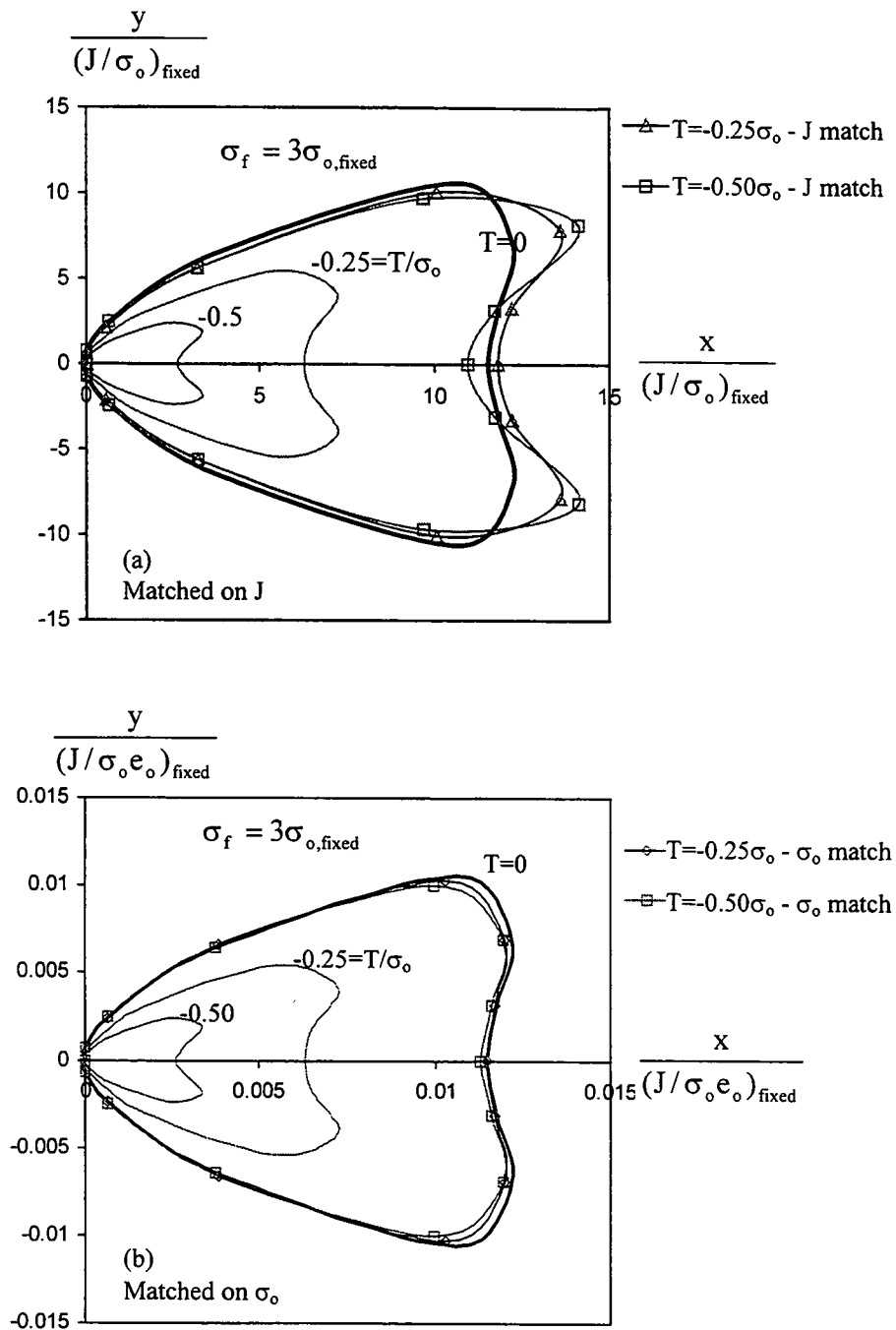


Figure 12.8:
 Unconstrained field is matched to the $T=0$ field at a local fracture stress of $\sigma_f = 3\sigma_{o,\text{fixed}}$, by J in (a) and yield stress in (b), as shown by contours of principal stress. Values are normalised with fixed J/σ_o ($J/\sigma_o e_o$) for the constrained field.

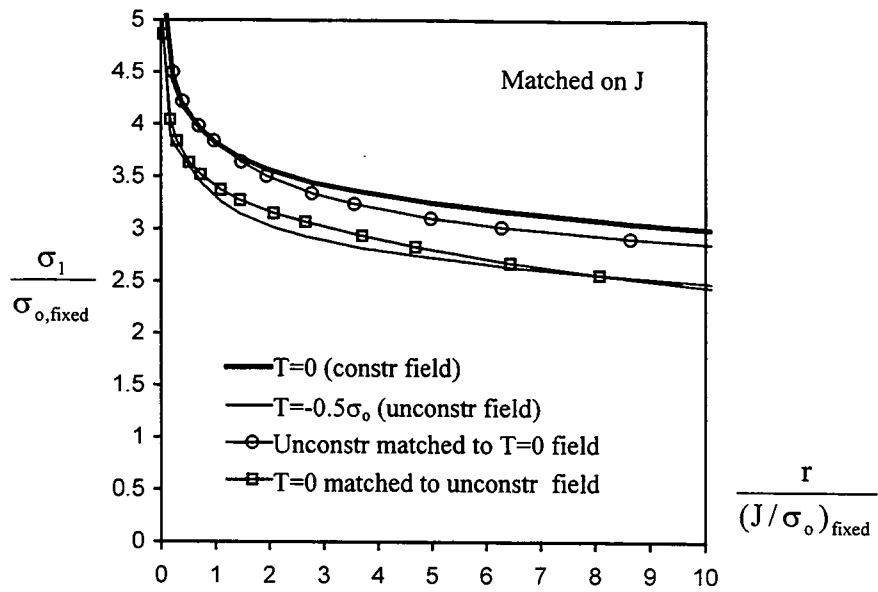


Figure 12.9:

Unconstrained and T=0 field match close to the crack tip by adjusting J, based on the small strain Weibull stress approach for $\lambda=3$ and $m=20$. Values normalised with fixed σ_o and J/σ_o .

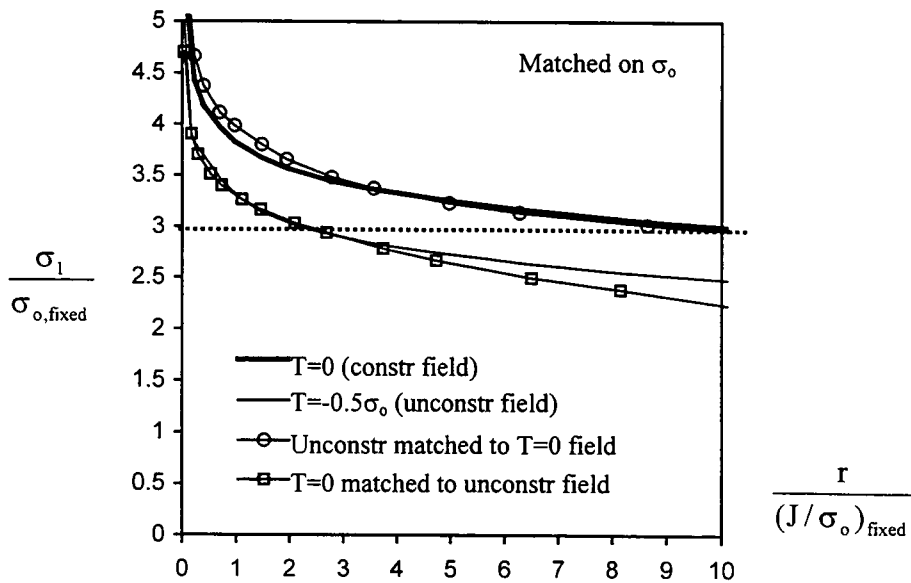


Figure 12.10:

Unconstrained and T=0 field match at a fracture process zone boundary ($\lambda=3$) by adjusting J, based on the small strain Weibull stress approach for $\lambda=3$ and $m=10$. Values normalised with fixed σ_o and J/σ_o .

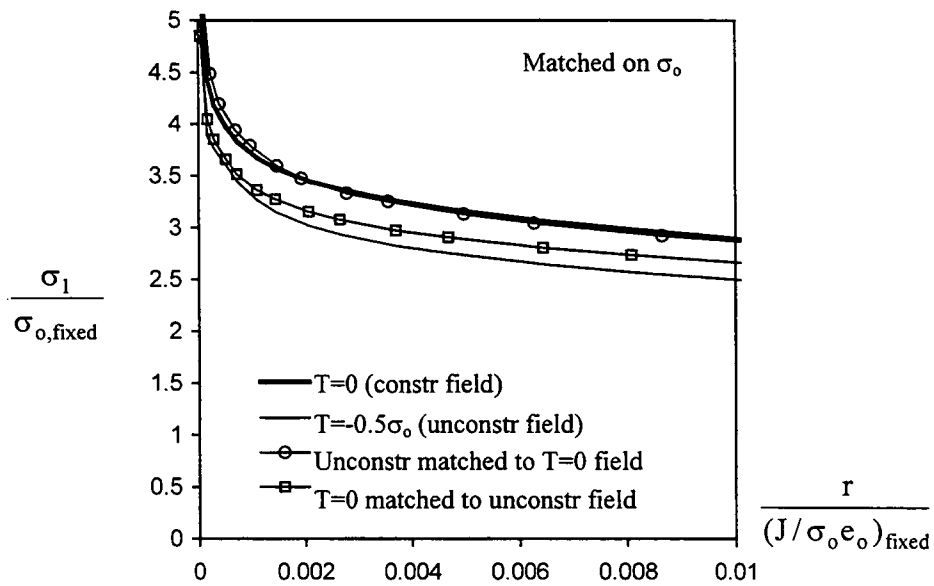


Figure 12.11:
 Unconstrained and $T=0$ field match close to the crack tip by adjusting yield stress. Based on the small strain Weibull stress approach for $\lambda=3$ and $m=20$. Values normalised with fixed σ_0 and $J/\sigma_0 e_0$.

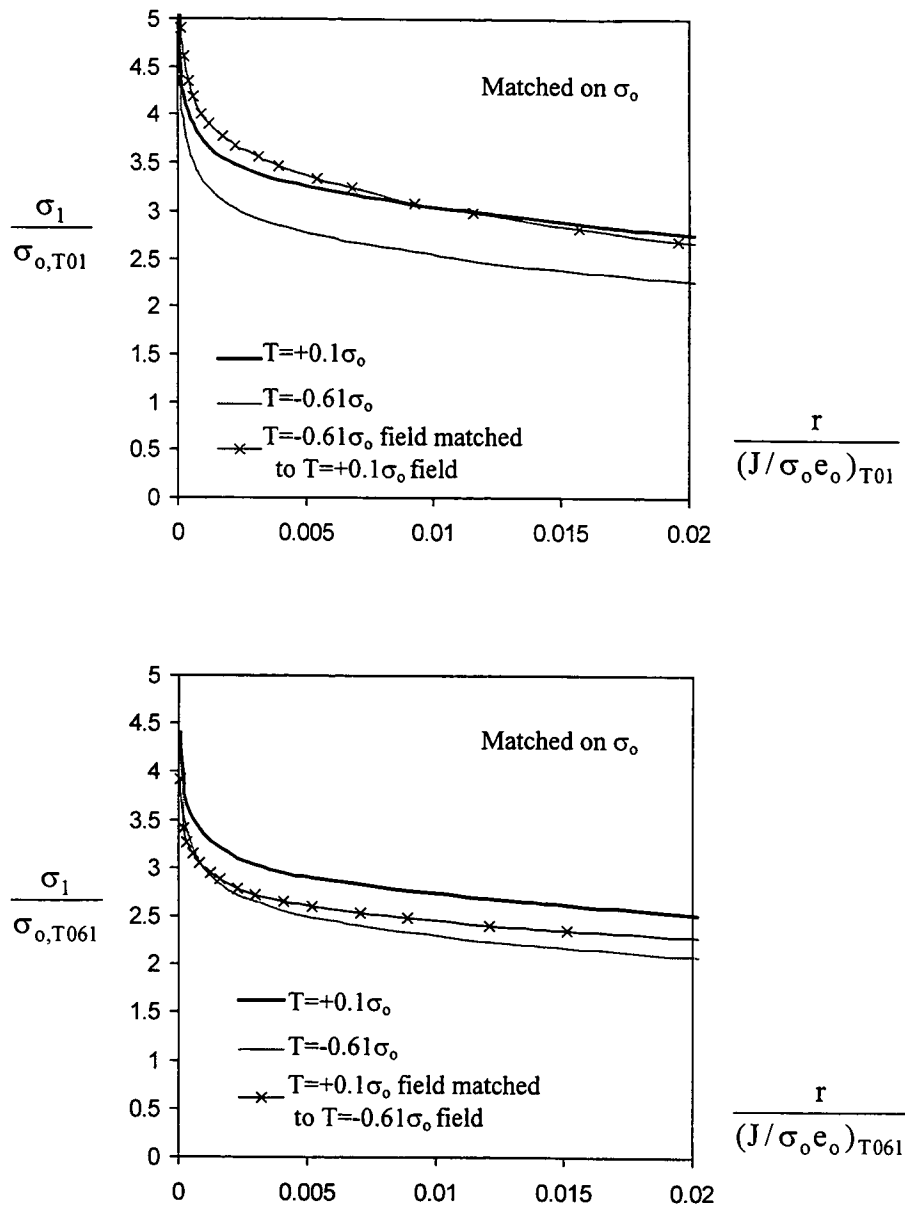


Figure 12.12:

Principal stress ahead of the crack for crack tip fields characteristic of $K_J=150-250\text{MPa}\sqrt{\text{m}}$ toughness data. The fields differ by constraint and temperatures (yield stresses) and are matched at a fracture stress taken as three times the yield stress of the field to which values are matched. All values normalised with a fixed value of σ_0 and $J/\sigma_0 e_0$ also taken for the field to which values are matched.

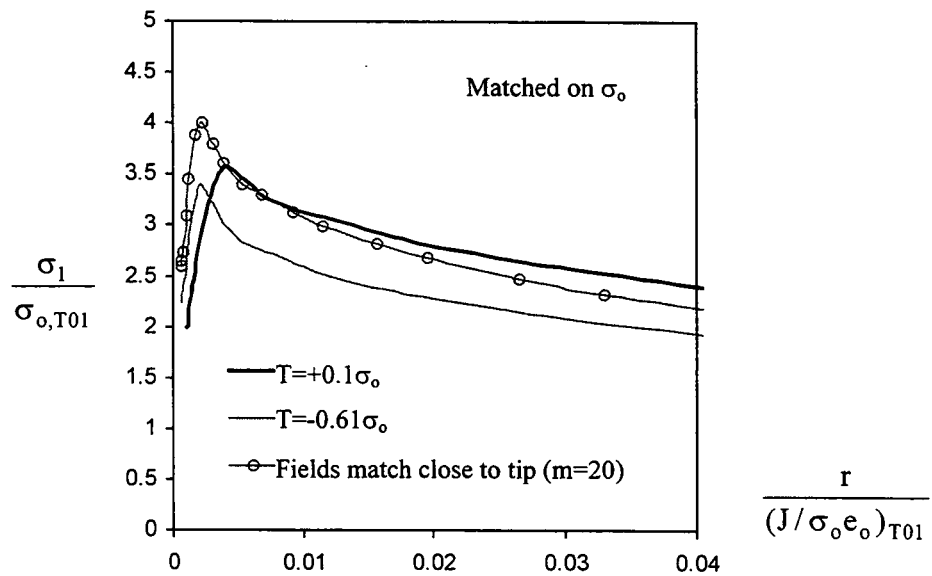


Figure 12.13:

Principal stress ahead of the crack for constrained ($T=+0.1\sigma_o$) and unconstrained ($T=-0.61\sigma_o$) field, characteristic of $K_J=150-250 \text{ MPa}\sqrt{\text{m}}$ toughness data. Fields are matched by yield stress computed from finite strain Weibull stress procedure in the plastic zone ($\lambda=1$) and normalised with a fixed value σ_o and $J/\sigma_o e_o$ for the constrained field.

Chapter 13

TEMPERATURE MARGINS DUE TO CONSTRAINT LOSS FOR A533B-1 DATA

13.1 Summary of experimental data

The procedures developed in Chapter 12 are applied to the experimental data of Sherry *et al* (2001), obtained from tests on shallow and deep cracked bend bars of A533B-1 pressure vessel steel. In Figure 13.1 the toughness data obtained from tests conforming to ASTM E813-88 on 50x50 and 50x67 mm specimens is presented as a function of temperature. The toughness is expressed in terms of K_J ($(JE/(1-\nu^2))^{1/2}$), although most tests below -100°C failed in contained yielding. Figure 13.2 shows the values of T-stress at failure for the specimens tested over a range of temperatures, while Figure 13.3 shows the J-T/Q toughness locus as a function of constraint and temperature. For clarity, the data points are fitted with solid lines. Due to small amount of valid data for the $a/w=0.1$ test configuration, the discussion focuses on a larger data set at $a/w=0.075$. The data show a significant increase in toughness due to constraint loss through-out the temperature range. Constraint in the experimental data is quantified by the T-stress and normalised with the yield stress at each test temperature, T/σ_0 . The Q parameter was calculated using the modified boundary layer formulation and $T=0$ as the reference field for the average values of experimental data and is listed in Tables 13.1 and 13.2. The temperature dependent yield stress is re-drawn in Figure 13.4 from Sherry *et al* (2001) and fitted with an expression:

$$\sigma_0(\phi) = -1.72\phi + 430, \quad (13.1)$$

valid for $-170^\circ\text{C} \leq \phi \leq -20^\circ\text{C}$, where ϕ is temperature in $[\text{C}]$ and σ_0 is the yield stress in $[\text{MPa}]$.

13.2 Determination of the local fracture stress

Plots of hoop stress directly ahead of the crack are shown in Figure 13.5 for the HRR field, the SSY ($T=0$) field and the $T=+0.1\sigma_0$ field, which is representative of the $a/w=0.5$ experimental data. Figure 13.5 suggests, that the experimental data can be described by taking the SSY field as the reference field, and setting the exponent of the leading term as $t=0.105$, corresponding to the average strain hardening exponent of 12 (Sherry *et al* (2001)).

High constraint data ($a/w=0.5$) was used to determine the local fracture stress by fitting the Ritchie-Knott-Rice model to the lower shelf toughness data, as shown in Figure 13.6. The strength of the leading singularity was identified with the small-scale yield (SSY) solution. Microstructural distances of $50\mu\text{m}$, $100\mu\text{m}$ and $200\mu\text{m}$, (Ritchie *et al* (1979), Bowen *et al* (1987)) were considered in the RKR model to represent a realistic range of grain sizes. The local fracture stress was taken to be 2300 MPa, corresponding to the average grain size of $120\mu\text{m}$, which is close to reports of Ortner and Hipsley (1994) for the same steel. Ritchie *et al* (1979) measured local fracture stress of 1830 MPa for a SA533B-1 steel of similar chemical composition.

13.3 Enhanced toughness margins from constraint loss

The elevation of toughness due to constraint loss can be quantified deterministically by matching crack tip fields at a local fracture stress (the RKR approach) and statistically by a Weibull stress approach, with results shown in Figures 13.7 and 13.8. The average constraint of $a/w=0.075$ data at each temperature was used in the procedure and the constraint for $a/w=0.5$ data was taken to be $T=+0.1\sigma_o$. The margin on toughness due to constraint loss can be quantified by matching principal stresses at a local fracture stress, giving:

$$\frac{K_{0.075}}{K_{0.5}} = \left[\frac{\sigma_f - Q_{0.075} \cdot \sigma_o}{\sigma_f - Q_{0.5} \cdot \sigma_o} \right]^{\frac{1}{2t}} \quad (13.2)$$

and shown in Figure 13.7. Here the subscript 0.075 denotes shallow cracked data ($a/w=0.075$) and subscript 0.5 represents the deep crack data ($a/w=0.5$). Using the Weibull stress approach, the $\tilde{\sigma}_w^m$ parameter was evaluated across the plastic zone ($\lambda=1$) and Weibull moduli was 15 and 20 were used. The margins on toughness follow as:

$$\frac{K_{0.075}}{K_{0.5}} = \left[\frac{(\tilde{\sigma}_w^m)_{0.5}}{(\tilde{\sigma}_w^m)_{0.075}} \right]^{\frac{1}{4}} \quad (13.3)$$

These are shown in Figure 13.8. Both approaches give good fit with the data close to the lower shelf, while in the ductile-brittle transition range (-120°C to -90°C) the deterministic model underpredicts the data, as observed by Ritchie *et al* (1979). As the Weibull stress was integrated over the entire plastic zone, it implicitly contains a temperature dependent distance term and therefore gives a better match with the experimental data, as shown in

Figure 13.8. However the approach is sensitive to the characterisation of the reliability of the data (Weibull modulus).

13.4 Enhanced temperature margins due to constraint loss

Just as the constrained and unconstrained data sets can be compared by a toughness shift at a constant temperature, the data can also be compared by a temperature shift at a constant toughness. An average constraint for both ($a/w=0.075$ and $a/w=0.5$) data sets was determined with matching average yield stress (temperature) at failure for toughness range increments of $100 \text{ MPa}\sqrt{\text{m}}$, and is given in Tables 13.1 and 13.2. The new yield stress of $a/w=0.5$ data ($\sigma_{o,0.5}^*$) to match the unconstrained data follows from:

$$\sigma_{o,0.5}^* = \frac{1}{\gamma} \sigma_{o,0.5} \quad (13.4)$$

where

$$\gamma = \frac{\sigma_{o,0.075}}{\sigma_{o,0.5}} \left(\frac{\sigma_f - Q_{0.075} \sigma_{o,0.075}}{\sigma_f - Q_{0.5} \sigma_{o,0.5}} \right)^{\frac{1}{2t-1}} \quad (13.5)$$

obtained from matching the fields at a local fracture stress directly ahead of the crack. It should be noted that at failure the critical stress intensification in a shallow cracked geometry is achieved by increasing the yield stress of the constrained field, as opposed to reducing the yield stress to match the crack tip fields in illustrations in Chapter 12. Using the Weibull stress procedure the factor γ is:

$$\gamma = \frac{\sigma_{o,0.075}}{\sigma_{o,0.5}} \left[\frac{(\tilde{\sigma}_w^m)_{0.075}}{(\tilde{\sigma}_w^m)_{0.5}} \right]^{\frac{1}{m-4}} \quad (13.6)$$

This is evaluated for the principal stress calculated from the finite strain boundary layer formulation and integrated over the plastic zone. The temperature shifts shown in Figure 13.9 to 13.11 follow by expressing the change in the yield stress for the constrained data as a temperature shift, using the empirical relation of Equation (13.1). When comparing fields at a fixed local fracture stress and microstructural distance, the temperature shift is underestimated in the ductile-brittle transition (Figure 13.10), with the magnitude of underprediction depending on the value of the local fracture stress, as shown in Figures 13.9 and 13.10.

The results of the statistical procedure using the Weibull stress applied to the A533B-1 data are shown in Figure 13.12. Good agreement with the experimental data is demonstrated using Weibull modulus of 20, characteristic of nuclear pressure vessel steel (Beremin (1983)).

13.5 The effect of simulated neutron irradiation on the temperature shift

The effects of neutron irradiation on material degradation must be considered in demonstrating structural integrity of operating nuclear power plant. The R6/4 code estimates that the neutron irradiation increases the yield stress and the tensile strength in ferritic steel through neutron interaction with point defects and dislocations. An increase of the yield stress from start-of-life value due to neutron irradiation can be approximated as (Ainsworth (2002)):

$$\Delta\sigma_o = 44.6 + 6.17 \cdot F_T \sqrt{D_f + 1.67D_t} \quad (13.7)$$

where

$\Delta\sigma_o$ Increase of the yield stress due to neutron irradiation

F_T Function of irradiation temperature

D_f Fast neutron dose

D_t Slow neutron dose

The maximum increase in the yield stress is limited to approximately 200 MPa and the increase in the tensile strength of irradiated material is taken as 80 percent of the increase of the yield stress ($\Delta\sigma_{TS} = 0.8\Delta\sigma_o$), with both increases taken independent of temperature. A temperature shifts due to constraint loss is then quantified for a start-of-life and irradiated material with the latter being based on the start-of-life yield stress.

First the strain hardening exponent and the elastic-plastic constraint parameter must be determined for both material conditions. The stress-strain curves are then derived for the irradiated material from which the new strain hardening exponent is estimated. Assuming that constraint loss is independent of irradiation effects fixes the level of constraint, parameterised with the applied T-stress or biaxiality, β , and allows comparisons to be made between temperature shifts for irradiated and unirradiated material. The procedure is applied to the unirradiated constrained ($a/w=0.5$) and unconstrained ($a/w=0.075$) A533B-1 data.

13.5.1 Stress-strain curves for the irradiated material

The available tensile test data for the unirradiated A533B-1 material consists of the yield stress as a function of temperature and a fixed strain hardening exponent of 12 (Sherry *et al* (2001)). A Ramberg-Osgood relation given by Eq. (12.2) was used to simulate a hardening behaviour of the material. Due to a non-proportional increase in the yield stress and tensile strength for irradiated material, a new strain hardening exponent must be determined for the irradiated material. The procedure consists of inverting the true stress-true strain curves obtained from Ramberg-Osgood relation for unirradiated material to give the engineering yield stress and tensile strength values, which are listed in Tables 13.1 and 13.2. These were then increased by irradiation effects: yield stress by 200 MPa and tensile strength by 160 MPa to simulate the conditions in severely irradiated material, and are listed Tables 13.3 and 13.4. The temperature dependent yield stress for simulated irradiated material was described by:

$$\sigma_o(\phi) = -1.72 \cdot \phi + 630 \quad (13.8)$$

which is valid for $-170^\circ\text{C} \leq \phi \leq -20^\circ\text{C}$, where ϕ is temperature in $[\text{C}]$ and σ_o is the yield stress in $[\text{MPa}]$. The strain hardening exponent for the simulated irradiated material was estimated using constancy of volume during plastic flow:

$$\frac{\sigma_{\text{TS}}}{\sigma_o} = \left(\frac{1}{0.002n} \right)^{\frac{1}{n}} \exp\left(-\frac{1}{n}\right) \quad (13.9)$$

and was found to be constant at a value of 21, as listed in Tables 13.3 and 13.4. The irradiated material is characterised with lower strain hardening rates compared to the unirradiated material. New true stress - true strain curves were then computed by merging Hooke's law into the Ramberg-Osgood relation for the yield stress of irradiated data using hardening exponent of 21 at each temperature.

13.5.2 Constraint effects for an irradiated material

The procedure used to quantify temperature shift relies on the description of the elastic-plastic crack tip fields with the small-scale yield term plus an elastic-plastic constraint term, Q , which depends on the strain hardening rate. As the strain hardening rate changes between unirradiated and irradiated material, the Q parameter was calculated for irradiated material response using modified boundary layer formulation with the applied T-stress as a boundary condition and $T=0$ as the reference field. The assumption is made that the neutron irradiation does not alter the constraint as described by the biaxiality parameter or

the applied T-stress. However the irradiation does change the parameterisation of constraint using the elastic-plastic parameter, Q , or T/σ_0 , due to elevation in the yield stress. The values of Q for irradiated material at fixed toughness are shown in Figure 13.12 and listed in Tables 13.3 and 13.4 and are close to the values of T/σ_0 , confirming observations of Du and Hancock (1991) that T-stress is approximately equivalent to $Q\sigma_0$ at low hardening rates.

13.5.3 The temperature shift for a simulated irradiated material

The temperature shift was derived for a simulated irradiated material by matching stress fields at a local fracture stress (the RKR approach) and by the Weibull stress model. The fracture stress was calibrated on the high constraint ($a/w=0.5$) unirradiated data to be 2300 MPa, and the value of 1830 MPa from Ritchie *et al* (1979) was also used. The local fracture stress was assumed to be unaffected by the irradiation effects, as the experimental evidence suggesting otherwise is not available. The Weibull stress was determined from a finite strain boundary layer formulation with boundary conditions corresponding to K and T for irradiated material, by integrating the principal stress over the plastic zone for a Weibull modulus of 20. The results of the procedure using the local fracture stress are shown in Figures 13.13 and 13.14, while Figure 13.15 shows the results from using Weibull stress procedure. In part due to higher yield stress and lower strain hardening rate, the constraint effects in simulated irradiated material are more pronounced, giving 10°C to 40°C greater temperature shifts, compared to the unirradiated material.

13.6 Main conclusions to the temperature shift due to constraint loss

- Crack tip stress field are self-similar with respect to yield stress under contained yielding and as a result the constrained crack tip field can be matched to the unconstrained field by change of J or a temperature dependent yield stress.
- This allows constraint loss to be quantified in terms of a toughness margin or as a temperature shift at a fixed toughness.

- The RKR model can be successfully applied over the lower end of the ductile-brittle temperature regime. At higher temperatures the critical micro-structural distance employed in the RKR model must be increased with temperature as cracked carbides develop as voids rather than unstable micro-cracks above critical levels of plastic strain.
- Temperature shift in a irradiated material is 10°C to 40°C greater compared to the start-of-life data, due to higher yield stress and lower strain hardening rates, assuming the irradiation does not affect local fracture properties of the material.

Average toughness K_J [MPa√m]	Temperature ϕ [°C]	Yield stress σ_o [MPa]	Constraint		
			T/σ_o	Q	T-stress [MPa]
100	-115	627.8	0.06	0.04	37.7
200	-72	553.8	0.10	0.065	55.4
300	-53	521.2	0.11	0.07	57.3
400	-41	500.5	0.11	0.07	55.1

Table 13.1:
Summary of average values of experimental data at a fixed toughness for high constrained ($a/w=0.5$) data.

Average toughness K_J [MPa√m]	Temperature ϕ [°C]	Yield stress σ_o [MPa]	Constraint		
			T/σ_o	Q	T-stress [MPa]
100	-136	663.9	-0.46	-0.45	-305.4
200	-117	631.2	-0.61	-0.67	-385.1
300	-110	619.2	-0.63	-0.70	-390.1
400	-96	595.1	-0.68	-0.77	-404.7

Table 13.2:
Summary of average values of experimental data at a fixed toughness for unconstrained ($a/w=0.075$) data.

Toughness K_J [MPa√m]	Temp ϕ [°C]	Yield stress σ_o [MPa]	Tensile strength σ_{TS} [MPa]	Hardening exponent n	Constraint		
					T/σ_o	Q	T-stress* [MPa]
100	-115	827.8	917.3	21	0.05	0.025	37.7
200	-72	753.8	830.0	21	0.07	0.048	55.4
300	-53	721.2	796.2	21	0.08	0.055	57.3
400	-41	700.5	773.1	21	0.08	0.055	55.1

*Assuming T-stress is not influenced by neutron irradiation effects

Table 13.3:

Summary of average values of irradiated constrained data ($a/w=0.5$) over a fixed toughness range.

Toughness K_J [MPa√m]	Temp ϕ [°C]	Yield stress σ_o [MPa]	Tensile strength σ_{TS} [MPa]	Hardening exponent n	Constraint		
					T/σ_o	Q	T-stress* [MPa]
100	-136	863.9	951.0	21	-0.35	-0.32	-305.4
200	-117	831.2	917.3	21	-0.46	-0.47	-385.1
300	-110	819.2	905.9	21	-0.48	-0.50	-390.1
400	-96	795.1	884.5	21	-0.51	-0.54	-404.7

*Assuming T-stress is not influenced by neutron irradiation effects

Table 13.4:

Summary of average values of irradiated unconstrained data ($a/w=0.075$) over a fixed toughness range.

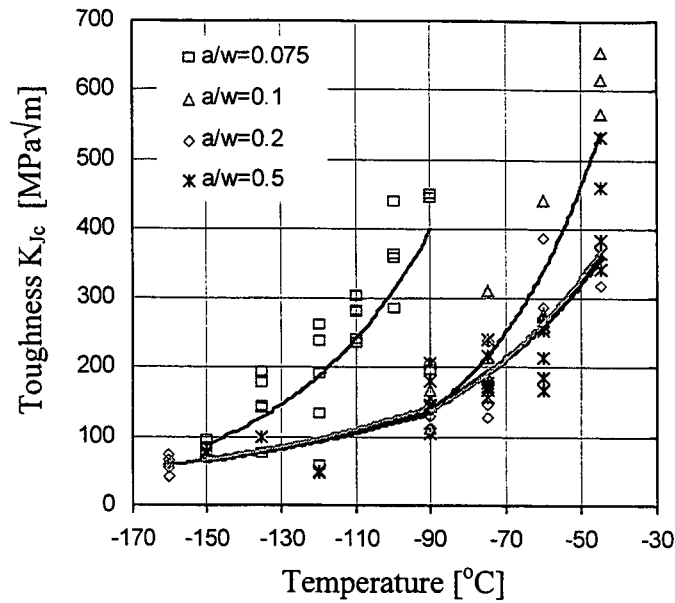


Figure 13.1:
Experimental low and high constraint toughness data from Sherry *et al* (2001) as a function of temperature. Data are curve-fit for clarity.

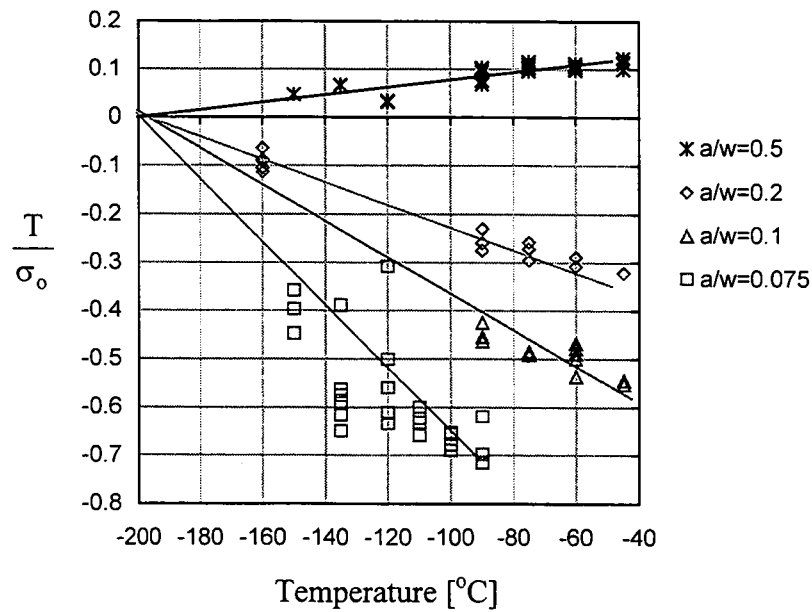


Figure 13.2:
Constraint values in experimental data from Sherry *et al* (2001) as a function of temperature.

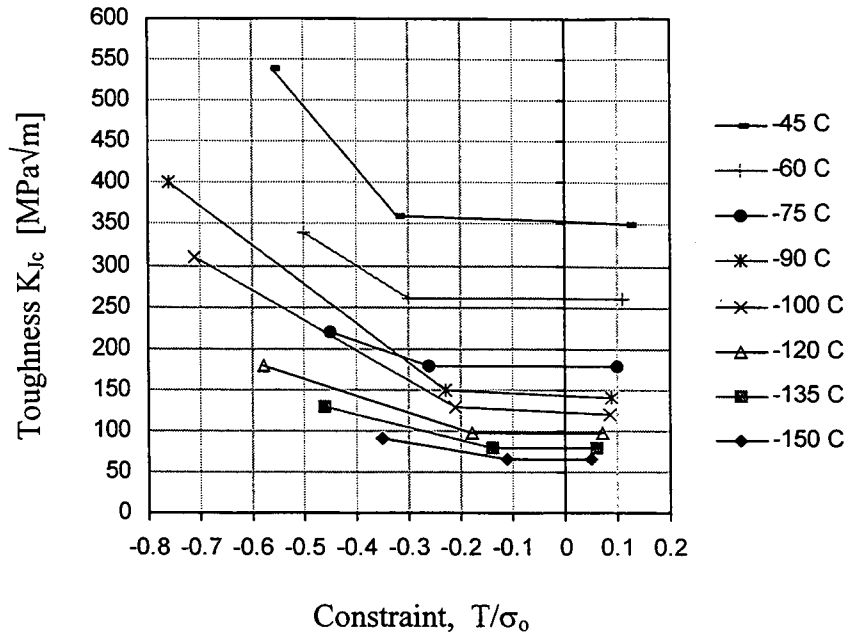


Figure 13.3:
Toughness data from Sherry *et al* (2001) as a function of constraint. Data are curve-fit for clarity.

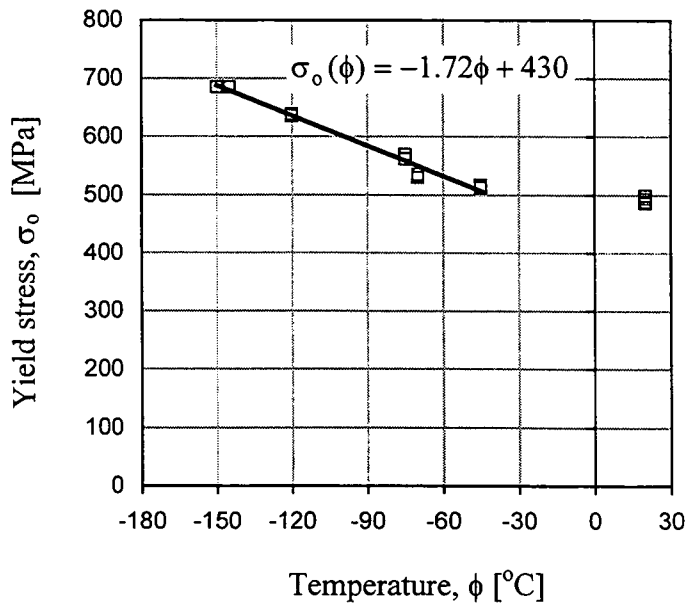


Figure 13.4:
Temperature dependent yield stress re-drawn from data of Sherry *et al* (2001). A linear curve-fit over the temperature range of interest is superimposed.

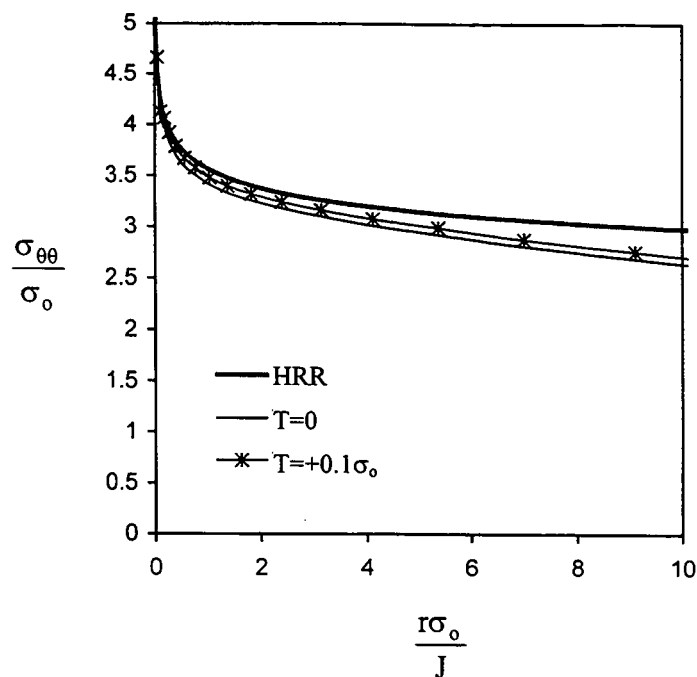


Figure 13.5:
The stress fields based on the HRR and SSY (T=0) singularity directly ahead of the crack. The hoop stress for the field representative of constrained (a/w=0.5) data with T=+0.1 σ_0 is superimposed .

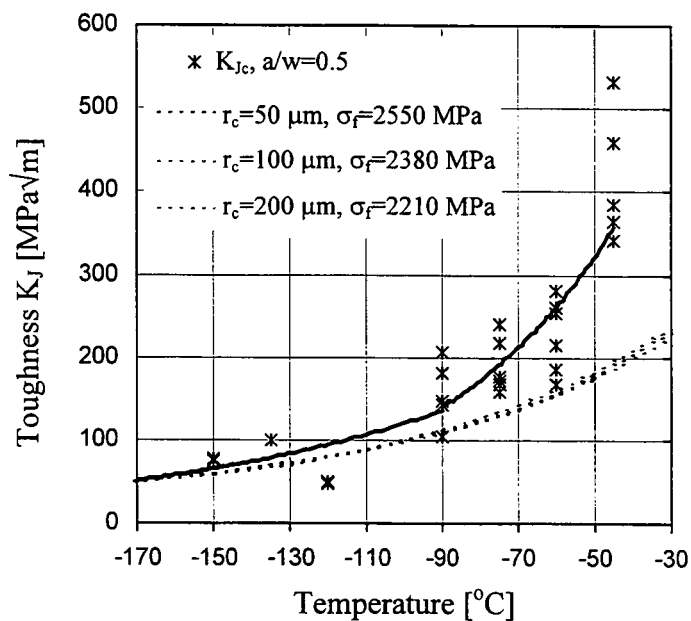


Figure 13.6:
High constraint (a/w=0.5) data fitted with the RKR model using SSY singularity on the lower shelf at three microstructural distances.

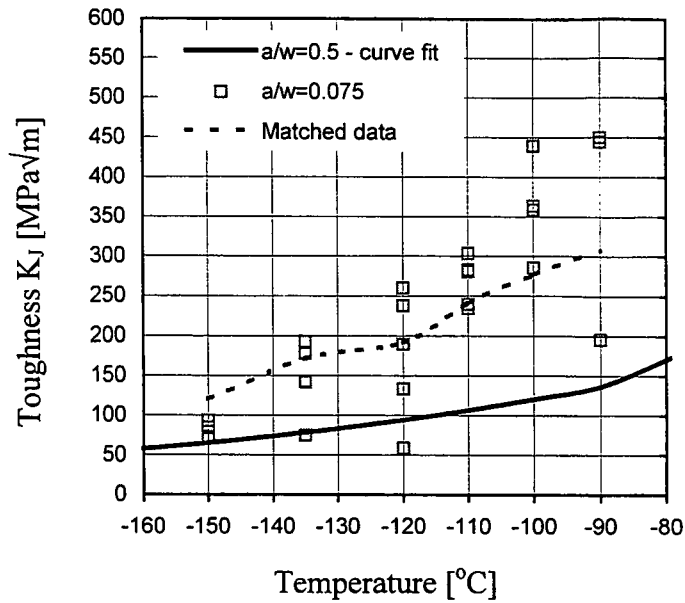


Figure 13.7:
Constraint correction to the shallow cracked ($a/w=0.075$) experimental data obtained by matching fields at a local fracture stress of $\sigma_f=2300$ MPa.

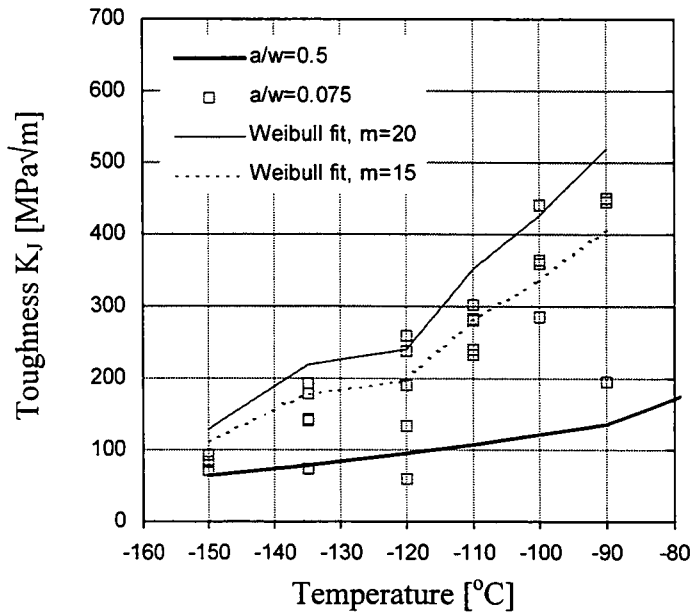


Figure 13.8:
Constraint correction to the shallow cracked ($a/w=0.075$) experimental data obtained by comparing stress fields using the Weibull stress model evaluated in the plastic zone ($\lambda=1$).

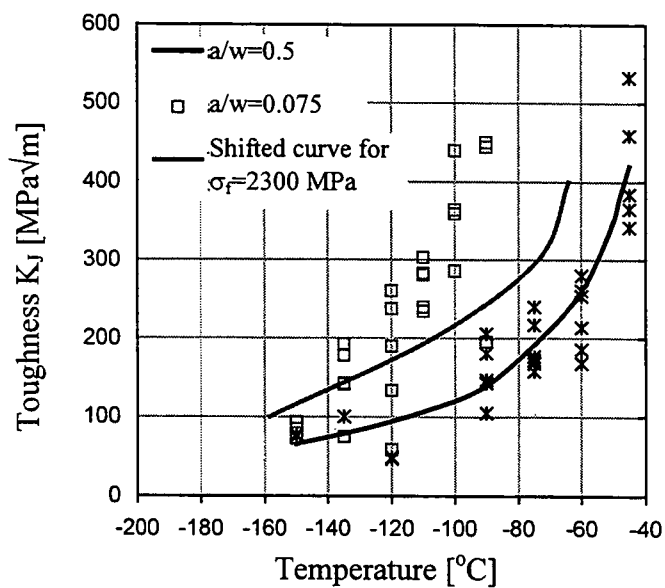


Figure 13.9:
Temperature shifts due to constraint loss for the $a/w=0.075$ data obtained by matching the crack tip fields at a local fracture stress of $\sigma_f=2300$ MPa.

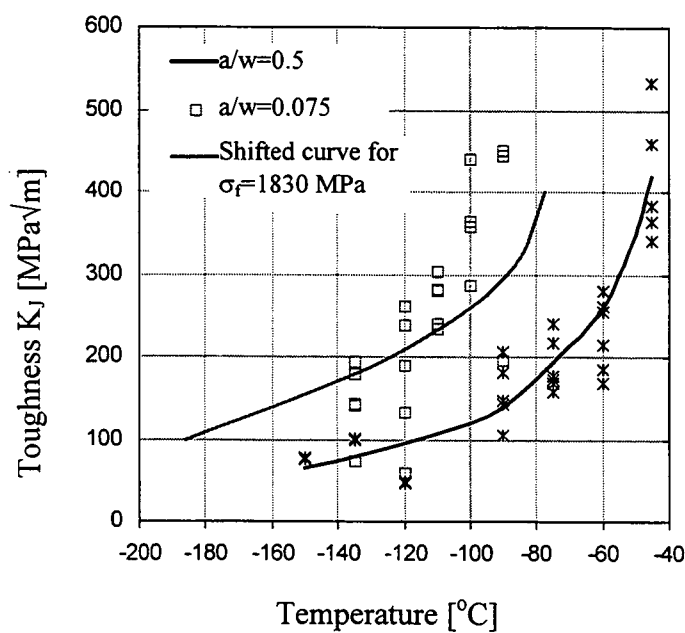


Figure 13.10:
Temperature shifts due to constraint loss for the $a/w=0.075$ data obtained by matching the crack tip fields at a local fracture stress of $\sigma_f=1830$ MPa after Ritchie *et al* (1979).

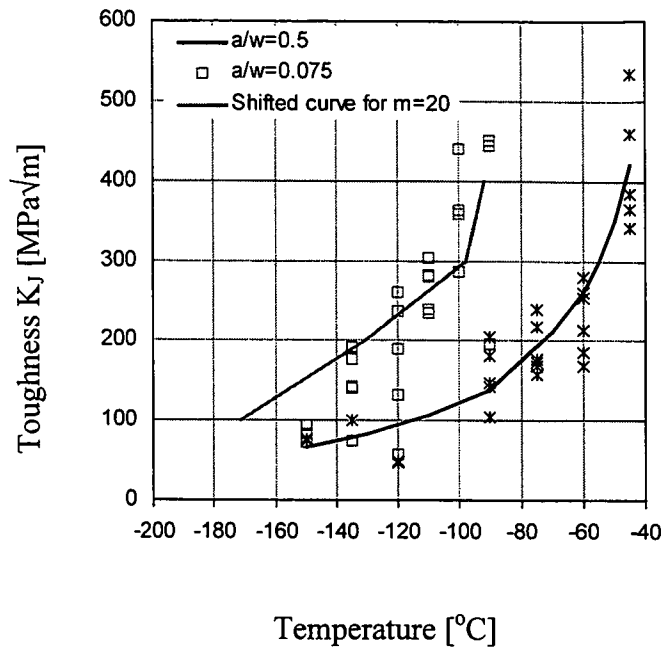


Figure 13.11:
Temperature shifts from constraint loss for the $a/w=0.075$ data, obtained using the Weibull stress evaluated in the plastic zone ($\lambda=1$).

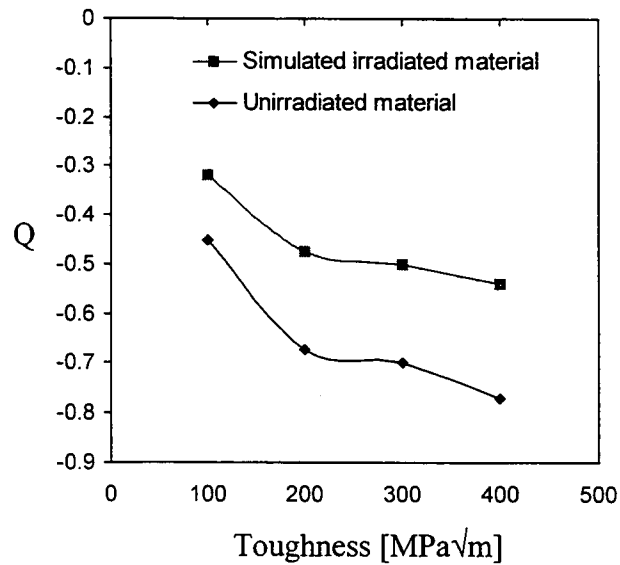


Figure 13.12:
Q parameter for the irradiated and unirradiated material, determined at a fixed toughness for the $a/w=0.075$ data set.

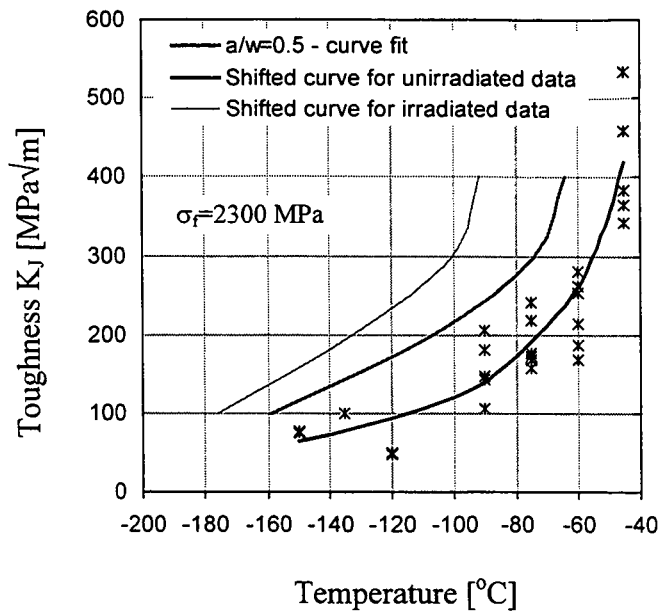


Figure 13.13:
Temperature shift due to constraint loss for unirradiated and irradiated $a/w=0.075$ data by matching stress fields directly ahead of the crack at a local fracture stress of 2300 MPa.

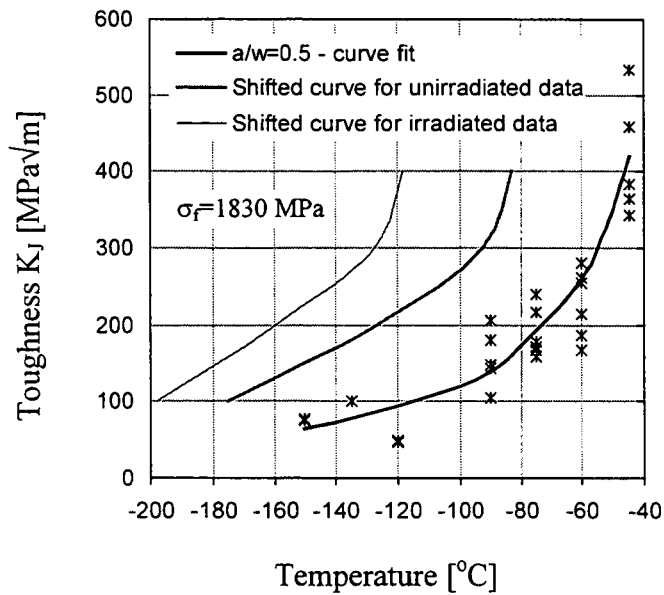


Figure 13.14:
Temperature shift due to constraint loss for unirradiated and irradiated $a/w=0.075$ data by matching stress fields directly ahead of the crack at a local fracture stress of 1830 MPa.

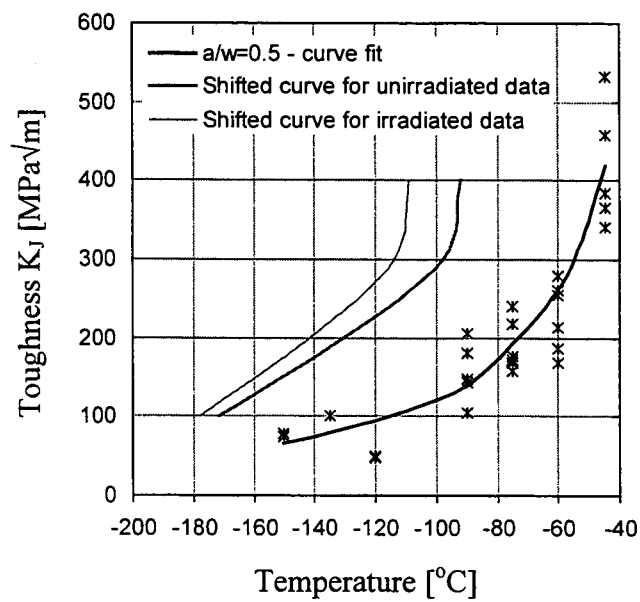


Figure 13.15:
 Temperature shift due to constraint loss for unirradiated and irradiated $a/w=0.075$ data using the Weibull stress model with Weibull modulus of 20 evaluated in the plastic zone.

Chapter 14

MODE I AND MIXED-MODE CRACK TIP FIELDS UNIFIED BY CONSTRAINT

In this section of the thesis Mode I and mixed-mode crack tip fields are shown to belong to the same family of fields and can be unified in a single toughness-mixity-constraint locus. First the structure of mixed mode fields under small scale yielding conditions is summarised following Li (1997). An extensive experimental programme was performed to measure fracture toughness and constraint for a family of unconstrained Mode I and mixed-mode cracks. The experiments combined with the numerical work of Li (1997) confirm a correlation between constraint and mixity through toughness measured by J .

14.1 Mixed-mode fields

14.1.1 Slip line fields

During perfectly-plastic deformation, the plastic strains at the crack tip are assumed to dominate the elastic components, such that deformation is almost incompressible. Under these circumstances the stress field is determined by the hydrostatic or mean stress, $\sigma_m = \sigma_{kk} / 3$, and the yield criterion. The hydrostatic stress at the tip ($r=0$) is illustrated as a function of angle θ in Figure 14.1 for five levels of mixity, while the angular span of the Mises stress is shown in Figure 14.2, obtained from boundary layer computations.

The structure of the plastic sectors of the field can be identified from the hydrostatic component. Rice and Tracey (1973) have shown that for incompressible plane strain deformation, combination of the yield criterion, the plane strain condition and the necessity for the crack tip stresses to be bounded allows the equilibrium equations to be written in the form:

$$\frac{\partial(\sigma_{rr} + \sigma_{\theta\theta})}{\partial\theta} \times \frac{\tau_{r\theta}}{\partial\theta} = 0 \quad (14.1)$$

This leads to two possible forms for the plastic sectors, either

$$\frac{\partial(\sigma_{rr} + \sigma_{\theta\theta})}{\partial\theta} = \frac{1}{2} \frac{\partial\sigma_m}{\partial\theta} = 0 \quad (14.2)$$

or

$$\frac{\partial \tau_{r\theta}}{\partial \theta} = 0 \quad (14.3)$$

The first condition corresponds to regions in which the mean stress does not change with angle around the tip, and thus comprises constant stress sectors in which the slip lines are straight. The second condition corresponds to the situation in which the shear stress in cylindrical co-ordinates does not change with angle. As the slip lines are trajectories of constant shear stress, this corresponds to centred fans, in which the hydrostatic stress varies linearly with angle.

In association with the yield criterion these observations enable the angular span of the elastic and plastic sectors to be identified, and allows the field to be assembled. In all the numerical examples shown in Figure 14.1, the regions of constant stress have an angular span of $\pi/2$ or $\pi/4$, leading to continuous stress fields. However the orientation of the constant stress diamond rotates with mixity. The angular span of the centred fans is determined from the angular range over the region in which the mean stress varies linearly with angle. Finally the fields are completed by noting the span over which the yield criterion is not satisfied corresponds to elastic wedges. The complete family of fields is assembled in Figure 14.3, where the angles given to the left of the slip line fields are the elastic displacement vectors on the crack flanks and the angle to the right are the orientation of the maximum hoop stress.

The mixed mode fields are simple distortions of the Mode I field corresponding to a rotation of the main constant stress diamond. This allows a continuous plastic field to extend to the crack flanks with a uniform stress triangle on the tensile side, while the elastic wedge on the compressive flank increases its angular span. This process continues with increasing mixity until the pure Mode II field is recovered. This field is identical to that discovered by Hutchinson (1968) as plasticity now fully surrounds the crack tip corresponding to the Mode II HRR field.

The angle of maximum hoop stress is the direction radially out through the apex of the constant stress diamond. This angle is of particular interest in terms of stress controlled brittle fracture. It is frequently argued that such failure occurs at the orientation at which the propagating crack extends in Mode I (Erdogan and Sih (1963), Williams and Ewing (1972)). In the case of non-hardening plasticity the crack tip stress at this angle may be

compared with the stress in an unconstrained Mode I field. In non-hardening plasticity it is convenient to focus attention at the tip, where mixed-mode fields can be correlated with Mode I fields which have the same level of constraint. In the pure Mode I field the direction of interest is directly ahead of the crack, whereas in the mixed-mode problem it is inclined at an angle which is a function of mixity.

14.1.2 Strain hardening solutions

It is now appropriate to turn attention to the effect of strain hardening. In uniaxial tension the material has been allocated an isotropic elastic response for stresses less than the uniaxial yield stress, σ_0 . Yield is determined by the Von Mises yield criterion and the associated flow rule using small strain theory. At stresses greater than the yield stress the material follows a law which approximates to a Ramberg-Osgood stress-strain relation.

Numerical calculations were performed by Li (1997) for the elastic mixities given in Table 14.1 with strain hardening exponent, $n=12$ and 6. Attention has been focused on the plane on which the maximum principal stress and minimum shear stress occur. In Mode I this is directly ahead of the crack but in the mixed-mode loading the angle is weakly dependent on the hardening rate over the range of interest (Shih 1974) and the numerical data have been taken from the radial node set closest to this angle. The stresses are non-dimensionalised with respect to the uniaxial yield stress, σ_0 , while the radial distance from the crack tip, r , is non-dimensionalised by J/σ_0 .

Figure 14.4 shows numerical results for a range of mixities ranging between 0 and 1. The important point is that the stress profiles for all the mixities are parallel. At this orientation, they can therefore be regarded as a family of fields which differ by a second order term which is independent of distance.

Figure 14.5 shows numerical results for Mode I modified boundary layer formulations, in which constraint loss is associated with T . Again the central observation is that for a given hardening rate all these stress profiles are parallel. That is to say, the stress level associated with a mixed mode problem can be identified with the loss of constraint in a Mode I loading. The relationship between mixity and Q or T is shown for these strain hardening calculations in Figures 14.6 and 14.7. O'Dowd and Shih (1991) have argued that Mode I

fields are deviatorically similar but differ largely hydrostatically through a parameter Q . In this context the maximum stress deviator, $S_{\theta\theta}$ directly ahead of the Mode I fields is given in Figure 14.8 for an unconstrained Mode I field and in Figure 14.9 for a mixed-mode field. Comparison of Figures 14.8 and 14.9 indicates that the mixed mode fields differ largely hydrostatically in the same manner as the Mode I J-Q/T fields.

14.2 Fracture Criteria

The constraint dependent fracture toughness which is observed in Mode I can be expressed as a fracture locus in which the toughness is given as a function of a constraint parameter Q/T. Extensive Mode I data have been presented by Sumpter and Hancock (1991), Sumpter and Forbes (1992), Kirk *et al* (1993) and complement the data presented in the later part of the work.

In Mode I, cleavage is often interpreted on the basis of local criteria which involve the attainment of a critical stress over a micro-structurally significant distance directly ahead of the crack as proposed by Ritchie-Knott-Rice (1973). In mixed mode loading, the direction of crack propagation has also been identified with the plane of maximum hoop stress (Erdogan and Sih (1963), Williams and Ewing (1972) and Budden (1987)) which occurs at an inclined angle, such that the propagating crack grows locally in Mode I.

The constraint of Mode I and mixed mode fields have been correlated in Figures 14.6 and 14.7. Constraint based Mode I failure loci can now be mapped into mixed-mode small scale yielding data for stress controlled fracture. The procedure is illustrated with the experimental data obtained from a tests on deep and shallow edge cracked bend bars in mode I and mixed mode I+II condition, on a plain carbon steel.

14.3 Experimental details

Specimens of width, $W=24$ mm, thickness, $B=11.5$ mm and length 130 mm were machined from bars of a plain carbon steel (En32). The chemical composition is given in Table 14.2 and the tensile properties are listed in Table 14.3. Specimens were notched with a slitting wheel and fatigue pre-cracked, in accordance with ASTM E399-88 (1988). Shallow cracked specimens were obtained by machining the deeply cracked specimens, while maintaining the width of the uncracked ligament. Fracture toughness tests were performed

using an environmental chamber cooled with liquid nitrogen. Tests were performed at -90°C , where failure occurred by cleavage in full plasticity with minor ductile tearing preceding failure in shallowest geometries. Temperature was measured with spot-welded thermocouples and was maintained within $\pm 2^{\circ}\text{C}$ during testing. Before applying the displacement controlled load at cross-head velocity of 0.5 mm/min , specimens were maintained at the test temperature for minimum of 12 minutes (1 min/mm width).

Mode I tests were performed on deep ($a/w=0.5$) and shallow ($a/w<0.3$) edge cracked bend bars in symmetric three-point-bending (3PB). The mixed-mode tests were performed in asymmetric four-point-bending arrangement (A4PB), described by Maccagno and Knott (1989), which allows the use of the same type of specimens and provides a wide range of mode mixities, by positioning the specimen in the stress field composed of shear and bending stresses, as illustrated in Figure 14.10.

The toughness values were characterised by J-integral and comprise of the elastic and plastic components, as discussed in Chapter 2. The elastic component of the J-integral in mixed mode loading is:

$$J_{\text{el}} = \frac{K_{\text{I}}^2 + K_{\text{II}}^2}{E} (1 - \nu^2) \quad (14.4)$$

where the stress intensity factors were calculated using expressions of Maccagno and Knott (1989):

$$K_{\text{I}} = \frac{M}{BW^{3/2}} Y_{\text{I}}, \quad K_{\text{II}} = \frac{Q}{BW^{1/2}} Y_{\text{II}}, \quad (14.5)$$

Here M is the bending moment, Q is the shear force and Y_{I} and Y_{II} are the Mode I and Mode II calibration functions. The Young's modulus was measured to be 217 GPa and ν was taken to be 0.3 . The plastic part of the J-integral was determined from the plastic work done under load – crack-mouth-opening-displacement record, using $\eta_{\text{J-C}}$ factors given by Kirk and Dodds (1993) for shallow mode I cracks. Specific $\eta_{\text{J-C}}$ factors were calculated using finite element model for each mixed-mode test configuration and are listed in Table 14.4. The fracture toughness was then expressed in stress intensity factor notation, as discussed in Chapter 2.

14.4 Experimental results

All failures occurred by cleavage in large scale plasticity, although minor ductile tears were observed for very shallow cracks ($a/w < 0.1$) and large mode mixities ($M^e < 0.66$). These were in all cases less than 0.3mm. Under these conditions constraint effects could be invoked for shallow cracked specimens and associated with higher fracture toughnesses compared to the deep cracked geometries. The test set-up, failure load and toughness (K_{Jc}) are given in Table 14.5 for Mode I configurations, while Table 14.6 summarises mixed-mode test results. Photographs of specimens fractured in mixed-mode loading are shown in Figure 14.11, while the fracture toughness values for both sets of tests are shown in Figure 14.12 as a function of constraint and mixity.

The data are analysed using failure assessment diagrams of R6/4 (2001), which are used to infer margins against failure by interpolating between elastic fracture and plastic collapse modes of failure of a cracked structure. For mixed-mode loading, the R6 recommends the use the effective stress intensity factor, defined by superposition of mode I and Mode II contributions. The loads are normalised by the limit load of each configuration, obtained from a full-field solution using ABAQUS, while K_{eff} on the ordinate is normalised with the lower bound deep cracked mode I value (R6/4 (2001)). In this manner both sets of results are assessed independently. The results of unconstraint mode I and mixed-mode tests are close, as shown in Figure 14.13, demonstrating that the two fields differ only by a hydrostatic component, and the T/Q constraint effects can be mapped into mixity.

Mixed-mode fracture toughness data are mapped into Mode I toughness-constraint locus, by using relation between constraint and mixity given in Figure 14.6 for $n=12$. The results are shown in Figure 14.14, where an excellent agreement between the Mode I data and mapped mixed-mode values is observed. The experimental fracture toughness data can also be used to generate the Q/T vs mixity locus, by correlating the constraint with mixity at a fixed fracture toughness value. This is shown in Figure 14.15 together with the correlation obtained by matching stress fields at a local fracture stress (Anderson and Dodds (1991)). Following Gao and Dodds (2001) the probabilistic Weibull stress model can also be used to match Mode I and mixed-mode data, hence infer constraint-mixity locus. The non-dimensional Weibull stress parameter is integrated in the plastic zone using finite strain

boundary layer formulation (Gao and Dodds (2001)) and the results are superimposed in Figure 14.15.

14.5 Conclusions

In mode I, in-plane constraint loss may give rise to a family of elastic-plastic crack tip fields which can be described by J and a second parameter, which determines the level of crack tip constraint (Q). This family of fields differs in a largely hydrostatic manner. Mixed mode field can be interpreted as belonging to the same family such that constraint loss by mixed mode loading results in a family of fields which differ largely hydrostatically on the plane of maximum hoop stress. For stress controlled brittle fracture this allows the constraint enhanced toughness observed in unconstrained Mode I fields to be correlated with the constraint enhanced toughness in mixed-mode loading.

It was shown by Li (1997) that the deformation fields of an interfacial crack at a rigid substrate can also be correlated with the deformation fields of a crack located in a homogeneous material. The same is true for an interfacial crack between strength mismatched materials, as observed by the deformation fields in non-hardening material and by the principal and deviatoric stress components for a strain hardening material. More generally, the constraint of mode I fields parameterised by Q can be correlated with the constraint of interfacial mixed mode fields parameterised by elastic mixity, as shown in Figure 14.16, allowing the fracture resistance of homogeneous mode I, mixed-mode I+II and interfacial configurations to be unified in a single constraint based fracture toughness locus.

Mixity	M^e
K_I	1.00
$K_I = 4 K_{II}$	0.84
$K_I = 2 K_{II}$	0.71
$K_I = K_{II}$	0.5
$K_I = 0.5 K_{II}$	0.30
K_{II}	0.00

Table 14.1:
Elastic mixity for range of plane strain mixed mode fields.

C	Si	Mn	P	S	Cr	Mo	V
0.18	0.26	0.70	0.014	0.027	0.10	0.02	<0.003

Table 14.2:
Chemical composition of En32 steel (in wt%)

	20 °C	-90 °C
Upper yield strength [MPa]	330	480
Lower yield strength [MPa]	316	429
Tensile strength [MPa]	507	610
% elongation	34 ⁺	26 ⁺⁺
Strain hardening exponent*	7	9

* Derived from constancy of volume during plastic flow

⁺ Measured on gauge length of 28 mm

⁺⁺ Measured on gauge length of 55 mm

Table 14.3:
Tensile properties of En32 steel.

Elastic mixity, M^e	0.91	0.87	0.78	0.66	0.50
Local mixity, M^p	0.93	0.85	0.80	0.78	0.68
η_{plCMOD}	0.6	0.57	0.49	0.43	0.40

Table 14.4:
 η_{plCMOD} calibration factors for deep cracked ($a/w=0.5$) bend bars over a range of mode-mixities in asymmetric four-point-bending.

Test	a/w	F _f [kN]	J _{el} [N/mm]	J _{pl} [N/mm]	K _{Jc} [MPa√m]	T/σ _o
M25	0.060	12520	11.6	965.7	482.8	-0.92
M17	0.105	10800	12.6	336.2	288.4	-0.63
M21	0.102	8600	7.8	46.8	114.1	-0.50
M18	0.173	9240	11.7	53.4	124.6	-0.34
M19	0.251	9940	13.7	64.4	136.5	-0.17
M10	0.512	16220 ⁺	17.7	0.0	64.9	+0.18
M20	0.510	9900	15.9	34.2	109.3	+0.15

⁺ Test performed in symmetric four-point bending at -100°C

Table 14.5:

Results of fracture toughness tests on Mode I cracks in three-point bending at -90°C.

Test	M ^o	F _f [kN]	K _{I,f} [MPa√m]	K _{II,f} [MPa√m]	J _{pl} [N/mm]	K _{Jc} [MPa√m]	φ [°]
M10	1.0	16220 ⁺	64.9	/	0.0	64.9	0
M20	1.0	9900 ⁺⁺	61.6	/	34.2	109.3	2
M16	0.91	16100 [*]	62.4	7.9	84.1	154.9	12
M23	0.87	40600	75.2	14.6	130.1	192.1	17
M15	0.78	45500	41.2	16.4	69.9	136.5	28
M13	0.66	57400	24.7	20.7	97.2	155.6	29
M14	0.66	62000	26.7	22.4	218.1	230.7	39
M22	0.50	69400	10.4	25.7	206.9	223.8	46

⁺ Test performed in symmetric four-point bending at -100°C

⁺⁺ Test performed in three-point bending

^{*} Test performed in three-point bending with a crack offset of 20mm

Table 14.6:

Results of fracture toughness tests on mixed-mode cracks having a/w=0.5 in asymmetric four-point bending at -90°C.

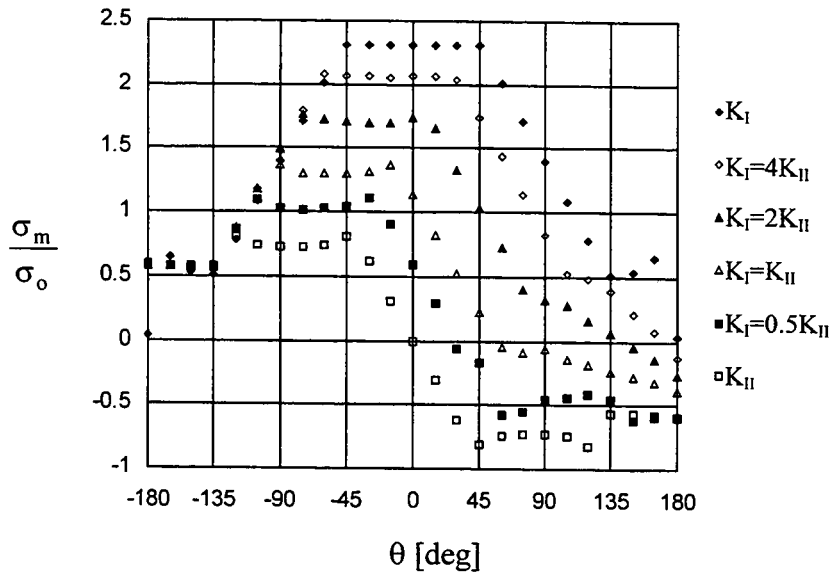


Figure 14.1:
Mean stress non-dimensionalised by the yield stress as a function of angle for a range of mixities in a non-hardening material, after Li (1997).

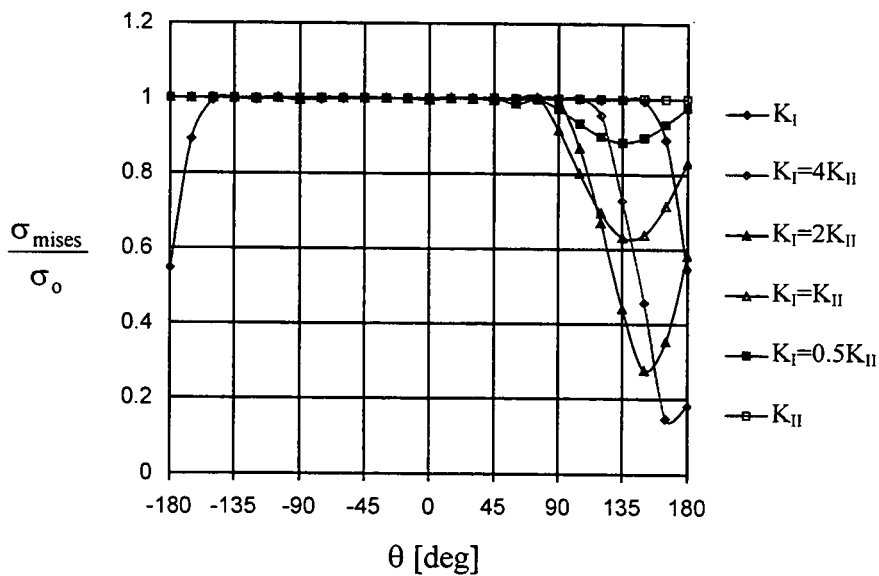


Figure 14.2:
Mises stress non-dimensionalised by the yield stress as a function of angle for a range of mixities in a non-hardening material, after Li (1997).

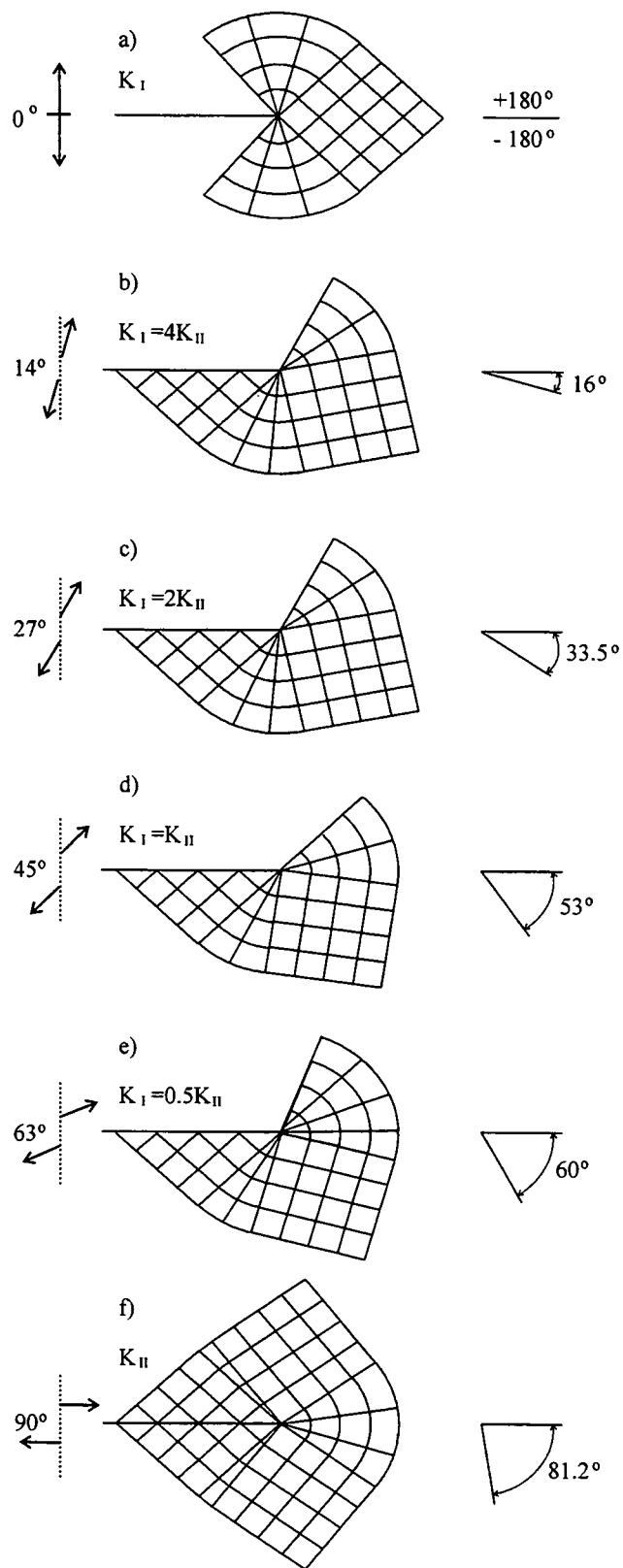


Figure 14.3:
Slip line fields for a family of mixed mode problems at $T=0$, after Li (1997).

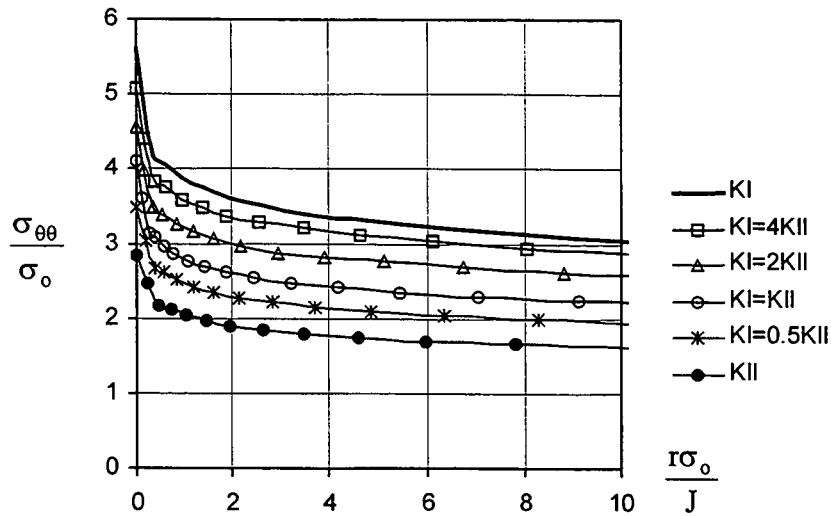


Figure 14.4:
The maximum hoop stress of mixed-mode cracks as a function of the non-dimensionalised distance from the crack tip, after Li (1997).

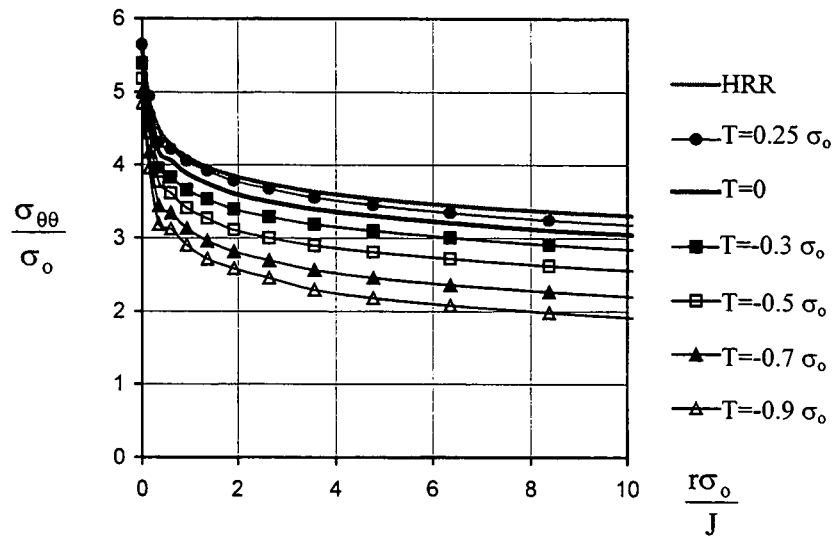


Figure 14.5:
The hoop stress directly ahead of a Mode I crack as a function of the non-dimensionalised distance from the crack tip for a range of $\frac{T}{\sigma_0}$ values, after Li (1997).

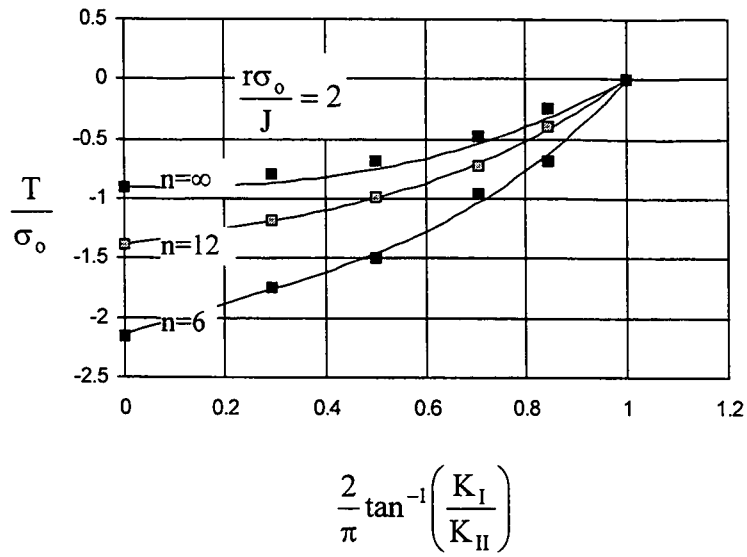


Figure 14.6:
T-stress as a function of mixity for a range of hardening rates, after Li (1997).

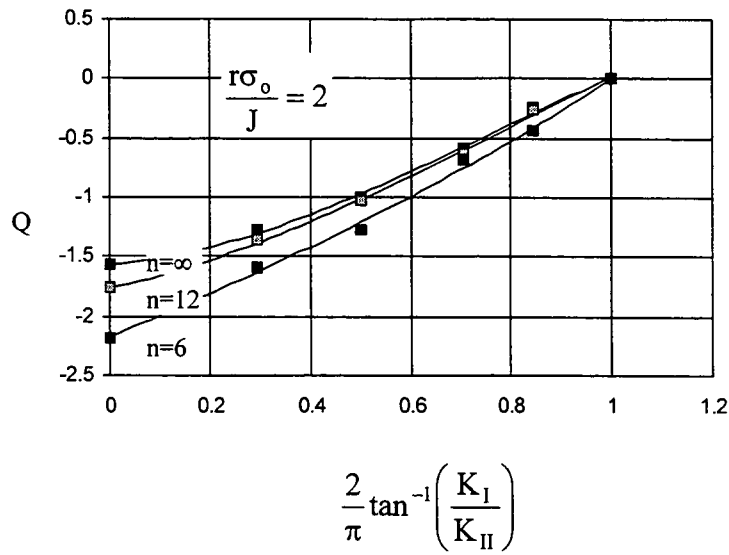


Figure 14.7:
Q as a function of mixity for a range of hardening rates, after Li (1997)

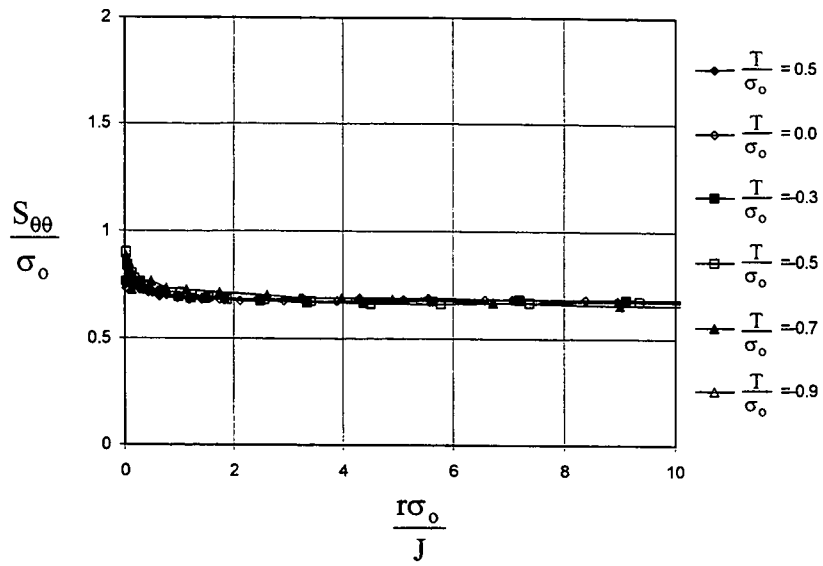


Figure 14.8:
The stress deviator, $S_{\theta\theta}$, non-dimensionalised by the yield stress directly ahead of Mode I crack for a range of $\frac{T}{\sigma_0}$ values, after Li (1997).

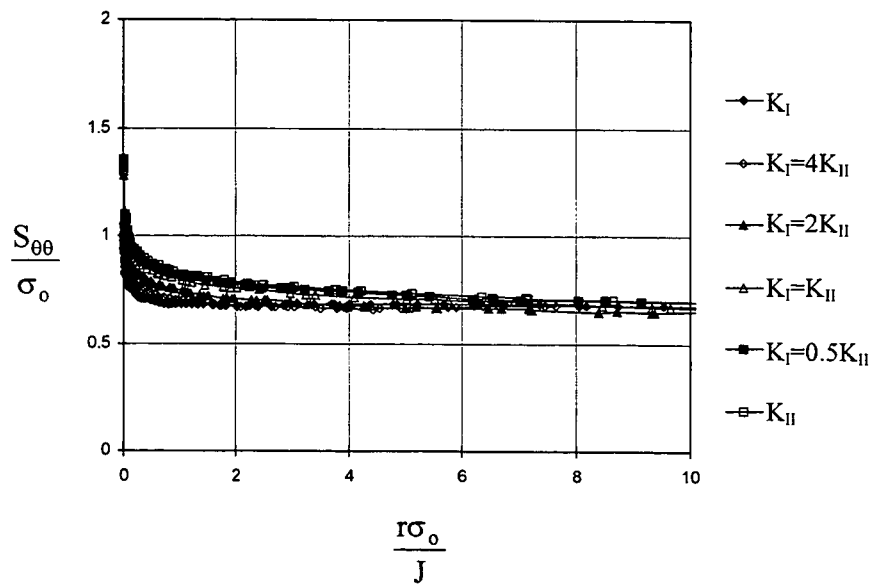


Figure 14.9:
The stress deviator, $S_{\theta\theta}$, non-dimensionalised by the yield stress on the plane of maximum hoop stress in mixed-mode cracks, after Li (1997).

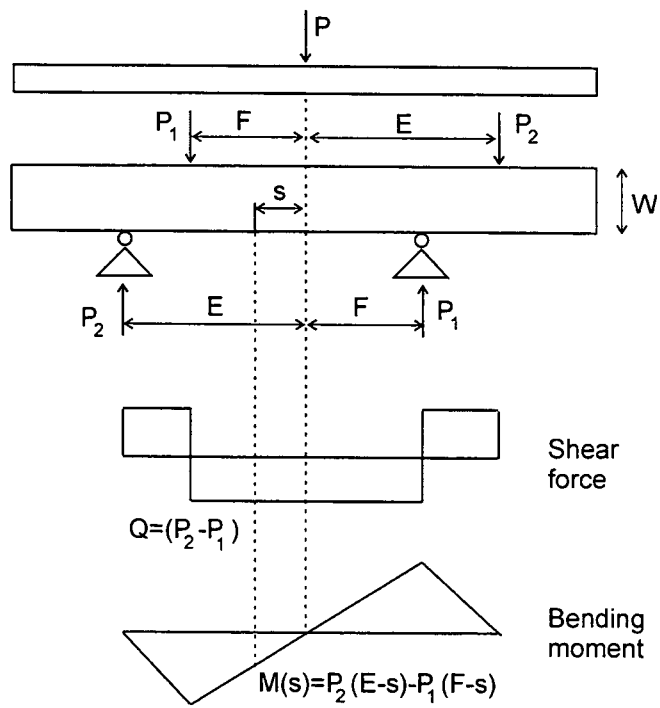


Figure 14.10:
 Illustration of the asymmetric four-point bend loading arrangement, after
 Maccagno and Knott (1989).

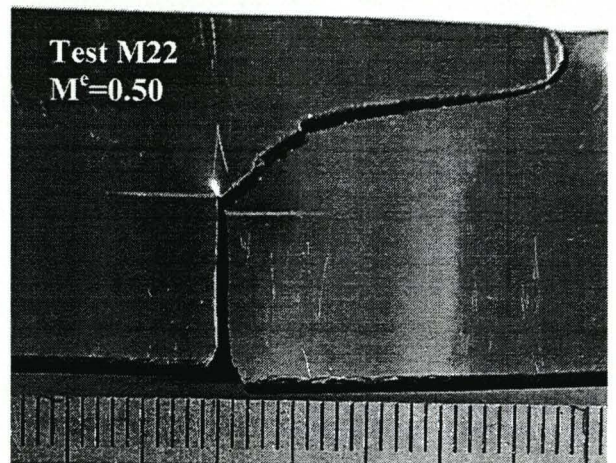
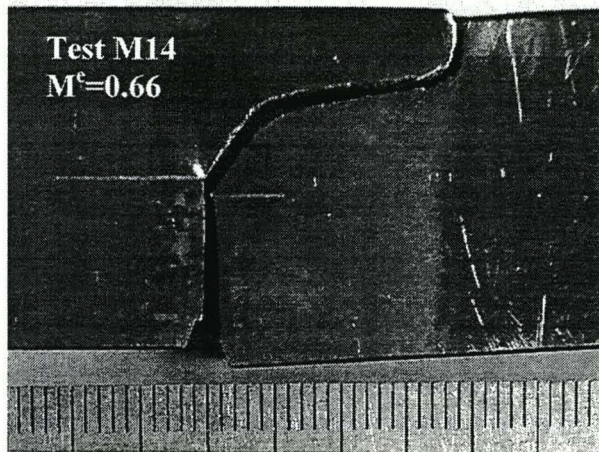
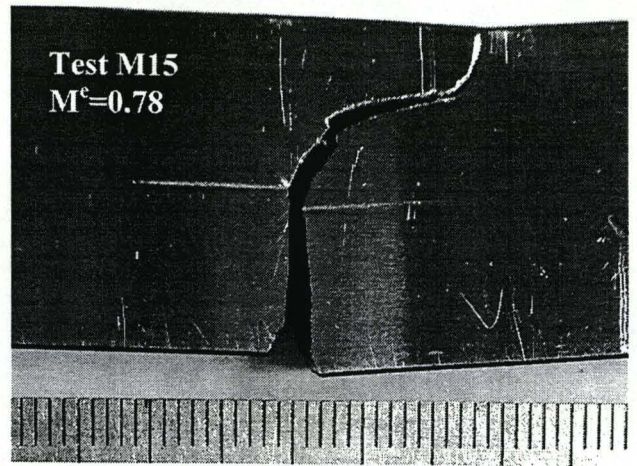
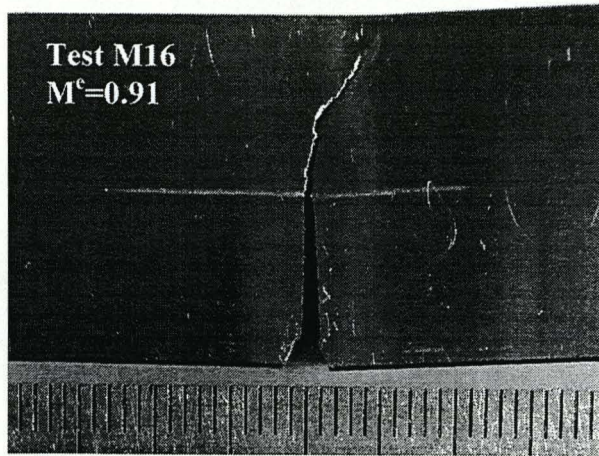


Figure 14.11:
Photographs of specimens tested to cleavage under mixed-mode loading, showing crack propagation direction as a function of mixity.

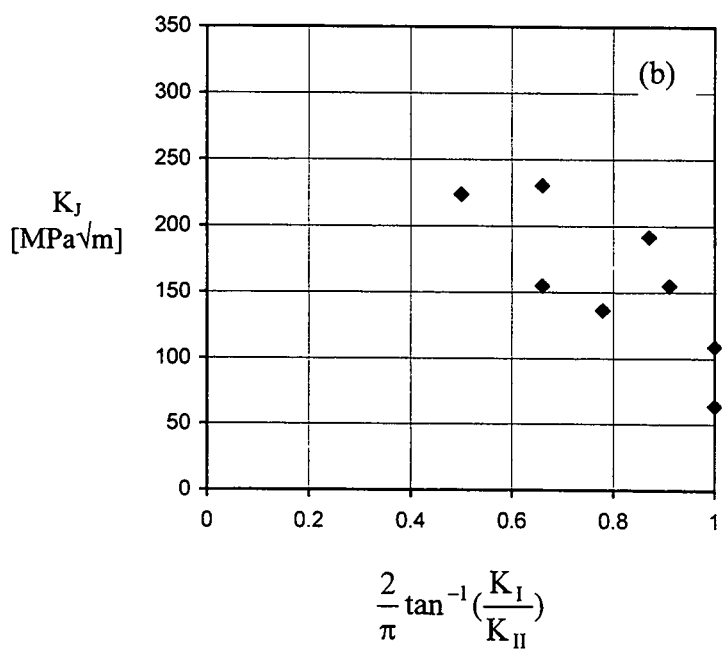
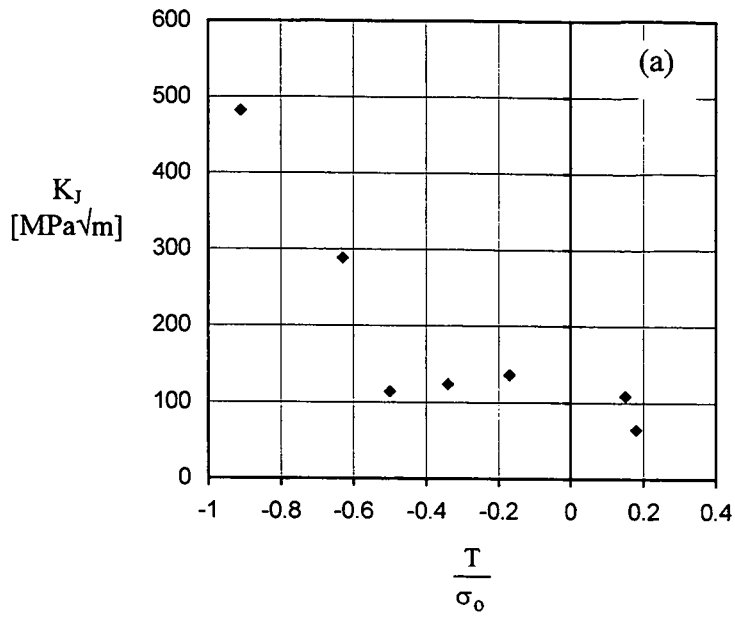


Figure 14.12:
 Results of fracture toughness tests on unconstrained Mode I cracks shown in (a) and mixed-mode I/II cracks shown in (b).

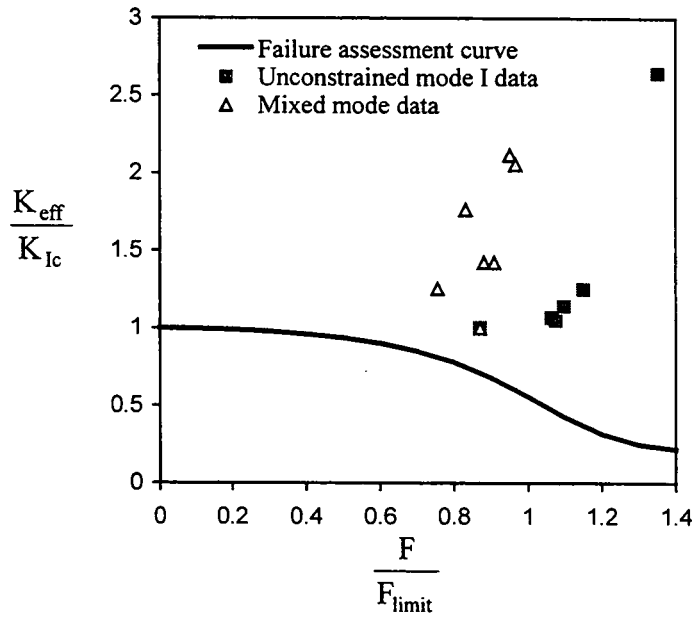


Figure 14.13:
Unconstrained Mode I and mixed-mode I/II toughness data plotted in a failure assessment diagram.

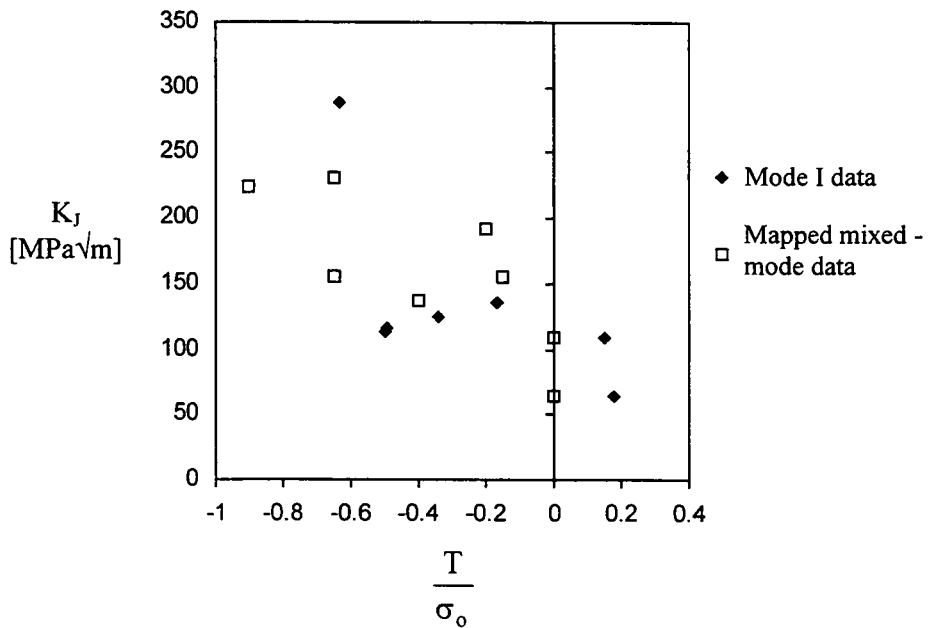


Figure 14.14:
Unification of mode-mixity and in-plane constraint loss, shown by Mode I data and mapped mixed mode I+II data into a common constraint-mixity locus.

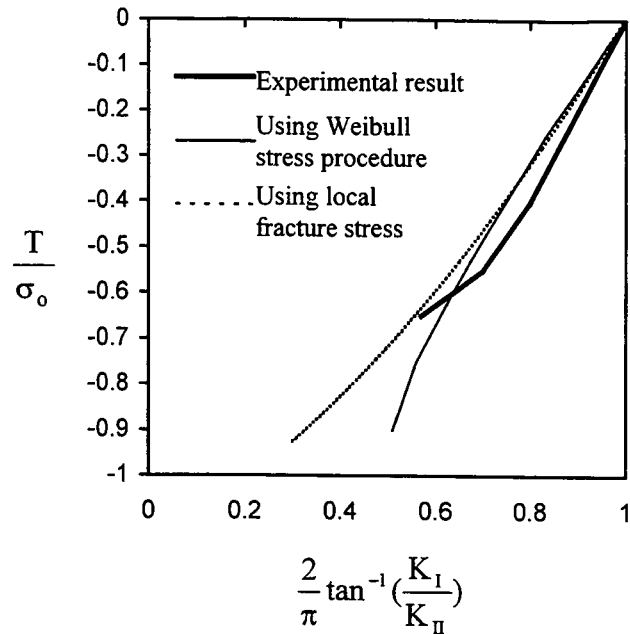


Figure 14.15: Constraint-mixity locus derived from the experimental data and superimposed predictions obtained by matching fields at a local fracture stress or by using the Weibull stress procedure of Gao and Dodds (2001).

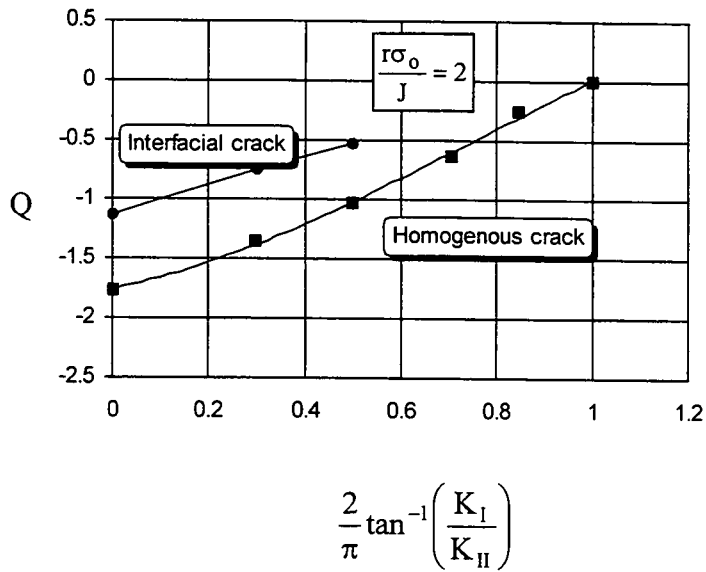


Figure 14.16: Correlation between the constraint parameter and remote mixity for interfacial cracks, after Li (1997).

Chapter 15

FRACTURE MECHANICS OF LASER WELDED JOINTS

15.1 Introduction

The components of welded structures often have elastically matched properties but may differ in strength. A crack in a strength mismatched joint may experience a spatial gradient in plastic deformation resistance which affects the crack tip stress and deformation fields. The relative strength of the constituents forming the joint is quantified by a strength mismatch, defined by the ratio of the yield stress of the weld to the base metal:

$$M = \frac{\sigma_{oW}}{\sigma_{oBM}} \quad (15.1)$$

Here σ_{oW} is the yield stress of the weld metal and σ_{oBM} of the base material. Welded joints are usually designed so that the weld metal is stronger than the base material, giving an overmatched joint. This is intended to restrict plastic deformation in the weldment. In undermatched welds the base material is stronger than the weld metal. As it is difficult to extract tensile specimens from weld microstructures to determine the local yield stresses, a relation between the yield stress (σ_o) and Vickers hardness measurements (HV) is used. BS 7448:2 (1997) recommends the use of the expressions:

$$\text{For parent material: } \sigma_o = 3.28\text{HV} - 221; \quad 160 < \text{HV} < 495 \quad (15.2a)$$

$$\text{For weld material: } \sigma_o = 3.15\text{HV} - 168; \quad 150 < \text{HV} < 300 \quad (15.2b)$$

to define strength mismatch for carbon steels.

15.2 Numerical examinations of crack tip fields in mismatched joints

The stress fields of cracks located in inhomogeneous material systems depend on the relative strengths of the constituents. Joch *et al* (1993) and Eripret *et al* (1997) have demonstrated that slip line fields in bending and tension depend on the yield stress of the base material adjacent to the weld material containing the crack. Burstow *et al* (1998) examined crack tip fields for a crack located in the weld centerline subject to undermatching and overmatching conditions. For undermatched welds the base material constrained the plasticity to the weld material, while the opposite effect occurred for the overmatched welds, as illustrated in Figure 15.1 taken from Burstow *et al* (1998). In both cases the asymptotic stress field of a crack in the weld metal is of a homogeneous nature,

until it reaches the weld-base material boundary. Under continuous loading the plastic zone then extends in the weaker material. As most welds are designed to be overmatched compared to the parent plate, asymmetric plastic zones develop and ductile crack extension occurs into the base material.

Parametric studies of the effects of weld width and mismatch on the opening stresses ahead of the crack by Burstow *et al* (1998) show that stress levels ahead of a crack located in the center of undermatched welds were higher than the homogeneous configuration subject to the same remote loading, as shown in Figure 15.2. For overmatched configurations the stresses were lower, producing an effect similar to applying a negative T-stress in a homogeneous material. Narrow welds are particularly sensitive to mismatch as the proximity of the material with different strength influences development of the crack tip field earlier during the loading history than in wider welds. These effects are illustrated in Figure 15.2, which is taken from Burstow *et al* (1998). A comparison of the contours of plastic strains for two weld widths (Figure 15.1), allowed Burstow *et al* (1998) to argue that the stress fields in welds of unequal widths are self similar when loaded to the same value of $J/h\sigma_{0W}$, where h is the weld semi-width and σ_{0W} is the yield stress of the weld metal. This is illustrated in Figure 15.3, where plots of normalized opening stresses for several weld widths loaded to the same $J/h\sigma_{0W}$ value clearly collapse to a single load and mismatch dependant curve. This allows the effect of material mismatch on the stress distribution to be assessed independently of the weld geometry and enables the change in crack tip constraint to be identified with material mismatch at a given load level. The stress distribution for a crack located in the center of the weld is governed by weld material properties close to the tip and steadily approaches a distribution governed by the base material properties remote from the crack tip, as shown in Figure 15.4 from Burstow *et al* (1998). The transition is strongly dependant on the mismatch and remote loading. A transition can be defined where the stress distribution becomes predominantly governed by the properties of the base material and the associated higher fracture toughness, even when the crack is located in the center of the weld.

Zhang *et al* (1996, 1997) have examined crack tip stress fields for a crack located at a strength mismatched bi-material interface. By measuring the stress distribution in the mismatched geometry with respect to a J-dominant reference solution they observed that

the stresses can be separated into a J-dominant reference solution and a difference field governed by mismatch effects:

$$\sigma_{ij} \approx \sigma_{ij}^{\text{ref}}(J) + M\sigma_{\text{oref}}f_{ij}(\theta) \quad (15.3)$$

the so-called M family of fields. Here σ_{oref} is the yield stress used in the reference solution. The difference field is self similar in nature and scaled by the mismatch constraint parameter M , which measures the strength of the mismatch effects on the stress field. Zhang *et al* showed that M depends on the angular position around the crack tip, but is not dependant on the radial distance. Using the small-scale yield solution as the reference field, Zhang *et al* (1996, 1997) observed near-linear relation between the material mismatch, M , and the mismatch constraint parameter, M . Overmatching reduced crack tip constraint and could be quantified by a negative M term, whilst undermatching increased constraint. As constraint due to material mismatching (M) is independent of the geometric constraint (Q), Zhang *et al* argued that the crack tip stress field can be expressed in an additive manner:

$$\sigma_{ij} \approx \sigma_{ij}^{\text{ref}}(J) + Q\sigma_{\text{oref}}\delta_{ij} + M\sigma_{\text{oref}}f_{ij}(\theta) \quad (15.4)$$

giving rise to the J-Q-M theory for mismatched joints, also discussed by Thaulow *et al* (1999).

15.3 Laser beam welding

Recent advances in laser technologies have enabled laser welding to become a competitive joining procedure to arc welding. Laser welding is a high energy density process, which allows a rapid production of low distortion welds. The process does not require special vacuum chambers, is not limited to electrically conductive materials, or influenced by magnetism.

High penetration beams of short wavelengths generated using the CO₂ or Nd:YAG mediums are used for joining metals. The beam is transferred to the workpiece where a concentrated beam of light is converted into thermal energy. A focal spot hundredths of mm in diameter may be focused on the weld surface or above or below it. On the surface melting occurs and progresses through the weld by heat transfer. Two important "figures of merit" which characterise laser welding are the energy transfer efficiency and the melting efficiency. The energy transfer efficiency is the ratio of the heat absorbed by the workpiece to that in the incident laser energy. The melting efficiency is the ratio of the heat necessary to melt the fusion zone to the heat absorbed by the workpiece. The energy transfer

efficiency indicates how much of the laser energy is absorbed by the component, while the melting efficiency indicates how effectively that absorbed energy is used to produce melting.

The lasers can be used in a continuous or pulsed mode in an autogeneous mode or with a filler material. With well calibrated instruments, benefits such as narrow welds, minimal distortion, small heat affected zones and excellent weld quality can be achieved, favouring this technique in particular for joining fine grained alloyed steels. Because the welds are narrow and the welding process is relatively rapid, the high cooling rates promote development of hard and brittle microstructures, such as martensite (Cam *et al* (1999)). These features may compromise the structural integrity of the weldments. Xie (2002) has suggested that by splitting a single laser beam in two equal beams following each other in tandem, the high cooling rates can be mitigated. This results in tougher welds with wider heat affected zones, and can also be achieved by the addition of a filler material, as observed by Sumpter (1999).

15.4 Fracture mechanics of laser welds

Fracture toughness testing procedures for laser welded joints have not been standardised. This is due largely to lack of information of the interaction between the base material and the fusion zone, which have significantly different tensile properties. During integrity assessments, a crack is assumed to be located in a fictitious material of uniform tensile and toughness properties, typically of the most brittle weld constituent (weld metal), to give a conservative defect assessment. To obtain more realistic estimates of fracture toughness the effects of specimen geometry (weld width, crack size, notch position, etc.) and the degree of strength mismatch on toughness have to be considered. Almost all laser welds are overmatched with high hardness and possibly low ductility of the weld metal (Cam *et al* (1999)). The weld geometry makes it almost impossible to determine the intrinsic fracture toughness properties of the weld region using Charpy V-notched specimens (Kristensen (1996)) or CTOD toughness testing procedures (Yeni *et al* (1996)), as the crack path deviates towards the softer base metal as a result of material mismatch. These techniques only provide information on fracture performance of the whole joint under impact and static bending conditions, but can not provide intrinsic toughness properties of

individual microstructural constituents due to the inevitable interaction between weld zone and base material.

Recent work in fracture mechanics of laser welds has endeavoured to:

- (1) Clarify the effect of strength mismatch on testing procedures (Eripret *et al* (1997), Hornet *et al* (1995)).
- (2) Examine the limit load behavior of weldments and modify existing failure assessment procedures (Schwalbe *et al* (1997), Joch *et al* (1993)).
- (3) An important area of interest are brittle fractures with emphasis on geometric (Q) and material (M) factors (Zhang *et al* (1997)).

Eripret *et al* (1997) have examined the effect of strength mismatch on using testing procedures developed for homogeneous specimens and adjusted for the limit load of the mismatched joint. For deep cracks in overmatched welds which are wide compared to weld length (as illustrated in Figure 15.5), the plastic zones are contained within the weld metal. Eripret *et al* (1997) argue that fracture is governed by the properties of the weld metal and can be assessed with the standard procedures for homogeneous material with weld metal properties. For shallow cracks and cracks in narrow welds, a second plastic zone develops at the interface marginally ahead of the crack and extends in the softer base material, as illustrated in Figure 15.5. Under increasing loading the two plastic zones grow and join together thus alleviating the crack tip stresses, as shown by Burstow *et al* (1998). The distinction between the plasticity patterns of a deep and shallow cracked configurations and the significance of mismatch effects can be measured through a geometrical parameter $h/(W-a)$, where h is the weld semi-width and $W-a$ is the unbroken ligament. Eripret *et al* (1997) suggest that for SENB configurations the homogeneous deep crack configuration develops when $h/(W-a)$ is more than 0.5 and the mismatch is less than 1.5. Conversely, for $h/(W-a)$ less than 0.25 and mismatched above 1.5, as is the case in laser welds, significant plasticity largely develops in the softer base material and limits weld metal deformation. Hence within geometric limitations on the ligament size and weld width the mismatch effects can be neglected for cracks in the weld metal, allowing test procedures for homogeneous material to be used with idealised weld or base material properties.

Ductile behaviour of weldments with limit load analysis and the application of the failure assessment procedures has been discussed by Joch *et al* (1993), Hornet *et al* (1995) and

Schwalbe *et al* (1997). The engineering approach to cracks in heterogeneous structures usually recommends that the tensile properties of the weaker base material and fracture properties of HAZ or weld metal should be used in the integrity assessments (Schwalbe *et al* (1997)). This approach is recognised to be conservative, however has limited experimental verification for highly overmatched laser welds. To provide more realistic basis for integrity assessments, the mechanisms of fracture and yield across the weld joint have to be understood and complemented with an experimental data base.

15.5 Limit load solutions for overmatched welds

An understanding of plastic collapse mechanisms is essential for defect assessment procedures based on failure assessment diagrams. Simple upper bound solutions to limit load can be obtained from slip line analysis of a cracked geometry obeying a rigid-plastic behaviour. From equilibrium considerations, the rate of work done by external forces at limit load is equal to the rate of dissipation of plastic energy in the deforming region. This allows expressions for limit loads for SENB and CCT geometries to be derived (Joch *et al* (1993), Hornet *et al* (1995)). Solutions to limit loads of a joint with crack located in the weld metal consist of suitable interpolation between the contribution to the limit load from a part of slip lines that extend into the base material and the part that develops in the weld (Joch *et al* (1993), Hornet *et al* (1995)). For SENB configurations where the weld metal is large enough to contain the plasticity, as shown in Figure 15.6a, Hornet *et al* (1995) estimate the limit load to be:

$$F_Y = 1.593 \cdot B \cdot \sigma_{ow} \frac{(W-a)^2}{4W} = M \cdot F_{YBM} \quad (15.5)$$

For narrow welds where plasticity develops outwith the weld metal, Figure 15.6b, the limit load can be estimated using a weighted contribution from the weld and base metal (Hornet *et al* (1995):

$$F_{YW} = 1.155 B \sigma_{oBM} \frac{(W-a)^2}{4W} \frac{(\beta - \alpha)M + \alpha}{\sin^2 \beta} \quad (15.6)$$

$$\alpha = \arccos \left(\cos \beta + \frac{2h}{(w-a)} \sin \beta \right) \quad (15.7)$$

which is a function of crack size, mismatch ratio and weld width. The angle β is attained by minimising the limit load F_{YW} .

15.6 Procedures for structural assessment of mismatched joints

The range of methods available for structural assessment of homogeneous materials are summarised in Figure 15.7 following Schwalbe *et al* (1997). These methods are being modified to incorporate mismatch effects. A three-level procedure is generally recommended:

- Level 1: Use of handbooks for stress intensity factor and limit load solutions. In mismatched structures the lowest yield stress and the highest strain hardening rates are recommended to provide conservatism.
- Level 2: Use of specific methods developed for mismatch. Examples include the ARAMIS code from EdF, modified EPRI handbook from EWI and the modified R6 approach from Nuclear Electric.
- Level 3: Perform detailed finite element analysis, using measured material properties on the mismatched structure.

Restricting the discussion to the modified R6 procedure, the mismatch limit load is the dominant parameter in J-estimates. The development of R6 for strength mismatch effects considers the mismatch effect for a bi-material system and introduces a limit load parameter defined as:

$$L_r = \frac{F}{F_{YM}} \quad (15.8)$$

F_{YM} is the mismatch limit load determined for a crack location, weld geometry and strength mismatch, which is tabulated in R6, Section IV.2 (2001) for CCP and SENB configurations.

Option 1 of R6 is unchanged for mismatch except for the cut-off L_r^{\max} which becomes a function of the mechanical properties of both constituents. Option 2 offers a more accurate assessment for a specific material parameters. The failure assessment curve is constructed for the equivalent stress-strain curve:

$$f_2(L_r) = \left[\frac{E\varepsilon}{L_r\sigma_{oe}} + \frac{L_r^3\sigma_{oe}}{2E\varepsilon} \right]^{-0.5} \quad (15.9)$$

where σ_{oe} is the 0.2% proof stress for the equivalent stress-strain curve, ε is the strain at $L_r\sigma_{oe}$ and the equivalent stress-strain curve for the mismatched joint is defined with a weighted average of the stress-strain curves of base and weld material:

$$\sigma_e(\varepsilon^p) = g\sigma_w(\varepsilon^p) + (1-g)\sigma_B(\varepsilon^p) \quad (15.10)$$

The weighting factor is deduced from the mismatch limit load:

$$g = \left(\frac{F_{YM}}{F_{YB}} - 1 \right) / (M - 1) \quad (15.11)$$

Under option 3 a detailed analysis of the cracked structure is required, either by treating structure as homogeneous and using the equivalent stress-strain curve of Eq. (15.10) or by allowing for different strengths in different regions. In both cases the J-integral should be evaluated using elastic and elastic-plastic analyses and the failure assessment curve constructed as:

$$f_3(L_r) = \left(\frac{J_{el}}{J} \right)^{1/2} \quad (15.12)$$

where J and J_{el} are J-integrals corresponding to the mismatch load L_r defined by Eq.(15.8). The cut-off L_r^{\max} for option 3 is defined as the ratio of equivalent flow stress, $\bar{\sigma}_e$, to equivalent yield stress, σ_{oe} , both depending on the material hardening characteristics and strength mismatch.

R6/4 recommends that the fracture toughness values should be those of the material at the crack tip, while the limit loads are the mismatch limit loads defined by Eq. (15.8). For option 2 and option 3 assessments a conservative assessment can be obtained by use of the flow properties of the weakest material at crack tip.

15.7 Estimation of J-integral from experimental quantities

To estimate the J-integral for cracks in mismatched structures, modifications to the standard procedure developed on deep cracks in homogeneous structures have been considered by Wang and Gordon (1992), Kirk and Dodds (1992), Joch *et al* (1993) and Hornet *et al* (1995)). Joch *et al* (1993) suggested that the J-integral should be evaluated from the plastic work done under the load-displacement curve in combination with an η_{pl} factor derived considering the relationship between deformation mechanisms and the limit load. Wang and Gordon (1992), and Kirk and Dodds (1992,1993) have considered the use of plastic work under load-CMOD records for mismatched structures. Based on finite element calculations they recommend a modification to Eq. (2.54) to include mismatch effects as:

$$\eta_{\text{plCMOD}} = (3.5 - 1.4167 \cdot a/w) \left(\frac{\sigma_{\text{oBM}}}{\sigma_{\text{oW}}} + \frac{1 - \sigma_{\text{oBM}}/\sigma_{\text{oW}}}{2} \right) \quad (15.13)$$

Hornet *et al* (1995) have checked both procedures experimentally and conclude that both fail to correctly include mismatch effects when gross-section yielding occurs. In particular Eq. (15.13) fails to account for the weld width ($2h$) although mismatch effects are a function of this geometric quantity. Hornet *et al* (1995) propose the use of load-CMOD curve to describe gross section yielding, and the calibration factor η_{plCMOD} has to be modified to account for strength mismatch on fracture behaviour of the specimen. For a configuration where weld metal is wide enough to fully contain the plasticity, the η_{plCMOD} factor is the same as for the homogeneous material (Wang and Gordon (1992)):

$$\eta_{\text{plCMOD}} = 3.5 - 1.4167 \cdot a/w \quad (15.14)$$

For narrow welds where plasticity extends into the base material, Hornet *et al* (1995) give the η_{plCMOD} factor as:

$$\eta_{\text{plCMOD}} = (3.5 - 1.4167 \cdot a/w) + \frac{2h}{W - a} \frac{\sin \beta}{\sin \alpha} \frac{1 - M}{\alpha + M(\beta - \alpha)} \quad (15.15)$$

Hornet *et al* (1995) have observed excellent correlation between J-integral estimations using this procedure and from detailed finite element model of the experimental geometry.

These expressions are limited to specific configurations where cracks are in the center of the weld. To apply these expressions with confidence the extent of plasticity must also be accurately determined. This may not always be straightforward. For cracks located near the fusion line or in the graded heat affected zone and for shallow cracks, analytic expressions are less readily available. Hornet *et al* (1995) demonstrated excellent agreement between the η_{plCMOD} factors computed using finite element techniques to those obtained from slip line analysis. In the light of this discussion the finite element approach is used in the current work to define η_{plCMOD} factors for specific crack configurations located in weld microstructures.

15.8 Fracture toughness of laser welded joints

The measurement of the intrinsic fracture toughness of a local microstructure on laser welded joint is difficult due to the small dimensions of the constituents forming the joint. Fracture toughness tests can be performed for a crack located in a particular microstructure, and the measured value is often termed the apparent fracture toughness

(Sumpter (1996)), because of the strong mismatch effects which affect the crack tip loading. The tests essentially quantify the fracture resistance of the whole joint. Sumpter (1996) argues that rather to strive to determine an intrinsic toughness of a particular microstructure, the apparent fracture toughness is more meaningful to engineering practice, as in real structures crack propagation samples stress field of the entire joint.

Despite the appealing nature of the laser welding, little data are available in literature on the fracture toughness of laser beam welded joints. The data are largely concerned with cracks located in the center of welds tested at the upper shelf temperatures (Cam *et al* (1999), Sumpter (1996), Sumpter (1999)). Fracture mechanics CTOD tests reported by Cam *et al* (1999) show similar CTOD values for cracks located in the center of the weld metal at room temperature and at -40°C . Due to the high strength mismatch and ductile nature of fracture in this temperature range, significant crack tip blunting and branching occurred, and the crack eventually extended into the more ductile base material, as shown in Figure 15.8 from Cam *et al* (1999). Sumpter (1996) has performed dynamic fracture toughness tests on laser welded plates at 0°C and -40° , and observed a consistently higher toughness for cracks located in the center of the weld, compared to the cracks in the HAZ. In these tests ductile initiation occurred at temperature close to upper shelf. Cracks located in the center of the weld or at the fusion line under dynamic conditions branched towards the base material and propagated as cleavage cracks in the base material following the HAZ, as shown in Figure 15.9 from Sumpter (1996). Crack branching and the path of a propagating crack may be associated with the mismatch constraint effects, discussed by Thaulow (1999) and Burstow (1998) which elevate the constraint along the crack path. Compared to arc welding, the toughness of the laser welded joint was comparable or higher at 0°C for cracks located in the weld centerline or at the fusion line (Sumpter (1996)).

A more recent study by Sumpter (1999) argued that the crack deviation also depends on the toughness of the weld, rather than solely on the hardness differential with the plate. If the weld is genuinely brittle, no deviations occur regardless of the hardness differential (mismatch). Sumpter (1999) suggests that crack deviation into the base material occurs when weld has high toughness that allows plasticity to develop into the base material before failure. Such welds can be produced by adding a filler material or by controlling the heat input to keep the hardness of the weld metal below 300 HV (Sumpter (1999)).

In practice structural integrity of welded components is often based on testing notched Charpy specimens. Typical of such tests performed on laser welds are fracture path deviations (FPD) (Hadley 2000, 2001) such that crack originating from a notch cut in the weld extends into the base material adjacent to the weld. This is largely due to narrow weld geometry of the laser welds combined with high hardness differential between the weld metal and the base material, leading to concerns that FPD could conceal possible low toughness of the weld metal. Recommendations have been given (Hadley 2001) that the full Charpy transition curve should be generated to determine with confidence the temperature range where crack propagates by FPD or through the weld metal. Charpy testing should then be performed for the lowest temperature where FPD does not occur (or the standard temperature, whichever is lower). For laser welds in low carbon steels ($C < 0.12\%$) having hardness mismatch > 2 , the FPD does not occur before lower shelf temperatures are reached, potentially questioning the applicability of such results to the operating environment closer on the upper shelf. Hadley (2001) also recognises that generating full transition curve can be potentially unreliable, as fracture by FPD may occur above a temperature for which the Charpy transition curve no longer predicts failure by FPD, due to statistical variation between batches.

Systematic data on the fracture behaviour of laser welded joints is needed, especially at lower temperatures, where contained plasticity develops for cracks in weld microstructures. The objective of the current work is to further advance studies on fracture path deviations in laser welds and to aid the development of testing standards for laser welded joints. Similarly the statistical aspects of crack propagation direction of strongly overmatched joints have not yet been addressed, and these are examined in subsequent chapters.

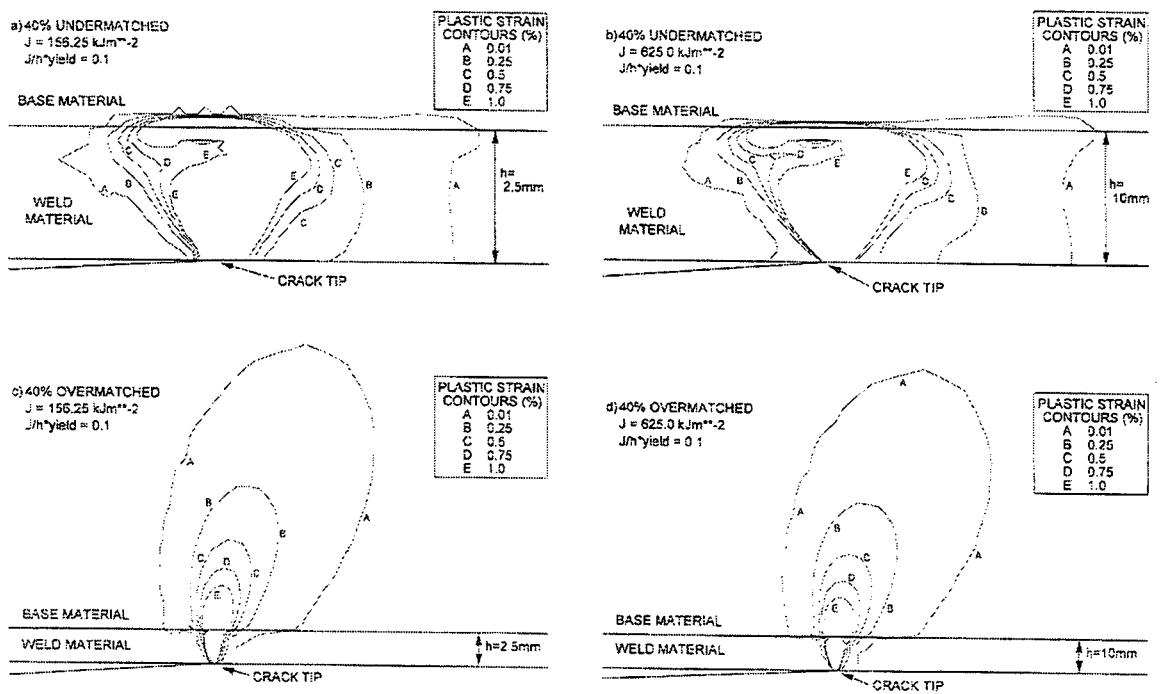


Figure 15.1:
 Comparison of plastic strain contours for 40% mismatched welds at two weld widths loaded to $J/h\sigma_{0W} = 0.1$, from Burstow *et al* (1998).

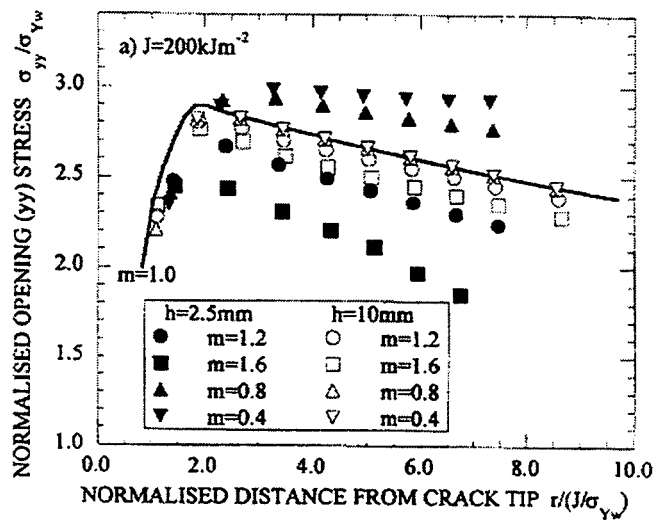


Figure 15.2:
The effect of mismatch, m , and weld width, $2h$, on the distribution of stresses ahead of a crack, from Burstow *et al* (1998).

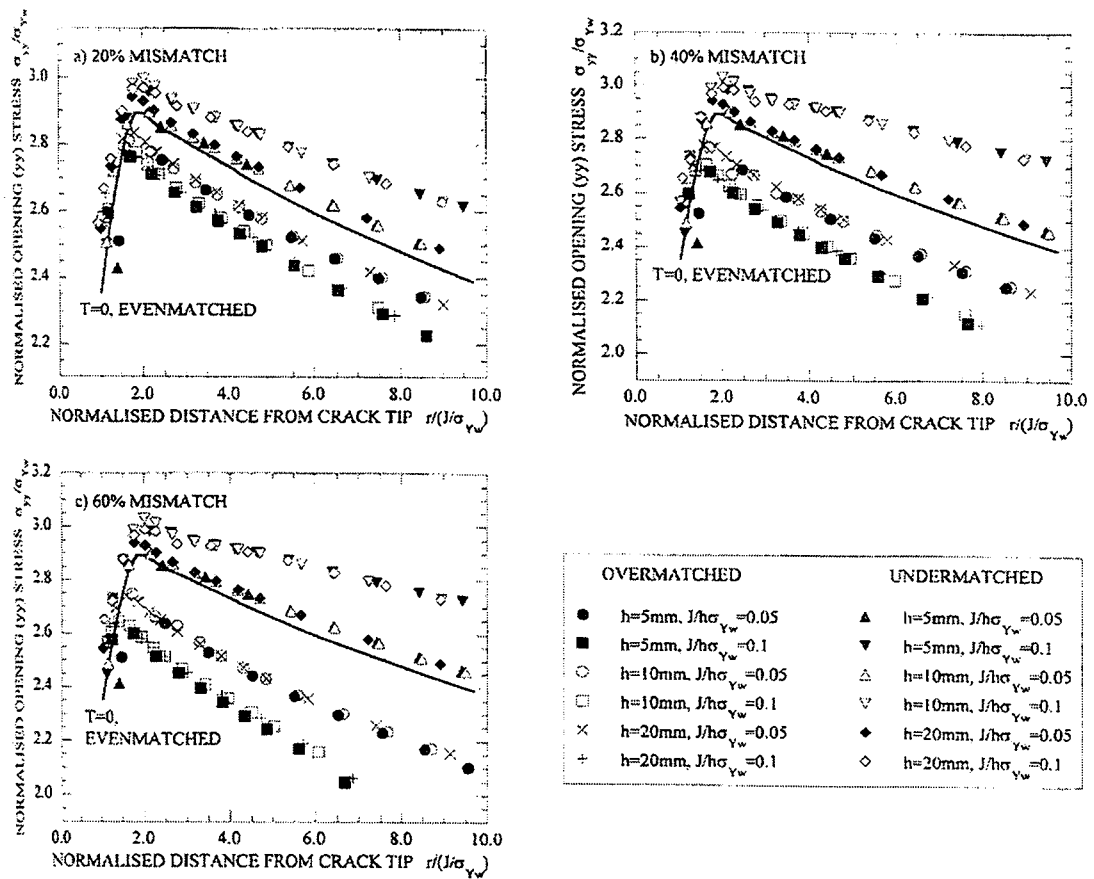


Figure 15.3:

The crack tip stresses directly ahead of the crack as a function of mismatch, showing self-similarity of crack tip fields when normalised by $J/h\sigma_{yw}$, after Burstow *et al* (1998).

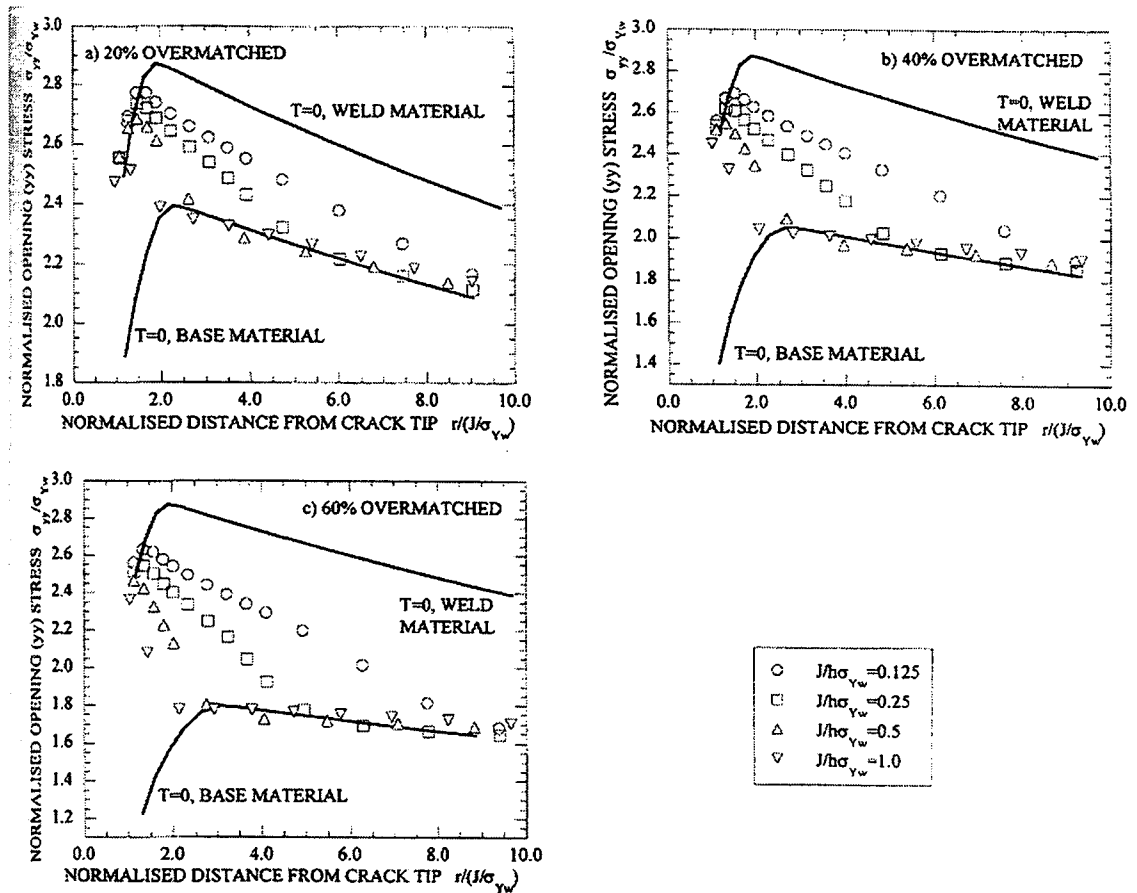


Figure 15.4:
Effect of base material strength on crack tip stress distribution with increasing load, after Burstow *et al* (1998).

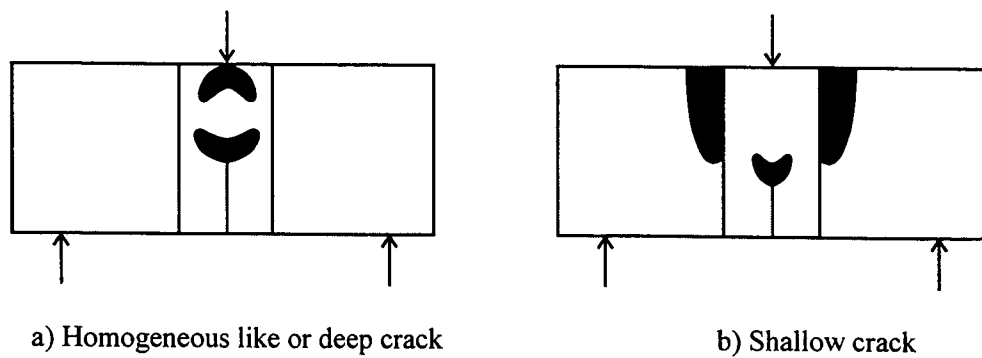


Figure 15.5:
Schematic representation of plasticity development in mismatched SENB specimens, after Eripret *et al* (1997).

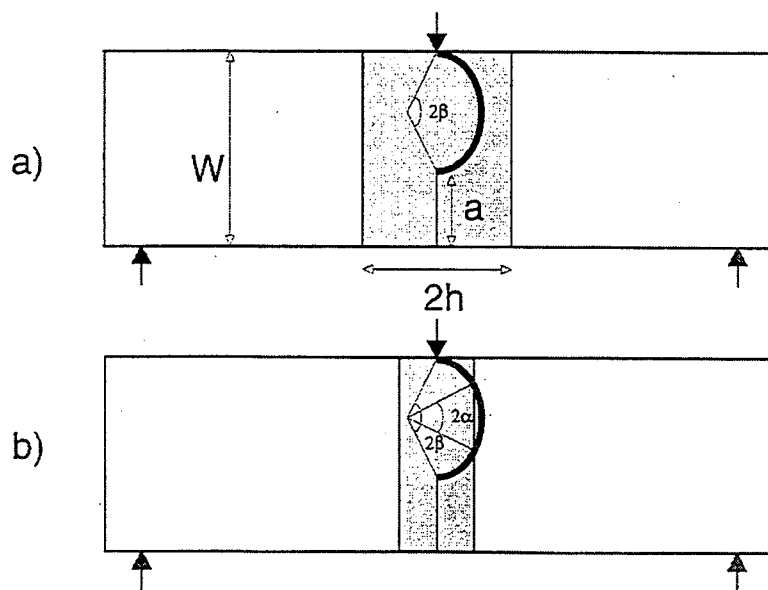


Figure 15.6:
The definition of the plasticity development patterns for mismatched SENB specimens: a) the weld joint is large enough to contain the plasticity and b) plasticity extends to the base material, after Hornet *et al* (1995).

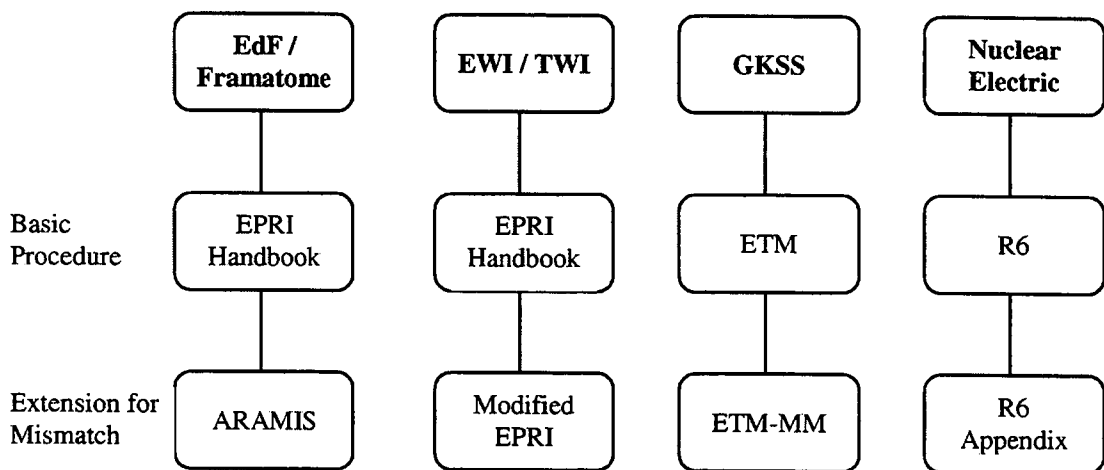


Figure 15.7:
 Defect assessment procedures for structural integrity and extension for mismatch effects, after Schwalbe *et al* (1997).

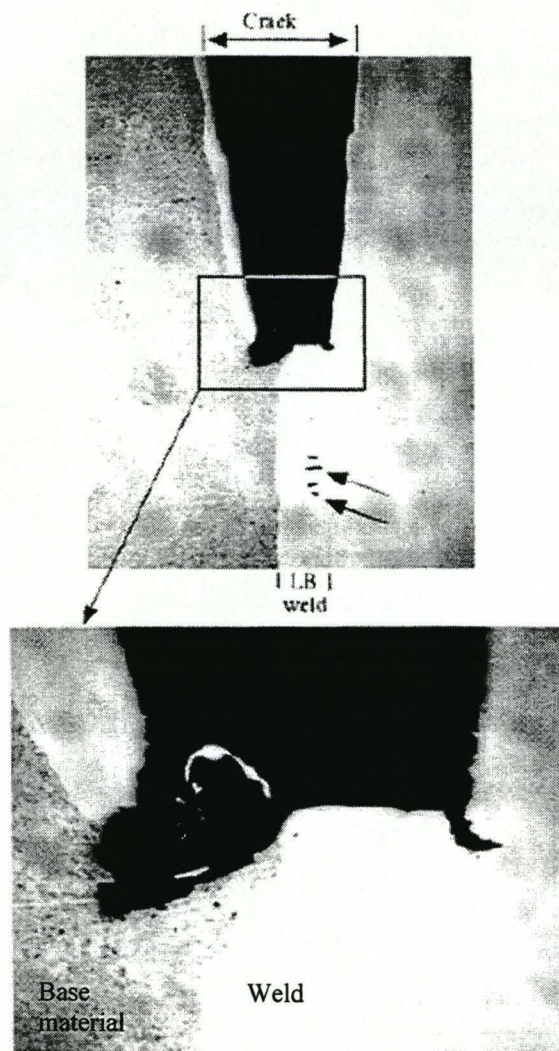


Figure 15.8:
Ductile tearing of a crack located in the weld centerline at 0°C, taken from Cam
et al (1999).

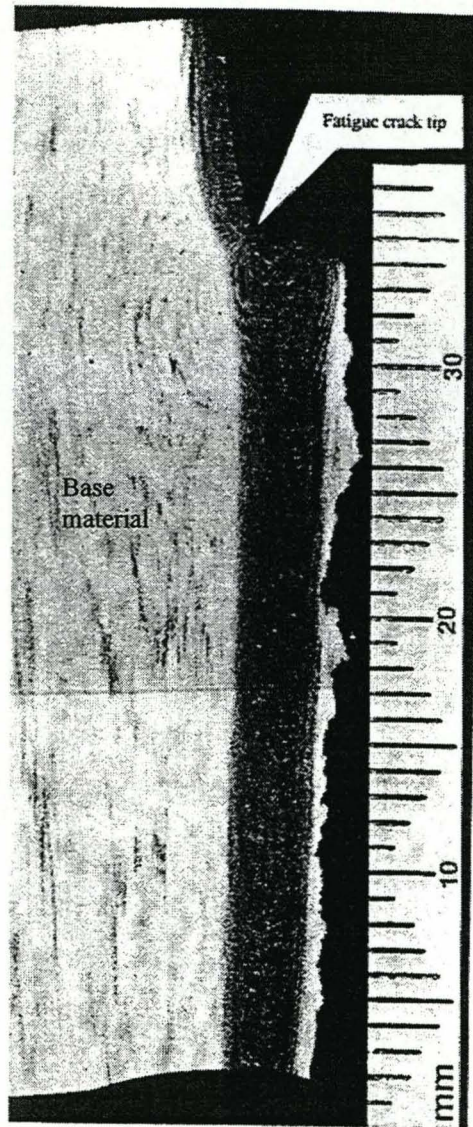


Figure 15.9:
Cleavage crack path for a crack located at the weld centerline under dynamic loading, after Sumpter (1996).

Chapter 16

WEAKEST LINK ANALYSIS OF A BI-MATERIAL JOINT

16.1 Introduction

The design of welded joints often requires the weld to have a higher yield strength than the parent plate. The need to apply defect assessment procedures to such joints requires fracture mechanics methods to be applied to cracks between elastically matched but strength mismatched materials. To ensure structural integrity the most detrimental conditions must be considered. These may involve cleavage. Fundamentals of fracture in welded joints can be simplified to a study of a bi-material joint containing a crack along the interface. The joint is composed of two elastically matched but strength mismatched homogeneous materials and analysed using a weakest link model, which is extended to a graded material in Chapter 18.

16.2 Procedure

Within the context of statistical fracture mechanics (Freudenthal (1968)), brittle failure can be modelled using weakest link statistics, based on the Weibull stress, as discussed in Chapter 10. The Weibull stress is typically computed for λ values ($\lambda = \sigma_f / \sigma_o$) of the order of 2.5~3, representative of lower shelf toughness data (Ritchie *et al* (1973), Bowen *et al* (1987)). The weakest link argument necessitates the value for the local fracture stress of each constituent. An argument based on the Ritchie-Knott-Rice (1973) model gives the relation between the local fracture stresses σ_{f1} and σ_{f2} as a function of the HRR fields for two different materials:

$$\frac{\sigma_{f1}}{\sigma_{f2}} = \frac{\sigma_{o1}}{\sigma_{o2}} \left(\frac{J_1 \alpha r_{c2} \sigma_{o2} e_{o2} I_n}{J_2 \alpha r_{c1} \sigma_{o1} e_{o1} I_n} \right)^{\frac{1}{n+1}} = M \quad (16.1)$$

In the present study the toughness and the strain hardening exponents of both halves of the joint are assumed in Eq. (16.1) to be the same ($n=10$ was used). However Eq. (16.1) has advantage of being more general: the effect of toughness gradient often negates the effect of the strength gradient. Secondly the expression in the round brackets approaches unity for weakly hardening materials of similar fracture properties with n values of 10~15, representative of joints in ferritic steels of different grades. Thus Eq. (16.1) can be used as a good approximation to local fracture stresses without detailed knowledge of the

micromechanical parameters or fracture properties. Equation (16.1) suggests that the critical local fracture stresses for two materials is approximately equal to the ratio of yield stresses at low strain hardening rates. The argument is supported by data of Bowen *et al* (1987) who showed experimentally on an A533B steel that the ratio of local fracture stresses is closely related to the ratio of yield stresses for two different microstructures, as illustrated in Figure 16.1. In Eq. (16.1) the strain hardening rate for both materials is assumed to be identical, although the argument can be applied to dissimilar strain hardening rates. This allows the same value for λ to be used for both halves of a mismatched joint. The volume V_0 used to determine the Weibull stress is regarded as a material constant and is taken to be identical for both halves of the joint.

To progress the discussion it is useful to introduce a non-dimensional Weibull stress, $\tilde{\sigma}_w$, which describes the structure of the strength mismatched crack tip field:

$$\tilde{\sigma}_w^m = \frac{\sigma_w^m V_0}{\sigma_0^{m-4} J^2 E^2 B} = f(M, n, \nu, \lambda, m) \quad (16.2)$$

and is a function of the mismatch, ν , λ , m and the strain hardening exponent, but is independent of the crack tip deformation (J/σ_0). The failure probability:

$$P = 1 - \exp\left(-\left(\frac{\sigma_w}{\sigma_u}\right)^m\right) \quad (16.3)$$

can then be expressed in terms of a non-dimensional Weibull stress and the loading parameter, J , for a mismatched joint:

$$P_{(M)} = 1 - \exp\left(-\frac{\tilde{\sigma}_{w(M)}^m \sigma_0^{m-4} E^2 B J^2}{V_0 \sigma_u^m}\right) \quad (16.4)$$

and for a homogeneous ($M=1$) joint:

$$P_{(M=1)} = 1 - \exp\left(-\frac{\tilde{\sigma}_{w(M=1)}^m \sigma_0^{m-4} E^2 B J^2}{V_0 \sigma_u^m}\right) \quad (16.5)$$

Here the properties of the weaker material are assigned to the interface containing a crack, and the homogeneous joint is taken to be of the same material. For a homogeneous material the mean value of toughness, \bar{J} , is:

$$\bar{J} = \int_0^\infty J \frac{\partial P_{(M=1)}}{\partial J} dJ = \left(\frac{V_0 \sigma_u^m}{\tilde{\sigma}_{w(M=1)}^m \sigma_0^{m-4} E^2 B} \right)^{\frac{1}{2}} \Gamma\left(1 + \frac{1}{2}\right) \quad (16.6)$$

$\Gamma(1 + \frac{1}{2})$ is the Gamma function. The failure probability of a mismatched material can then be expressed with the mean toughness, \bar{J} , of a homogeneous ($M=1$) material:

$$P_{(M)} = 1 - \exp - \frac{\tilde{\sigma}_{w(M)}^m}{\tilde{\sigma}_{w(M=1)}^m} \left(\frac{J}{\bar{J}} \Gamma(1 + \frac{1}{2}) \right)^2 \quad (16.7)$$

In Chapter 4 arguments were developed to allow the scaling constant K_0 in the expression for failure probability to be expressed in terms of the mean value and Gamma function. Similar arguments are developed here to relate the scaling constant σ_u with the average local strength:

$$\bar{\sigma} = \int_0^{\infty} \sigma \cdot p(\sigma) \cdot d\sigma = \sigma_u \cdot \Gamma(1 + \frac{1}{m}) \quad (16.8)$$

where probability density function describing the strength distribution in a volume V_0 is:

$$p(\sigma) = \frac{\partial}{\partial \sigma} \left[1 - \exp \left(- \left(\frac{\sigma}{\sigma_u} \right)^m \right) \right] \quad (16.9)$$

By identifying the average local strength in Eq. (16.8) to be the average local fracture stress, $\bar{\sigma}_f$, the σ_u can be written as:

$$\sigma_u = \frac{\bar{\sigma}_f}{\Gamma(1 + \frac{1}{m})} = \frac{\lambda \sigma_0}{\Gamma(1 + \frac{1}{m})} \quad (16.10)$$

16.3 Crack propagation direction

The argument may be extended to consider the statistics of crack propagation direction. Weakest link statistics do not require a single failure initiation site, or in the present context, a single crack propagation direction. However interest is now restricted to low failure probabilities and the low loads of most interest in structural integrity assessments. Under these circumstances it may be shown that multiple failures may be neglected in comparison to a single failure initiation. In addition it is assumed that interface failure does not occur. The most likely (modal) crack propagation direction follows from failure probabilities of each crack tip segment evaluated using Eq. (16.4), as discussed in Chapter 10. The area under the pdf curve is unity when the pdf is taken as:

$$\text{pdf}_{(\theta)} = \frac{P_{(M,\theta)}}{P_{(M)\text{total}} \cdot \Delta\theta} \quad (16.11)$$

which also makes the pdf independent of the V_0 and σ_u parameters. This follows from a Taylor expansion of the failure probability, where at low loads the leading terms are dominant and V_0 and σ_u in Eq. (16.11) cancel out. To attain low failure probabilities (low loads), a value for J of 1/100 of the average critical value for a homogeneous material was used, although the results are not very sensitive as long as the failure probability is low.

16.4 Numerical method

The near crack-tip stress field was modeled using boundary layer formulations, as described by Rice and Tracey (1973). Mode I plane strain conditions at the crack tip were analysed using a finite strain formulation and a blunt crack with crack tip radius of $r/R=2.8 \times 10^{-6}$, where R is the outer radius of the mesh. The uniaxial material behavior was linear elastic below the yield stress and merged into a Ramberg-Osgood relation, as discussed in Chapter 12. To model strength mismatched bi-material joints, the lower half of the mesh ($-\pi < \theta < 0$) was assigned a yield stress $M\sigma_0$ ($M \geq 1$), while the upper half ($\pi > \theta > 0$) was given a yield strength σ_0 . Both halves were considered to be elastically identical, with identical hardening exponents and Weibull moduli.

16.5 Results and discussion

Figure 16.2(a) shows the principal stress contours of constant $\sigma_1/\sigma_0 (= \lambda)$ ratio of 2.5 for homogeneous and bi-material joints. Contours are non-dimensionalised by J and the yield stress of the softer side of the joint (σ_0). The stresses in bi-material joints exhibit a discontinuity in radial stress at the interface, while equilibrium requires continuity of hoop and shear stresses. The size of the process zone and the radius of the plastic zone, shown in Figure 16.2(b), reduce on the harder side of the joint with increasing strength mismatch, M .

The Weibull stress and the cumulative probability have been determined numerically for both halves of the joint. In Figure 16.3, the failure probability is shown for homogeneous and bi-material joints as a function of the loading parameter, J , and strength mismatch. The loading parameter, J , is normalised with the mean toughness, \bar{J} , of the weaker homogeneous material. For both, $m=10$ and $m=20$, an increase in mismatch increases the failure probability at a given applied loading. The effect is most pronounced for higher moduli, where failure is dominated by small volume of material close to the crack tip. In

Figure 16.4 the toughness of the joint is considered at a fixed failure probability. It can be seen that at high moduli, the influence of the process zone size diminishes and a reduction in toughness is observed with an increase in mismatch.

The probability that the crack propagation direction lies between θ and $\theta+d\theta$ is indicated by a probability density function, shown in Figure 16.5 for a range of mismatches. The results for the homogeneous system ($M=1$) at low Weibull moduli ($m=10$) interestingly exhibits a distinct bi-modal distribution, symmetric across the crack plane, with peaks at $\pm 40^\circ$ due to the large volume at these angles. This suggests that macroscopic crack propagation at $\theta=0$ occurs by cleavage on alternate inclined planes (Becker *et al* (2002)). At higher moduli ($m=20$) the microscopic crack propagation direction is directly ahead of the crack. In bi-material joints the greatest value of the pdf is consistently exhibited by the softer side of the joint and approaches the interface with an increase of the mismatch. Similar trends are observed in the average crack propagation angle, shown in Figure 16.6, where at low moduli the greater sampling volume on the softer side of the joint influences greater angles compared to those for higher moduli. Both, the probability density function and the average angle indicate failure of the softer side in a bi-material joint with a possibility of interface failure at high mismatches.

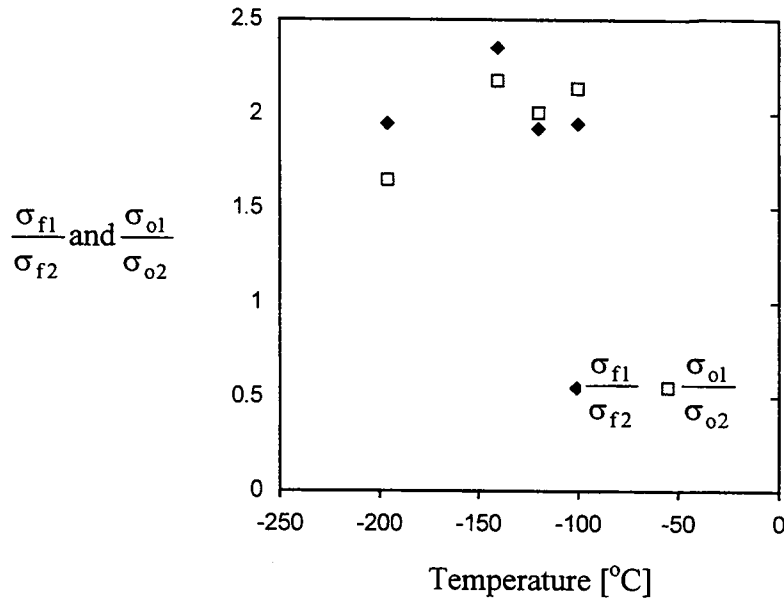


Figure 16.1:
The ratio of the local fracture stresses and yield stresses of the two microstructures in A533B steel, using data of Bowen *et al* (1987).

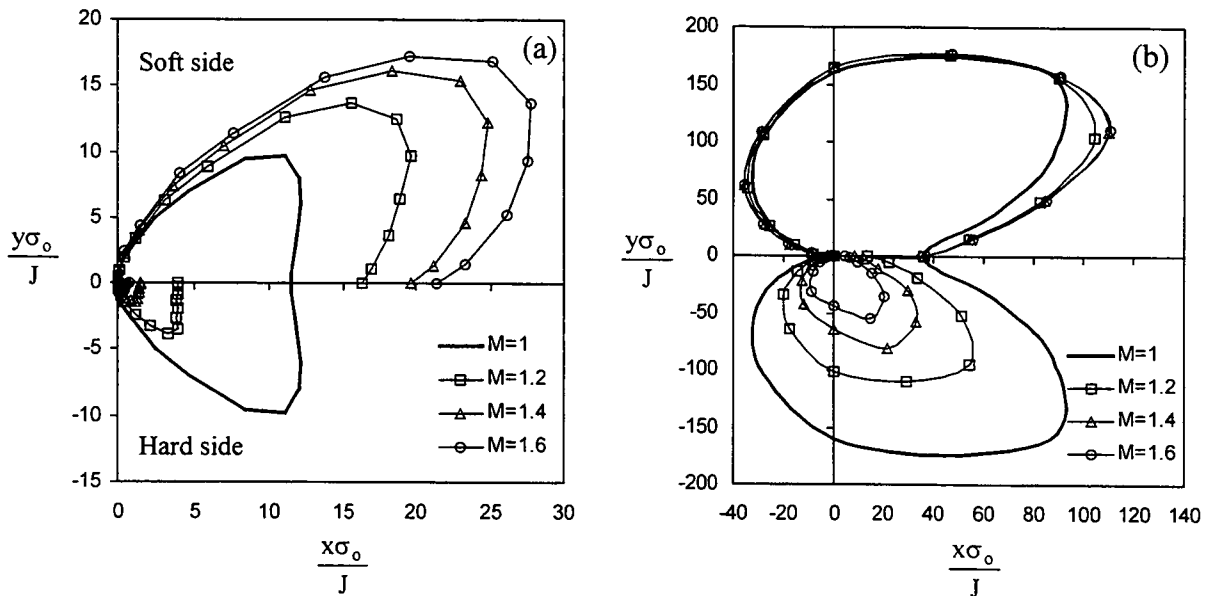


Figure 16.2:
Contours of principal stress for $\lambda=2.5$ and plastic zone sizes for a range of strength mismatches in Mode I plane strain.

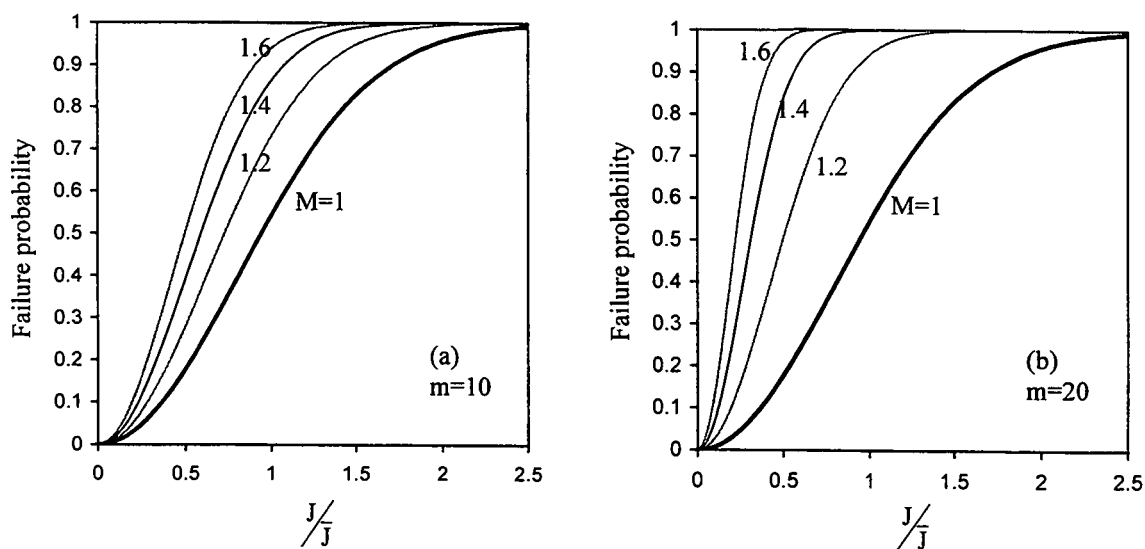


Figure 16.3: Failure probability for a bi-material joint as a function of normalised load in plane strain. λ is 2.5 and Weibull modulus is 10 in Figure 16.3(a) and 20 in Figure 16.3(b).

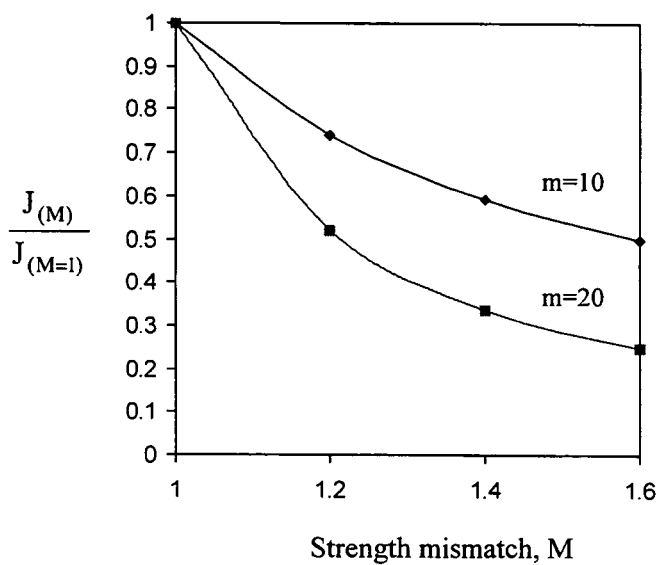


Figure 16.4: The dependence of toughness in a bi-material joint on the strength mismatch and Weibull modulus at $\lambda=2.5$.

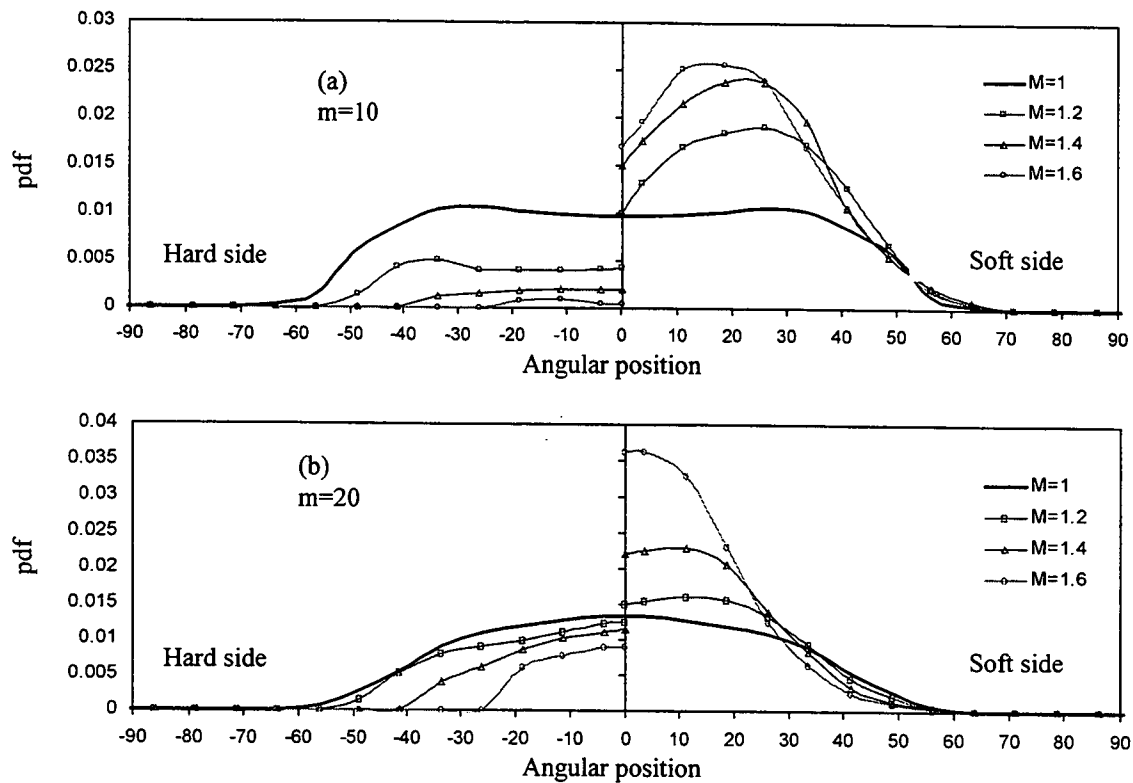


Figure 16.5:

The probability density function for a bi-material joint as a function of angle over a range strength mismatches at $\lambda=2.5$. The Weibull modulus is 10 in Figure 16.5(a) and 20 in Figure 16.5(b).

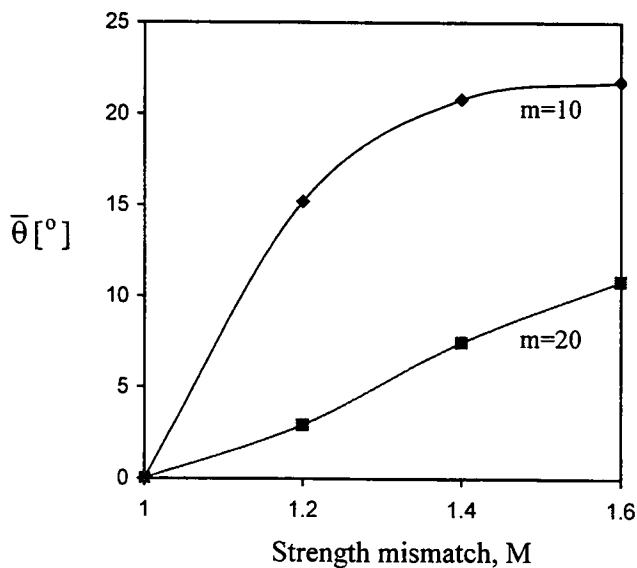


Figure 16.6:

Average crack propagation angle into the soft side of a bi-material joint at $\lambda=2.5$, as a function of strength mismatch and Weibull modulus (m).

Chapter 17

AN EXPERIMENTAL EXAMINATION OF THE INTEGRITY OF LASER WELDED JOINTS

17.1 Experimental details

The integrity of weldments in a ferritic steel plate fabricated using a laser beam welding procedure has been investigated for cracks located in a range of weld microstructures. The weld was fabricated in Lloyds Grade L36N low carbon steel of shipbuilding specifications from Danish Steel. The chemical composition is given in Table 17.1. This steel is particularly suited for laser welding due to limits on the amount of carbon, phosphorus and sulphur. Tensile tests were performed at room temperature on standard specimens cut from the base material. The base material had a yield stress of 390 MPa, a tensile strength of 516 MPa and a strain hardening exponent of 10. Fracture mechanics specimens were cut from a large 11.5 mm thick plate containing a butt weld produced by autogeneous CO₂ laser at TWI, and machined to dimensions shown in Figure 17.1. The welding parameters are summarised in Table 17.2. Cracks were introduced in the weld metal, the heat affected zone (henceforth HAZ) and in the base material near HAZ using a machined notch and fatigue pre-cracking under mixed-mode loading. In all cases the final fatigue crack extended to half the specimen width (11 mm).

Attempts to locate a crack in a particular microstructure are difficult due to the Y shaped profile of the weld, which is illustrated in Figures 17.2 and 17.3. The width of the weld also varies along the length of the plate, between 1.6 and 2.0 mm. The notch was generally cut perpendicularly to the plate surface and in some cases at small angles, to sample more uniform microstructure along the crack width. Post-test metallographic examination revealed that the final fatigue pre-crack location with respect to the microstructure between the two notch orientations was small. It was also noted that in perpendicular cut notches the final fatigue pre-crack tends to align itself in the microstructure so that sections of the crack front deviate from the notch plane. These effect have been neglected in calculations of J . From a 3-dimensional finite element model of a homogeneous material with a similar thickness, Wang (2002) suggested that the stresses near the surface are low and cleavage initiation is unlikely. Therefore the crack position with respect to the microstructure in the center region of the specimen effectively governs the fracture behaviour.

Metallographic examinations revealed a microstructural variation across the laser weld, similar to that observed by Sumpter (1999) and Cam *et al* (1999). The ferritic/pearlitic microstructure of the base material transforms into a martensitic/bainitic microstructure of the weld metal, while the heat affected zone largely comprised bainite and pearlite. The Vickers hardness was measured across the width of the weld and is shown in Figure 17.4. In Figure 17.4(a) the Vickers hardness (HV) is measured on the specimen taken from near the end of the plate and clearly shows higher HV values compared to a series of measurements on a specimen taken from the centre of the plate, shown in Figure 17.4(b). The single pass welding process with high travel speed resulted in high cooling rate that produced a hard weld metal. The hardness rapidly reduces as a function of position across the HAZ to the hardness value of the parent plate. The ratio between the hardness of the weld metal and base material is on average 2.25 times. BS 7448:2:1997 gives a relation between hardness and yield stress for arc welds. In the absence of specific correlations between hardness and yield stress for laser welds and due to high hardness of the weld metal which exceed the bounds of the empirical correlations given in BS 7448:2:1997, the strength mismatch is defined from the ratio of HV measured across the microstructures and the value of the base material, measured remote from the weld, as shown in Figure 17.5. The yield strength gradient across the weld then follows from the mismatch and the yield strength of the base material.

17.2 Results from cleavage tests in contained yielding

17.2.1 Fracture toughness

Fracture mechanics tests were performed on laser welded specimens at $-130\text{ }^{\circ}\text{C}$, to give cleavage failure in contained yielding, under four point bending. The specimens were cooled with liquid nitrogen using an environmental chamber, which kept the temperature constant during testing to within $\pm 3\text{ }^{\circ}\text{C}$. The temperature was measured near the fatigue crack tip using spot welded thermocouples. All failures were under contained yielding and load-displacement and load-crack-mouth-opening-displacement records were linear to final failure. Plots of the plastic zone at failure obtained from the numerical model discussed later are shown in Figure 17.6 for a representative sample of test configurations. The apparent fracture toughness for the welded joint was calculated from the Irwin expression ($Y\sigma\sqrt{\pi a}$) in which the geometry function, Y , was taken from Tada (1973). The fracture toughness results are shown in Figure 17.7 as a function of crack position measured from

the centerline of the weld and summarised in Table 17.3. The lowest toughness was recorded for a joint containing a crack in the centre of the weld and at the edge of the heat affected zone. In the first instance the crack tip field sampled a small region which was fully contained in the weld (see specimen LW-15 in Figure 17.9), where the high hardness was associated with a low fracture toughness. Cracks located in the HAZ benefit from the mismatch gradient which causes large plastic zones to develop into the softer side of the weld. It has been shown numerically (Burstow *et al* 1998) that the crack located at the foot of the yield strength gradient experiences higher constraint levels introduced by material inhomogeneity. This is reflected in the present results where the apparent fracture toughness for the crack at the edge of HAZ is half the value for a crack located in the HAZ. The results are also in agreement with the numerical study of Rashid and Tvegaard (2003) who examined cracks in a graded zone between two homogeneous solids. They discuss toughness in terms of specific energy per unit crack extension using a cohesive zone model and show the configuration corresponding to a crack at a fusion line is nearly twice as tough as a configuration with a crack near the interface in the softer or the harder homogeneous material surrounding the graded zone.

17.2.2 Crack path

Photographs of the crack paths are shown in Figures 17.8 and 17.9. Figure 17.9 shows the crack path with respect to the weld microstructure on the surface of the specimen, while Figure 17.8 shows the corresponding crack paths in the centre of the specimen. A distinct difference in the orientation of crack paths can be observed between the surface and centre positions. In the centre of the specimen cracks located in the coarse grained HAZ (Specimens LW-1, LW-3 and LW-10) deviated from the HAZ in the direction of the high strength material, towards the fusion line and finally propagated along the fusion line. The orientation of the initial crack path measured from the tip of the fatigue pre-crack were between 9.7° (Specimens LW-1) and 17° (Specimen LW-10), with higher angles recorded for cracks located closer to the fusion line, see Table 17.3. A configuration with a crack on the fusion line (Specimen LW-5) showed that the crack propagated straight ahead along the fusion line. Similarly for a configuration in which the crack was located in the weld, 0.2 mm from the fusion line (Specimen LW-4), the crack initially propagated towards and then along the fusion line. An exception to this trend was observed for specimen LW-2, where the crack was positioned at the edge of the HAZ, and the crack propagated towards the parent plate at an initial angle of 5° .

A marked surface effect was observed in all specimens, which effects the crack propagation direction within 1.5~2 mm from the specimen surface. As shown in photographs in Figure 17.9, surface cracks consistently propagate down the yield strength gradient, away from the weld. This may be due to lower stress triaxialities close to the surface where plane stress conditions prevail and for which numerical calculations show that plasticity is predominantly restricted into the softer material, as shown in Figure 17.10. After the initial deviations at an angles between 15° to 51° on the surface, under pure bending cracks propagated in a largely straight path, along the transition between the fine grained HAZ to the parent plate. Under three point bending (Specimen LW-5), a crack located on the fusion line propagated into the HAZ and along the fine grained HAZ. This was marked with significant pop-in effects, which were not observed under pure bending. A similar configuration (Specimen LW-4) containing a crack in the weld, 0.2 mm from fusion line, showed that the crack propagated along the fusion line on the weld side of the joint. When the crack was positioned between the refined and coarse grained HAZ (Specimen LW-2), the initial crack propagation in pure bending was towards the coarse HAZ at an angle of 8° . The crack then gradually turned towards the refined HAZ and propagated along the transition between refined HAZ and parent plate. Similarly a crack positioned into the base material, near HAZ (Specimen LW-8), clearly deviated towards the weld, until it approached the refined HAZ, when it propagated along the refined HAZ. Lastly, a crack positioned in a centre of the weld (Specimen LW-15) propagated straight ahead, unaffected by the strength gradients at this temperatures.

The surface path of a propagating crack is influenced by the fracture behaviour in the centre of the specimen. After initiation, crack paths on the surface and in the centre unified and are governed by the plane strain conditions in the centre of the specimen.

17.3 Results of cleavage tests in ductile-brittle transition

Deep and shallow cracked bend specimens were tested at -90°C and at -60°C , allowing plasticity and constraint to develop prior to cleavage failure. Shallow cracked specimens were machined from the deep cracked specimens to an a/w ratio of 0.1. Fracture toughness values were calculated from supposition of elastic and plastic parts of the J-integral, as discussed in Chapter 2. The plastic part was obtained from the area under the load-CMOD (crack mouth opening displacement) curve, using the specific η_{plCMOD} factors computed

from a full field finite element model of the test configuration. Details of the finite element modelling are given in Chapter 18. The model was a plane strain representation of the test geometry, with highly focused mesh at the crack tip. The knife edges, on which CMOD values were measured during the test, were also included. The lower yield strength of the base material was measured with a tensile test to be 470 MPa at $-90\text{ }^{\circ}\text{C}$, and 420 MPa at $-60\text{ }^{\circ}\text{C}$ and strain hardening exponent of 10 was used. A strength mismatch of 2.25 was assumed between the weld metal and the parent plate and a bilinear transition was idealised for the HAZ (See Figure 18.2). Crack was positioned in the model in such a manner, that it closely represented the individual test geometry with respect to the crack position measured in the centre of the specimen (plane strain conditions). The η_{PICMOD} values are listed in Table 17.4 and 17.5 for deep and shallow cracks for test conditions.

17.3.1 Deep cracks

Deep cracks ($a/w=0.5$) were tested at $-60\text{ }^{\circ}\text{C}$ under four point bending. The fracture toughness values are summarised in Table 17.4 and in Figure 17.11. At this temperature final failure was in full plasticity and preceded by several pop-in events, as shown in the load-displacement records redrawn in Figure 17.12. Each pop-in was evaluated according to BS 7448:2 and in all cases the first pop-in event was classified as a critical event. The fracture toughness was calculated using the load at the critical pop-in and the corresponding plastic work under the load versus CMOD curve and is shown in Figure 17.11. A similar spatial variation can be observed for present results and those obtained in contained yielding. The lowest toughness was observed for a crack in the weld centerline and increases for a crack in the heat affected zone. For cracks located at the edge of the heat affected zone the fracture toughness is reduced and comparable to that of the weld metal, as observed in tests at $-130\text{ }^{\circ}\text{C}$.

Photographs of specimens are shown in Figure 17.13, taken on two cross-sections in the center of the specimen 2mm apart. Cracks located in the weld centerline (Specimen LW-22) initiated straight ahead, while cracks near the fusion line in the weld metal (Specimens LW-23, LW-30) or HAZ side (Specimen LW-11) initiated into the weld metal. Unlike to the behaviour at $-130\text{ }^{\circ}\text{C}$, the crack does not follow the fusion line but propagates directly into the weld metal. Cracks located at the edge of heat affected zone (specimens LW-13 and LW-24) initiated towards the base material. In this set the highest toughness was

observed for a crack located in the heat affected zone that propagated into the weld metal, complementing results from $-130\text{ }^{\circ}\text{C}$ tests. A configuration with a crack in the base material gave the toughness of the base material to be $310\text{ MPa}\sqrt{\text{m}}$ and the crack propagated towards and along the edge of heat affected zone.

Specimen LW-31 which had a crack fully contained in the weld, 0.1mm from fusion line and is identical to LW-30 was used to examine the extent of pop-in effects observed in all tests at $-60\text{ }^{\circ}\text{C}$. The specimen was prepared and tested in the same manner as before. The load-displacement curve is the same as that of specimen LW-30, redrawn in Figure 17.12. Test was stopped when pop-in failure occurred. The extent of pop-in was marked by fatigue crack growth, after which the specimen was cooled in liquid nitrogen and broken open. The fracture surface of the specimen is shown in Figure 17.14. The cleavage fracture originated only in the centre of the specimen where plane strain conditions prevail and the maximum extent of the pop-in was 1.4 mm.

17.3.2 Shallow cracks

Shallow cracks with an a/w ratio of 0.1 were tested at $-90\text{ }^{\circ}\text{C}$ under three point bending. Photographs of crack position along the weld width prior to cleavage test are shown in Figure 17.15, while the paths of cleavage cracks in the centre of the specimens are shown in Figure 17.16. Cracks on the weld metal propagated straight ahead (Specimens LW-17, LW-20 and LW-25), while cracks in the heat affected zone (Specimen LW-18) propagated along the edge of the heat affected zone in the base material. In specimens LW-19 and LW-33 crack is positioned in the base material near HAZ and propagated towards the HAZ and along the HAZ – base material region for several millimetres before turning into the base material.

Extensive plasticity and crack blunting developed in all configurations prior to failure. All failures were by cleavage with no prior ductile tearing or pop-in events, with the exception of specimen LW-25, where a critical pop-in event terminated the test. In the configuration in which the crack was located in the weld (Specimens LW-17 and LW-20) negligible crack tip blunting was observed and plasticity was predominantly confined to the base material. Fracture toughness values are shown in Figure 17.17 and summarised in Table 17.5 with failure load and specific η_{PICMOD} factors. Constraint effects were measured by the

T-stress and normalised with the yield stress of the crack tip material and are shown in Figure 17.18. Cracks located in the base material near the heat affected zone showed the highest toughness with matching lowest negative T-stresses.

Contrary to results of deep cracks, preliminary results on shallow cracks show nearly constant value of apparent fracture toughness for all crack locations. This is in part due to extensive plastic yielding that develops in the base material for nearly all configurations, including those containing cracks in the weld metal, associating such configurations with higher toughness. High values of toughness for cracks located in the weld metal are in part also influenced by the experimental error. Toughness was determined from the measured area under the load-CMOD record, with the CMOD values were measured using knife edges. The knife edges were bonded on the base material portion of the specimen near the weld. Due to extensive plastic deformation of the softer base material surrounding the weld, the knife edges have erroneously recorded larger crack mouth opening, thus giving larger than expected toughness values.

17.4 Ductile tearing of laser welded joint

Configurations containing a crack at the fusion line and in the base material near HAZ were examined for extensive ductile tearing at room temperature. Photographs of the crack location in the centre of the specimen are shown in Figure 17.18. In both cases plastic strains develop asymmetrically into the base material and the crack extends in the direction of the lower strength gradient, into the base material.

17.5 Charpy V-notched tests

17.5.1 Impact tests

Standard 10x10 mm V-notched Charpy specimens were cut from the weld plate and 45° notch of 2 mm in depth was cut along the fusion line. Impact tests were performed at 0 °C, -40 °C, -70 °C and -85 °C and photographs of fractured specimens are shown in Figure 17.20. In all cases crack propagated away from the weld, into the base material. Comparable Charpy impact values were recorded for tests at 0 °C (284 J) and -40 °C (288 J) and crack propagated in ductile manner. At -70 °C and -90 °C the impact energies were 240 J and 148 J, respectively and crack initiated in ductile manner and propagated by cleavage.

17.5.2 Slow bend Charpy tests

Elongated 10x10 mm specimens machined to Charpy specifications were notched on the fusion line and tested at -85 °C and -70 °C under quasi-static three point bending, using the testing arrangement for fracture mechanics tests. Crack path in both tests initiated close to the notch tip and propagated into the base material, along the edge of the HAZ, as shown in Figure 17.21. The -70 °C test was stopped before cleavage failure. The results are consistent with the impact Charpy tests, and show the opposite crack propagation direction to that obtained from fatigue pre-crack test geometries. A possible explanation for this fracture behaviour is given in the next chapter, section 18.4.

17.6 Discussion

The results of deep and shallow cracked laser welds tested through the ductile-brittle transition show similar trends, both in terms of fracture toughness and crack propagation direction. The highest toughness of the weld joint was observed for cracks located in the heat affected zone. This may be influenced by the local mixity induced by the strength gradient. Cracks located near the weld centerline and near the edge of the heat affected zone exhibit the lowest failure loads and fracture toughness values. Further from the weld the toughness then increased to the value of base material. The trends are shown as curve fits to the -130 °C data in Figure 17.22. Crack initiation angles and crack paths generally follow the toughness gradient and are much less influenced by the strength mismatch, Figure 17.22. This is consistent with the suggestion of Sumpter (1999) that autogeneous laser welds tend to produce high hardness of the weld metal in excess of the 300 HV which are associated with low fracture toughnesses. Sumpter (1999) suggests that in such welds crack path is largely governed by the toughness of individual microstructures rather than by the material strength.

The results of Charpy tests are consistent with those of Sumpter (1999), Kristensen (1996) and Hadley (2000, 2001) in that under impact loading crack propagates into the base material at ductile-brittle transition temperatures. Conversely the quasi-static fracture mechanics tests in ductile-brittle transition where crack initiated by cleavage at minimum plastic distortions show opposite trends with crack propagating into the less tough phase. Charpy tests are commonly performed to characterise the weld and combined with

assumption that fracture properties of the material into which crack propagates govern failure. Such practice can give misleading conclusions about the integrity of laser welds.

Hadley (2000, 2001) addressed the fracture path deviations (FPD) by testing Charpy specimens machined from several laser welds manufactured to commercial specifications with carbon content limited to 0.12% (Lloyd's register (1997)) and laboratory welds with purposely embrittled weld metal. Steel of specifications used in this work has also been included in their study. A general observations was made that FPD is related to but does not conceal genuinely brittle weld metal. However a dual fracture mode with failure by FPD or through the weld metal at considerably lower fracture energies has also been observed at the transitional temperatures, this being more pronounced for embrittled welds ($>0.16\%$ C). Hadley (2001) recommends that the full Charpy transition curve is generated to determine the temperature range of the bi-modal fracture behaviour, although Hadley also recognises that such method lacks simplicity and may not be reliable or cost effective. To avoid ambiguity due to the bi-modal Charpy behaviour and recognising that the weld metal is the weakest constituent of the joint, a recommendations is made that standard Charpy testing of laser welds should be complemented with fracture mechanics testing of the weld metal. Laser weld may be considered fit for service if Charpy and fracture mechanics testing at the lowest operational or standard temperature (whichever is lower) shows that:

- In Charpy tests failure occurs by FPD and impact toughness is in excess of 27J for low-strength steels or 47J for high-strength steels (Hadley 2001) and
- Fracture toughness testing of the weld metal shows no FPD and the toughness, measured by K_{Jc} , of the weld metal is in excess of the minimum value, typically $125 \text{ MPa}\sqrt{\text{m}}$ (Sumpter 1999) for tests at 0°C and stress intensity rate of $10^4 \text{ MPa}\sqrt{\text{m}}/\text{sec}$. Should FPD occur at this temperature and $K_{Jc} > 125 \text{ MPa}\sqrt{\text{m}}$ is also indicative of sufficient toughness of the weld metal to allow the weld to be considered fit for service.

C	Mn	Si	S	P	Ni
0.10	1.36	0.48	0.002	0.007	0.35
Cr	Mo	Nb	Cu	Al	
0.058	0.016	0.024	0.13	0.032	

Table 17.1:
Chemical composition of Lloyd's Grade L36N steel [in wt%]

Laser power	13 kW at workpiece (continuous wave)
Focal length mirror	500 mm
Focal position	at surface (0 mm)
Travel speed	0.9 m/min
Gas shielding and plasma control via angled jet (4mm diameter at 45°) following the beam with He at 40l/min.	
Plates were machined and degreased prior to welding.	

Table 17.2:
Welding specifications

Specimen	Crack location	Distance from weld centerline [mm]	Test temperature [°C]	Failure load [kN]	K_c [MPa√m]	Crack initiation angle [degree]	Comments
LW-15	Weld centerline	0	-131	12.75	56.4	Straight	
LW-4	Weld, near FL	0.9	-132	19.55	88.1	Straight	
LW-5	On fusion line	1	-136	10.50 ⁺	78.9	Straight	
LW-1	Heat affected zone	1.425	-126	25.55 ⁺⁺	95.1	11.5°, 9.3°	
LW-10	Heat affected zone	1.475	-129	18.60	83.8	44°, 17°	Notch cut at a 4° angle
LW-3	Heat affected zone	1.525	-135	17.10	77.1	23.5°, 12.7°	
LW-2	Base material near HAZ	1.82	-133	14.65	66	5°*	
LW-8	Base material near HAZ	2.1	-135	13.30	59.9	13°	
LW-0	Base material	/	-128	18.90	103	Straight	Specimen cut from base material

* Crack propagates to base material

⁺ Three-point bending test

⁺⁺ 25 mm wide geometry

Table 17.3:

Summary of tests on laser welds in contained yielding (-130 °C). Test were performed on deep cracks ($a/w=0.5$) in four-point bending. Crack initiation angle is measured at two positions, 2 mm apart in the centre of the specimen. For crack path see Figure 17.8.

Specimen	Crack location	Distance from weld centerline [mm]	Test temperature [°C]	Failure load [kN]	η_{plCMOD}	K_I [MPa \sqrt{m}]	Crack initiation angle [degree]	Comments
LW-22	Weld centerline	0	-60	16.6	1.36	92.7	Straight	1 st pop-in failure $A_{CMOD}=1.07$ Nm
LW-23	Weld	0.75	-60	16.3	1.57	112.5	26°, 19° to weld	1 st pop-in failure $A_{CMOD}=2.33$ Nm
LW-30	Weld, near fusion line	0.85	-59	20.3	1.59	189.8	11°, 22° to weld	1 st pop-in failure $A_{CMOD}=8.9$ Nm
LW-31	Weld, near fusion line	0.9	-60	19.8	1.59	175.2	8.5°, 6° to weld	1 st pop-in failure $A_{CMOD}=7.3$ Nm
LW-11	Heat affected zone	1.4	-59	18.7	1.62	174.7	32°, 16° to weld	1 st pop-in failure $A_{CMOD}=7.4$ Nm
LW-24	Edge of HAZ	1.6	-60	18.9	1.60	121.9	19°, 22° to BM	1 st pop-in failure $A_{CMOD}=2.25$ Nm
LW-13	Base material, near HAZ	1.75	-59.5	17.95	1.61	156.2	26°, 19.5° to BM	1 st pop-in failure $A_{CMOD}=5.66$ Nm
LW-32	Base material	2.4	-59	22.3	1.63	310.8	11.5°, 10° to HAZ	1 st pop-in failure $A_{CMOD}=27.0$ Nm

Table 17.4:

Summary of tests on laser welds in ductile-brittle transition at -60 °C. Test were performed on deep cracks ($a/w=0.5$) in four-point bending. Crack initiation angle is measured at two positions, 2 mm apart in the centre of the specimen. For crack path see Figure 17.13.

Specimen	Crack location	Distance from weld centerline [mm]	Test temperature [°C]	Failure load [kN]	η_{plCMOD}	K_J [MPa√m]	Crack initiation angle [degree]	Comments
LW-17	Weld centerline	0	-93	11.06	3.71	353.2	Straight	
LW-21*	Weld centerline	0	-91	10.18	3.46	194.9	Straight	*a/w=0.13
LW-20	Weld	0.25	-90	11.64	3.72	427.3	Straight	
LW-25	Near fusion line	0.95	-92	9.52	3.90	164.2	Straight	Pop-in failure
LW-18	Heat affected zone	1.35	-92	10.78	4.74	368.4	9°, 10°, to BM	
LW-19	Base material near HAZ	2.20	-92	11.72	4.79	474.3	23°, 17°, to HAZ	
LW-33	Base material near HAZ	2.7	-91	11.60	4.9	524.6	11.5°, 11°, to HAZ	

Table 17.5:

Summary of tests on shallow cracked ($a/w=0.1$) laser welds at -90 °C. Test were performed in three-point bending. Crack initiation angle is measured at two positions, 2 mm apart in the centre of the specimen. For crack path see Figure 17.16.

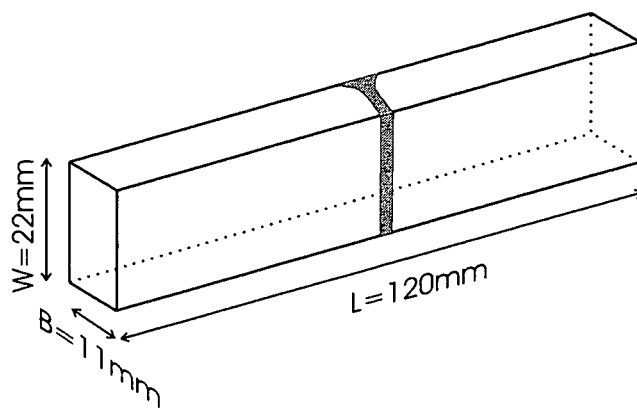


Figure 17.1:
Geometry of laser welded specimens.

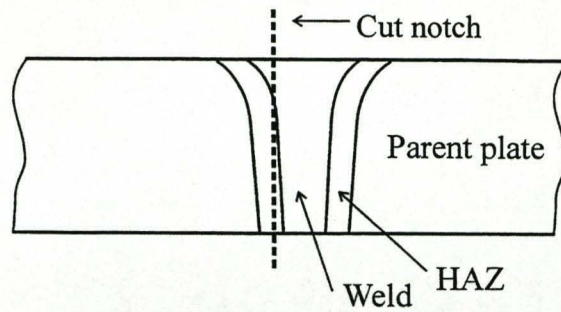


Figure 17.2:

Illustration of typically weld cross-section and a crack location in the heat affected zone, near fusion line.

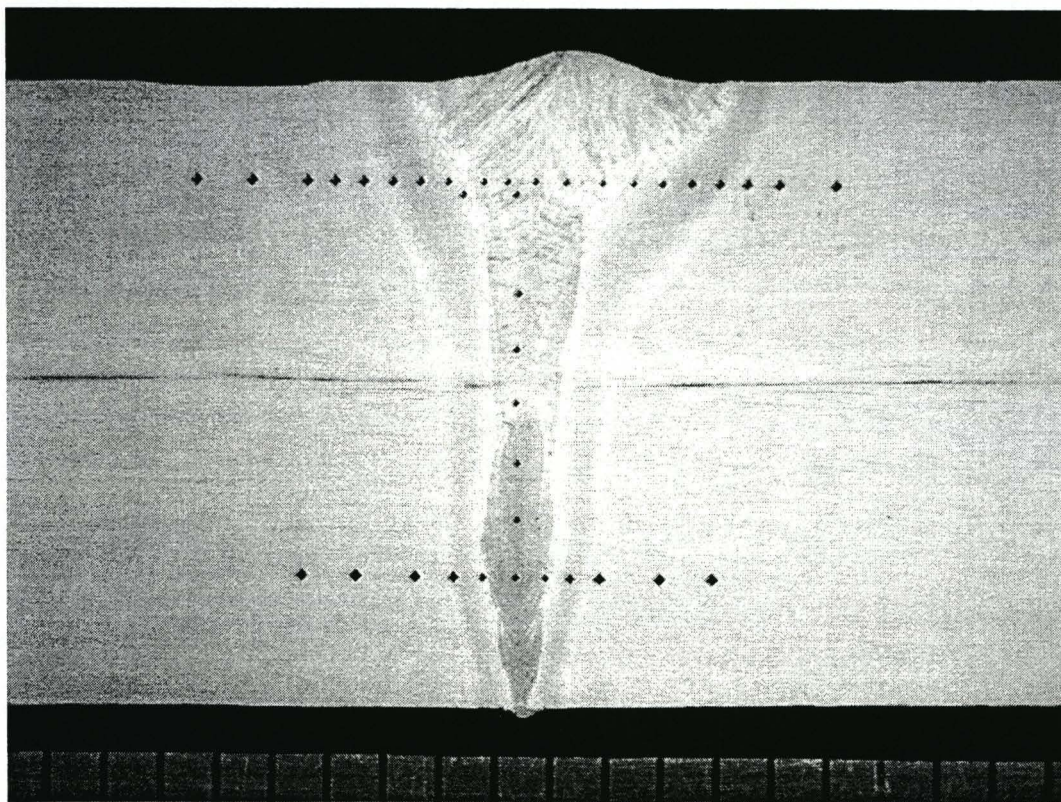


Figure 17.3:

Cross-section of laser weld showing and example of a crack located in the heat affected zone (HAZ), near fusion line and a photograph of the cross-section. The indentations from Vickers hardness measurements are visible. Note that the section is taken from the end of the plate where the weld is narrower.

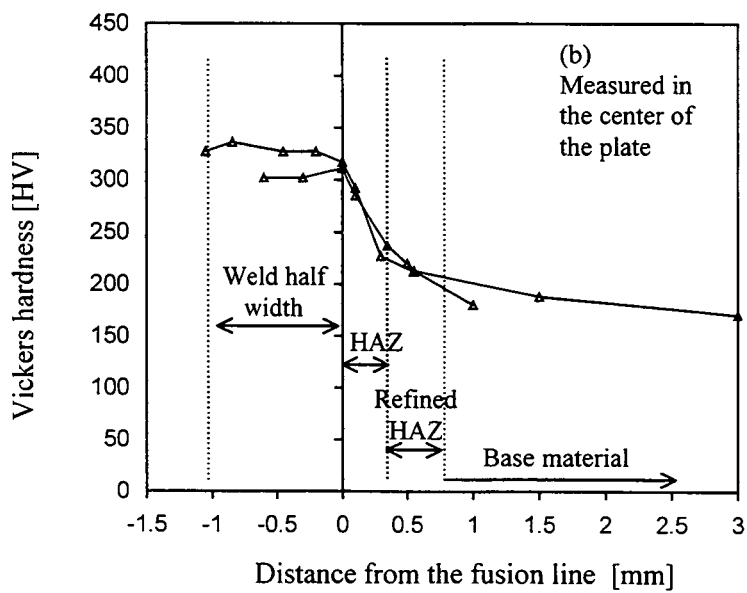
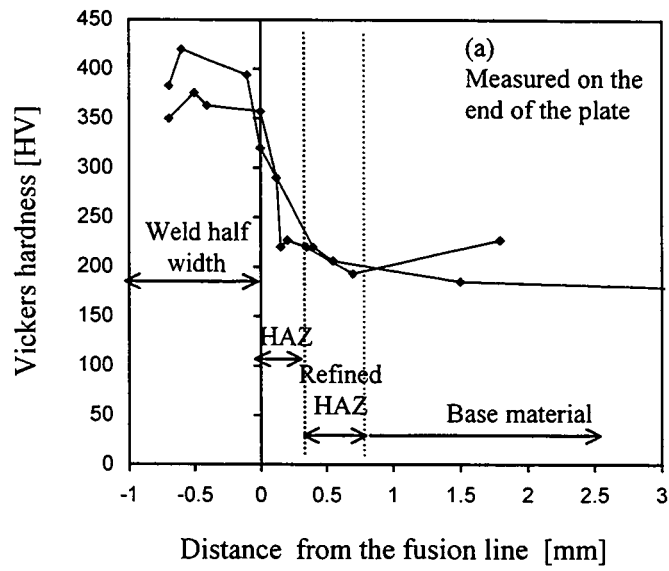


Figure 17.4:

Measurement of Vickers hardness across the width of the weld, starting from the fusion line. Measurements were performed on two specimens taken from the edge of the plate (Figure 17.4(a)) and on two specimens taken from the centre of the plate (Figure 17.4(b)).

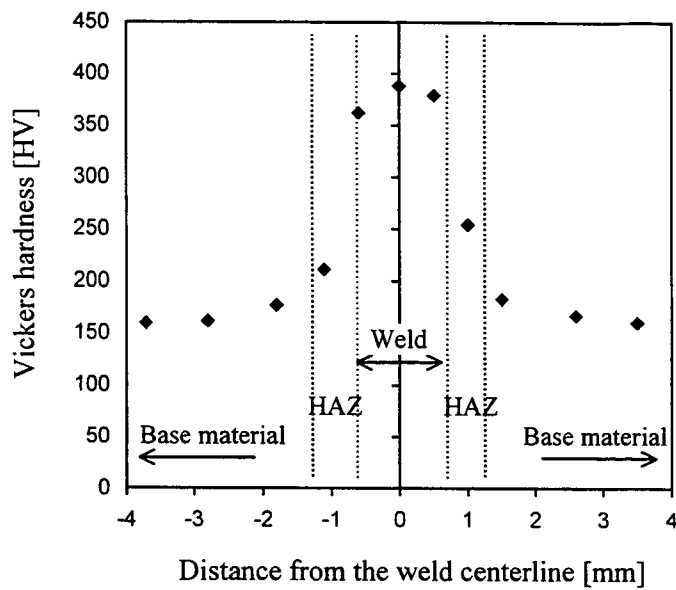


Figure 17.4(c): TWI measurement of Vickers hardness across the width of the weld. Photograph of measurement positions is shown in Figure 17.3. Note that these are taken at the end of the plate, where the weld is narrower.

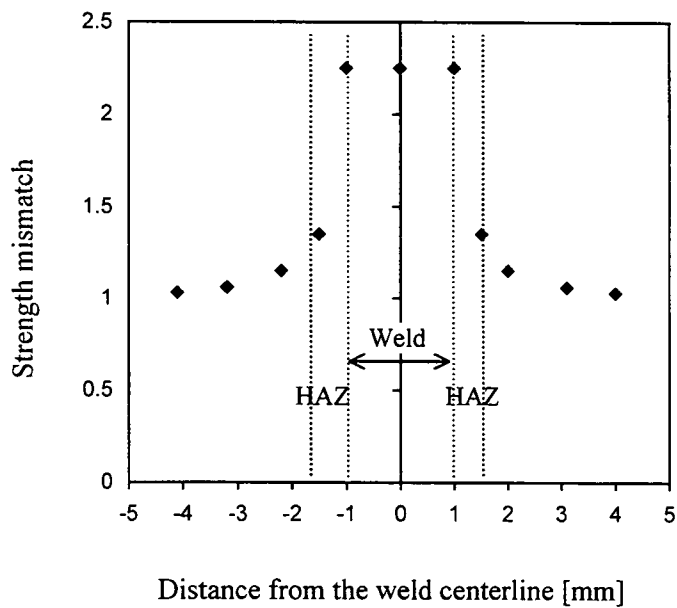


Figure 17.5: Strength mismatch from collection of hardness measurements across the laser welded joint, simplified for use in the finite element model.

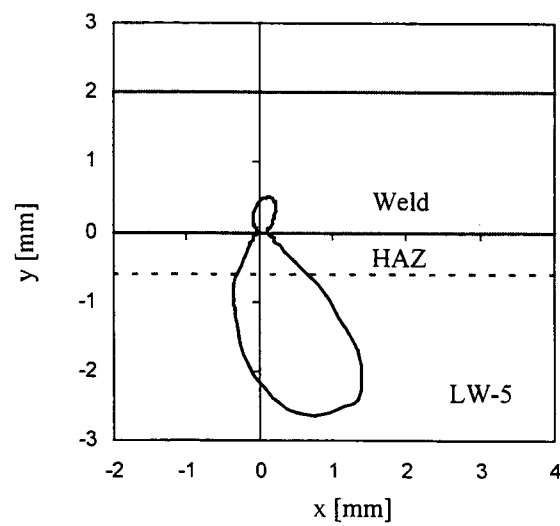
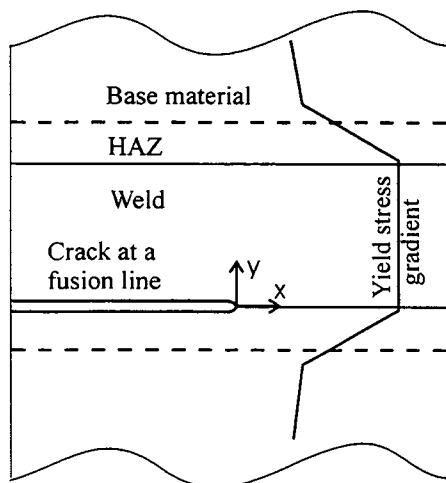
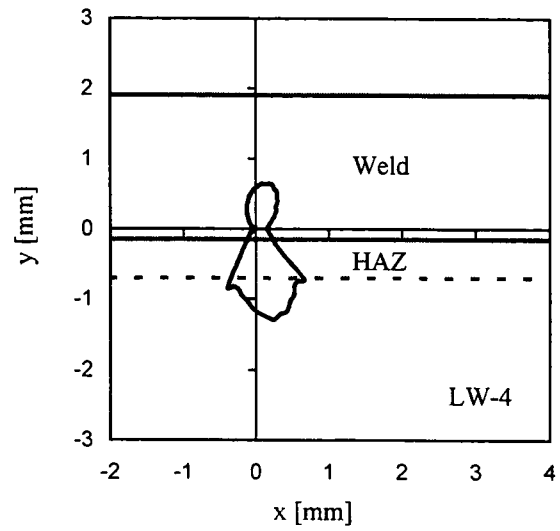
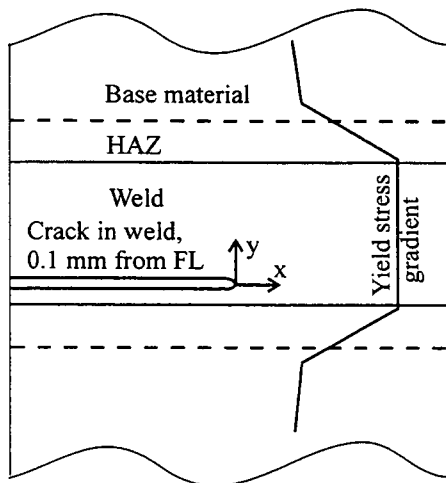
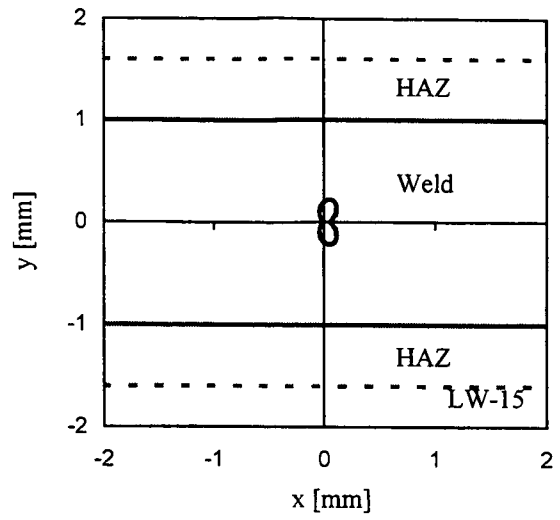
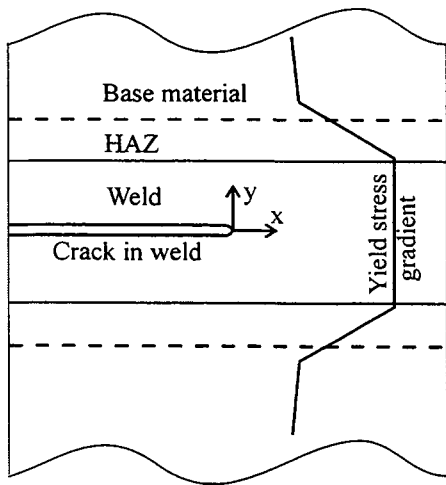


Figure 17.6:
Schematic representation of crack locations in test geometries and associated plots of the plastic strains.

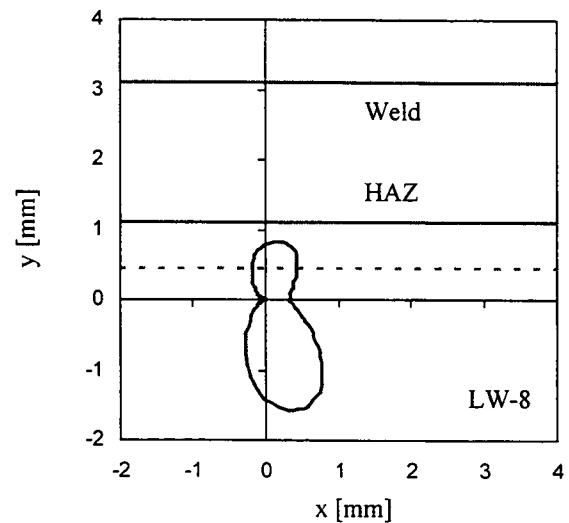
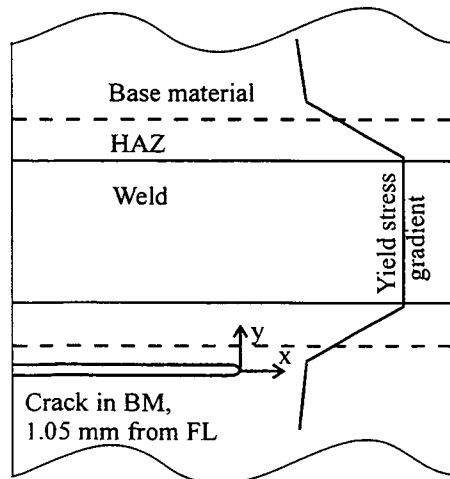
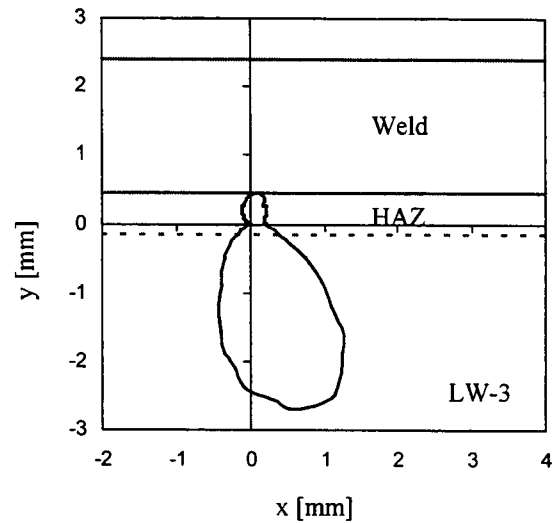
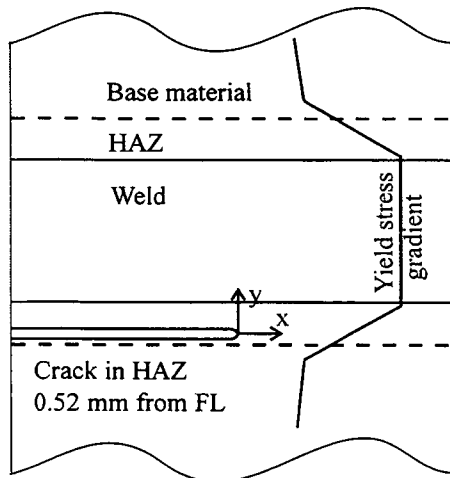
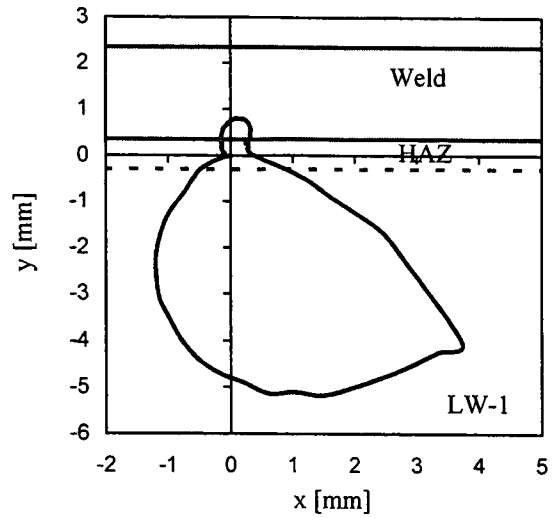
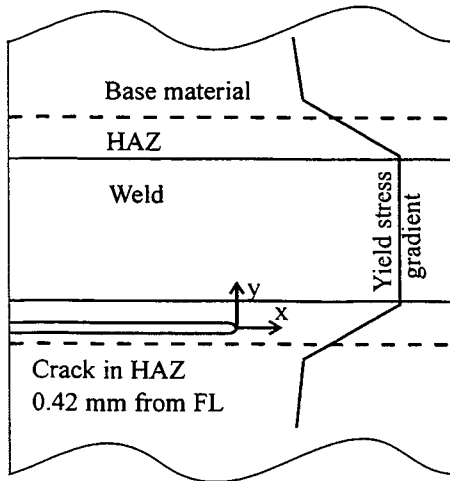


Figure 17.6 (cont):
Schematic representation of crack locations in test geometries and associated plots of the plastic strains.

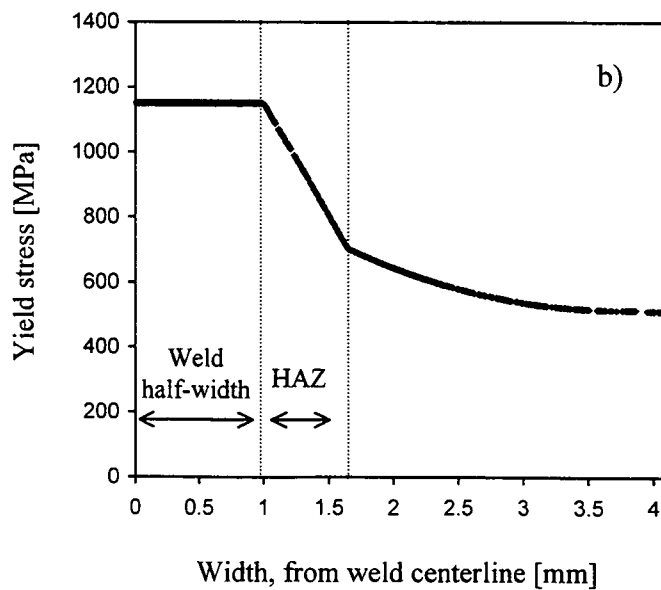
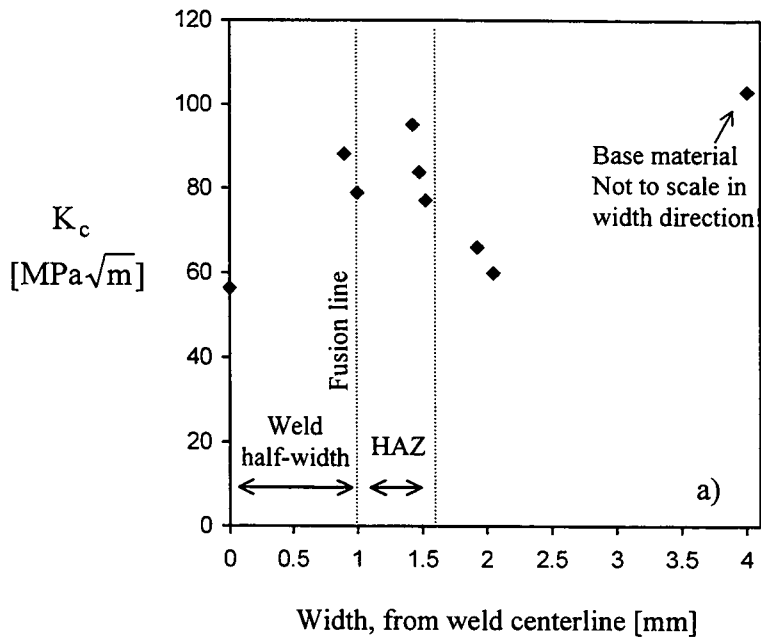


Figure 17.7:
Fracture toughness in contained yielding at $-130\text{ }^{\circ}\text{C}$ for a range of crack configurations, with crack location measured in the centre of specimens. The local yield stresses are shown in Figure 18.7(b).

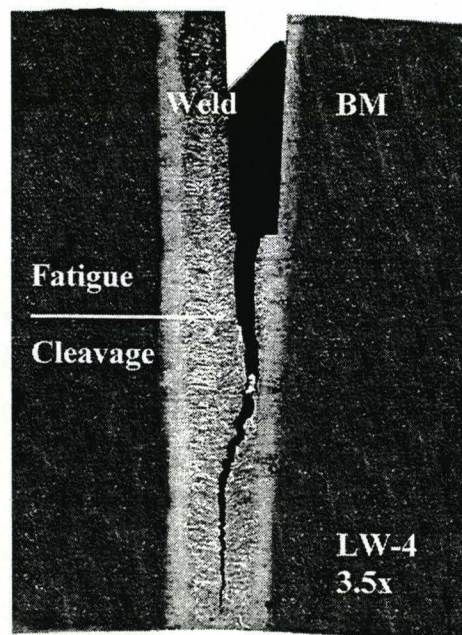
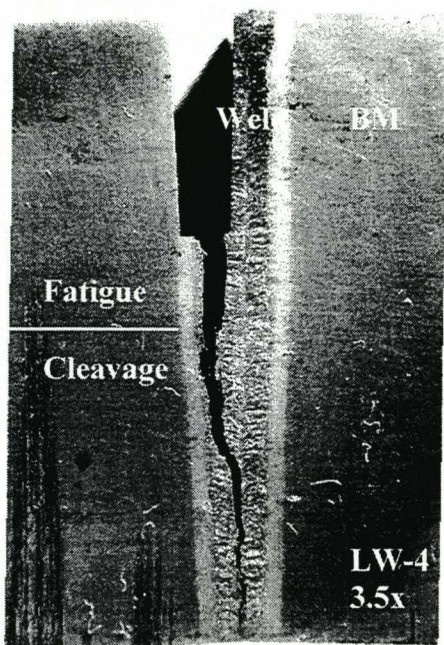
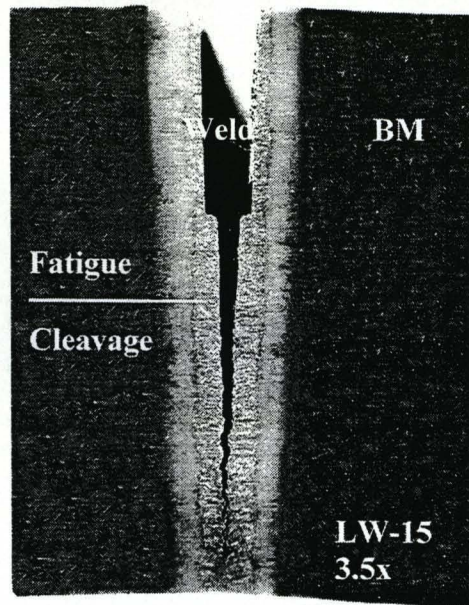
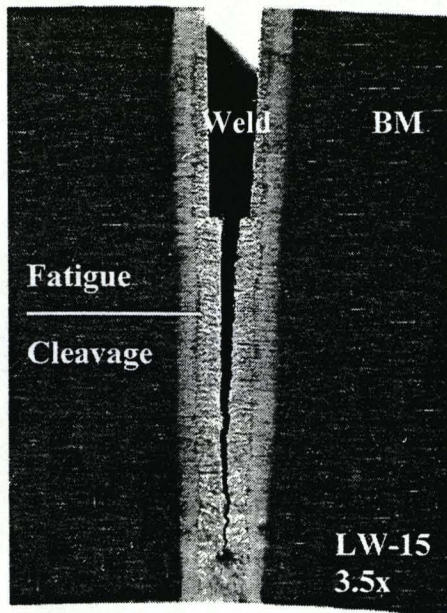


Figure 17.8:
Photographs of crack paths at -130°C tests in the center of the specimen,
measured on cross-sections 2 mm apart.

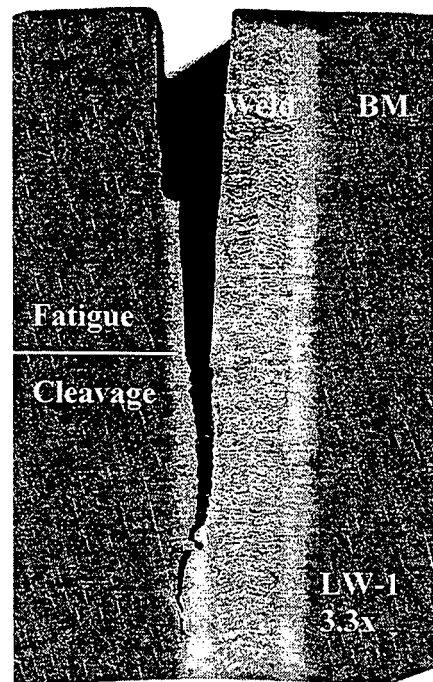
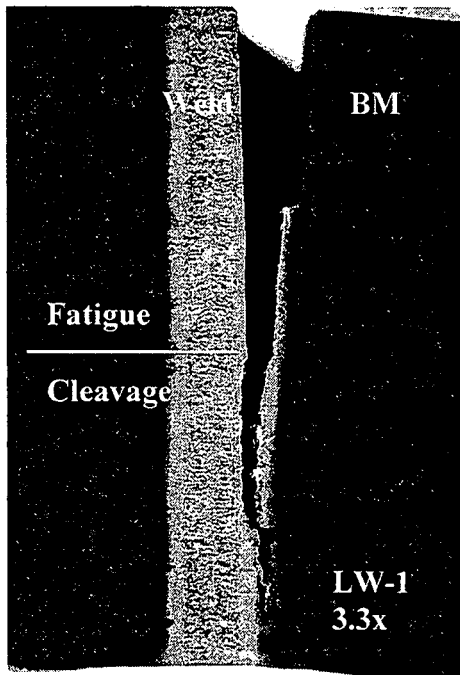
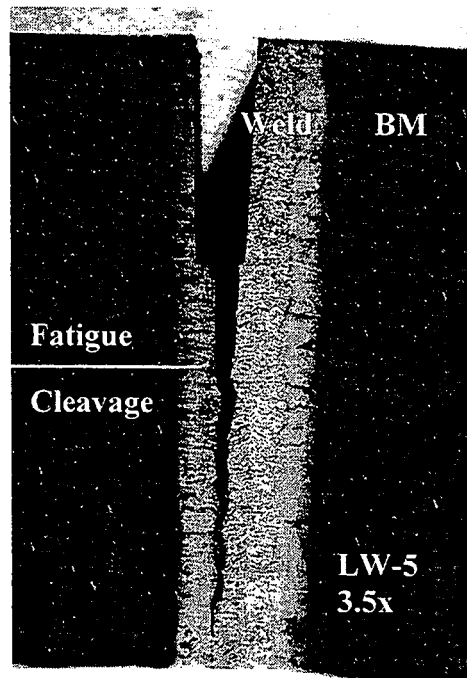
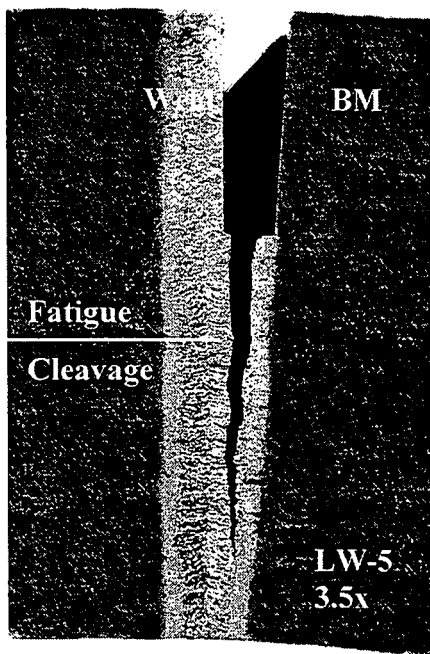


Figure 17.8 (cont):
Photographs of crack paths at -130°C tests in the center of the specimen,
measured on cross-sections 2 mm apart.

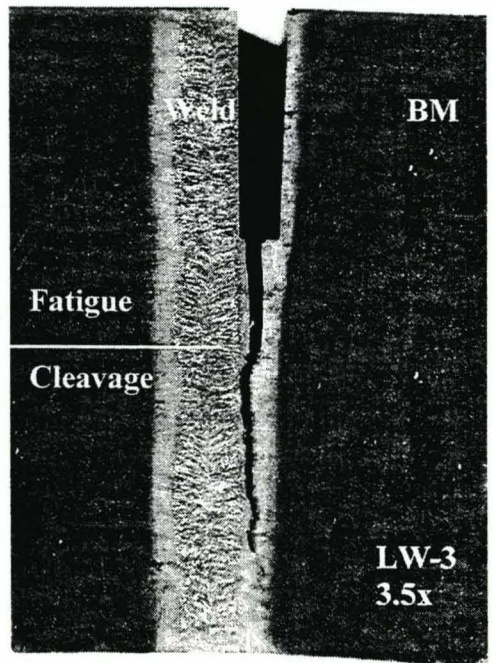
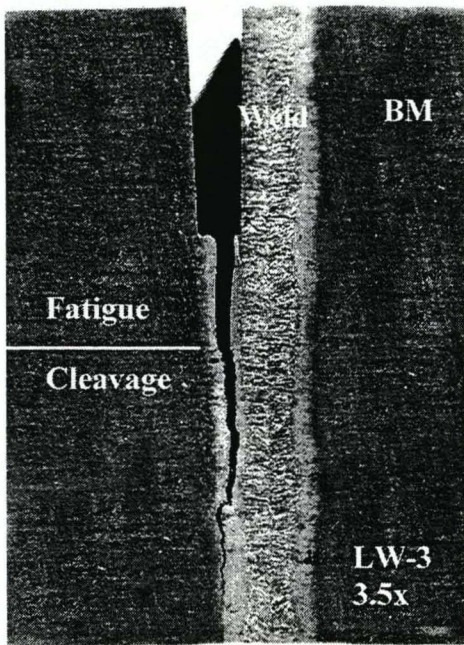
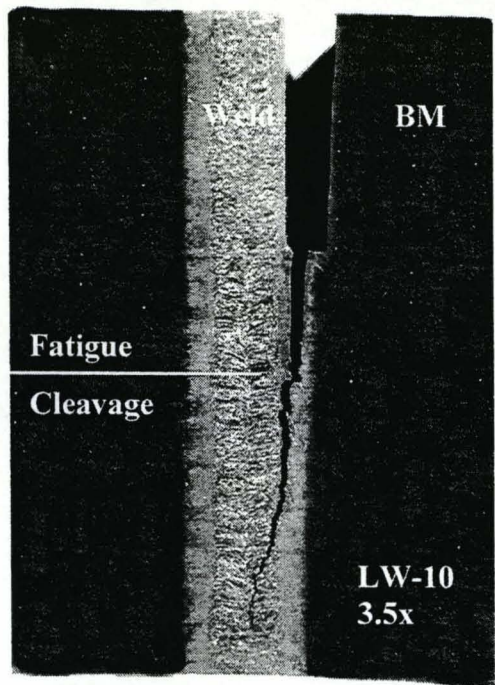
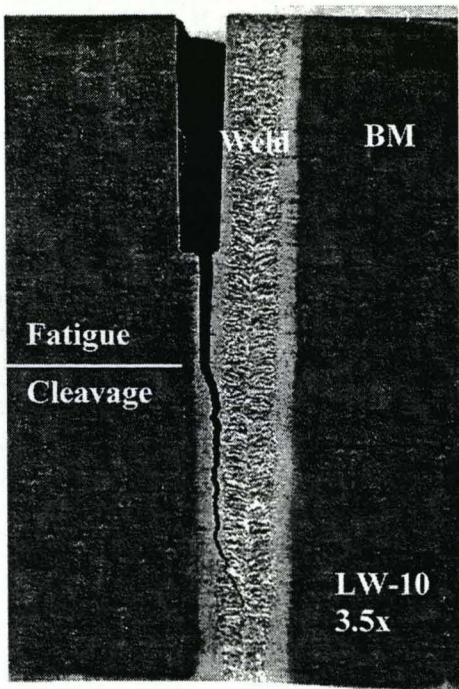


Figure 17.8 (cont):
Photographs of crack paths at $-130\text{ }^{\circ}\text{C}$ tests in the center of the specimen,
measured on cross-sections 2 mm apart.

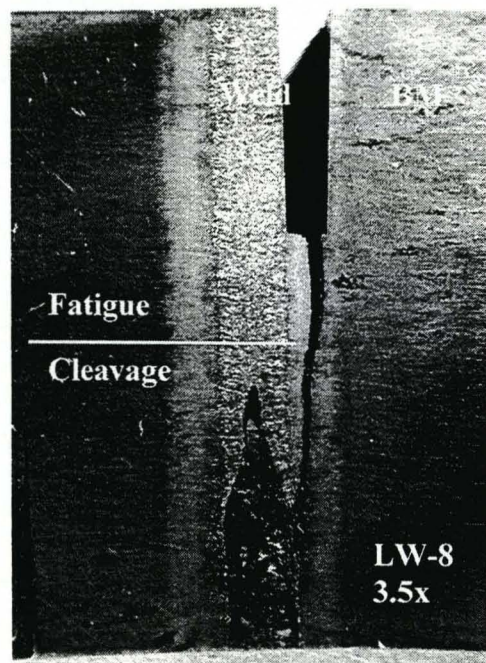
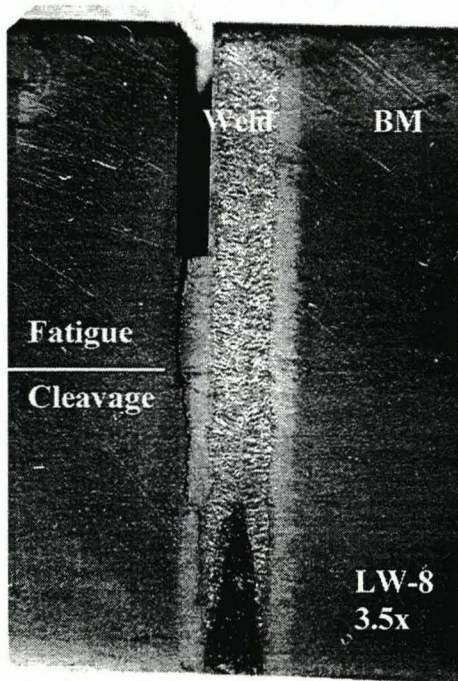
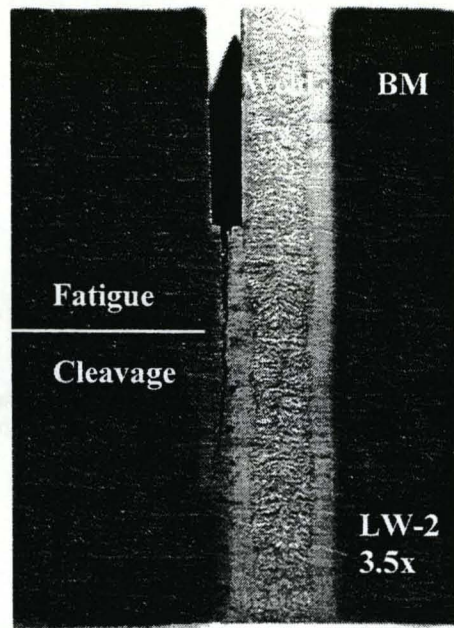
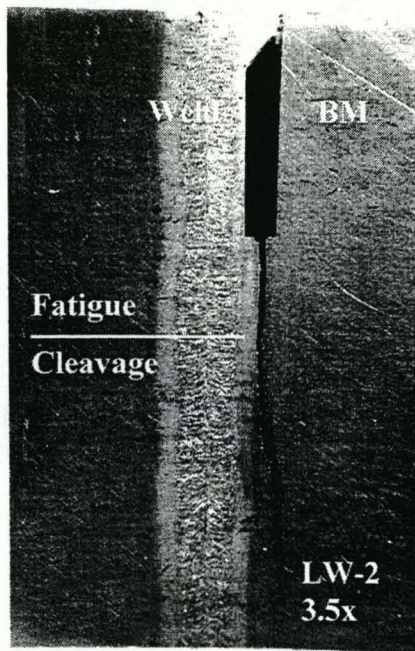


Figure 17.8 (cont):
Photographs of crack paths at -130°C tests in the center of the specimen,
measured on cross-sections 2 mm apart.

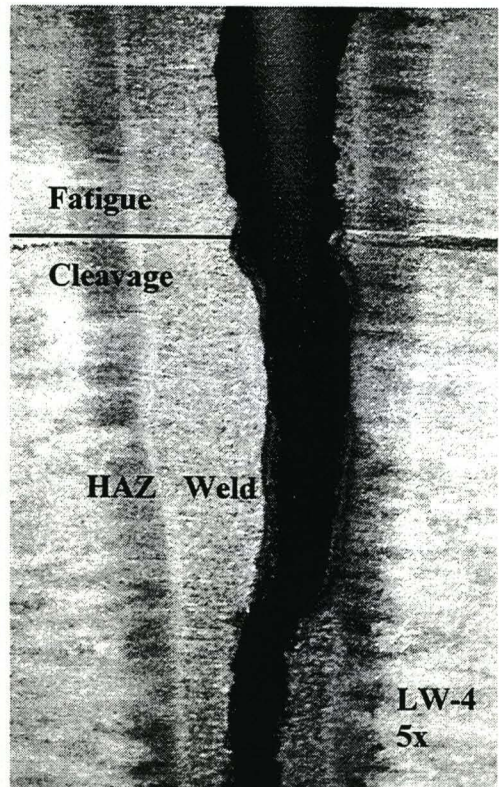
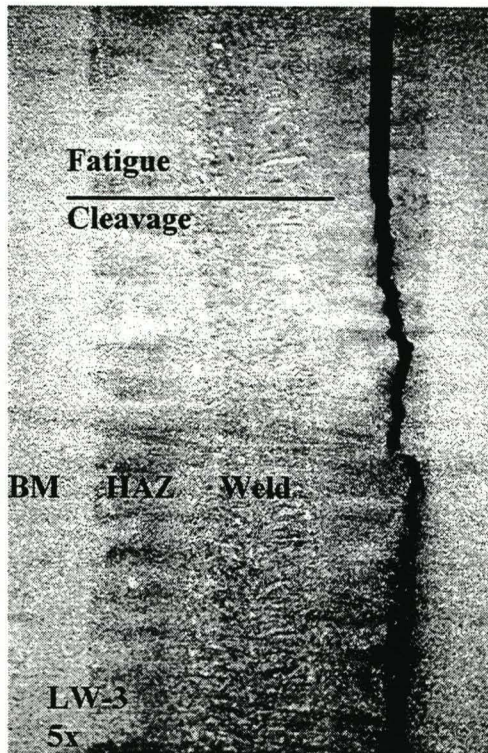
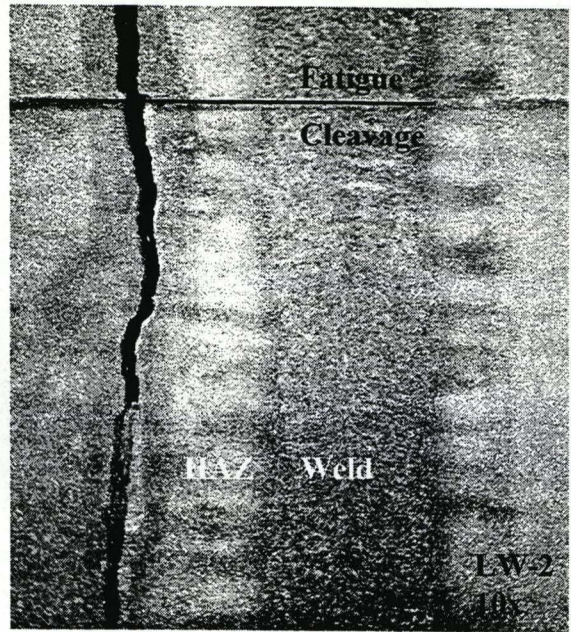
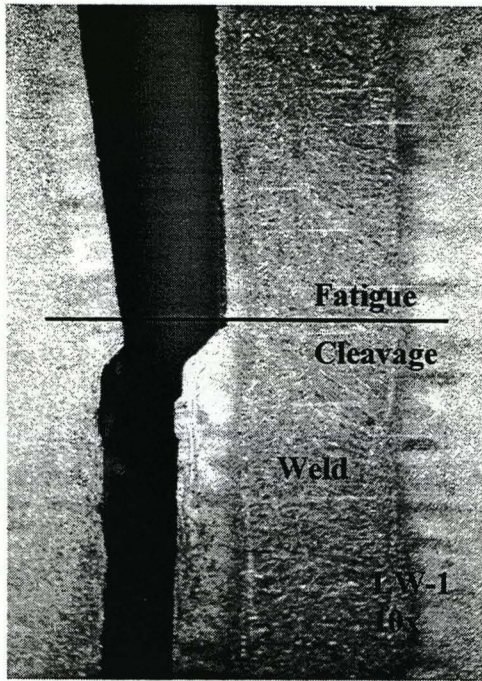


Figure 17.9:
Photographs of crack path on the surface of laser welded specimens, tested at -130 °C.

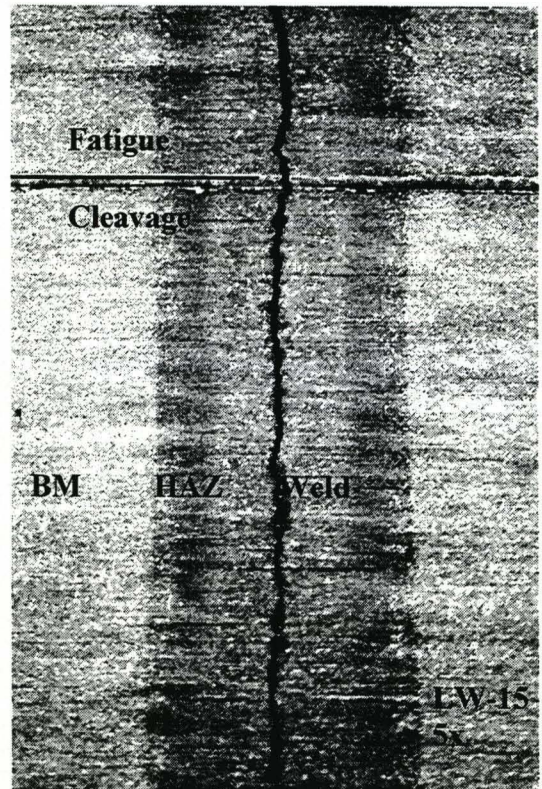
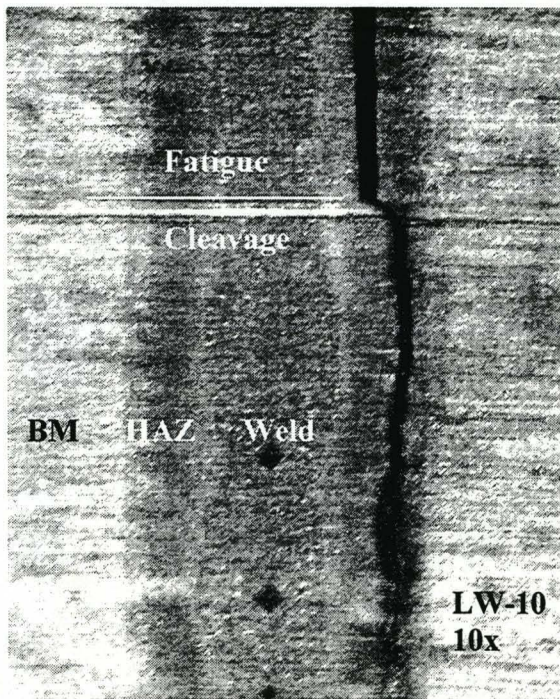
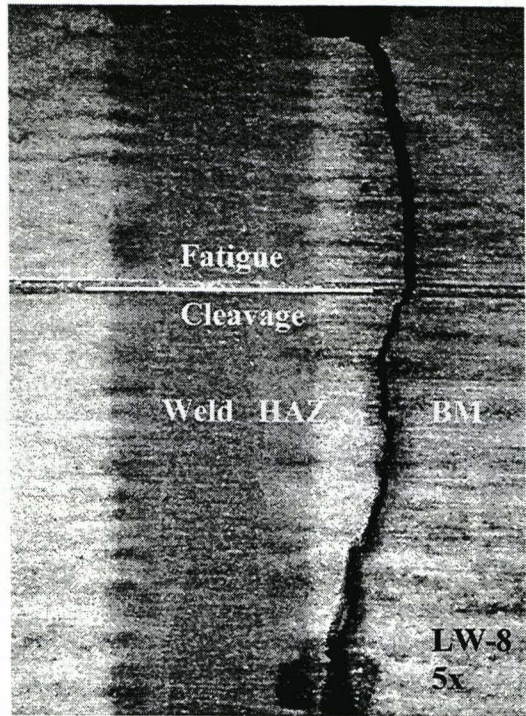
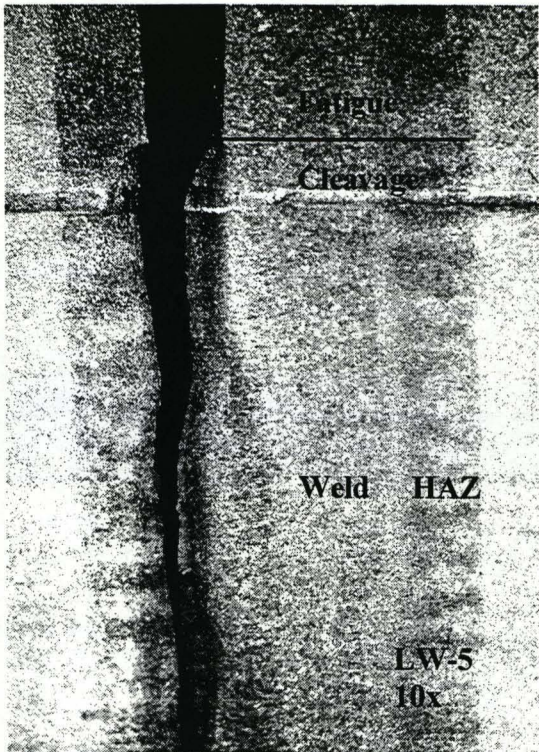


Figure 17.9 (cont):
Photographs of crack path on the surface of laser welded specimens, tested at -130°C .

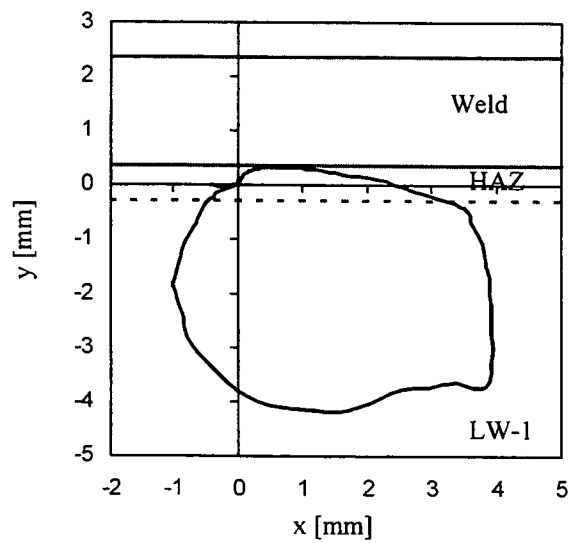
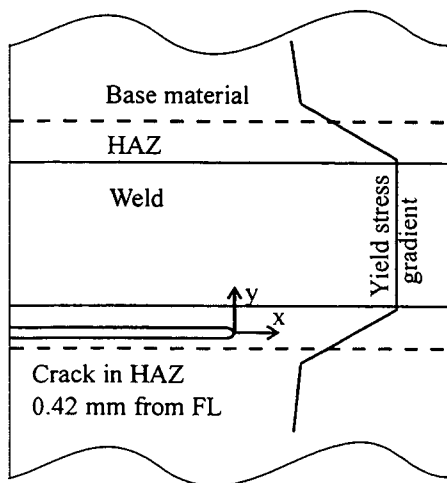
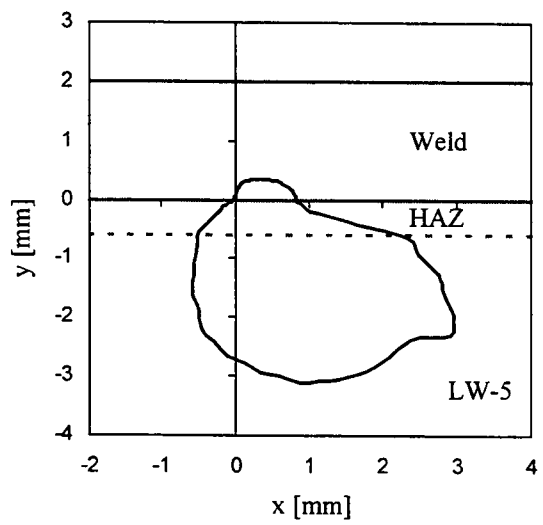
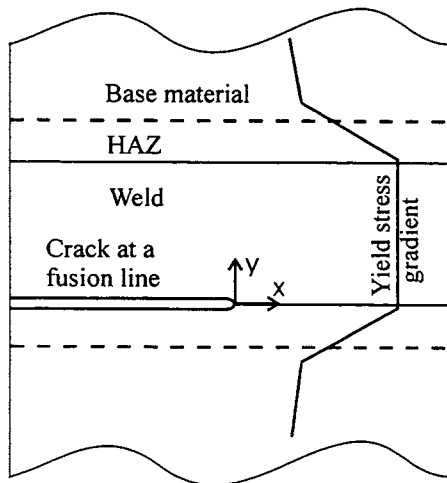
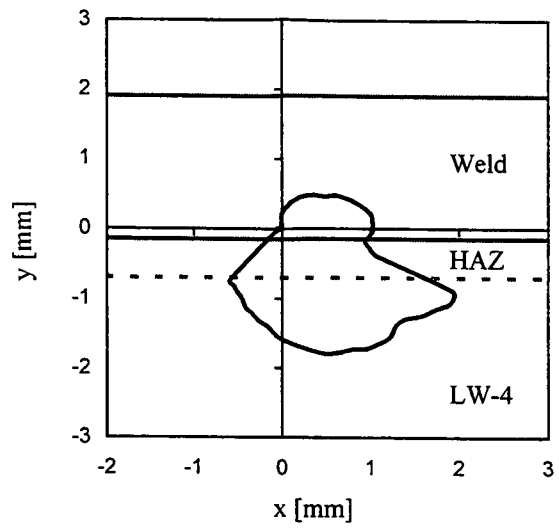
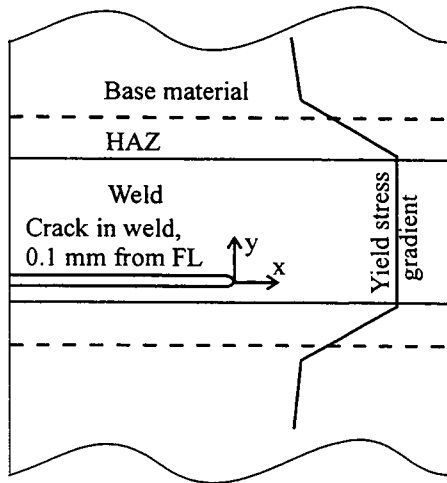


Figure 17.10:

Plots of the plastic strains under plane stress conditions for a representative sample of test geometries at -130°C conditions.

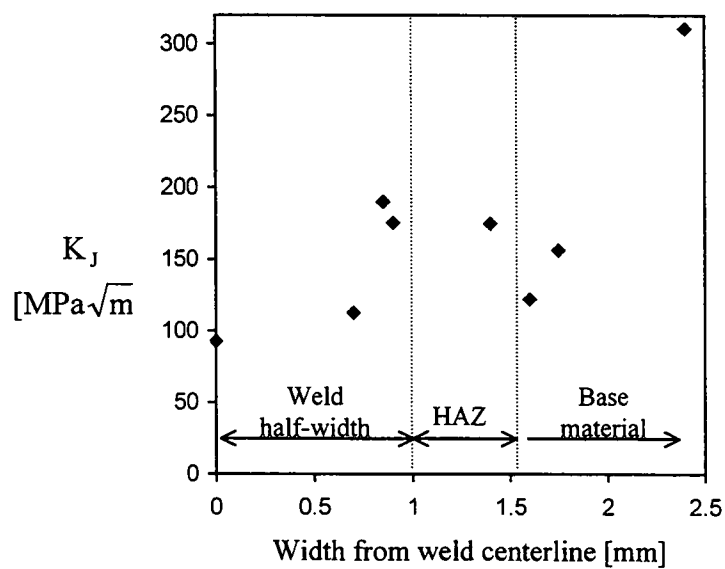


Figure 17.11:
Fracture toughness for a deep crack ($a/w=0.5$) configuration in ductile-brittle transition at -60 C. Crack location is measured in the centre of the specimen.

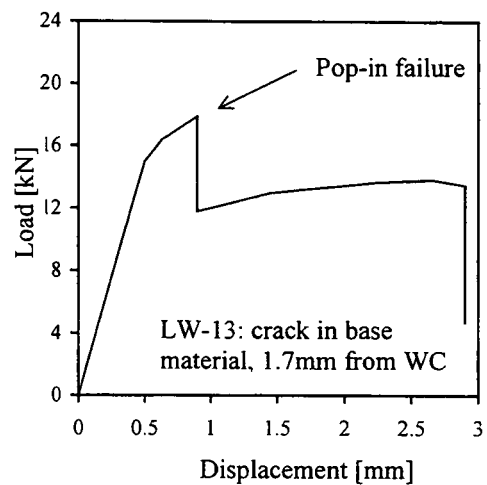
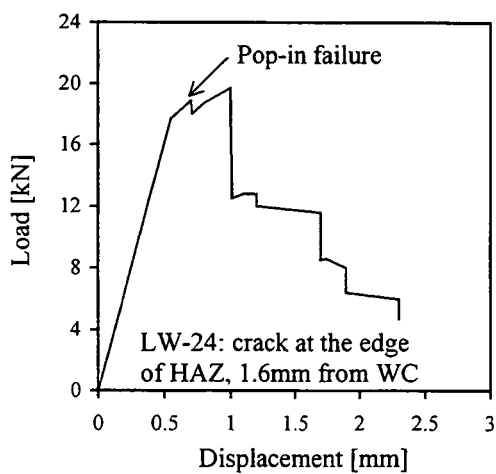
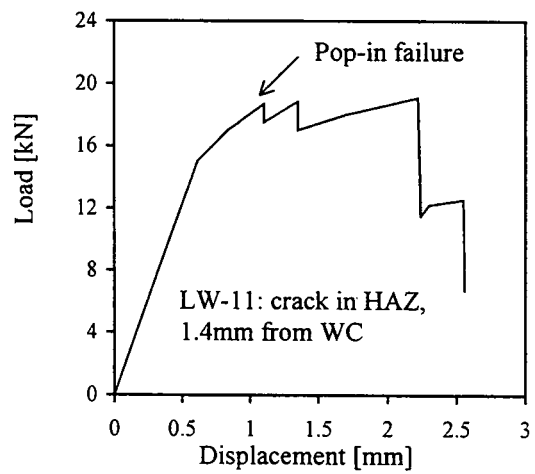
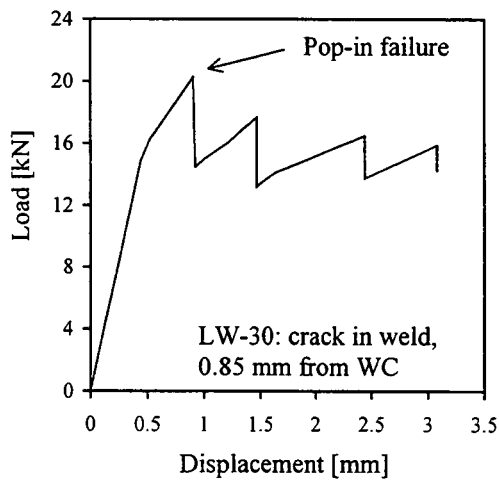
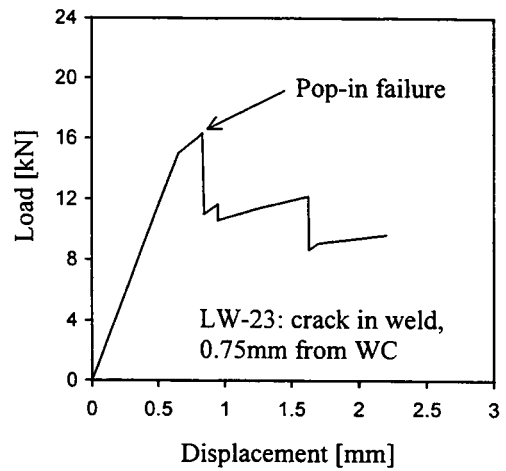
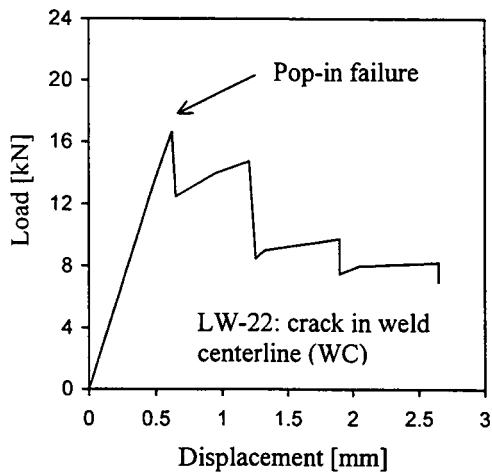


Figure 17.12: Load – load-line-displacement records from tests on deep cracks at -60°C , showing pop-in failures.

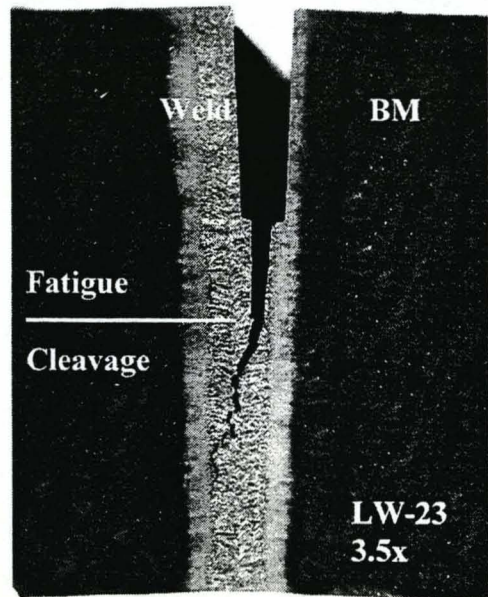
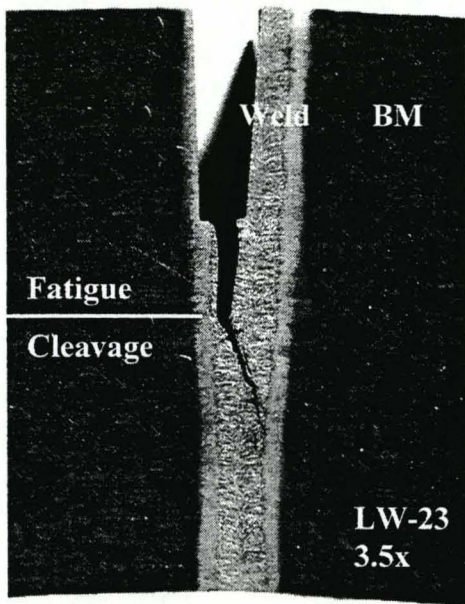
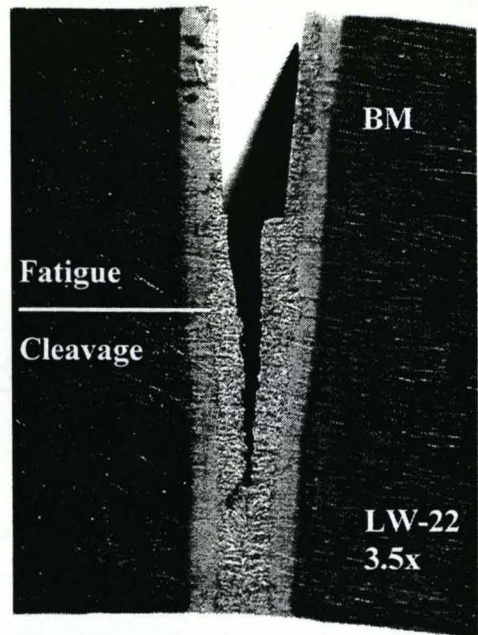
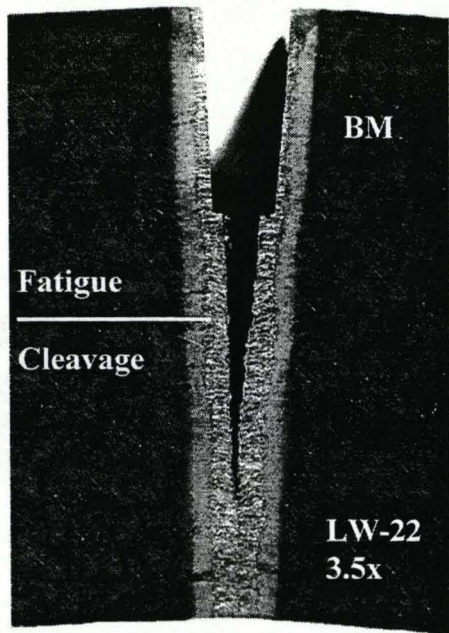


Figure 17.13:
Photographs of crack paths in the center of laser welded specimens, for $a/w=0.5$ configurations tested at -60°C . Photographs are taken at cross-sections 2mm apart.

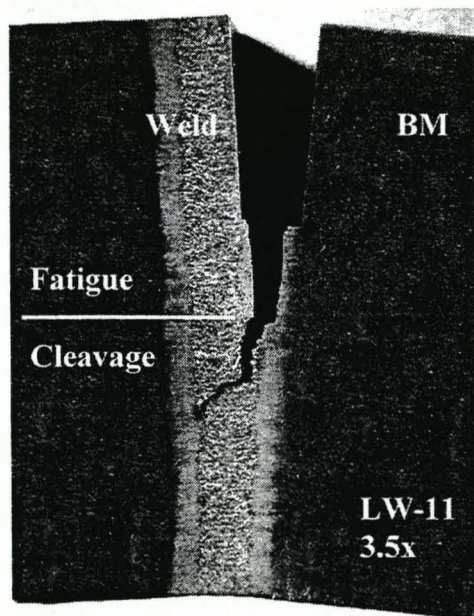
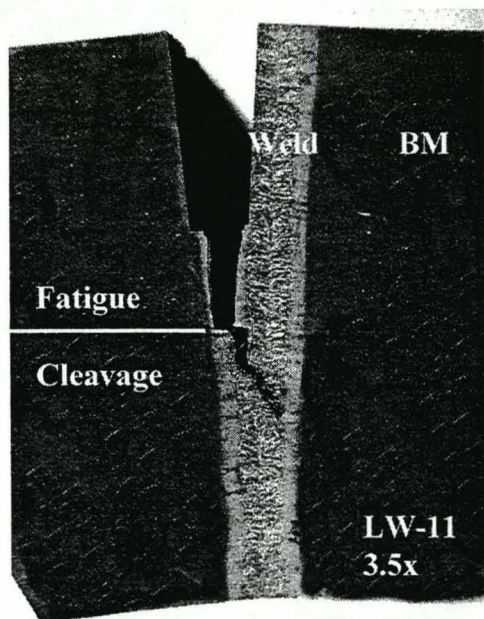
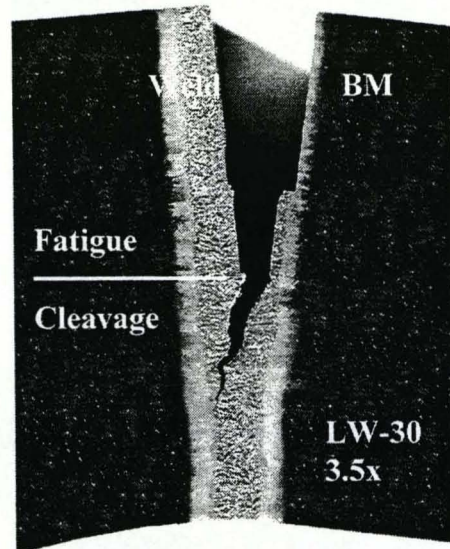
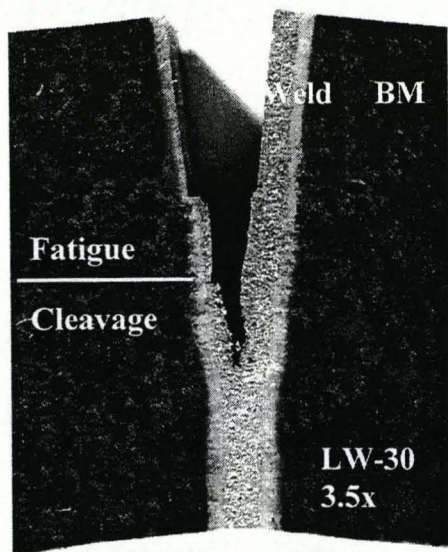


Figure 17.13 (cont):
Photographs of crack paths in the center of laser welded specimens, for $a/w=0.5$ configurations tested at -60°C . Photographs are taken at cross-sections 2mm apart.

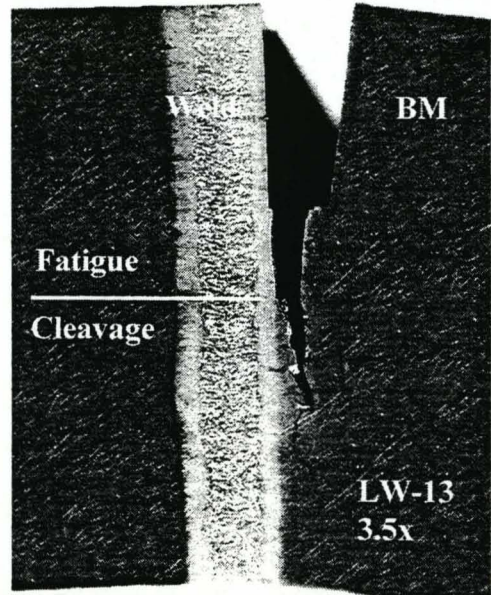
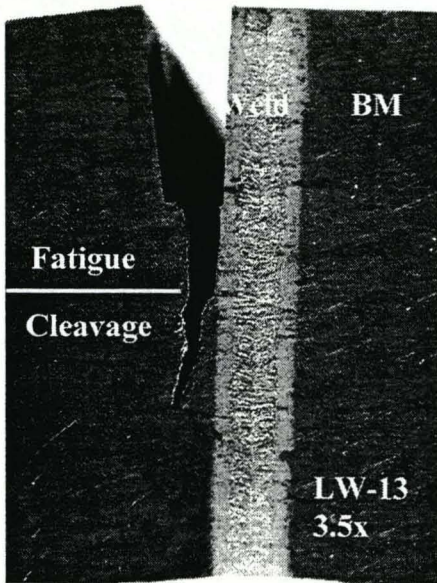
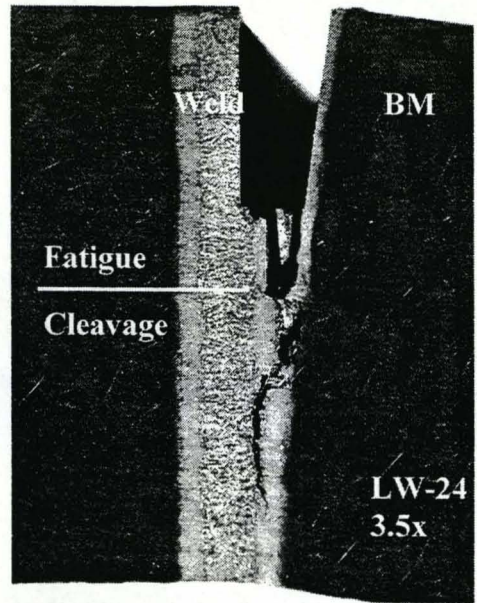
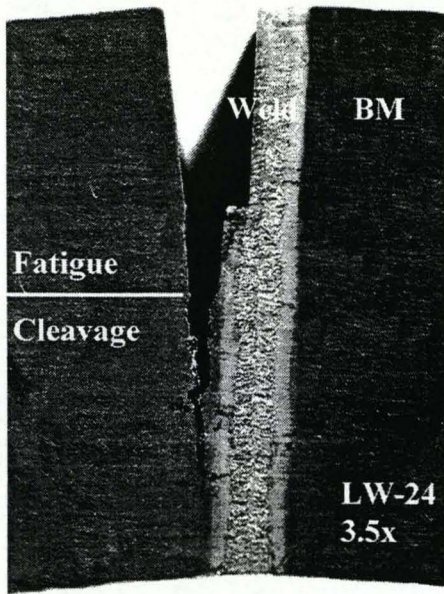


Figure 17.13 (cont):
Photographs of crack paths in the center of laser welded specimens, for $a/w=0.5$ configurations tested at $-60\text{ }^{\circ}\text{C}$. Photographs are taken at crosssections 2mm apart.

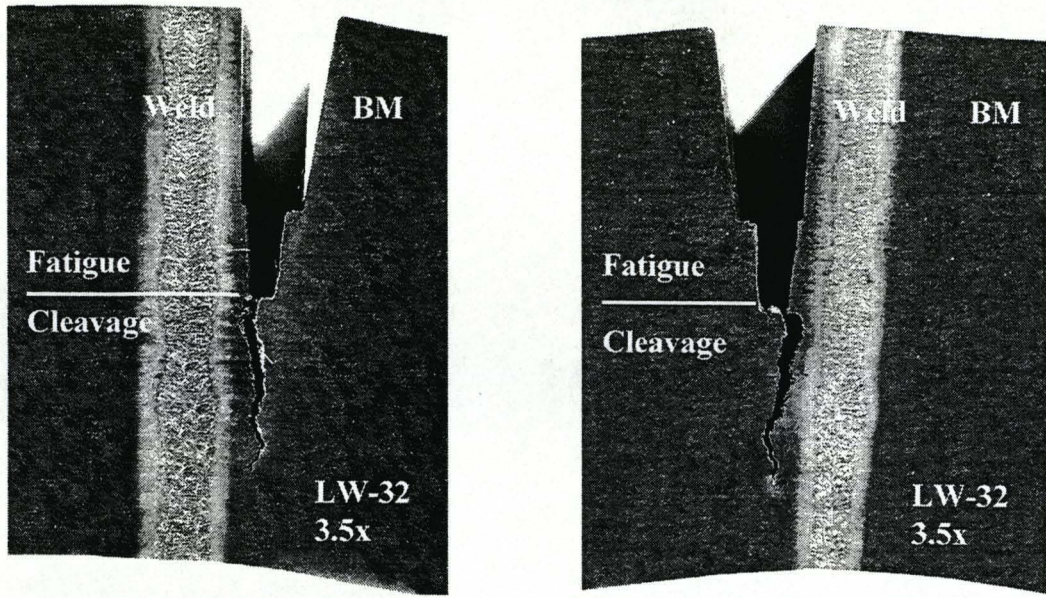


Figure 17.13 (cont):
Photographs of crack paths in the center of laser welded specimens, for $a/w=0.5$ configurations tested at $-60\text{ }^{\circ}\text{C}$. Photographs are taken at crosssections 2mm apart.

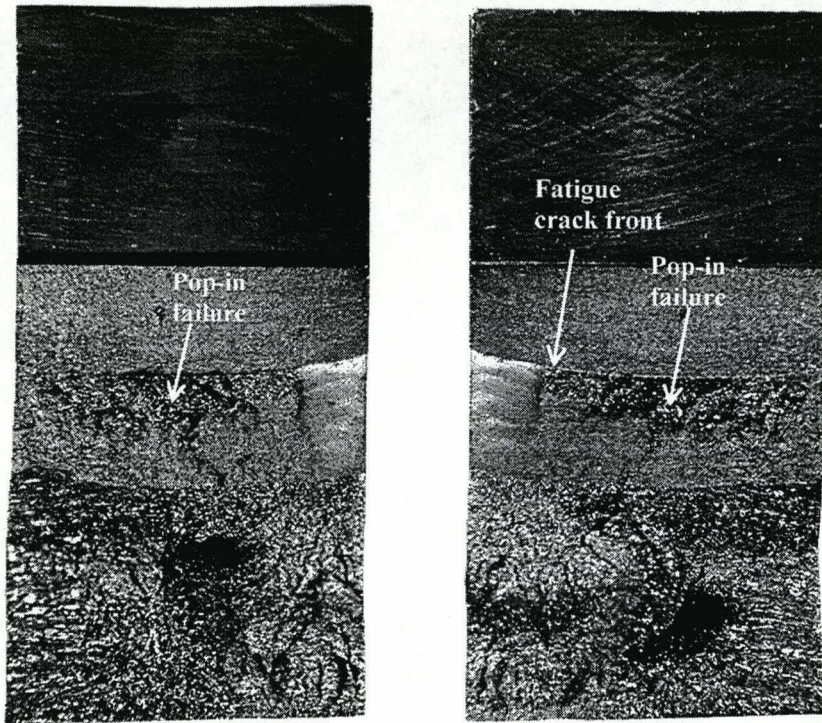


Figure 17.14:
Photograph of a fracture surface of specimen LW-31 showing pop-in failure.
The specimen had a crack front fully contained in the weld metal.

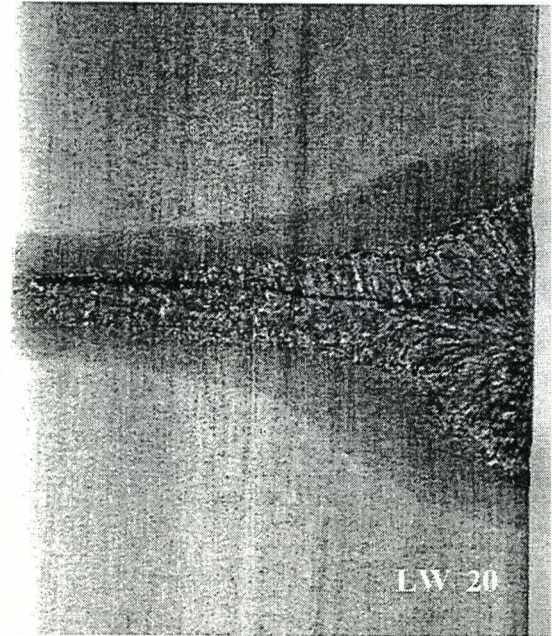
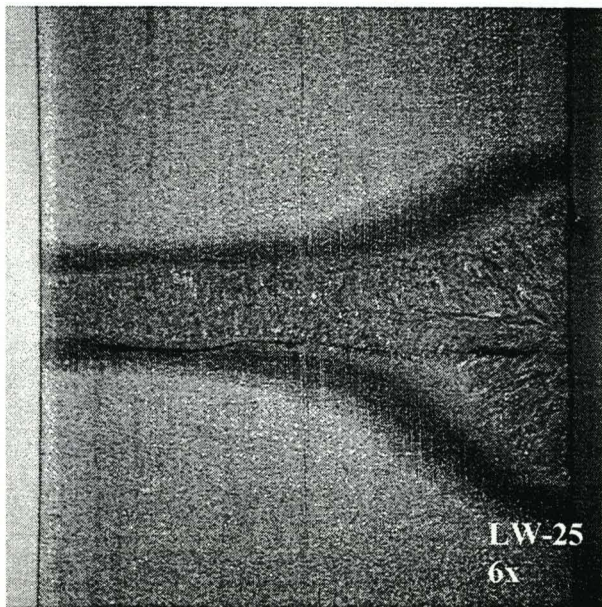
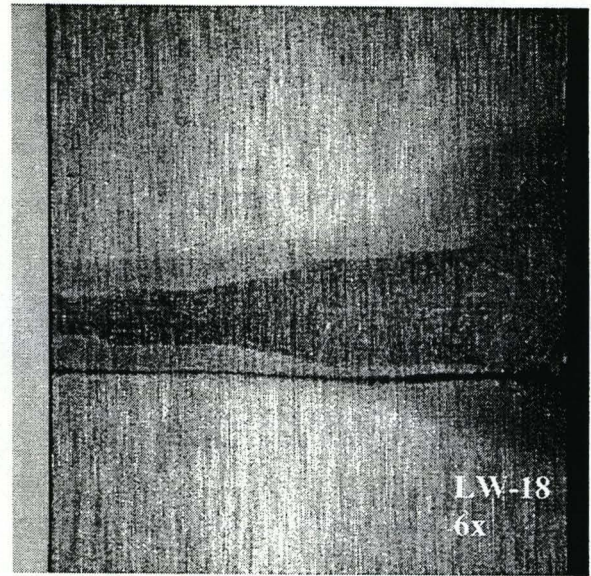
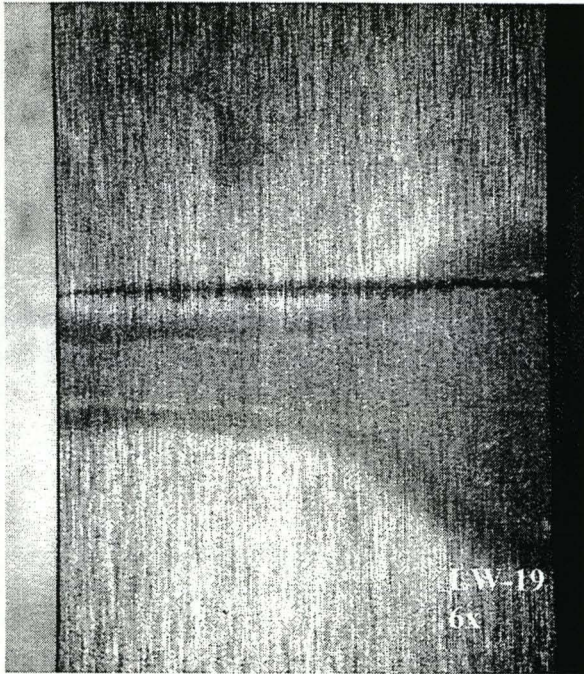


Figure 17.15:
Photographs of crack location along the width of the weld for $a/w=0.1$ crack prior to cleavage tests.

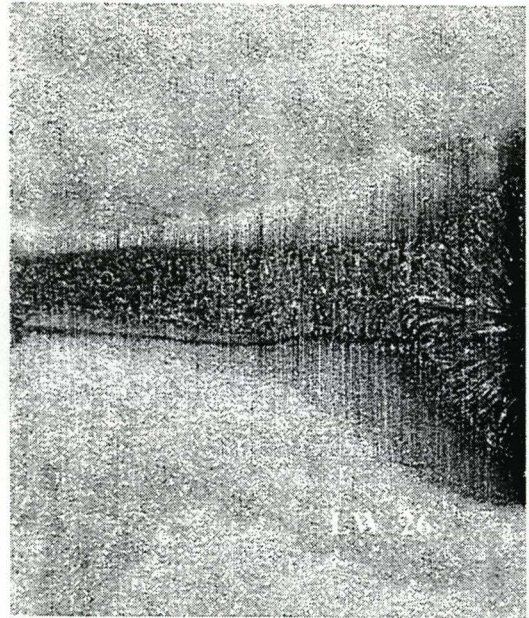
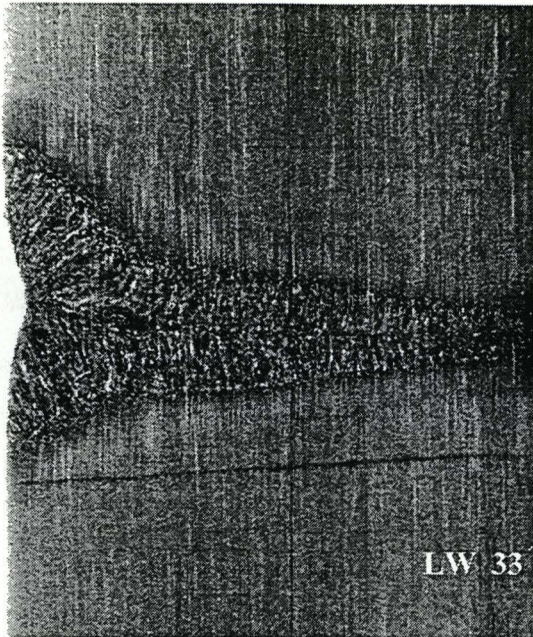


Figure 17.15 (cont):
Photographs of crack location along the width of the weld for $a/w=0.1$ crack prior to cleavage tests.

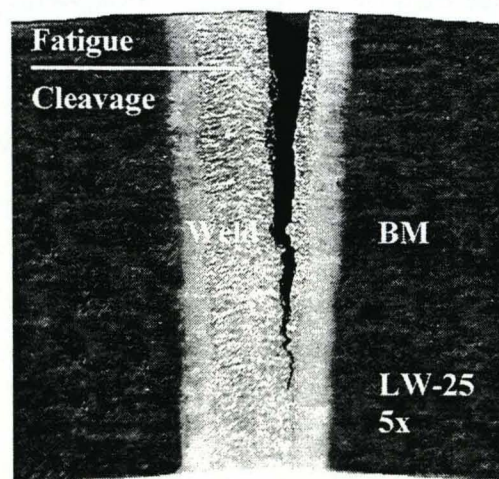
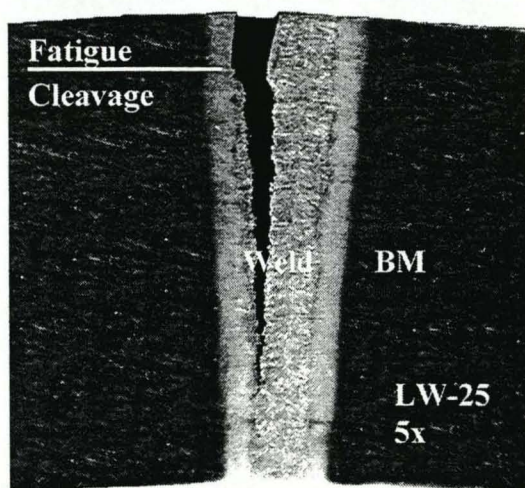
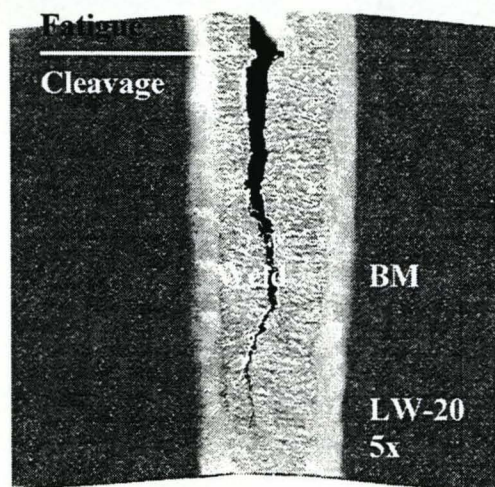
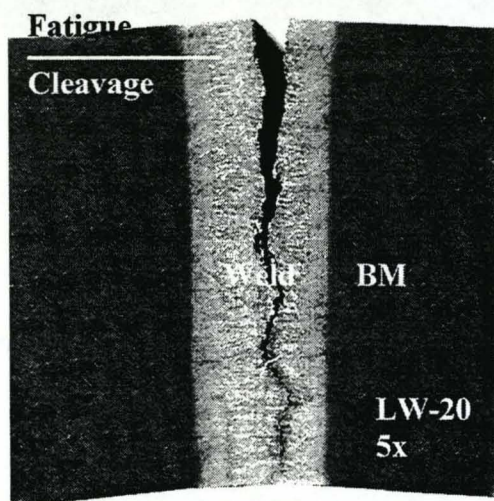
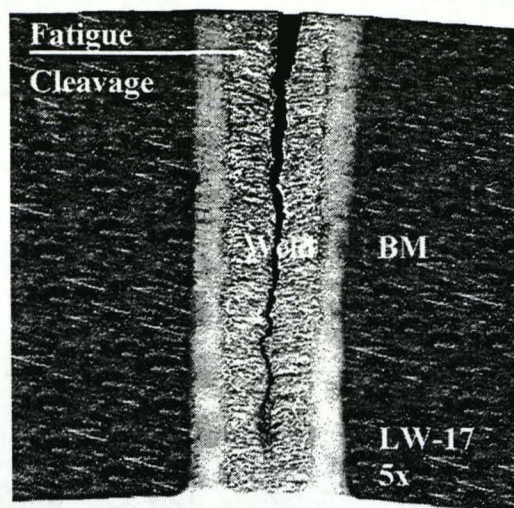
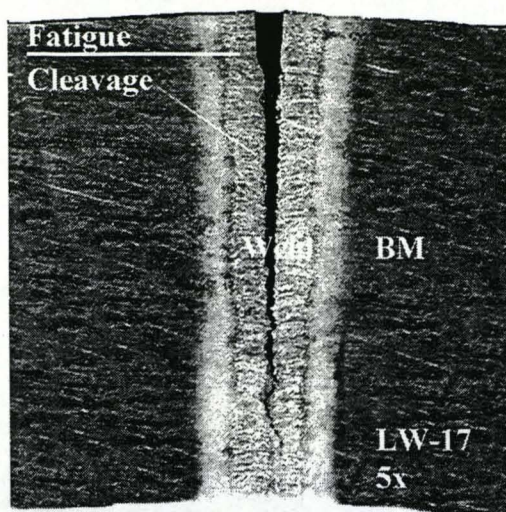


Figure 17.16:
Photographs of crack paths in the center of laser welded specimens, for $a/w=0.1$ configurations tested at -90°C . Photographs are taken at cross-sections 2 mm apart.

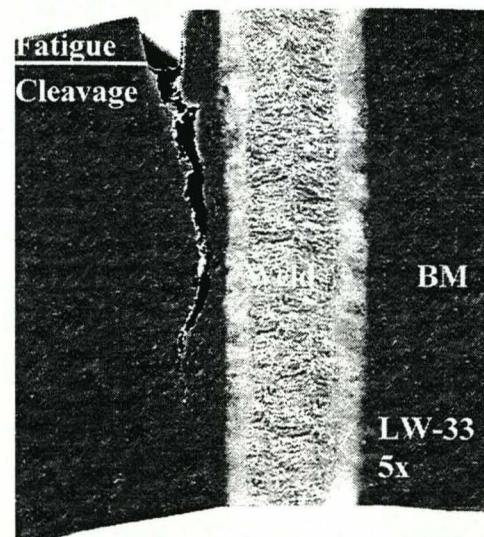
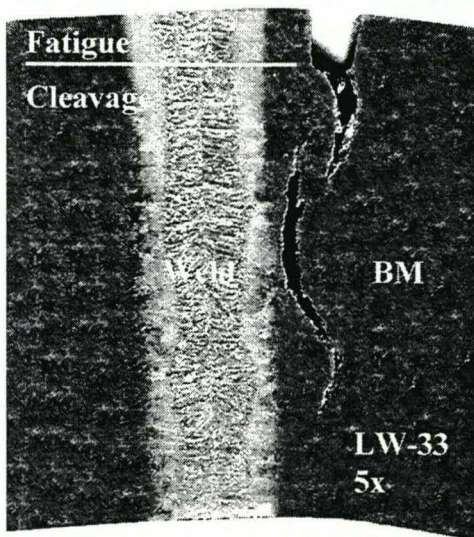
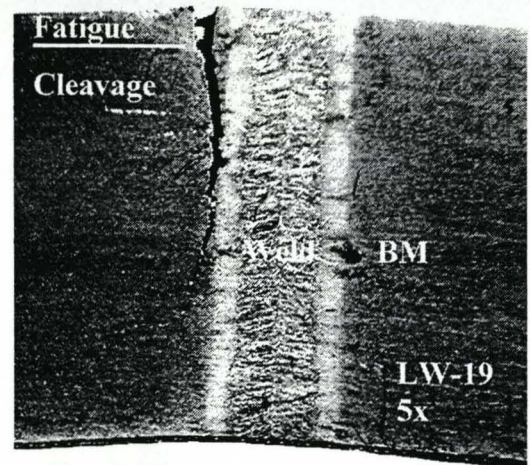
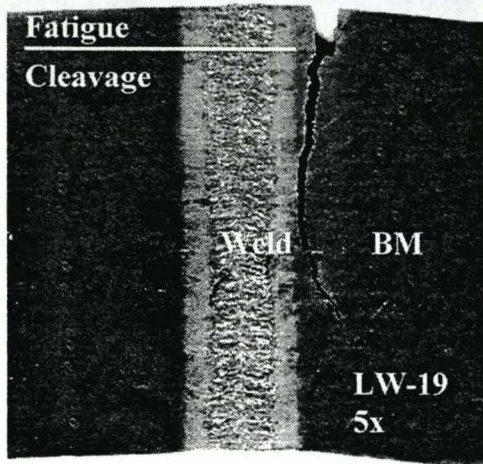
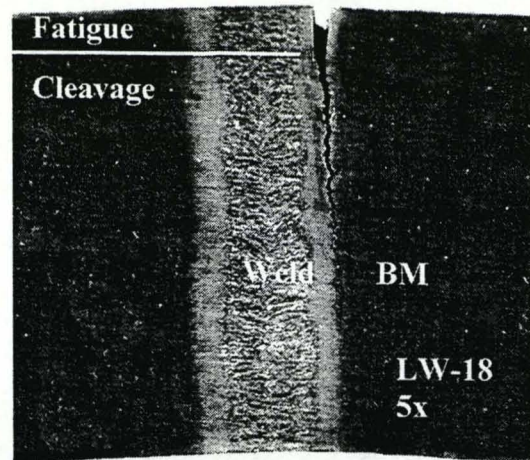
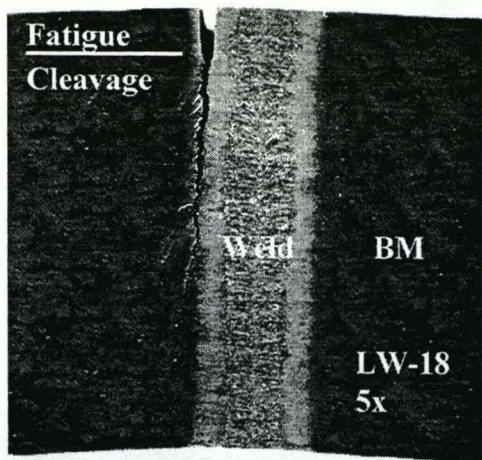


Figure 17.16 (cont):
Photographs of crack paths in the center of laser welded specimens, for $a/w=0.1$ configurations tested at -90°C . Photographs are taken at cross-sections 2 mm apart.

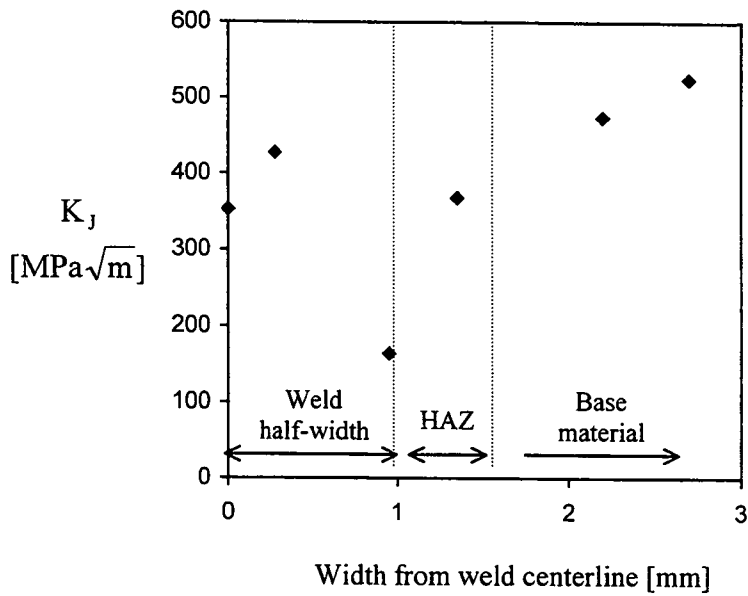


Figure 17.17: Fracture toughness for shallow crack ($a/w=0.1$) configurations in ductile-brittle transition at $-90\text{ }^\circ\text{C}$. Crack location is measured in the centre of the specimen.

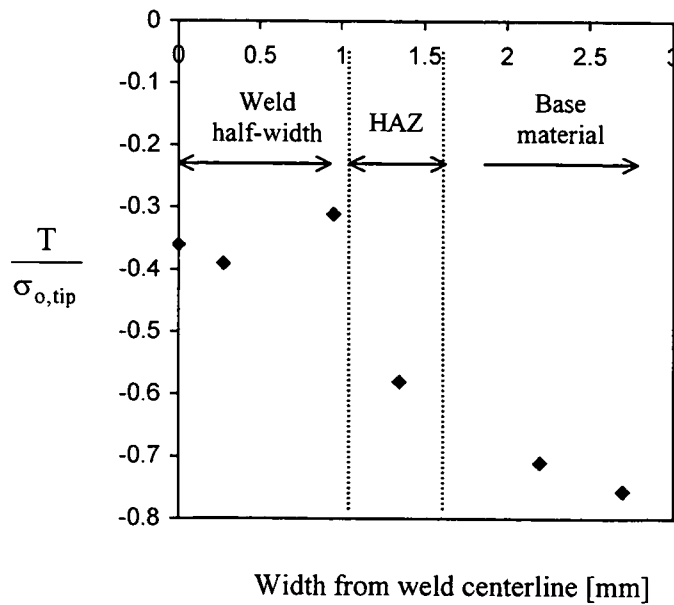


Figure 17.18: T-stress for shallow crack ($a/w=0.1$) configurations in ductile-brittle transition at $-90\text{ }^\circ\text{C}$. Crack location is measured in the centre of the specimen and T-stress is normalised with the yield stress of material at the crack tip.

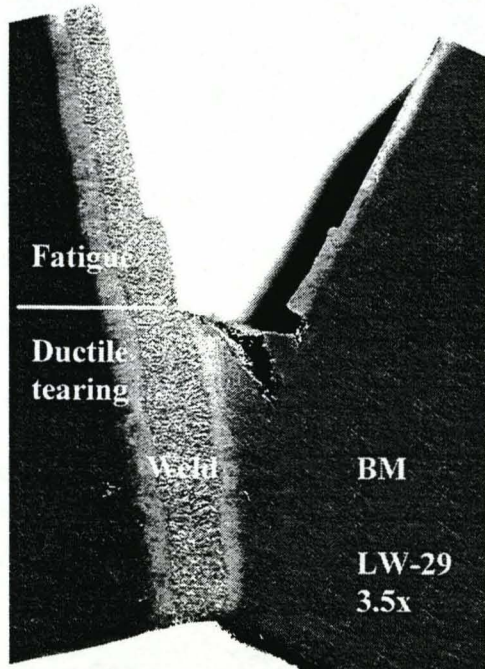
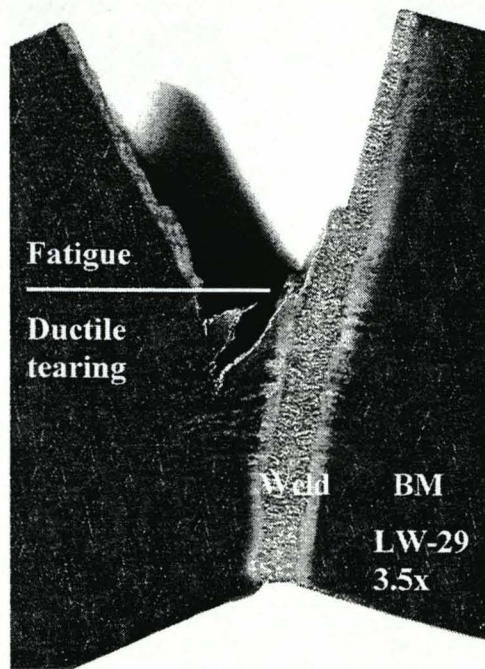
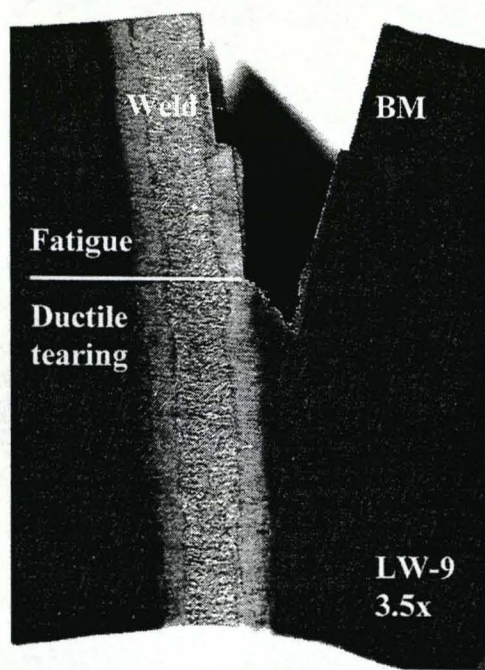
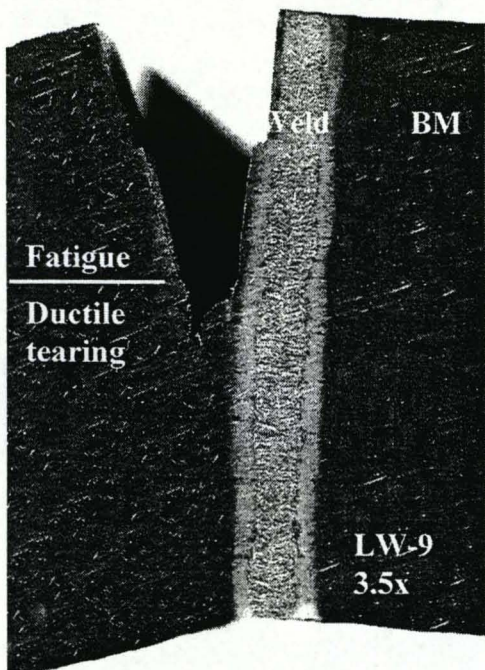


Figure 17.19:
Photographs showing ductile tearing of laser welded joint at room temperature.

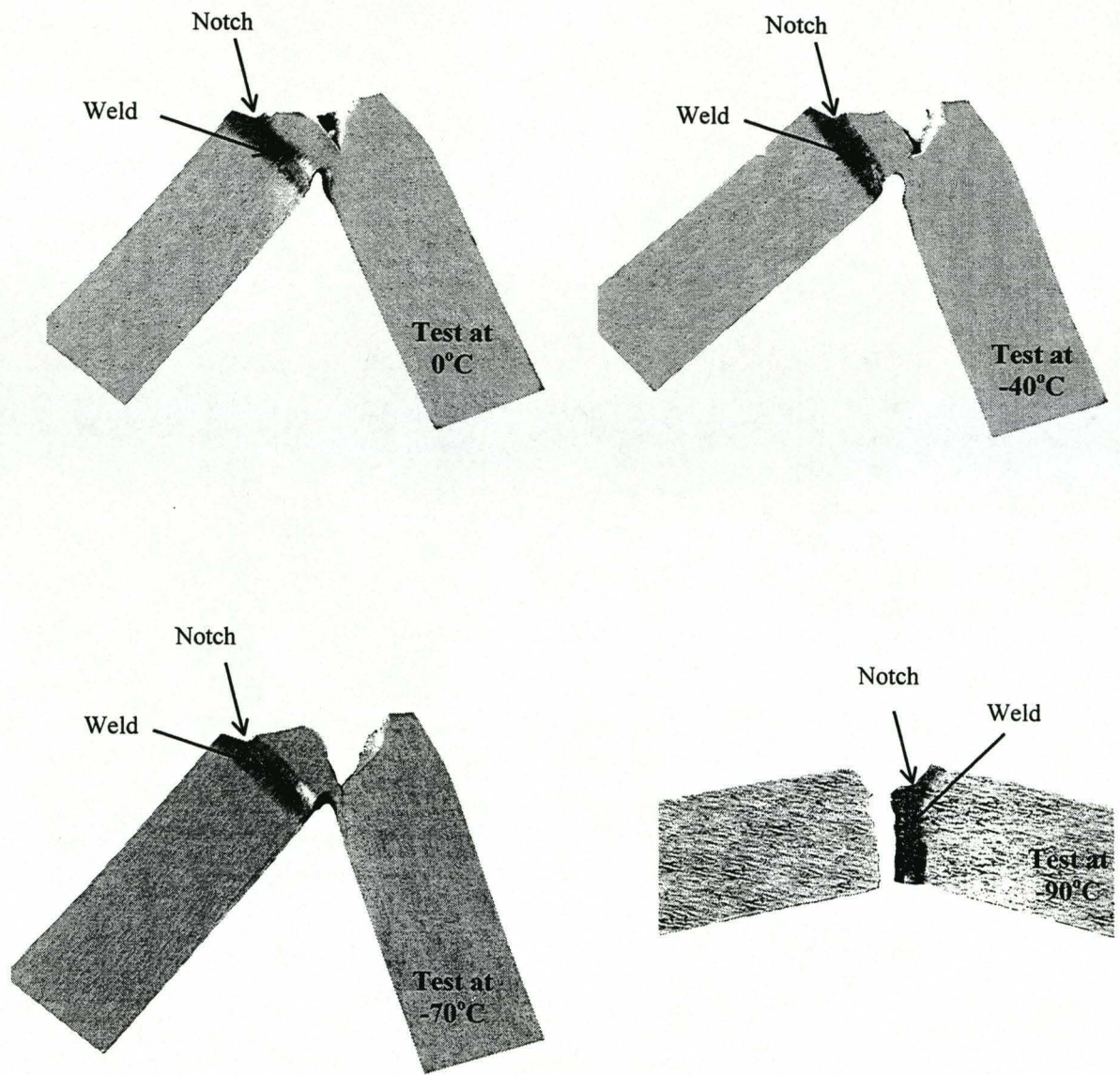


Figure 17.20:
Photographs of Charpy specimens tested in ductile-brittle transition.
Notch was cut along the fusion line.

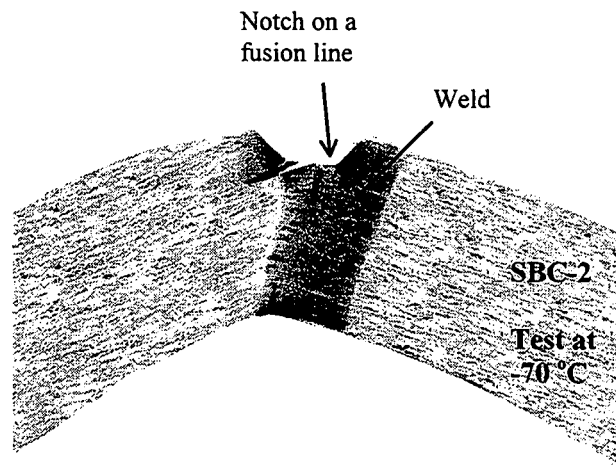
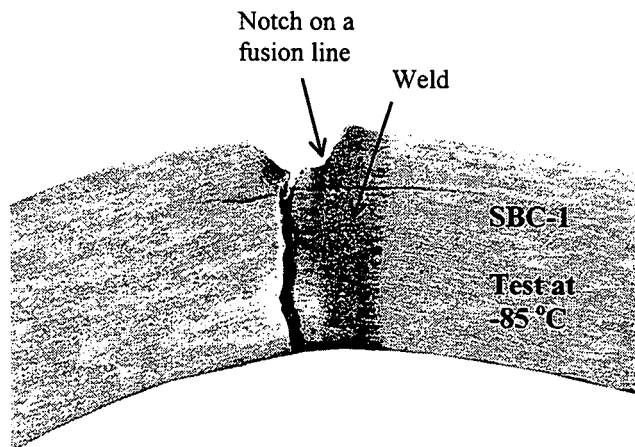


Figure 17.21:
Photographs of Charpy geometries tested under quasi-static three-point bending.

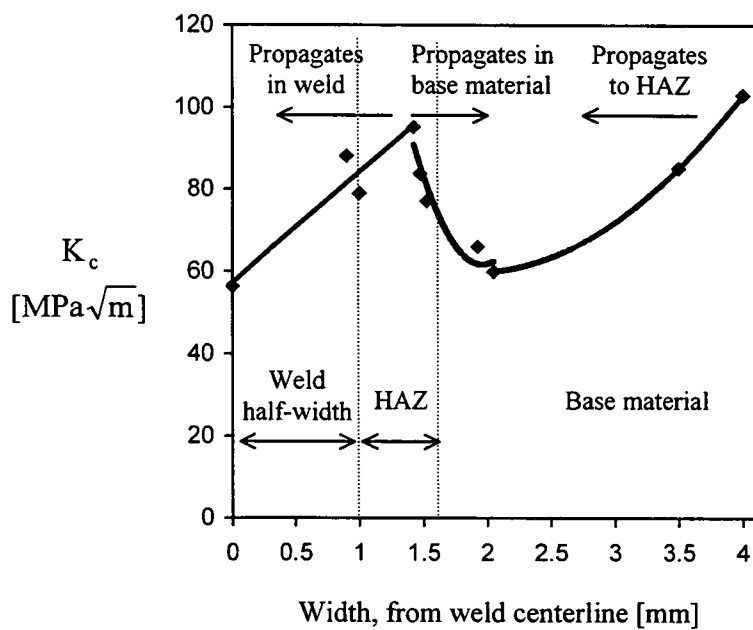


Figure 17.22:
 Curve-fit to the deep crack K_c data at $-130\text{ }^\circ\text{C}$ and crack propagation direction with respect to fracture toughness gradients.

Chapter 18

FRACTURE ASSESSMENT OF LASER WELDED JOINTS

The fracture performance of laser welded joints is assessed in this chapter using deterministic and probabilistic methods, ranging from simple R6 type approach to the detailed local approach methods. Attention is given to the prediction of crack path in graded joints.

18.1 Numerical model

The deep cracked ($a/w=0.5$) experimental geometry discussed in Chapter 17 was modelled with a detailed plane strain finite element model comprising 3000 isoparametric second order solid elements focused at the crack tip, which had radius of a $5\mu\text{m}$, as shown in Figure 18.1. The model was loaded in three and four point bending using ABAQUS as a solver. The geometry consisted of a weld, which was idealised as 2 mm wide, a heat affected zone 0.65 mm wide, while the remainder of the specimen was modelled with base material properties. These dimensions were derived from optical observations and Vickers hardness measurements (see Figure 17.4) and represent the average values for the laser welds. The material was idealised as linear elastic below the yield stress and merged into Ramberg-Osgood relation above the yield stress, as discussed previously. The yield stresses for the weld metal and HAZ were determined by combining the strength mismatch with the yield stress of the base material. The strain hardening coefficient was measured on base material to be 10 and was assumed identical for all the weld microstructures.

Three representative crack configurations were analysed. Configuration of specimen LW-5 had crack located on the fusion line, while configurations LW-1 and LW-3 had a crack in the HAZ and LW-2 and LW-8 had a crack in the base material near the HAZ. The crack locations in relation to the yield stress profile at $-130\text{ }^{\circ}\text{C}$ are shown in Figure 18.2.

Material gradation was introduced in the model through a user defined variable, which was associated with the yield stress. The variable used was the nodal temperature which has the flexibility to model material gradients by assigning corresponding yield stresses to nodes. Thus the graded material zone was defined by interpolating nodal properties between those of the weld and base material. For accuracy several stress-strain curves were introduced for

every 50 MPa increase of yield stress, to allow an accurate interpolation. A benchmark for the procedure is shown in Figure 18.3, where a contour of a process zone is shown for a bi-material joint. The solid line show the contour obtained from the model, where two yield stresses are associated directly with the elements in the lower and upper half of the model. The symbols represent contour where the yield stresses are prescribed as a function of nodal temperatures. In both cases the same stress-strain relation is used. Clearly the contours are in excellent agreement and the J-integral values also match to within 0.1%, giving confidence in the procedure.

18.2 Assessment using failure assessment diagrams

Experimental results have been analysed using failure assessment diagrams for mismatched structures, as specified in Chapter III.8 of R6/4 (2001), and are shown in Figures 18.4 and 18.5. Specific failure assessment curves (FAC) were constructed using finite element analyses for the weld configurations, and are shown in Figures 18.4. Specific FACs were also determined for a homogeneous crack tip material and are superimposed in Figure 18.4. The loads in Figure 18.4 are normalised with the corresponding limit loads, determined from the finite element model and are shown in Figure 18.6 for weld configurations and Figure 18.7 for homogeneous crack tip material. The limit loads of laser welded joints are close to the values for the base material, as extensive plasticity develops into the base material. Using the limit load of the base material in assessments as suggested in R6/4 is conservative, however the reserve margins on load are small. The specific FACs of the weld and the homogeneous crack tip material are close, as shown in Figure 18.4. This suggests that assessment of the weld joint could be simplified by using specific FAC for the homogeneous crack tip material, while the mismatch effects are accounted for by using the limit load of the weld configuration to define L_r for the assessment point. The cut-off in the diagram was determined by the ratio of equivalent flow to yield stress, and the flow properties of the base material. If the flow properties of the crack tip material are used, the cut-offs differ by 4%.

The test geometries are assessed in Figure 18.5 using general and specific FACs. The abscissa is normalised with the limit load of the weld configuration, while on the ordinate J_{elastic} is normalised with J_{mat} which is identified with the measured J_c values for the weld configuration. Although R6/4 suggests that the J_{mat} should be identified with the intrinsic fracture toughness of the material containing the crack tip, such values are difficult to

obtain for laser welded joints. By taking J_{mat} equal to J_c of the weld configurations the assessments are realistic. It should be noted however that the failure assessment diagrams are intended as a failure avoidance procedure, in which case use of apparent J_{mat} is likely to overestimate margins against elastic failure. For transferability schemes of the J_c between laboratory specimens and real structures the statistical size and shape arguments discussed in Chapter 4 should also be considered.

18.3 Crack initiation directions using maximum hoop stress criteria

The initiation angles of a cleavage crack have been analysed using maximum hoop stress criteria (Erdogan and Sih (1963), Williams and Ewing (1972)), as discussed in Chapter 10. The angles are representative of the effects of the strength mismatch at an assumed fixed toughness of the microstructures. Plots of the hoop stress are shown in Figure 18.8 for the three crack configurations. The hoop stresses are evaluated at a radial distance of $2J/\sigma_{o,\text{tip}}$ where $\sigma_{o,\text{tip}}$ is the yield stress of the crack tip material. Numerical results using the maximum hoop stress criteria suggest that cracks tend to propagate in the direction of the higher yield stress (to weld metal). The values of crack initiation angles are given in Figure 18.8, although they are dependant on angular mesh refinement.

18.4 Crack initiation direction based on the local stress triaxiality

The triaxial constraint induced by geometry and material inhomogeneity may influence initiation and path of a propagating crack in a mismatched structure. The local stress triaxiality featuring in the experimental data is examined, using plane strain fullfield finite element model of the test geometries. The material properties were defined by a Ramberg-Osgood relation using the measured yield stress and strain hardening exponent and were modelled under three or four point bending corresponding to the experimental arrangement. Specimen LW-23 containing a fatigue pre-crack in the weld near fusion line tested at -60°C and specimen SBC-1 containing a Charpy V-notch on the fusion line tested at -85°C were modelled. The results are shown through Figures 18.10 to 18.13 by plots of plastic zone sizes, principal plastic strains and the stress triaxialities. The latter has been examined along three locations parallel to the fusion line: directly ahead of the crack, along the base material near the edge of the HAZ and along the weld metal, as illustrated in Figure 18.9.

18.4.1 Charpy V-notch geometry

Ahead of the blunt notch large asymmetric plastic zones develop with plasticity predominantly extending into the base material, as shown in Figure 18.10. At the tip of the blunt notch the stress triaxiality is low, as shown in Figure 18.11, large strains promote plastic flow on the surface of the notch and the cleavage originator has to be sampled further from the notch root. A competition occurs between the distance from the stress concentrator (notch) and the sufficiently high stress state to promote cleavage. For the laser welds this results in large fracture process zone compared to weld dimensions that samples most of the microstructure. With increasing distance from the notch root triaxiality rises more rapidly in the edge of the heat affected zone due to the contribution from the strain hardening of the base material, compared to the values on the fusion line or in the weld metal, where material overmatch reduces stress state. This is also illustrated by plots of 2% principal plastic strain contours in Figure 18.12 that show plastic strains predominantly developing in the base material. Failure site is sampled at the edge of HAZ close to base material and the crack originating from a notch thus propagates in the base material.

18.4.2 Geometry with a fatigue pre-crack

Conversely failure of a constrained fatigue pre-crack occurs well before extensive plastic flow elevates stresses at the edge of the HAZ, as shown in Figure 18.12 with the plot of a principal plastic strain contour. The fracture process zone thus samples a relatively small zone close to the crack tip, making it less sensitive to the adjacent strength gradients. Plots of stress triaxialities ahead of the constrained fatigue pre-crack located on the fusion line are shown in Figure 18.13. To distances within 500 μm from the crack tip, typical of the cleavage fracture process zone for fatigue pre-cracks (Wall (1996), Bowen (1987), Ritchie (1979)), triaxiality is highest directly ahead of the crack and much lower at the edge of the HAZ or in the weld. The constraint induced by geometry and material combined by the lower ductility of the hard weld metal influence the fatigue pre-crack to extend into the weld metal by cleavage, as observed in the experiments.

18.5 Statistics of crack propagation in a graded material

The probability of failure can be described by a two parameter cumulative distribution function, such as that proposed by Weibull and discussed in Chapter 10:

$$P = 1 - \exp\left(-\left(\frac{\sigma_w}{\sigma_u}\right)^m\right) \quad (18.1)$$

A weakest link representation of the graded material requires that a spatially distributed loading and strength of the material must be considered, as discussed in Chapter 4. For a homogeneous material under contained yielding the Weibull stress can be written in terms of applied J and yield stress (see Chapter 12):

$$\sigma_w^m = \tilde{\sigma}_w^m \frac{J^2 E^2 \sigma_o^{m-4} B}{V_o} \quad (18.2)$$

where $\tilde{\sigma}_w^m$ is the non-dimensional Weibull stress in a J -dominant configuration and is a function of strain hardening, Weibull modulus and process zone size, λ . In a homogeneous material the strength has the same statistical distribution in all crack tip sectors. The Weibull stress describes loading, while the scaling constant σ_u is a material property, independent of loading. The σ_u term can be related to the mean strength of the material through the mean Weibull stress:

$$\bar{\sigma}_w = \int_0^{\infty} \sigma_w \frac{\partial P}{\partial \sigma_w} d\sigma_w \quad (18.3)$$

which is proportional to the mean fracture toughness at failure ($\bar{\sigma}_w \propto \bar{J}_C$):

$$\sigma_u^m = \tilde{\sigma}_w^m \frac{\bar{J}_c^2 E^2 \sigma_o^{m-4} B}{V_o \Gamma(1 + \frac{1}{m})^m} \quad (18.4)$$

For a graded material σ_u is sampled over a process zone and thus becomes dependant on the material and loading. Separation into the loading and material terms is no longer possible as the failure probability for a graded material becomes:

$$P = 1 - \exp\left(-\left(\frac{1}{E^2 B} \int_V \frac{\sigma_1^m}{\sigma_o^{m-4} \bar{J}_c^2} \frac{\Gamma(1 + \frac{1}{m})^m}{\tilde{\sigma}_w^m} dV\right)\right) \quad (18.5)$$

This integral is evaluated in the process zone, V , and Weibull modulus is considered to be spatially dependant. A value of 22 was obtained by Beremin (1983) for ferritic steel at liquid nitrogen temperatures. Recently, using the master curve toughness data and a three parameter Weibull function, Laukkanen *et al* (2003) suggest that the Weibull modulus increases with temperature in the ductile-brittle transition. Weibull moduli of 22 and 30 were thus considered for the ferritic base material in the analysis of test data obtained at -130°C . A Weibull modulus of 10 was assigned to the weld metal, which has mechanical

properties between those of brittle materials, such as ceramics ($m \sim 3-5$) and ductile ferritic steels ($m \sim 20-30$). The Weibull moduli, $\tilde{\sigma}_w$ and $\Gamma(1 + \frac{1}{m})$ for cracks in the HAZ were linearly interpolated between the values of the base and weld metals. As the spatially distributed mean fracture toughness of each weld constituent is not available, the experimental data measured on the entire weld joint was used instead (see Figure 17.22). Strain hardening exponent and volume V_0 are taken to be spatially independent, although the extension is straightforward.

18.5.1 Plastic zones and process zones

Contours of plastic zones were determined by comparing the Mises stress with the local yield stress. In Figure 18.14 the plastic zones are shown for a configuration LW-5 where crack is located at a fusion line, tested at -130°C . At low loads, $F/F_{lim} < 0.5$, plastic zones are small and material gradation has little effect on the development of plasticity. With increased loading, plasticity become distinctly asymmetric and extends down the gradient towards the lower yield stress, of the base material, as discussed by Burstow *et al* (1998). Similar results were observed for a configuration LW-1 with crack located in the heat affected zone, as illustrated in Figure 18.15.

The process zone in which failure is sampled must be contained within the plastic zone and a zone in which principal stresses exceed a local fracture stress. Large plastic strains close to the crack tip must also be excluded, as they promote particle debonding over microcracking (Wall *et al* (1994), Wang *et al* (2002b)). However the precise value of the local fracture stress for the base material is not known. The local fracture stress of the martensitic/bainitic microstructure of the weld metal and HAZ are likewise not available and are difficult to estimate, as the values depend on the volume fractions and the size of microstructural constituents. The Weibull stress was calculated in the process zone limited by the size of the plastic zone at failure. For Weibull moduli greater than 10 the results are less sensitive to the process zone size as the dominant contribution to the Weibull stress arises close to crack tip (within 1-2 mm) (Lei *et al* (1998)). Wang (2002b) suggests that in a mild steel a plastic strain greater than 2% gives rise to particle debonding and arrests existing microcracks. The inner cut-out of the process zone was defined by contours of 2% plastic strain. The process zones are shown in Figure 18.16.

18.5.2 Results

Failure probabilities were evaluated in the fracture process zone for each 4.5° angular wedge surrounding the crack tip. Probability density functions were then determined as discussed in Chapter 10 and used to determine average crack initiation angles. The angles are examined as a function of applied load in Figure 18.17 and summarised in Table 18.1 with test results. Probability density functions of crack initiation angles are shown in Figures 18.18 to 18.20, showing distribution of most likely failure sites at low ($L_r=0.3$) and high ($L_r=1$) loads. The experimentally measured crack initiation angles are superimposed.

At low loads the process zones are small, the near tip field converges to a homogeneous problem and strength mismatch effects have only a small influence on the crack initiation direction. Thus in both configurations, the crack on a fusion line and in HAZ, crack initiates straight ahead. At higher loads ($L_r>0.4$), asymmetric process zones sample material inhomogeneities that influence the average crack initiation angles. For a configuration with the crack on the fusion line, crack initiates towards the weld at small angles, as shown in Figures 18.17(a) and 18.18. For a crack in the HAZ the strength gradient decisively swings the crack towards the softer side when the base material has assigned Weibull modulus of 22, as shown in Figure 18.17(b). The direction of crack initiation contrasts with the experimentally observed behaviour although the magnitudes of the angles are comparable. Assigning the Weibull modulus of 30 for the base material, the Weibull stress samples small zone near the crack tip and the crack in HAZ propagates straight ahead. The results suggests the crack initiation angles are sensitive to the scatter in the data, as measured by m .

18.6 Discussion

Failure probabilities and crack initiation angles are important in demonstrating the structural integrity of graded joints. Experimental results show important and previously unreported trends, in that crack path systematically follows the fracture toughness patterns, and the highest fracture toughness values are observed for cracks in the heat affected zone. Using local stress triaxiality an insight into the mechanics of crack initiation and subsequent crack path deviations can be given. Maximum principal stress, σ_1 , can be written in terms of mean stress and stress deviator:

$$\sigma_1 = \sigma_m + 2/3(\sigma_1 - \frac{1}{2}(\sigma_2 + \sigma_3)) \quad (18.6)$$

and the magnitude of the latter quantity can be written in terms of plastic strains:

$$\sigma_1 = \sigma_m + 2/3 \left(\frac{de_1^p}{d\bar{e}^p} \right) \bar{\sigma} \quad (18.7)$$

where de_1^p is in increment of principal plastic strain, $d\bar{e}^p$ is the increment of equivalent plastic strain and $\bar{\sigma}$ is the equivalent (von Mises) stress (Hancock and Cowling (1980)). In unconstrained geometries the magnitude of the principal stress needed to initiate cleavage fracture can thus only be achieved by contribution from strain hardening. Conversely in high constrained sharp pre-cracked geometries stresses at the crack tip exceed local fracture stress before significant plastic strains develop in the softer base material.

The Weibull stress model was extended to consider the spatially distributed strength and fracture toughness. The fracture toughness values measured on the entire weld joint are available, although the intrinsic fracture toughness of each weld constituent should ideally be used. The plastic strains and the spatially dependant reliability of the material were also considered in the model. Despite these extensions the model has a limited success in matching experimental observations in a strongly graded material, with yield strength gradient in excess of 600 MPa/mm (i.e. HAZ). In such cases heavily asymmetric process zones develop and extend towards the lower strength material. Statistically the crack propagation in such materials are largely governed by the volume effects. For configurations where crack is located in a moderate strength gradient of 80 MPa/mm (i.e. base material near HAZ), experimental results at both, -130 °C and -60 °C are close to the results of the Weibull stress model. The failures in laser weld joints may also be influenced by the residual stresses or dominated by the intrinsic toughness of weld metal, as suggested by Sumpter (1999).

Specimen	Crack location	Distance from weld centerline [mm]	Measured angle [degree]	Computed angle [degree]	
				No plastic strain	2% plastic strain
LW-5	Fusion line	1.0	0	2.5	4.2
LW-1	HAZ	1.42	9.3	-11.9	-9.5
LW-3	HAZ	1.52	12.7	-7.5	-6.2
LW-10	HAZ	1.47	17	-8.9	-8.3
LW-2	Base material near HAZ	1.9	-5	-4.7	-4.2
LW-8	Base material near HAZ	2.1	13	-4.1	-4.8

a) $m=22$ for base material and $m=10$ for weld

Specimen	Crack location	Distance from weld centerline [mm]	Measured angle [degree]	Computed angle [degree]	
				No plastic strain	2% plastic strain
LW-5	Fusion line	1.0	0	1.9	3.8
LW-1	HAZ	1.42	9.3	0.4	3.0
LW-3	HAZ	1.52	12.7	0	1.4
LW-10	HAZ	1.47	17	0.2	2.4
LW-2	Base material near HAZ	1.9	-5	-2.1	-1.7
LW-8	Base material near HAZ	1.9	13	-2	-1.9

b) $m=30$ for base material and $m=10$ for weld

Table 18.1:
Measured and computed average crack initiation angles using Weibull stress model for $-130\text{ }^{\circ}\text{C}$ test conditions.

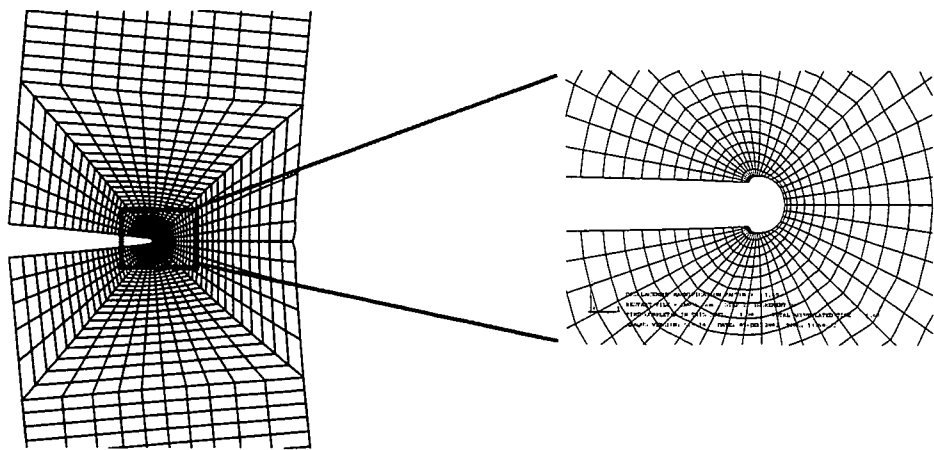


Figure 18.1:
Detail of the finite element mesh near the crack tip.

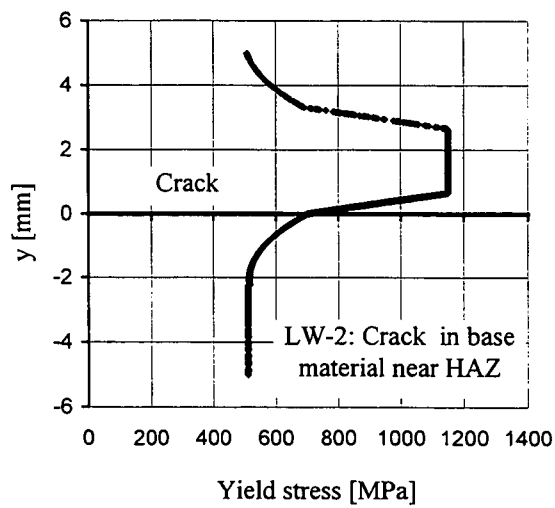
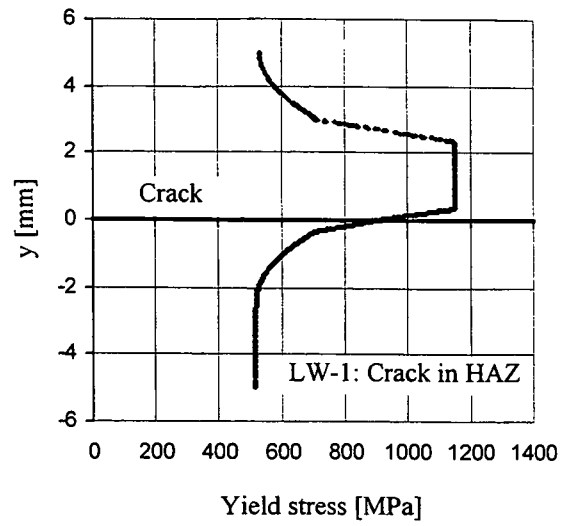
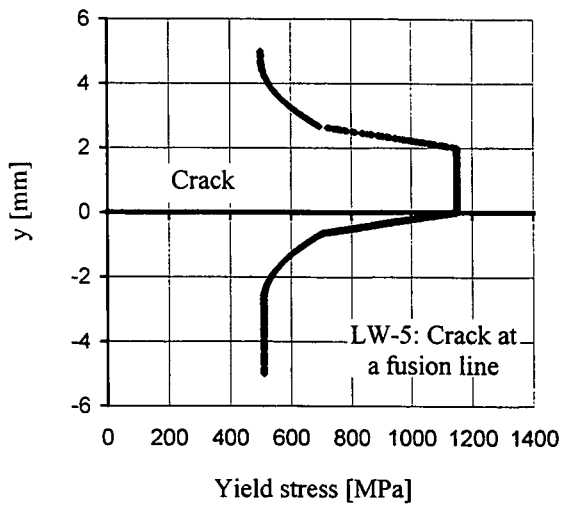


Figure 18.2:
Illustration of crack locations in the yield stress gradient at -130°C .

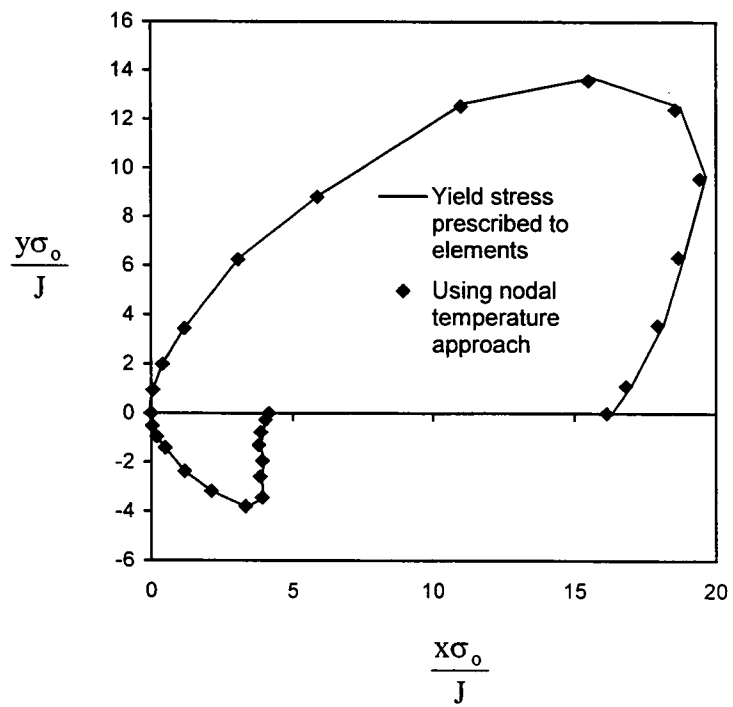
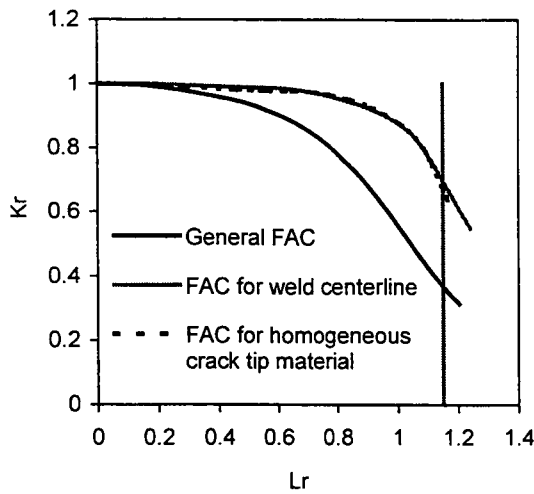
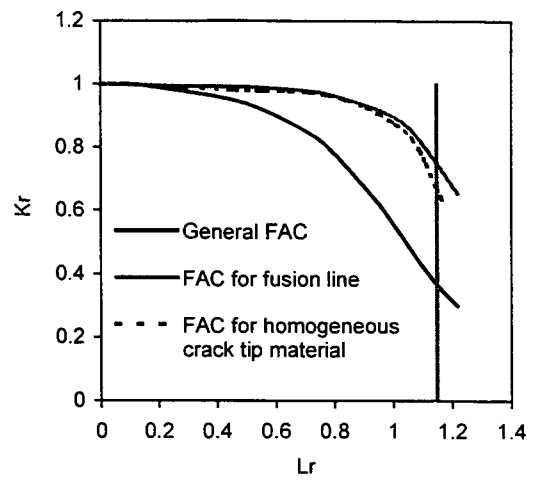


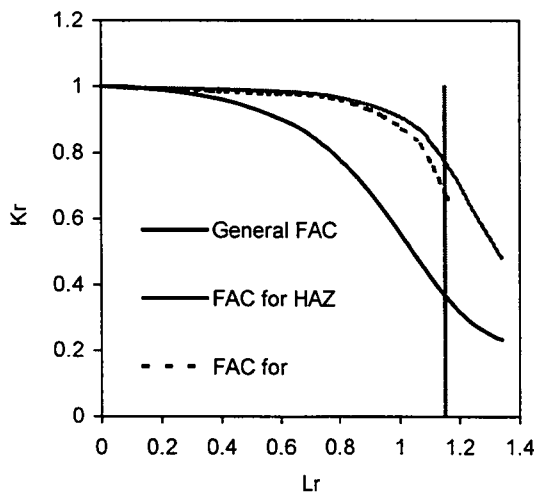
Figure 18.3:
 Benchmark of the procedure where nodal temperature are used to prescribe the stress-strain relation to elements.



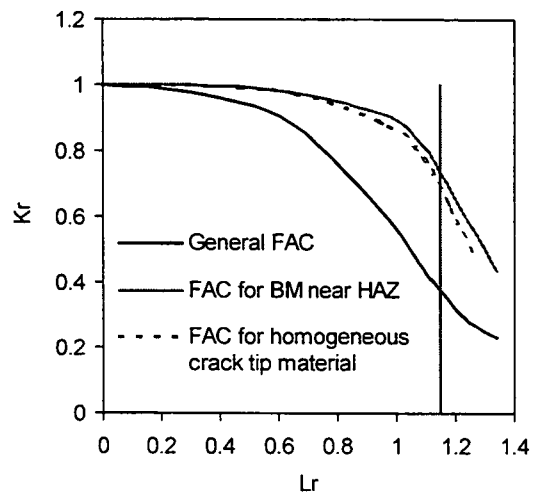
a) Weld centerline configuration



b) Fusion line configuration



c) HAZ configuration



d) Base material near HAZ configuration

$$L_r = \frac{F}{F_{lim,configuration}}$$

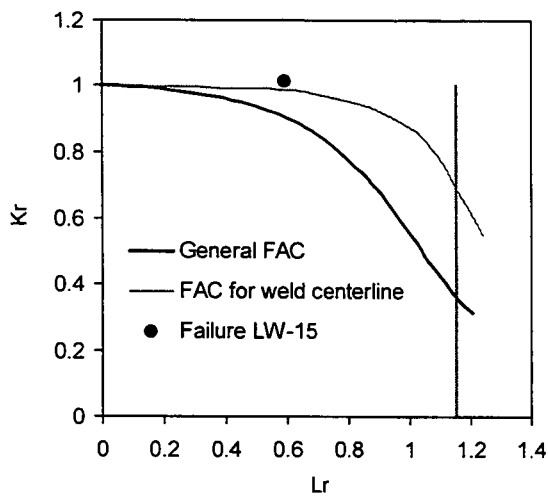
for a weld configuration and

$$L_r = \frac{F}{F_{lim,homogeneous}}$$

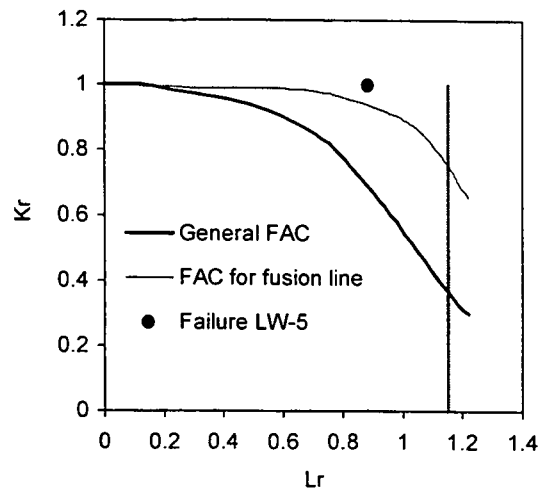
for a homogeneous crack tip material

Figure 18.4:

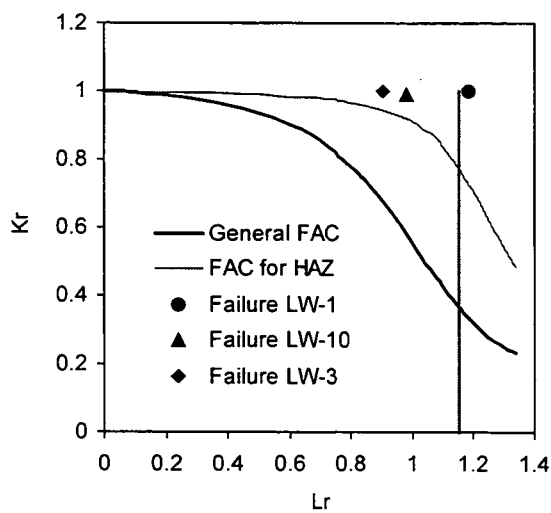
Failure assessment diagrams for cracks in laser welded joints, showing general (Option 1) and geometry and material specific (Option 3) failure assessment curves (FAC).



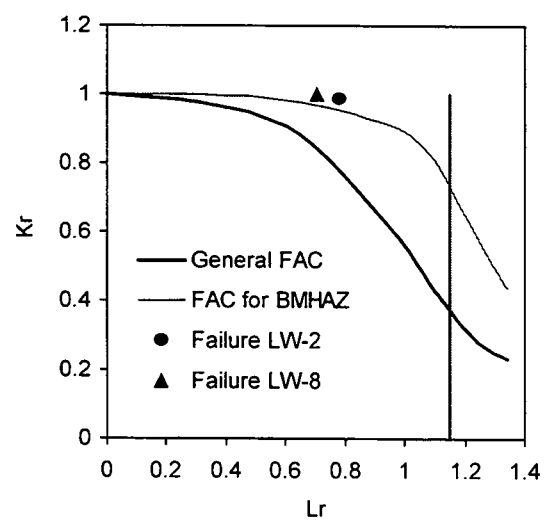
a) Weld centerline configuration



b) Fusion line configuration



c) HAZ configuration



d) Base material near HAZ configuration

Figure 18.5:

Assessment of configurations tested at $-130\text{ }^{\circ}\text{C}$ using failure assessment diagrams. J is non-dimensionalised with the J_c measured on the weld configuration and load with the limit load of the configuration.

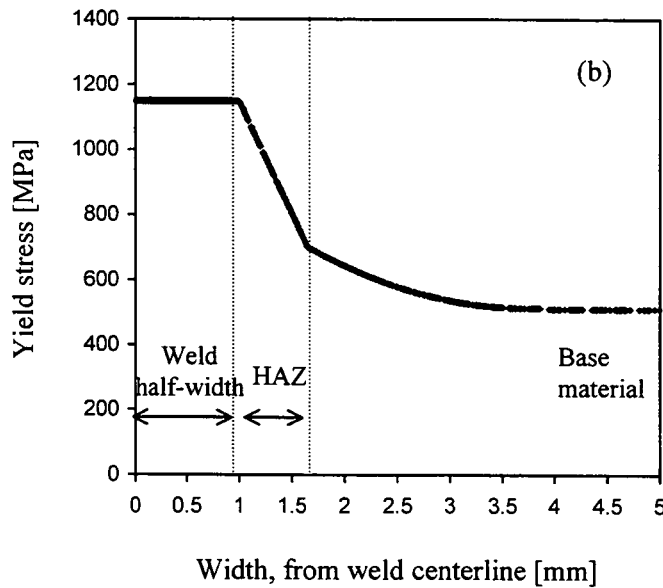
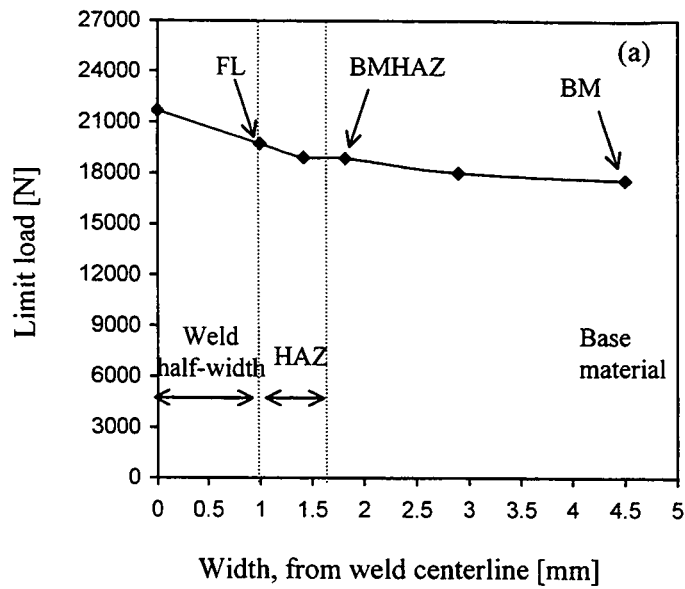


Figure 18.6:
Limit loads for cracks in the laser welded joint are shown in figure (a) and illustrated with respect to the yield stress gradient in figure (b).

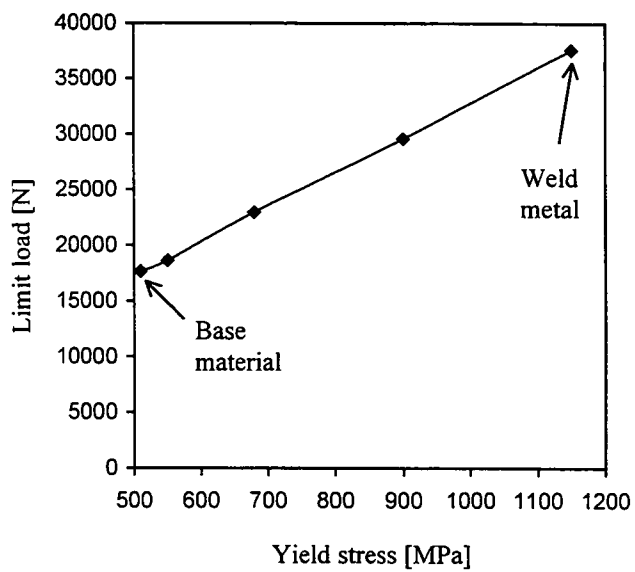
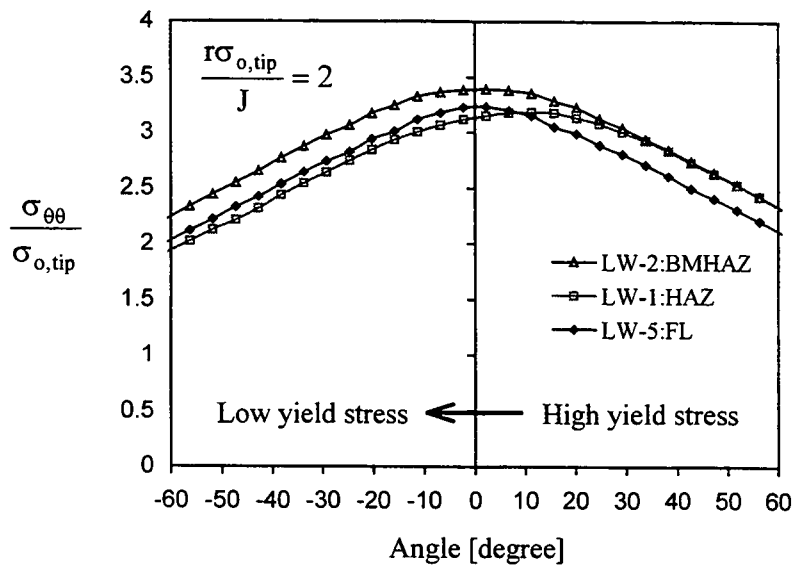


Figure 18.7:
Limit load of a homogeneous crack tip material, as a function of crack tip yield stress.



Configuration	Angle of crack initiation*
LW-5: FL	2.25°
LW-1: HAZ	11.75°
LW-2: BMHAZ	2.25°

* Note: Angular mesh refinement is 2.25°.

Figure 18.8:
Plots of maximum hoop stress around the crack tip for experimental configurations. Stresses are normalised with the crack tip yield stress and distances with crack tip yield stress and measured J.

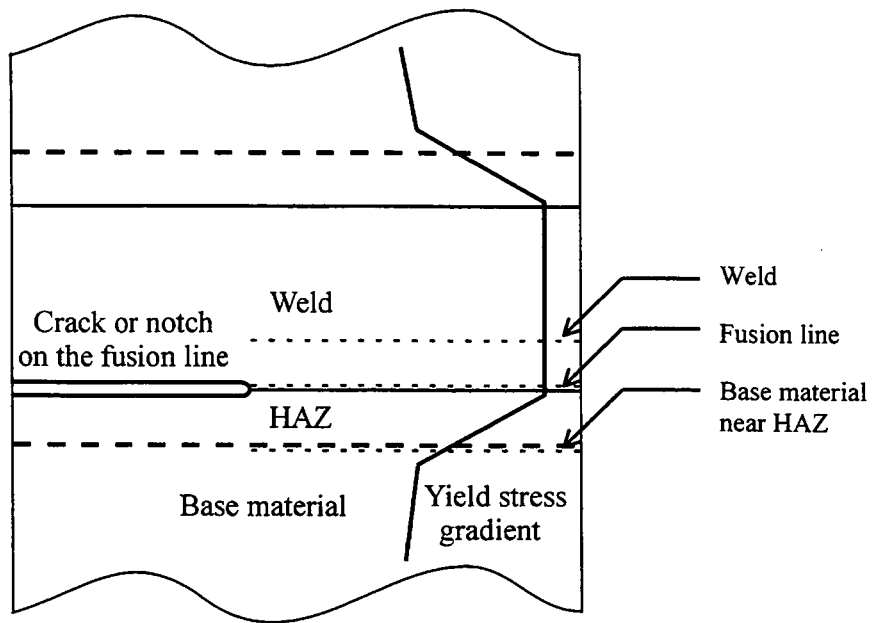


Figure 18.9:
Illustration of the configuration with crack on the fusion line, showing paths along which stress triaxiality was determined.

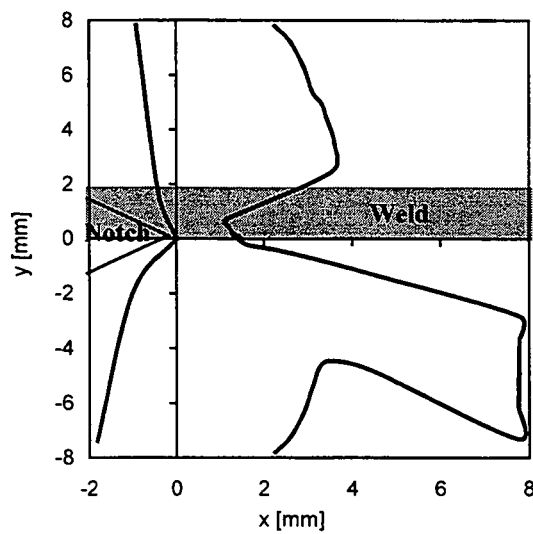


Figure 18.10:
Plastic zone size for slow bend Charpy geometry at failure at -85 °C.

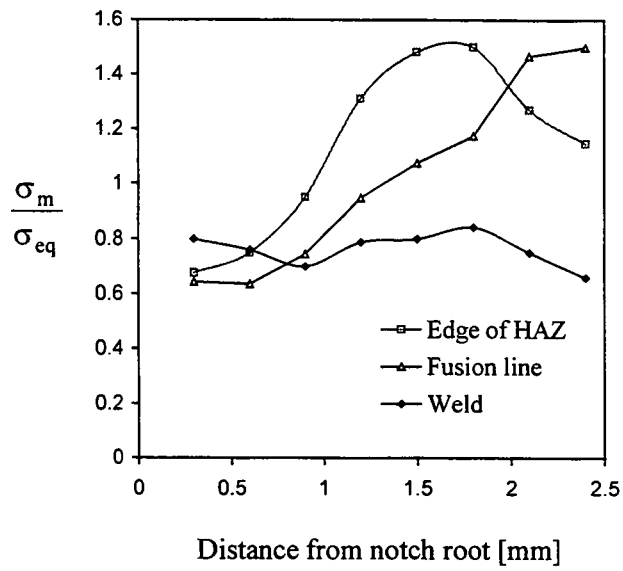


Figure 18.11:
Stress triaxiality ahead of the Charpy V-notch located on the fusion line.

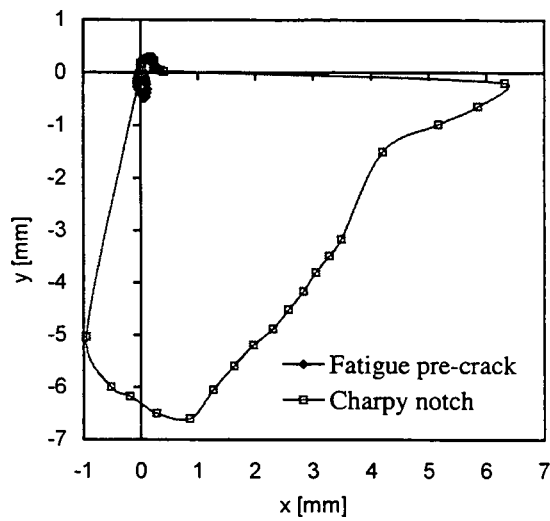


Figure 18.12:
Contours of 2% principal plastic strain ahead of a fatigue pre-crack and Charpy notch.

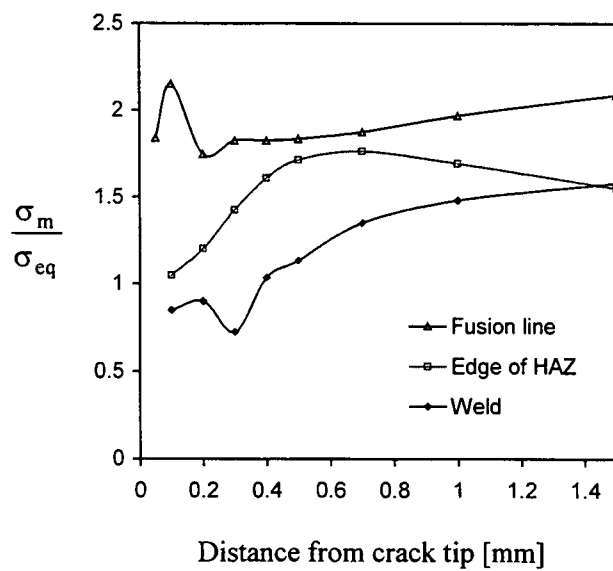


Figure 18.13:
Stress triaxiality ahead of the fatigue pre-crack located on the fusion line.

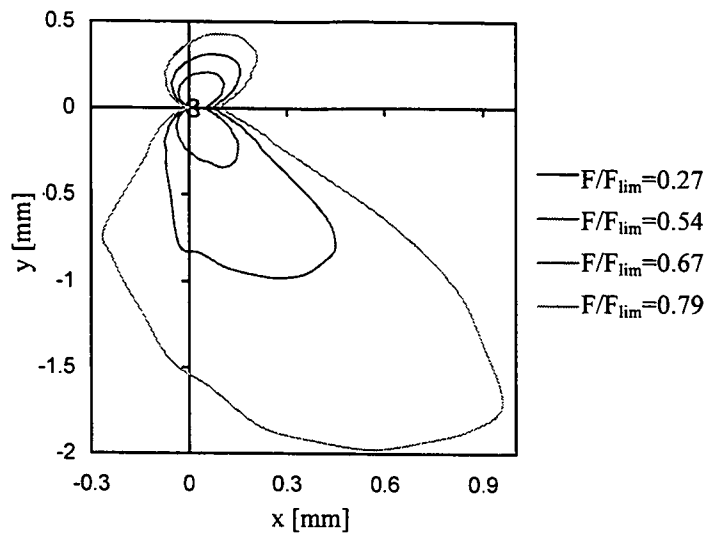
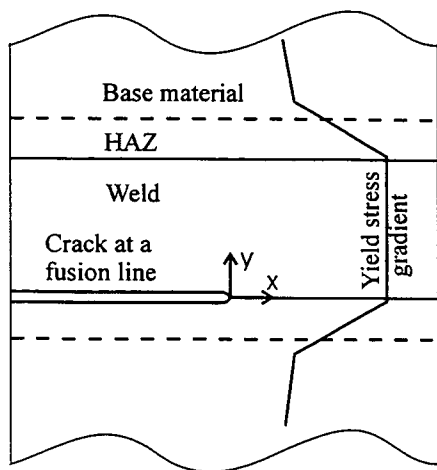


Figure 18.14:
Evolution of plastic zone with increased loading, for a crack located at a fusion line.

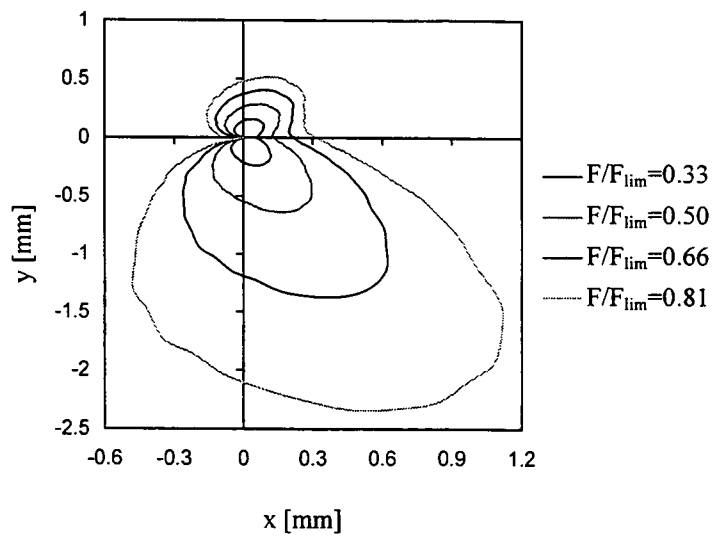
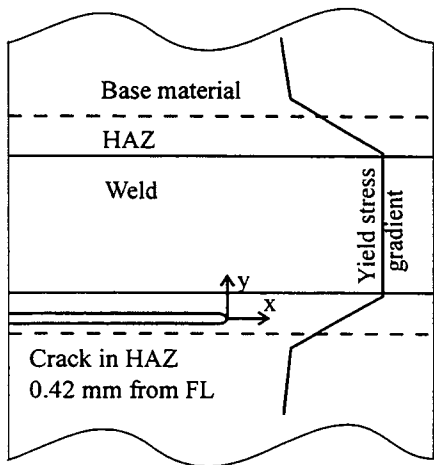
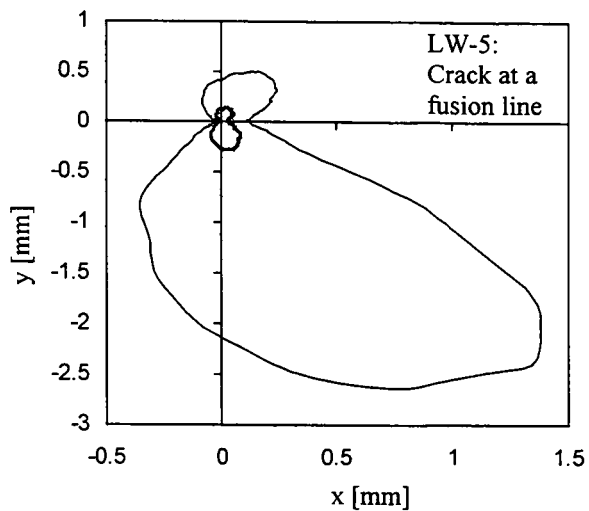
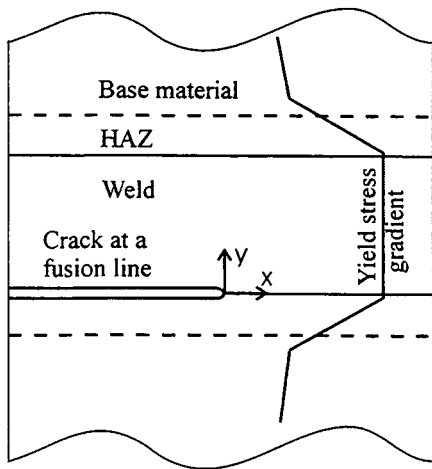
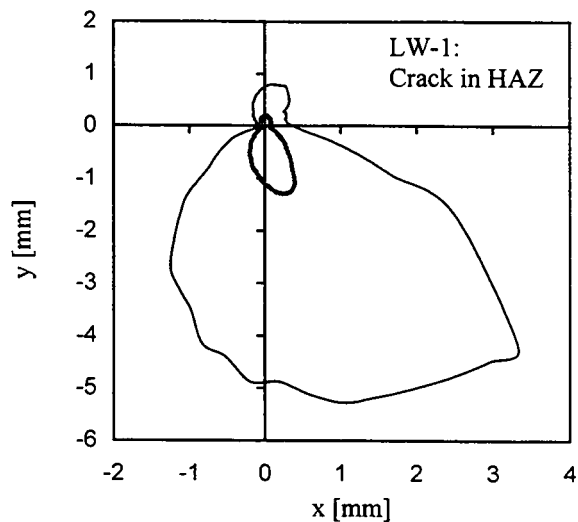
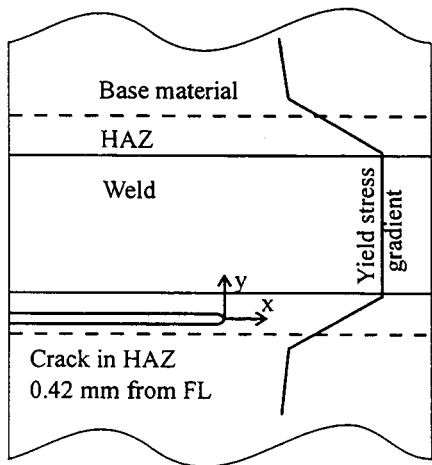


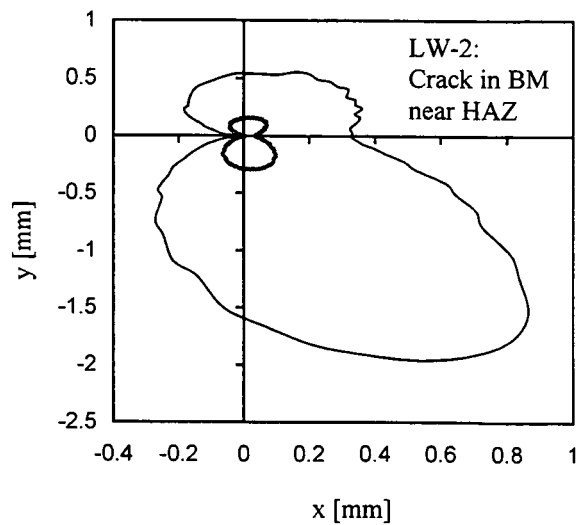
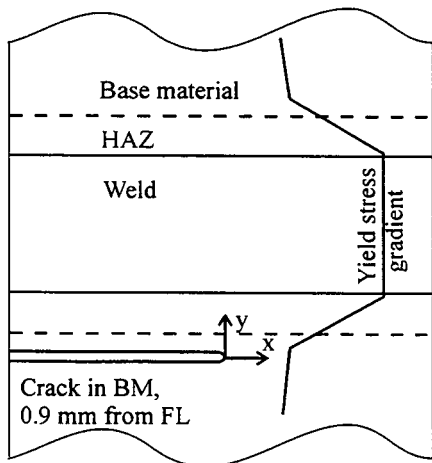
Figure 18.15:
Evolution of plastic zone with increased loading, for a crack located in the heat affected zone.



— Plastic zone
 — 2% plastic strain



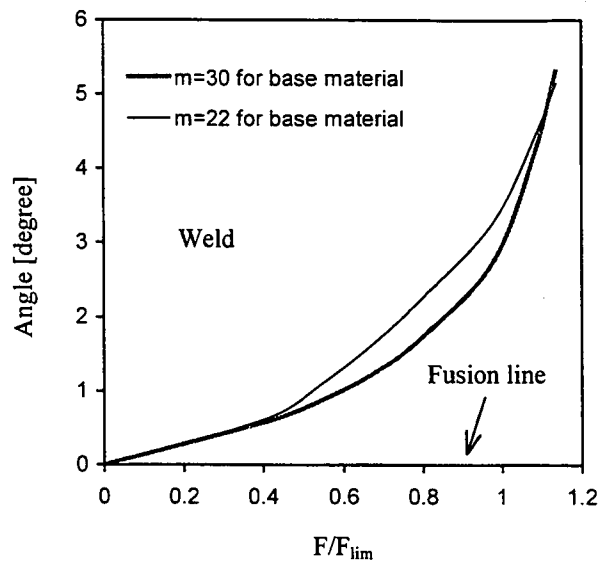
— Plastic zone
 — 2% plastic strain



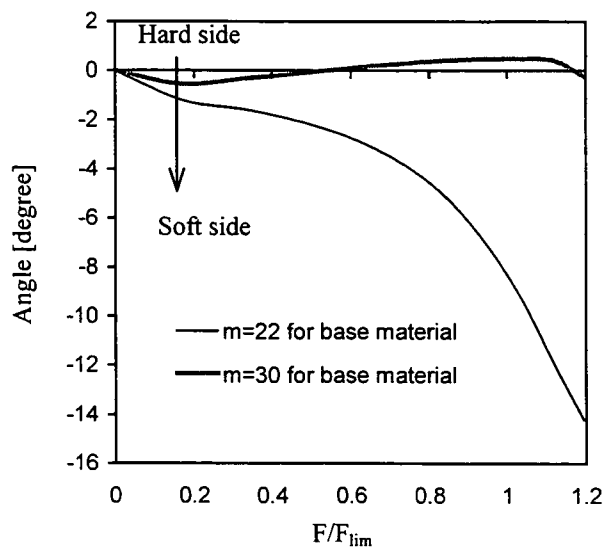
— Plastic zone
 — 2% plastic strain

Figure 18.16:

The process zone for a crack in a laser welded joint, defined with plastic zone size and contour of 2% plastic strain.



(a) Crack on a fusion line



(b) Crack in HAZ

Figure 18.17:
Average crack initiation angles as a function of load for cracks on a fusion line and in HAZ. Weibull moduli are 22 and 30 for the base material and interpolated to the value of 10 for the weld metal.

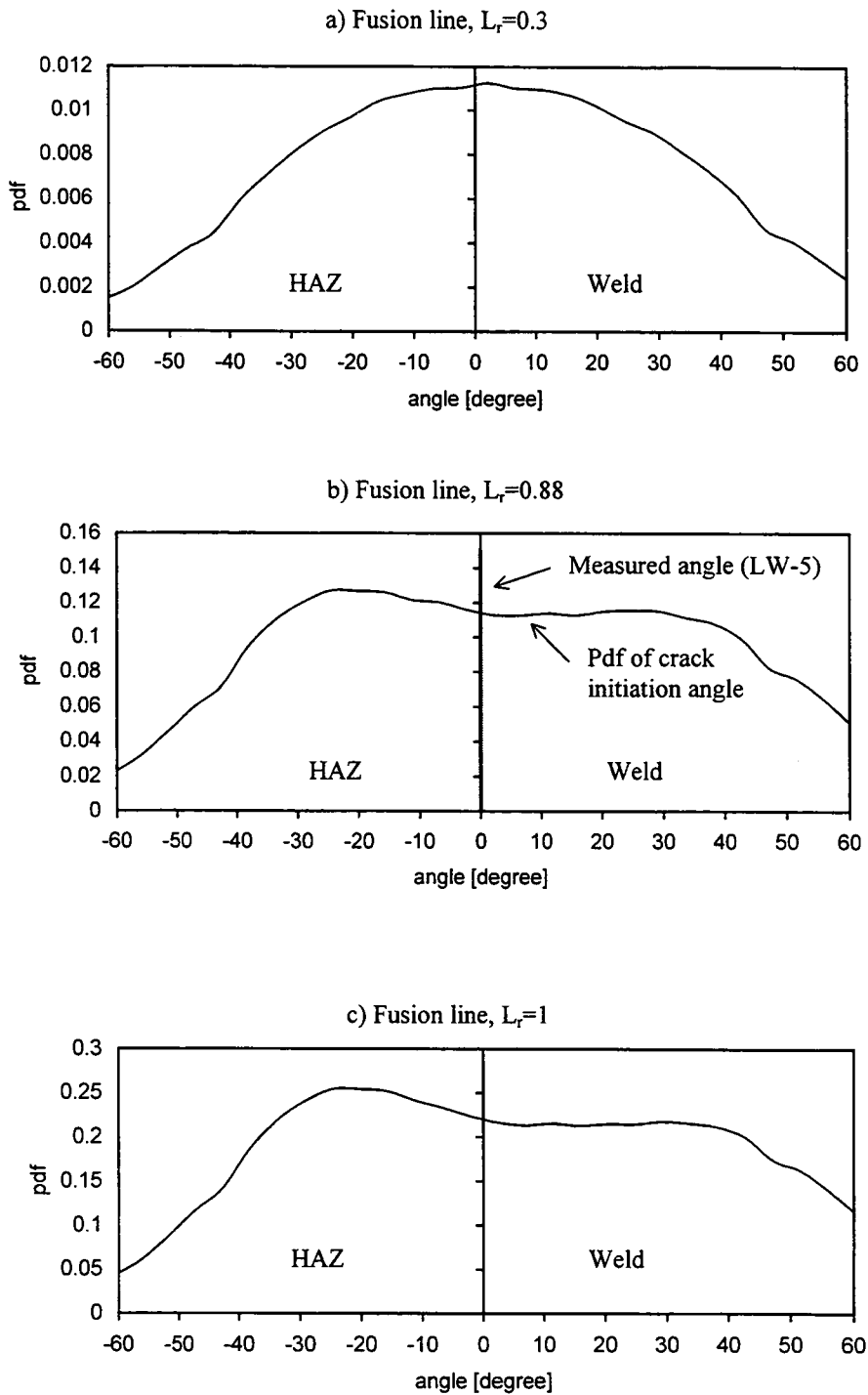


Figure 18.18: Probability density functions for a crack on the fusion line at low and high loads. Weibull modulus is 22. Measured angle from specimen LW-5 is superimposed.

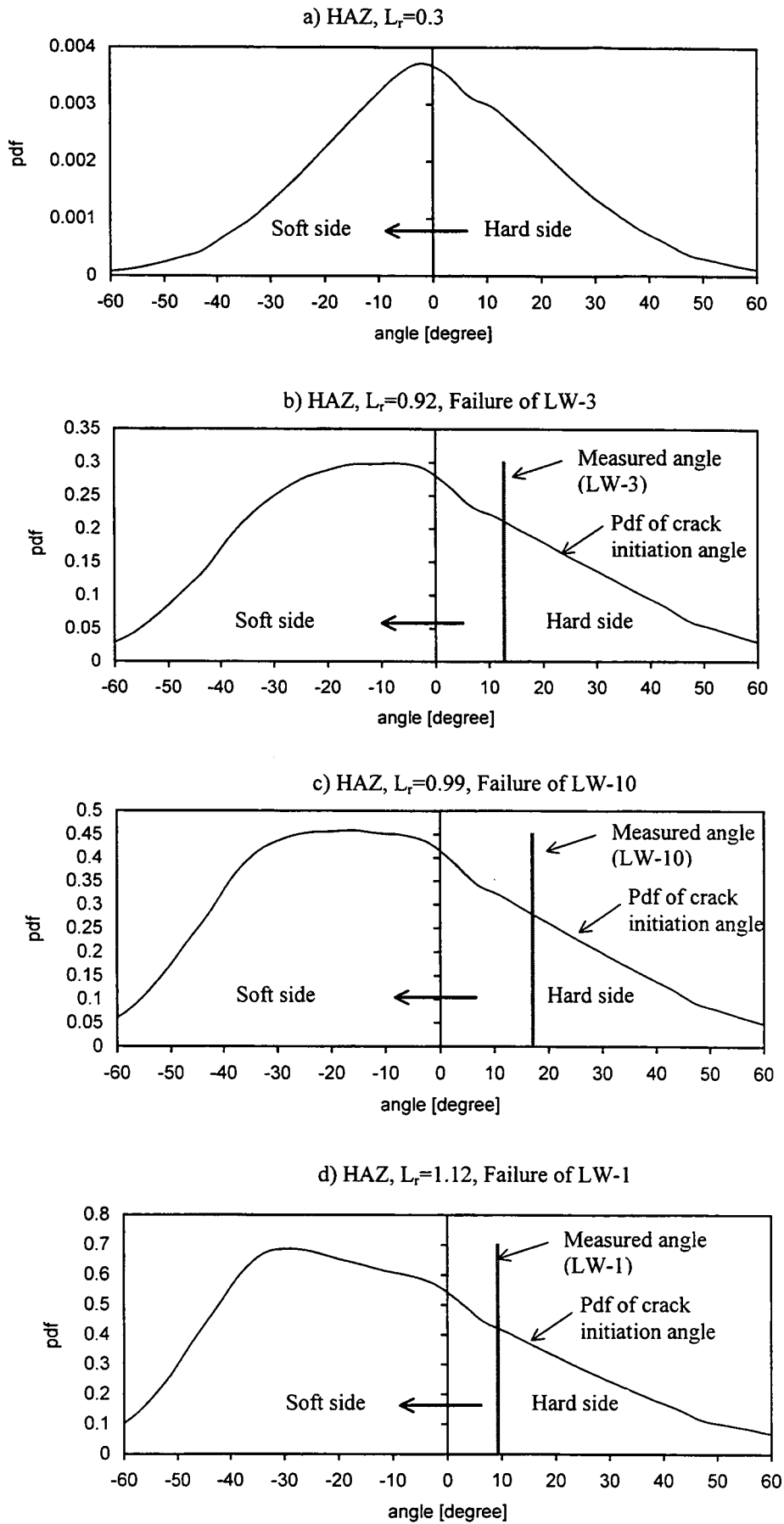


Figure 18.19: Probability density functions for a crack in the heat affected zone at low and high loads. Weibull modulus is 22. Measured angles from experiments are superimposed.

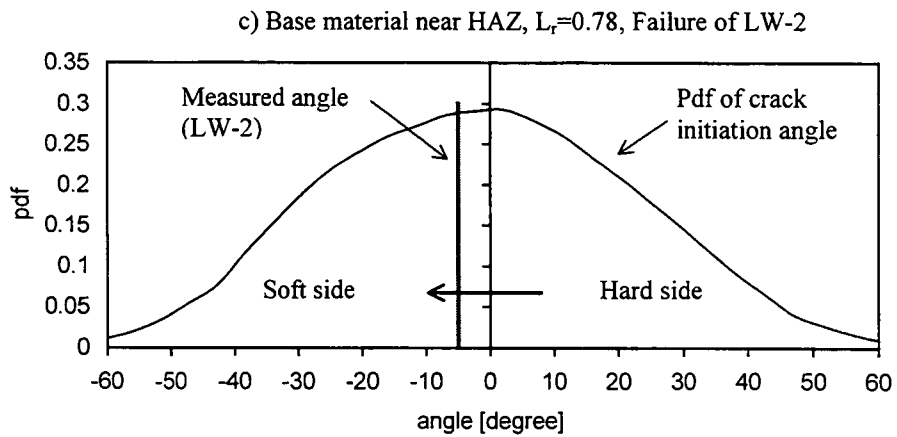
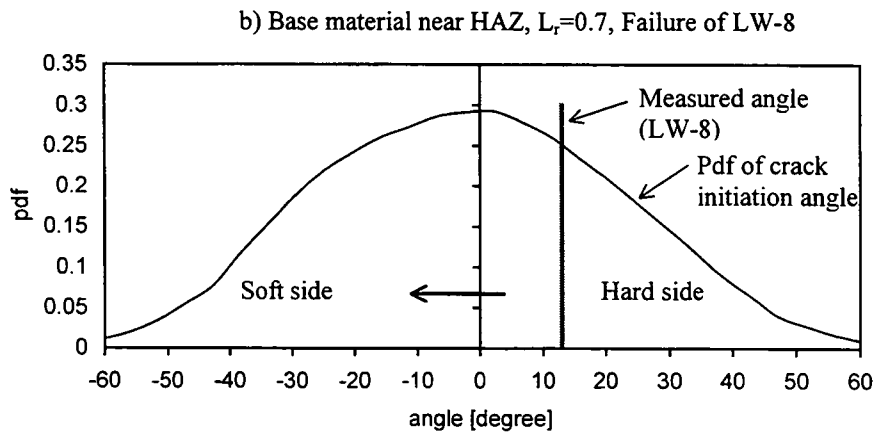
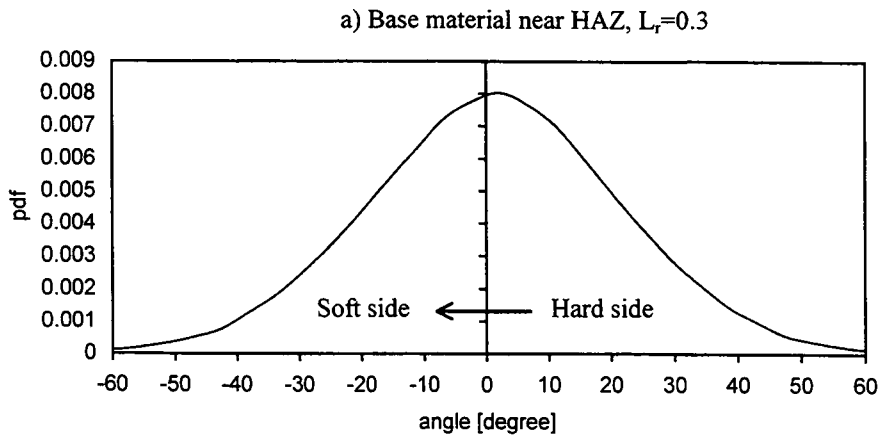


Figure 18.20:
Probability density functions for a crack in the base material near heat affected zone, at low and high loads. Weibull modulus is 22. Measured angles from experiments are superimposed.

Chapter 19

OVERALL CONCLUSIONS

Cleavage and its implications for structural integrity assessments have been addressed for cracks in homogeneous and mismatched structures, in the context of statistical and constraint effects. The first part of the work examined the re-characterisation procedure applied to fatigue, ductile tearing and cleavage. In the second part of the work the micromechanics of cleavage fracture was addressed and discussed in the context of temperature and toughness transferability schemes. The integrity of laser welded joints has also been examined experimentally and numerically within the context of constraint based fracture mechanics.

A systematic investigation of an infinite periodic sinusoidal crack has emphasised the dependency of the crack driving force and constraint parameter on crack front perturbation. A consistent shift in crack driving force was observed from the advanced segments to the retarded crack segments and was related with the crack perturbation under both, elastic and elastic-plastic conditions. A qualitative crack front stability argument based on a crack front perturbation was presented. Loss of crack tip constraint under high and low constraint conditions was correlated with the local redistribution of forces and moments, giving rise to predominantly compressive T-stresses due to crack front curvature.

Numerical and experimental studies investigated the interaction of two co-planar surface breaking defects and the failures from defects with re-entrant sectors. Complex defects with re-entrant sectors exhibit high local stress intensity factors. An experimental programme examined cleavage failures from such defects and re-characterised bounding defects. This demonstrated that the re-characterisation procedure is not conservative when failure occurs at small fractions of the limit load. The observation is confirmed with deterministic and a probabilistic analyses, in which the re-characterised defect is found to be less detrimental than the complex defect. Failures close to the limit load benefit from constraint loss which counteract the amplified crack driving forces in re-entrant sectors and cause re-characterised defects to be more detrimental than the original complex defects. In such cases re-characterisation is conservative, as shown by the deterministic and a probabilistic analyses. Benefit may be taken from statistical size effects, which are strongly

dependent on the crack geometry. It is recommended that statistical size and shape corrections should be used only when they result in a reduction in the critical value of size and shape corrected stress intensity.

Re-characterisation procedures, such as those given in BS 7910 and R6/4, are conservative for fatigue and ductile tearing, since in both failure modes the crack advances from the re-entrant sector towards the re-characterised shape. The re-characterisation procedure for defects with re-entrant sectors which fail in cleavage is non-conservative for failures at small fractions of the limit loads. At such low loads there is no benefit from constraint loss, but statistical size and shape corrections may recover the conservatism of the assessment.

In the second part of the work, constraint – temperature transferability schemes have been discussed. Crack tip stress fields are self-similar with respect to yield stress under contained yielding and as a result the constrained crack tip field can be matched to the unconstrained field by a J or by a temperature dependent yield stress when the fracture mechanism is temperature independent. This allows constraint loss to be quantified in terms of a toughness margin or as a temperature shift at a fixed toughness.

The Ritchie-Knott-Rice model has been examined in the context of temperature dependant microstructural parameters. As the local fracture stress has been experimentally observed to be temperature independent, the necessary conclusion is that the critical microstructural distance increases with temperature in the ductile-brittle transition.

Mode I and mixed-mode I/II crack tip fields have been shown to belong to the same family of fields and can be unified in a single toughness-mixity-constraint locus. In mode I, in-plane constraint loss gives rise to a family of elastic-plastic crack tip fields which can be described by J and a second parameter which determines the level of crack tip constraint (Q/T). This family of fields differs in a largely hydrostatic manner. Mixed mode field can be interpreted as belonging to the same family such that constraint loss by mixed-mode loading results in a family of fields which differ largely hydrostatically on the plane of maximum hoop stress. For stress controlled brittle fracture this allows the constraint enhanced toughness observed in unconstrained Mode I fields to be correlated with the

constraint enhanced toughness in mixed-mode loading. The argument has been confirmed by an extensive testing programme under mode I and mixed-mode I+II conditions.

It has been shown by Li (1997) that the deformation fields of an interfacial crack at a rigid substrate can be correlated with the deformation fields of a crack located in a homogeneous material. The same is true for an interfacial crack between strength mismatched materials, as observed by the deformation fields in non-hardening material and by the principal and deviatoric stress components for a strain hardening material. More generally, the constraint of mode I fields parameterised by Q can be correlated with the constraint of interfacial mixed mode fields parameterised by elastic mixity. This allows the fracture resistance of homogeneous mode I, mixed-mode I+II and interfacial configurations to be unified in a single constraint based fracture toughness locus.

The integrity of single-pass laser welded joints has been examined experimentally in ductile-brittle transition temperatures and at room temperature. The results show the highest fracture toughness for cracks located in the heat affected zone of the weld joint. For the weld centerline and the region near the edge of the heat affected zone the lowest failure loads and fracture toughness were measured. The crack initiation angles and crack paths followed the spatially distributed gradients of the fracture toughness and were much less influenced by the gradations in yield strength.

Results of Charpy tests are consistent with those of Sumpter (1999) and Kristensen (1996) in that under impact loading the crack propagates into the base material. Conversely the quasi-static low temperature fracture mechanics tests where crack initiated from a sharp pre-crack by cleavage at minimum plastic distortions show opposite trends with crack propagating into the less tough phase. Charpy tests are commonly performed to characterise the weld and combined with assumption that fracture properties of the material into which crack propagates govern failure. Such practice can give misleading conclusions about the integrity of single-pass laser welds.

The strength and toughness gradation have been considered in the extension of the Weibull stress model applied to graded materials. The model however suggests that crack in a material with a large strength gradient initiates in the direction of lower yield strength, into

the base material. Results obtained from a deterministic maximum hoop stress criteria agree with experimental observations in that crack initiates towards the harder phase.

Most of the work has been extensively communicated to the industrial partners and scientific community at international conferences. The list of conference publications is attached in the Appendix A. Two papers have been accepted for publication in the *Engineering Fracture Mechanics* journal and another is in final draft. The journal papers are attached in the Appendix B.

BIBLIOGRAPHY

- Ainsworth, R.A., (2002), Private communication.
- Ainsworth, R.A. and O'Dowd, N.P., (1995), *Constraint in the failure assessment diagram approach for fracture assessment*, International Journal of Pressure Vessels and Piping, Vol. 117, pp: 260-267
- Al-Ani, A. and Hancock, J.W., (1991), *J-Dominance of short cracks in tension and bending*, Journal of the Mechanics and Physics of Solids, Vol. 39, No.1, pp:23-43
- Anderson, T. L., (1995), "Fracture mechanics: fundamentals and applications", Second Edition, CRC Press, Boca Roca, Florida
- Anderson, T.L., Dodds, R.H., (1991), *Specimen size requirements for fracture toughness testing in the ductile-brittle transition region*, Journal of Testing and Evaluation, Vol. 19, pp.123-134
- ASME, Section XI (1992), Boiler and pressure vessel design code, American Society of Mechanical Engineers, Philadelphia, USA
- ASTM E399 (1988), *Standard method for plane strain fracture toughness testing of metallic metals*, Vol. 03.01, American Society for Testing and Materials, Philadelphia
- ASTM E813-88, (1988), *Standard test method for J_{IC} , a measure of fracture toughness*, American Society of testing and Materials, Philadelphia
- ASTM E1921, (1997), *Standard method for determination of reference temperature T_0 for ferritic steels in the transition range*, American Society for Testing and Materials, Philadelphia
- Bayley, C.J., Bell, R., (1997), *Experimental and numerical investigation of coplanar fatigue crack coalescence*, International Journal of Pressure Vessels and Piping, Vol.74, pp.33-37
- Becker, T.L., Cannon, R.M., Ritchie, R.O., (2002), *Statistical fracture modelling: crack path and fracture criteria with application to homogeneous and functionally graded materials*, Engineering Fracture Mechanics, Vol. 69, pp.1521-1555
- Bennet, P.E., Sinclair, G.M. (1966), *Parameter representation of low-temperature yield behaviour of body centered cubic transition metals*, Journal of Basic Engineering, Transactions ASME, Vol.88, pp.518-524
- Beremin, F.M., (1983), *A local criterion for cleavage fracture of nuclear pressure vessel steel*. Metallurgical Transactions, Vol.14(A), pp.2277-2287
- Bergly, J.A. and Landes, J.D. (1972a), *The effect of specimen geometry on J_{IC}* , ASTM STP 514, pp:24-39

- Bergly, J.A. and Landes, J.D. (1972b), *The J-integral as a fracture criterion*, ASTM STP 514, pp:1-20
- Betegón, C. and Hancock, J.W., (1991), *Two-parameter characterisation of elastic-plastic crack-tip fields*, Journal of Applied Mechanics, Vol. 58, pp:104-110
- Bezensek, B., Hancock, J.W., (2001), *The non-coplanar coalescence of interacting defects in fatigue*, In: Proc Int Conf SAE Brasil Fatigue 2001, Ed: Pimenta PM *et al*, São Paulo, Brasil, 2001
- Bezensek, B., Hancock, J.W., (2003), *The re-characterisation of complex defects. Part 2: Cleavage*, To appear in Engineering Fracture Mechanics
- Bilby, B.A., Cardew, B.A., Goldthorpe, M.R. and Howard, I.C., (1986), *A finite element investigation of the effect of specimen geometry and the field of stress and strain at the tip of stationary cracks*, In 'Size effect in Fracture', Inst. Mech. Eng. London, UK, pp:37-46
- Bowen, P., Druce, S.G., Knott, J.F., (1987), *Micromechanical modelling of fracture toughness*, Acta Metallurgica, Vol. 35, No. 7, pp.1735-1746
- Bruckner-Fort, A, Ehl, W., Munz, D., Trolldenier, B., (1990), *The size effect of microstructural implications of the weakest link model*, Fatigue and Fracture of Engineering Materials and Structures, Vol. 13, pp.185-200
- BS 7910 (1999), "Guidance on methods for assessing the acceptability of flaws in metallic structures", British Standard Institution, London
- BS 7448 (1997), "Fracture mechanics toughness tests, Part 2: Method for determination of K_{Ic} , critical CTOD and critical J values of welds in metallic materials." British Standard Institution, London, UK
- Budden, P.J., (1987), Journal of Mechanics and Physics of Solids, Vol.35, pp.457-478
- Burdekin, F.M. and Stone, D.E.W., (1966), *The crack opening displacement approach to fracture mechanics in yielding*, Journal of Strain Analysis, No. 1, pp: 145-153
- Burstow, M.C., Howard, I.C., Ainsworth, R.A., (1998), *The influence of constraint on crack-tip stress fields in strength mismatched welded joints*, Journal of the Mechanics and Physics of Solids, Vol. 46, No. 5, pp.845-872
- Cam G, Erim S, Yeni C, Kocak M, (1999), *Determination of mechanical and fracture properties of laser beam welded steel joints*, Welding research, Supplement to the Welding journal, June 1999, pp.193-s – 201-s
- Cherepanov, G.P., (1967), *Crack propagation in continuous media*, USSR, J. Appl. Math. and Mech. Translation, Vol. 31, p: 504

- Cottrell, B. and Rice, J.R., (1984), *Slightly curved or kinked cracks*, International Journal of Fracture, Vol. 16, No. 2, pp:155-169
- Curry DA, (1980), *Comparison between two models of cleavage fracture*, Metal Science, Vol. 14(2), pp:78-80
- Curry DA, Knott JF, (1978), *Effects of microstructure on cleavage fracture stress in steel*, Metal Science, Vol. 12, pp. 511-514
- Curry DA, Knott JF, (1979), *Effects of microstructure on cleavage fracture toughness of quenched and tempered steels*, Metal Science, Vol. 13, pp. 341-345
- Dowling, A.R. and Townley, C.H.A., (1975), *The effect of defects on structural failure: A two-criteria approach*, International Journal of Pressure Vessels and Piping, Vol. 3, pp: 77-137.
- Dugdale, D.S., (1960), *Yielding of steel sheets containing slits*, Journal of the Mechanics and Physics of Solids, Vol. 8, pp: 100-108
- Du, Z.Z. and Hancock, J.W., (1991), *The effect of non-singular stresses on crack tip constraint*, Journal of the Mechanics and Physics of Solids, Vol. 39, pp:555-567
- Erdogan F and Sih GC, (1963), Journal of Basic Engineering, Vol. 85, p. 519
- Eripret, C., Hornet, P., (1997), *Fracture toughness testing procedures for strength mismatched structures*, Mis-Matching of Interface and Welds, Ed. K.H. Schwalbe, M. Kocak, GKSS Research Center Publications, Geesthacht, FRG, pp.17-34
- Eshelby, J.D. (1968), *Stress analysis of cracks*, ISI Publication, Vol. 121, pp: 13-48
- EPRI (1981), "An Engineering Approach for Elastic-Plastic Fracture Analysis", Electric power research institute, Schenectady, New York
- ESIS P1-92 (1992), "ESIS Recommendations for determining the fracture resistance of ductile materials."
- Freudenthal, A.M., (1968), *Statistical approach to brittle fracture*, In: Fracture: an advanced treatise. Ed: Liebowitz H. Academic Press: New York. Vol.2, pp.591-619
- Frise, P.R., Bell, R., (1992), *Modelling fatigue crack growth and coalescence in notches*, International Journal of Pressure Vessels and Piping, Vol.51, pp.107-126
- Gahm, H., and Jeglitsch, F., (1981), *Colour methods and their application in metallography*, Microstructural Science, Vol.9, 65-80
- Gao, X., and Dodds, R.H., (2001), *An engineering approach to assess constraint effects on cleavage fracture toughness*, Engineering Fracture Mechanics, Vol. 68, p.263

- Griffith, A.A., (1921), *The phenomenom of rupture and flow in solids*, Phil. Trans. Roy. Soc. of London, Ser. A, Vol. 221, pp:163-197
- Green, A.E. and Sneddon, I.N., (1950), *The distribution of stress in the neighbourhood of a flat elliptical crack in an elastic solid*, Proc. of the Cambridge Philisophical Society, vol. 46, pp. 159-163
- Hadley, I, (2000), *Testing the waters-shipbuilding laser welds face toughness trial*, TWI research bulletin, Vol. 41(5),September/October 2000, p. 67
- Hadley, I, (2000), *Testing the waters-shipbuilding laser welds face toughness trial Part II: the findings...*, TWI research bulletin, Vol. 41(6),November/December 2000
- Hadley, I, (2001), *Charpy testing laser welds – the significance of fracture path deviation*, TWI research bulletin, Vol. 42(5),September/October 2001
- Hancock, J.W. and Cowling, M.J., (1980), *Role of state of stress in crack-tip failure process*, Metal Science, pp.293-304
- Hancock, J.W., Gall, D.S. and Huang, X., (1986), *Fatigue crack growth due to random loading in air and sea water with applications to the growth of semi-elliptical cracks in the tubular welded joints of offshore structures*, Inst. Of Mechanical Engineers, Technical report C144/86, pp.49-58
- Hancock, J.W., Reuter, W.A. and Parks, D.M., (1993), *Toughness and constraint parameterized by T*, In 'Constraint effects in fracture', ASTM STP 1171, American Society for Testing and Materials, Philadelphia, pp: 121-140
- Hasegawa, K., (2002), Private communication.
- Hasegawa, K., Miyazaki, K., Kanno, S., (2001), *Interaction criteria for multiple flaws on the basis of stress intensity factors*, In: Proc Int Conf ASME Pressure Vessels and Piping 2001, Atlanta, Ga, 22-26 July 2001
- Hertzberg RW, (1989), 'Deformation and Fracture Mechanics of Engineering Materials', 3rd ed, John Wiley and Sons
- HKS, (1998), ABAQUS/Standard, V 5.8, Hibbitt, Karlsson and Sorensen, inc, Providence, Rhoad Island
- Hornet, P., and Eripret, C., (1995), *Experimental J evaluation from a load-displacement curve fro homogeneous and overmatched SENB or CCT specimens*, Fatigue and Fracture of Engineering Materials and Structures, Vol. 18, No. 6, pp.679-692
- Hutchinson, J.W., (1968), *Singular behaviour at the end of a tensile crack in hardening material*, Journal of the Mechanics and Physics of Solids, Vol. 16, pp: 13-31
- Iida, K., Ando, K. and Hirata, T., (1984), *An evaluation technique for fatigue life of multiple surface cracks*, Naval Arch. And Ocean Engineering, Vol. 22, pp. 177-199

- Iida, K. and Kawahara, M., (1980), *Propagation and coalescence of fatigue cracks initiated from collinear or parallel adjacent surface flaws*, 4th International conference on pressure vessel technology, I.Mech.E. London
- Inglis, C.E., (1913), *Stresses in a plate due to presence of cracks and sharp corners*, Trans. Inst. Naval Architects, Vol. 55, pp:219-241
- Irwin, G.R., (1957), *Journal of Applied Mechanics*, Transactions ASME, Vol. 24, p:361
- Irwin, G.R., (1958), 'Fracture Handbook der Physik VI', pp:551-590, Springer-verlag, Berlin, 1958
- Irwin, G.R., (1960), *Plastic zone near a crack and fracture toughness*, Proc. 7th Sagamore Conf., p.IV-63
- Irwin, G.R., (1962), *Crack extension force for a part-through crack in a plate*, Trans. ASME, *Journal of Applied Mechanics*, Vol. 29, pp. 651
- Joch, J., Ainsworth, R.A., Hyde, T.H., (1993), *Limit load and J-estimates for idealised problems of deeply cracked welded joints in plane strain bending and tension*, Fatigue and Fracture of Engineering Materials and Structures, Vol. 16, No. 10, pp.1061-1079
- Karstensen, A.D., (1996), 'Constraint estimation schemes in fracture mechanics', PhD Thesis, University of Glasgow, UK
- Kfoury, A.P., (1986), *Some evaluations of the elastic T-term using Eshelby's method*, International Journal of Fracture, Vol. 30, pp. 301-315
- Kirk, M.T., and Dodds, R.H., (1992), "Effect of weld strength mismatch on structural integrity assessments", EWI report J6154-11-94
- Kirk, M.T., and Dodds, R.H., (1993), *J and CTOD estimation equations for shallow cracks in single edge notch bend specimens*, Journal of Testing and Evaluation, Vol. 21(4), pp.228-238
- Kirk, M.T., Koppenhoefer, K.C., and Shih, C.F., (1993), In: Hackett, E.M. (Eds), 'Constraint Effect in Fracture' ASTM STP 1171, American Society for Testing and Materials, Philadelphia, pp.79-103
- Kristensen, J.K., (1996), *Procedure qualification, process monitoring, NDT and adaptive welding control*, Int. Conf. on Exploitation of Laser Processing in Shipyards and Structural Steelworks, Glasgow UK.
- Kobayashi, A.S., Chiu, S.T. and Beeuwkes, R.A. (1973), *A numerical investigation on the use of the J-integral*, Engineering Fracture Mechanics, Vol. 5, pp: 293-305
- Landes, J.D., and Shaffer, D.H., (1980). In: Fracture Mechanics: Twelfth Conference, ASTM STP 700

- Larsson, S.G. and Carlsson, A.J., (1973), *Influence of non-singular stress terms and specimen geometry on small-scale yielding at crack tips in elastic plastic material*, International Journal of Fracture, Vol. 19, pp: 263-278
- Laukkanen, A., Nevesmaa, P., Kainanen, H., Wallin, K., (2003), *Fracture toughness transferability study between the master curve method and pressure vessel nozzle using local approach*, PVP-Vol. 462, Application of Fracture Mechanics to Failure Assessment, Proc. Int. Conf. ASME PVP 2003, Cleveland, OH, July 2003
- Leek, T.H. and Howard, I.C., (1996), *An examination of methods of assessing interacting surface cracks by comparison with experimental data*, International Journal of Pressure Vessels and Piping, Vol. 68, pp: 181-201
- Leevers, P.S. and Radon, J.C., (1986), *Inherent stress biaxiality in various fracture specimen geometries*, International Journal of Fracture, Vol. 19, pp: 942-955
- Lei, Y., O'Dowd, N.P., Busso, E.P., Webster, G.A., (1998), *Weibull stress solutions for 2-D cracks in elastic and elastic-plastic materials*, International Journal of Fracture, Vol. 89, p. 245
- Li, J., (1997), 'Elastic-plastic interfacial crack problems', PhD Thesis, University of Glasgow, UK
- Li, F.Z., Shih, C.F., Needleman, A., (1985), *A comparison of methods for calculating energy release rates*, Engineering Fracture Mechanics, Vol. 21, pp.405-421
- Li, Y. and Wang, Z., (1986), *High-order asymptotic field of tensile plane-strain nonlinear crack problem*, Scientia Sinica (Series A), Vol. 29, pp:941-955
- Lidbury, D.P.G., (1990), "Effects of specimen size on the fracture toughness transition properties of a Seizwell B specific A508 Class 3 steel forging and comparison with the additional RPV materials", AEA Technology Report No. PWR/RDMC/MWG/P(89)248M, Risley, UK
- Lidbury, D.P., Sherry, A.H., Beardsmore, D.W., Wilkes, M., Dowling, A.R., Connors, D.C. Parsons, A.B., (1999), *Application of local approach modelling of constraint contributions to the ductile-brittle transition*, Proc. Int. Conf. ASME PVP2000, PVP-Vol.392, p.259
- Maccagno, T.M., and Knott, J.F., (1989), *The fracture behaviour of PMMA in mixed modes I and II*, Engineering Fracture Mechanics, Vol. 34, pp.65-86
- MacLennan, I.J., (1996), "Two parameter engineering fracture mechanics", PhD Thesis, University of Glasgow, UK
- MacLennan, I.J. and Hancock, J.W., (1995), *Constraint-based Failure Assessment Diagrams*, Proc. Royal Society London, Series A, Vol. 451, pp: 757-777

- McClintock, F.A., (1968), *A criterion for ductile fracture by the growth of holes*, Journal of Applied Mechanics, Vol. 35, pp:363-371
- McMeeking, R.A., (1977), *Finite deformation analysis of crack tip opening in elastic-plastic material and implications for fracture*, Journal of the Mechanics and Physics of Solids, Vol. 25, pp.357-381
- McMeeking, R.A. and Parks, D.M., (1979), *On criteria for J-Dominance of crack tip fields in large scale yielding*, In Landes, J. (Ed.). 'Elastic-Plastic Fracture, ASTM STP 668', American Society for Testing and Materials, Philadelphia, pp:175-194
- Melin, S., (1983), *Why do cracks avoid each other?*, International Journal of Fracture, Vol. 23, pp: 37-45
- Miyazaki, H., Kaneko, H. and Murakata, T., (1989), *Stress intensity factor analyses of interacting elliptical cracks using line-spring boundary element method*, International Journal of Pressure Vessels and Piping, Vol. 38, pp:1-14
- Moussa, W.A., Bell, R., Tan, C.L., (1999), *The interaction of two parallel non-coplanar identical surface cracks under tension and bending*, International Journal of Pressure Vessels and Piping, Vol.76, pp.135-145
- Murakami, Y. and Nisitani, (1981), *Stress intensity factors for interacting two semi-elliptical surface cracks in tension*, Trans. Japan Soc. Mechanical Engineers, Ser. A, Vol. 47, No. 415, pp. 295-303
- Murakami, Y. and Nemat-Nasser, S., (1982), *Interacting dissimilar semi-elliptical surface flaws under tension and bending*, Engineering Fracture Mechanics, Vol. 16, No. 3, pp. 373-386
- Murakami, Y. (1987), 'Stress Intensity Factor Handbook', Volume 1, Pergamon Press
- Nekkal, A. and Hancock, J.W., (1994), "A method to quantify and use the enhanced toughness of small defects in high strength weldments, Report No. GR/H48576, University of Glasgow
- O'Donoghue, P.E., Nishioka, T. and Atluri, S.N., (1984), *Multiple surface cracks in pressure vessels*, Engineering Fracture Mechanics, Vol. 20, No. 3, pp. 545-560
- O'Dowd, N.P. and Shih, C.F., (1991a), *Family of crack tip fields characterized by a triaxiality parameter: Part I - structure of fields*, Journal of the Mechanics and Physics of Solids, Vol. 39, pp:939-963
- O'Dowd, N.P. and Shih, C.F., (1991b), *Family of crack tip fields characterized by a triaxiality parameter: Part II- fracture application*, Journal of the Mechanics and Physics of Solids, Vol. 40, pp:989-1015
- Orowan, E., (1952), *Fundamentals of brittle behaviour of metals*, Fatigue and Fracture of Metals, Wiley, New York, pp:139-167

- Ortner, S.R., and Hipsley, C.A., (1996), *Two component description of ductile to brittle transition in ferritic steel*, Materials Science and Technology, Vol. 12, pp.1035-1042
- PD 6493 (1991), "Guidance on methods for assessing the acceptability of flaws in fusion welded structures", Document PD 6493, British Standard Institution, 1991
- Paris, P.C. and Erdogan, F., (1963), *A critical analysis of crack propagation laws*, Journal of Applied Mechanics, Transactions ASME, Ser. D, Vol. 85, pp:528-534
- Parks, D.M. (1981), *The Inelastic line-spring: Estimates of elastic-plastic fracture mechanics parameters for surface-cracked plates and shells*. J Pressure Vessel Technol Trans ASME. Vol. 246, p.254
- Parks, D.M. and White, C.S. (1982), *Elastic-plastic line-spring finite elements for surface cracked plates and shells*, Journal of Pressure Vessels Technology, Vol. 104, pp: 287-292
- Perl, M., Levy, C., Wang, J., (1997), *Interaction effects in combined arrays of radial and longitudinal semi-elliptical surface cracks in pressurised thick-walled cylinder*, Journal of Pressure Vessel Technology, Transactions ASME, Vol.119, pp.167-173
- R6, (2001), "Assessment of the integrity of structures containing defects", Revision 4, British Energy Generation Ltd, Gloucester, UK
- Raju, I.S., Newman, J.C., Jr, (1981), *An empirical stress-intensity factor equation for the surface crack*, Engineering Fracture Mechanics, Vol. 15, pp: 185-192
- Rashid, M.M. and Tveegaard, V., (2003), *On the path of a crack near a graded interface under large scale yielding*, International Journal of Solids and Structures, Vol. 40, pp: 2819-2831
- Rice, J.R., (1968), *A path independent integral and the approximate analysis of strain concentration at notches and cracks*, ASME Journal of Applied Mechanics, Vol. 35, pp: 379-386
- Rice, J.R., (1972), International Journal of Solids and Structures, Vol. 8, pp:751-758
- Rice, J.R., (1974), *Limitations to the small scale yielding approximation for crack tip plasticity*, Journal of The Mechanics and Physics of Solids, Vol. 22, pp: 17-26
- Rice, J.R., (1985), *First-order variation in elastic fields due to variation in location of a planar crack front*, Journal of Applied Mechanics, Vol. 52, pp: 571-579
- Rice, J.R. and Johnson, M.A., (1970), 'Inelastic behaviour of solids', McGraw-Hill, New York
- Rice, J.R. and Levy, N. (1972), *The part-through surface crack in an elastic plate*, Journal of Applied Mechanics, Vol. 39, No. 1, March 1972, pp: 185-194

- Rice, J.R. and Rosengren, G.F., (1968), *Plane strain deformation near a crack tip in power-law hardening material*, Journal of the Mechanics and Physics of Solids, Vol. 16, pp: 1-12
- Rice, J.R. and Tracey, D.M.,(1973), *Computational fracture mechanics*, In: "Numerical and computational methods in structural mechanics", Academic Press, New York
- Ritchie, R.O., Knott, J.F., Rice, J.R.,(1973), *On the relationship between critical tensile stress and fracture toughness in mild steel*, Journal of the Mechanics and Physics of Solids, Vol.21, p.395
- Richie, R.O., Server, W.L., Wullaert, R.A., (1979), *Critical fracture stress and fracture strain models for the prediction of lower and upper shelf toughness in nuclear pressure vessel steels*, Metallurgical Transactions, Vol. 10A, pp.1557-1570
- Robinson, J.N., (1976), *An experimental investigation of the effect of specimen type on the crack tip opening displacement and J-integral fracture criteria*, International Journal of Fracture, Vol. 12, pp: 723-737
- Robinson, J.N. and Tetelman, A.S., (1973), *The critical crack-tip opening displacement and microscopic and macroscopic fracture criteria for metals*, Un. Cal. Los Angeles Rep. Eng. 7360
- Schijve, J., (2003), *Fatigue of structures and materials in the 20th century and the state of the art (review article)*, International Journal of Fatigue, Vol. 25, pp.679-702
- Schwalbe, K.H., Ainswort, R.A., Eripret, C., Franco, Ch., Gilles, Ph., Kocak, M., Pisarski, H., Wang, Y.Y., (1997), *Common views on the effects of yield strength mismatch on testing and structural assessment*, In: "Mis-Matching of Interface and Welds", Ed. K.H. Schwalbe, M. Kocak, GKSS Research Center Publications, Geesthacht, FRG, pp.99-132
- Scott, P.M. and Thorpe, T.W., (1981), *Prediction of semi-elliptic crack shapes development during fatigue crack growth*, Report R-10104, Atomic Energy Research Establishment, Harwell, United Kingdom
- Sham, T.L., (1991), 'The determination of the elastic T-term using higher order weigh functions', *International Journal of Fracture*, vol. 48, pp.81-102
- Sherry, A.H., Lidbury, D.P.G., Beardsmore, D.W., (2001), "Validation of constraint based structural integrity assessment methods. Final report." Report No. AEAT/RJCB/RD01329400/R003, AEA Technology, UK
- Shih, C.F., (1974), *Small scale yielding analysis of mixed-mode plane-strain crack problems*, In: "Fracture problems" ASTM, STP 560, American Society for Testing and Materials, Philadelphia, pp.187-210

- Shih, C.F., (1981), *Relationship between the J-integral and the crack tip opening displacement for stationary and extending cracks*, Journal of the Mechanics and Physics of Solids, Vol. 29(4), pp. 305-326
- Shih, C.F. and German M.D.,(1981), *Combined loading of a fully plastic ligament ahead of an edge crack*, Journal of Applied Mechanics, Vol. 53, pp:27-43
- Slatcher, S., and Oystein, E., (1986), *Practical application of the weakest-link model to fracture toughness problems*, Engineering Fracture Mechanics, Vol.24, p.495
- Soboyejo, W.O., Knott, J.F., Walsh, M.J., Cropper, K.R., (1990), *Fatigue crack propagation of coplanar semi-elliptical cracks in pure bending*, Engineering Fracture Mechanics, Vol.37, pp.323-340
- Stoker, J.J., (1969), 'Differential Geometry', Wiley-Interscience, New York
- Sumpter, J.D.G., (1987), *Jc determination for shallow notched welded bend specimens*, Fatigue and Fracture of Engineering Materials and Structures, Vol. 10, pp.1061-1079
- Sumpter, J.D.G., (1996), *Fracture toughness of laser welds in ship steel*, Advanced Performance Materials, Vol. 3, pp.393-405
- Sumpter, J.D.G., (1999), *Fracture toughness evaluation of laser welds in ship steels*, European Symposium on Assessment of Power beam Welds, GKSS Research Center, Geesthacht, Germany, February 4-5
- Sumpter J.D. and Hancock, J.W., (1991), *Shallow crack toughness of HY80 welds: an analysis based on the T stress*, International Journal of Pressure Vessels and Piping, Vol. 45, pp: 207-221
- Sumpter, J.D.G. and Forbes, A.T., (1992), *Constraint based analysis of shallow cracks in mild steel*, In Dawes, M.G. (Ed.), 'Shallow crack fracture mechanics, Toughness Tests and Applications', The Welding Institute, Abington, Publishing Cambridge, England, Cambridge CB1 6AL, UK.
- Tada, H., Paris, P., Irwin, G., (1973), 'The Stress Analysis of Cracks Handbook', Del Research Corporation, Missouri
- Thaulow, C., Hauge, M., Zhang, Z.L., Ranestad, O., Fattorini, F., (1999), *On the interrelationship between fracture toughness and material mismatch for cracks located in the fusion line of weldments*, Engineering Fracture Mechanics, Vol. 64, pp.367-382
- Twaddle, B.R. and Hancock, J.W., (1986), *The Development of Cracks by Defect Coalescence*, Fatigue of Offshore Structures, EMAS
- Wall, M., Lane, C.E., Hipplesley, C.A, (1994), *Fracture criteria for hydrogen and temper embrittlement in 9Cr1Mo steel*, Acta Metallurgica and Materialia, Vol. 42, pp.1295-1309

- Wallin, K., (1984), *The scatter in K_{IC} results*, Engineering Fracture Mechanics, Vol.19, p.1085
- Wallin, K., (1985), *The size effect in K_{IC} results*, Engineering Fracture Mechanics, Vol.22, pp.149-163
- Wallin, K., (2000), *T-stress based correction for the Master Curve transition temperature T_0* . In: Proc ASME PVP2000, PVP Vol 412, Seattle, USA
- Wallin, K., Saario, T., Torronen, K., (1984), Metal Science, Vol. 18, p.13
- Wang, Y.Y., (1993), *On the two-parameter characterisation of elastic-plastic crack-front field in surface cracked plates*, In Hackett, E.M., Schwable, K.H. and Dodds, R.H., (ed.), 'Constraint Effect in Fracture, ASTM STP 1171, American Society for testing and Materials, Philadelphia, PA., pp:120-138
- Wang, G.Z., Chen, J.H., Wang, J.G., (2002), *On the measurement and physical meaning of the cleavage fracture stress in steel*, International Journal of Fracture, Vol. 118, pp.211-227
- Wang, G.Z., Chen, J.H., Liu, G.H., (2002b), *On the characteristic distance and minimum fracture toughness for cleavage fracture in a C-Mn steel*, International Journal of Fracture, Vol. 118, pp.57-76
- Wang, Y.Y., and Gordon, J.R., (1992), *The limits of applicability of J and CTOD estimation procedures for shallow-cracked SENB specimens*, In: Shallow Crack Fracture Mechanics, Toughness tests and Applications, Ed. MG Dawes, Cambridge, UK, September 23-24
- Wang, Y.Y., and Parks, D.M., (1992), *Evaluation of the T-stress in surface cracked plates using line spring method*, International Journal of Fracture, Vol. 59, pp.25-44
- Wells, A.A., (1961), *Unstable crack propagation in metals – cleavage and fast fracture*, Proc. Crack propagation symposium, Cranfield, pp: 210-230
- Westergaard, H.M., (1939), *Bearing pressures and cracks*, Journal of Applied Mechanics, Vol. 61, pp. A49-A53
- Williams, M.L., (1957), *On the stress distribution at the base of a stationary crack*, Asme Journal of Applied Mechanics, vol. 24, pp.111-114
- Williams, M.L., Ewing, P.D., (1972), International Journal of Fracture Mechanics, Vol. 8, p. 441
- Xie, J., (2002), *Dual beam laser welding*, Welding research, Supplement to the Welding Journal, October 2002, pp.223-s – 230-s

- Yeni, C., Erim, S., Cam, G., Kocak, M., (1996), *Microstructural features and fracture behaviour of laser welded similar and dissimilar steel joints*, Int. Welding Technology 96 Symposium, Istanbul, Turkey, pp.235-247
- Zhang, Z.L., Hauge, M., Thaulow, C., (1996), *Two parameter characterisation of the near tip stress fields for bi-material elastic-plastic interface crack*, International Journal of Fracture, Vol. 79, pp.65-83
- Zhang, Z.L., Thaulow, C., Hauge, M., (1997), *Effects of crack size and weld metal mismatch on HAZ cleavage toughness*, Engineering Fracture Mechanics, Vol. 57, pp.653-664

Appendix A

LIST OF CONFERENCE PUBLICATIONS

- [1] B. Bezensek and J.W. Hancock, *Increased temperature margins due to constraint loss*, In: Proc. Int. Conf. ASME PVP03: Application of fracture mechanics in failure assessment, PVP-462, Ed: P.S. Lam *et al*, Cleveland, Oh, USA, July 2003, pp: 49-56, [ISBN 0-7918-4153-7]
- [2] B. Bezensek, *Application of linear graph theory in designing fracture mechanics experiments.* Proc. Int. Conf. Advanced Engineering Design 2003, Paper No. 57, Prague, June 2003, [ISBN 90-86059-35-9]
- [3] B. Bezensek and J.W. Hancock, *A statistical fracture mechanics analysis of crack path deviations in strength mismatched joints*, In: Proc. Int. Conf. Engineering Structural Integrity Assessment: Needs and Provision (ESIA 6), Ed: P.E.J.Flewitt *et al*, EMAS Publishing, Manchester, October 2002, pp:291-299, [ISBN emas.co.uk]
- [4] B. Bezensek and J.W. Hancock, *A constraint based statistical approach to failure from complex defects*, In: Proc. Int. Conf. ECF 14: Fracture Mechanics Beyond 2000, Vol. I, Ed: A.Neimitz, *et al*, EMAS Publishing, Krakow, Poland 2002, pp:249-256, [ISBN 1901537366]
- [5] B. Bezensek and J.W. Hancock, *Ductile tearing of interacting surface breaking defects*, In: Proc. Int. Conf. 10th Congress on Fracture, Ed: T.Kishi *et al*, Paper No. ICF100557OR, Honolulu, Hi, USA, December 2001, p. 537, [ISBN 0080440428]
- [6] B. Bezensek and J.W. Hancock, *The non-coplanar coalescence of interacting defects in fatigue*, In: Proc. Int. Conf. SAE Brasil Fatigue 2001, Ed: P.M.Pimenta *et al*, Paper No. 2001-01-4052, São Paulo, Brazil, Dec. 2001, pp:151-159
- [7] B. Bezensek, Z.Ren and J.W. Hancock, *A study of complex defects failing by fatigue, ductile tearing and cleavage*, In: Proc. Int. Conf. Nuclear Energy in Central Europe 2001, Ed: I.Jencic, B.Glumac, Paper No. 402, Portoroz, Slo, September 2001, [ISBN 961-6207-17-2]
- [8] B. Bezensek and J.W. Hancock, *Brittle fracture from interacting surface breaking defects*, In: PVP-423, Ed: D. Lidbury, Proc. Int. Conf. ASME Pressure Vessels and Piping 2001, Atlanta, Ga, USA, July 2001, pp: 25-31, [ISBN No. 0-7918-1678-8]

Appendix B:
COPIES OF PAPERS TO APPEAR IN
“ENGINEERING FRACTURE MECHANICS” JOURNAL

- [1] Bezensek B. and Hancock JW., *The Re-characterisation of Complex Defects, Part I: Fatigue and Ductile tearing*, Accepted for publication in Engineering Fracture Mechanics, October 2002.
- [2] Bezensek B. and Hancock JW., *The Re-characterisation of Complex Defects, Part II: Cleavage*, Accepted for publication in Engineering Fracture Mechanics, October 2002.



PERGAMON

Available online at www.sciencedirect.com

SCIENCE @ DIRECT®

**Engineering
Fracture
Mechanics**

Engineering Fracture Mechanics xxx (2003) xxx–xxx

www.elsevier.com/locate/engframech

The re-characterisation of complex defects Part I: fatigue and ductile tearing

B. Bezensek ^{*,1}, J.W. Hancock*Department of Mechanical Engineering, University of Glasgow, Glasgow G12 8QQ, Scotland, UK*

Received 11 July 2002; received in revised form 16 April 2003; accepted 17 April 2003

Abstract

Defect assessment codes idealise complex defects as simple shapes which are amenable to analysis in a process known as re-characterisation. The present work examines the re-characterisation of complex defects which extend by fatigue, ductile tearing or cleavage. A family of representative defects were analysed numerically, while a related experimental programme investigated defect interaction and failure. Part I of the paper focuses on fatigue and ductile tearing. Part II examines cleavage. The numerical and experimental results are discussed within the context of the re-characterisation procedures described in BS 7910 (Guidance on methods for assessing the acceptability of flaws in metallic structures. London, UK: British Standard Institution; 1999 [Chapter 7]) and R6/4 (Assessment of the integrity of structures containing defects. Gloucester: British Energy Generation Ltd.; 2001 [Revision 4, Chapters I and II.3]).

The level of conservatism of the re-characterisation procedures for fatigue and ductile tearing are discussed. A possible non-conservatism of the re-characterisation for cleavage is discussed in Part II, within the framework of constraint based statistical fracture mechanics.

© 2003 Published by Elsevier Science Ltd.

Keywords: Complex defects; Re-characterisation; Line-spring analysis; Fatigue; Ductile tearing

1. Introduction

Defect assessment procedures ensure the integrity of structures which may contain cracks or flaws. Assessments are based on toughness data obtained from standard tests on specimens with straight crack fronts. The integrity of the structure is then demonstrated by comparing a characterising parameter, such as the stress intensity factor, K , or the J -integral, J , around the perimeter of a real or idealised defect with critical values obtained from standard test geometries. However real structures may contain neighbouring defects, or defects with complex shapes. Codes, such as BS 7910 [1], R6/4 [2] and ASME Section XI [3], invoke procedures which allow multiple interacting or complex defects to be idealised as simpler shapes, which are more amenable to analysis. To ensure the procedure is conservative, the re-characterised defects

* Corresponding author. Tel.: +44-141-330-4722; fax: +44-141-330-4343.

E-mail addresses: b.bezensek@eng.gla.ac.uk (B. Bezensek), j.hancock@eng.gla.ac.uk (J.W. Hancock).

¹ On leave from University of Maribor, Faculty of Mechanical Engineering, Slovenia.

must be demonstrated to be more detrimental than the original defect. Although the re-characterisation procedures are primarily intended for complex defects which extend by fatigue, they may also be applied to monotonic loading failures under both cleavage and ductile tearing conditions.

Re-characterisation can be applied to single defects, or to multiple interacting defects, on a single or adjacent planes. Multiple non-co-planar defects are assessed either as co-planar defects or as separate defects, depending on proximity rules set out in the codes. The procedure is approached in two stages illustrated in Fig. 1 for defects on a single plane. The defect is enclosed in a rectangular box and a re-characterised defect is generated by inscribing a semi-elliptical profile for a surface breaking defect, or an elliptical profile for sub-surface defect, within the box. One axis of the semi-ellipse is parallel to the free surface length, while the other axis extends in the through-thickness direction.

Experimental studies [4–7] have demonstrated limited crack interaction effects under bending as the adjacent crack tips approach, and numerical analyses [7–10] show enhanced values of stress intensity factors for very closely spaced crack tips. Recent revisions of BS 7910 and R6/4 incorporate limited interaction effects in fatigue but preclude the contribution of coalescence to the fatigue life, by re-characterising interacting defects when the adjacent crack tips touch.

The first part of the work considers the conservatism of the re-characterisation procedure and interaction rules, given in BS 7910 and R6/4 for interacting and complex defects, extending by fatigue and ductile tearing. The fatigue study considers the safety margins introduced by the new crack proximity rules in the BS7910 standard in relation to the coalescence and re-characterisation of adjacent defects extending by fatigue. The fatigue study is also used to generate a family of complex cracks with re-entrant sectors. Such defects exhibit enhanced fatigue crack growth rates in the re-entrant sectors [4,6,11], associated with amplified values of the local stress intensity factor. In this context a particular concern arises from failure under monotonic loading. This is examined for ductile tearing in the later sections of Part I, while Part II focuses on cleavage and addresses the appropriateness of the interaction rules and the re-characterisation procedure.

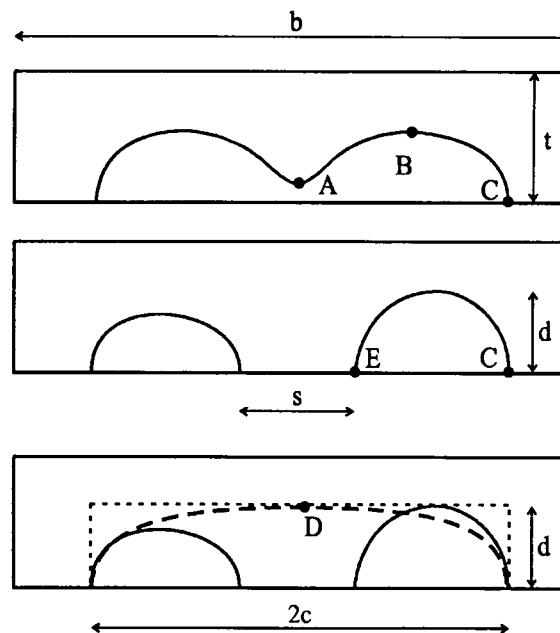


Fig. 1. Crack geometry and the re-characterisation of complex defects.

2. Geometry and numerical procedure

2.1. Geometry

The experimental and related numerical work is focused on the interaction of two surface breaking defects which develop from two co-planar notches by fatigue under three point bending. The experimental work was performed on a plain carbon-manganese 50D steel (BS 4360). Specimens were manufactured to the geometry shown in Fig. 2, using two co-planar starter notches cut with a circular slitting wheel to a nominal depth of 2 mm, surface length of 25 mm and an initial separation of 25 mm.

2.2. Crack configurations

The crack configurations shown in Fig. 3 were retrieved from the experimental programme. Under fatigue the two notches developed into two semi-elliptical defects which extended largely independently of each other until adjacent crack tips met on the free surface, usually with the formation of a shear step. Subsequently a single complex defect with a re-entrant sector formed. The re-entrant sector initially had a high local curvature and rapidly evolved towards a convex bounding shape. Six configurations representing the stages of coalescence towards a bounding defect, shown schematically with solid lines in Fig. 3 were analysed in detail. The configurations are defined by the crack depth in the re-entrant sector. This ranged from $0.12t$ for a configuration with pronounced (shallow) re-entrant sector, to a deep bounding crack of depth $0.52t$, where t is the plate thickness. The analysis focused on the development of the crack front segment in the re-entrant sector (referred to as position A) and at the deepest crack sections (referred to as position B). Each crack was analysed individually and the results compared with results of neighbouring cracks to indicate the development of the complex crack. The effect of a step resulting from non-co-planar coalescence is also analysed.

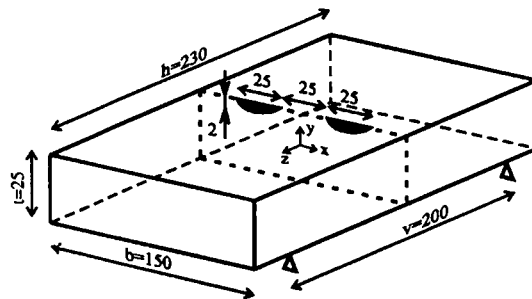


Fig. 2. Experimental geometry; all units are in mm.

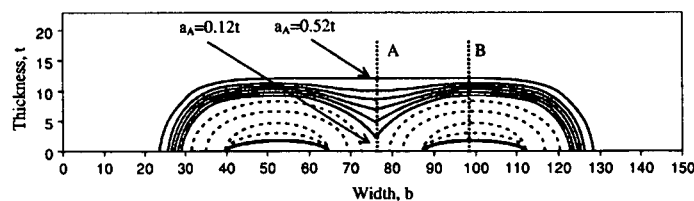


Fig. 3. A family of interacting and complex cracks, originating from two co-planar notches by fatigue, $b = 6t$. Crack configurations are denoted with the depth at position A.

2.3. Line spring technique

Rice and Levy [12] introduced the elastic line spring technique as a computationally efficient way of analysing surface cracked plates and shells. The method essentially idealises a part-through surface crack of surface length $2c$ as a through crack with a series of one-dimensional springs placed across the crack faces. The compliance of each spring is matched to the compliance of a plane strain edge crack bar of matching local crack depth. The additional rotations and displacements arising from the increased compliance due to the cracked bar are combined in a constitutive relation to give the local force and bending moments per unit length along the crack front. The stress intensity factors are then determined from the local forces and moments using the geometry calibration functions for a plane strain edge crack bar. The line spring method was extended by Parks and White [13] to include elastic-plastic behaviour. Limit load behaviour is introduced using an upper bound solution for the limit load of an edge cracked strip in combined tension and bending, while the J -integral is determined from the plastic work done [13]. The accuracy of elastic and elastic-plastic line spring solutions is discussed by Parks and White [13] and Parks [14], and shown to give acceptable level of accuracy when compared with the detailed three-dimensional solutions of Newman and Raju [15]. Using line springs the T -stress [16] can be calculated by combining forces and moments [17] with the calibration functions of T -stress of an edge crack bar given by Sham [18].

2.4. Finite element model

A symmetric quarter of the experimental geometry was modelled with the finite element mesh schematically shown in Fig. 4. The mesh comprised 660 isoparametric second order small strain shell elements and was solved using the ABAQUS [19] finite element code. A crack was represented by uniformly distributed symmetric line spring elements on the lower edge of the model. Displacement controlled three point bending was examined under both elastic and elastic-plastic conditions. The linear elastic analysis used a Young's modulus of 210 GPa and Poisson's ratio of 0.3 to represent the experimental material, although non-dimensional results are presented where appropriate. An elastic perfectly-plastic response was used for a nearly incompressible material (Poisson's ratio of 0.49) to determine the limit load, while the

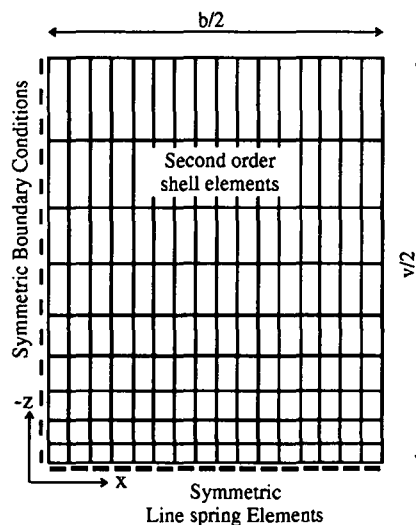


Fig. 4. Finite element mesh of a symmetric quarter of the experimental geometry.

strain hardening response representative of mild steel was modelled with a Ramberg–Osgood power hardening law with a power hardening exponent of 9, which describes the uni-axial tensile test data on the experimental material. The uni-axial stress–strain relation was generalised to multi-axial loading with a Mises yield criterion and an associated flow rule. The yield discontinuity (Lüder's extensions) was not included in the model and the yield stress was set at a 350 MPa, to match experimental tensile data at 20 °C.

3. Numerical study

3.1. Linear elastic analysis

The stress intensity factors (henceforth SIF) and the T -stress are presented in Figs. 5–7 for the crack configurations shown in Fig. 3. The SIFs are normalised by the nominal outer fibre stress and the maximum crack depth of each configuration. Fig. 5 shows the SIF at the deepest point of the both defects (position B) until a bounding semi-ellipse is formed, while position A tracks the SIF at the line-of-coalescence in the re-entrant sector. Fig. 6 shows the stress intensity factor between the line-of-coalescence and the deepest segment. Strongly amplified values of stress intensity factors are exhibited in the re-entrant sector, however these reduce as the re-entrant shape develops into a bounding profile. The re-entrant sectors exhibit amplified SIFs, but remote from the re-entrant sector there is no significant effect on the stress intensity factor.

In-plane crack tip constraint is parameterised by the T -stress [16,20] which is the first non-singular term in the Williams expansion [21] of the asymptotic elastic stress field. The T -stress is presented in Fig. 7 between positions A and B, normalised by the outer fibre stress. The crack shape causes significant in-plane constraint loss in the shallow re-entrant sector, as indicated by a compressive (negative) T -stress. The deeper crack segments exhibit a positive T -stress and are fully constrained.

The variation of SIF and T along the profile of a complex crack is determined by the distribution of the local forces and bending moments per unit length, as shown in Figs. 8 and 9. The local force per unit surface length of the crack, $N_{(x)}$, is shown in Fig. 8. The bending moment, $M_{(x)}$, defined as the bending stress per unit surface length of the crack, is shown in Fig. 9. Both are presented between positions A and B and normalised with the remotely applied values, given in Figs. 8 and 9. In three point bending the complex crack produces a tensile local forces and amplified bending moments in the shallow re-entrant sectors, while

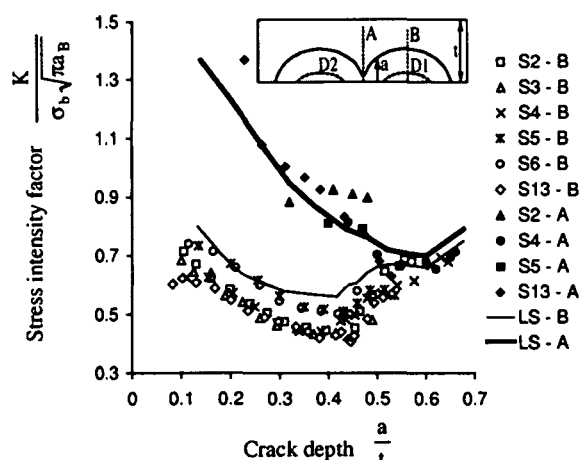


Fig. 5. Stress intensity factor in the re-entrant sector and at the deepest segment from fatigue and line spring (LS) study. The test specimens are denoted with letter S and number.

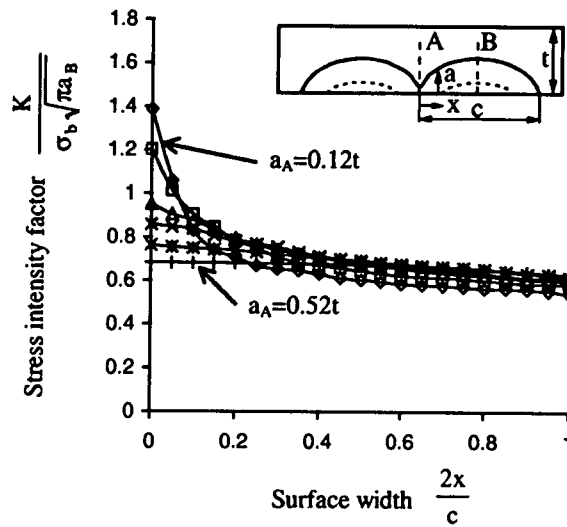


Fig. 6. Stress intensity factor between positions A and B, showing amplified values in the re-entrant sector.

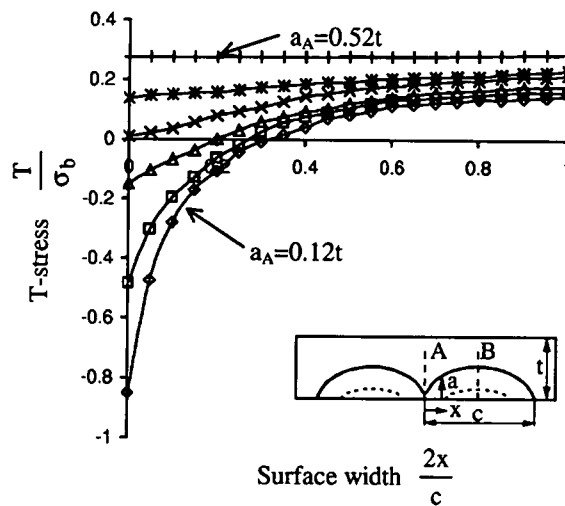


Fig. 7. Non-singular T -stress between positions A and B, showing compressive T -stress in pronounced re-entrant sectors.

the deeper crack segments feature reduced bending moments and compressive forces. The corresponding values for an edge crack are superimposed on Figs. 8 and 9, for three point bending. The normalised force is zero for a straight edge crack subject to bending, while the normalised bending moment is unity.

3.2. Elastic analysis of a crack front with a shear step

An elastic line spring analysis was used to examine the effects of a step in a crack front, by using line spring elements available in ABAQUS [19], which show the stress intensity factors of opening and shear modes. The analysis focused on the family of cracks shown in Fig. 3, where the two cracks are parallel but

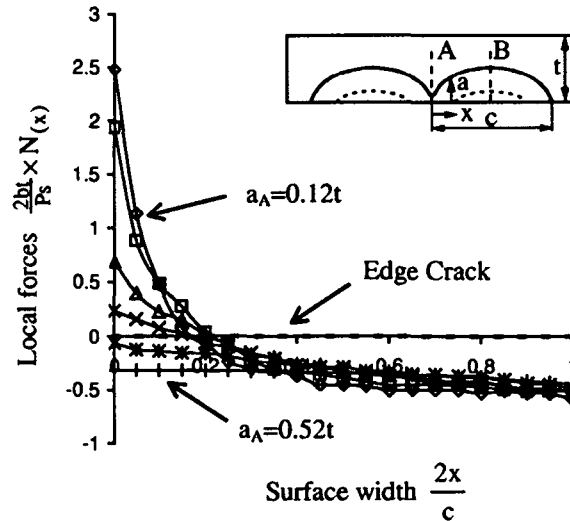


Fig. 8. Non-dimensionalised local forces per unit crack length, between positions A and B, showing amplified values in the re-entrant sector.

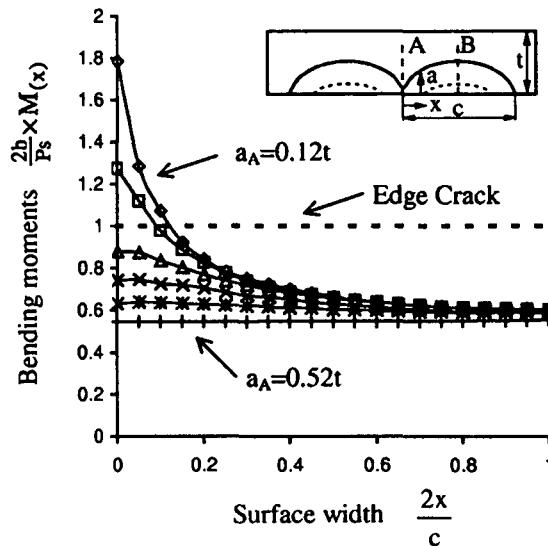


Fig. 9. Non-dimensionalised bending moments per unit crack length, between positions A and B, showing the amplified values in the re-entrant sector.

misaligned by a step, as shown schematically in Fig. 10. The planar sections of the crack were dominated by Mode I and the associated stress intensity factor, K_I , while the step exhibited a strong local Mode III component. This is shown in Figs. 11 and 12 as function of the crack depth at position A for a planar profile and a profile with a step. The amplification of Mode I stress intensity factor in the re-entrant sector of a planar coalesced geometry (Fig. 11) is reduced by the step, which introduces a Mode III component, as shown in Fig. 12. Further increases in the step height reduce the Mode I stress intensity factor in the re-entrant sector, but the strongest effect on the Mode I component occurs from the initial introduction of

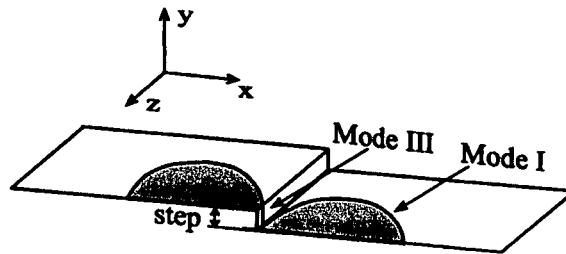


Fig. 10. Geometry with a crack front step, showing Mode I and Mode III stress intensity factors.

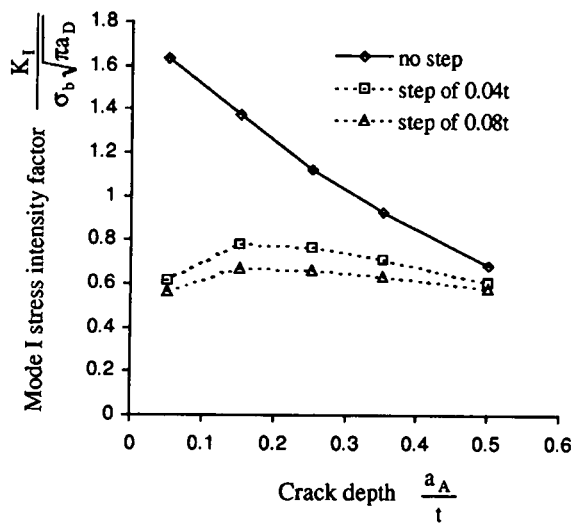


Fig. 11. Mode I stress intensity factor in the re-entrant sector for co-planar and non-co-planar cracks.

the step. The reduction in K_I and increase in K_{III} were not observed to have a significant effect on the fatigue crack growth rates in the re-entrant sector, where rapid fatigue crack growth rates were observed without any local retardation due to the step.

The T -stress in the re-entrant sector for the co-planar and non-co-planar cracks is presented in Fig. 13, normalised with the outer fibre stress. The amplified values of compressive T -stress, which are characteristic of co-planar cracks, are reduced by the non-co-planar coalescence. However both, the Mode I stress intensity factor and the T -stress reduce in the same way, so that the biaxiality parameter β , defined by Leevers and Radon [22]:

$$\beta = \frac{T\sqrt{\pi a}}{K}, \tag{1}$$

is similar for both the co-planar and non-co-planar configurations, as shown in Fig. 14.

3.3. Elastic-plastic analysis

Elastic-plastic line spring analysis [12-14] was performed to determine the development of complex defects under elastic-plastic conditions. Elastic perfectly-plastic line spring analysis was used to determine limit loads. The local limit load is the load to develop full plasticity in the local ligament for a

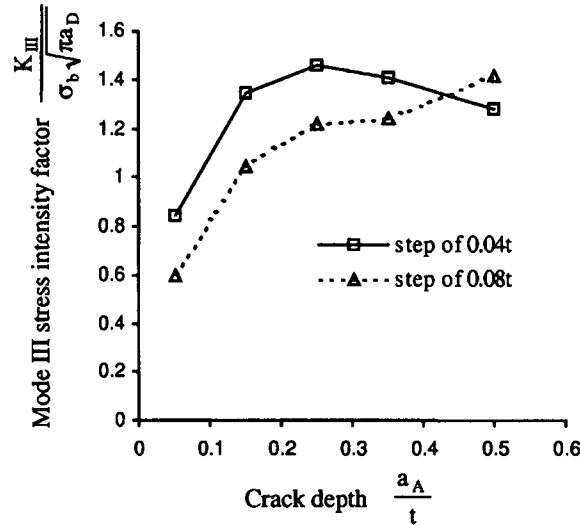


Fig. 12. Mode III stress intensity factor in the re-entrant sector for two step heights.

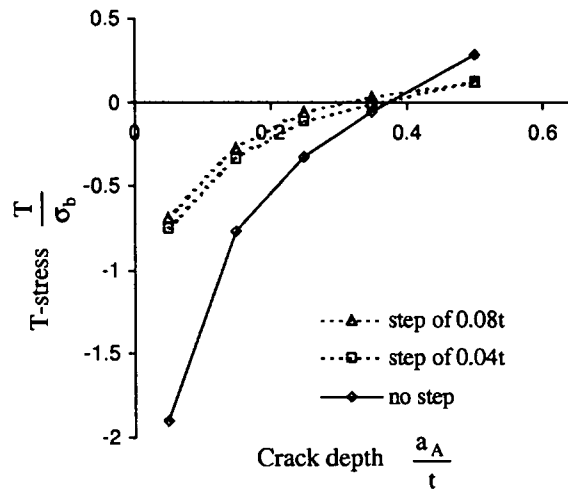


Fig. 13. T-stress in the re-entrant sector for co-planar and non-co-planar cracks.

non-hardening perfectly-plastic material, while the global limit load is that to cause plastic collapse of the whole structure. The local and global limit loads are shown in Fig. 15, normalised with the (global) limit load of the uncracked geometry (P_0). The analysis shows that the smallest local limit load occurs in the configuration with the most pronounced re-entrant sector. In this configuration plasticity develops across the ligament at a significantly lower load than the global plastic collapse load. As the pronounced re-entrant sector develops towards the bounding shape, the local limit load in the re-entrant sector approaches that of the deepest sections. Unlike the local limit load, the shape of the re-entrant sector does not significantly affect the global limit load, which largely depends on the total load bearing area. The calculated load-displacement response obtained by line-spring analysis of a strain hardening material is shown in Fig. 16. The load is normalised by the limit load of the uncracked body, P_0 , and the local limit load in the re-entrant sector and the global limit loads are indicated.

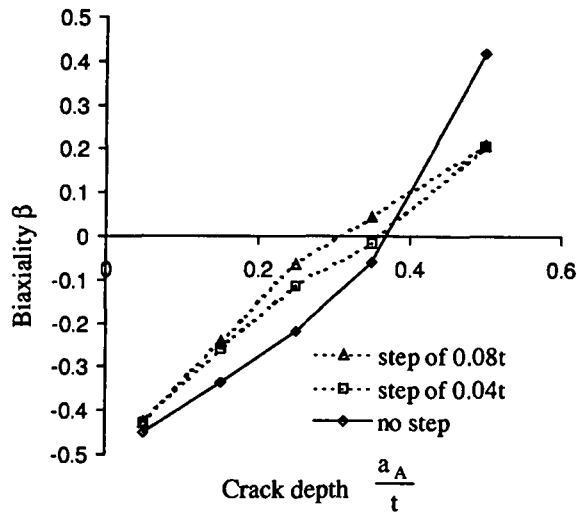


Fig. 14. Biaxiality ratio in the re-entrant sector for co-planar and non-co-planar cracks.

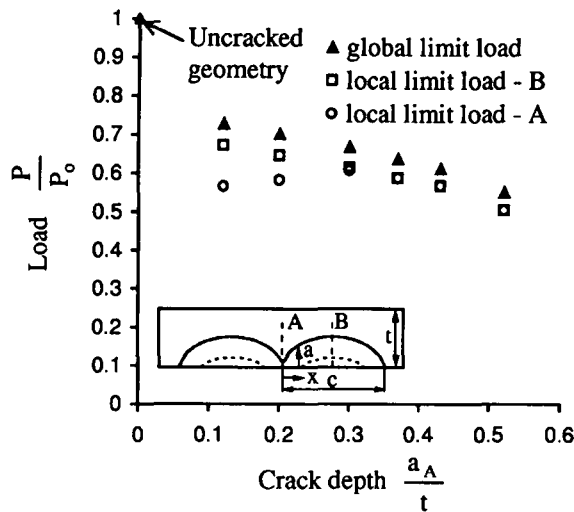


Fig. 15. Local and global limit loads for complex cracks developed by fatigue.

The crack driving force quantified by the J -contour integral [23] was determined for defects with re-entrant sectors under large scale yielding. The J -contour integral is presented in Figs. 17 and 18 for the re-entrant and the deepest position of the complex defect. J is normalised by the tensile yield stress (σ_0) and the smallest ligament ($t - a_B$) of each configuration. The development of J in the re-entrant sector is presented for a series of cracks at the same remotely applied load in Fig. 17 and for the same remote displacement in Fig. 18. The applied load is normalised with the (global) limit load of an uncracked geometry, and the applied displacement is normalised with the thickness (t). The values of J in the re-entrant sector are compared to the J values in the deepest segments, by presenting the data sets for positions A and B with the same abscissa value. This allows a comparison of J at two positions on the same complex crack front. The elastic-plastic analysis shows amplified values of J in the pronounced re-entrant sectors

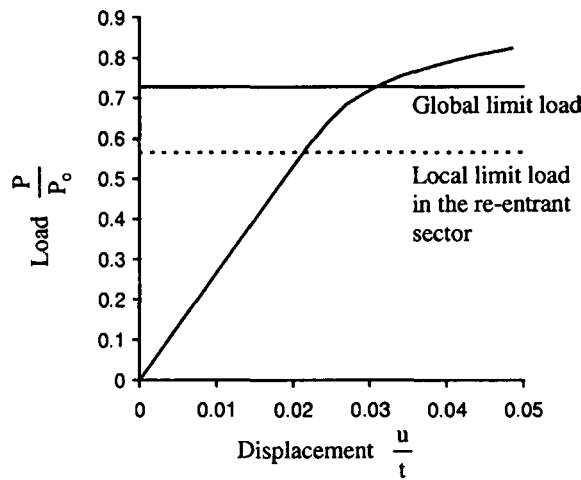


Fig. 16. Calculated load-displacement response for $a_A = 0.12t$ configuration. The local limit load in the re-entrant sector and the global limit loads are superimposed.

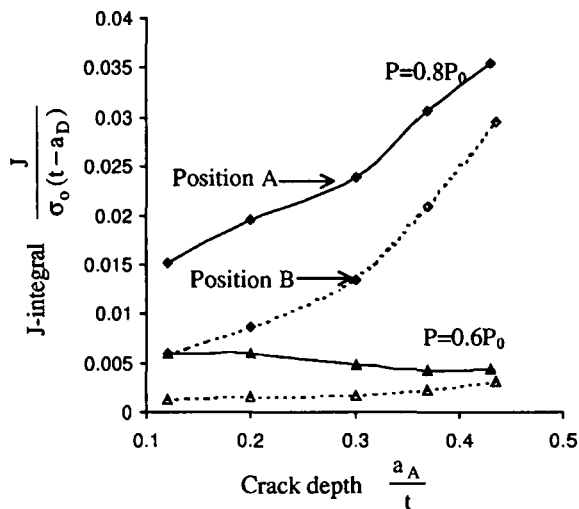


Fig. 17. J -integral evaluated at a constant load and compared at positions A and B on a complex crack.

accompanied with lower local limit loads compared to the deeper crack segments for all applied loads and displacements.

In Fig. 19 the development of the T -stress is presented in the re-entrant sector under large scale yielding. The T -stress was chosen as the constraint parameter, following arguments developed by Betegón and Hancock [20] and Hancock et al. [24]. It is argued that T provides a good practical measure of crack tip constraint even within large scale yield conditions. In Fig. 19, T is presented at four applied loads, normalised with the limit load of the uncracked geometry. The non-linear results complement the linear analysis and indicate a compressive T -stress in the re-entrant sector, whose magnitude depends on the extent of coalescence. The results demonstrate a loss of in-plane constraint in pronounced re-entrant sectors. For modest re-entrant sectors and bounding (or re-characterised) defects, the T -stress becomes positive along the majority of the crack front.

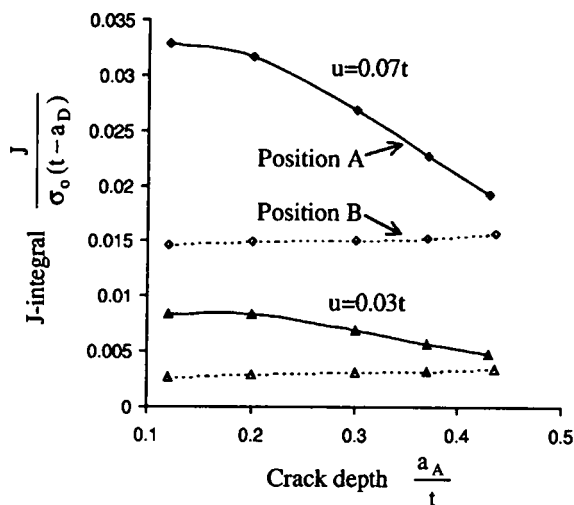


Fig. 18. J -integral evaluated at a constant displacement and compared at positions A and B on a complex crack.

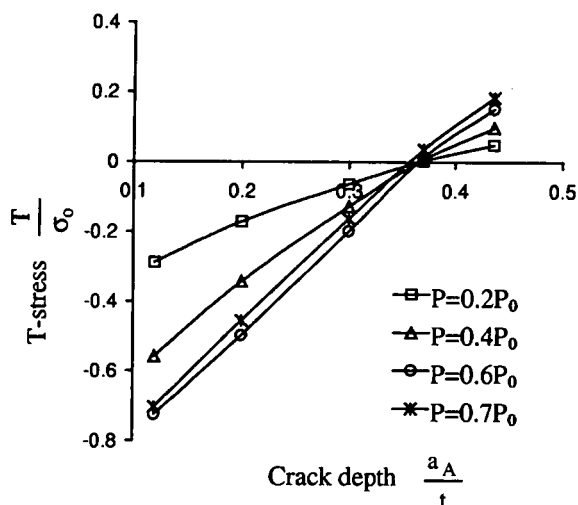


Fig. 19. T -stress evaluated at fixed applied load in the re-entrant sector on a complex crack.

4. Fatigue

4.1. Experimental procedure and observations

Fatigue tests were conducted on a servo hydraulic testing machine under three point bending at a frequency of 4 Hz and at a stress ratio of 0.1, keeping the applied stress intensity factor less than $30 \text{ MPa} \sqrt{\text{m}}$ during the test. The development of the crack shape was monitored using a "beach mark" technique, which produced distinct striations on the fracture surface. This was achieved by altering the load ratio at a constant frequency, such that the minimum load amplitude during beach marking is the mean amplitude during the main fatigue growth, while keeping the maximum load fixed. A fractograph of the broken specimen showing beach marks on the fatigue surface is illustrated in Fig. 20. The two cracks initially



Fig. 20. Sequence of cracks developed in fatigue. Minor interaction effects occur before coalescence. During coalescence the rapid fatigue crack growth extends the crack towards a bounding defect.

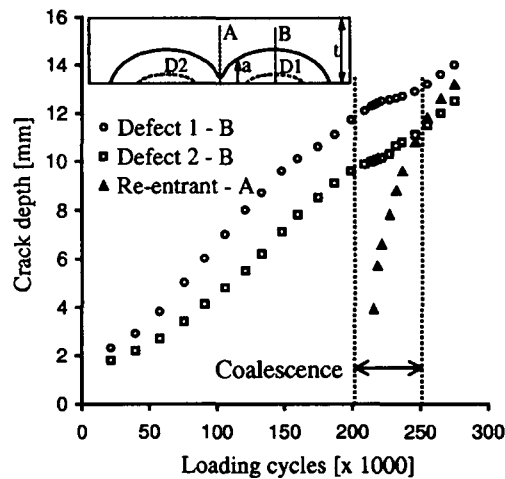


Fig. 21. Crack depth in the re-entrant sector (position A) and at deeper segments (position B) for semi-elliptical cracks extending by fatigue.

developed largely independently of each other until they coalesced and formed a complex crack with a re-entrant sector. During coalescence the complex crack exhibited strongly enhanced fatigue crack growth rates in the re-entrant sector, as shown in Figs. 20 and 21. This allows the complex defect to evolve rapidly into a bounding semi-elliptical defect at a small fraction of the total test duration.

In all fatigue tests the free surface crack path deviated locally from the notch plane [4,6,7,11]. The cracks either overlapped and isolated a small cone-shaped piece of material, Fig. 22(b), or coalesced by shearing the small ligament and forming a step in the crack front, as shown in Fig. 20 and illustrated schematically in Fig. 22(a). The mode of coalescence is determined by the size of the ligament between the two crack tips as discussed by Bezensek and Hancock [25]. Shearing between the adjacent crack tips occurs when the ligament is small, otherwise the cracks overlap and coalesce sub-surface in the notched plane. Crack overlap leads to modest re-entrant sectors, while the most highly curved shallow re-entrant sectors develop when the overlap is small. Experimental effects arising from the loading system are insufficient to explain this effect. Attempts to enforce co-planar coalescence by a surface groove were also unsuccessful [25].

4.2. Analysis of fatigue data

The local fatigue crack growth rates measured in the experiments were used to derive local stress intensity factors for the deepest position of the crack (position B), the re-entrant sector (position A), and the

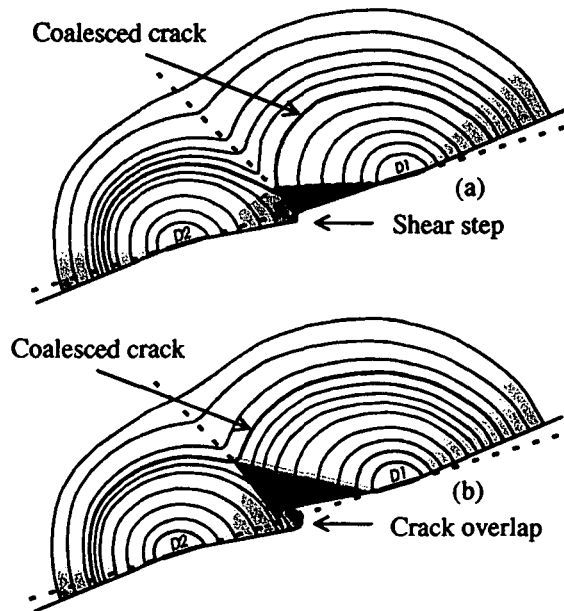


Fig. 22. Coalescence by a shear step (a) and sub-surface by a crack overlap (b).

position on the free surface (positions C and E), as shown schematically in Fig. 1. The local stress intensity factors were inferred from the beach marks spacing using a Paris law:

$$\frac{\Delta a}{\Delta N} = C(\Delta K)^n \quad (2)$$

The constants C and n were determined from fatigue tests on standard 25 mm thick edge crack geometries in three point bending to be $8 \times 10^{-12} (\text{MPa}\sqrt{\text{m}})^{-n} \text{ m/cycle}$ and 2.92, which is consistent with reported data [26] on this grade of steel.

The experimentally determined stress intensity factors are shown as data points in Fig. 5, normalised with the outer fibre stress and the maximum crack depth. Initially the highest values of stress intensity occur at the deepest locations of the separate semi-elliptical defects (position B) but these reduce as the aspect ratio (a/c) decreases with crack growth. The lowest SIF at site B occurs just before coalescence, followed by a gradual increase as the coalesced defect develops towards the single bounding defect. At the point of coalescence the stress intensity in the re-entrant sector was extremely high. However as the crack depth in the re-entrant sector developed towards the bounding defect, the stress intensity factors at A and B converged. The crack depth ($0.53t$ in Fig. 5) where this occurs completes the coalescence process and the stress intensity factor distribution around the crack front approaches that of a single semi-elliptical defect, as shown in Section 3. Superimposed on Fig. 5 are the numerical stress intensity factors from the line spring analysis of the family of coalescing cracks. The results show excellent correlation between the numerical and the experimental data.

Interaction effects between the adjacent separate defects can be quantified by comparing the fatigue growth rates on the free surface, as shown in Fig. 23 and by the ratio of applied stress intensity factors at surface positions C and E, shown in Fig. 24. Interaction effects only become significant when the crack tip spacing becomes less than half the depth of the deepest defect ($s < d/2$). The magnitude of the interaction is dependent on the thickness of the out-of-plane ligament separating the adjacent crack tips which

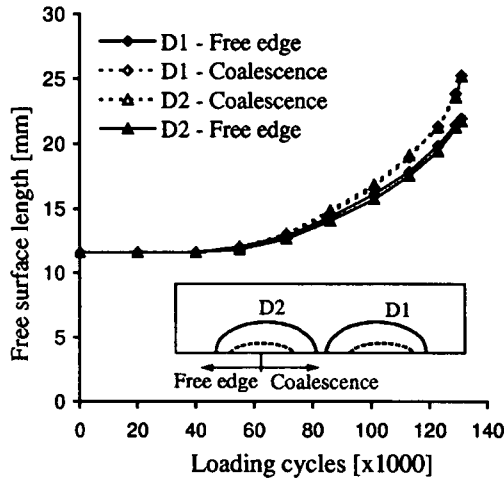


Fig. 23. Crack length on free surface towards and away from the adjacent defect.

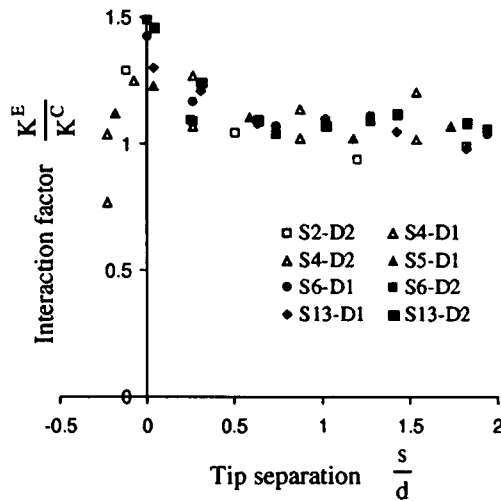


Fig. 24. Interaction factor defined as the ratio of stress intensity factors for free surface tips C and E from fatigue tests.

determines the mode of coalescence. In cases of crack overlap, interaction effects elevate the local SIF by 20 per cent compared to a single isolated defect, while coalescence by a shear step causes a 40 per cent increase in SIF as $s \rightarrow 0$.

5. Ductile tearing

5.1. Experimental procedure

A series of experiments were performed at 20 °C to investigate crack interaction and the development of the crack shape by ductile tearing on the upper shelf. Ductile tearing was investigated for a configuration

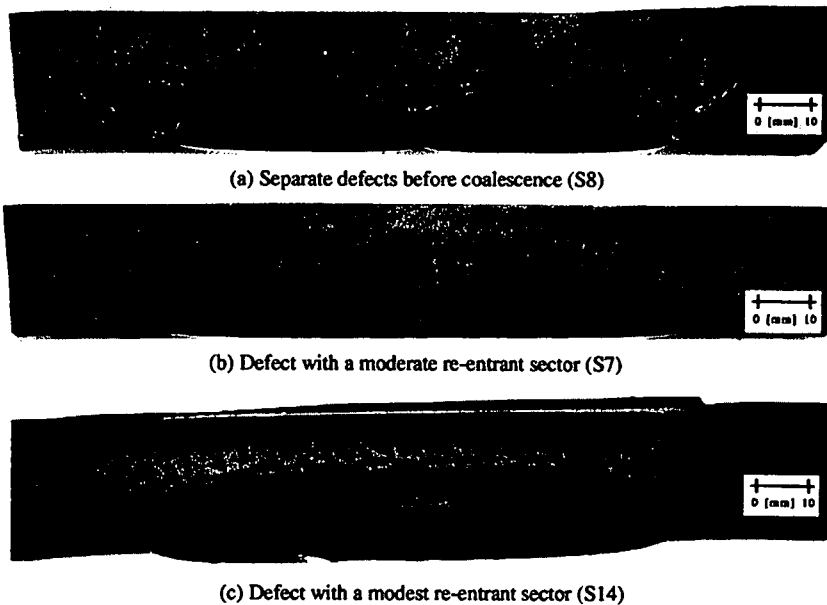


Fig. 25. Fractographs of fracture surface of ductile torn configurations. Arrows indicate boundary of ductile tearing.

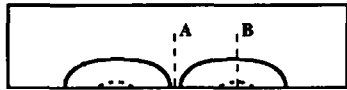
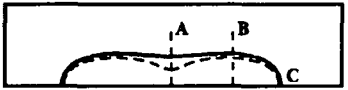
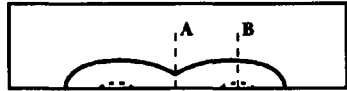
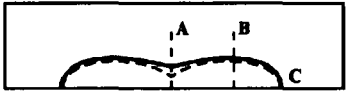
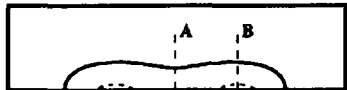
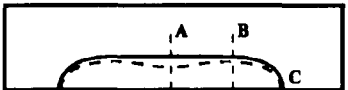
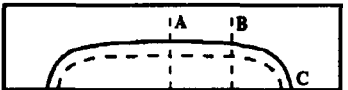
with two separate defects, shown in Fig. 25(a), followed by two tests on a complex defect with a re-entrant sector, shown in Fig. 25(b) and (c). The test configurations were produced by fatigue, as described in Section 4. The ductile tearing experiments were conducted using a servo hydraulic test machine in three point bending at a cross-head velocity of 1 mm/min. Large amounts of displacement controlled ductile tearing were performed in two stages. Crack advance was monitored with a heat tinting technique after the first stage, followed by brittle fracture in liquid nitrogen after further crack advance in the second stage. In the heat tinting process the specimen was heated to 300 °C for 6 h to oxidise the fracture surface. The fatigue surface develops a light blue colour, whereas the ductile tear is marked by a dark blue shade. In the case of specimen S14 cleavage occurred at room temperature after extensive plastic deformation and ductile tearing, as given in Table 1.

5.2. Results

The significant dimensions of the crack shapes are presented in Table 1, with a schematic representation of the crack shape developed by ductile tearing. The crack depths in the re-entrant sector, at the deepest segments and the extension on the free surface are given in Table 1, with the load to cause gross plasticity in each stage of the experiment. The fracture surfaces are shown in Figs. 25 and 26.

Ductile tearing started in the re-entrant sector, allowing the crack to develop towards a single bounding defect. The rest of the crack front exhibited only small amounts of crack extension, while crack advance on the free surface was negligible. After a semi-elliptical crack front had been established, the crack advanced around the entire crack front, including the free surface. In the configuration with two separate interacting defects a shearing mechanism connected the two adjacent non-co-planar crack tips into a planar crack front with a modest re-entrant sector before the second stage of ductile tearing.

Table 1
 The coalescence of two surface breaking defect by ductile tearing. The crack depths at positions A and B are shown at the end of each stage, with the load to initiate gross plasticity in each stage and the extension on the free surface, Δc

Fatigue phase		Ductile phase								
a_A [mm]	a_B [mm]	Stage 1				Stage 2				
		P_1 [kN]	a_A [mm]	a_B [mm]	Δc [mm]	P_2 [kN]	a_A [mm]	a_B [mm]	Δc [mm]	
<i>Separate defects before coalescence (S8)</i>										
										
NA	11.3	141	6.4	12.3	0.0	224	10.8	13.0	0.0	
<i>Defect with a moderate re-entrant sector (S7)</i>										
										
7.0	11.9	128	9.0	12.4	0.0	191	11.8	12.8	0.0	
<i>Defect with a modest re-entrant sector (S14) (large tear followed by cleavage at 20 °C)</i>										
										
9.8	11.6	131	13.2	12.8	0.0	212	16.6	16.2	3.0	

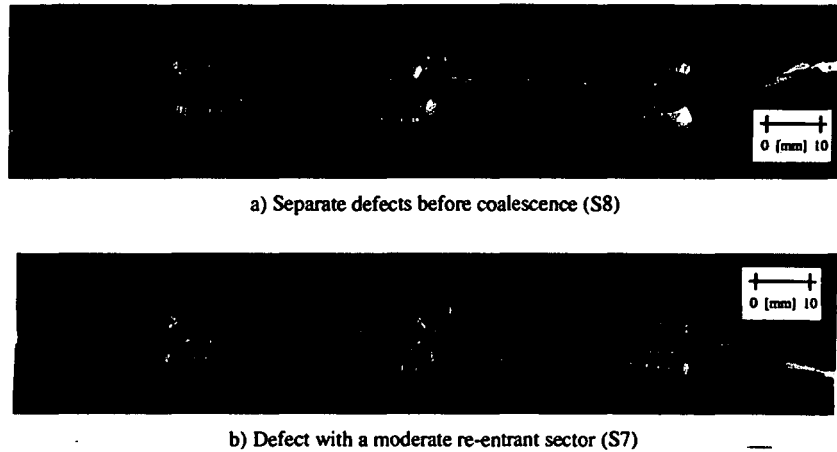


Fig. 26. A view of the configurations at the free surface, showing deviation from notch plane during fatigue phase of the test.

6. Discussion

6.1. Fatigue

During fatigue, co-planar surface breaking defects developed largely independently until the adjacent crack tips met and coalesced. Small interaction effects, which are sensitive to shear and overlap effects, occurred before adjacent crack tips came in contact. The observations are consistent with the finite element work of Moussa et al. [27] and Perl et al. [9] on the interaction of non-co-planar surface breaking cracks and the analysis of Bayley and Bell [11] and Murakami and Nemat-Nasser [28] on the interaction of co-planar surface breaking cracks. Small under-predictions of the fatigue life arise if interaction effects are omitted. However this is counteracted by re-characterising the defect as soon the crack tips touch. Although the two effects may not be equal, the resulting effect is usually conservative.

Coalescence is a rapid local process affecting the local region where a re-entrant sector is formed. The fraction of the fatigue life spent in coalescence was approximately 15 per cent in the present work, matching previous reports [4,6,7], although Frise and Bell [29] found that coalescence could constitute up to 87 per cent of total test time, depending on the geometry, defect spacing, and the type of loading. In engineering applications both, crack interaction and coalescence may constitute a useful part of the operational life. Re-characterisation procedures which discard both, interaction and coalescence, shorten the operational life. Allowing a limited amount of defect interaction but precluding coalescence, as recommended in R6/4 and BS 7910 defect assessment codes, and proposed for the revised ASME XI code [30] rationalises the assessment while maintaining the necessary conservatism. The present experimental work confirms suggestions of Twaddle and Hancock [4], Iida and Hirata [5], and Iida and Kawahara [31], and agrees with observations of Leek and Howard [6] and Soboyejo et al. [7], that the defect interaction and coalescence phases in fatigue growth may be neglected and simplified procedures for fatigue life are conservative and support the revised defect re-characterisation rules of BS 7910 and R6/4.

6.2. Ductile tearing

The configurations developed by the coalescence of two initially separate co-planar defects in fatigue formed the basis for the numerical and experimental analysis of ductile tearing. The results show the crack

advance initiates in the re-entrant sector, confirming the numerically determined enhanced crack driving forces and low local limit loads in the re-entrant sector. The constraint loss effects observed in the numerical analysis did not feature significantly in the experiments due to moderate re-entrant sectors exhibited by the test configurations. The unconstrained crack tip fields in bending develop only for crack depths less than $0.36t$ [32], whereas test geometries had crack depths in re-entrant sectors exceeding $0.25t$, where t is the geometry thickness.

The experimental studies showed that re-entrant sectors start to evolve in a similar way in both fatigue and ductile tearing. Tearing starts in the re-entrant sector, allowing the crack to develop towards the bounding defect shape, followed by the remainder of crack front. This suggests that current re-characterisation procedures, BS 7910 and R6/4 applied to such defects extending by ductile tearing are conservative, since the crack develops in a similar manner to fatigue.

For surface breaking defects there are distinct differences in the evolution of crack segments close to the free surface in fatigue and ductile tearing. In fatigue, crack advance occurs around the entire crack front, with high crack growth rates near the free surface, whereas in ductile tearing the crack is initially suppressed at the free surface, due to the loss of constraint associated with out-of-plane effects.

7. Conclusions

The crack driving force, quantified by K and J , was investigated for a family of complex cracks developed by fatigue. The results indicate presence of amplified stress intensity factors in the re-entrant sectors, confirmed by the experimentally observed rapid fatigue crack growth rates. Experimental fatigue and ductile tearing studies initially show similar development of complex cracks towards the re-characterised shape, confirming the inherent conservatism in the re-characterisation procedure of BS 7910 and R6/4. However it will be shown in Part II, that the re-characterisation process is potentially non-conservative when cleavage failure occurs at small fraction of the limit load.

Acknowledgements

The authors are pleased to acknowledge support of British Energy Generation Limited and helpful discussion with Dr. R.A. Ainsworth. The access to ABAQUS under academic licence at the University of Glasgow is gratefully acknowledged to Hibbitt, Carlsson and Sorensen. B. Bezensek wishes to thank the Ministry of Science, Sport and Education of Slovenia for financial support and the Faculty of Mechanical Engineering, University of Maribor, Slovenia, for granting leave of absence to complete this work in the University of Glasgow.

References

- [1] BS 7910. Guidance on methods for assessing the acceptability of flaws in metallic structures. London, UK: British Standard Institution; 1999 [Chapter 7].
- [2] R6. Assessment of the integrity of structures containing defects. Gloucester: British Energy Generation Ltd.; 2001 [Revision 4, Chapters I and II.3].
- [3] ASME Boiler and pressure vessel design code. Section XI. Philadelphia: American Society of Mechanical Engineers; 1992.
- [4] Twaddle BR, Hancock JW. The development of cracks by defect coalescence. In: Fatigue of offshore structures. EMAS. 1986.
- [5] Iida K, Ando K, Hirata T. An evaluation technique for fatigue life of multiple surface cracks. *Naval Arch Ocean Engng* 1984;22:177-99.

- [6] Leek TH, Howard IC. An examination of methods of assessing interacting surface cracks by comparison with experimental data. *Int J Pressure Vessels Piping* 1996;68:181-201.
- [7] Soboyejo WO, Knott JF, Walsh MJ, Cropper KR. Fatigue crack propagation of coplanar semi-elliptical cracks in pure bending. *Engng Fract Mech* 1990;37:323-40.
- [8] O'Donoghue PE, Nishioka T, Atluri SN. Multiple surface cracks in pressure vessels. *Engng Fract Mech* 1984;20:545-60.
- [9] Perl M, Levy C, Wang J. Interaction effects in combined arrays of radial and longitudinal semi-elliptical surface cracks in pressurised thick-walled cylinder. *J Pressure Vessel Technol Trans ASME* 1997;119:167-73.
- [10] Hasegawa K, Miyazaki K, Kanno S. Interaction criteria for multiple flaws on the basis of stress intensity factors. In: *Proc Int Conf ASME Pressure Vessels and Piping 2001*, Atlanta, Ga. 22-26 July 2001.
- [11] Bayley CJ, Bell R. Experimental and numerical investigation of coplanar fatigue crack coalescence. *Int J Pressure Vessel Piping* 1997;74:33-7.
- [12] Rice JR, Levy N. The part-through surface crack in an elastic plate. *J Appl Mech* 1972;39:185-94.
- [13] Parks DM, White CS. Elastic-plastic line-spring finite elements for surface cracked plates and shells. *J Pressure Vessel Technol Trans ASME* 1982;104:287-92.
- [14] Parks DM. The inelastic line-spring: estimates of elastic-plastic fracture mechanics parameters for surface-cracked plates and shells. *J Pressure Vessel Technol Trans ASME* 1981;246:254.
- [15] Newman Jr JC, Raju IS. An empirical stress-intensity factor equation for the surface crack. *Engng Fract Mech* 1981;15:185-92.
- [16] Rice JR. Limitations to the small scale yielding approximation for crack tip plasticity. *J Mech Phys Solids* 1974;22:17-26.
- [17] Wang YY, Parks DM. Evaluation of the elastic T -stress in surface plates using the line-spring method. *Int J Fract* 1992;56:25-40.
- [18] Sham TL. The determination of the elastic T -term using higher order weigh functions. *Int J Fract* 1991;48:81-102.
- [19] ABAQUS/Standard. V5.8. Hibbit, Karlsson and Sorensen Inc. Providence, RI, 1998.
- [20] Betegón C, Hancock JW. Two-parameter characterisation of elastic-plastic crack-tip fields. *J Appl Mech Trans ASME* 1991;58:104-10.
- [21] Williams ML. On the stress distribution at the base of a stationary crack. *J Appl Mech Trans ASME* 1957;24:111-4.
- [22] Leever PS, Radon JC. Inherent stress biaxiality in various fracture specimen geometries. *Int J Fract* 1983;19:942-55.
- [23] Rice JR. A path independent integral and the approximate analysis of strain concentration at notches and cracks. *J Appl Mech Trans ASME* 1968;35:379-86.
- [24] Hancock JW, Reuter WA, Parks DM. Toughness and constraint parameterised by T . In: *Constraint effects in fracture*. ASTM STP, vol. 1171. Philadelphia: American Society for Testing and Materials; 1993. p. 121-40.
- [25] Bezensek B, Hancock JW. The non-coplanar coalescence of interacting defects in fatigue. In: Pimenta PM, Ricardo LC, editors. *Proc Int Conf SAE Brasil Fatigue 2001*, São Paulo, Brasil, 2001.
- [26] Hancock JW, Gall DS, Huang X. Fatigue crack growth due to random loading in air and sea water with applications to the growth of semi-elliptical cracks in the tubular welded joints of offshore structures. In: *Inst Mechanical Engineers. Technical report C144/86*. 1986:49-58.
- [27] Moussa WA, Bell R, Tan CL. The interaction of two parallel non-coplanar identical surface cracks under tension and bending. *Int J Pressure Vessel Piping* 1999;76:135-45.
- [28] Murakami Y, Nemat-Nasser S. Interacting dissimilar semi-elliptical surface flaws under tension and bending. *Engng Fract Mech* 1982;16:373-86.
- [29] Frise PR, Bell R. Modelling fatigue crack growth and coalescence in notches. *Int J Pressure Vessel Piping* 1992;51:107-26.
- [30] Hasegawa K. Private communication, 2002.
- [31] Iida K, Kawahara M. Propagation and coalescence of fatigue cracks initiated from collinear or parallel adjacent surface flaws. In: *Proc 4th Int Conf Pressure Vessel Technol*. IMechE, London, 1980.
- [32] Al-Ani A, Hancock JW. J -dominance of short cracks in tension and bending. *J Mech Phys Solids* 1991;39:23-43.



PERGAMON

Available online at www.sciencedirect.com

SCIENCE @ DIRECT®

Engineering Fracture Mechanics xxx (2003) xxx–xxx

**Engineering
Fracture
Mechanics**www.elsevier.com/locate/engfracmech

The re-characterisation of complex defects Part II: cleavage

B. Bezensek ^{*,1}, J.W. Hancock*Department of Mechanical Engineering, University of Glasgow, Glasgow G12 8QQ, Scotland, UK*

Received 11 July 2002; received in revised form 16 April 2003; accepted 17 April 2003

Abstract

The re-characterisation of complex defects with re-entrant sectors has been addressed for cracks extending by fatigue, ductile tearing and cleavage. In Part I crack extension by fatigue and ductile tearing was discussed. In Part II cleavage data are presented for a family of complex defects with re-entrant sectors. Experimental tests on complex and re-characterised profiles are analysed using deterministic and probabilistic approaches. The work addresses the conservatism of re-characterisation procedures when applied to cleavage failure on the lower shelf and in the ductile–brittle transition.

© 2003 Published by Elsevier Science Ltd.

Keywords: Complex defects; Cleavage failure; Line spring analysis; Re-characterisation; Statistical fracture mechanics; Constraint

1. Introduction

The integrity of critical engineering structures is assured by considering realistic defects under severe operating conditions. This may involve cleavage failure when unstable crack propagation may occur under near elastic conditions. In general, defect assessment procedures try to avoid detailed numerical analyses and advocate simplified but conservative procedures, in which complex defects are idealised as a simple shapes in a process known as defect re-characterisation. Re-characterisation is usually applied to defects which extend by fatigue or ductile tearing, as discussed in Part I of the current work. This work demonstrated that complex defects exhibit amplified values of the stress intensity factor and the J -integral in re-entrant sectors. This may compromise the conservatism of the re-characterisation procedure when failure occurs by cleavage.

The present work examines cleavage failures from complex and re-characterised defects on the lower shelf and in the ductile–brittle transition. Detailed analyses of the test results are presented using deterministic and probabilistic approaches. The deterministic analysis compares the maximum stress intensity

* Corresponding author. Tel.: +44-141-330-4722; fax: +44-141-330-4343.

E-mail addresses: b.bezensek@eng.gla.ac.uk (B. Bezensek), j.hancock@eng.gla.ac.uk (J.W. Hancock).

¹ On leave from Faculty of Mechanical Engineering, University of Maribor, Slovenia.

factor or the J -integral, to a critical value obtained from tests on standard test geometries or from the Master curve [1]. The probabilistic analysis is based on the weakest link statistics applied to cleavage failure. Both the deterministic and probabilistic approaches have been extended to include constraint effects.

2. Experimental details

2.1. Experimental procedure

Specimens with a developing family of separate, complex, and single bounding defects have been examined experimentally. The specimens were developed by fatigue as described in Part I. Semi-elliptical cracks with shapes similar to those of re-characterised defects were also tested. A statistical experimental study of brittle failures has not been attempted: rather representative configurations have been tested and analysed, to address the effect of the enhanced stress intensity factor in re-entrant sectors on cleavage failure.

Tests were performed at $-196\text{ }^{\circ}\text{C}$ to represent cleavage on the lower shelf and at $-100\text{ }^{\circ}\text{C}$ to represent cleavage in the ductile–brittle transition. The reference temperature at which failure occurs by cleavage instability before gross plastic deformation was estimated following the ASTM E1921 [1] procedure to be $-130\text{ }^{\circ}\text{C}$. The test temperatures were obtained by cooling the specimens with liquid nitrogen: the temperature being measured at two surface positions with spot welded thermocouples. The fracture toughness on the lower shelf ($-196\text{ }^{\circ}\text{C}$) was measured on a set of five 25 mm thick three point bending specimens as $53 \pm 5\text{ MPa}\sqrt{\text{m}}$ and in the ductile–brittle regime ($-100\text{ }^{\circ}\text{C}$) estimated from the Master curve [1] as $165 \pm 23\text{ MPa}\sqrt{\text{m}}$, which is close to the experimentally measured $180\text{ MPa}\sqrt{\text{m}}$, reported by MacLennan [2].

The temperature dependent yield stress was estimated from a relation suggested by Bennet and Sinclair [3]:

$$\sigma_y = 745.6 - 0.056 \cdot \Theta \cdot \ln \left(\frac{\zeta}{\sqrt{2\dot{\epsilon}}} \right) \quad (1)$$

Here Θ is the temperature in Kelvin, ζ is a constant equal to 10^8 s^{-1} , $\dot{\epsilon}$ is the strain rate, and σ_y is the yield stress in MPa. At room temperature this relation gives a yield stress of 350 MPa, at strain rate of $8.33 \times 10^{-6}\text{ s}^{-1}$, which is close to the experimentally measured 345 MPa for grade 50D steel. The yield stress in the cleavage regime was estimated to be 510 MPa at $-100\text{ }^{\circ}\text{C}$ and 640 MPa at $-196\text{ }^{\circ}\text{C}$. The temperature dependence of Young's modulus is described with an expression suggested by Lidbury [4] for ferritic steels:

$$E(\phi) = 210 - 0.054\phi \quad [\text{GPa}] \quad (2)$$

where ϕ is the temperature in $^{\circ}\text{C}$. At room temperature Young's modulus is 209 and 220 MPa at $-196\text{ }^{\circ}\text{C}$.

2.2. Experimental results

The failure loads of the test geometries shown in Fig. 1 are given in Table 1, in which the tests are denoted with the letter S followed by a number. The test configurations include defects with adjacent but separate defects (S3, S10), complex defects with re-entrant sectors (S2, S5, S6, S11, S12), as well as bounding semi-elliptical defects (S4, S13, S15, S16). The last series of defects arises from complete coalescence of initially separate defects, and result in a series of semi-elliptical defects with similar shapes to those, which would result from re-characterisation. In all cases the load-displacement records were linear until the final catastrophic failure, except for specimen S5 tested at $-100\text{ }^{\circ}\text{C}$ which exhibited gross plasticity prior to failure. Table 1 also gives the local and global limit loads calculated by elastic–plastic line spring

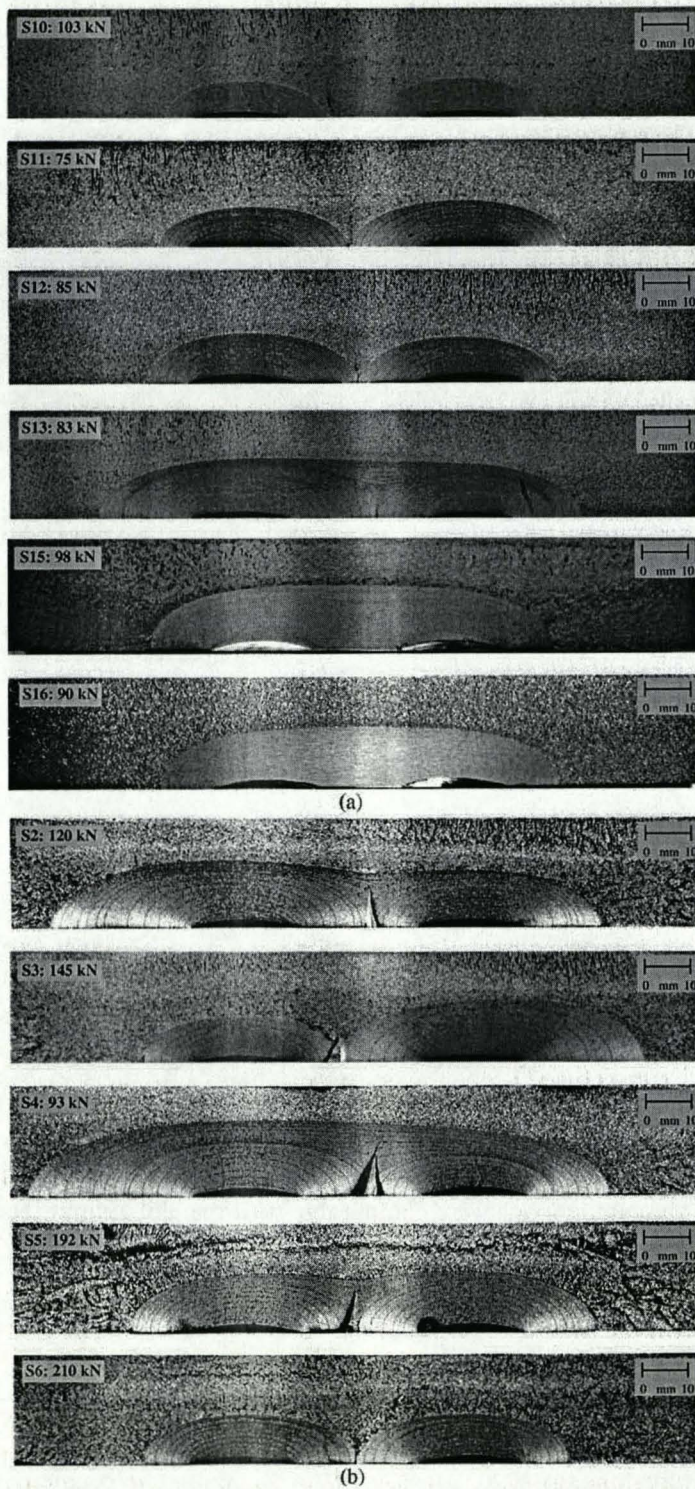


Fig. 1. Showing fractographs of the tested crack configurations, with the recorded failure loads to cleavage at (a) $-196\text{ }^{\circ}\text{C}$ and (b) $-100\text{ }^{\circ}\text{C}$.

Table 1

Results of experimental cleavage tests showing characterising crack dimensions, failure and limit loads of real defect and the failure load for the re-characterised defect, obtained from statistical procedure (Eq. (18))

Test	Complex defect with a re-entrant sector					Re-characterised defect		
	Crack depth at A, a_A [mm]	Failure load, P_f [kN]	Local limit load, $P_{lim,local}$ [kN]	Global limit load, $P_{lim,global}$ [kN]	Yield stress, σ_y [MPa]	Crack depth at D, a_D [mm]	Free surface length, $2c$ [mm]	Estimated failure load, $P_{re-charact.}$ [kN]
<i>Lower shelf regime (-196 °C)</i>								
Separate defects before coalescence								
S10	-	103	-	289	640	9.3	82.2	100
Defect with a pronounced re-entrant sector								
S11	2.0	75	220	256	640	11.2	92	92
S12	1.0	85	216	251	640	11.4	96	89
Semi-elliptical defect								
S13 ^a	-	83	190	217	640	13.2	105	-
S15	-	98	206	229	640	13.7	86.9	-
S16	-	90	203	225	640	13.5	87	-
<i>Ductile-brittle regime (-100 °C)</i>								
Individual defect before coalescence (defects overlapped)								
S3	-	145	-	170	510	14.2	110	112
Defect with a modest re-entrant sector								
S2	12.1	120	125	132	510	15.4	121.6	100
S5 ^b	11.8	192	150	162	510	13.9	112.9	109
Defect with a pronounced re-entrant sector								
S6	2.2	210	143	197	510	11.5	94	127
Semi-elliptical defect								
S4 ^a	-	93	102	108	510	17.2	127.4	-

Refer to Part I for definition of nomenclature.

^a Tested defect exceeded the size of a recommended re-characterised defect.

^b Gross plasticity preceded cleavage failure.

analysis for the crack profiles using the temperature dependent yield stress given by Eq. (1), and the dimensions of re-characterised defects.

On the lower shelf the failure loads for complex defects with re-entrant sectors were up to 23 per cent lower than those for the bounding defects. However, the reverse trend was observed in the ductile-brittle transition, where the highest failure load was noted for the complex defect and the lowest for a bounding defect. On the lower shelf the failure loads were only a small fraction of the global limit load, while in the ductile-brittle transition the failure loads were comparable with the global limit load.

3. Deterministic analysis

3.1. Deterministic procedure

In defect assessment procedures the applied stress intensity factor around the crack front is usually compared with the fracture toughness, K_{IC} , measured on standard test geometries with straight crack fronts. In real engineering structures, defects seldom have simple straight crack fronts and frequently have a

varying depth. In such cases the crack driving force varies spatially with crack tip position. The resistance to crack advance may also vary spatially due to constraint, temperature or environmental effects, such as irradiation. Without loss of generality, the failure criterion can be defined as the ratio of an applied stress intensity factor, $K_{(t)}$, to a local resistance to crack extension, K_{mat} , both of which may be function of the crack tip position, t :

$$K_r = \frac{K_{(t)}}{K_{\text{mat}}} \quad (3)$$

In the present work the local fracture toughness, K_{mat} , is considered to be a function of constraint, as measured by T [5]. The effect of constraint on cleavage is quantified by an expression suggested by Wallin [6]:

$$\begin{aligned} K_{\text{mat}} &= 20 + (K_{\text{IC}} - 20) \exp \left\{ 0.019 \left(-\frac{T_{(t)}}{10} \right) \right\} & \text{for } T < 0 \\ K_{\text{mat}} &= K_{\text{IC}} & \text{for } T > 0 \end{aligned} \quad (4)$$

Here K_{IC} is the plane strain fracture toughness of standard deep crack test specimen.

Configurations with pronounced re-entrant sectors (S6, S11 and S12) and the corresponding re-characterised configurations were analysed in detail using the line spring technique of Rice and Levy [7] as extended by Parks and White [8] to include elastic-plastic behaviour. A symmetric half of the experimental geometry was modelled at the experimental failure load. The material response was idealised as linear elastic below the yield stress and merged into a Ramberg-Osgood relation with the appropriate temperature dependant yield stress (510 MPa at -100 °C and 640 MPa at -196 °C). The strain-hardening exponent was determined from uni-axial test data at room temperature to be 9 and given the low strain hardening can be assumed to be largely temperature independent.

The analysis determined the distribution of the elastic-plastic stress intensity factor, K_J , and the T -stress around the crack front. Although line spring analysis is a computationally efficient and effective numerical technique, it has limited accuracy near the free surface. Consequently the K_J on the free surface was identified with the stress intensity factor and determined from fatigue crack growth data, using the beach mark spacing. Line spring analysis was used for most of the crack front. For segments close to the free surface the values of K_J were interpolated by using a polynomial to match the value on the free surface with the value obtained from fatigue data. The same polynomial was used to determine the value of T -stress for the near-surface crack tips and the K_J and T -stress of the re-characterised defect.

3.2. Results of a deterministic analysis

The analyses of a complex geometries (S6, S11 and S12) and the related re-characterised geometries are summarised in Fig. 2. Fig. 2(a) shows the digitised complex and the re-characterised crack shapes and Fig. 2(b) shows the corresponding elastic-plastic stress intensity factors (K_J) for both geometries. The elastic-plastic stress intensity factors are normalised with the outer fibre stress in bending and the greatest crack depth (at position D, using the nomenclature defined in Part I), and are plotted along the surface length of the defect. The T -stress is shown in Fig. 2(c), normalised with the outer fibre stress in bending. As noted in Part I, pronounced re-entrant sectors of complex defects exhibit amplified stress intensity factors and loss of in-plane crack tip constraint, as shown by a negative T -stress.

The ratio of the local elastic-plastic stress intensity factor, $K_{J(t)}$, to the local constraint matched toughness, K_{mat} , is given in Fig. 2(d) and (e) for a complex and the re-characterised defect. Fig. 2(d) shows data for tests (S11) and (S12) at -196 °C and Fig. 2(e) for test (S6) at -100 °C. The deterministic analysis shows that failure is strongly affected by in-plane constraint effects, which depend on the applied load. Failures (S11) and (S12) on the lower shelf (-196 °C) occurred at small fractions of the limit load, and as

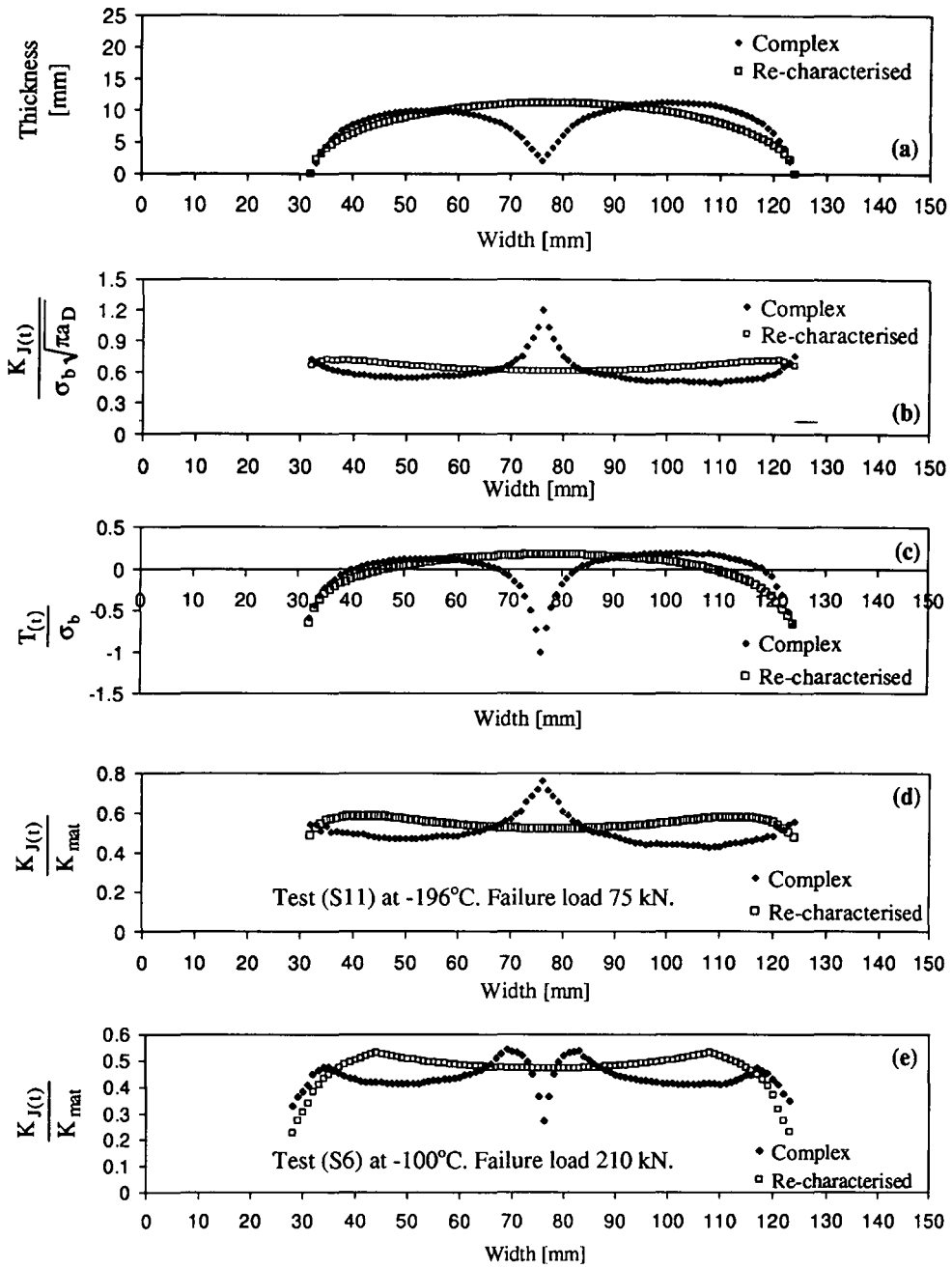


Fig. 2. Deterministic assessment of complex defects (S11 at -196°C and S6 at -100°C) and re-characterised defects: (a) crack profiles, (b) normalised elastic-plastic stress intensity factors and (c) normalised T -stress. The failure criterion K , is shown in (d) for the complex defect (S11) and in (e) for the complex defect (S6). Results of assessment of test (S12) are identical to results from test (S11).

such do not benefit from any increase in toughness due to constraint loss. Failure is determined by the stress intensity factor alone. This is shown by the distinct peak in the ratio $K_{J(t)}/K_{mat}$ in the re-entrant sector in

Fig. 2(d). However in the ductile–brittle transition, failure (S6) occurred close to the global limit load and benefited from a constraint enhanced toughness in the re-entrant sector, as shown in Fig. 2(e). The enhanced toughness, K_{mat} , associated with constraint loss counter-balances the amplified crack driving forces in the re-entrant sector. Although the complex defect is more detrimental than the re-characterised defect on the lower shelf when constraint effects are weak, the constraint enhanced toughness in the ductile–brittle transition recovers the conservatism of the re-characterisation procedure in this temperature range.

4. Probabilistic analysis

4.1. Statistical Fracture Mechanics

The failure of brittle materials has been widely discussed as a statistical process [9] and analysed using weakest link statistics [10–12]. The weakest link argument partitions the crack front into small segments of sufficient volume to contain a second phase particle from which cleavage originates [13]. The failure of each segment is considered to be statistically independent and described with a cumulative distribution function, F , such as that proposed by Weibull:

$$F^i = 1 - \exp - \left(\frac{K - K_{\min}}{K_0} \right)^n \quad (5)$$

Here F^i is a probability of failure of segment i at or below the stress intensity factor, K reduced by the cut-off K_{\min} , and K_0 is a material property with dimensions of $\text{MPa} \sqrt{\text{m}}$. If a crack front of length s , is divided into incremental segments of length s_0 , the survival of the crack front requires survival of all segments, giving:

$$1 - F = (1 - F^i)^{s/s_0} \quad (6)$$

For a straight crack of length s , subject to uniform stress intensity factor, K , the probability of failure, F , can be written as:

$$F = 1 - \exp - \left\{ \frac{s}{s_0} \left(\frac{K - K_{\min}}{K_0} \right)^n \right\} \quad (7)$$

where K_0 and s_0 are scaling constants, and the cut-off in the distribution below which failure does not occur is commonly taken as $20 \text{ MPa} \sqrt{\text{m}}$ [1]. Wallin [11] has argued that the shape factor for J -dominant cracks should be 4. Without loss of generality the material property, K_0 , can be written in terms of the mean toughness, \bar{K} :

$$\bar{K} = K_0 \Gamma \left(1 + \frac{1}{n} \right) + K_{\min} \quad (8)$$

where $\Gamma(1 + 1/n)$ is the Gamma function. This allows Eq. (7) to be re-written as:

$$F = 1 - \exp - \left\{ \frac{1}{s'_0} \left(\frac{K - K_{\min}}{\bar{K} - K_{\min}} \right)^n \right\} \quad (9)$$

where

$$s'_0 = \frac{s_0}{\Gamma(1 + \frac{1}{n})} \quad (10)$$

The mean fracture toughness, \bar{K} , is now considered to be a function of constraint, K_{mat} , as expressed by Eq. (4). In general the constraint and the mean local toughness vary with spatial position, allowing Eq. (9) to be written more generally as:

$$F = 1 - \exp - \left\{ \frac{1}{s'_0} \int_s \left(\frac{K_{(t)} - K_{\text{min}}}{K_{\text{mat}} - K_{\text{min}}} \right)^n dt \right\} \quad (11)$$

$K_{(t)}$ is the stress intensity factor at position t on the crack front, and K_{mat} is the corresponding constraint matched toughness. The failure probability is determined by integrating the ratio $(K_{(t)} - K_{\text{min}})/(K_{\text{mat}} - K_{\text{min}})$ along the entire crack front. For simplicity the argument is now restricted to a two parameter distribution by setting K_{min} to zero.

The stress intensity factor, $K_{(t)}$, can always be separated into load and geometry dependent parts using a reference stress intensity factor, K_{ref} , and a non-dimensional function of geometry, $\alpha_{(t)}$:

$$K_{(t)} = K_{\text{ref}} \cdot \alpha_{(t)} \quad (12)$$

The reference stress intensity factor can be chosen in a number of ways. In the present context it is advantageous to identify K_{ref} with the maximum stress intensity factor along the crack front. The probability of failure can then be expressed by substituting Eq. (12) into the cumulative failure probability of Eq. (7):

$$F = 1 - \exp - \left\{ \frac{\xi}{s_0} \left(\frac{K_{\text{ref}}}{K_0} \right)^n \right\} \quad (13)$$

where ξ is:

$$\xi = \int_s \alpha_{(t)}^n dt \quad (14)$$

Slatcher and Oystein [14] shows that ξ is essentially an effective crack front length. This may readily be evaluated for geometries for which a closed-form expression for the non-dimensional stress intensity factor is available or by a numerical evaluation of computational results.

The probability density function is defined by differentiating the cumulative probability function:

$$p = \frac{\partial F}{\partial K_{\text{ref}}} \quad (15)$$

This allows the mean value of K_{ref} to be written as:

$$\bar{K}_{\text{ref}} = \int_0^\infty K_{\text{ref}} \cdot p \cdot dK_{\text{ref}} = K_0 \left(\frac{s_0}{\xi} \right)^{1/n} \Gamma \left(1 + \frac{1}{n} \right) \quad (16)$$

The ratio of the mean values of K_{ref} for two configurations, A and B, then depends on the ratio of the effective crack front length parameters, ξ^A and ξ^B :

$$\frac{\bar{K}_{\text{ref}}^A}{\bar{K}_{\text{ref}}^B} = \left(\frac{\xi^B}{\xi^A} \right)^{1/n} \quad (17)$$

Two geometries may have different geometric shapes and sizes, but for straight cracks in similar shaped test specimen, Eq. (17) is equivalent to the statistical size corrections of ASTM E1921 [1]. Eq. (17) can also be used to map fracture mechanics parameters from one geometry to another, by invoking size and shape

Table 2
Benchmark of Eq. (18) with cleavage tests on semi-elliptical, complex and standard 25 mm thick geometries in three point bending at $-196\text{ }^{\circ}\text{C}$ ($\zeta_{\text{straight}} = 25\text{ mm}$)

Test No.	Test geometry data		Comparison	
	Characteristic crack dimension, a_D [mm]	Effective crack front length, ζ [mm]	$(p^{\text{test}}/p^{\text{straight}})$ measured	$(p^{\text{test}}/p^{\text{straight}})$ from Eq. (18)
S11	11.2	21.51	3.0	3.4
S12	11.0	24.50	3.4	3.3
S13	14.0	17.60	3.3	3.2
S15	13.7	7.51	3.9	4.0
S16	13.5	7.36	3.6	4.1

Characteristic crack dimension and effective crack front length are listed with measured load and approximated average failure load for the geometry using Eq. (18).

corrections. Given the ratio of the reference stress intensity factors in two configurations, it is also straightforward to compare the failure loads:

$$\frac{\bar{P}^A}{\bar{P}^B} = \frac{\psi^A}{\psi^B} \left(\frac{\zeta^B}{\zeta^A} \right)^{1/n} \quad (18)$$

where ψ is function of geometry and the dimension chosen to define K_{ref} .

This procedure is applied to a series of cleavage tests on complex defects, semi-elliptical surface breaking defects and standard straight crack 25 mm thick three point bend specimens. The effective crack front length, ζ , was determined numerically by integrating the elastic-plastic stress intensity factor calculated by line spring analysis. The results given in Table 2 demonstrate good agreement between the ratio of experimental failure loads and the average values derived from the size and shape corrections, using Eq. (18), suggesting that failure can be described by weakest link arguments. Semi-elliptical cracks were also analysed using the Newman-Raju [15] solutions for ζ and the results agree closely with the line spring analysis.

The predicted failure loads of re-characterised defects were obtained by use of Eq. (18) from the experimentally measured failure load on a bounding defect (S4 at $-100\text{ }^{\circ}\text{C}$ and S15 at $-196\text{ }^{\circ}\text{C}$) and are given in Table 1.

4.2. Results of probabilistic analysis

Probabilistic aspects of cleavage failure have been addressed using weakest link statistics for the complex and re-characterised geometries and are shown in Fig. 3. The relative failure probability of the complex and re-characterised defect depends on the applied load, which affects the constraint term in a non-linear manner. The relative failure probabilities quantify the level of conservatism in the re-characterisation procedure. For the procedure to be conservative the probability of failure of the complex defect must be less than the re-characterised defect.

At small fractions of the limit load, constraint effects are negligible and failure is essentially governed by the stress intensity factor. This is shown in Fig. 3(b), in which geometrically similar complex defects (S11) and (S12) with re-entrant sectors have a higher failure probability than the re-characterised defect at the failure load. In contrast, close to limit load (S6 at $-100\text{ }^{\circ}\text{C}$), shown in Fig. 3(c), the complex defect has a lower failure probability due to the beneficial effects of constraint loss in the re-entrant sector. The probability analysis thus confirms that the re-characterisation procedure is non-conservative on the lower shelf, but is conservative when the constraint effects are invoked in the ductile-brittle transition.

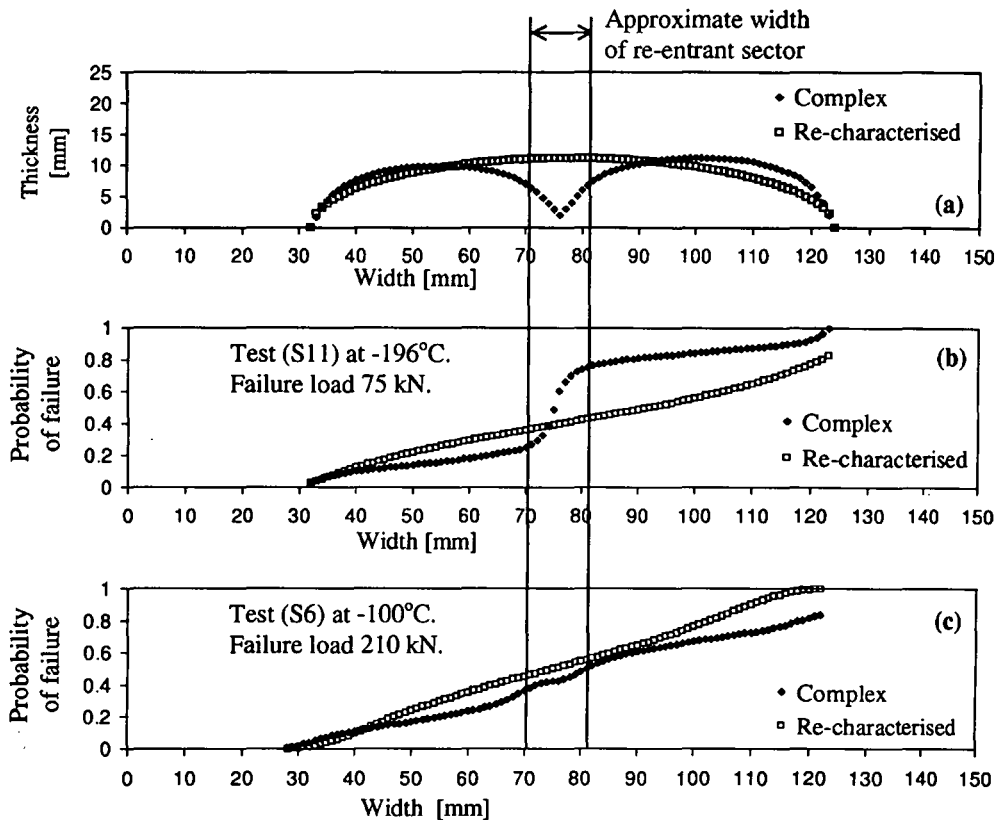


Fig. 3. Probability of failure of complex defects (S11) at -196°C and (S6) at -100°C and re-characterised defects, at measured failure load on complex defects. Results of assessment of test (S12) are identical to results from test (S11).

5. Failure assessment diagrams

5.1. Introduction

Cleavage failures on the lower shelf and in the ductile–brittle transition have been analysed using failure assessment diagrams (FADs) described in R6, revision 4 [16], as shown in Figs. 4–7. FADs assess the proximity to failure by comparing the stress intensity factor, K , with a material property, K_{mat} , to cause crack extension. The general (Option 1) and material and geometry specific (Option 3) failure assessment curves (FAC) were constructed from the elastic and total J values, obtained from elastic–plastic line spring analysis. The experimentally measured failure load was normalised with the local limit load, given in Table 1. For both, complex and re-characterised defects only the maximum elastic–plastic stress intensity factor along the crack front is considered. This is normalised with a lower bound fracture toughness data, corresponding to 5% failure probability of the standard fracture mechanics test specimen. The maximum elastic–plastic stress intensity factor is located in the re-entrant sector for a complex defect and near surface for the re-characterised defect. Initially in Section 5.2 the fracture toughness data from 25 mm thick three point bend specimens has been used without constraint or statistical size and shape corrections. The re-characterisation procedure is then applied to the defect and the analysis is performed for the same failure

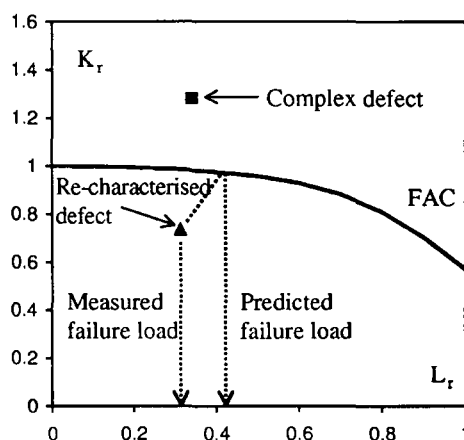


Fig. 4. Assessment of the complex defect (S11) tested at $-196\text{ }^{\circ}\text{C}$ and the re-characterised defect using general FAD. The elastic-plastic stress intensity factor is normalised with lower bound fracture toughness, measured on 25 mm thick specimens, without applying constraint or statistical size corrections. Load is normalised with the local limit load.

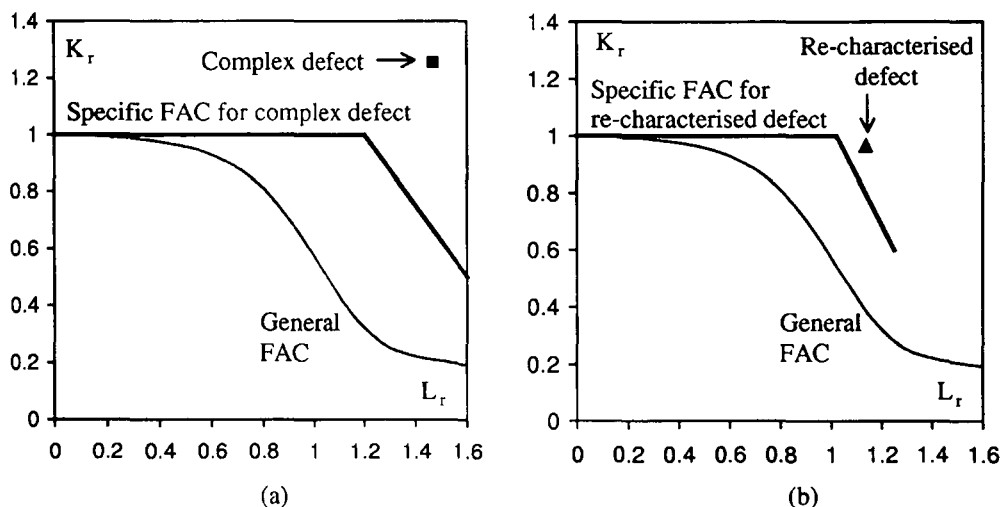


Fig. 5. Assessment of the complex defect (S6) tested at $-100\text{ }^{\circ}\text{C}$ is shown in (a) and the re-characterised defect in (b) using general FAD. The elastic-plastic stress intensity factor is normalised with lower bound fracture toughness using the Master Curve at $-100\text{ }^{\circ}\text{C}$, without constraint or statistical size corrections. The load is normalised with the local limit load.

load. In Section 5.3 assessment is repeated invoking the constraint enhanced fracture toughness and finally in Section 5.4 by incorporating the statistical size and shape effects.

5.2. General FAD

Fig. 4 shows the analysis of a complex defect (S11) tested at $-196\text{ }^{\circ}\text{C}$, and Fig. 5 the analysis of a complex defect (S6) tested at $-100\text{ }^{\circ}\text{C}$ using the general FAD. The analysis of the complex defects indicates a failure point above the general and specific failure assessment curves at both test temperatures. In

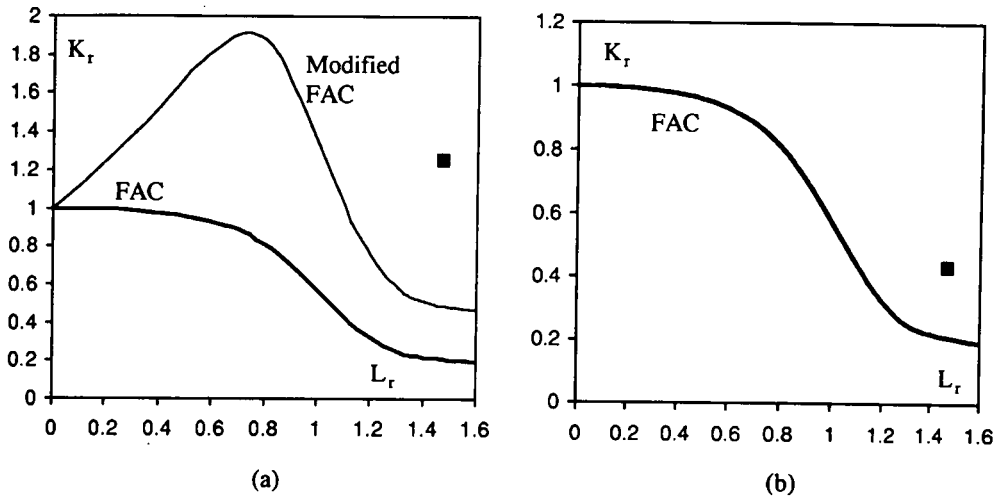


Fig. 6. Assessment of a complex tested (S6) at $-100\text{ }^\circ\text{C}$ using constraint modified failure assessment diagram. In (a) the modified failure assessment curve is constructed for the re-entrant sector of a complex defect, by combining option 1 FAC with Eq. (4). The elastic-plastic stress intensity factor is normalised with lower bound toughness from Master curve [1] at $-100\text{ }^\circ\text{C}$. In (b) the elastic-plastic stress intensity factor is normalised with constraint enhanced lower bound toughness. The load is normalised with the local limit load.

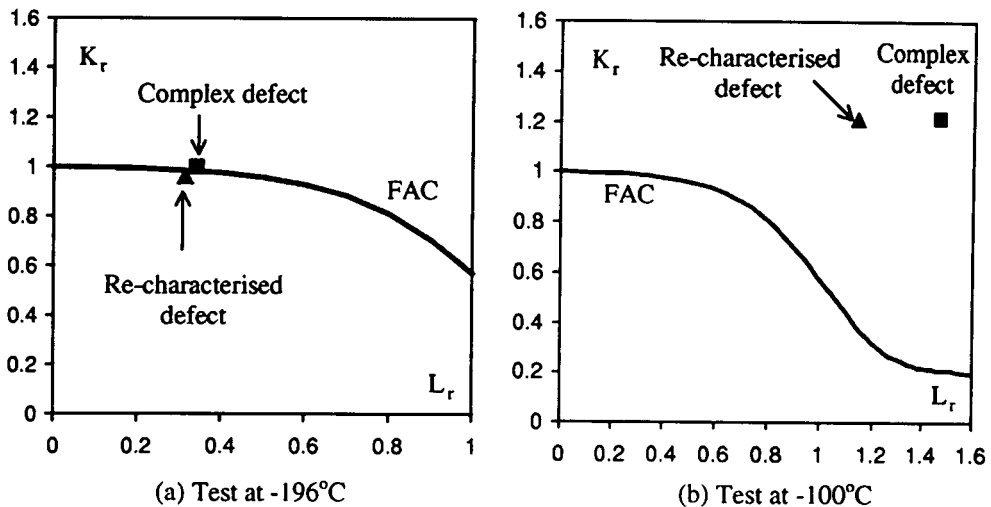


Fig. 7. Assessment of complex defects (S11 at $-196\text{ }^\circ\text{C}$ and S6 at $-100\text{ }^\circ\text{C}$) and re-characterised defects using FAD including statistical size and shape corrections. The elastic-plastic stress intensity factor is normalised with lower bound size and shape corrected toughness, while measured failure load is normalised with the local limit load.

contrast, the failure point of the re-characterised defect is inside the FAD at $-196\text{ }^\circ\text{C}$, while at $-100\text{ }^\circ\text{C}$ it falls above both, the general and specific FACs. If the re-characterisation procedure was applied to the complex defect (S11) at $-196\text{ }^\circ\text{C}$, the procedure would predict a failure load obtained by extending the loading path from the origin through the failure point of the re-characterised defect to the general failure assessment curve, as shown in Fig. 4. Clearly the re-characterisation procedure overestimates the failure on the lower shelf and is non-conservative.

5.3. Constraint modified FAD

Constraint modified FADs defined in Chapter III.7 of R6/4 [16] have been constructed for the cleavage failure of a complex defect (S6) at $-100\text{ }^{\circ}\text{C}$ and its re-characterised form. The diagrams are presented in terms of the local limit loads, which are close to the global limit loads. The elastic-plastic stress intensity factor is normalised in Fig. 6(a) by a lower bound critical value, K_{IC} , obtained from the Master curve for 25 mm thick specimen at $-100\text{ }^{\circ}\text{C}$. Constraint effects were examined for the re-entrant sector using Eq. (4) and were introduced in the FAD by combining these expressions with the general failure assessment curve to produce a constraint modified failure assessment curves, as discussed by Ainsworth and O'Dowd [17]. In Fig. 6(b) the applied K_I is normalised with a constraint enhanced fracture toughness, K_{mat} , retaining the general failure assessment curve as the relevant assessment curve, as discussed by MacLennan and Hancock [18].

At $-100\text{ }^{\circ}\text{C}$ the constraint enhanced toughness derived from constraint loss moves the failure outside the failure assessment curves, as shown in Fig. 6. This confirms that the detrimental effects associated with enhanced stress intensity factors in re-entrant sectors can be offset by invoking constraint enhanced toughness.

5.4. FAD with statistical size effects

Complex defects differ in the length and shape from the re-characterised defects and from the standard straight crack test specimens. Statistical size and shape corrections become relevant in assessments of such defects and are examined for a complex defect with a re-entrant sector and its re-characterised form. Weakest link arguments are employed for this purpose. For clarity the in-plane constraint effects are not combined with size and shape corrections. In practise these effects may be applied individually or combined, to give the most realistic integrity assessments. The maximum elastic-plastic stress intensity factor is located in the re-entrant sector for the complex defect (as shown in Fig. 2) and near surface for the re-characterised defect. The reference stress intensity factor is identified with the maximum value and the effective crack front lengths determined using Eq. (14) are summarised in Table 3, for complex and re-characterised defects and standard 25 mm thick edge cracked bend bars.

At $-196\text{ }^{\circ}\text{C}$ the effective critical elastic-plastic stress intensity factor for the complex defect is greater than that of the straight crack test specimen due to a decrease in the effective crack front length parameter, ξ . In contrast the effective critical elastic-plastic stress intensity factor for the re-characterised defect is less than that of the straight edge crack geometry due to an increase in effective crack front length. The re-characterised defect has physical crack front length four times greater than the straight crack and statistically has lower resistance to crack propagation. The physical crack front length of the complex defect is

Table 3

The physical and effective crack front lengths are given with the size and shape corrected mean values of fracture toughness, \bar{K}_{mat} , and the standard deviation, σ

	$-100\text{ }^{\circ}\text{C}$			$-196\text{ }^{\circ}\text{C}$		
	Complex crack	Re-characterised crack	Straight crack	Complex crack	Re-characterised crack	Straight crack
Physical crack length [mm]	109.9	100.9	25.0	105.2	98.3	25.0
Effective crack length, ξ [mm]	26.8	63.8	25.0	9.3	71.1	25.0
\bar{K}_{mat} [MPa $\sqrt{\text{m}}$]	167.8	130.5	165.0	67.8	40.8	53.0
σ [MPa $\sqrt{\text{m}}$]	22.6	18.2	23.0	6.4	3.9	5.0

also approximately 4 times longer than the straight cracked three point bend specimen, but the enhanced elastic-plastic stress intensity factor in the short re-entrant sector decreases the effective crack front length. The competition between the physical crack front length and local amplification of stress intensity becomes less apparent at $-100\text{ }^{\circ}\text{C}$ where more plasticity develops in the re-entrant sector.

The assessment of complex and re-characterised defects is shown in Fig. 7 for tests at -196 and $-100\text{ }^{\circ}\text{C}$, using the size and shape corrected lower bound fracture toughness. Both configurations fall on the general failure assessment curve at $-196\text{ }^{\circ}\text{C}$ and outside the curve at $-100\text{ }^{\circ}\text{C}$. The failure of the re-characterised defect is correctly predicted at $-196\text{ }^{\circ}\text{C}$ after employing size and shape corrections. Failure of the complex defect (S11) at $-196\text{ }^{\circ}\text{C}$ coincides with the FAC due to an increase in K_{mat} resulting from size and shape corrections. To ensure conservatism, it is recommended that the lower of either, the size and shape corrected or the deterministically measured toughness, should be used in the assessment.

6. Failure initiation site

In analysing failures from complex defects it is relevant to identify the failure initiation site. The deterministic approach in this problem compares the crack driving force and the constraint enhanced toughness. A probabilistic approach identifies the site of the maximum probability density function as the most likely site from which failure initiates.

Both, deterministic and probabilistic approaches show that configurations with pronounced re-entrant sectors fail from re-entrant sectors at a small fraction of the limit load. This is shown by the distinct peak in K_r , shown in Fig. 2(d) for test (S11) and by the modal value of the probability density function in Fig. 8(b). Close to the limit load (S6 at $-100\text{ }^{\circ}\text{C}$) constraint effects shift the origin of failure from the re-entrant sector towards deeper crack segments, as shown by the low values of K_r in the re-entrant sector (Fig. 2(e)) and by the change in pdf (Fig. 8(c)). The failure site is located close to the re-entrant sector, where there is a modest amplification of the stress intensity factor, but no loss of constraint to enhance the local toughness.

It is relevant to compare the probability of failure from the short re-entrant sector with the probability of failure from the remaining crack front (Fig. 3). The contribution to the failure probability from the short re-entrant sector is approximately equal to the contribution from the rest of the crack front at $-196\text{ }^{\circ}\text{C}$. Although the re-entrant sector is the single most likely failure initiation site, failure has nearly the same probability of initiating from the rest of the crack front due to its greater length. At $-100\text{ }^{\circ}\text{C}$ constraint effects clearly favour initiation outside the re-entrant sector (Fig. 3(c)).

Whether the complex defect fails from the re-entrant sector or the deeper parts of the crack is determined by the constraint loss in the re-entrant sector. The argument may be developed to quantify the constraint loss necessary to make the re-characterised defect more detrimental than the complex defect. The deeper crack front locations are fully constrained and failure is governed by the general failure assessment curve. Failure from shallow re-entrant sectors is governed by modified failure assessment curves, which depend on the constraint sensitivity of the fracture toughness [17,18]. In order to compare failure at two sites using a single FAD, sites are compared at the same load. This can be achieved by using the elastic-plastic stress intensity factor of the re-characterised defect, K_D , as the loading parameter in the ordinate of the FAD. In the re-entrant sector the enhanced stress intensity causes failure at K_D/K_{mat} less than unity at low loads. However constraint enhanced toughness in the re-entrant sector elevates the FAC above the general curve as the limit load is approached. The modified and general FAC intersect, as shown in Fig. 9, defining the transition of failure from the re-entrant sector to the deeper sites of a complex defect or to the re-characterised defect (Fig. 9). The constraint effects in the re-entrant sector may be estimated using Eq. (4), through the amplification of the stress intensity factor in the re-entrant sector, which may be assessed from a detailed finite element analysis or from the approximate procedure described in Appendix A. The FAD

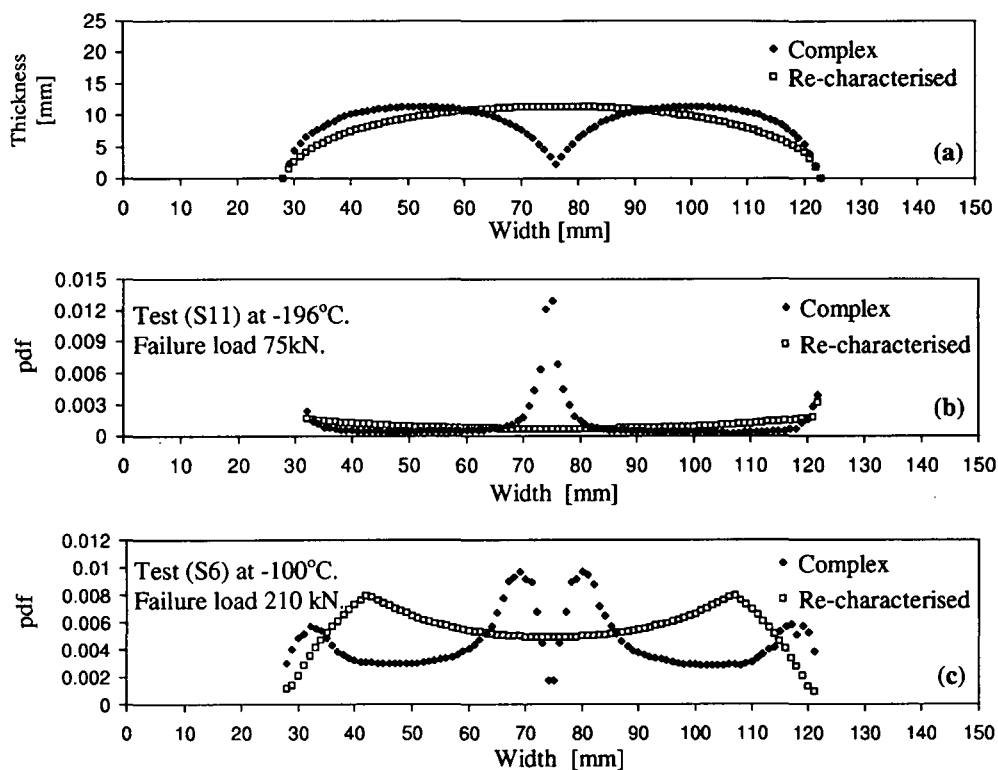


Fig. 8. Probability density function (pdf) for complex defects (S11) at -196°C and (S6) at -100°C and the re-characterised defects, at measured failure loads on complex defects.

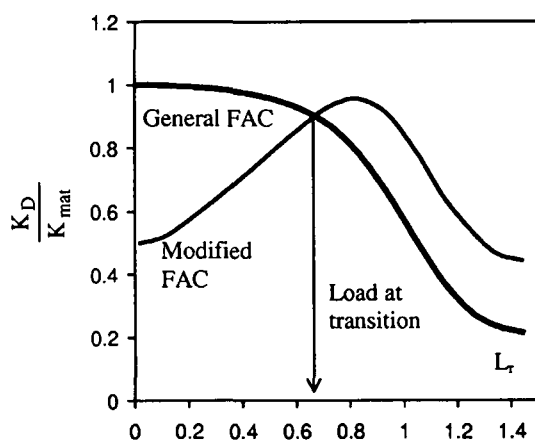


Fig. 9. The transition of failure from a complex defect to a re-characterised defect determined using a modified FAD. The transition is governed by the constraint effects in the re-entrant sectors.

shown in Fig. 9 thus expresses the lack of conservatism of the re-characterisation procedure at $L_r < 0.67$, while conservatism is recovered due to the loss of constraint at $L_r > 0.67$.

7. Discussion

On the lower shelf complex defects exhibited lower failure loads than the predicted failure loads for the re-characterised defects. However at $-100\text{ }^{\circ}\text{C}$ the failure loads of the complex defects were greater than the re-characterised defects due to constraint enhanced toughness. For failures at loads very much less than the global limit load (S11 and S12) on the lower shelf, the loss of crack tip constraint is negligible and insufficient to compensate for the amplified crack driving forces which develop in pronounced re-entrant sectors. In this case failure is governed by the applied crack driving force alone and failure initiates from the re-entrant sector. On the lower shelf, the re-characterisation procedure has been demonstrated to be non-conservative as exemplified by the FAD in Fig. 4. Conservatism is recovered when constraint effects can be invoked to compensate for the amplified crack driving forces at failures close to the limit load, shown by test (S6) at $-100\text{ }^{\circ}\text{C}$ and by the FAD in Fig. 6. Conservatism of re-characterisation procedure can also be recovered by employing statistical size and shape correction to fracture toughness (Fig. 7(a)). Both corrections may be applied concurrently.

Statistical size and shape corrections to the fracture toughness measured on standard test specimens should be employed in assessing cleavage failure. Size and shape effects can be quantified through an effective crack front length parameter, ζ , which allows the fracture resistance to be size and shape corrected. Corrections may result either in increase or decrease in the toughness, K_{mat} , as measured on standard straight crack specimens. Physically this depends on whether the resistance to crack propagation is governed by large sections of the crack front or small sections with high stress intensity factors. It is recommended that a decrease in K_{mat} associated with an increase in the effective crack length parameter, ζ , should always be used. However an increase in K_{mat} due to a decrease in the effective length parameter, ζ , should be taken with caution. The recommendation is that size and shape corrections should only be used if they results in decrease in K_{mat} , to ensure a conservative assessment procedures.

Re-characterisation rules for adjacent but separate defects applied to cleavage failure must allow sufficient safety margins to account for the statistical nature of cleavage. In the present work a test was performed on a configuration containing two separate co-planar defects, with separation of adjacent crack

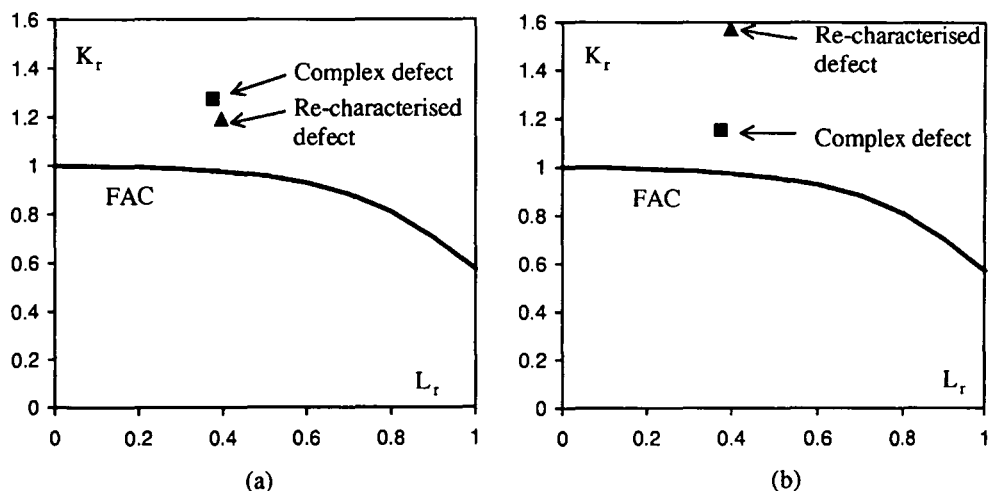


Fig. 10. Assessment of a complex defect (S10) tested at $-196\text{ }^{\circ}\text{C}$ and the re-characterised defect using FAD. In (a) the elastic-plastic stress intensity factor is normalised with lower bound toughness from standard 25 mm thick specimen and in (b) with size and shape corrected toughness. The load is normalised with the local limit load.

tips equal to the crack depth, (specimen S10 in Fig. 1) tested at $-196\text{ }^{\circ}\text{C}$. A small difference between the measured failure load of 103 kN and the failure load for the hypothetical re-characterised defect of 100 kN was noted (Table 1). In configuration (S10) the crack tips had not met, and according to BS 7910 [19] and R6/4 [16] the defects should be treated separately and independently. Fig. 10 shows assessment of the configuration as individual defects and as a re-characterised defect in the FAD using both, measured and statistical size and shape corrected fracture toughness. In both cases the defect configuration falls close to failure assessment curve. In cases where the separation of the crack tips is greater than depth of the larger defect, $s > d$, small interaction effects are present and assessment of individual defects is more realistic. As the crack tips approach, $s < d$, interaction becomes significant and must be included in the assessment. The re-characterisation procedures are non-conservative for $s < d$ and it is recommended that the procedures should only be applied for defects which are more widely separated ($s > d$).

8. Conclusions

Defect re-characterisation has been addressed in the context of statistical and constraint based fracture mechanics. A numerical and experimental study investigated the interaction of two co-planar surface breaking defects and the failures from defects with re-entrant sectors.

Complex defects with a re-entrant sectors exhibit high local stress intensity factors. An experimental programme examined cleavage failures from such defects and demonstrated that the re-characterisation procedure is not conservative when failure occurs at small fractions of the limit load. The observation is reconfirmed with both, deterministic and a probabilistic analyses, in which the re-characterised defect is found to be less detrimental than the complex defect. Failures close to the limit load benefit from constraint loss which counteract the amplified crack driving forces in re-entrant sectors and cause re-characterised defects to be more detrimental than the original complex defects. In such cases re-characterisation is conservative, as shown by the deterministic and a probabilistic analyses. Benefit may be taken from statistical size effects, which are strongly dependent on the crack geometry. It is recommended that statistical size and shape corrections should be used only when they result in a reduction in the critical value of size and shape corrected stress intensity.

Re-characterisation procedures, such as those given in BS 7910 and R6/4, are conservative for fatigue and ductile tearing, since in both failure modes the crack advances from the re-entrant sector towards the re-characterised shape (see Part I). The re-characterisation procedure for defects with re-entrant sectors which fail in cleavage is non-conservative for failures at small fractions of the limit loads. At such low loads there is no benefit from constraint loss, but statistical size and shape corrections may recover the conservatism of the assessment.

It is proposed that two levels of assessment should be used to ensure safety margin against cleavage for complex defects with re-entrant sectors:

- (1) Assess the constraint effects in the re-entrant sector of a complex defect for the design load. If the constraint effects are sufficient to counteract the amplified values of crack driving force in the re-entrant sector, the re-characterisation procedure (BS 7910, R6/4) is conservative.
- (2) Re-characterise the complex defect following guidelines of defect assessment codes using statistical size and shape corrections for the re-characterised defect.

Re-characterisation of separate interacting defects must take account of interaction effects which elevate the stress intensity factors of adjacent crack tips. The present data indicates that the re-characterisation procedure is conservatively applied to such defects only when the tip separation is greater than the depth of the deeper defect.

Acknowledgements

The authors are pleased to acknowledge support of British Energy Generation Limited and helpful discussion with Dr. R.A. Ainsworth. The access to ABAQUS under academic licence at University of Glasgow is gratefully acknowledged to Hibbitt, Carlsson and Sorensen. B. Bezensek wishes to thank the Ministry of Science, Sport and Education of Slovenia for financial support and the Faculty of Mechanical Engineering, University of Maribor, Slovenia, for granting leave of absence to complete the work in the University of Glasgow.

Appendix A. Approximate amplification factors

Simple geometry based amplification factors for the crack driving force and constraint effects in the re-entrant sector of complex defects are defined. The crack with a re-entrant sector is re-characterised and the crack driving force is determined for the deepest position of the re-characterised defect. The amplification of crack driving force in the re-entrant sector is determined by multiplying this solution by an amplification factor, χ_K . The crack with a re-entrant sector is characterised with a length on the free surface, A, the depth of the re-entrant sector, B, and the width of the re-entrant sector, C, as shown in Fig. 11. The tip of the re-entrant sector is approximated by a 60° circular arc to define the local curvature in the re-entrant sector, $\rho = 1/r$. The amplification factor χ_K is:

$$\begin{aligned} \chi_K &= \left[\rho \frac{A \cdot B}{C} \right]^\zeta & \text{for } r \ll A \\ \chi_K &= \left[\rho \frac{A \cdot B}{C} \right]^{-\zeta} & \text{for } r \approx A \text{ and } B > 1 \text{ unit} \end{aligned} \tag{A.1}$$

from fitting the exponent of Eq. (A.1) with the detailed line spring data. The evaluation of the approximate procedure with the detailed line spring calculations gives conservative assessments when the exponent ζ is 1/10.

A similar procedure is defined for assessing amplification for constraint effects in the re-entrant sector. The amplification factor for the T -stress is defined using the above described approximation to the complex geometry and is used in conjunction with the T -stress solutions of standard edge crack bar in bending (SENB) [20]. The exponent, ζ , of 1/8 gives a good agreement with the detailed line spring computations:

$$\begin{aligned} \frac{T}{\sigma_0} \Big|_{\text{re-entrant}} &= \chi_T \cdot \frac{T}{\sigma_0} \Big|_{\text{SENB}} \\ \chi_T &= \left[\rho \frac{A \cdot B}{C} \right]^\zeta \end{aligned} \tag{A.2}$$

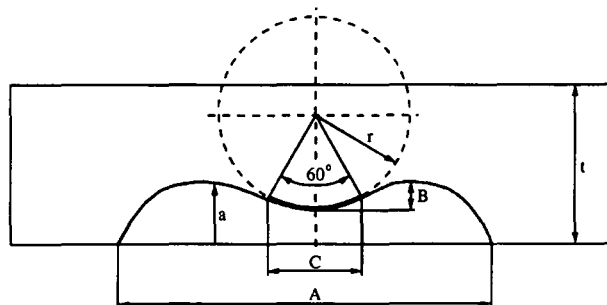


Fig. 11. The definition of complex geometry as used in defining the approximate amplification factors.

References

- [1] ASTM E1921. Standard method for determination of reference temperature T_0 for ferritic steels in the transition range. American Society for Testing and Materials, Philadelphia, 1997.
- [2] MacLennan IJ. Two parameter engineering fracture mechanics. PhD Thesis, University of Glasgow, UK, 1996.
- [3] Bennet PE, Sinclair GM. Parameter representation of low-temperature yield behaviour of body centered cubic transition metals. *J Basic Engng Trans ASME* 1966;88:518-24.
- [4] Lidbury DPG. Effects of specimen size on the fracture toughness transition properties of a Seizwell B specific A508 Class 3 steel forging and comparison with the additional RPV materials. AEA Technology Report No. PWR/RDMC/MWG/P(89)248M. Risley, UK, 1990.
- [5] Betegón C, Hancock JW. Two-parameter characterisation of elastic-plastic crack-tip fields. *J Appl Mech Trans ASME* 1991;58:104-10.
- [6] Wallin K. T -stress based correction for the Master Curve transition temperature T_0 . In: Proc ASME PVP2000, PVP, vol. 412. Seattle, USA, 2000.
- [7] Rice JR, Levy N. The part-through surface crack in an elastic plate. *J Appl Mech Trans ASME* 1972;39(1):185-94.
- [8] Parks DM, White CS. Elastic-plastic line-spring finite elements for surface cracked plates and shells. *J Pres Ves Technol Trans ASME* 1982;104:287-92.
- [9] Freudenthal AM. Statistical approach to brittle fracture. In: Liebowitz H, editor. Fracture: an advanced treatise, vol. 2. New York: Academic Press; 1968. p. 591-619.
- [10] Beremin FM. A local criterion for cleavage fracture of nuclear pressure vessel steel. *Metal Trans A* 1983;14:2277-87.
- [11] Wallin K. The scatter in K_{IC} results. *Engng Fract Mech* 1984;19:1085.
- [12] Landes JD, Shaffer DH. In: Fracture mechanics: twelfth conference, ASTM STP 700, 1980.
- [13] Ritchie RO, Knott JF, Rice JR. On the relationship between critical tensile stress and fracture toughness in mild steel. *J Mech Phys Solids* 1973;21:395.
- [14] Slatcher S, Oystein E. Practical application of the weakest-link model to fracture toughness problems. *Engng Fract Mech* 1986;24(4):495.
- [15] Newman JC, Raju IS. An empirical stress-intensity factor equation for the surface crack. *Engng Fract Mech* 1981;15:185-92.
- [16] R6. Assessment of the integrity of structures containing defects, Revision 4. British Energy Generation Ltd., Gloucester, 2001.
- [17] Ainsworth RA, O'Dowd NP. Constraint in the failure assessment diagram approach for fracture assessment. *Int J Pres Ves Pip* 1995;117:260-7.
- [18] MacLennan IJ, Hancock JW. Constraint-based failure assessment diagrams. *Proc R Soc London A* 1995;451:757-77.
- [19] BS 7910. Guidance on methods for assessing the acceptability of flaws in metallic structures. British Standard Institution, London, UK, 1999.
- [20] Sham TL. The determination of the elastic T -term using higher order weigh functions. *Int J Fract* 1991;48:81-102.

